# The University of Sheffield




# Global Optimisation and Manufacturing Tolerance Investigation of Surface-mounted and Interior Permanent Magnet Motors for Power Steering Application

**Karl Buhagiar**

A thesis submitted for the degree of Doctor of Philosophy
Department of Electronic and Electrical Engineering
The University of Sheffield, UK

March 2021

# ABSTRACT

Cogging torque in Permanent Magnet (PM) motors, as a kind of torque ripple produced by the interaction between the rotor PM field and the stator slots, is critical in Electrical Power Steering (EPS) applications. Manufacturing tolerances in mass-production process result in deviations in stator and rotor geometries that, in turn, affect cogging torque. This thesis investigates the influence of manufacturing tolerances on the cogging torque, identifies the worst-case scenarios of manufacturing tolerances, and quantifies the uncertainty of cogging torque due to manufacturing tolerances, in 12-slot/8-pole, 12-slot/10-pole, and 12-slot/14-pole Surface-mounted PM (SPM) and Interior PM (IPM) motors for EPS applications.

Throughout the thesis, two-dimensional Finite Element Analysis (FEA) is used for analysis and an existing EPS 12-slot/8-pole IPM motor is used as a baseline. Three-dimensional effects in PM motors are non-negligible, however, two-dimensional FEA is adopted to compromise between model accuracy and computational effort. The Genetic Algorithm (GA) is used to optimise the motors under investigation with a set of constraints. Single-objective optimisation is only used initially to identify the maximum average torque and multi-objective optimisation is used to finalise the optimal designs with a compromise between average torque and torque ripple. The optimally designed SPM and IPM motors with three slot and pole number combinations are subsequently used for investigating cogging torque sensitivity to both stator and rotor manufacturing tolerances. Then the worst-case scenarios are identified using a global search algorithm combined with a simplified motor model based on a series of FEA simulations. Finally, cogging torque uncertainty is quantified using a Monte-Carlo simulation with a sample size of 100 motors using various statistical distributions to fit the number of occurrences of the amplitudes and harmonics of cogging torque and thereby quantify the skewness and dispersion of the distributions.

The Pareto-fronts of multi-objective optimisation of the IPM and SPM motors show that the SPM motors allow for a better compromise between average torque and torque ripple at the optimised operating point. Thus, even with a larger air-gap for accommodating the retaining of PMs, SPM motors can produce lower torque ripple and higher average torque than IPM motors with the same slot and pole number combination. The discrepancy between the Pareto-fronts of the IPM and SPM motors increases with increasing rotor pole number.

Cogging torque is composed of native harmonic components (NHCs) inherent to the motor topologies and additional harmonic components (AHCs) due to manufacturing tolerances. Stator and rotor tolerances result in fundamental cogging torque AHCs with an order equal to the rotor pole number and stator slot number, respectively. The directions and locations of stator and rotor tolerances resulting in the cogging torque worst-case scenario are identified. Cogging torque of both IPM and SPM motors is most sensitive to tolerances in stator tooth radial position, slot opening, rotor pole-shoe height and PM height, but varies with the slot and pole number combinations and rotor topologies.

It has been found that with increasing rotor pole number, (a) the worst-case cogging torque due to combined stator and rotor tolerances of IPM motors decreases, but it the opposite is true for SPM motors; (b) the uncertainty of the peak-to-peak cogging torque due to stator tolerances decreases, but that due to rotor tolerances increases significantly; (c) the skewness of the distribution of the peak-to-peak cogging torque due to the increase of combined stator and rotor tolerances in SPM motors; (d) the dispersion of the distributions of the IPM motors decreases but those of the SPM motors increases.. It has also been found that the uncertainty of the native cogging torque components of 12-slot/10-pole and 12-slot/14-pole motors due to tolerances is very low, but that of 12-slot/8-pole motors is non-negligible.

# ACKNOWLEDGEMENTS

Firstly, I would like to extend my deepest gratitude to my academic supervisor, Prof. Zi-Qiang Zhu, for his continuous support, encouragement, invaluable advice, and patience during my studies. I would also like to thank my industry supervisor from ZF-TRW, Dr. David Moule, for his guidance and advice with regards to my studies and career development.

I thank ZF-TRW for the financial support to my PhD study.

It has been a great pleasure to be a part of the Electrical Machines and Drives Research Group at the University of Sheffield. The assistance, collaboration, and technical discussions with fellow colleagues over the years have been insightful and inspiring.

My sincere thanks go to Dr. Nicholas Sammut for being my mentor during my undergraduate studies and encouraging me to pursue further studies abroad.

On a personal note, I consider myself lucky that during my tertiary education, spanning four countries, I have crossed paths with many friends from all over the globe, gained invaluable experiences and deep friendships. Special thanks go to Răzvan, Büşra, Özgün, Vimanyu, Cindy, and Ezra who have supported me throughout the highs and lows of my doctoral journey.

# CONTENTS

**ABSTRACT** ..... ii

**ACKNOWLEDGEMENTS** ..... iv

**LIST OF SYMBOLS** ..... xi

**LIST OF ABBREVIATIONS** ..... xiii

1 GENERAL INTRODUCTION ..... 1

1.1 Introduction ..... 1

1.2 Power Steering Systems ..... 1

1.2.1 Hydraulic Power Steering ..... 1

1.2.2 Electrohydraulic Power Steering ..... 3

1.2.3 Electric Power Steering ..... 4

1.3 Permanent Magnet Machines ..... 7

1.3.1 BLDC and BLAC Machines ..... 7

1.3.2 Stator Winding Topologies ..... 8

1.3.3 Rotor Topologies ..... 9

1.3.4 Combinations of Number of Slots and Number of Poles ..... 12

1.4 Torque Pulsation in Permanent Magnet Machines ..... 12

1.5 Design Optimisation Methods ..... 14

1.6 Design Optimisation of PM Motors for EPS Applications ..... 17

1.7 Manufacturing Tolerances ..... 21

1.8 Scope and Contributions of Thesis ..... 25

2 ANALYSIS OF ELECTROMAGNETIC PERFORMANCE OF BASELINE IPM MOTOR ..... 27

2.1 Introduction ..... 27

2.2 Analysis of Electromagnetic Performance ..... 30

2.3 Influence of Design Parameters on Motor Torque ..... 34

2.4 Influence of Load and Current Angle on Motor Torque ..... 38

2.5 Comparison with Experimental Results ..... 41

2.6 Conclusion ..... 42

**3 SINGLE- AND MULTI-OBJECTIVE OPTIMISATION OF IPM MOTORS** ..... 44
3.1 Introduction ..... 44
3.2 Single-objective Optimisation of IPM Motors ..... 46
3.2.1 Optimisation of 12-slot/8-pole IPM Motor ..... 46
3.2.2 Analysis of Optimised 12-slot/10-pole IPM Motor ..... 49
3.2.3 Analysis of Optimised 12-slot/14-pole IPM Motor ..... 51
3.3 Multi-objective Optimisation of IPM motors ..... 53
3.3.1 Optimisation of 12-slot/8-pole IPM Motor ..... 53
3.3.2 Optimisation of 12-slot/10-pole IPM Motor ..... 56
3.3.3 Optimisation of 12-slot/14-pole IPM Motor ..... 58
3.4 Comparison of Single-objective and Multi-objective Optimisation ..... 60
3.5 Comparison of Optimised 12-slot/8-pole IPM Motor with Baseline IPM Motor ..... 63
3.6 Conclusion ..... 68
**4 SINGLE- AND MULTI-OBJECTIVE OPTIMISATION OF SPM MOTORS** ..... 70
4.1 Introduction ..... 70
4.2 Single-objective Optimisation of SPM Motors ..... 71
4.2.1 Analysis of Optimised 12-slot/8-pole SPM Motor ..... 71
4.2.2 Analysis of Optimised 12-slot/10-pole SPM Motor ..... 73
4.2.3 Analysis of Optimised 12-slot/14-pole SPM Motor ..... 75
4.3 Multi-objective Optimisation of SPM Motors ..... 77
4.3.1 Optimisation of 12-slot/8-pole SPM Motor ..... 77
4.3.2 Optimisation of 12-slot/10-pole SPM motor ..... 79
4.3.3 Optimisation of 12-slot/14-pole SPM motor ..... 81
4.4 Comparison of Single-Objective and Multi-Objective Optimisation of SPM Motors ..... 84
4.5 Comparison of Single-Objective and Multi-Objective Optimisation of IPM and SPM Motors 88
4.6 Conclusion ..... 91
5 ANALYSIS OF COGGING TORQUE SENSITIVITY TO MANUFACTURING TOLERANCES IN IPM AND SPM MOTORS ..... 94
5.1 Introduction ..... 94

5.2 Motors under Investigation ..... 95
5.3 Manufacturing Tolerances under Investigation ..... 98
5.4 Analysis of Cogging Torque Sensitivity to Stator Tolerances in IPM Motors ..... 101
5.4.1 Analysis of Cogging Torque Sensitivity of 12-slot/8-pole IPM motor ..... 101
5.4.2 Analysis of Cogging Torque Sensitivity of 12-slot/10-pole IPM motor ..... 104
5.4.3 Analysis of Cogging Torque Sensitivity of 12-slot/14-pole IPM motor ..... 106
5.4.4 Comparison of Cogging Torque Sensitivity of IPM Motors ..... 109
5.5 Analysis of Cogging Torque Sensitivity to Stator Tolerances in SPM Motors ..... 111
5.5.1 Analysis of Cogging Torque Sensitivity of 12-slot/8-pole SPM motor ..... 111
5.5.2 Analysis of Cogging Torque Sensitivity of 12-slot/10-pole SPM motor ..... 113
5.5.3 Analysis of Cogging Torque Sensitivity of 12-slot/14-pole SPM motor ..... 116
5.5.4 Comparison of Cogging Torque Sensitivity of SPM Motors ..... 119
5.6 Analysis of Cogging Torque Sensitivity to Rotor Tolerances in IPM Motors ..... 122
5.7 Analysis of Cogging Torque Sensitivity to Rotor Manufacturing Tolerances in SPM Motors 128
5.8 Comparison of Cogging Torque Sensitivity of IPM and SPM Motors to Stator Tolerances ... 134
5.9 Comparison of Cogging Torque Sensitivity of IPM and SPM Motors to Rotor Tolerances ... 138
5.10 Comparison with Experimental Results ..... 142
5.11 Conclusion ..... 145
6 INVESTIGATION OF WORST SCENARIOS OF COGGING TORQUE IN IPM AND SPM MOTORS DUE TO MANUFACTURING TOLERANCES ..... 148
6.1 Introduction ..... 148
6.2 Determination of Worst-Case Scenarios of the Cogging Torque Due to Tolerances in the Radial Position of the Stator Teeth Profile of IPM and SPM motors ..... 149
6.2.1 Worst-Case Scenarios of Cogging Torque of 12-slot/8-pole IPM Motor ..... 151
6.2.2 Worst-Case Scenarios of Cogging Torque of 12-slot/10-pole IPM Motor ..... 156
6.2.3 Worst-Case Scenarios of Cogging Torque of 12-slot/14-pole IPM Motor ..... 163
6.2.4 Comparison of Worst-Case Scenarios of Cogging Torque of IPM Motors with Different Slot/Pole Number Combinations ..... 170
6.2.5 Comparison of Worst-Case Scenarios of Cogging Torque of IPM and SPM Motors ..... 172
6.3 Investigation of Worst-Case Scenarios Due to Stator Tolerances in IPM motors ..... 175

6.4 Investigation of Worst-Case Scenarios Due to Stator Tolerances in SPM motors ..... 178
6.5 Comparison of Cogging Torque Worst-Case Scenarios Due to Stator Tolerances only in IPM and SPM motors ..... 181
6.6 Investigation of Worst-Case Scenario of Cogging Torque Due to Rotor Tolerances in IPM motors 183
6.6.1 Worst-Case Scenarios of Cogging Torque of 12-slot/8-pole IPM Motor ..... 183
6.6.2 Worst-Case Scenarios of Cogging Torque of 12-slot/10-pole IPM Motor ..... 185
6.6.3 Worst-Case Scenarios of Cogging Torque of 12-slot/14-pole IPM Motor ..... 186
6.7 Investigation of Worst-Case Scenario of Cogging Torque Due to Rotor Tolerances in SPM motors 188
6.7.1 Worst-Case Scenarios of Cogging Torque of 12-slot/8-pole SPM Motor ..... 188
6.7.2 Worst-Case Scenarios of Cogging Torque of 12-slot/10-pole SPM Motor ..... 190
6.7.3 Worst-Case Scenarios of Cogging Torque of 12-slot/14-pole SPM Motor ..... 191
6.8 Comparison of Cogging Torque Worst-Case Scenarios Due to Rotor Tolerances only in IPM and SPM motors ..... 193
6.9 Investigation of Worst-Case Scenario of Cogging Torque Due to Combined Stator and Rotor Tolerances in IPM motors ..... 195
6.9.1 Worst-Case Scenarios of Cogging Torque of 12-slot/8-pole IPM Motor ..... 195
6.9.2 Worst-Case Scenarios of Cogging Torque of 12-slot/10-pole IPM Motor ..... 198
6.9.3 Worst-Case Scenarios of Cogging Torque of 12-slot/14-pole IPM Motor ..... 200
6.10 Investigation of Worst-Case Scenario of Cogging Torque Due to Combined Stator and Rotor Tolerances in SPM motors ..... 202
6.10.1 Worst-Case Scenarios of Cogging Torque of 12-slot/8-pole SPM Motor ..... 202
6.10.2 Worst-Case Scenarios of Cogging Torque of 12-slot/10-pole SPM Motor ..... 205
6.10.3 Worst-Case Scenarios of Cogging Torque of 12-slot/14-pole SPM Motor ..... 208
6.11 Comparison of Cogging Torque Worst-Case Scenarios Due to Combined Stator and Rotor Tolerances in IPM and SPM motors ..... 211
6.12 Conclusion ..... 212
7 UNCERTAINTY ANALYSIS OF COGGING TORQUE IN IPM AND SPM MOTORS DUE TO MANUFACTURING TOLERANCES ..... 214
7.1 Introduction ..... 214

7.2 Uncertainty Analysis of Cogging Torque in IPM and SPM Motors due to Stator Tolerances 217

7.3 Uncertainty Analysis of Cogging Torque of IPM and SPM Motors due to Rotor Tolerances 222

7.4 Uncertainty Analysis of Cogging Torque of IPM and SPM Motors due to Stator and Rotor Tolerances ..... 226

7.5 Conclusion ..... 233

8 CONCLUSIONS AND DISCUSSION ..... 237

8.1 Motivation and Methodology ..... 237

8.2 Electromagnetic Performance of Baseline IPM Motor ..... 238

8.3 Single-Objective and Multi-Objective Optimisation of IPM and SPM Motors ..... 240

8.4 Cogging Torque Sensitivity to Manufacturing Tolerances in IPM and SPM Motors ..... 241

8.5 Worst Scenarios of Cogging Torque in IPM and SPM Motors ..... 243

8.6 Uncertainty of Cogging Torque Due to Manufacturing Tolerances in IPM and SPM motors 247

8.7 Future Work ..... 248

REFERENCES ..... 251

**APPENDIX A CALCULATION OF THE TORQUE-SPEED CHARACTERISTICS OF PM MOTORS** ..... 261

A.1 Calculation of the Torque-speed Envelope of PM Motors ..... 261

A.2 Calculation of Efficiency Maps and Other Parameter Maps ..... 262

**APPENDIX B DETERMINATION OF WORST-CASE SCENARIOS OF THE COGGING TORQUE DUE TO TOLERANCES IN THE RADIAL POSITION OF THE STATOR TEETH PROFILE OF SPM MOTORS** ..... 264

B.1 Worst-Case Scenarios of Cogging Torque of 12-slot/8-pole SPM Motor ..... 264

B.2 Worst-Case Scenarios of Cogging Torque of 12-slot/10-pole SPM Motor ..... 270

B.3 Worst-Case Scenarios of Cogging Torque of 12-slot/14-pole SPM Motor ..... 278

**APPENDIX C ANALYSIS OF INFLUENCE OF SAMPLE SIZE ON COGGING TORQUE UNCERTAINTY** 286

# LIST OF SYMBOLS

| Symbol | Description | Unit |
|---|---|---|
| $N_s$ | Number of stator slots | |
| $\Psi_d$ | d-axis flux linkage | Wb |
| $\Psi_q$ | q-axis flux linkage | Wb |
| $B_n$ | Radial air-gap flux density component | T |
| $I_d$ | d-axis current | A |
| $I_{max}$ | Maximum current | A |
| $I_q$ | q-axis current | A |
| $L_d$ | d-axis inductance | H |
| $L_q$ | q-axis inductance | H |
| $T_{AHC}$ | Cogging torque due to additional harmonic components | Nm |
| $T_{NHC}$ | Cogging torque due to native harmonic components | Nm |
| $T_{cogging}$ | Cogging torque | Nm |
| $T_{ripple_{absoute}}$ | Absolute torque ripple | Nm |
| $T_{ripple_{relative}}$ | Relative torque ripple | Nm |
| $V_{lim}$ | Voltage limit | V |
| $\delta_{PM\ height}$ | Manufacturing tolerance in permanent magnet height | mm |
| $\delta_{iron\ cavity}$ | Manufacturing tolerance in rotor iron cavity | mm |
| $\delta_{iron}$ | Manufacturing tolerance in rotor iron profile | mm |
| $\delta_{lateral\ position}$ | Manufacturing tolerance in lateral position of permanent magnet | mm |
| $\delta_{radial\ position}$ | Manufacturing tolerance in radial position of permanent magnet | mm |
| $\delta_{sleeve}$ | Manufacturing tolerance in rotor sleeve | mm |
| $\omega_s$ | Mechanical angular frequency | rad/s |
| $\phi_z$ | Phase of $n^{\text{th}}$ order additional harmonic component | ° |

| | | |
|---|---|---|
| N | Fundamental component of cogging torque without tolerances | |
| $p$ | Number of rotor pole pairs | |
| $q$ | Number of slots per pole per phase | |
| $T$ | On-load torque | Nm |
| $n$ | Order of additional harmonic component | |

# LIST OF ABBREVIATIONS

| | |
|---|---|
| AHC | Additional harmonic component |
| BLAC | Brushless alternating current |
| BLDC | Brushless direct current |
| ECU | Electrical Control Unit |
| EMF | Electromotive force |
| EPAS | Electric power-assisted steering |
| EPHS | Electrically-powered hydraulic steering |
| EPS | Electric power steering |
| EPSapa | Axle parallel-type electric power steering |
| EPSc | Column-type electric power steering |
| EPSdp | Dual pinion-type electric power steering |
| EPSp | Pinion-type electric power steering |
| EPSrc | Rack-concentric-type electric power steering |
| FEA | Finite-element analysis |
| FSCW | Fractional-slot-concentrated-winding |
| GCD | Greatest common divisor |
| HPS | Hydraulic power steering |
| IPM | Interior permanent magnet |
| LCM | Least common multiple |
| MMF | Magnetomotive force |
| MPU | Motor pump unit |
| MTPA | Maximum torque per ampere |
| NHC | Native harmonic component |
| PM | Permanent magnet |
| PMSM | Permanent magnet synchronous machines |
| RSM | Response surface methodology |

| | |
|---|---|
| SPM | Surface-mounted permanent magnet |
| THD | Total harmonic distortion |

# 1 GENERAL INTRODUCTION

## 1.1 Introduction

Permanent magnet (PM) synchronous machines (PMSMs) are extensively used in a wide variety of applications due to the attributed potentials in terms of power density, efficiency, and reliability [ZHU14]. Furthermore, PMSMs provide high overload capabilities, wide operating range, and good fault-tolerance capability [ZHU14]. The inherent advantages and capabilities of PMSMs have motivated consideration in domestic, industrial, transportation, military, aerospace, and automotive among other applications [GIE02].

Power steering systems in the automotive industry have evolved over the years and electrical motors are increasingly applied in a wide range of vehicles [HAR17]. The steering system allows the driver to guide the vehicle laterally through rotation of the steering wheel. Power assisted steering is required to reduce the torque which the driver has to apply, thereby allowing for a comfortable driving experience. Disruptive interference from the road surface needs to be filtered from the driver, without suppressing useful feedback [HAR17]. Advances in electrical motors, sensors, power electronics and control systems have allowed for extensive application in power steering systems

## 1.2 Power Steering Systems

Motor vehicles can be steered by the driver through the steering assembly, which is a part of the chassis. All the forces acting between the vehicle body and the road, other than the aerodynamic forces, are transmitted via the chassis [HAR17]. The steering assembly is composed of the steering wheel, steering column, steering gear and tie rods (steering linkage) [HAR17]. It has become common to implement the steering gear as a rack-and-pinion drive. More information about the history of steering systems can be found in [HOL02, HAR17].

Modern steering systems provide a more consistent steering feel at all speeds and reduce the required steering wheel torque in order to steer the vehicle in a particular direction. Such systems are known as power steering systems or power-assisted steering systems. There are three types of power steering systems, i.e. hydraulic power steering, electrohydraulic power steering, and electric power steering.

### 1.2.1 Hydraulic Power Steering

Hydraulic power steering systems comprise a pump, which is driven by the engine through an accessory belt, and therefore operate continuously whenever the engine is running. The most common type of pump used in hydraulic power steering systems is the vane-type pump. However, there are other pumps that could

be applied to hydraulic power steering, such as the radial piston and the tandem pump [HAR17].

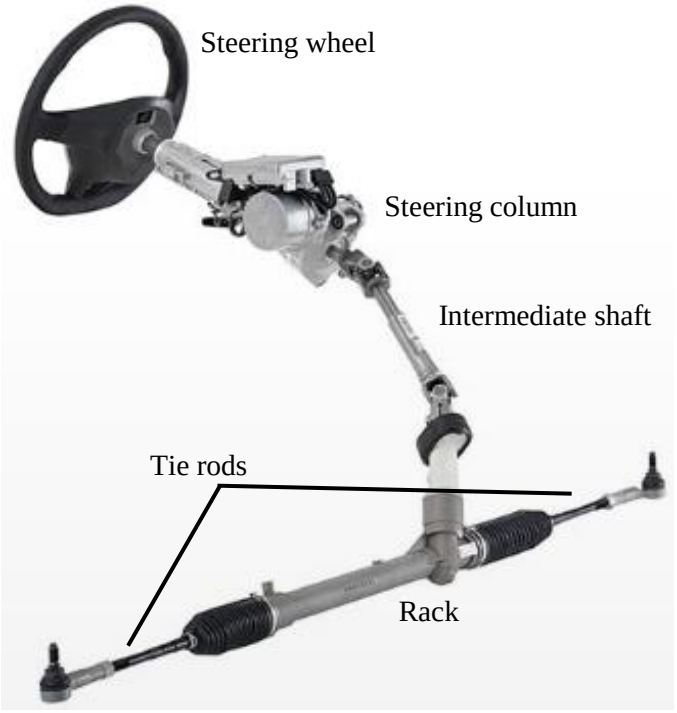



Fig. 1.1. Components of a column-type steering assembly [ZF21].

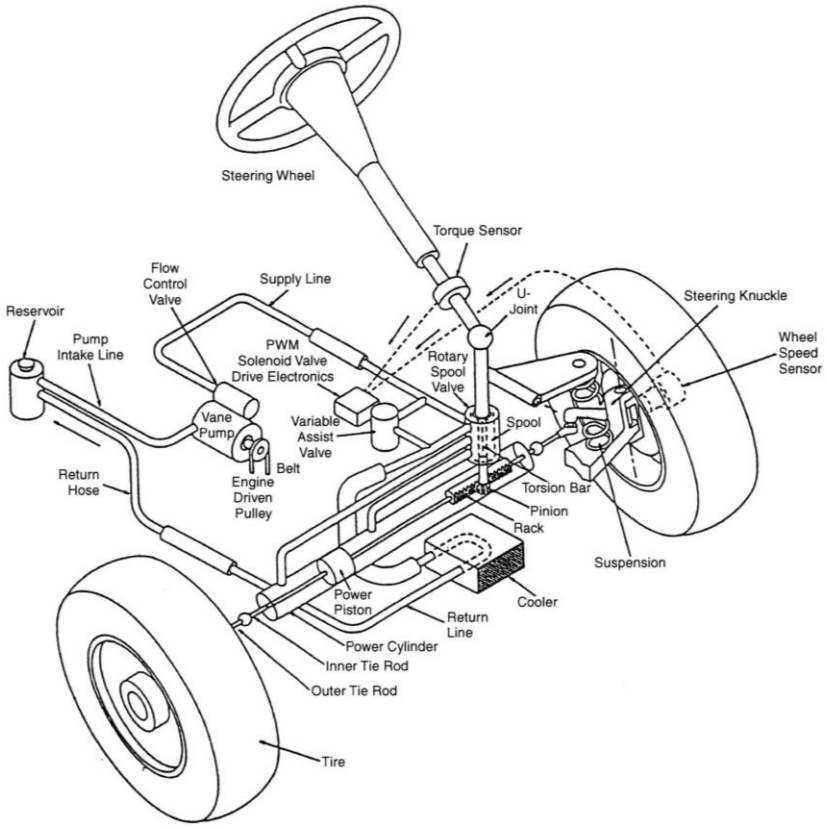
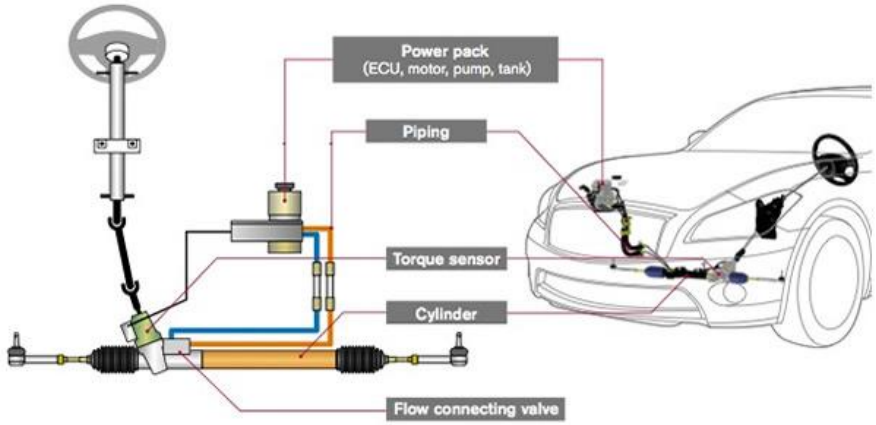



Fig. 1.2. Example of a hydraulic rack and pinion power steering system [HOL02].

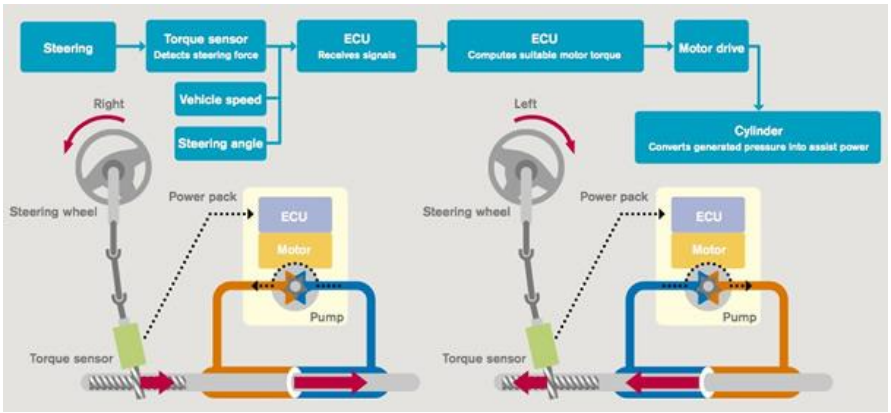
Hydraulically supported steering systems are limited by the fact that a high mechanical steering power is usually required at lower speeds, when the engine is generating a low power. Conversely, the engine generates a high power at high speeds but the steering power required at these speeds is much lower than that required at low speeds. Furthermore, hydraulic power steering systems place a load on the engine and result in higher fuel consumption.

### 1.2.2 Electrohydraulic Power Steering

The Electrically-Powered Hydraulic Steering (EPHS) or Electrohydraulic Power Steering (EHPS) was developed in the early 1990s as a response to the demand of a steering system that can be controlled independently from the engine [HAR17]. The electrohydraulic power steering includes a motor pump unit (MPU) which has a hydraulic part with external gear pump, hydraulic resonator and check/pressure relief valve, as well as an electric motor with an Electrical Control Unit (ECU) [HAR17]. Electrohydraulic power steering systems provide more flexibility in terms of packaging because the hydraulic pump is powered by an electrical motor, rather than by the engine [HOL02].




(a) Configuration of an EHPS system




(b) Operation of an EHPS system

Fig. 1.3. Configuration and operation of an EHPS system [NIS21]

### 1.2.3 Electric Power Steering

Electric Power-Assisted Steering (EPAS), or Electric Power Steering (EPS), generates the power-assist by means of an electric motor whose force is fed into the rack or steering column by a servo gear unit. The electric motor is powered by the on-board wiring and actuated by power electronics integrated into the electric ECU of the EPS. Steering wheel movement results in a rotation of the torsion bar and the required power-assist is computed by the ECU using torsion bar torque measurements. Advances in power density of electric motors permit EPS systems to be installed in vehicles which require higher steering power.

EPS systems are operated only when needed, and therefore, they are also referred to as power-on-demand systems. EPS systems have established themselves due to various advantages including reduced system weight and volume, increased recyclability, reduced impact on the environment due to the avoidance of hydraulic fluid and reduced energy consumption, which in turn leads to better mileage, higher efficiency, and lower emissions [BUR03, GAE17]. Furthermore, EPS may provide additional functionalities for vehicle safety, ride comfort and driver-assist [GAE17].

The types of EPS systems that are used with rack-and-pinion systems are column, pinion, dual-pinion, axle-parallel, and rack-concentric [HOL02, GAE17]. The power-assist performance and the steering rack force for each EPS type are illustrated in Fig. 1.4.

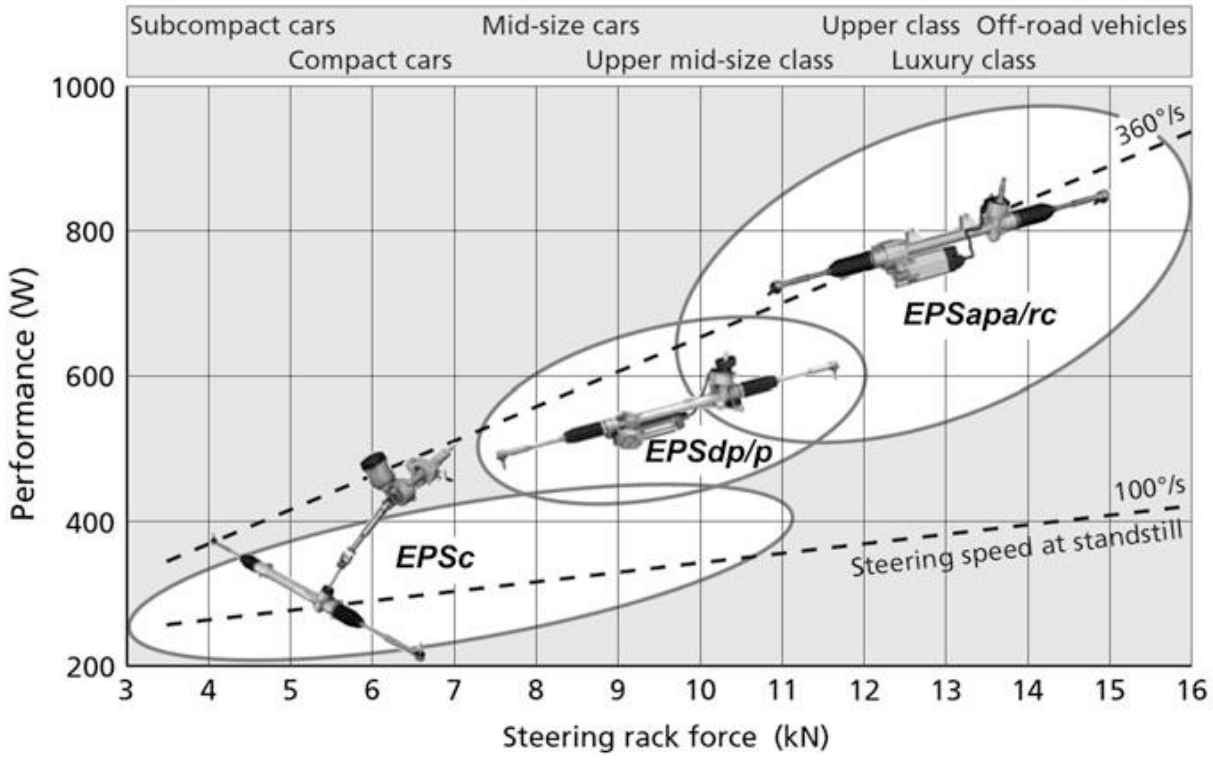



Fig. 1.4. Operation areas of EPS steering systems [GAE17].

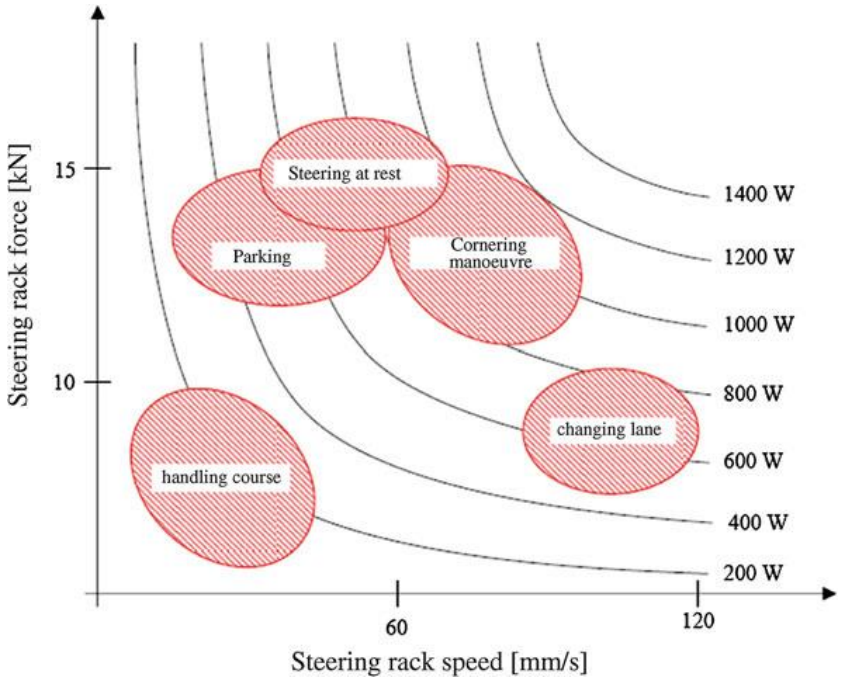



Fig. 1.5. Example of mechanical steering power of an SUV [HAR17].

The column-type EPS (EPSc), shown in Fig. 1.4, is one of the most widely applied EPS systems in small- and middle-size vehicles and can be assembled in a module and be just slightly more intrusive that the column-type steering in a manual steering system. Therefore, the column mount can be mounted under the dash of small vehicles, thereby isolating the electrical motor and control unit from the underhood environmental conditions [HOL02, GAE17]. The location of the column-type EPS leads to stricter temperature requirement and a poor crash response due to the proximity of the power-assist unit to the driver [HOL02, GAE17]. The torques of the power-assist unit are transferred along steering column, intermediate steering shaft and pinion and the limits of each part have to be considered when calculating the highest possible steering force with this EPS type [GAE17].

Fig. 1.6 shows examples of pinion, dual-pinion, axle-parallel, and rack-concentric EPS systems. The power-assist unit of the pinion-type EPS (EPSp) is mounted at the gearbox, right at the point where the steering pinion is in contact with the rack. The system can generate a higher steering force due to the isolation of the power-assist unit from the steering column and intermediate steering shaft.

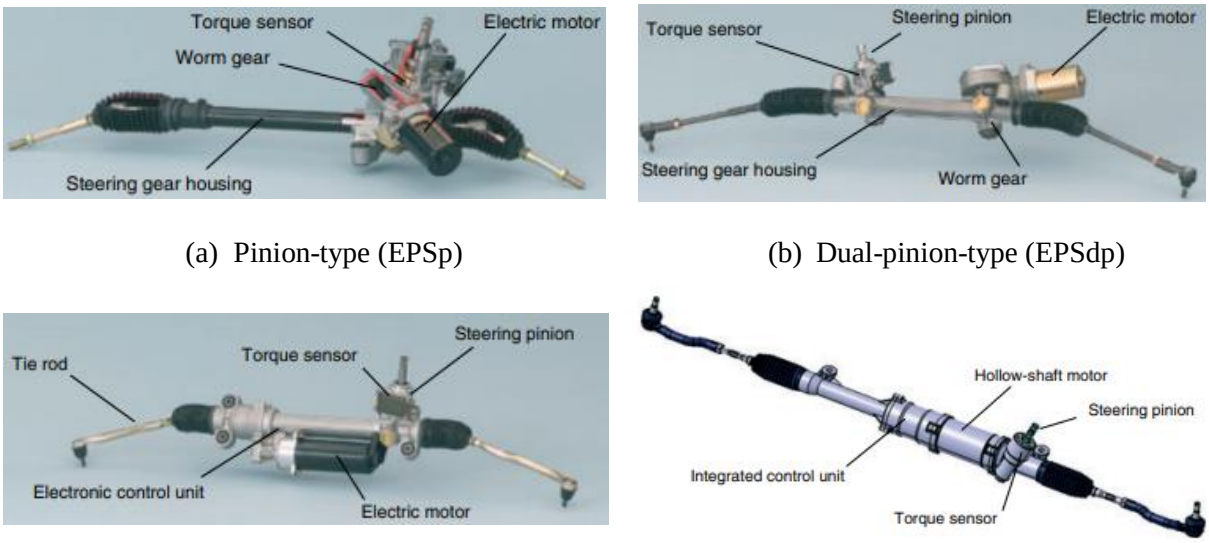
The dual-pinion-type EPS (EPSdp) is applied in medium and upper middle class vehicles. The power-assist unit is mounted at a second pinion and can be positioned by a worm gear, thereby providing adaptability to difficult installation spaces and improved crash response given careful placement of the EPS system [GAE17].

Axle-parallel-type EPS (EPSapa) is applied in dynamic sports cars, upper middle class cars, and high load vehicles. The force generated by the electrical motor is transferred through the rack by a combination of a ball screw and a timing belt gearbox [GAE17].

Rack-concentric-type EPS (EPSrc) is applied in vehicles with larger rack loads. The steering rack passes through the electrical motor leading to a compact system, but requiring the motor to have a hollow shaft. Rack-concentric-type EPS systems do not include a gearbox as the axle-parallel-type and therefore the electrical motor is required to generate a higher torque, possibly requiring a larger motor [GAE17].

Dual-pinion, axle-parallel, and rack-concentric type EPS systems require that the power-assist unit is placed closer to the engine, and therefore, the power-assist unit must be designed to meet higher requirements in terms of vibrations, temperatures, and other environmental conditions.

The EPS systems discussed in this section feature a mechanical connection between the steering wheel and the tyres, which means that the driver has direct mechanical access even after EPS system failure. Steer-by-wire systems measure the steering input and electronically control a mechanical system that is mechanically isolated from the steering wheel, as discussed in [BEN05, BIA06]. Steer-by-wire systems have the advantages of flexibility in space utilisation, avoidance of steering shafts, and avoidance of standardisation of left-hand or right-hand drive systems. On the other hand, steer-by-wire systems require very careful considerations to meet the safety requirements of EPS applications.




(a) Pinion-type (EPSp) (b) Dual-pinion-type (EPSdp)

(c) Axle-parallel-type (EPSapa) (d) Rack-concentric-type (EPSrc)

Fig. 1.6. Types of EPS systems [WUE13], [HAR17].

## 1.3 Permanent Magnet Machines

### 1.3.1 BLDC and BLAC Machines

A PM machine is generally designed as either trapezoidal back-EMF or sinusoidal back-EMF machine [HEN94]. The corresponding control strategies are commonly referred to as brushless direct current (BLDC) or alternating current (BLAC) [JAH83].

Ideally, a trapezoidal back-EMF machine should be operated in BLDC mode and a sinusoidal back-EMF machine should be operated in BLAC mode. In practice, back-EMF waveforms may depart significantly from the ideal and the machines may operate in both BLDC and BLAC modes, at the cost of compromising efficiency and torque ripple capability [ZHU14].

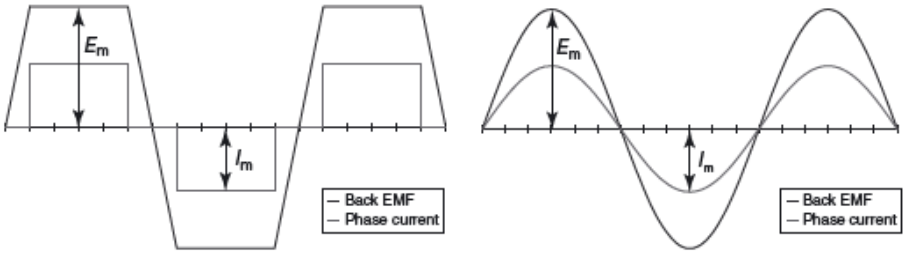



Fig. 1.7. Ideal back-EMF waveforms and phase currents for PM machines [ZHU14].

Control of BLDC and BLAC drives requires rotor position information acquired via position sensors. BLAC drives require high precision, and consequently higher costs sensors compared to BLDC drives. This has motivated research into sensorless control techniques that have been developed for both types of electrical machine drives [ZHU14]. Control of BLAC machines is facilitated by vector control theory in which the current and voltage waveform can be transformed into d- and q- axis components and vice-versa. On the other hand, on-line control of BLDC machines based on advanced commutation can be more complex.

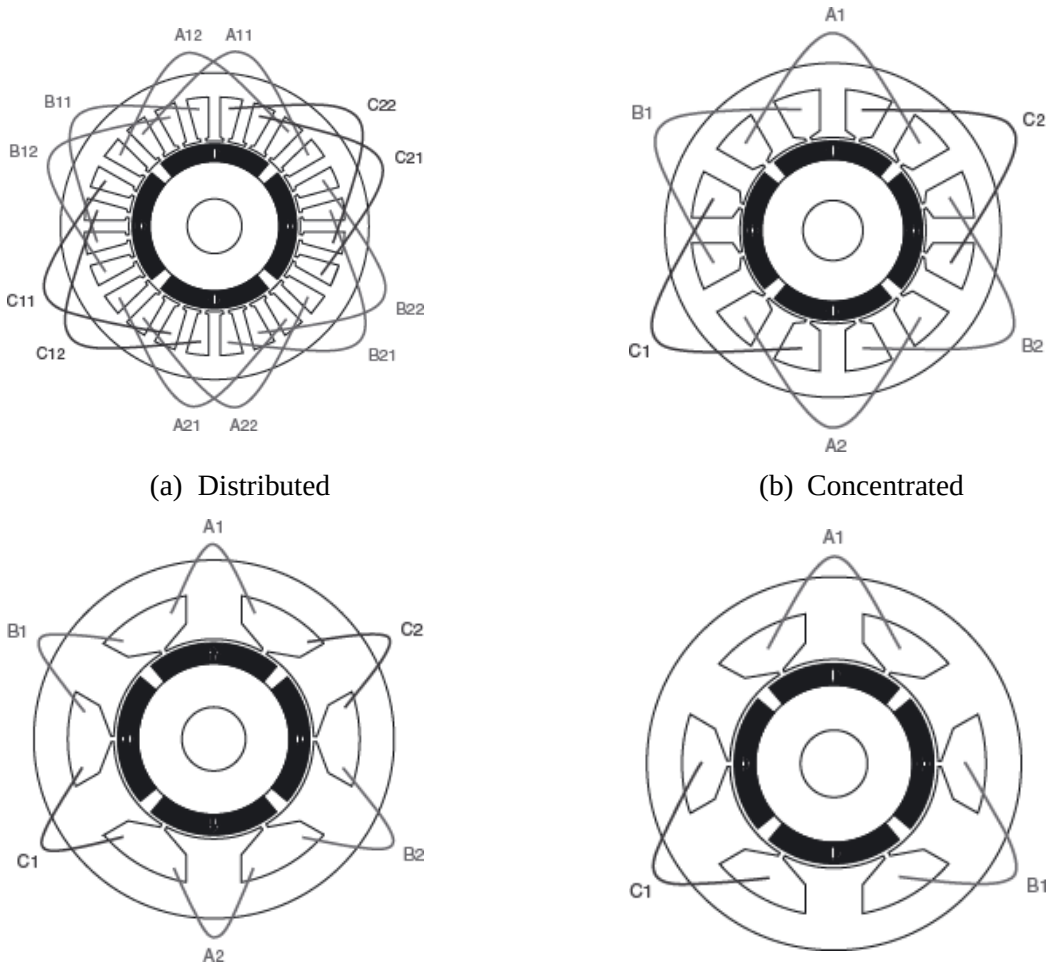
Low order current harmonics in BLDC drives lead to high iron and eddy current losses and higher acoustic noise. Eddy current losses in PM machines result in increase of PM temperature and may lead to partial demagnetisation depending on the operating point of the machine. Thus, BLAC drives are preferred in a variety of applications due to their potential in terms of torque density, efficiency and machine control [ZHU14].

### 1.3.2 Stator Winding Topologies

Stator windings can be concentrated or distributed along a number of slots. In general, distributed windings are overlapping while concentrated windings can be either overlapping or non-overlapping. Furthermore, non-overlapping windings can be double-layer windings, where all teeth are wound, or single-layer windings, where alternate teeth are wound.

The choice of stator winding arrangement can be based on the advantages and disadvantages presented by each topology. Overlapping windings have longer end-windings but the coil pitch can be designed to be closer to the pole pitch in order to exploit reluctance torque. Conversely, non-overlapping windings have shorter end-windings and reduced reluctance torque capability. Reluctance torque capability is also determined by the rotor topology as outlined in Section 1.3.3.

The length of the end-windings affects the axial length of the machine. Longer end-windings result in higher winding resistance and therefore result in a lower efficiency due to increased resistive losses. Furthermore, larger phase resistances may present an issue in low voltage systems due to the higher voltage drop and may compromise high-speed performance of the machine.




(a) Distributed (b) Concentrated

(c) All teeth wound (d) Alternate teeth wound

Fig. 1.8. Stator winding configurations in electrical machines [ZHU14].

Distributed (overlapping) windings are attributed to more sinusoidal back-EMF waveforms leading to lower torque ripple. Concentrated non-overlapping windings result in MMF harmonics leading to higher stator iron losses, rotor iron losses and permanent magnet eddy current losses. Concentrated non-overlapping windings enable stator segmentation for easier manufacturing and additional winding isolation making the winding arrangement suitable for safety and fault-tolerant applications.

Flux linkage of alternate teeth wound single-layer machines can be maximised by using unequal tooth widths, and thereby maximising the coil pitch to pole pitch ratio, at the cost of increased rotor losses. This topology results in a higher self-inductance, higher d-axis inductance and negligible mutual inductances, thus making the machine ideal for fault-tolerant applications [ZHU14].

### 1.3.3 Rotor Topologies

The two most commonly used PM machine topologies are surface-mounted permanent magnet (SPM) machines and interior permanent magnet (IPM) machines. PM machines can be designed with an external rotor or an internal rotor to better-fit application requirements such as machine torque and rotor inertia. SPM motors comprise PMs which are shaped, magnetised and mounted on the rotor iron. Certain applications may require a rotor sleeve to aid retention of PMs and to provide mechanical integrity. Rotors of IPM machines comprise PMs embedded in the rotor iron, thus utilising the rotor iron to retain the PMs.

There are various SPM rotor topologies in which the geometry and PM magnetisation are designed to achieve certain application requirements. Some examples of SPM rotor topologies are shown in Fig. 1.9a and Fig. 1.9b are relatively simple rotor structures in which the PM is mounted onto a circular motor. Air spaces can be introduced in the rotor iron geometry to reduce rotor inertia as well as manipulate flux to obtain better overload and demagnetisation capabilities [ZHU14]. Furthermore, the rotor and PMs are often shaped in different ways to reduce material scrap, improve assembly, and obtain lower torque pulsation, as will be discussed in subsequent sections. Fig. 1.9c and Fig. 1.9d show examples of pseudo-Halbach and Halbach rotors, respectively, which utilise specific PM magnetisation to obtain lower flux leakage resulting in lower cogging torque and higher torque capability. An example of surface-inset PM rotor is shown in Fig. 1.9e. This topology allows better retention of the PMs and increased saliency ratio at the cost of higher flux leakage. Fig. 1.9f shows an example of a consequent pole motor in which PMs magnetised in the same direction are removed, thus resulting in lower PM volume.

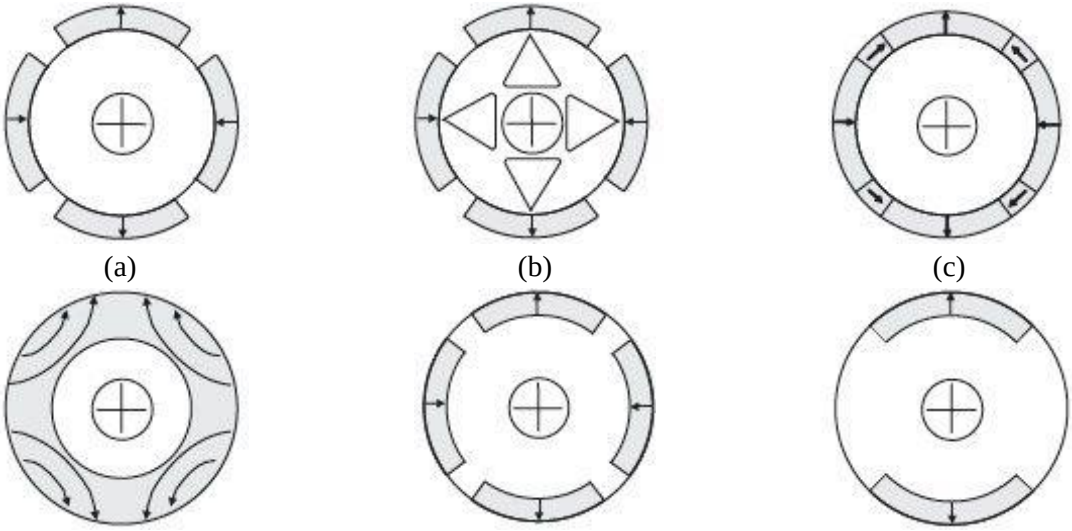



Fig. 1.9. Examples of different SPM rotor designs [ZHU14].

Some examples of IPM rotor designs are shown in Fig. 1.10. IPM rotors employ rectangular PMs resulting in a lower manufacturing cost due to the scrap attributed to shaped PMs as well as the complexity of shaping PMs with certain tolerances. Rotor PMs are shielded by the rotor iron in the instance of an opposite magnetic field. Consequently, IPM machines provide a better demagnetisation withstand capability and better flux weakening capability [WAN11a]. Furthermore, IPM machines have a higher winding self-inductance which makes the topology favourable for fault-tolerant applications. IPM rotors have a higher saliency ratio due to different d- and q- axis reactances. Therefore, reluctance torque can be exploited to minimise PM volume requirement.

The rotor iron provides additional flux leakage paths and this effect is decreased using air spaces, often referred to as flux barriers, and adopting narrower rotor ribs and rotor bridges. The thicknesses of the rotor ribs and rotor bridges are limited by the lamination material properties, lamination thickness, and mechanical stress over the operating speed range of the IPM machine.

Design of rotor PMs and flux barriers can be adapted to achieve better demagnetisation capabilities (Fig. 1.10b) or a flux focusing effect by arranging multiple PMs in particular configurations (Fig. 1.10c). Spoke-type rotors, as shown in Fig. 1.10d to Fig. 1.10f, utilise PMs that are laterally magnetised and flux barriers that are arranged to obtain lower flux leakage, flux focusing, and various degrees of saliency. The shaft of spoke-type rotors is required to be non-magnetic to avoid flux leakage.

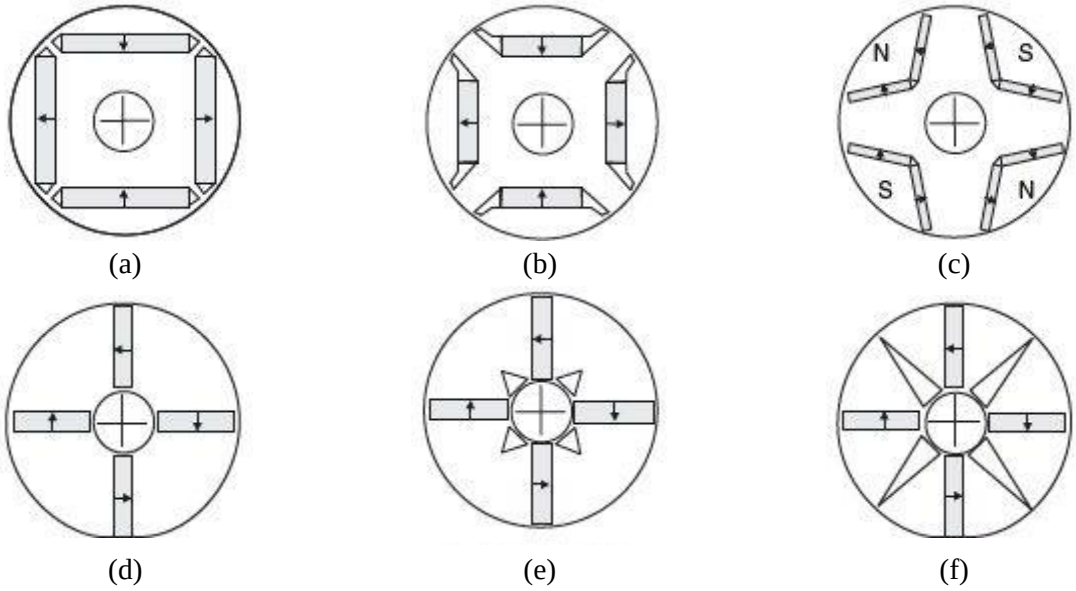



Fig. 1.10. Examples of different IPM rotor designs [ZHU14].

IPM and SPM rotor topologies exhibit different merits and demerits. IPM rotors are favoured because of lower PM manufacturing costs since bar magnets are easier to manufacture and a higher manufacturing tolerance may be adequate. However, the significant flux leakage through the rotor iron results in a higher PM volume requirement. PM shaping in SPM motors requires a stricter manufacturing tolerances and results in PM scrap which can be costly. A rotor sleeve may be required for PM retention resulting in a higher number of required components and assembly steps. SPM rotors result in significantly lower flux leakage through the rotor iron, thus leading to a lower PM volume requirement.

In general, SPM machines provide higher air-gap flux than IPM machines since flux leakage through the rotor iron is significantly lower. The magnitude of the air-gap flux density has a direct impact on flux-linkage and magnetic saturation that, in turn, affect torque, back-EMF harmonics, and torque harmonics, among other factors. Certain applications requiring high safety standards, such as EPS applications, require a rotor sleeve resulting in a slightly higher effective air-gap. Saliency in SPM motors is often very low compared to that of IPM machines and thus IPM machines have better reluctance torque capability, leading to a lower PM volume requirement for a given resultant torque. This compromises the high requirement of PM volume due to flux leakage. Magnetic field in the reverse direction of the PM magnetisation may result in partial demagnetisation. The rotor iron shields the PM in IPM machines, thus resulting in better demagnetisation withstand capabilities than SPM motors.

Optimal machine flux weakening capability is obtained when the characteristic current is equal to the rated current [SCH94, SOO90], where the characteristic current is equal to the PM flux linkage divided by the d-axis inductance. Traditional SPM machines with distributed windings tend to have a high PM flux linkage and low d-axis inductance, resulting in a high characteristic current and poor flux weakening capability. Fractional slot concentrated winding SPM machines have a significantly higher inductance and can provide good flux weakening performance [ELR05]. IPM machines comprise a lower effective air-gap and

consequently have better flux weakening capabilities.

### 1.3.4 Combinations of Number of Slots and Number of Poles

There are various possible combinations of number of slots, $N_s$, and number of poles, $P$ that can be applied in PM machine design. Machines with a number of slots per pole per phase $q$ equal to an integer, e.g. 1, are referred to as integer slot machines, while machines with $q$ not equal to an integer, often lower than 1, are known as fractional slot machines.

Fractional slot machines are favourable due to lower cogging torque and increased fault-tolerant capability. Furthermore, fractional slot concentrated-winding machines have shorter end-windings and overall length, resulting in lower resistive losses, higher efficiency and higher torque density [ZHU09a].

Fractional slot machines have higher armature magnetomotive force (MMF) subharmonics leading to increased rotor losses, increased torque ripple, and low winding factor in some instances [BIA06a]. Furthermore, fractional slot machines may have a low order of the vibration mode, which may not be suitable for low-noise applications [ZHU09a].

## 1.4 Torque Pulsation in Permanent Magnet Machines

The output torque in electrical machines is composed of three components, mutual torque due to the interaction of the stator and rotor MMF distributions, reluctance torque due to the difference between the d- and q-axis inductances, and torque pulsation due to the permeance distribution in the air-gap.

Torque pulsation at no-load condition is commonly referred to as cogging torque or detent torque, and torque pulsation under load condition is referred to as torque ripple. Generally, cogging torque and torque ripple have different waveform characteristics due to the change in permeance distribution from no-load to on-load condition [ISL09]. Furthermore, the torque ripple amplitude is a function of the current amplitude and the current phase-advance angle [OMB11].

One of the main goals of designing an electrical machine is to obtain a high average torque and minimum torque pulsation. Minimisation of torque pulsation can be performed through electrical machine design methods and control methods [JAH96]. This section will outline literature on torque ripple minimisation through electrical machine design.

The periodicity of the cogging torque is related to the least common multiple between the stator slot number and the rotor pole number, i.e. LCM($2p$,$N_s$). A higher LCM results in a higher frequency and lower amplitude of the cogging torque. Zhu *et al.* [ZHU00] proposed another factor for indication of the cogging torque amplitude which is equal to the ratio of the product of the pole and slot numbers to the aforementioned LCM.

Cogging torque may be decreased by adding notches in the stator teeth, also referred to as auxiliary slots,

dummy slots, or bifurcated teeth [ZHU00, BIA02, KOH03, YAN07]. The number of notches influences the torque pulsation amplitude and periodicity, and therefore the number of notches must be chosen carefully in order to obtain an optimal improvement in torque pulsation.

One of the main factors which determines the torque pulsation characteristic is the interaction of the rotor magnets and the stator slots. Thus, stator slot opening width and stator teeth width influence torque pulsation. The influence of stator slot opening on torque pulsation was studied in [ZHU00, ZHU09] and it was determined that its influence depends on the slot/pole number combination. Stator slot pairing [YAN05] and stator teeth pairing [HWA00, FEI10] have been found to be effective techniques in torque pulsation minimisation.

The outer profile of the stator lamination often includes features, such as notches and keybar slots to allow for easier manufacturing. An example of a motor with keybar slots in the stator is shown in Fig. 1.16. Zhu *et al.* [ZHU08] studied the influence of features in the outer surface of the stator and determined that keybar slots result in local saturation and an increase in the cogging torque amplitude.

The pole-arc width directly influences the air-gap flux, and consequently, the machine torque. The pole-arc width should be designed to span an integer number of slot pitches and is dependent on the permanent magnet magnetisation type, the air-gap thickness and the slot opening width [BIA02]. The influence of the pole-arc to pole-pitch ratio on the cogging torque is dependent on the slot/pole number combination [ZHU00, ZHU03]. Zhu *et al.* [ZHU00] have suggested that a high ratio of the LCM($2p$,$N_s$) to the slot number indicates a higher number of feasible pole-arc to pole-pitch ratios for minimum cogging torque.

Asymmetric placement of the rotor permanent magnets is a technique used to manipulate the instants when a particular magnet interacts with the stator slots. Shifting of the permanent magnets results in torque components of different phases at each rotor magnet, and with careful design can result in a net reduction in torque pulsation. The technique was first presented by Li *et al.* [LI88], was applied by Breton *et al* [BRE00], and was further refined and generalised by Bianchi *et al.* [BIA00, BIA02]. Bianchi *et al.* [BIA02] note that asymmetric placement of the magnets influences the back-EMF, particularly in machines with parallel connected windings.

Segmentation of the rotor magnet composing a single pole into multiple magnets can also be used to minimise torque pulsation in SPM machines [LAT06]. The technique is particularly effective for reducing the amplitude of the lower torque pulsation harmonics, given an optimal number of magnets per pole and optimal distance between the magnets within the pole and adjacent poles [LAT06].

Torque pulsation can be reduced, or even eliminated, by skewing the stator or the rotor of the machines at the expense of lower average torque, increased leakage inductance, and increased stray losses [JAH96]. The main challenges are the increased complexity in winding fabrication of skewed stators and the production and magnetisation of skewed rotor permanent magnets [GE17]. The option of stator skewing is often discounted due to the complexity in machine windings, particularly in mass production. On the other

hand, rotor skewing has been extensively applied to machines in different applications. Rotor skewing can be implemented by either skewing both rotor laminations and permanent magnets or by displacing the rotor laminations and permanent magnets at intermediate steps resulting in easier manufacturing [ZHU00, BIA02]. Traditional rotor skewing introduces an asymmetry along the axis of the motor resulting in undesirable axial magnetic forces affecting the shaft and bearings. Unbalanced forces due to rotor skewing can be mitigated using skew patterns that are symmetrical in the axial direction [ZHA15].

Torque pulsation is influenced by the magnet shape in SPM machines and the rotor shape in IPM machines. The former has been studied by Islam *et al.* [ISL09] and the technique was applied to machines with different slot/pole number combinations. Permanent magnet shaping can also be applied in the axial direction to obtain an effect similar to rotor skewing [SHA12, ZHA14]. Rotor shaping in IPM machines has been applied by [EVA10, WAN14]. The addition of air-spaces in IPM machines was also found to be effective in torque pulsation minimisation [KIO06].

## 1.5 Design Optimisation Methods

Optimisation can be defined as the process of methodically finding one or more solutions from a solution space that satisfy one or more objective functions subject to a number of constraints on the design variables [MAR04]. The design variables can be continuous or discrete depending on the problem to be optimised. Terminology can vary vastly in literature; the solution space is also referred to as the objective, criterion or cost space and the objective functions are also referred to as the fitness, criteria or cost functions, and the design space are also referred to as the search or decision space.

The difficulty of the optimisation problem is dependent on the properties of each objective function such as linearity and convexity (or lack thereof). For instance, a convex function, shown in Fig. 1.11, has a local minimum that is always equal to the global minimum. However, in most applications, the objective functions tend to have properties such as discontinuity and local minima that are not equal to the global minimum, as shown in Fig. 1.12.




(a) Convex function (b) Non-convex function

Fig. 1.11. Definition of convex function [SUD14].




(a) Discontinuity (b) Local extremes

Fig. 1.12. Function properties [SUD14].

Optimisation methods can be classified as exact, approximate, and metaheuristic [TAL09]. Exact methods are a family of algorithms, generally applied to combinatorial problems that always solve the problem to a guaranteed optimality [PUC05]. Examples of exact methods include algorithms such as dynamic programming, branch-and-bound, Lagrangian relaxation based methods, and linear and integer programming based methods [PUC05]. Approximate methods comprise approximation and heuristic algorithms, the former provides proven solutions in provable run-time bounds, while the latter is problem-dependent and provides reasonably "good" solutions in a reasonable time [TAL09]. Metaheuristic methods are problem-independent techniques that can be applied to a broad range of problems and are particularly effective in the optimisation of large and complex problems in a reasonable time. There is a plethora of metaheuristic methods, including evolutionary algorithms, such as genetic algorithm and differential evolution, simulated annealing and swarm-based algorithms [TAL09].

Evolutionary algorithms are inspired by biological evolutionary principles in which a population of individuals is exposed to environmental pressure leading to processes such as reproduction mutation, crossover and selection of the fittest individuals. The fitness of the population can be expressed as either a single-objective function or multi-objective functions.

Genetic algorithms are evolutionary search and optimisation algorithms based on natural selection thus mimicking biological evolution. An initial population is determined randomly or using data obtained a priori. Selection of an appropriate population size is essential to adequately represent the variability of the objective function [DEB01]. The population size is dependent on the optimisation problem, particularly on the number of design parameters to be optimised. The objective function(s) are evaluated for the given population and the processes of selection, reproduction, crossover, and mutation are applied to produce a new population for a given number of generations.

The key difference between single-objective and multi-objective problems is that the outcome of a multi-objective optimisation problem is not a single solution but a set of solutions with varying degrees of each objectives. The aim of multi-objective optimisation is to identify the trade-off between the multiple objectives. This is performed by obtaining a set of Pareto-optimal solutions. A solution is Pareto-optimal if it is not possible to improve a given objective without deteriorating a least another objective [TAL09].

The set of Pareto-optimal solutions form a curve in the solution space of the optimisation problem referred to as the Pareto-optimal front, or Pareto-front [DEB01]. An example of a Pareto-front of a multi-objective optimisation problem, in which both objectives are minimised, is shown in Fig. 1.13.

The preferred solution considering the trade-off can then be determined a posteriori. It is worth noting that a set of Pareto-optimal solutions exist only if all the objectives of the optimisation problem are conflicting. The set of Pareto-optimal solutions reduces to a single solution if all objectives are non-conflicting.

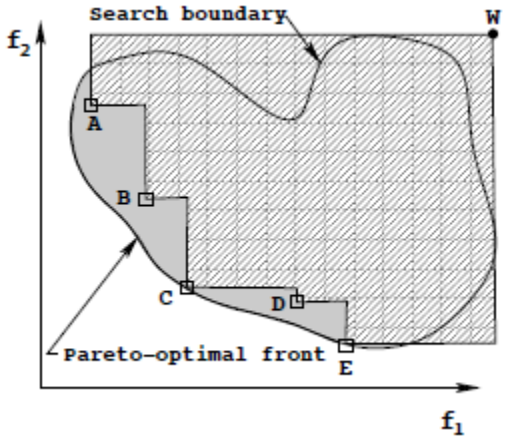



Fig. 1.13. Example of Pareto-front of multi-objective optimisation [DEB01].

Classical optimisation methods attempt multi-objective optimisation by scalarising the multiple objectives into a single objective function [DEB01]. Examples of classical optimisation methods include the weighted sum method and other weighted metric methods. Optimisation using classical methods is generally performed using a priori knowledge of the optimisation problem at hand but can be problematic since the multiple objectives may be of different orders of magnitude and the individual objectives may vary in a non-linear manner in response to the input variables. Classical optimisation methods fail to locate certain Pareto-optimal solutions if the solution space is non-convex [DEB01].

The optimisation process of a multi-objective problem using a particular optimisation algorithm, illustrated in Fig. 1.14, starts with the definition of the optimisation objectives and the required constraints. The parameters to be optimised are identified through an analysis of the main effects of the parameters on the optimisation objectives and the parameter space and any design constraints are then defined.

Main effects refer to the average effects of multiple independent variables (or factors) on a particular quantity [SAL12]. Main effects analysis provides a better understanding of the sensitivity of a particular quantity, for instance the average torque of a PM motor, to changes in independent variables such as machine dimensions. Main effects can be determined using single-factor experiments, also referred to as the one-variable-at-a-time method or a design of experiments [SAL12].

The solution space is then determined using the optimisation algorithm and the designer selects the optimal solution/s considering the trade-offs between the objectives. The selected solutions are then verified and to

ensure adherence to any application-specific requirements. Design selection and post-optimisation analysis and verification may need to be repeated until a satisfactory design meeting all requirements is found.

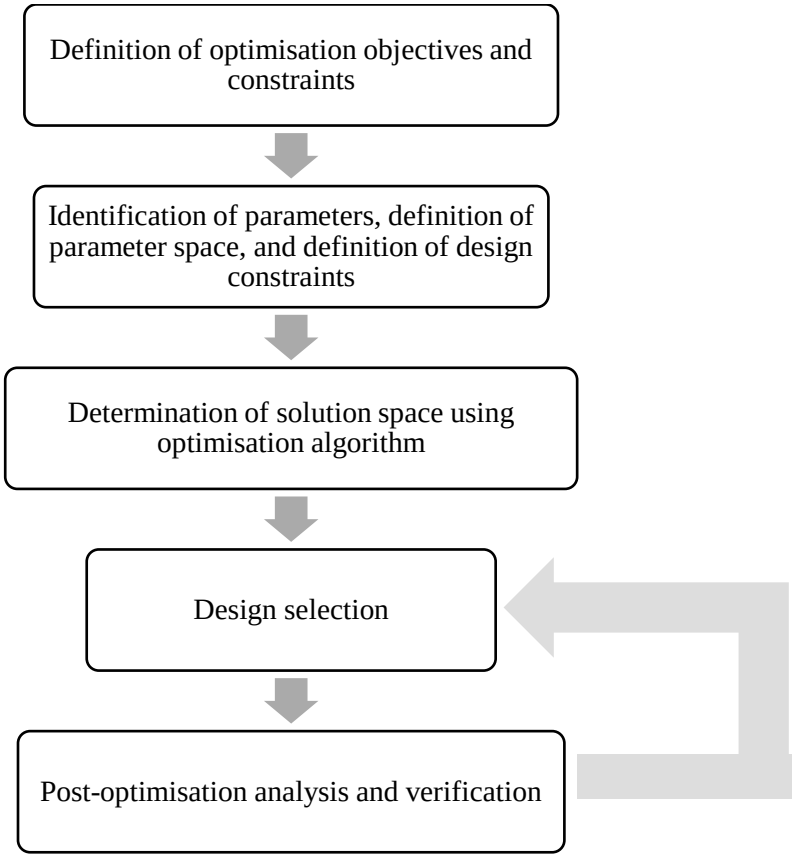



Fig. 1.14. The process of multi-objective optimisation.

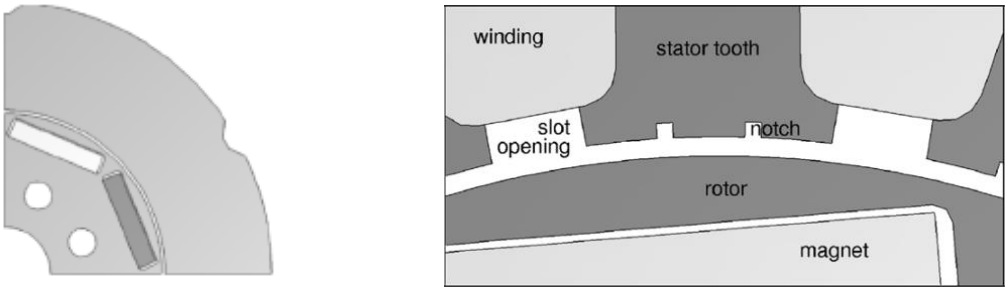
## 1.6 Design Optimisation of PM Motors for EPS Applications

The problem of optimisation of PM motor design is very complex due to the wide range of topologies and materials, the non-linearity of the magnetic circuit in response to variation of the input electrical power and environmental conditions, such as temperature and pressure, and 3D effects such as end-region flux leakage and rotor eccentricity. Furthermore, the optimisation problem is made more complex by the often conflicting nature of the various optimisation objectives, such as torque, motor mass and volume, efficiency, and cost, as well as constraints that are dependent on the application.

Some of the PM motor topologies that have been optimised for various applications include SPM motors [DUA09, DUA13, LIP15], IPM motors [BIA02, PEL10, ALO11], spoke-type IPM motors [HWA07, RAH16, SI16], and PM-assisted synchronous reluctance motors [CHE12, BAR16, STI16].

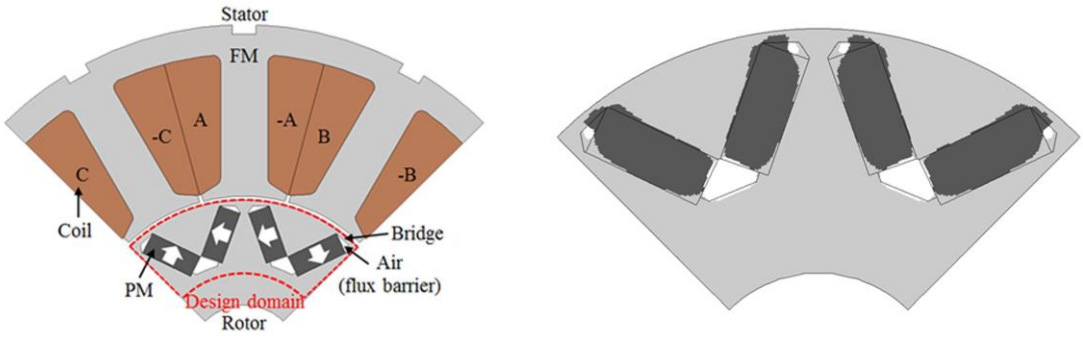
Various PM motor topologies have been proposed for EPS applications. The proposed machine designs have been analysed using analytical equations, FEA, or experimental measurements or a combination of the three methods.

A 12-slot/8-pole IPM machine with dummy slots and notches in the stator was optimised by Schlensok *et al.* [SCH06] using a combined analytical and numerical method. A flux-focusing rotor design using the same slot/pole number combination was optimised by Lim *et al.* [LIM15] using magnetic-thermal coupled equations to enable assessment of the permanent magnet demagnetisation due to temperature. The authors focused on shaping the rotor magnets, rather than the rotor iron, and presented a magnet design that provides optimal machine performance. The optimised magnet design eliminates magnet areas that contribute to additional flux-leakage such as the bottom corners of the magnet. However, the magnet design leads to higher costs attributed to manufacturing such an intricate design. Alternatives that mitigate flux-leakage include the introduction of additional air spaces around the corners of magnets and thinner flux-leakage paths while also considering rotor stresses. A similar 12-slot/8-pole flux-focusing IPM motor was optimised by Kim *et al.* [KIM16] considering the influence of certain manufacturing tolerances.




(a) Rotor design (b) Optimised notch shape

Fig. 1.15. 18-slot/8-pole IPM motor studied in [SCH06].




(a) Initial machine design (b) Optimised permanent magnet design

Fig. 1.16. 12-slot/8-pole IPM motor studied in [LIM15].

Spoke-type fractional slot concentrated winding IPM machines have been designed for EPS applications by Carraro *et al* in [CAR14] and [CAR18]. The former publication focuses on optimisation of five spoke-type IPM motors with different slot/pole number combinations for minimum PM volume. The most recent publication comprises design and analysis of eight spoke-type IPM motors with different slot/pole number combinations and heavy rare earth free PM materials. The electromechanical performance and stator deformation of the motors was analysed. It was concluded that torque density of motors with a low number

of poles is lower than that of motors with a higher pole number. Analysis of stator deformation due to magnetic forces concluded that noise and vibration is dependent on the periodicity of the motor, as expected. It was concluded that there is no slot/pole number combination that meets all the performance targets at the same time. The 12-slot/14-pole spoke-type IPM motor was found to yield satisfactory performance, high torque density and lowest cost among the analysed topologies.

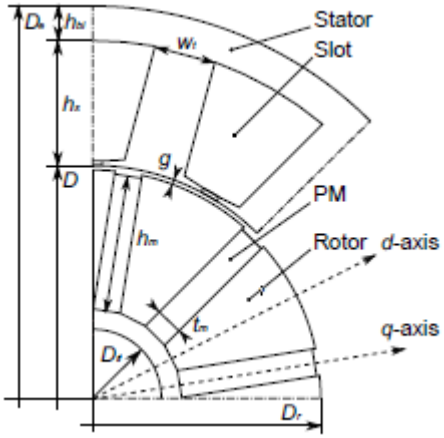



Fig. 1.17. Cross-section of a spoke-type IPM motor studied in [CAR14].

Ombach and Junak compared 9-slot/8-pole SPM and IPM motors in [OMB07] considering various machine parameters. The IPM motor requires a lower permanent magnet volume compared to the SPM motor due to the additional reluctance torque. Generally, motors with a slot/pole number combination with a periodicity of 1, such as 9-slot/8-pole motors, are not considered for EPS applications due to the unbalanced magnetic forces and high noise and vibration. The aforementioned publication analysed the average torque over the speed range of the motor and demagnetisation capability. However, the motors might not be adequate for EPS due to noise and vibration.



(a) (b)

Fig. 1.18. 9-slot/8-pole SPM and IPM machines studied in [OMB07].

A 12-slot/8-pole SPM machine with unequal tooth width was optimised for the required cogging torque and torque ripple by Sim *et al.* [SIM12]. The study considered four design parameters: eccentricity, angle of the larger tooth-tips, width of the smaller teeth, and the pole arc angle.

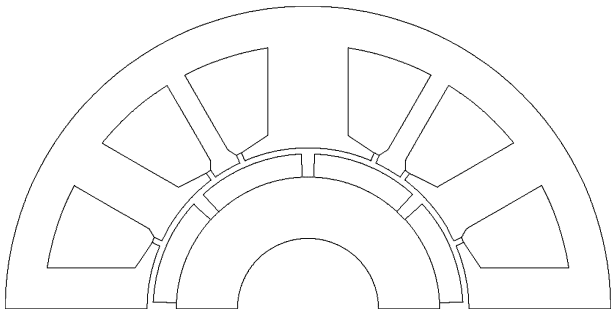


Fig. 1.19. 12-slot/8-pole SPM machine with unequal tooth widths studied in [SIM12].

The performance of 6-slot/4-pole, 12-slot/8-pole, and 12-slot/10-pole SPM motors was investigated by Lee *et al.* [LEE14] using FEA and experiments. It was proposed that the 12-slot/10-pole SPM machine should be considered for EPS because of the satisfactory results in terms of space harmonics of the radial forces, back-EMF waveforms and cogging torque. The experimental acoustic noise measurements for the pole/slot number combinations clearly show that the 12-slot/10-pole machine generated the highest acoustic noise level. The authors argue that the stator of the 12-slot/10-pole machine could be redesigned to avoid resonance and therefore the choice of the 12-slot/10-pole machine as the optimal topology remains. However, this argument was not sustained by analytical, numerical, or experimental results.

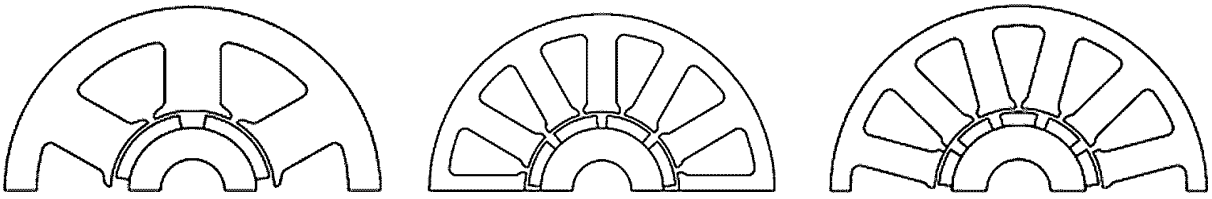


Fig. 1.20. SPM machines studied in [LEE14].

Benedetti *et al.* [BEN05] and Bianchi *et al.* [BIA06] presented solutions for permanent magnet machines applied in a steer-by-wire EPS system. Benedetti *et al.* [BEN05] presented a redundant-motor drive and considered EPS mechanical requirements, motor fault currents and braking torque, motor design, and motor control. Furthermore, the system was simulated and tested using an experimental test-rig. Bianchi *et al.* [BIA06] defined the design parameters of the proposed IPM motors, which were selected to match the required base operating point, flux weakening operating point, and a prefixed maximum braking torque. Torque ripple reduction was achieved by rotor step skewing and by optimising the position of rotor flux-barriers. Finite-element and experimental results confirming the analytical results have been presented.

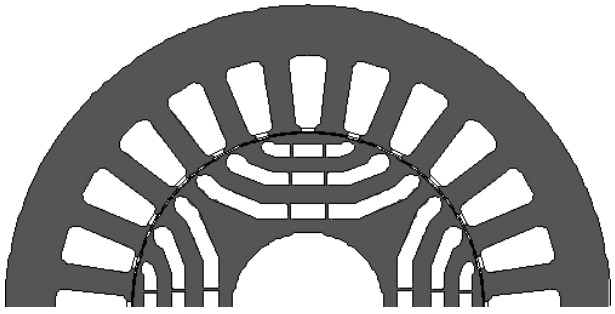


Fig. 1.21. IPM machine studied in [BEN05, BIA06].

Huang *et al.* [HUA20] analysed the demagnetisation capability of the 12-slot/8-pole IPM motor shown in Fig. 1.22 using 2D and 3D finite-element models. The analysis was performed for motors with different PM thicknesses and the demagnetisation performance of the improved motor design was verified experimentally.

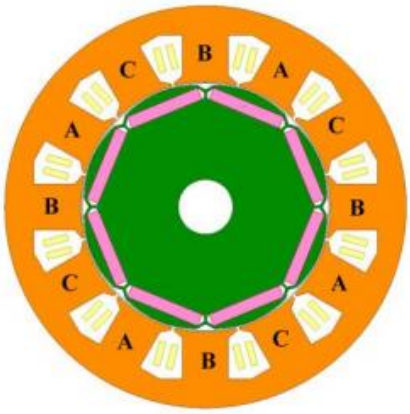



Fig. 1.22. IPM machine studied in [HUA20].

## 1.7 Manufacturing Tolerances

Mass-produced electrical machines are inevitably subjected to manufacturing tolerances which result in a deviation in the expected performance of the electrical machine. Manufacturing tolerances may affect the assembly of stator and rotor laminations, magnet dimensions and placement, and stator and rotor concentricity among other factors [ISL04]. Rotor eccentricity is an important factor in the assembly of an electrical machine as it results in unbalanced magnetic forces and consequently in higher noise and vibration.

The predicted geometry of the electrical machine is in fact modified by the lamination manufacturing processes, such as punching and laser cutting, by the lamination stacking processes, such as welding and interlocking. Furthermore, there may be other materials in the housing which are not accounted for in the design phase.

The properties of the materials used in the electrical machines are also subjected to manufacturing tolerances. Such issues include minor anisotropies in the laminations material, differences in remanent magnetic flux density of the permanent magnets and deviations in the magnetisation direction of the permanent magnets.

The issue of minimisation of cogging torque due to manufacturing tolerances has been addressed by an investigation of the influence of certain manufacturing errors [ISL04, GAS08, GAS09, ZHU12, KHA14, KIM16, GE17, MUE19, TAR19, KOL20, YAN20] or as a geometry optimisation problem using stochastic methods [OMB07a, COE11, COE12].

The fundamental component of cogging torque of a motor without any deviations from the nominal design is defined by the Least Common Multiple (LCM) of the number of rotor PM poles ($2p$)and the number of stator slots $N_s$ [ZHU00], as defined in (1.1),

$$N = LCM(2p, N_s) \tag{1.1}$$

The cogging torque of a motor is composed of the inherent Native Harmonic Components (NHCs) and Additional Harmonic Components (AHCs) due to factors resulting from a deviation from the nominal geometry of the motor, such as manufacturing tolerances [GAS08, GAS09]. The instantaneous value of the cogging torque can be expressed as the addition of the cogging torque due to NHCs and cogging torque due to AHCs, as defined in 1.2.

$$T_{cogging} = T_{NHC} + T_{AHC} \tag{1.2}$$

where

- $T_{cogging}$ is the cogging torque
- $T_{NHC}$ is the inherent cogging torque (NHCs)
- $T_{AHC}$ is the cogging torque due to AHCs

Gašparin *et al* [GAS08, GAS09] investigated manufacturing tolerances in the dimensions and assembly of the permanent magnets using FEA and experimental measurements. Permanent magnet misplacements and thickness variations resulted in additional harmonic components with negligible influence on the native harmonic components. On the other hand, permanent magnet width variations cause an increase in the amplitude of the native harmonic components with no significant increase in the amplitude of the additional harmonic components.

Fractional slot concentrated winding (FSCW) machines are often segmented for an easier winding process, as outlined in Section 1.5. The assembly of the segments can result in stator gaps between the teeth and the back-iron or between the modules. Zhu *et al.* [ZHU12] investigated the influence of these stator gaps on the cogging torque and the back-EMF using FEA and experimental results. Uniform additional stator gaps of 0.05 mm resulted in an increased effective air-gap and lower cogging torque and gaps of 0.1 mm or larger led to an increase in flux leakage through the tooth tips and slot iron bridges resulting in a higher cogging torque. The cogging torque periodicity and the back-EMF were not affected by the stator gaps. Non-uniform additional stator gaps led to an increase in cogging torque amplitude and periodicity which is dependent on the location of the additional stator gaps. The influence of the stator gaps on the back-EMF was negligible.

Khan *et al.* [KHA14] considered manufacturing tolerances in the rotor magnet dimensions of a 6-pole/9-slot FSCW SPM machine with a 3-step skewed rotor using the design of experiment method according to one of the matrices in Taguchi's method [TSU92]. The magnet dimensions of a batch of 200 magnets were

measured. The accuracy of these measurements was not reported. The magnets required to construct 40 rotors were selected and divided into four batches within specific ranges of magnet dimensions. The cogging torque and back-EMF of the 40 rotors were measured and four FEA models of rotors with magnets within the specified dimensions ranges were simulated. The exact dimensional limits of the modelled rotors were not specified. The results obtained from FEA and experimental measurements were compared.

Kim *et al.* [KIM16] considered stator and rotor asymmetries in a 9-slot/6-pole FSCW SPM motor using FEA and experiments. Stator asymmetries and static eccentricity resulted in increased amplitude of the $6^{th}$ cogging torque harmonic, while rotor asymmetries and dynamic eccentricity resulted in increased amplitude of the $9^{th}$ cogging torque harmonic. As expected, the cogging torque order influenced by manufacturing errors in the stator is a multiple of the rotor pole number, and conversely, the cogging torque order influenced by rotor manufacturing tolerances is a multiple of the stator slot number.

Ge *et al.* [GE17] investigated the influence of manufacturing tolerances in the roundness of the stator bore and PM magnetisation diversity on the cogging torque of 12-slot/8-pole and 12-slot/10-pole IPM motors. The influence of multiple manufacturing tolerances has an additive effect on the cogging torque of PM motors.

The influence of manufacturing tolerances on the on-load torque and radial teeth force of an IPM motor was investigated in [MUE19]. The study considered tolerances in the stator teeth dimensions, magnet remanence, dimensions, and placement, and eccentricity. It was concluded that the influence of manufacturing tolerance is dependent on the motor operating point and influence of multiple tolerances on the on-load torque is correlated. Furthermore, the influence of the analysed manufacturing tolerances on the radial teeth force is non-negligible. Taran *et al.* [TAR19] conducted a similar study based on the IEEE Std 1812 guide and concluded that the motor ratings, magnetic loading and topology have a considerable influence on motor sensitivity to manufacturing tolerances.

An analytical model was used to analyse the cogging torque sensitivity of a 12-slot/8-pole, 12-slot/10-pole, and 18-slot/16-pole IPM motors in [YAN20]. It was proposed that the robustness of the cogging torque to manufacturing tolerances can be improved through selection of an adequate pole-arc to pole-pitch ratio and stator slot-opening width.

The influence of various manufacturing tolerances on the on-load torque of a 9-slot/6-pole IPM motor was investigated in [KOL20]. A design of experiments with variables expressed as a probability distribution was used to identify the motor sensitivity to manufacturing tolerances. The motor under investigation is very sensitive to the housing radius, rotor radius, and static eccentricity.

Statistical methods have been applied to optimise the geometry of electrical machines in order to produce a design with a cogging torque characteristic which is more resilient to deviations in the machine geometry. Coenen *et al.* [COE11] applied this approach to the geometry of an 8-pole PM machine considering manufacturing tolerances in magnetisation of the rotor magnets. The PM machine topology was not

reported.

The methodology in [COE11] was used to investigate the no-load an on-load torque of two IPM machines in [COE12]. The authors described an approach combining analytical and numerical solutions and compared the results with those obtained using FEA. The results of the proposed method and FEA differed but the qualitative distribution was identical.

Design of experiments and FEA were combined and applied to 18 worst-case rotor configurations, previously identified in [SCH06a]. The faulty magnets in each configuration had a reduction in remanence of 5%. The probability of occurrence of each configuration was calculated and a weighted average for the chosen design parameter showed a cogging torque reduction of 7%. The optimum design determined using this method was then validated using two stochastic FEA tests. Each test was based on 50 configurations in which the remanent flux density of the rotor magnets varies randomly with a margin of $\pm$4% and $\pm$6%, respectively. The resulting frequency distributions showed that the average amplitude of the cogging torque was decreased by 9% and 10%, respectively.

A design methodology of a 12-slot/8-pole FSCW IPM motor considering manufacturing tolerances was presented by Ombach and Junak [OMB07a]. Their study confirmed that cogging torque is sensitive to all production processes. It was proposed that tolerance analysis can be performed using a combination of either design of experiments and FEA or Monte Carlo and analytical equations. The authors identified the most important manufacturing tolerances that affect each machine parameter and calculated a probability distribution of the manufacturing tolerances given a realistic mean and standard deviation obtained from current mass-production processes. The statistical distributions of various machine parameters were then calculated and compared to experimental measurements.

Lee *et al.* [LEE14a] used a variation of Taguchi's method to find the optimal machine dimensions for maximum back-EMF considering a set of permanent magnet manufacturing tolerances. The results showed that the average back-EMF was increased by 12.87 % with respect to the initial design but the influence of the machine dimensions on the harmonics of the back-EMF was not reported. Other studies utilising the Taguchi method to optimise permanent magnet motors considering manufacturing tolerances include [LEI19, KIM20, LEE20, GOP21]. The six-sigma methodology is extensively applied in industry to improve quality of processes through identification and mitigation of the causes of variation in the response of a process [PAT18]. The performance of an electrical machine can be regarded as analogous to a process allowing various process analysis methods to be employed. Robust design optimisation of PM machines considering manufacturing tolerances to obtain six-sigma quality has been performed using different methods in [JUN17, PAU19, BRA20, RAF20].

## 1.8 Scope and Contributions of Thesis

The main aims of the thesis are as follows:

- Analyse the performances of a baseline 12-slot/8-pole IPM motor
- Single-objective optimisation of IPM and SPM motors of different slot/pole number combinations for maximum average torque
- Multi-objective optimisation of IPM and SPM motors of different slot/pole number combinations for maximum average torque and minimum torque ripple
- Identification of a set of multi-objective optimised IPM and SPM motors of different slot/pole number combinations with the same volume and similar torque performance
- Analysis of cogging torque sensitivity of multi-objective optimised motors to manufacturing tolerances
- Identification of worst-case scenarios of manufacturing tolerances of multi-objective optimised motors
- Analysis of cogging torque uncertainty of multi-objective optimised motors due to manufacturing tolerances

The performance of the motors under investigation could not be determined experimentally due to the unprecedented circumstances brought by the COVID-19 global pandemic. The finite-element model is adapted to the motor analysed and tested in [GE16a] to demonstrate the efficacy of the applied 2D FEA model.

The thesis is organised as follows:

**Chapter 1** presents an introduction to power steering systems, PM machines, the problem of design optimisation, and manufacturing tolerances.

**Chapter 2** analyses the electromagnetic performance of a baseline 12-slot/8-pole IPM motor and the sensitivity of design parameters. Furthermore, the electromagnetic performance of the baseline motor is compared with the experimental results in [GE16a] to validate the finite-element model of the motor under investigation.

This thesis aims to analyse the influence of manufacturing tolerances on IPM and SPM motors with different slot/pole number combinations applied in EPS systems. **Chapter 3** and **Chapter 4** are global optimisation of 12-slot/8-pole, 12-slot/10-pole, and 12-slot/14-pole IPM and SPM motors, respectively. Single-objective optimisation for maximum average torque gives a set of design constraints. Furthermore, the compromise between average torque and torque ripple of IPM and SPM motors is investigated using multi-objective optimisation. The optimised IPM motors are compared to the baseline IPM motor in

Chapter 3. The IPM and SPM motors identified using single-objective and multi-objective optimisations are compared in Chapter 4.

**Chapter 5** analyses the cogging torque sensitivity to manufacturing tolerances of IPM and SPM motors with different slot/pole number combinations obtained using multi-objective optimisation. This chapter considers the influence of various manufacturing tolerances in the identified stator and rotor of IPM and SPM motors. The finite-element model used in this analysis is adapted to 12-slot/8-pole and 12-slot/10-pole IPM motor designs used in the experimental tests performed in [GE16a] to validate the finite-element models used in this thesis.

**Chapter 6** identifies the worst-case scenarios of cogging torque due to stator manufacturing tolerances in the IPM and SPM motors under investigation, rotor manufacturing tolerances, and manufacturing tolerances in both stator and rotor.

**Chapter 7** utilises a stochastic approach to analyse the uncertainty of cogging torque of the IPM and SPM motors under investigation. Uncertainty analysis of the cogging torque is performed on motors subjected to stator tolerances only, rotor tolerances only, and both stator and rotor tolerances. These are executed to identify the contributions of the various manufacturing tolerances to the uncertainty of the cogging torque in IPM and SPM motors with different slot/pole number combinations.

**Chapter 8** provides a summary of the findings of this thesis and presents a discussion for future work.

# 2 ANALYSIS OF ELECTROMAGNETIC PERFORMANCE OF BASELINE IPM MOTOR

## 2.1 Introduction

The design parameters of the baseline motor are listed in Table 2.1 and the cross-section of the motor is shown in Fig. 2.1. The stator and rotor irons are made out of the same lamination material and the B-H characteristic is shown in Fig. 2.2. Some of the key characteristics of the baseline motor are:

- Fractional-slot motor, with 12 stator slots and 8 rotor poles
- Modular stator with open slots and concentrated windings connected in parallel
- IPM rotor with 3-step skewing (see Fig. 2.3)
- Eccentric rotor pole-shaping with a minimum air-gap of 0.6 mm
- High PM grade
- Rotor bridge as thick as the lamination
- Base rotational speed of 1500 rpm

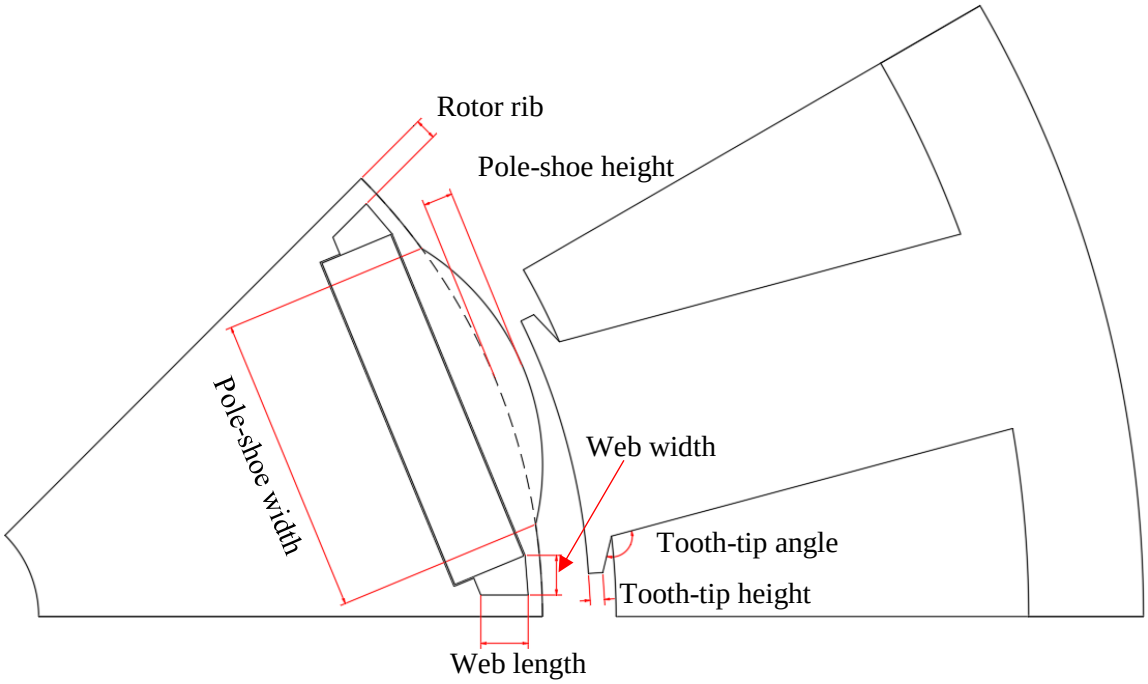



Fig. 2.1. Cross-section of a stator slot and a rotor pole of baseline 12-slot/8-pole IPM motor.

Table 2.1. Design parameters of baseline 12-slot/8-pole IPM motor

| **Parameter** | **Value** | **Unit** |
|---|---|---|
| Stack length | 37.50 | mm |
| Lamination thickness | 0.50 | mm |
| Air-gap length | 0.60 | mm |
| Outer diameter | 85.00 | mm |
| Inner diameter (bore) | 46.40 | mm |
| Split ratio | 0.539 | N/A |
| Back-iron thickness | 4.00 | mm |
| Tooth width | 7.00 | mm |
| Slot opening width | 3.00 | mm |
| Tooth tip height | 0.50 | mm |
| Tooth tip angle | 115 | ° |
| Number of turns | 27 | N/A |
| Wire diameter (bare copper) | 1.20 | mm |
| Parallel branches | 4 | N/A |
| Maximum peak current | 95 | A |
| Pole-shoe height (max.) | 1.05 | mm |
| Pole-arc to pole-pitch ratio | 0.62 | N/A |
| Bridge width | 0.50 | mm |
| Rib width | 1.50 | mm |
| Web width | 1.50 | mm |
| Web length | 1.65 | mm |
| PM cavity height | 2.71 | mm |
| PM cavity with | 12.20 | mm |
| PM height | 2.61 | mm |
| PM width | 12.10 | mm |
| Rotor skew angles | -5.25/0/5.25 | ° |
| PM Br | 1.38 | T |
| PM Coercive force | -1100 | kA/m |

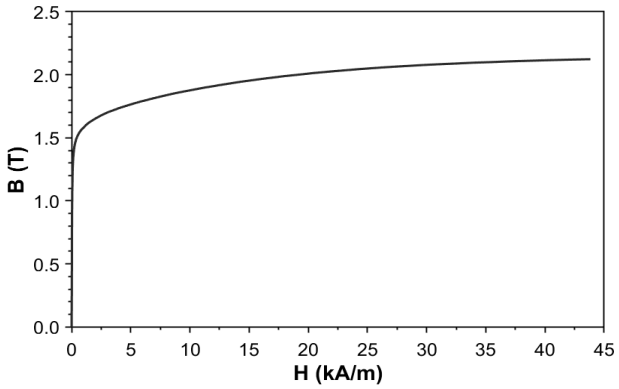



Fig. 2.2. B-H characteristic of the stator and rotor lamination material.

The rotor of the baseline IPM motor comprises 3-step rotor skew, as shown in Fig. 2.3. The rotor is composed of three segments, often referred to as pucks, that are rotated by particular angles, listed in Table 2.1, with respect to the middle segment. Rotor skewing is implemented to minimise torque ripple, as outlined in Chapter 1. The torque ripple of the motor is required to be below 5% to meet the requirements of EPS applications.

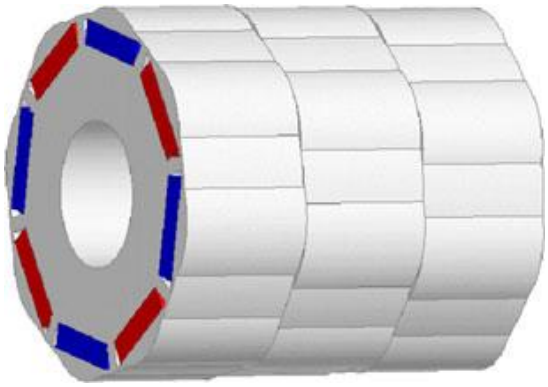


Fig. 2.3. Example of rotor 3-step skew of an 8-pole IPM motor [GE16].

The baseline motor is modelled using the finite-element software, ANSYS Maxwell. The motor is modelled using 2D finite-element analysis and axial effects are neglected. Three-dimensional effects in PM motors are non-negligible, however, two-dimensional FEA is adopted to compromise between model accuracy and computational effort. The dominant axial effects in the baseline motor are leakage flux where the rotor pucks come in contact and end-effects in both the stator and rotor. The electromagnetic torque of motors with step-skewed rotors can be calculated as the summation of the torque due to each rotor step divided by the number of rotor steps.

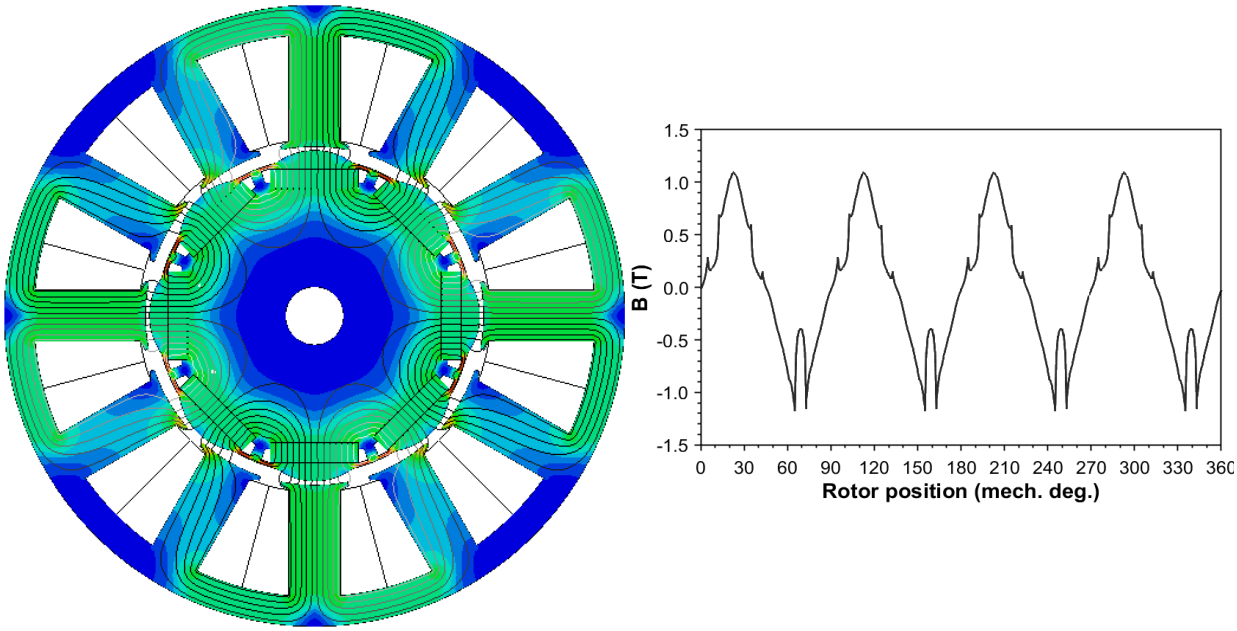
The electromagnetic performance of the motor is analysed at the base speed and maximum current operating point with zero current advance angle. The sensitivity of the design parameters of the motor is then determined through a one-at-a-time parametric analysis. The influence of load and current angle on the motor torque and torque ripple will also be investigated.

The experimental performance of the baseline motor could not be compared with the experimental

performance of prototypes of the baseline motor due to the unprecedented circumstance brought by the COVID-19 global pandemic. The finite-element model is adapted to the motor analysed and tested in [GE16] to demonstrate the efficacy of the applied 2D FEA model.

## 2.2 Analysis of Electromagnetic Performance

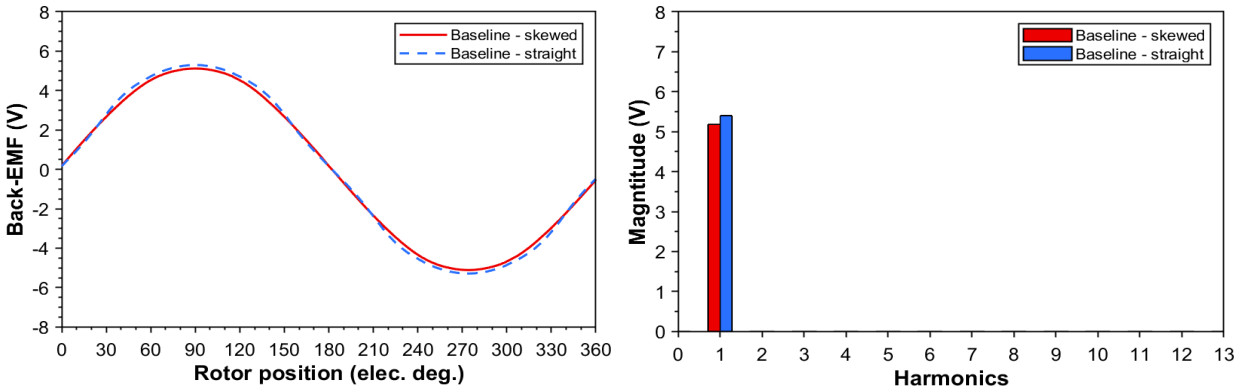
The electromagnetic performance of the baseline 12-slot/8-pole IPM motor is analysed using 2D FEA. The equipotential lines of the motor and the air-gap magnetic flux density under no-load condition are shown in Fig. 2.4. There is significant inter-pole flux leakage through the rotor bridges as well as some flux leakage through the stator teeth, as expected in IPM motors. The peak air-gap magnetic flux density is 1.18 T, and this is attributed to the high grade of the PM material.




(a) Equipotential lines and flux density (b) Air-gap magnetic flux density

Fig. 2.4. Equipotential lines and air-gap magnetic flux density of baseline motor under no-load condition.

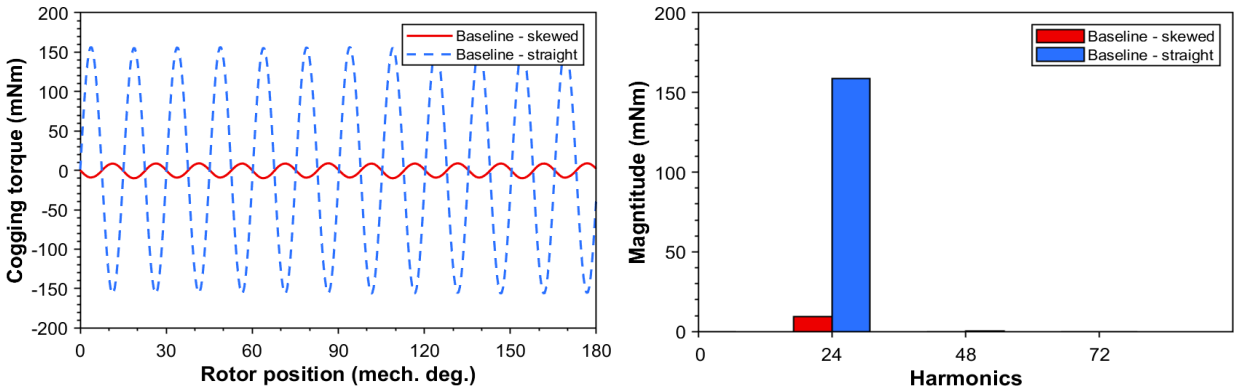
Analysis of the electromagnetic performance is carried out for the baseline motor, comprising a rotor with 3-step skew, and the baseline motor with a non-skewed rotor for completeness. The back-EMF of the motor with skewed and non-skewed rotors is shown in Fig. 2.5. The back-EMF waveform of the motor is sinusoidal with negligible THD. Rotor step-skewing results in a reduction in the magnitude of the fundamental harmonic of the back-EMF of 3.8%.




(a) Waveforms (b) Harmonics

Fig. 2.5. Back-EMF waveforms and harmonics of the baseline IPM motor.

The cogging torque of the baseline motor is shown in Fig. 2.6. The peak-to-peak cogging torques of the baseline motor with a skewed rotor and with a non-skewed rotor are 18.8 mNm and 313.6 mNm, respectively. Thus, rotor step-skewing results in a reduction of the peak-to-peak cogging torque of 94.0%. The fundamental harmonic of the motor cogging torque is determined by the least common multiple of the stator slot number and the rotor slot number. Thus, the cogging torque is composed of the fundamental 24$^{th}$ order harmonic, which is the least common multiple between the rotor pole number (8) and the stator slot number (12).




(a) Waveforms (b) Harmonics

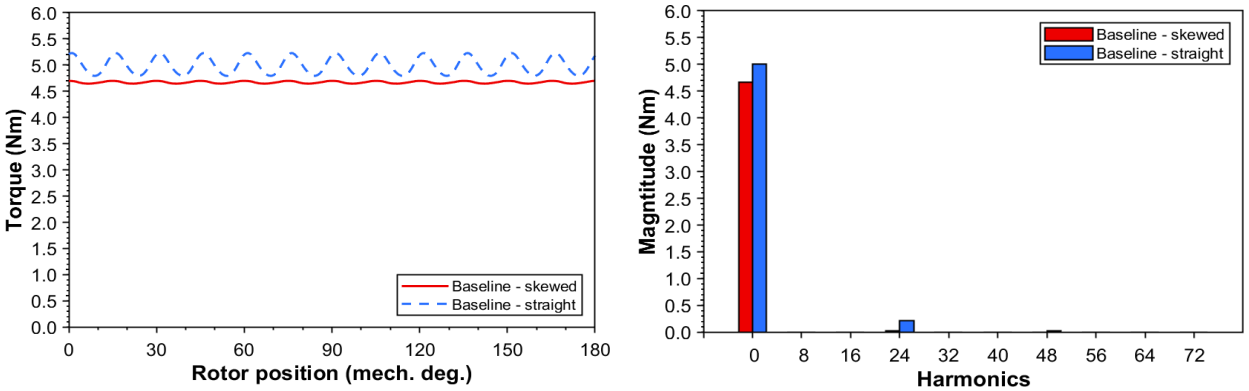
Fig. 2.6. Cogging torque waveforms and harmonics of the baseline IPM motor.

The on-load torque of the baseline motor at base speed, maximum current and zero current angle is shown in Fig. 2.7. The average torques of the baseline motor with a skewed rotor and a non-skewed rotor are 4.6 Nm and 4.9 Nm, respectively. The absolute torque ripples of the two motors are 6.0 mNm and 44.2 mNm, respectively, resulting in a relative torque ripple of 1.3% and 9.0%, respectively.

The absolute torque ripple of the motor and relative torque ripple of a motor are defined as follows:

$$T_{ripple_{absoute}} = \max\big(T(\theta)\big) - \min(T(\theta)) \tag{3}$$

$$T_{ripple_{relative}} = 100 * \frac{\max\big(T(\theta)\big) - \min(T(\theta))}{mean(\max\big(T(\theta)\big) - \min\big(T(\theta)\big))} \tag{4}$$




(a) Waveforms (b) Harmonics

Fig. 2.7. On-load torque of the baseline IPM motor at maximum current and zero current advance angle.

Thus, rotor step skewing, results in reductions of maximum back-EMF and average on-load torque of 3.8% and 6.1%, respectively. Furthermore, the reductions in peak-to-peak cogging torque and on-load absolute torque ripple due to rotor step-skewing are 94.0% and 86.4%, respectively.

PM motors are often required to operate over a range of rotational speeds and the torque-speed operational envelope is a good indicator of motor performance. The operating points of a PM motor are determined by a vector control scheme aimed at exploiting the characteristics of a motor to obtain the best performance. The Maximum Torque per Ampere (MTPA) control algorithm determines the minimum current magnitude and the corresponding current advance angle required at a specific operating point in the torque-speed range of the motor. The MTPA control algorithm is independent of motor losses such as mechanical losses, iron losses, and copper losses.

The torque-speed envelope of the motor defines the maximum average torque of the motor that can be obtained throughout the speed range of the motor given constraints on the maximum voltage and maximum current of the motor.

The average torque of a PM motor can be approximated analytically using (3), where $p$ is the pole-pair number, $\Psi_d$ and $\Psi_q$ are the d- and q- axis flux linkages, and $I_d$ and $I_q$ are the d- and q- axis current vectors. The constraints on the voltage and the current are determined by (4) and (5), where $\omega_s$ is the rotational speed. The voltage limit $V_{lim}$ and the maximum current $I_{max}$ are defined by the specifications of the inverter used in the particular application.

$$T = \frac{3}{2} p(\Psi_d I_q - \Psi q I_d) \tag{5}$$

$$\omega_s \sqrt{\Psi_d^2 + \Psi_q^2} \leq V_{lim} \tag{6}$$

$$\sqrt{I_d^2 + I_q^2} \leq I_{max} \tag{7}$$

The cross-coupling of the d- and q-axis flux linkages is a result of the saturation in the magnetic material due to the d- and q-axis currents. Therefore, accurate calculation of the average torque requires the flux linkages to be expressed as a function of $I_d$ and $I_q$, as indicated in (6).

$$T = \frac{3}{2} p\left[\Psi_d(I_d, I_q) I_q - \Psi q(I_d, I_q) I_d\right] \tag{8}$$

Goss et al. [GOS13] obtained the d- and q-axis flux linkages over a range of $I_d$ and $I_q$ using 2D FEA. The variation of the flux linkages with $I_d$ and $I_q$ was expressed as a second order polynomial function and the coefficients were determined using a least squares fitting of the data obtained using FEA computations. The torque-speed envelope is then obtained by calculating the maximum average torque using (3) for a given speed $\omega_s$ and maximum current $I_{max}$ over the speed range of the motor.

The torque-speed envelope, shown in Fig. 2.8, is obtained using the method outlined in [GOS13] with the difference that the voltage limit of the motors is set to be equal to the maximum voltage at the base speed, maximum current, and MTPA current angle. This is performed to obtain torque-speed envelopes with the same base speed, thus allowing for a fair comparison of the torque-speed envelopes of the baseline motor with a step-skewed rotor and a non-skewed rotor. Fig. 2.8 shows that the discrepancy between the torque-speed envelopes of the baseline motor with a step-skewed rotor and a non-skewed rotor above base speed decreases with increasing rotational speed.

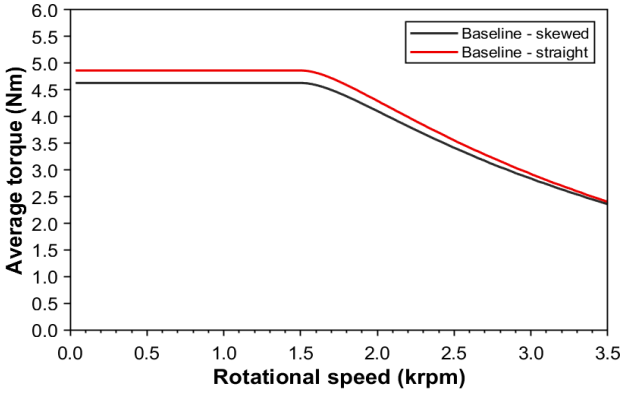



Fig. 2.8. Torque-speed envelope of baseline 12-slot/8-pole IPM motor.

## 2.3 Influence of Design Parameters on Motor Torque

The sensitivity of the cogging torque to various design parameters was analysed using a o one-variable-at-a-time parametric sweep [WAH13]. The influence of the analysed design parameters on the cogging torque is shown in Fig. 2.9, Fig. 2.10, and Fig. 2.11.

The cogging torque decreases slightly with increasing split ratio since the pole-area increases while the PM volume is constant, thus resulting in a decrease in air-gap magnetic flux density. The influence of the stator back-iron width and the rotor rib width on the cogging torque is very low since the B-H operating point of the material does not vary significantly under no-load condition. The influence of an increase in stator tooth width above the nominal value on the cogging torque is negligible. However, a lower tooth width results in lower cogging torque due to magnetic saturation in the tooth. As can be seen in Fig. 2.10(b), cogging torque increases significantly with the slot opening width.

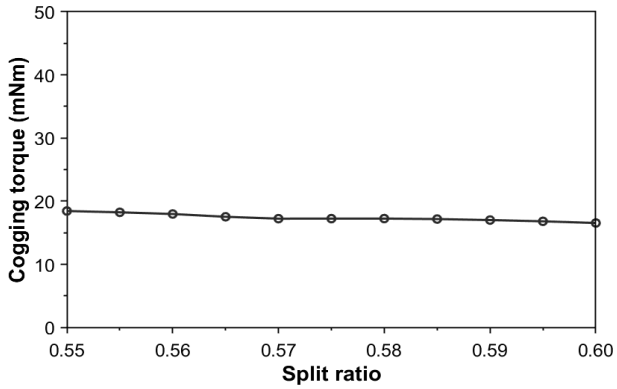
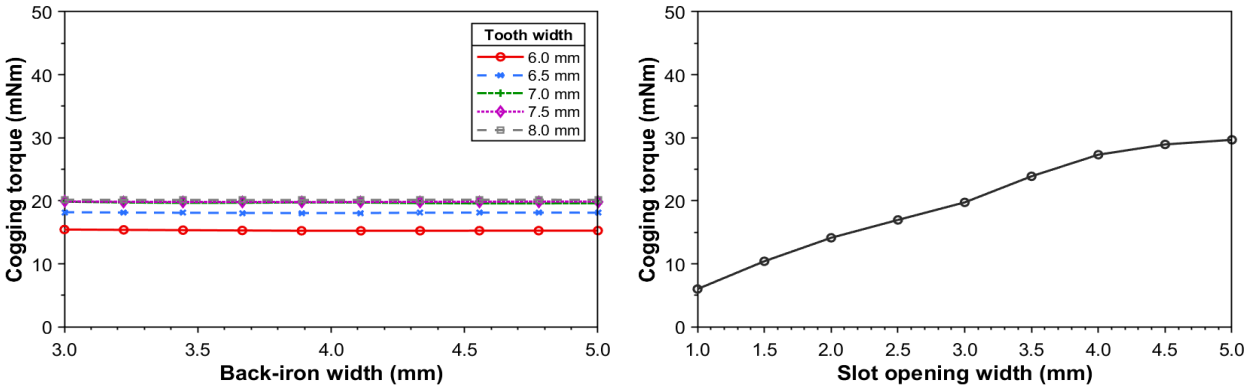


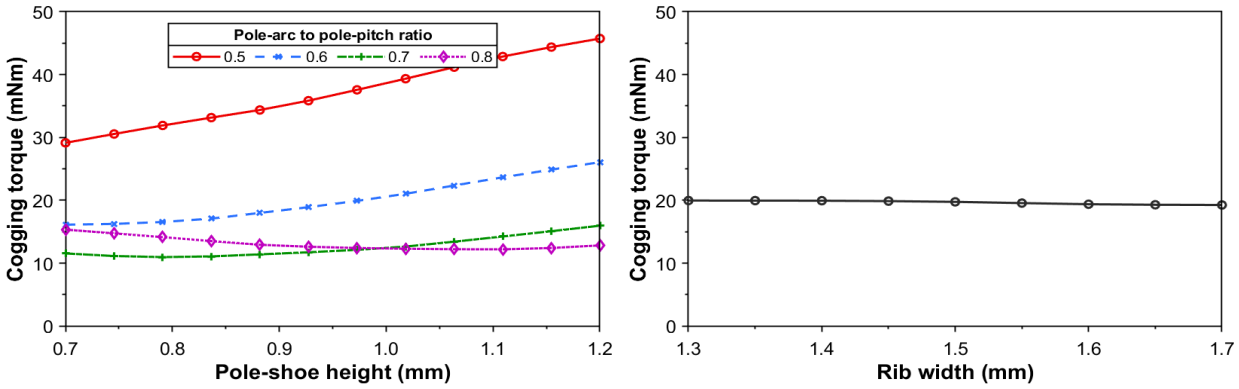

Fig. 2.9. Influence of split ratio on cogging torque of baseline IPM motor.




(a) Stator back-iron and tooth widths (b) Slot opening width

Fig. 2.10. Influence of stator design parameters on cogging torque of baseline IPM motor.

The rotor pole-shoe dimensions affect the saliency of the motor, and consequently, the cogging torque. The cogging torque decreases with increasing pole-shoe height. The sensitivity of the cogging torque to a change in pole-shoe height decreases with increasing pole-arc to pole-pitch ratio. The cogging torque increases with increasing pole-shoe height in motors with lower pole-arc to pole-pitch ratio.




(a) Pole-shoe height (b) Rib width

Fig. 2.11. Influence of rotor design parameters on cogging torque of baseline IPM motor.

The one variable at a time analysis is repeated for the operating point at base speed, maximum current, and zero current angle to investigate the sensitivity of the average torque and torque ripple to design parameters. The influence of the analysed design parameters on average torque is shown in Fig. 2.12, Fig. 2.13, and Fig. 2.14.

The average torque decreases with increasing split ratio, stator tooth width, and stator back iron width, due to the decreasing air-gap magnetic flux density. Similarly, wider stator teeth and back-iron result in lower average toque due to the lower magnetic flux density in the stator material. The influence of that stator slot opening width on the average torque is low. However, narrower slots lead to increased inter-pole flux leakage through the stator teeth resulting in lower average torque.

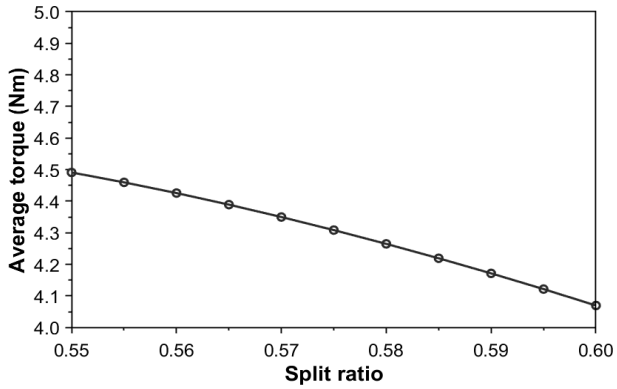
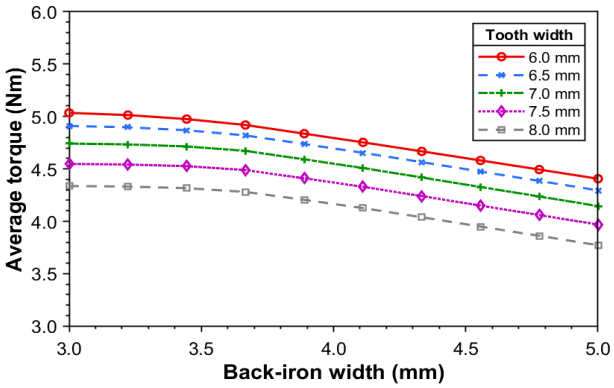
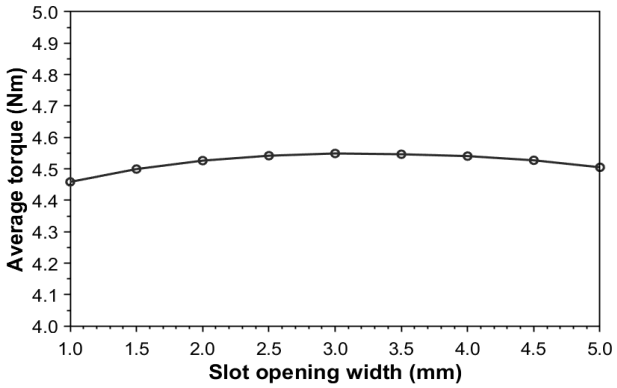



Fig. 2.12. Influence of split ratio on average torque of baseline IPM motor.



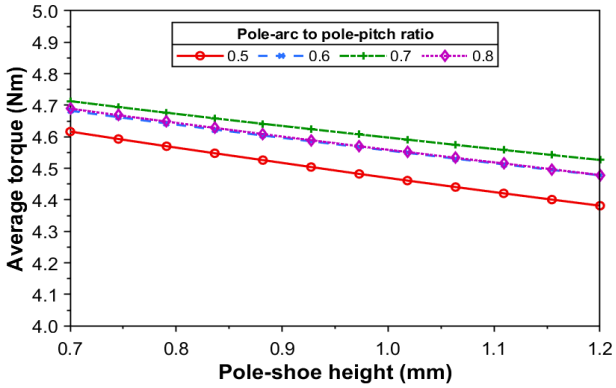

(a) Stator back-iron and tooth widths



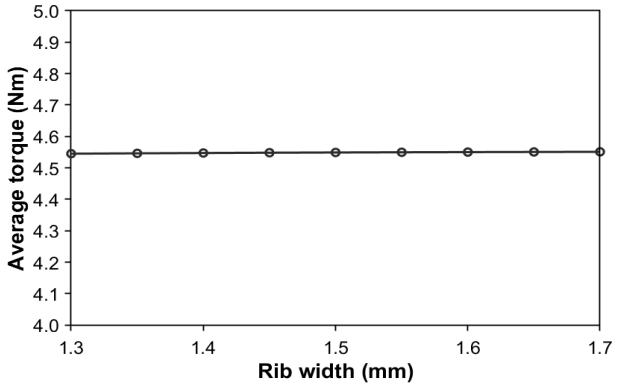

(b) Slot opening width

Fig. 2.13. Influence of stator design parameters on average torque of baseline IPM motor.

Higher pole-shoe heights lead to an increased maximum air-gap length, and consequently, to increased saliency. The average torque decreases with increasing pole-shoe height. The motor saliency is also determined by the pole-arc to pole-pitch ratio. The average torque of motors with a pole-arc to pole-pitch ratio of 0.6 and 0.8 is almost identical, independent from the value of the pole-shoe height. The influence of the rib width on the average torque of the motor is negligible since the increase in flux leakage through the saturated rotor rib is very small.




(a) Pole-shoe dimensions




(b) Rib width

Fig. 2.14. Influence of rotor design parameters on average torque of baseline IPM motor.

The torque ripple increases with increasing split ratio and this may be attributed to the fact that the PM cavity geometry changes as the split ratio increases given that the PM dimensions and rotor rib dimensions are kept constant. The influence of the stator back iron and the tooth dimensions on the torque ripple is non-linear. A thin back-iron and tooth results in increased material saturation, and consequently, in increased torque ripple. A thicker back-iron combined with a thicker tooth results in increased torque ripple attributed to the increased slot leakage. The torque ripple increases in the case of slot openings above the nominal value due to the lower tooth-tip width. Furthermore, low slot opening results in increased torque ripple due to the increased inter-pole flux leakage through the stator tooth-tip.

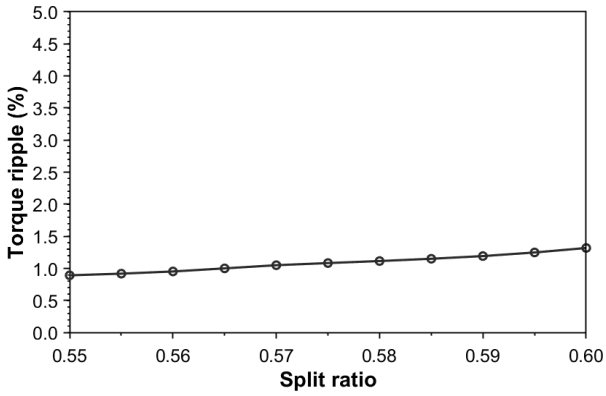
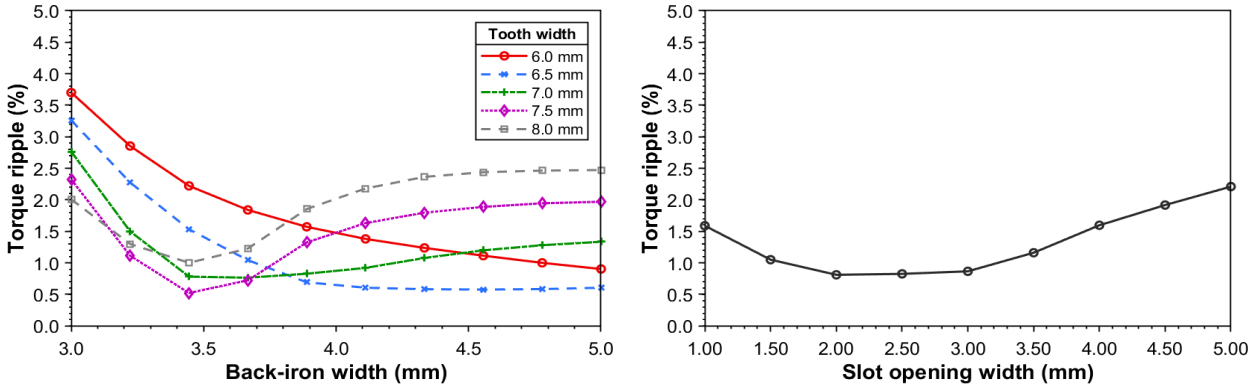


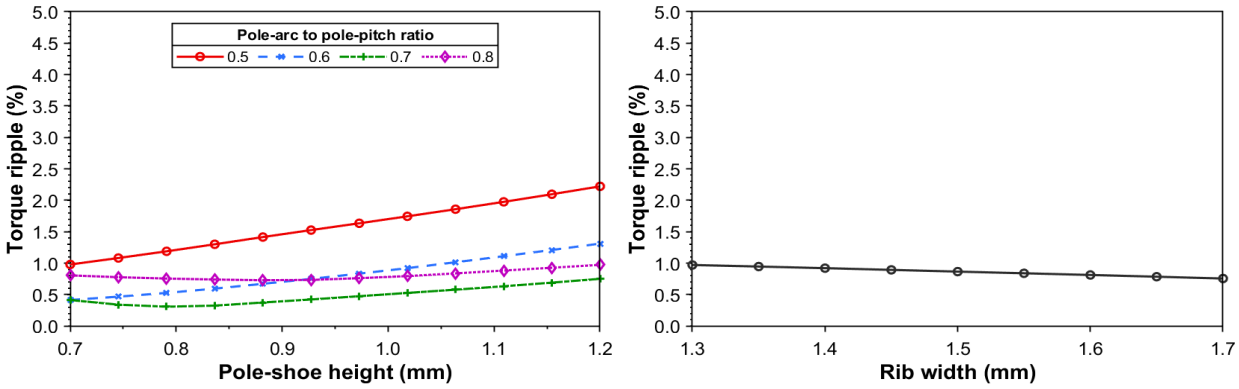

Fig. 2.15. Influence of split ratio on torque ripple of baseline IPM motor.




(a) Stator back-iron and tooth widths (b) Slot opening width

Fig. 2.16. Influence of stator design parameters on torque ripple of baseline IPM motor.

Higher pole-shoe heights lead to an increased maximum air-gap length, and consequently, to increased saliency. The influence of the pole-shoe height on the torque ripple decreases with increasing pole-arc angle. The torque ripple increases with increasing pole-shoe height for lower values of the pole-arc angle. The influence of the rib width on the torque ripple is low. The torque ripple decreases with increasing rib width despite the negligible change in average torque.

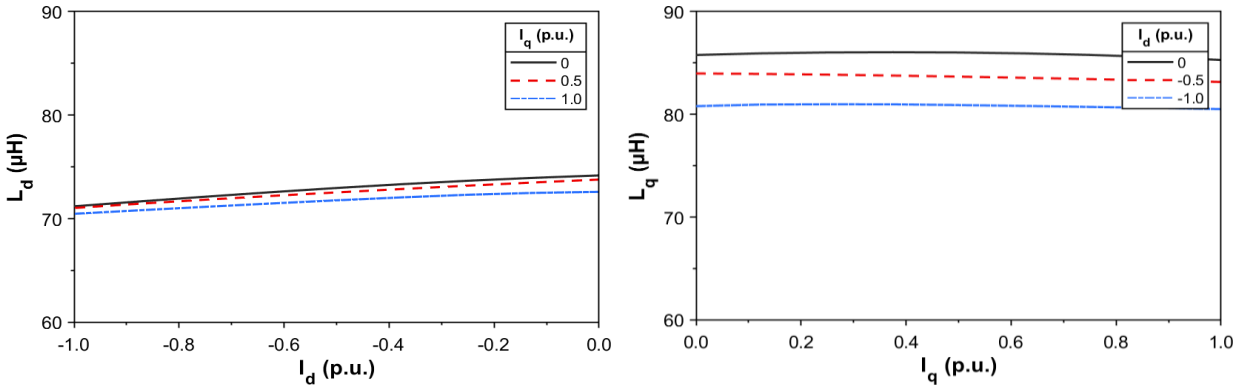



(a) Pole-shoe dimensions (b) Rib width

Fig. 2.17. Influence of rotor design parameters on torque ripple of baseline IPM motor.

## 2.4 Influence of Load and Current Angle on Motor Torque

The influence of electric load and current angle on the d- and q- axis inductances is shown in Fig. 2.18. The motor inductances are calculated using ANSYS Maxwell which computes an inductance matrix based on the energy stored in a structure given certain excitations. The d-axis inductance is lower than the q-axis inductance, thus resulting in reluctance torque. The d-axis inductance decreases with increasing negative d-axis current since negative d-axis current results in lower flux linkage. The d-axis inductance decreases slightly with increasing q-axis current. The q-axis inductance does not change significantly with increasing q-axis current. Negative d-axis current results in a flux weakening effect affecting flux linkage and q-axis inductance.




(a) $L_d$ (b) $L_q$

Fig. 2.18. Influence of d- and q-axis currents on d- and q-axis inductances of baseline IPM motor.

The average torque of the motor increases linearly with the q-axis current magnitude resulting in a torque constant $k_T$ of 48.4 kNm/A, as shown in Fig. 2.19. The absolute and relative torque ripples, defined in (3) and (4), respectively, of the motor are shown in Fig. 2.20. The absolute torque ripple increases with increasing load level by up to 29 mNm, while the relative torque ripple decreases with increasing load level.

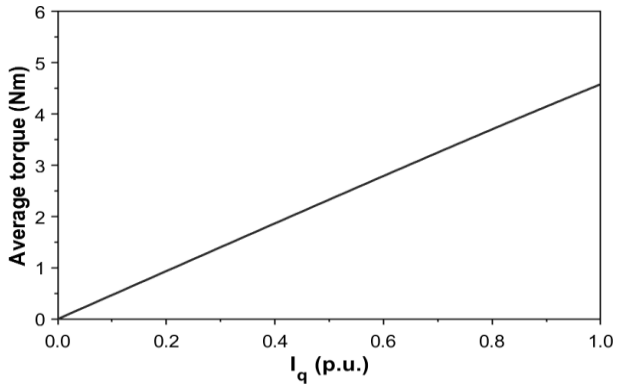
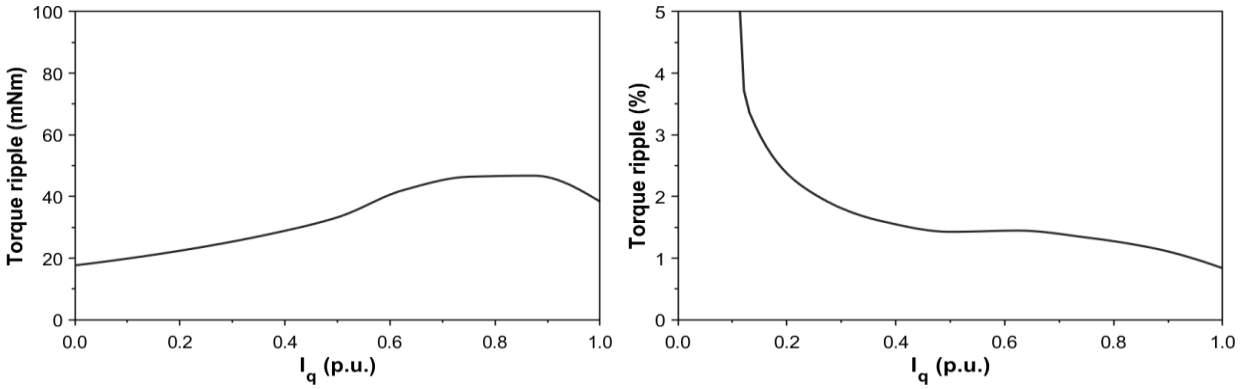


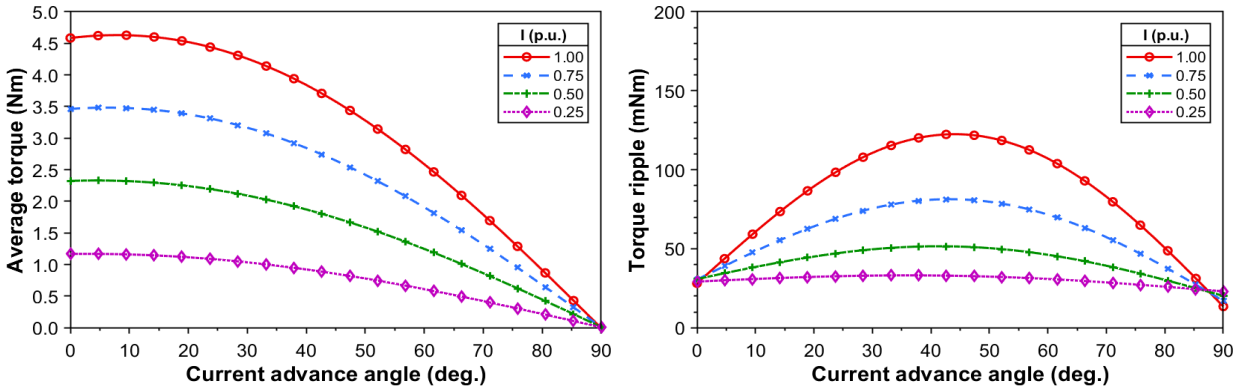

Fig. 2.19. Influence of q-axis current on average torque of baseline IPM motor given zero d-axis current.




(a) Absolute torque ripple (b) Relative torque ripple

Fig. 2.20. Influence of load on torque ripple of baseline IPM motor given zero d-axis current.

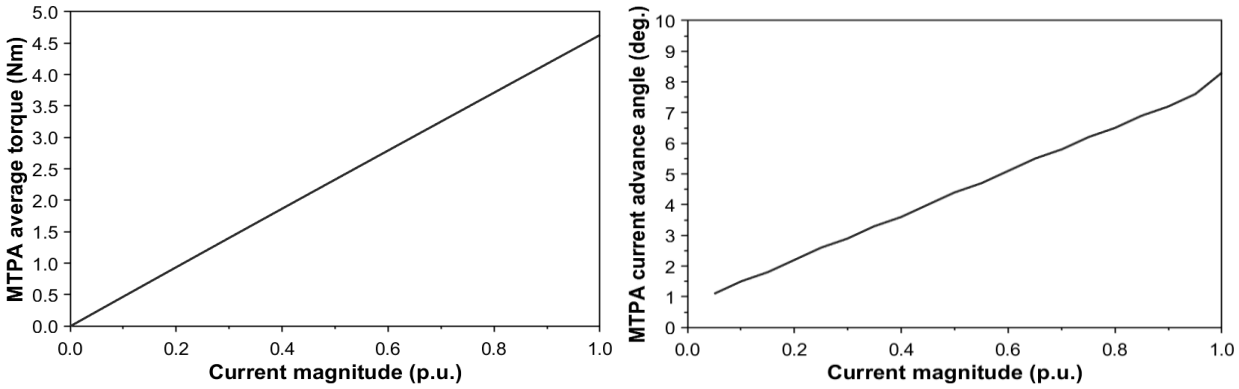
The influence of load and current angle on the average torque and torque ripple of the baseline motor is shown in Fig. 2.21. The maximum average torque of the motor is obtained at a non-zero current angle due to the saliency of the motor and the optimal current angle for maximum average torque is dependent on the load level. The variation of the torque ripple with current angle increases with increasing load level. The torque ripple at low load levels is slightly higher than the cogging torque.




(a) Average torque (b) Torque ripple

Fig. 2.21. Influence of load and current angle on average torque and torque ripple of baseline IPM motor.

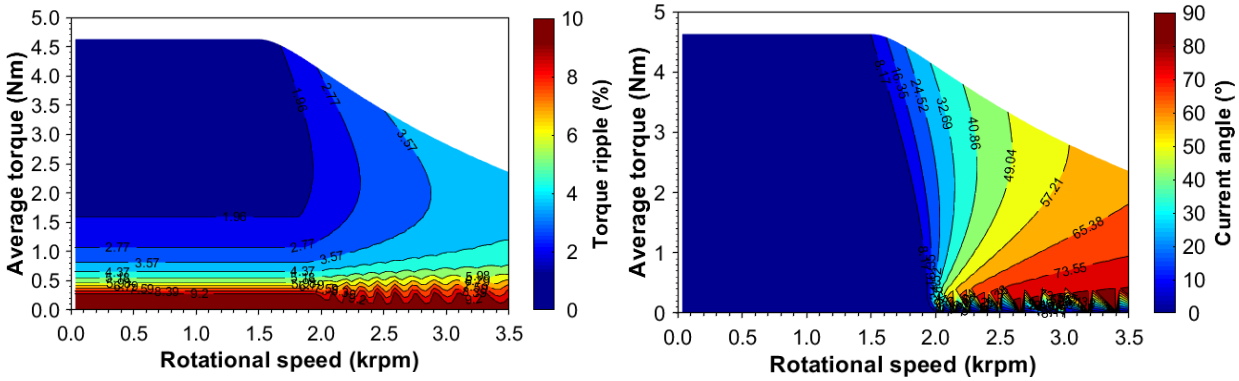
The MTPA average torque and the corresponding current advance angle for a given current magnitude at the base speed are shown in Fig. 2.22. The MTPA average torque increases linearly with increasing current magnitude. Similarly, the current angle increases in a quasi-linear manner with increasing current angle since the saliency of the motor is dependent on load level.




(a) MTPA average torque (b) MTPA current advance angle

Fig. 2.22. Influence of current magnitude on the MTPA average torque and current angle of baseline IPM motor at base speed.

Response Surface Methodology (RSM) is used to calculate the flux linkage, average torque, and torque ripple as a function of the d- and q-axis currents. The parameters are combined with the MTPA algorithm to obtain the average torque, torque ripple, load, and current angle across the operating range of the motor. The method is discussed in more detail in Appendix. The torque ripple and current angle maps of the baseline motor are shown in Fig. 2.23. The torque ripple at low load levels is very high since the average toque is very low. The torque ripple in the constant torque region does not vary significantly with a change in load given that the average torque is higher than approximately 1.5 Nm. The torque ripple in the flux-weakening region increases with increasing rotational speed due to the increase in current angle required to maintain the voltage constant.




(a) Torque ripple (b) Current angle

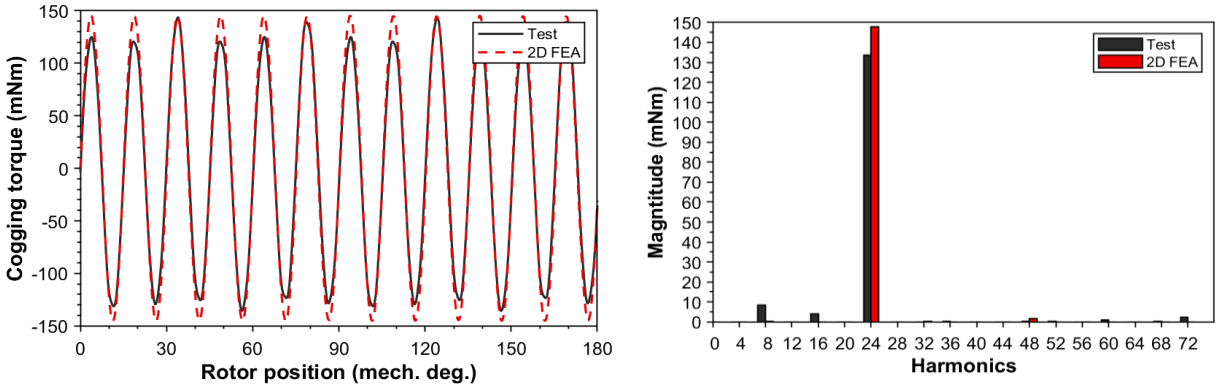
Fig. 2.23. Torque ripple and current angle maps of baseline IPM motor across the operating range.

## 2.5 Comparison with Experimental Results

The unprecedented circumstances brought by the global pandemic at the time of writing affected the development and experimental testing of prototypes of the baseline motor.

The baseline motor was used in an experimental study performed in [GE16] that analysed the influence of the various skew configurations on the cogging torque. The utilised PMs have a remanence of 1.32 T and coercivity of 972.6 kA/m. The baseline motor is modelled with a non-skewed rotor and with 3-step skew by an angle of -5°, 0°, and 5°. Thus, the constructed 2D FEA model is adapted to the motor tested in [GE16] to demonstrate the efficacy of the constructed 2D FEA model.

The cogging torque of the motor with a non-skewed rotor obtained experimentally and using FEA is shown in Fig. 2.24. The cogging torque obtained using FEA has a slightly higher fundamental 24$^{th}$ order harmonic than that obtained experimentally. The cogging torque obtained experimentally has 8$^{th}$ and 16$^{th}$ order torque harmonics attributed to tolerances in the stator geometry, as will be discussed in the subsequent chapters. The difference in peak-to-peak cogging torque between the two waveforms is 5%.

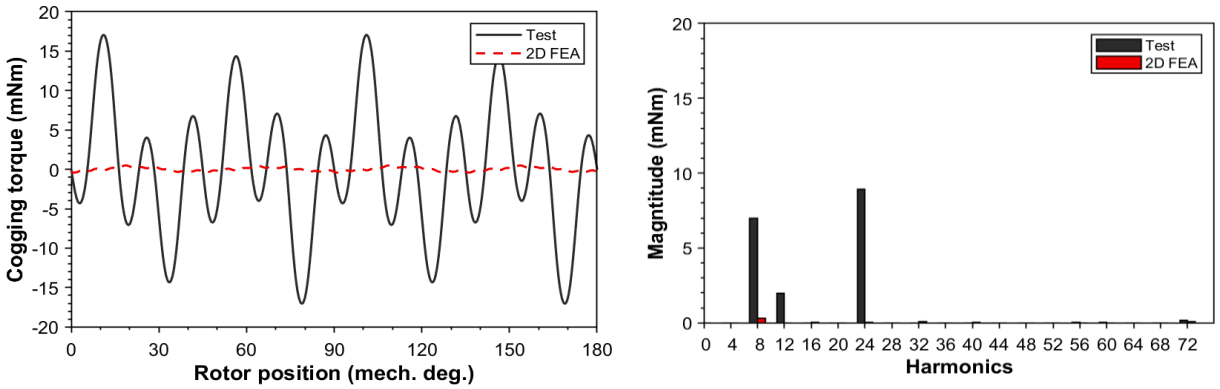



(a) Waveforms (b) Harmonics

Fig. 2.24. Cogging torque of the baseline motor with a non-skewed rotor.

The cogging torque of the baseline motor with 3-step-skewing (-5°, 0°, and 5°) is shown in Fig. 2.25. Theoretically, the a motor with 3-step rotor skew with skewing angles of -5°, 0°, and 5° results in almost zero cogging torque. Thus, the cogging torque obtained using 2D FEA is negligible.

The cogging torque of the prototype motor is significantly higher than that obtained using 2D FEA. The cogging torque obtained experimentally is composed of a fundamental 24$^{th}$ order harmonic as well as the 8$^{th}$ and 12$^{th}$ order harmonic components. The 8$^{th}$ order harmonic is attributed to imperfections in the stator and the 12$^{th}$ order harmonic is attributed to imperfections in the rotor, as will be discussed in subsequent chapters. The 24$^{th}$ order harmonic is attributed to axial effects such as end-effects and the interaction between adjacent rotor pucks.




(a) Waveforms (b) Harmonics

Fig. 2.25. Cogging torque of the baseline motor with step-skewed rotor.

## 2.6 Conclusion

The electromagnetic performance of the baseline 12-slot/8-pole IPM motor is analysed using 2D FEA. The baseline motor has a modular stator allowing easier implementation of concentrated windings. The rotor comprises eccentric pole shaping and 3-step-skew to mitigate cogging torque.

The motor torque is analysed under no-load and on-load condition given zero d-axis current. The peak-to-peak cogging torque is 19.4 mNm, the on-load average torque is 4.6 Nm, and the torque ripple is 34.6 mNm.

The influence of design parameters on the no-load and on-load torque of the motor given zero d-axis current is investigated. The influence of changes in the split ratio, stator back-iron width, and rib width on the cogging torque is not significant. The cogging toque increases with increasing slot opening width. The influence of the pole-shoe height on the cogging torque decreases with increasing pole-arc to pole-pitch ratio.

The average torque is sensitive to changes in the split ratio, stator back-iron width, stator tooth width, and pole-shoe dimensions due to the significant impact on the air-gap magnetic flux density and the operating point of the stator material. Similarly, the torque ripple is very sensitive to changes in the stator back-iron width, stator tooth width, and pole-shoe dimensions.

The influences of electric load and current angle on the motor inductances and torque characteristics are investigated. The d-axis inductance is lower than the q-axis inductance resulting in reluctance torque. The influence of the q-axis current on the d-axis inductance is fairly low. Conversely, the influence of negative d-axis current on the q-axis inductance is significant due to the inherent flux weakening effect attributed to negative d-axis currents. The average torque increases linearly with load and the relative torque ripple decreases with increasing load.

Analysis of the influence of the current angle on the average torque shows that the maximum average torque occurs at a current angle of 8.3° and that the magnitude of the reluctance torque decreases with

decreasing load level. The sensitivity of the absolute torque ripple to current angle increases significantly with increasing load. Maps of the torque ripple and current angle across the entire torque-speed operating range of the motor were calculated. The torque ripple does not vary significantly in the constant toque region and increases significantly with increasing rotational speed due to the increase in current angle.

A prototype of the baseline motor with some minor modifications to the PM material and the rotor step-skewing angles has been tested in a previous study [GE16]. The 2D FEA model used in this analysis was adapted to the prototype and the cogging torque of the motor with and without rotor step-skew was analysed. The difference peak-to-peak cogging torque of the motor without rotor step-skew obtained experimentally and using 2D FEA is 5%. The cogging torque of the motor with rotor step-skew obtained using 2D FEA is negligible compared that obtained experimentally. This discrepancy is due to the fact that axial effects such as end-effects and interaction between rotor steps are not accounted for in 2D FEA. It is shown that the measured peak cogging torque and harmonics are significantly higher than those obtained using 2D FEA, attributed to imperfections in the stator and the rotor, which clearly demand an in-depth investigation on the influence of manufacturing tolerance and imperfections, as will be discussed in subsequent chapters.

# 3 SINGLE- AND MULTI-OBJECTIVE OPTIMISATION OF IPM MOTORS

## 3.1 Introduction

Global optimisation can be used to determine the limit of a particular design objective or the compromise between two or more objectives, as discussed in Chapter 1. Single-objective optimisation is usually used to identify the motor design that produces the highest average torque, and the multi-objective optimisation is often used to identify the compromise between the average torque and torque ripple of the motors.

The first step of the design optimisation process is to identify the optimisation algorithm and the optimisation objective(s), to define the design constraints, i.e. the fixed parameters of the motor, and any overall assumptions adopted during the optimisation process. The genetic algorithm is adopted in this chapter using a population of 64 motors and 50 generations, and is used in the single- and multi-objective optimisation of the IPM motors with different slot/pole number combinations. The number of variable parameters directly affects the required population size and the number of generations used in the genetic algorithm. A higher number of parameters requires a larger population to ensure an adequate representation of the parameter space, and a higher number of generations to ensure adequate convergence in single-objective optimisation and parameter diversity on the Pareto-front(s) of multi-objective optimisation.

Design optimisation is performed at maximum current and at base speed, and the optimisation constraints are listed in Table 2.2. Material properties and certain application dependent dimensions of the baseline motor are fixed during the optimisation process. The outer diameter and stack length of the motors, as well as the air-gap length and the rotor iron bridge width are fixed. The gross slot current density, and consequently, the Ampere-turns of the motor, is fixed to ensure that the optimised motors have similar thermal characteristics. The rotor of the baseline motor comprises a three-step skew. However, the optimisation is performed on the motors with non-skewed rotors for simplicity. It is assumed that the temperature and winding resistance are constant for all motors and all losses are neglected. As a rule of thumb, the iron bridge width of the IPM motor must be at least as thick as the lamination itself, and therefore, a thickness of 0.5 mm is chosen.

Table 2.2. Fixed design parameters of the IPM motor optimisation

| Parameter | Value |
|---|---|
| Outer diameter | 85 mm |
| Stack length | 37.5 mm |
| Gross slot current density | 9.57 A/mm$^2$ |
| Air-gap length | 0.6 mm |
| Rotor skew | N/A |
| Rotor bridge width | 0.5 mm |
| PM remanence | 1.38 T |
| PM coercivity | -1100 kA/m |
| Operating temperature | 20°C |

The variable design parameters in the single- and multi-objective optimisations are:

- Split ratio
- Stator back-iron width
- Stator tooth width
- Stator slot opening width
- Rotor pole-arc to pole-pitch ratio
- Rotor pole-shoe height
- Rotor iron rib width
- PM width
- PM height

The motor designs obtained using single- and multi-objective optimisation of 12-slot/8-pole, 12-slot/10-pole, and 12-slot/14-pole IPM motors are outlined in this chapter. The sensitivity of the torque to changes in variable design parameters is then analysed and a torque ripple map over the torque-speed operating range is determined using the method in Appendix A.

The selection of slot/pole number combinations to be considered was steered by industry research interest and limitations attributed to the given outer stator diameter. Furthermore, 9-slot/8-pole and 9-slot/10-pole motors could not be considered for this application due to inherent high acoustic noise attributed to unbalanced magnetic force and low vibration mode number.

There are various methods that can be used to determine the sensitivity of a quantity due to changes in design parameters. The one-variable-at-a-time method is used in this chapter to produce a 2-level experimental design of the optimised motor at the optimised operating point. The two levels of each variable are set to be above and below the nominal value by a certain amounts the main effect plots of the average torque and the torque ripple are determined. The main effect plot is used to understand how a set of variables at different levels affect the mean of a response.

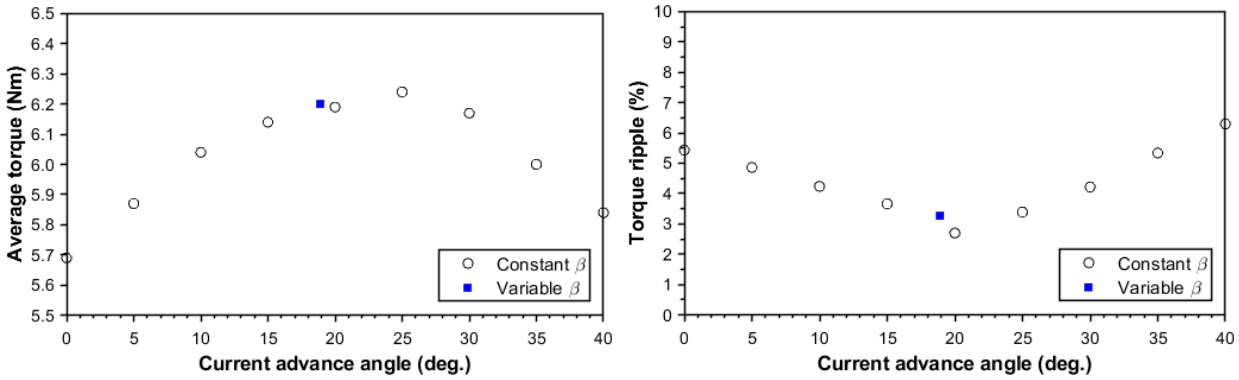
The motor designs obtained by single- and multi-objective optimisations are then analysed to understand the key differences between different topologies, and the optimised designs are compared with the baseline IPM motor.

## 3.2 Single-objective Optimisation of IPM Motors

### 3.2.1 Optimisation of 12-slot/8-pole IPM Motor

The single-objective optimisation is performed with constant current angle and with the current angle as a design variable respectively to identify the merits of the two methods. The optimisation with a constant current angle is repeated for different current angles to show the influence of the current angle on the maximum average torque and for comparison with the optimisation with variable current angle.

Fig. 2.26 shows the maximum average torque of the motors optimised with constant or variable current angle, and the corresponding torque ripple of the optimised motors. The optimisation with variable current angle is converged to a current angle of 18.9° and the torques of the motors with constant current angle are approximately the same for current angles equal to 20°, 25°, and 30°. The torque ripple of the optimised is the lowest at the current angle equal to 20° and increases almost linearly with changing current angle.




(a) Average torque (b) Torque ripple

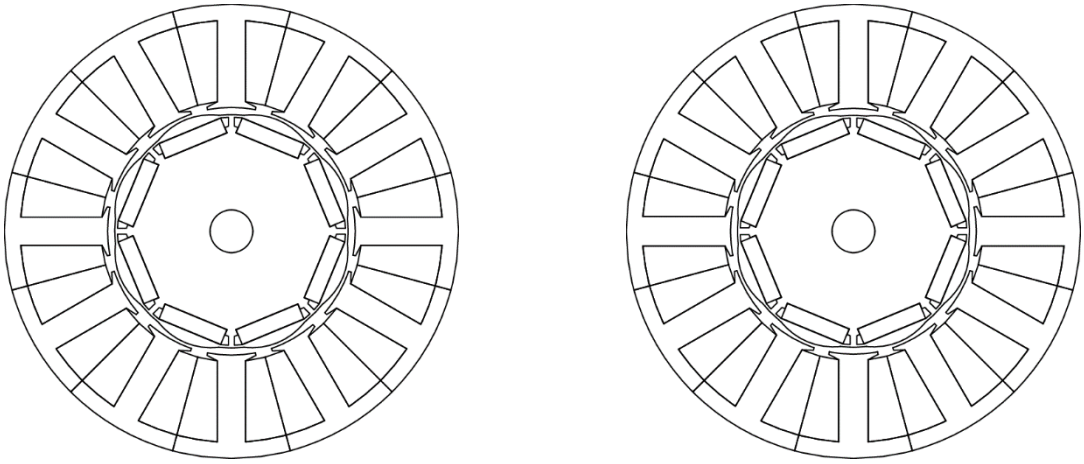
Fig. 2.26. Influence of current angle on torque of optimised motors.

The design parameters of the motors optimised with a constant current angle of 25° and with current angle as a variable are listed in Table 2.3, and the cross-sections are shown in Fig. 2.27. The torque-speed characteristics of the optimised motors and the torque ripples across the torque-speed range are shown in Fig. 2.28. The relative torque ripple increases with decreasing average torque. Furthermore, the torque ripple increases with increasing rotational speed.

The two methods of optimisation converged to designs with almost identical average torque, torque ripple and motor cross-sections. Optimisation with a constant current angle is useful to identify the maximum average torque for a motor design at a particular current magnitude and current angle. However, this method requires multiple runs to obtain the maximum average torque and the optimum current angle. Thus, while both methods are effective at optimising the average torque, optimisation with constant current angle actually requires a significant increase in computational time since the optimisation is repeated for a set of current angle values. The subsequent motor optimisations are therefore performed with the current angle as a design variable.

Table 2.3. Design parameters of optimised 12-slot/8-pole IPM motor

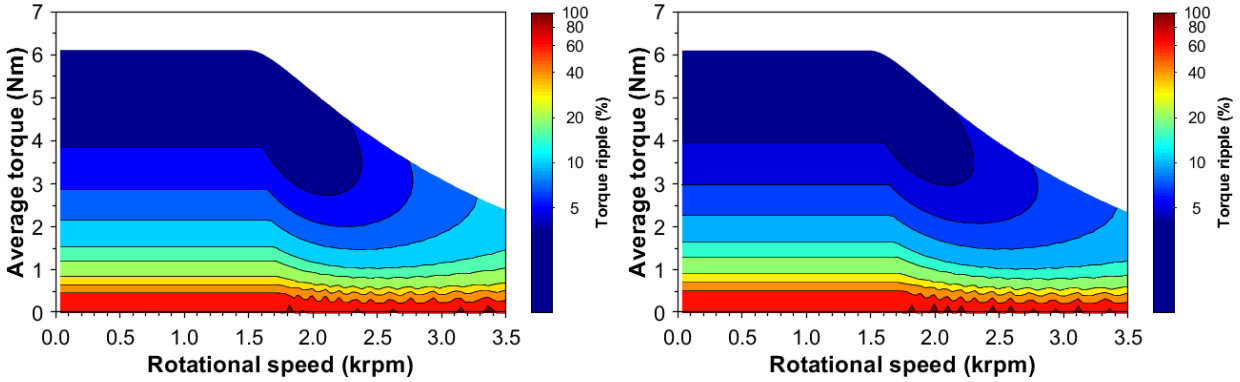
| **Parameter** | **Units** | **Values** | |
|---|---|---|---|
| | | **Constant $\beta$** | **Variable $\beta$** |
| Average torque | Nm | 6.2 | 6.2 |
| Torque ripple | % | 3.1 | 3.0 |
| Current advance angle | ° | 25.0 | 18.9 |
| Pole-arc to pole-pitch ratio | N/A | 0.725 | 0.717 |
| Pole-shoe height | mm | 0.75 | 0.71 |
| Rib width | mm | 1.08 | 1.26 |
| Tooth width | mm | 5.28 | 5.52 |
| Back-iron width | mm | 3.03 | 3.03 |
| Split ratio | N/A | 0.538 | 0.534 |
| Slot opening width | mm | 3.13 | 2.95 |
| PM height | mm | 2.97 | 2.98 |
| PM width | mm | 12.49 | 12.48 |
| PM volume | $cm^3$ | 11.12 | 11.17 |
| Torque per Volume | Nm/L | 29.14 | 29.14 |
| Torque per PM Volume | $Nm/cm^3$ | 0.557 | 0.555 |



(a) Constant current angle (b) Variable current angle

Fig. 2.27. Cross-sections of optimised 12-slot/8-pole IPM motors.

Adopting unified slot opening width across a set of motors is useful in the manufacturing process of the motors. Therefore, the slot opening width of the optimised motor is set to 3 mm, and identical to that of the baseline IPM motor. Of course, the slot opening may be varied in the manufacturing process, particularly for a modular stator. Thus, its influence will also be investigated.




(a) Constant current angle (b) Variable current angle

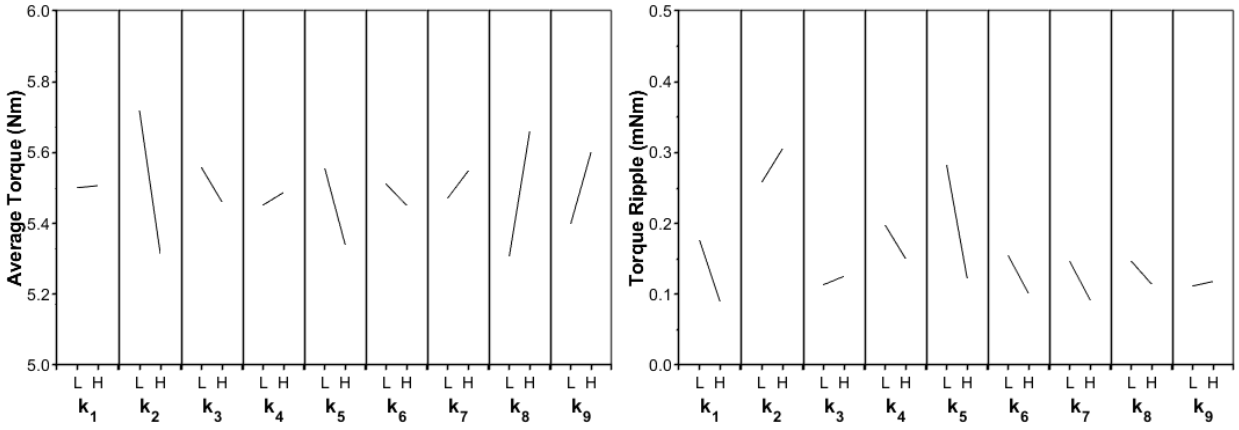
Fig. 2.28. Torque-speed characteristics of optimised 12-slot/8-pole IPM motors.

The sensitivity analysis of the motor to changes in design parameters is performed using the one-variable-at-a-time method in which each design parameter is set to be at two levels. The two levels are respectively lower and higher than the nominal value by the amounts listed in Table 2.4 and indicated by L and H in Fig. 2.29. The main effect plot shows the response, in this case the average torque and torque ripple, connected by a line. The gradient of the line indicates the increase or decrease of the response. The change in the response is not necessarily linear and thus further analysis is required to determine the linearity of the response due to a change in a design parameter.

The average torque of the optimised 12-slot/8-pole IPM motor is particularly sensitive to changes in the pole-shoe height and the PM dimensions. The pole-arc to pole-pitch ratio, the tooth width, the split ratio, and the slot opening width do not have a significant influence on the average torque, within the parameter variation ranges. The torque ripple of the IPM motor is very sensitive to changes in the stator back-iron width since a thinner back-iron results in an increase in saturation.

Table 2.4. Nominal design parameters of optimised 12-slot/8-pole IPM motor and the change in parameters used in the analysis

| | **Design parameter** | **Units** | **Change in parameter** | **Nominal value** |
|---|---|---|---|---|
| $k_1$ | Pole-arc to pole-pitch ratio | N/A | ±0.05 | 0.670 |
| $k_2$ | Pole-shoe height | mm | ±0.5 mm | 1.22 |
| $k_3$ | Iron rib width | mm | ±0.5 mm | 1.35 |
| $k_4$ | Tooth width | mm | ±0.5 mm | 5.39 |
| $k_5$ | Back-iron width | mm | ±0.5 mm | 3.29 |
| $k_6$ | Split ratio | N/A | ±2% | 0.543 |
| $k_7$ | Slot opening width | mm | ±0.5 mm | 3.0 |
| $k_8$ | PM height | mm | ±0.5 mm | 2.98 |
| $k_9$ | PM width | mm | ±0.5 mm | 12.07 |




(a) Average torque (b) Torque ripple

Fig. 2.29. Influence of change in design parameters on torque of optimised 12-slot/8-pole IPM motor, calculated using finite element analysis.

### 3.2.2 Analysis of Optimised 12-slot/10-pole IPM Motor

The genetic algorithm with a population of 64 motors and 50 generations is used to optimise the 12-slot/10-pole IPM motor for maximum average torque. The design parameters of the optimised 12-slot/10-pole IPM motor are listed in Table 2.5 and the cross-section is shown in Fig. 2.30. The slot opening width of the optimised motor is fixed to 3 mm and the torque-speed characteristic and the torque ripple map of the motors with optimised and fixed slot opening width are shown in Fig. 2.31.

Table 2.5. Average torque and design parameters of optimised 12-slot/10-pole IPM motor

| **Parameter** | **Units** | **Values** |
|---|---|---|
| Average torque | Nm | 6.1 |
| Torque ripple | % | 1.7 |
| Current advance angle | ° | 16.5 |
| Pole-arc to pole-pitch ratio | N/A | 0.699 |
| Pole-shoe height | mm | 0.73 |
| Iron rib width | mm | 0.87 |
| Tooth width | mm | 5.28 |
| Back-iron width | mm | 3.10 |
| Split ratio | N/A | 0.532 |
| Slot opening width | mm | 3.42 |
| PM height | mm | 2.99 |
| PM width | mm | 9.47 |
| PM volume | $cm^3$ | 10.60 |
| Torque per Volume | Nm/L | 28.67 |
| Torque per PM Volume | $Nm/cm^3$ | 0.575 |

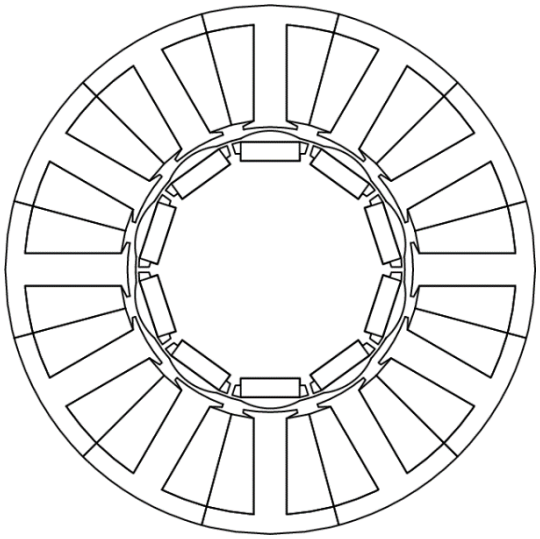
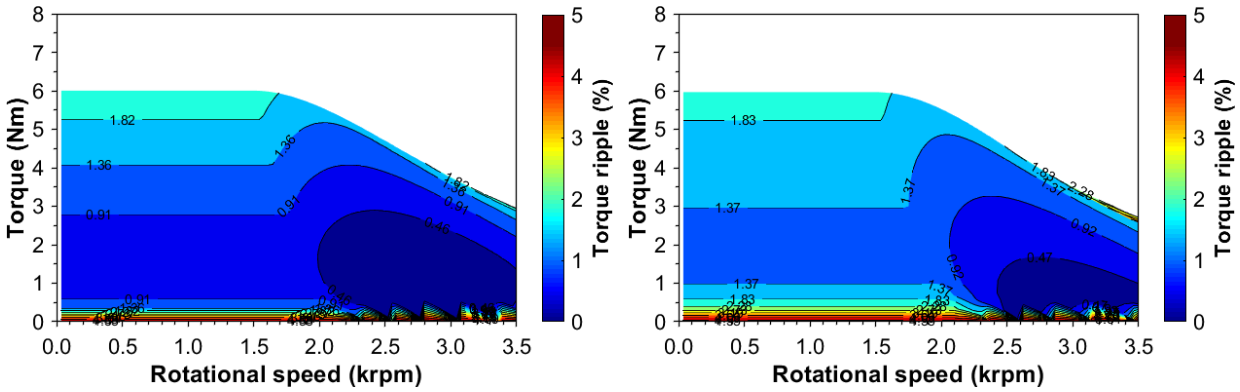


Fig. 2.30. Cross-section of optimised 12-slot/10-pole IPM motor.

The torque ripple at the torque-speed envelope of motor with optimised and fixed slot opening are almost identical. The torque ripple decreases with decreasing average torque and the change in torque ripple is more pronounced in the low speed region. The torque ripple of the motor with a fixed slot opening is higher than that of the motor with an optimised slot opening across the torque-speed range, particularly at lower average torque levels.




(a) Optimised slot opening width (b) Fixed slot opening width

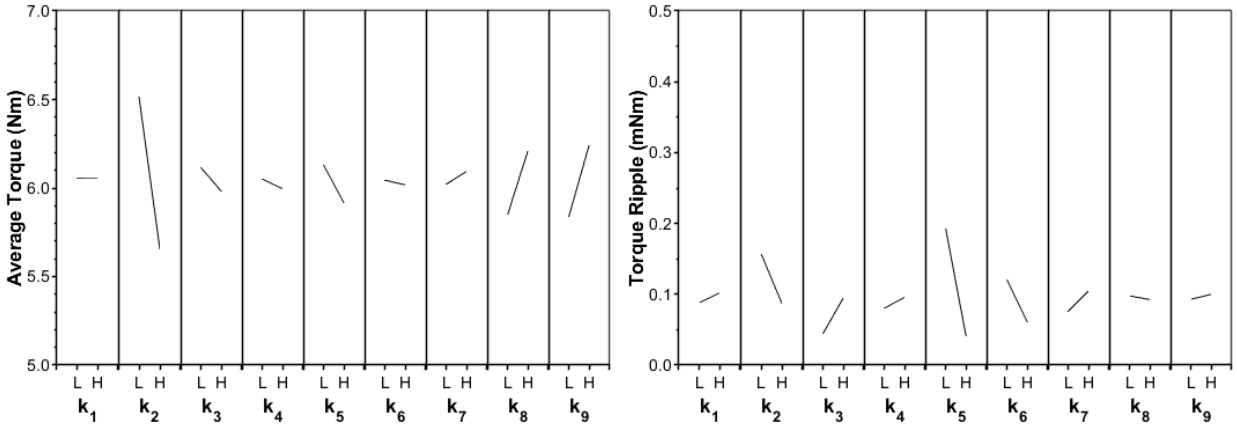
Fig. 2.31. Torque-speed characteristics and torque ripple of optimised 12-slot/10-pole IPM motor.

The main effect plots of the average torque and the torque ripple, based on a 2-level experimental design, are shown in Fig. 2.32. The two levels of each variables are set to be above and below the nominal value by the amounts listed in Table 2.6.

Table 2.6. The nominal design parameters of optimised 12-slot/10-pole IPM motor and change in parameters used in the analysis.

| | **Design parameter** | **Units** | **Change in parameter** | **IPM** |
|---|---|---|---|---|
| $k_1$ | Pole-arc to pole-pitch ratio | N/A | ±0.05 | 0.751 |
| $k_2$ | Pole-shoe height | mm | ±0.5 mm | 0.80 |
| $k_3$ | Iron rib width | mm | ±0.5 mm | 1.65 |
| $k_4$ | Tooth width | mm | ±0.5 mm | 5.27 |
| $k_5$ | Back-iron width | mm | ±0.5 mm | 3.11 |
| $k_6$ | Split ratio | N/A | ±2% | 0.538 |
| $k_7$ | Slot opening width | mm | ±0.5 mm | 3.0 |
| $k_8$ | PM height | mm | ±0.5 mm | 2.81 |
| $k_9$ | PM width | mm | ±0.5 mm | 12.10 |

The pole-shoe height of the IPM motor has a high influence of the average torque of the motor, comparable to that of the PM dimensions. The stator back-iron width has a higher influence on the average torque than the other stator design parameters. The torque ripple is very sensitive to changes in the stator back-iron width due to the attributed saturation levels.




(a) Average torque (b) Torque ripple

Fig. 2.32. Influence of change in design parameters on torque of optimised 12-slot/10-pole IPM motor.

### 3.2.3 Analysis of Optimised 12-slot/14-pole IPM Motor

The cross-section of the optimised 12-slot/14-pole IPM motor using the genetic algorithm is shown in Fig. 2.33 and the design parameters are listed in Table 2.7. The slot opening width of the optimised motor is fixed to 3 mm and the torque-speed characteristic and the torque ripple map of the motors with optimised and fixed slot opening width are shown in Fig. 2.34.

Table 2.7. Average torque and design parameters of optimised 12-slot/14-pole IPM motor

| **Parameter** | **Units** | **Values** |
|---|---|---|
| Average torque | Nm | 5.5 |
| Torque ripple | % | 3.0 |
| Current advance angle | ° | 9.9 |
| Pole-arc to pole-pitch ratio | N/A | 0.663 |
| Pole-shoe height | mm | 0.81 |
| Iron rib width | mm | 0.90 |
| Tooth width | mm | 5.11 |
| Back-iron width | mm | 3.20 |
| Split ratio | N/A | 0.560 |
| Slot opening width | mm | 3.29 |
| PM height | mm | 2.88 |
| PM width | mm | 7.43 |
| PM volume | $cm^3$ | 11.23 |
| Torque per Volume | Nm/L | 25.85 |
| Torque per PM Volume | $Nm/cm^3$ | 0.490 |

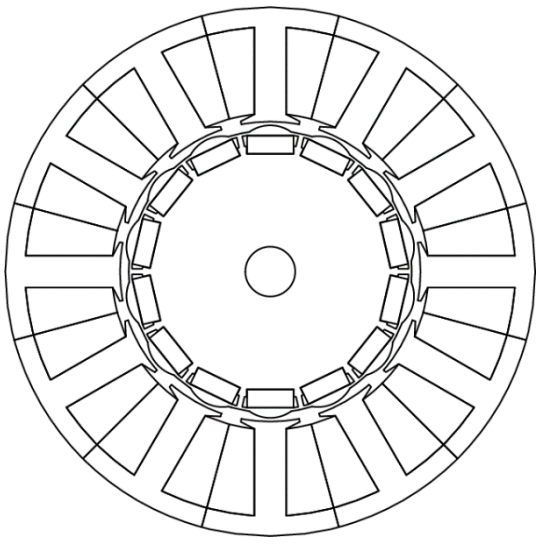
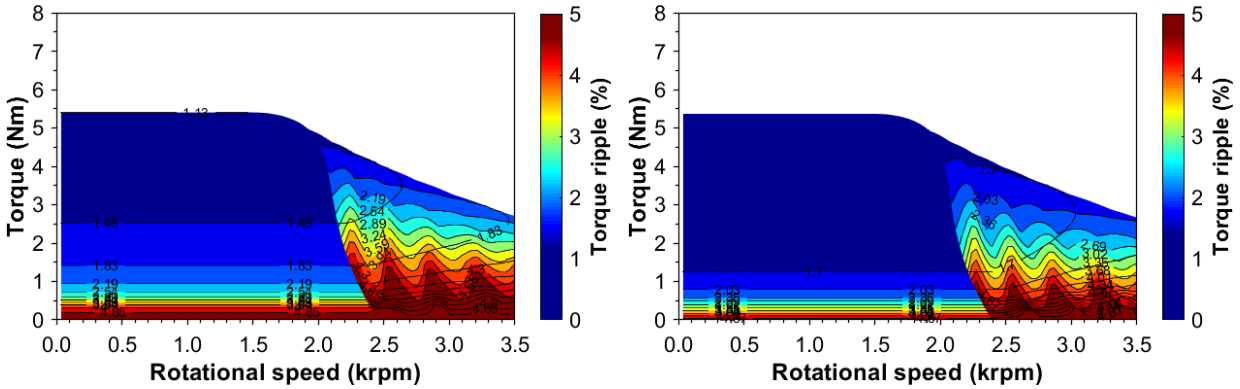


Fig. 2.33. Cross-section of optimised 12-slot/14-pole IPM motor.

The torque-speed characteristics of the motor with optimised and fixed slot opening width are shown in Fig. 2.34. The change in the torque-speed envelope is negligible and the torque ripple map of the motor with fixed slot opening width indicates a net decrease in torque ripple over the torque-speed range.




(a) Optimised slot opening width (b) Fixed slot opening width

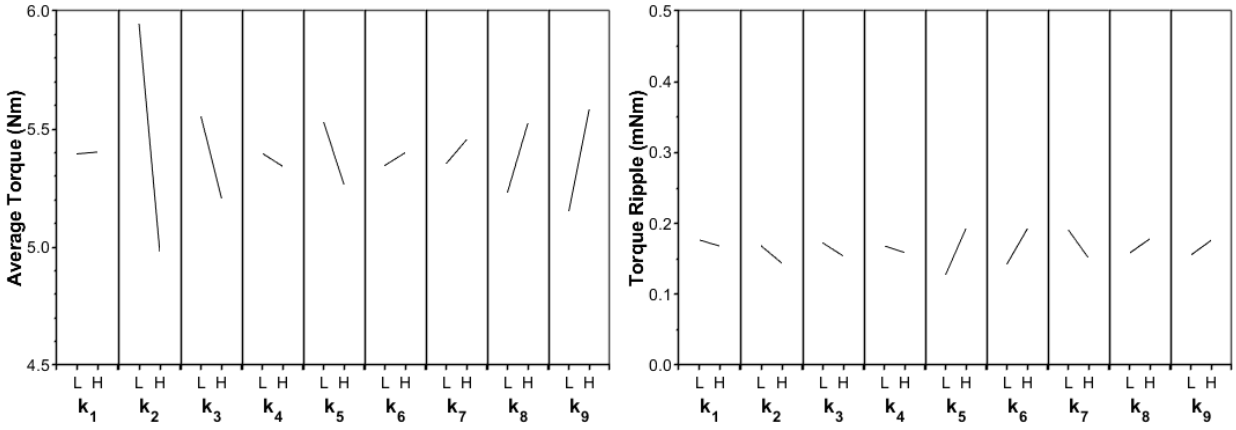
Fig. 2.34. Torque-speed characteristic and torque ripple of optimised 12-slot/14-pole IPM motor.

The main effect plots of the average torque and the torque ripple, based on a 2-level experimental design, are shown in Fig. 2.35. The two levels of each variables are set to be above and below the nominal value by the amounts listed in Table 2.8.

Table 2.8. The nominal design parameters of optimised 12-slot/14-pole IPM motor and change in parameters used in the analysis

| | **Design parameter** | **Units** | **Change in parameter** | **Nominal value** |
|---|---|---|---|---|
| $k_1$ | Pole-arc to pole-pitch ratio | N/A | ±0.05 | 0.663 |
| $k_2$ | Pole-shoe height | mm | ±0.5 mm | 0.81 |
| $k_3$ | Iron rib width | mm | ±0.5 mm | 0.90 |
| $k_4$ | Tooth width | mm | ±0.5 mm | 5.11 |
| $k_5$ | Back-iron width | mm | ±0.5 mm | 3.20 |
| $k_6$ | Split ratio | N/A | ±2% | 0.560 |
| $k_7$ | Slot opening width | mm | ±0.5 mm | 3.29 |
| $k_8$ | PM height | mm | ±0.5 mm | 2.88 |
| $k_9$ | PM width | mm | ±0.5 mm | 7.43 |

The average torque of the 12-slot/14-pole IPM motor is sensitive to the changes in the pole-shoe height and the PM dimensions. The PM width has a slightly higher influence on the average torque than the PM height. The influence of the rib width on the average torque is significant since the high number of rotor ribs results in a higher number of flux leakage paths. The torque ripple is sensitive to changes in the stator tooth width, back-iron, and slot opening width.




(a) Average torque (b) Torque ripple

Fig. 2.35. Influence of change in design parameters on torque of optimised 12-slot/14-pole IPM motor.

## 3.3 Multi-objective Optimisation of IPM motors

### 3.3.1 Optimisation of 12-slot/8-pole IPM Motor

Multi-objective optimisation of the 12-slot/8-pole IPM motor is performed for two objectives: maximum average torque and minimum torque ripple. The aim of the multi-objective optimisation is to locate a Pareto-optimal solution and to identify the Pareto-front showing the compromise between the two objectives in a given solution space. Thus, the limits of the two objectives produced by the selected motors may not be indicative of the actual limits of the motor.

The average torque and torque ripple of the solution space of the optimisation is shown in Fig. 2.36. The colour of the marker indicates the PM volume of each motor design. The torque ripple of the IPM motor is as low as approximately 0.5% and the torque ripple increases as the average torque increases. The solutions with lower average torque have a low PM volume, regardless of the torque ripple. This is expected since the average torque of a motor is directly related to the PM volume of the motor.

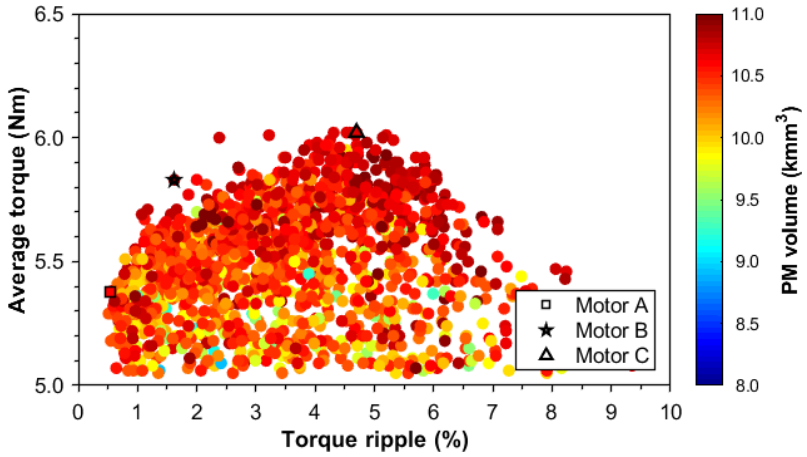


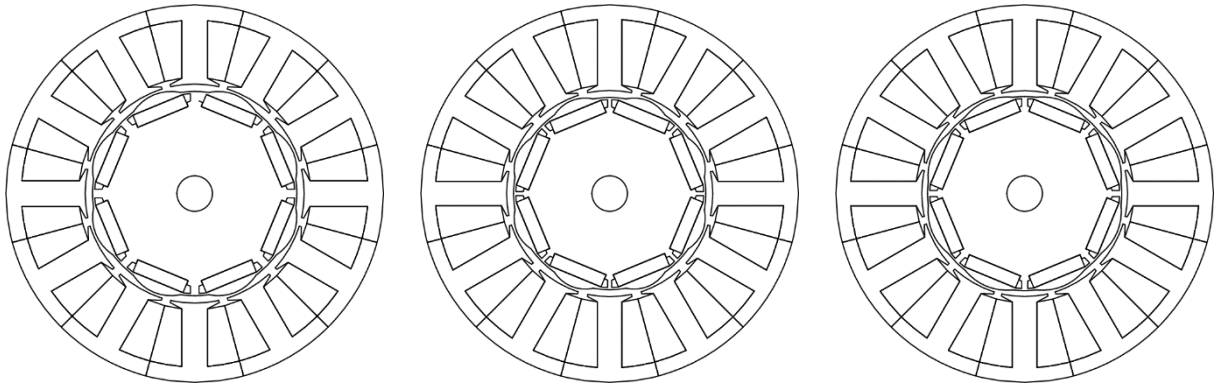

Fig. 2.36. Solution space of multi-objective optimisation of 12-slot/8-pole IPM motor.

The compromise between the average torque and torque ripple, and the impact on the motor design parameters, is investigated by selecting three solutions along the Pareto-front of the solution space, indicated in Fig. 2.36.

The design parameters of the selected motor designs are listed in Table 2.9 and the motor cross-sections are illustrated in Fig. 2.37. The average torque of the selected motors increases from 5.4 Nm to 6.0 Nm and the torque ripple increases from 0.6% to 4.7%. The change in optimised current angle is very low, and the current angles of Motors B and C are identical. The pole-shoe height and the split ratio decrease with increasing average torque. The PM volume of Motor B is 1.8% higher than that of Motor C, however, the average torque is 3.3% lower. The back-iron width decreases with increasing torque and torque ripple while the tooth width increases with increasing torque and torque ripple. This is attributed to the fact that wider teeth result in higher flux linkage and in turn leads to higher average torque. Furthermore, thinner back-iron width results in increased saturation in the stator back iron that in turn leads to higher torque ripple. Furthermore, the average torque and the torque ripple increase with decreasing rotor pole-shoe height.

Table 2.9. Average torque and design parameters of optimised 12-slot/8-pole IPM motors

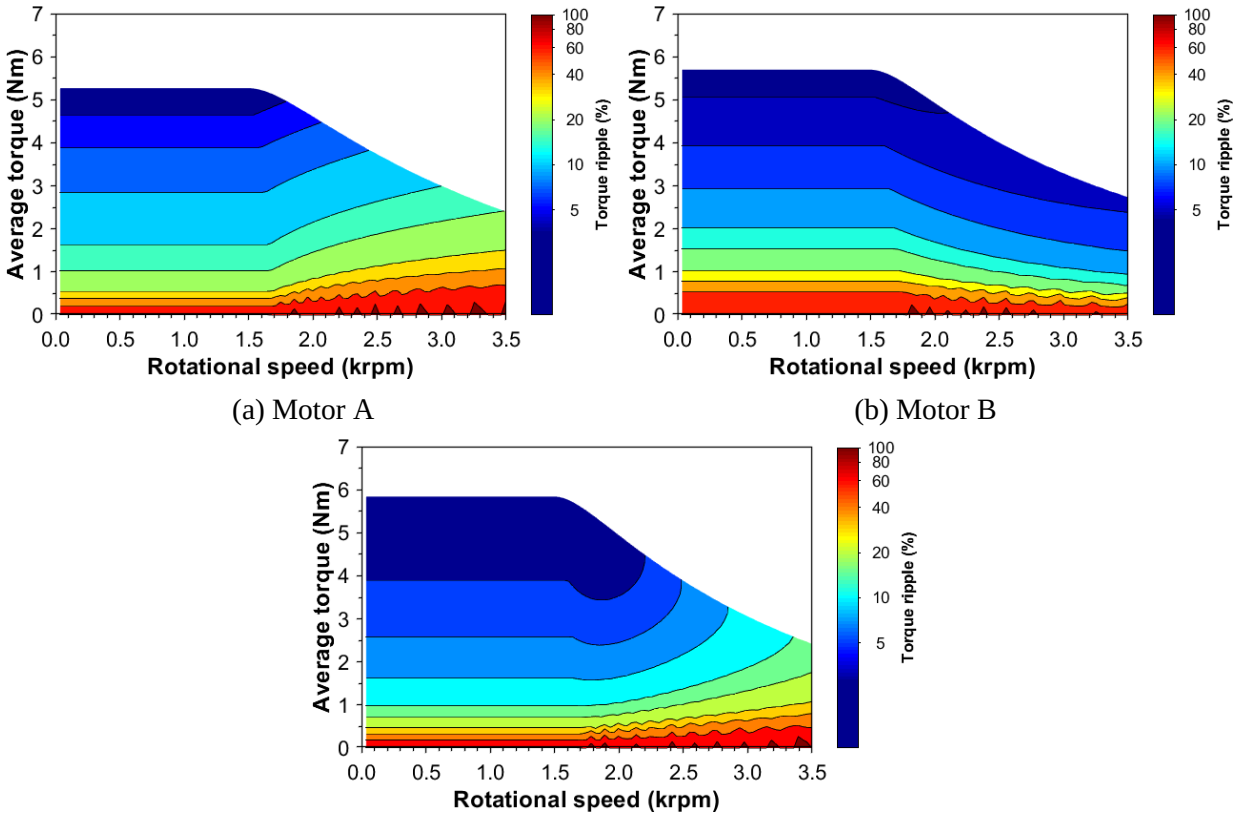
| **Parameter** | **Units** | **Values** | | |
|---|---|---|---|---|
| | | **Motor A** | **Motor B** | **Motor C** |
| Average torque | Nm | 5.4 | 5.8 | 6.0 |
| Torque ripple | % | 0.6 | 1.6 | 4.7 |
| Current advance angle | ° | 17.7 | 18.7 | 18.7 |
| Pole-arc to pole-pitch ratio | N/A | 0.638 | 0.560 | 0.679 |
| Pole-shoe height | mm | 1.06 | 0.97 | 0.70 |
| Iron rib width | mm | 1.93 | 0.93 | 1.36 |
| Tooth width | mm | 5.82 | 5.47 | 5.55 |
| Back-iron width | mm | 3.49 | 3.25 | 3.25 |
| Split ratio | N/A | 0.573 | 0.539 | 0.538 |
| Slot opening width | mm | 1.99 | 2.25 | 1.80 |
| PM height | mm | 2.90 | 2.92 | 2.88 |
| PM width | mm | 12.21 | 12.47 | 12.42 |
| PM volume | $cm^3$ | 10.61 | 10.91 | 10.72 |
| Torque per Volume | Nm/L | 25.38 | 27.26 | 28.2 |
| Torque per PM Volume | $Nm/cm^3$ | 0.509 | 0.532 | 0.560 |



(a) Motor A (b) Motor B (c) Motor C

Fig. 2.37. Cross-sections of 12-slot/8-pole IPM motors selected from multi-objective optimisation solution space.

The torque-speed characteristics and the torque ripple across the operating range of the three motors are shown in Fig. 2.38. The torque ripples of the three motors increase with decreasing current magnitude since the change in torque ripple due to current magnitude is lower than that of the average torque. The torque ripple is shown using a logarithmic scale to permit clear interpretation of the torque ripple across the relevant operating range.




(a) Motor A (b) Motor B

(c) Motor C

Fig. 2.38. Torque-speed characteristics and torque ripple of selected 12-slot/8-pole IPM motors.

The torque ripple of Motor A is low at the optimisation operating point, however, the torque increases significantly as the speed increases. The torque ripple of this motor is in excess of 20% in certain areas of the flux-weakening region presenting an issue for most applications. The torque ripple of Motor C follows a similar trend to that of Motor A, however, the torque ripple level is lower.

Motor B has a low torque ripple the maximum current magnitude and does not change significantly with a change in rotational speed. The increase in torque ripple with decrease in current magnitude is almost linear.

### 3.3.2 Optimisation of 12-slot/10-pole IPM Motor

The solution space of the multi-objective optimisation of the 12-slot/10-pole IPM motor is shown in Fig. 2.39. The multi-objective optimisation converged to a non-continuous Pareto-front, in which a narrower Pareto-front at the bottom left corner of the plot is followed by a much wider Pareto front that is considered in this analysis. The PM volume of the motors varies by over 20% throughout the solution space and the highest PM volume is attributed to the motors with the highest average torque along the Pareto-front.

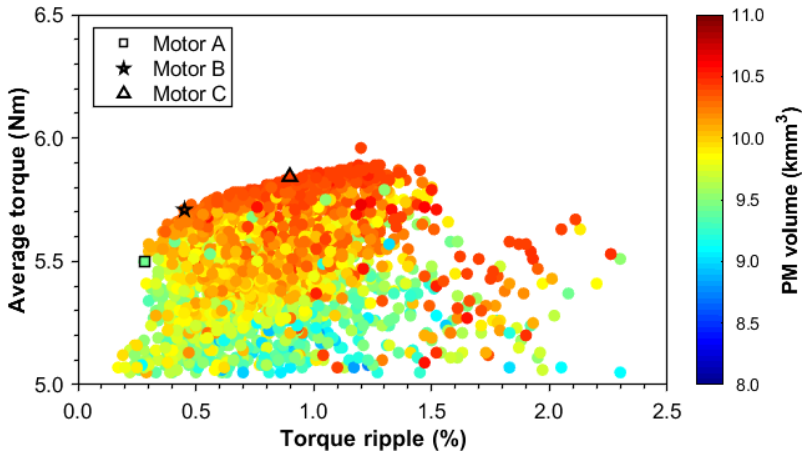


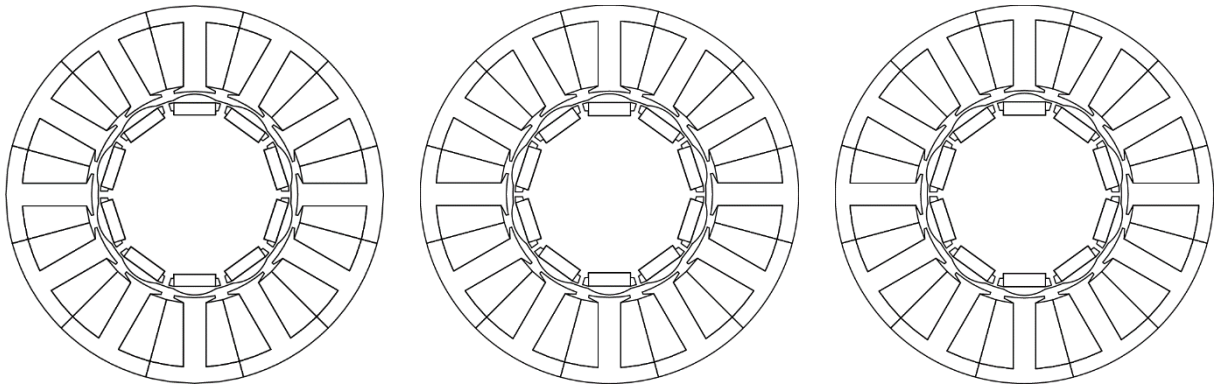

Fig. 2.39. The solution space of multi-objective optimisation of 12-slot/10-pole IPM motor.

The compromise between the average torque and torque ripple, and the impact on the motor design parameters, is investigated by selecting three solutions along the Pareto-front of the solution space, indicated in Fig. 2.39. The cross-sections of the motors are shown in Fig. 2.40 and the design parameters are listed in Table 2.10.

The average torque of the selected motors increases from 5.5 Nm to 5.8 Nm, the torque ripple increases from 0.3% to 0.9%, and the difference in current angle is very low. The motor designs are very similar and the main differences are in the PM height, rib width, and stator back-iron width. The PM height increases as the average torque and torque ripple increase, resulting in higher PM volume. The rotor rib width decreases as the average torque and torque ripple increase due to the decreased flux leakage. Similarly, the torque ripple increases as the stator back-iron width decreases due to the increased saturation.

Table 2.10. Average torque and design parameters of optimised 12-slot/10-pole IPM motor

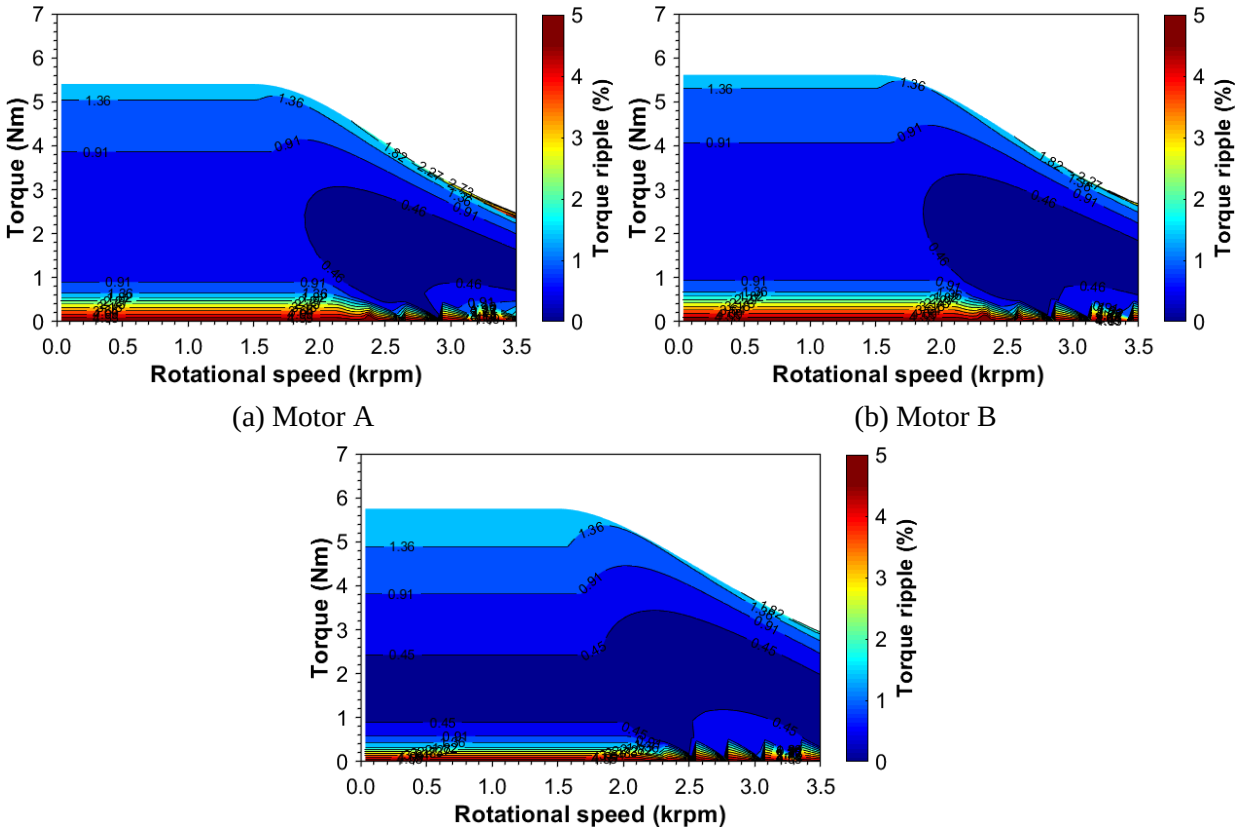
| **Parameter** | **Units** | **Values** | | |
|---|---|---|---|---|
| | | **Motor A** | **Motor B** | **Motor C** |
| Average torque | Nm | 5.5 | 5.7 | 5.8 |
| Torque ripple | % | 0.3 | 0.5 | 0.9 |
| Current advance angle | ° | 12.4 | 12.8 | 13.4 |
| Pole-arc to pole-pitch ratio | N/A | 0.703 | 0.709 | 0.684 |
| Pole-arc height | mm | 0.890 | 0.890 | 0.889 |
| Iron rib width | mm | 1.55 | 1.06 | 1.06 |
| Tooth width | mm | 5.12 | 5.12 | 5.05 |
| Back-iron width | mm | 3.66 | 3.52 | 3.26 |
| Split ratio | N/A | 0.539 | 0.538 | 0.541 |
| Slot opening width | mm | 2.93 | 2.89 | 3.27 |
| PM height | mm | 2.69 | 2.93 | 2.95 |
| PM width | mm | 9.37 | 9.37 | 9.41 |
| PM volume | $cm^3$ | 9.44 | 10.30 | 10.41 |
| Torque per Volume | Nm/L | 25.85 | 26.79 | 27.26 |
| Torque per PM Volume | $Nm/cm^3$ | 0.583 | 0.554 | 0.557 |



(a) Motor A (b) Motor B (c) Motor C

Fig. 2.40. Cross-sections of 12-slot/10-pole IPM motors selected from multi-objective optimisation solution space.

The torque-speed characteristics and the torque ripples across the operating range of the three motors are shown in Fig. 2.41. The torque ripple maps of the three motors are very similar, and the main difference lies in the constant torque region of the motors. As the maximum average torque increases, the torque ripple at lower current levels decreases.




(a) Motor A (b) Motor B

(c) Motor C

Fig. 2.41. Torque-speed characteristics of optimised 12-slot/10-pole IPM motors.

### 3.3.3 Optimisation of 12-slot/14-pole IPM Motor

The solution space of the multi-objective optimisation of the 12-slot/14-pole IPM motor is shown in Fig. 2.42. The average torque along the shown Pareto-front varies between 4 and 5.11 Nm and the torque ripple varies between 0.2 and 2.7%. The PM volume of the motors along the Pareto-front varies between approximately 7 to 8 kmm$^3$.

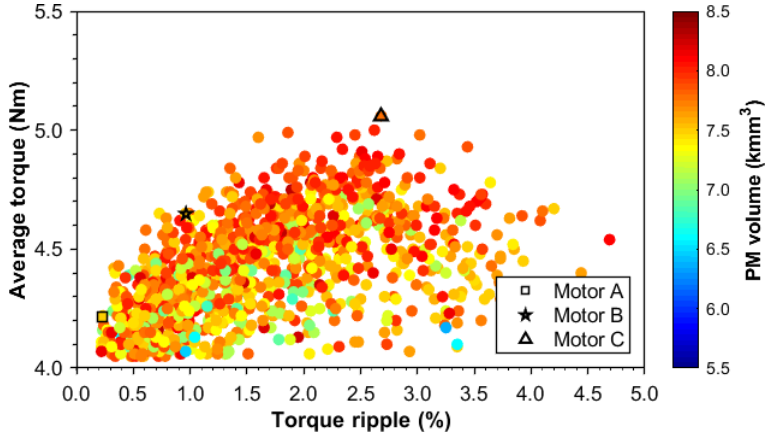


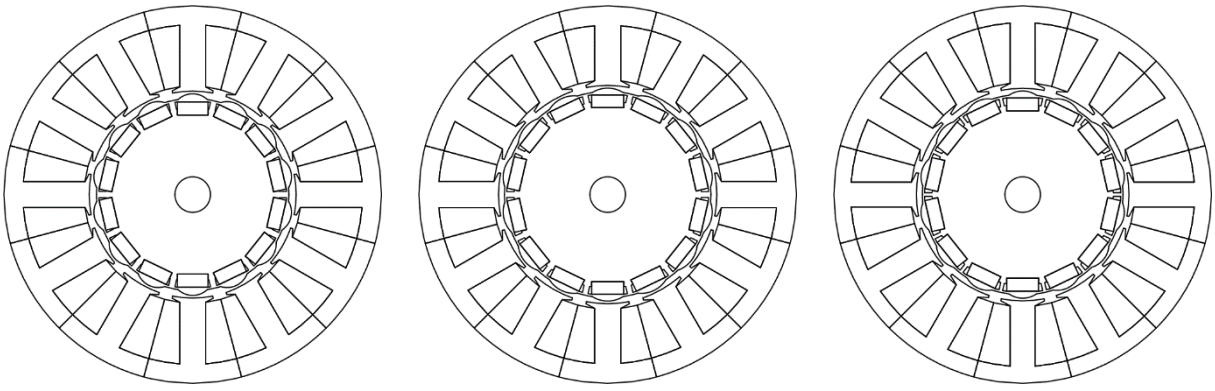

Fig. 2.42. Solution space of multi-objective optimisation of 12-slot/10-pole IPM motor.

The compromise between the average torque and torque ripple, and the impact on the motor design parameters, is investigated by selecting three solutions along the Pareto-front of the solution space, as indicated in Fig. 2.43. The cross-sections of the motors are shown in and the design parameters are listed in Table 2.11.

The average torque of the selected motors varies between 4.2 and 5.1 Nm, the torque ripple varies between 0.2 and 2.7%, and the current angle varies between 8.8 and 14.6°. The PM dimensions increase with increasing average torque. The pole-shoe dimensions and the rotor rib width decrease with increasing average torque. Furthermore, the stator back-iron width and tooth width decrease with increasing average torque and torque ripple.

Table 2.11. Average torque and design parameters of optimised 12-slot/14-pole IPM motor

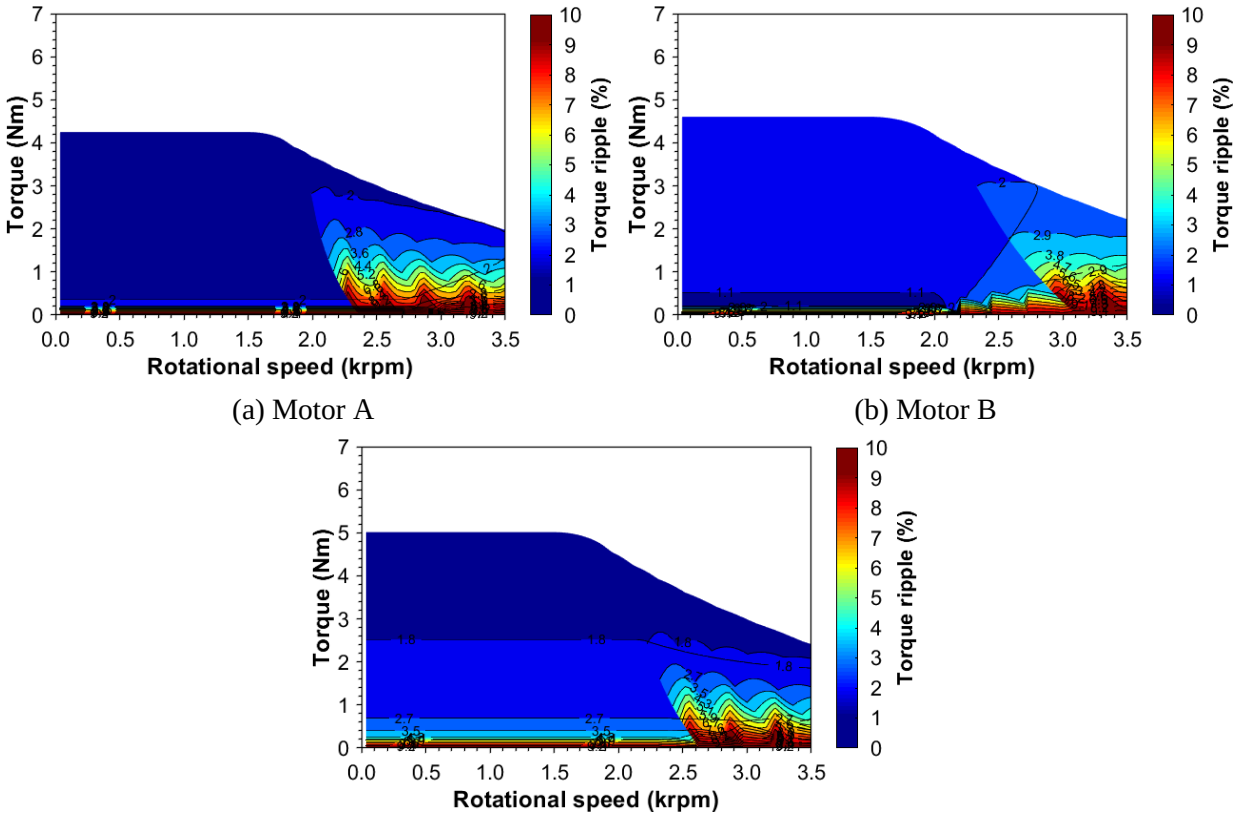
| **Parameter** | **Units** | **Values** | | |
|---|---|---|---|---|
| | | **Motor A** | **Motor B** | **Motor C** |
| Average torque | Nm | 4.2 | 4.6 | 5.1 |
| Torque ripple | % | 0.2 | 1.0 | 2.7 |
| Current advance angle | ° | 14.6 | 7.4 | 8.8 |
| Pole-arc to pole-pitch ratio | N/A | 0.682 | 0.669 | 0.610 |
| Pole-shoe height | mm | 1.05 | 0.74 | 0.75 |
| Iron rib width | mm | 1.44 | 1.28 | 0.82 |
| Tooth width | mm | 5.87 | 5.90 | 5.62 |
| Back-iron width | mm | 4.28 | 4.39 | 3.80 |
| Split ratio | N/A | 0.541 | 0.571 | 0.556 |
| Slot opening width | mm | 3.10 | 3.24 | 2.85 |
| PM height | mm | 2.89 | 2.78 | 2.91 |
| PM width | mm | 6.89 | 7.22 | 7.13 |
| PM volume | $cm^3$ | 10.45 | 10.54 | 10.89 |
| Torque per Volume | Nm/L | 19.74 | 21.62 | 23.97 |
| Torque per PM Volume | $Nm/cm^3$ | 0.402 | 0.437 | 0.468 |



(a) Motor A (b) Motor B (c) Motor C

Fig. 2.43. Cross-sections of optimised 12-slot/14-pole IPM motors.

The torque-speed characteristics and the torque ripple across the operating range of the three motors are shown in Fig. 2.44. The torque ripple of the Motors A and B is very low in the constant-torque region, while that of Motor C is low at high torque and increases with decreasing average torque. The torque ripple of the motors in the flux-weakening region increases significantly with decreasing average torque.




(a) Motor A

(b) Motor B

(c) Motor C

Fig. 2.44. Torque-speed characteristics of optimised 12-slot/14-pole IPM motors.

## 3.4 Comparison of Single-objective and Multi-objective Optimisation

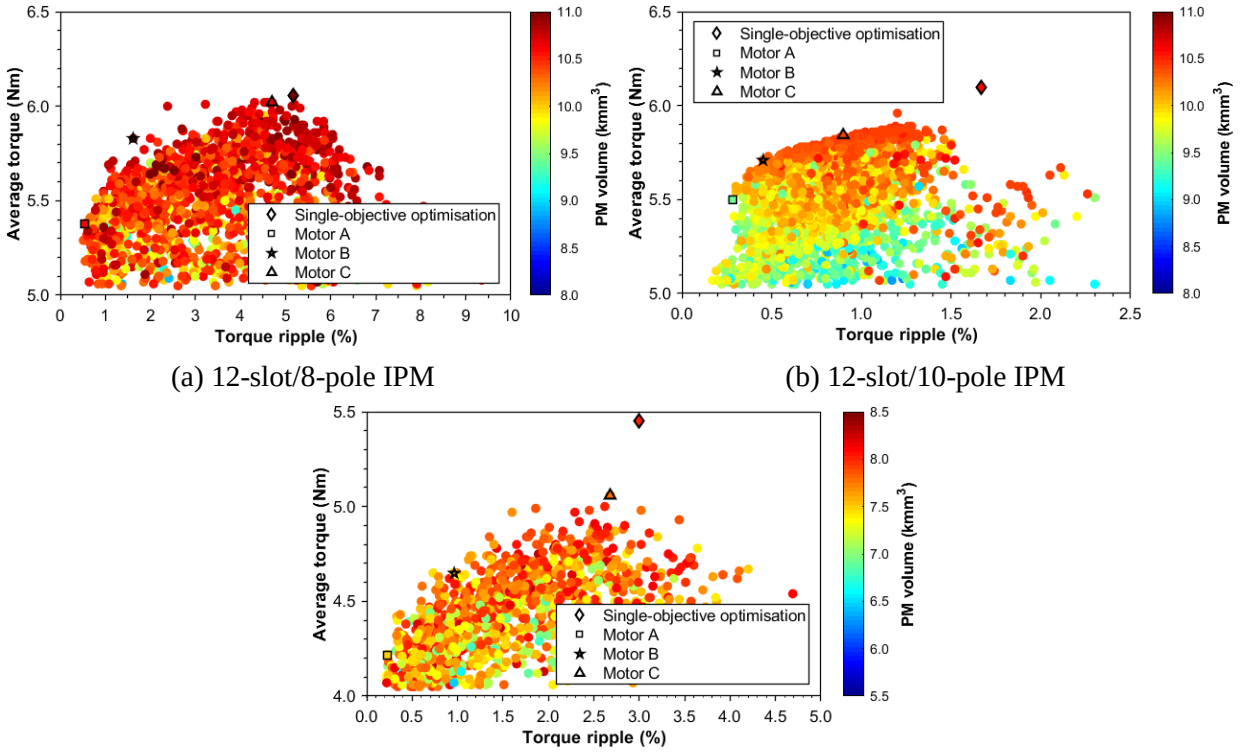
The solution spaces of the multi-objective optimisation of 12-slot/8-pole, 12-slot/10-pole, 12-slot/14-pole IPM motors, together with the motors optimised using the single-objective optimisation are shown in Fig. 2.45.

Some observations can be found from Fig. 3.20 as follows:

- Multi-objective optimised motors usually have lower torque ripples;
- Single-objective optimised motors for maximum average torque only always result in higher average torque than the multi-objective optimised motors due to the compromise amongst different objectives.

The 12-slot/8-pole IPM motor optimised for the single-objective optimisation, i.e. average torque only, lies on the upper portion of the Pareto-front, thereby indicating that the Pareto-front is a good estimation of the average torque and torque ripple limits of the motor. On the other hand, the 12-slot/10-pole and 12-slot/14-pole IPM motors optimised for the single-objective optimisation, i.e. average torque only, are well beyond the Pareto-front of the solution space of the multi-objective optimisation.

The Pareto-front of the two objectives can be discontinuous, i.e. composed of multiple convex or concave Pareto-fronts, as can be noted in the bottom left corner of Fig. 2.45(b). Furthermore, the solution space obtained using the multi-objective optimisation may not be sufficient to obtain the complete Pareto-front, which means that the optimisation may need to be repeated with a larger population. In most cases, the Pareto-front is used to determine solutions around the knee point of a convex Pareto-front to identify the design parameters responsible for the compromise between the two objectives. Thus, obtaining a Pareto-front that includes both limits of the optimisation objectives is not the aim of this analysis.




(a) 12-slot/8-pole IPM

(b) 12-slot/10-pole IPM

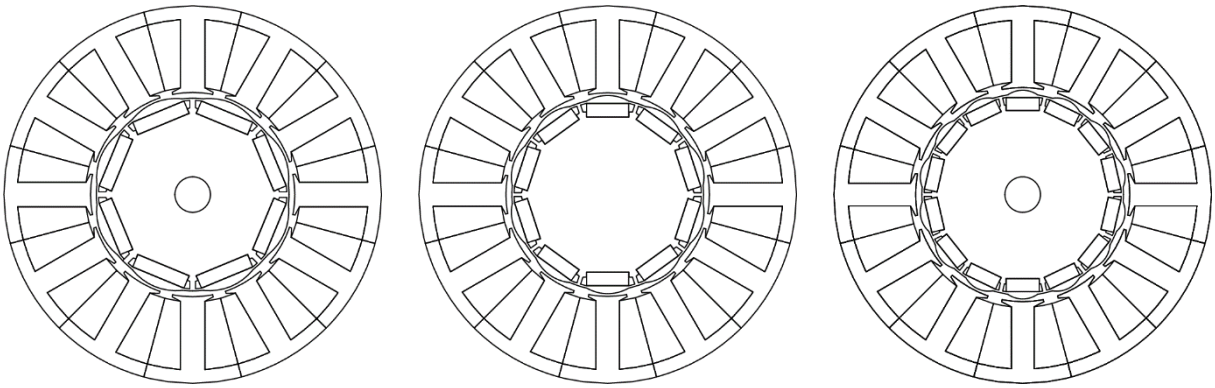
(c) 12-slot/14-pole IPM

Fig. 2.45. Solution space of multi-objective optimisation of IPM motors.

The design parameters of the IPM motors optimised for maximum average torque are listed in Table 2.12 and the cross-sections are shown in Fig. 2.46. The optimised 12-slot/8-pole and 12-slot/10-pole IPM motors for maximum average torque only have a comparable average torque, however, the torque ripple and the PM volume of the 12-slot/10-pole IPM motor are significantly lower. The average torque and PM volume of the12-slot/14-pole IPM motor optimised for average torque only is lower than those of the remaining motors.

Table 2.12. Torque and design parameters of IPM motors optimised for average torque only

| **Parameter** | **Units** | **Values** | | |
|---|---|---|---|---|
| | | **12-slot/8-pole** | **12-slot/10-pole** | **12-slot/14-pole** |
| Average torque | Nm | 6.2 | 6.1 | 5.5 |
| Torque ripple | % | 3.0 | 1.7 | 3.0 |
| Current advance angle | ° | 18.9 | 16.5 | 9.9 |
| Pole-arc to pole-pitch ratio | N/A | 0.717 | 0.699 | 0.663 |
| Pole-shoe height | mm | 0.71 | 0.73 | 0.81 |
| Rib width | mm | 1.26 | 0.87 | 0.90 |
| Tooth width | mm | 5.52 | 5.28 | 5.11 |
| Back-iron width | mm | 3.03 | 3.10 | 3.20 |
| Split ratio | N/A | 0.534 | 0.532 | 0.560 |
| Slot opening width | mm | 2.95 | 3.42 | 3.29 |
| PM height | mm | 2.98 | 2.99 | 2.88 |
| PM width | mm | 12.48 | 9.47 | 7.43 |
| PM volume | $cm^3$ | 11.17 | 10.60 | 11.23 |
| Torque per Volume | Nm/L | 29.14 | 28.67 | 25.85 |
| Torque per PM Volume | $Nm/cm^3$ | 0.555 | 0.575 | 0.490 |



(a) 12-slot/8-pole (b) 12-slot/10-pole (c) 12-slot/14-pole

Fig. 2.46. Cross-sections of IPM motors optimised for maximum average torque only.

## 3.5 Comparison of Optimised 12-slot/8-pole IPM Motor with Baseline IPM Motor

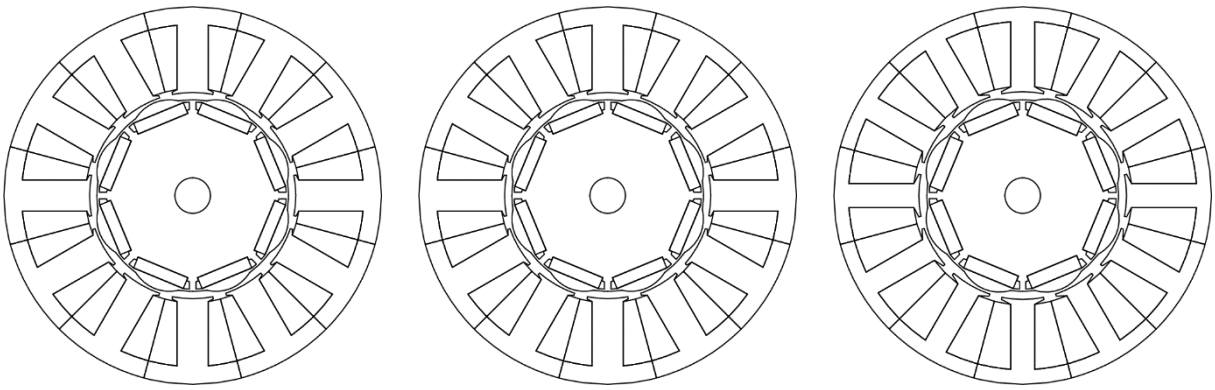
The baseline motor is compared with the 12-slot/8-pole motors obtained using single and multi-objective optimisation to identify key differences in design parameters and motor performance. The torque and design parameters of the three motors are listed in Table 2.13. The baseline IPM motor has a skewed rotor and therefore the performance of the baseline motor with a non-skewed rotor is included for a fair and complete analysis. The multi-objective optimised Motor A is selected from the previous analysis since the motor yields the average torque and torque ripple in the proximity of the knee point of the Pareto-front.

The average torque of the single-objective optimised motor is 34.8% higher than that of the baseline motor with a skewed rotor and the average torque per PM volume is 13.9% higher. The torque ripple of the single-objective optimised motor is 2.5 times that of the baseline motor with a skewed rotor. The increase in average torque with respect to the baseline motor is attributed to the lower pole-shoe height, thinner teeth and back-iron, higher PM volume, and higher flux linkage due to the lack of rotor skew. The increase in air-gap magnetic flux density combined with the thinner stator flux linkage paths results in higher stator saturation and increased torque ripple. The average torques of the single-objective optimised motor are 34.8% and 26.5% higher than those of the baseline motor with skewed and non-skewed rotors, respectively. Furthermore, the differences in relative torque ripples of the optimised motor and the baseline motor with skewed and non-skewed rotors are 1.8% and 5%, respectively. The single-objective optimised motor has significantly higher average torque and lower torque ripple than the baseline motor with non-skewed rotor.

The multi-objective optimised motor produces a 17.4% higher average torque, an increase in average torque per PM volume of 4.5% and a decrease in torque ripple by 50% with respect to the baseline motor with a skewed rotor. Furthermore, the average torque of the multi-objective optimised motor is 10.2% higher than that of the baseline motor with non-skewed rotor. However, the average torque per PM volume of the multi-objective optimised motor is 1.9% lower than that of the baseline motor with non-skewed rotor. The motor has a 6.3% higher split ratio than the baseline motor, 12.4% higher PM volume, and wider rotor ribs. The pole-shoe dimensions of the multi-objective optimised motor and the baseline motor are very similar, however, the stator teeth and back-iron are narrower. Thus, the increase in flux per pole and the decreased width of the stator teeth and back-iron result in higher average torque.

Table 2.13. Torque and design parameters of baseline and optimised 12-slot/8-pole IPM motors

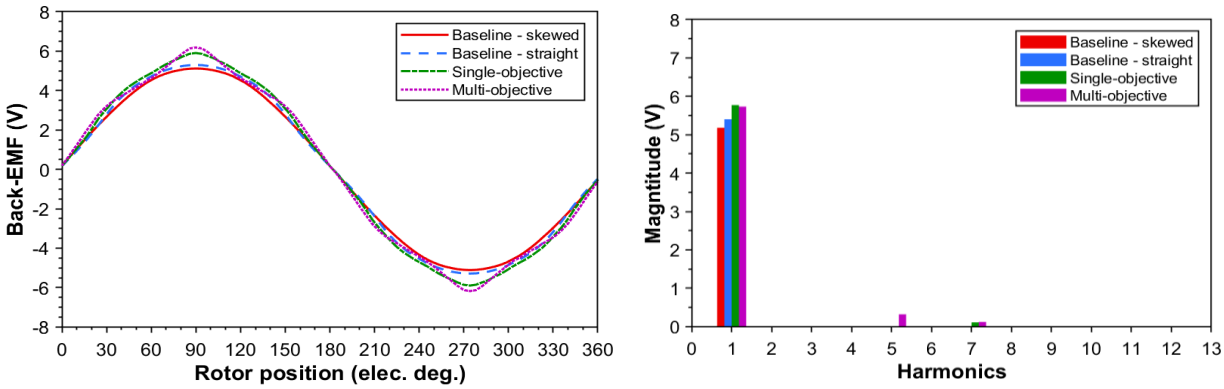
| **Parameter** | **Unit** | **Values** | | | |
|---|---|---|---|---|---|
| | | **Baseline (skewed rotor)** | **Baseline (non-skewed rotor)** | **Single-objective** | **Multi-objective** |
| Average torque | Nm | 4.6 | 4.9 | 6.2 | 5.4 |
| Torque ripple | % | 1.2 | 8.8 | 3.0 | 0.6 |
| Current advance angle | ° | 8.3 | 9.4 | 18.9 | 17.7 |
| Pole-arc to pole-pitch ratio | N/A | 0.620 | | 0.717 | 0.638 |
| Pole-shoe height | mm | 1.05 | | 0.71 | 1.06 |
| Rib width | mm | 1.50 | | 1.26 | 1.93 |
| Tooth width | mm | 7.00 | | 5.52 | 5.82 |
| Back-iron width | mm | 4.00 | | 3.03 | 3.49 |
| Split ratio | N/A | 0.539 | | 0.534 | 0.573 |
| Slot opening width | mm | 3.00 | | 3.00 | 3.00 |
| PM height | mm | 2.60 | | 2.98 | 2.90 |
| PM width | mm | 12.10 | | 12.48 | 12.21 |
| PM volume | $cm^3$ | 9.44 | | 11.17 | 10.61 |
| Torque per Volume | Nm/L | 21.62 | 23.03 | 29.14 | 25.38 |
| Torque per PM Volume | $Nm/cm^3$ | 0.487 | 0.519 | 0.555 | 0.509 |



(a) Baseline (b) Single-objective (c) Multi-objective

Fig. 2.47. Cross-sections of baseline and optimised 12-slot/8-pole IPM motors.

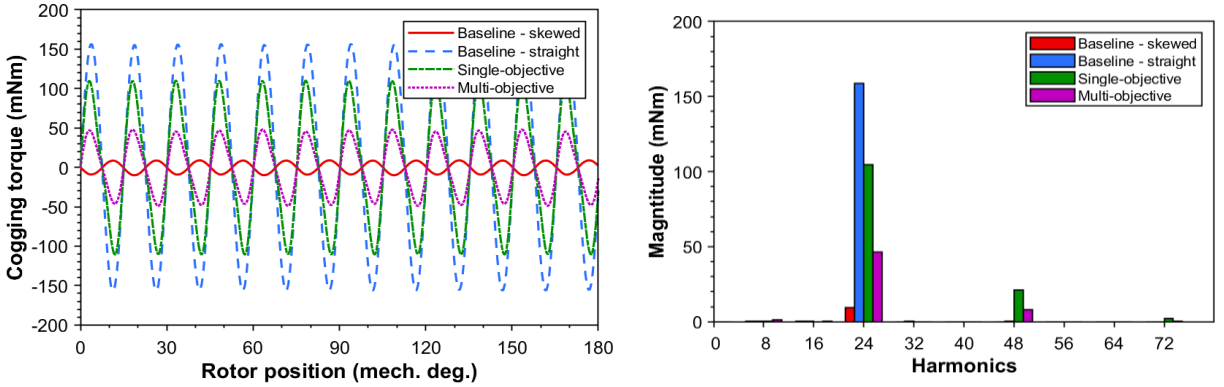
The back-EMF of the baseline and optimised motors is shown in Fig. 2.5. The rotor step skew of the baseline motor leads to an almost sinusoidal back-EMF waveform at the cost of lower flux linkage. The multi-objective optimised motor has the highest peak back-EMF due to the $5^{th}$ and $7^{th}$ harmonics. The back-EMF of the single-objective optimised motor has the highest fundamental back-EMF harmonic. The magnitude of the $7^{th}$ back-EMF harmonic of the single- and multi- objective optimised motors are almost identical.




(a) Waveforms (b) Harmonics

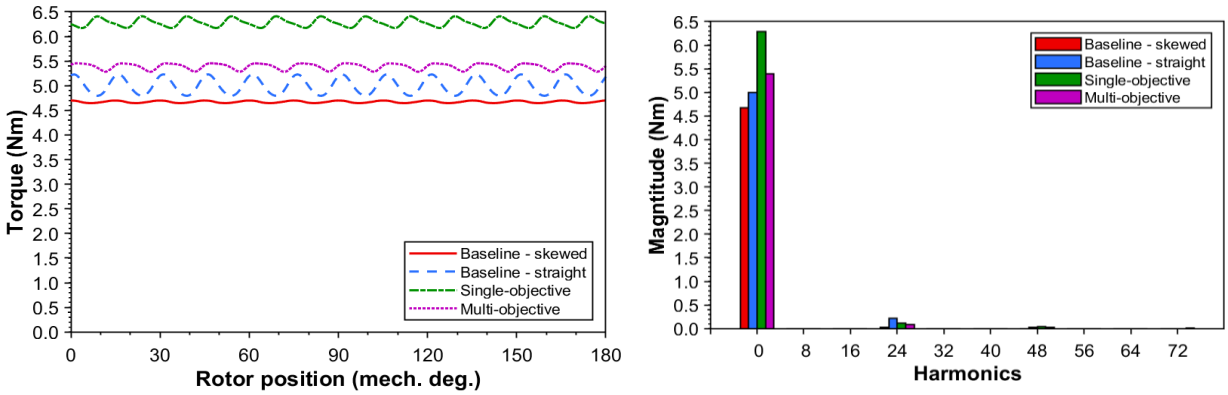
Fig. 2.48. Back-EMF of baseline and optimised 12-slot/8-pole IPM motors.

The cogging torques of the 12-slot/8-pole IPM motors are shown in Fig. 2.49 and the on-load torque is shown in Fig. 2.50. The cogging torque of the baseline motor with a non-skewed rotor is significantly higher than the optimised motor and the baseline motor with rotor skew. The cogging torques of the motors under investigation mainly comprise the $24^{th}$ and $48^{th}$ harmonic components, but also the tiny $8^{th}$ and $16^{th}$ harmonic components which can be attributed to numerical noise due to meshing etc..




(a) Waveforms (b) Harmonics

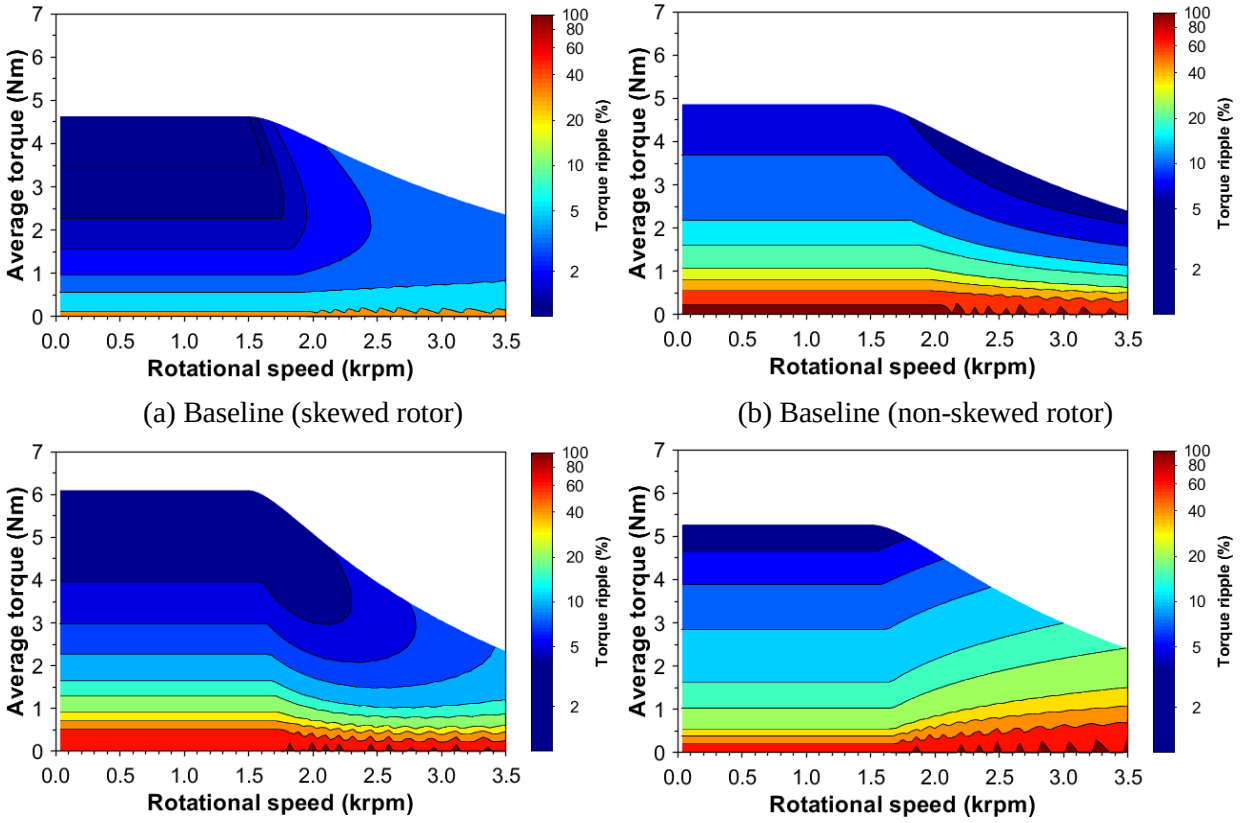
Fig. 2.49. Cogging torques of baseline and optimised 12-slot/8-pole IPM motors.




(a) Waveforms (b) Harmonics

Fig. 2.50. On-load torques of baseline and optimised 12-slot/8-pole IPM motors.

The torque speed characteristics and torque ripple maps of the baseline and optimised motors are shown in Fig. 2.51. The average torques of the motors in the constant torque region are listed in Table 2.13. The torque ripples of the analysed motors increase with decreasing electrical load. The torque ripple of the baseline motor with rotor skew is very low in the constant torque region and increases in the flux-weakening region. The torque ripples of the baseline motor with a non-skewed rotor and the optimised motors increase significantly with decreasing load and increasing current angle. The torque ripple of the multi-objective optimised motor is lower than that of the baseline motor with rotor skew at the corner speed, however, the torque ripple increases significantly at other operating points.




(a) Baseline (skewed rotor)

(b) Baseline (non-skewed rotor)

(c) Single-objective optimised

(d) Multi-objective optimised

Fig. 2.51. Torque-speed characteristics and torque ripple of baseline and optimised 12-slot/8-pole IPM motors.

A sensitivity analysis of the main design parameters of the motors under investigation is performed and the sensitivities of the average torque and torque ripple at the knee point of the torque-speed envelope are analysed. The one-variable-at-a-time method is used to produce a 2-level experimental design of the optimised motor. The design parameters and the changes in the parameters below and above the nominal value are listed in Table 2.14.

The average torque and torque ripple of the motors given a change in each design parameters is shown in Fig. 2.52. A straight line connects the values of the average torque and torque ripple above and below the nominal value of each design parameter for clarity. However, the response to a change in design parameters

is not necessarily linear.

Table 2.14. Design parameters of 12-slot/8-pole IPM motors under investigation considered in sensitivity analysis and change in design parameters

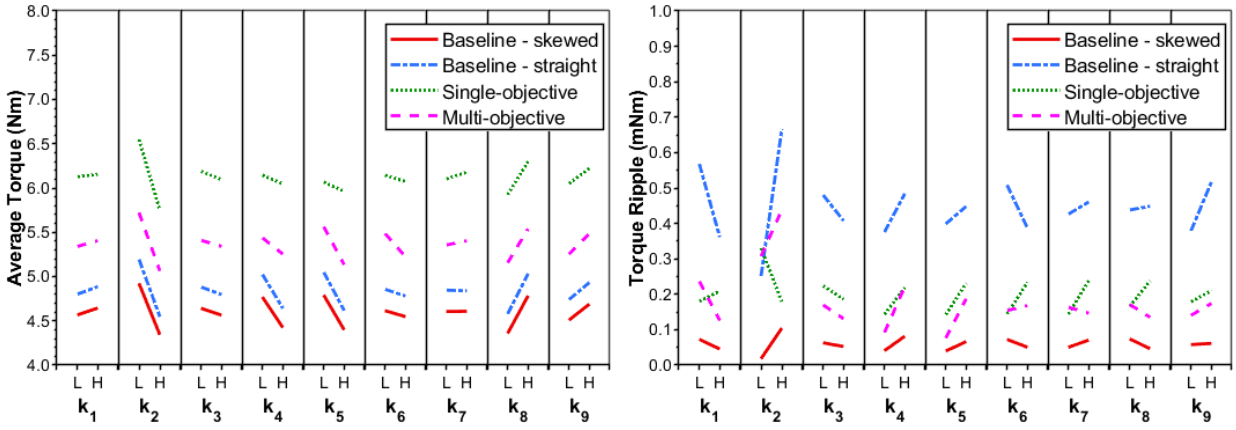
| | **Design parameter** | **Units** | **Change in parameter** |
|---|---|---|---|
| $k_1$ | Pole-arc to pole-pitch ratio | N/A | ±0.05 |
| $k_2$ | Pole-shoe height | mm | ±0.5 mm |
| $k_3$ | Rib width | mm | ±0.5 mm |
| $k_4$ | Tooth width | mm | ±0.5 mm |
| $k_5$ | Back-iron width | mm | ±0.5 mm |
| $k_6$ | Split ratio | N/A | ±2% |
| $k_7$ | Slot opening width | mm | ±0.5 mm |
| $k_8$ | PM height | mm | ±0.5 mm |
| $k_9$ | PM width | mm | ±0.5 mm |

The influence of design parameters on average torque of the three motors is relatively similar. However, the influence of design parameters on torque ripple differs significantly. The pole-shoe height has the highest influence on average torque of the three motors.

The average torque of the baseline motor with rotor skew varies by up to 4.1 % from the nominal given a change in the tooth width of 0.5 mm, and by up to 5.5% given a change in PM height of 0.5 mm. The average torque of the multi-objective optimised motor varies by up to 3% from the nominal given a change in split ratio of 2%.

The torque ripples of the motors are very sensitive to changes in the rotor pole-shoe height. The torque ripple of the baseline motor is the least sensitive to changes in design parameters. This effect can be attributed to the lower air-gap magnetic flux density harmonics due to rotor step skewing. Thus, a change in design parameter would result in a lower change in magnetic flux density harmonics and consequently to lower change in torque ripple.

A change in the pole-shoe height of the multi-objective optimised motor results in the highest change in torque ripple of up to 197.1% the nominal value. The torque ripple of the motors increases with increasing stator tooth and back-iron width. Wider rotor iron ribs result in increased rotor flux leakage and decrease in air-gap magnetic flux density. Therefore, the average torque and torque ripple decrease with increasing iron rib width. The sensitivity of the torque ripple to changes in the rotor pole-shoe dimensions, split ratio, slot opening, and PM height vary for every motor.




(a) Average torque (b) Torque ripple

Fig. 2.52. Influence of changes in design parameters on torque of baseline and optimised 12-slot/8-pole IPM motors.

## 3.6 Conclusion

Global optimisation using the genetic algorithm was performed on 12-slot/8-pole, 12-slot/10-pole, and 12-slot/14-pole IPM motors for given fixed volume, gross slot current density, air-gap length, and rotor bridge width. Single objective optimisation is used to determine the maximum average torque given the aforementioned constraints and multi-objective optimisation is performed to identify the compromise between the average torque and the torque ripple.

Single-objective optimisation of the average torque of the 12-slot/8-pole IPM motor is carried out with the current angle as a constant and with the current angle as a design variable. Optimisation with the current angle as a constant is useful to identify the maximum average torque that can be obtained given a particular current angle value and the corresponding torque ripple. However, multiple runs are required to identify the optimum current angle resulting in a significant increase in computation time. Single-objective optimisation with the current angle as a constant and as a design variable converge to approximately the same motor design. Thus, subsequent optimisations are performed with the current as a constant to minimise computational time.

The solution spaces of the single- and multi-objective optimisation of motors with different slot/pole number combinations are compared. The average torque of the single-objective optimised motors is higher than the maximum average torque of the solution space of the multi-objective optimisation. The maximum average toque of the 12-slot/14-pole IPM motor is significantly lower than those of the 12-slot/8-pole and 12-slot/10-pole IPM motors due to lower PM volume and higher rotor flux leakage.

The Pareto-front of the solution space of the multi-objective optimisation shows the compromise between the average torque and torque ripple of the motors. The torque ripple of the 12-slot/8-pole IPM motor can be as low as 0.5% at the cost of lower average torque. The 12-slot/10-pole IPM and 12-slot/14-pole exhibit

inherently low torque ripple and the minimum torque ripple is lower than 0.5%. The 12-slot/10-pole IPM motor exhibits better compromise between the average torque and torque ripple.

The performances of the baseline, single- and multi- objective optimised 12-slot/8-pole IPM motors are compared. The multi-objective optimised motor is selected to be on the knee of the Pareto-front to obtain the lowest torque ripple at a reasonable average torque. The back-EMF of the baseline motor is almost sinusoidal and has the lowest magnitude of the fundamental harmonic due to the lower flux linkage attributed to rotor step skewing. The single-objective optimised motor comprises the $7^{th}$ back-EMF harmonic and the multi-objective optimised motor comprised the $5^{th}$ and $7^{th}$ back-EMF harmonics resulting in a higher peak back-EMF. The baseline motor has the lowest cogging torque due to the rotor step-skewing. The cogging torque of the single-objective optimised motor is over twice that of the multi-objective optimised motor.

The torque ripple maps over the torque-speed operating range of the motors show that the torque ripple increases with decreasing electric load. The torque ripple of the baseline moor is low in the constant torque region and slightly higher in the flux-weakening region. The influence of electric load on the torque ripple of the baseline motor in the flux-weakening region is lower than that of the constant torque region. The torque ripple of the single-objective optimised motor is significantly higher than the baseline motor and increases with increasing current angle. The torque ripple of the multi-objective optimised motor is very low at the knee point of the torque-speed envelope and increases significantly with decreasing load and increasing current angle.

# 4 SINGLE- AND MULTI-OBJECTIVE OPTIMISATION OF SPM MOTORS

## 4.1 Introduction

Global optimisation using the genetic algorithm was performed on 12-slot/8-pole, 12-slot/10-pole, and 12-slot/14-pole IPM motors in Chapter 3. Global optimisation is repeated for 12-slot/8-pole, 12-slot/10-pole, and 12-slot/14-pole SPM motors given similar constraints on motor volume, gross slot current density, and air-gap length. The values of the fixed design parameters used in motor optimisation are listed in Table 2.2. SPM motors in EPS applications require a rotor sleeve resulting in a higher effective air-gap. Thus, the air-gap length of the SPM motors is 0.3 mm larger than that of the IPM motors.

Table 2.15. Fixed design parameters of the SPM motor optimisation

| Parameter | Value |
|---|---|
| Outer diameter | 85 mm |
| Stack length | 37.5 mm |
| Gross slot current density | 9.57 A/mm$^2$ |
| Air-gap length | 0.9 mm |
| Rotor skew | N/A |
| PM remanence | 1.38 T |
| PM coercivity | -1100 kA/m |
| Operating temperature | 20°C |

The variable design parameters in the single- and multi-objective optimisations are:

- Split ratio
- Stator back-iron width
- Stator tooth width
- Stator slot opening width
- PM pole-arc to pole-pitch ratio
- PM pole-shoe height
- PM height

Design optimisation is performed at maximum current and base speed. The SPM motors under investigation are optimised from maximum average torque using single-objective optimisation. Multi-objective optimisation of the average torque and torque ripple is performed to identify the compromise between the average torque and the torque ripple. The performance of motor designs along the Pareto-front of the multi-objective optimisation is analysed.

Unified slot opening width is adopted across the set of optimised IPM motors in Chapter 3. The slot opening width of the single-objective optimised SPM motors is set to 3 mm and the influence of slot opening width

on motor performance is investigated.

The performances of 12-slot/8-pole, 12-slot/10-pole, and 12-slot/14-pole SPM motors optimised for maximum average torque are compared. Furthermore, the solution spaces of the multi-objective optimisation of the three SPM motor topologies are analysed.

The solutions identified using the single-objective optimisation of IPM and SPM motors are compared. The Pareto-fronts of the multi-objective optimisation of the IPM and SPM motors are compared and the compromise between average torque and torque ripple of the various topologies is identified.

## 4.2 Single-objective Optimisation of SPM Motors

### 4.2.1 Analysis of Optimised 12-slot/8-pole SPM Motor

The design parameters of the optimised 12-slot/8-pole SPM motor are listed in Table 2.16 and the cross-section is shown in Fig. 2.53. The slot opening width of the optimised motor is fixed to 3 mm and the torque-speed characteristic and the torque ripple map of the motors with optimised and fixed slot opening widths are shown in Fig. 2.54.

Table 2.16. Average torque and design parameters of optimised 12-slot/8-pole SPM motor

| **Parameter** | **Units** | **Values** |
|---|---|---|
| Average torque | Nm | 6.7 |
| Torque ripple | % | 7.4 |
| Current advance angle | ° | 8.9 |
| Split ratio | N/A | 0.485 |
| Back-iron width | mm | 3.05 |
| Tooth width | mm | 5.35 |
| Slot opening width | mm | 2.61 |
| PM pole-shoe height | mm | 0.71 |
| PM pole-arc to pole-pitch ratio | mm | 0.919 |
| PM height | mm | 3.00 |
| PM volume | $cm^3$ | 9.73 |
| Torque per Volume | Nm/L | 29.14 |
| Torque per PM Volume | $Nm/cm^3$ | 0.637 |

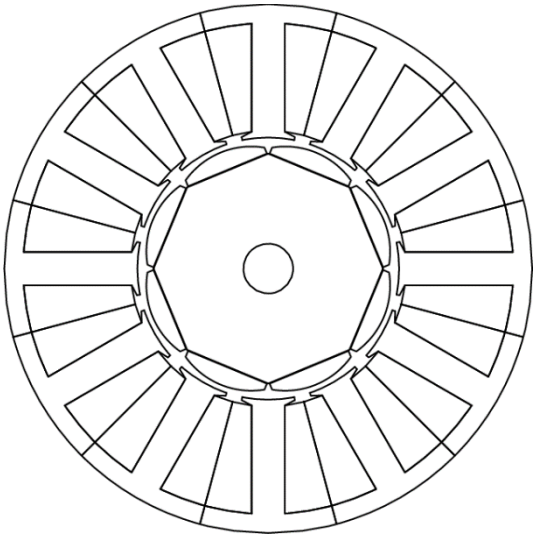
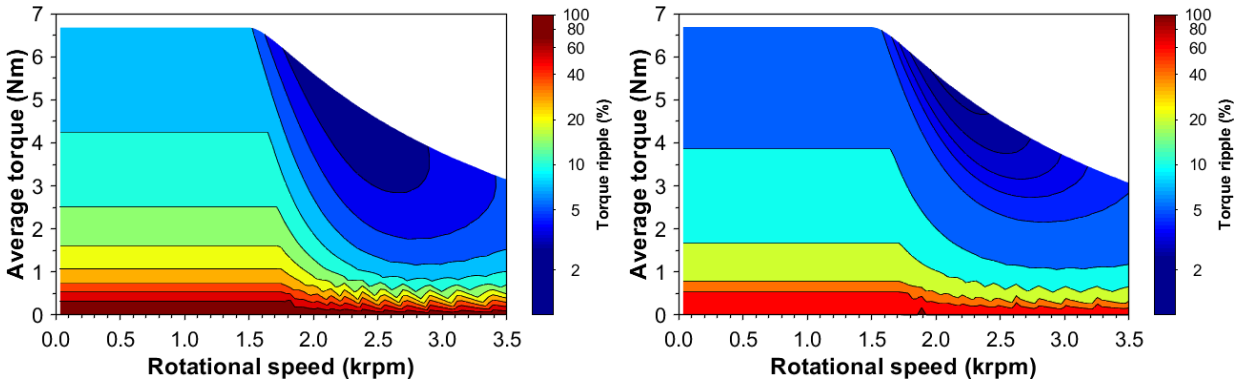


Fig. 2.53. Cross-section of optimised 12-slot/8-pole SPM motor.

The torque-speed characteristics and torque ripple maps of the motors with optimised and fixed slot opening are similar. The torque ripple in the constant torque region increases significantly with decreasing electrical load. The torque ripple in the flux-weakening region at high electrical load is very low and increases gradually with decreasing electrical load. The torque ripple of the motor with fixed slot opening width is lower than the motor with optimised slot opening width and the increase in torque ripple with decreasing electrical load is lower.




(a) Optimised slot opening width (b) Fixed slot opening width

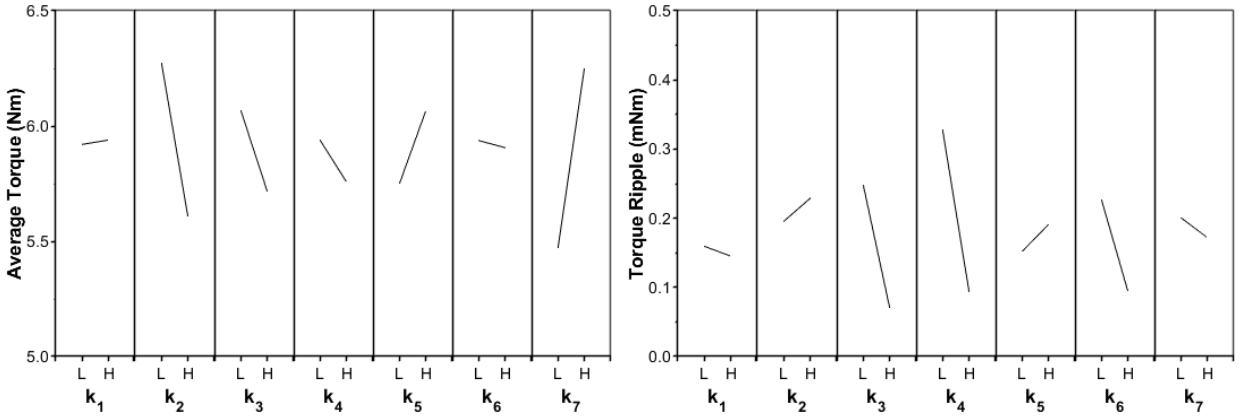
Fig. 2.54. Torque-speed characteristics and torque ripple of optimised 12-slot/8-pole SPM motor.

The main effect plots of the average torque and the torque ripple, based on a 2-level experimental design, are shown in Fig. 2.55. The two levels of each variables are set to be above and below the nominal value by the amounts listed in Table 2.17.

Table 2.17. Change in design parameters of SPM motor used in main effects analysis

| | **Design parameter** | **Units** | **Change in parameter** |
|---|---|---|---|
| $k_1$ | Pole-arc to pole-pitch ratio | N/A | ±0.025 |
| $k_2$ | Pole-shoe height | mm | ±0.5 mm |
| $k_3$ | Tooth width | mm | ±0.5 mm |
| $k_4$ | Back-iron width | mm | ±0.5 mm |
| $k_5$ | Split ratio | N/A | ±2% |
| $k_6$ | Slot opening width | mm | ±0.5 mm |
| $k_7$ | PM height | mm | ±0.5 mm |

The average torque of the SPM motor is very sensitive to changes in the pole-shoe height and PM dimensions. The average torque is more sensitive to changes in the tooth width than the back-iron width. However, the torque ripple is more sensitive to changes in the back-iron width. Smaller back-iron width results in higher saturation and in a considerable increase in torque ripple.




(a) Average torque (b) Torque ripple

Fig. 2.55. Influence of change in design parameters on torque of 12-slot/8-pole SPM motor with fixed slot opening width.

## 4.2.2 Analysis of Optimised 12-slot/10-pole SPM Motor

The design parameters of the optimised 12-slot/10-pole SPM motor are listed in Table 2.18 and the cross-section is shown in Fig. 2.56. The slot opening width of the optimised motor is fixed to 3 mm and the torque-speed characteristic and the torque ripple map of the motors with optimised and fixed slot opening width are shown in Fig. 2.31.

Table 2.18. Average torque and design parameters of optimised 12-slot/10-pole SPM motor

| **Parameter** | **Units** | **Values** |
|---|---|---|
| Average torque | Nm | 7.4 |
| Torque ripple | % | 3.0 |
| Current advance angle | ° | 8.6 |
| Split ratio | N/A | 0.527 |
| Back-iron width | mm | 3.02 |
| Tooth width | mm | 5.14 |
| Slot opening width | mm | 3.03 |
| PM pole-shoe height | mm | 0.73 |
| PM pole-arc to pole-pitch ratio | mm | 0.902 |
| PM height | mm | 2.99 |
| PM volume | $cm^3$ | 11.31 |
| Torque per Volume | Nm/L | 34.78 |
| Torque per PM Volume | $Nm/cm^3$ | 0.655 |

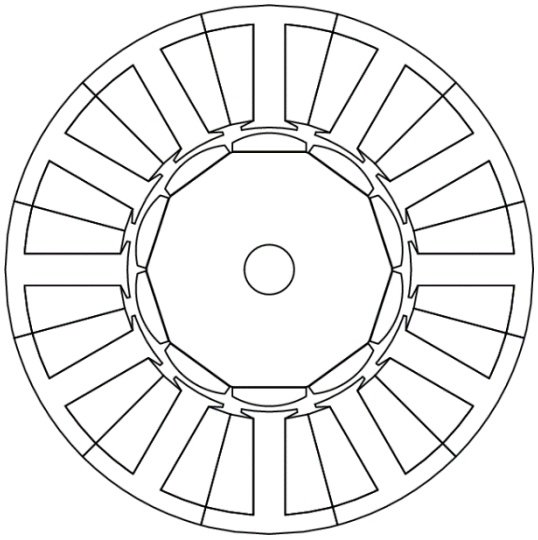
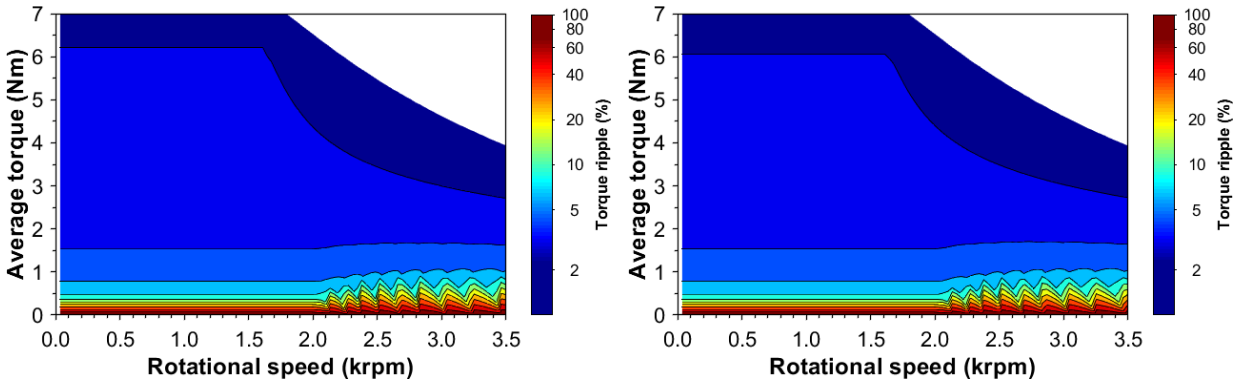


Fig. 2.56. Cross-section of optimised 12-slot/10-pole SPM motor.

The torque-speed characteristics and torque ripple maps of the motor with optimised and fixed slot opening with are almost identical since the change in slot opening width is very small. The torque ripple map of the optimised 12-slot/10-pole SPM motor has a similar characteristic to that of the 12-slot/8-pole SPM motor. The torque ripple increases with decreasing electrical load and the change in torque ripple is significantly higher in the constant torque region.




(a) Optimised slot opening width (b) Fixed slot opening width

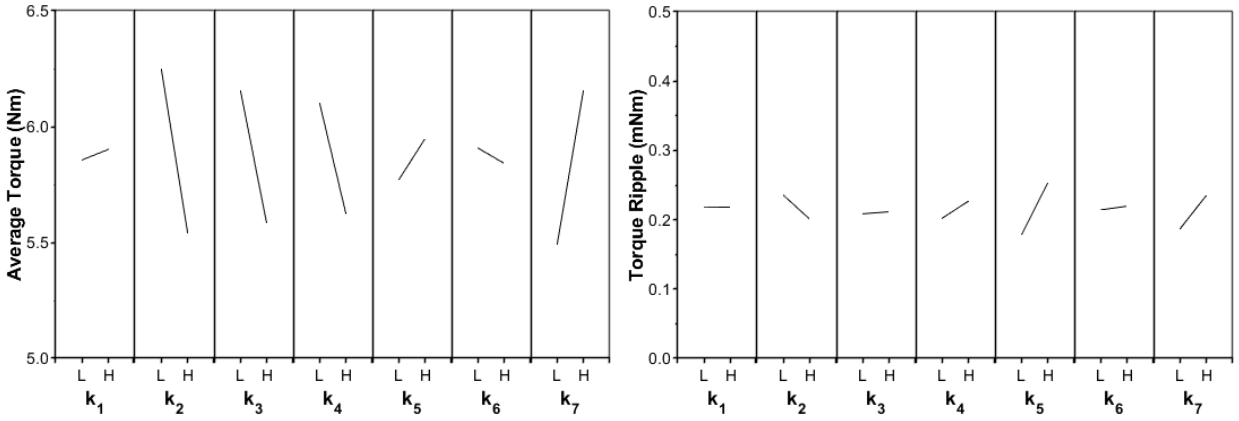
Fig. 2.57. Torque-speed characteristics and torque ripple of optimised 12-slot/10-pole SPM motor.

The main effect plots of the average torque and the torque ripple, based on a 2-level experimental design, are shown in Fig. 2.32. The two levels of each variables are set to be above and below the nominal value by the amounts listed in Table 2.19.

Table 2.19. Change in design parameters of SPM motor used in main effects analysis

| | **Design parameter** | **Units** | **Change in parameter** |
|---|---|---|---|
| $k_1$ | Pole-arc to pole-pitch ratio | N/A | ±0.025 |
| $k_2$ | Pole-shoe height | mm | ±0.5 mm |
| $k_3$ | Tooth width | mm | ±0.5 mm |
| $k_4$ | Back-iron width | mm | ±0.5 mm |
| $k_5$ | Split ratio | N/A | ±2% |
| $k_6$ | Slot opening width | mm | ±0.5 mm |
| $k_7$ | PM height | mm | ±0.5 mm |

The average torque of the optimised 12-slot/10-pole SPM motor is very sensitive to changes in the pole-shoe height, PM dimensions and dimensions of the stator teeth and back-iron. The influence of changes in design parameters on the torque ripple of the motor is very low. The motor split ratio has the highest influence on the motor torque ripple and a low influence on the average torque of the motor.




(a) Average torque (b) Torque ripple

Fig. 2.58. Influence of change in design parameters on torque of optimised 12-slot/10-pole SPM motor.

### 4.2.3 Analysis of Optimised 12-slot/14-pole SPM Motor

The cross-section of the optimised 12-slot/14-pole SPM motor using the genetic algorithm is shown in Table 2.20 and the design parameters are listed in Fig. 2.59. The slot opening width of the optimised motor is fixed to 3 mm and the torque-speed characteristic and the torque ripple map of the motors with optimised and fixed slot opening width are shown in Fig. 2.34.

Table 2.20. Average torque and design parameters of optimised 12-slot/14-pole SPM motor

| **Parameter** | **Units** | **Values** |
|---|---|---|
| Average torque | Nm | 7.0 |
| Torque ripple | % | 2.5 |
| Current advance angle | ° | 8.8 |
| Split ratio | N/A | 0.559 |
| Back-iron width | mm | 3.12 |
| Tooth width | mm | 5.52 |
| Slot opening width | mm | 3.11 |
| PM pole-shoe height | mm | 0.79 |
| PM pole-arc to pole-pitch ratio | mm | 0.866 |
| PM height | mm | 2.97 |
| PM volume | $cm^3$ | 8.41 |
| Torque per Volume | Nm/L | 25.85 |
| Torque per PM Volume | $Nm/cm^3$ | 0.654 |

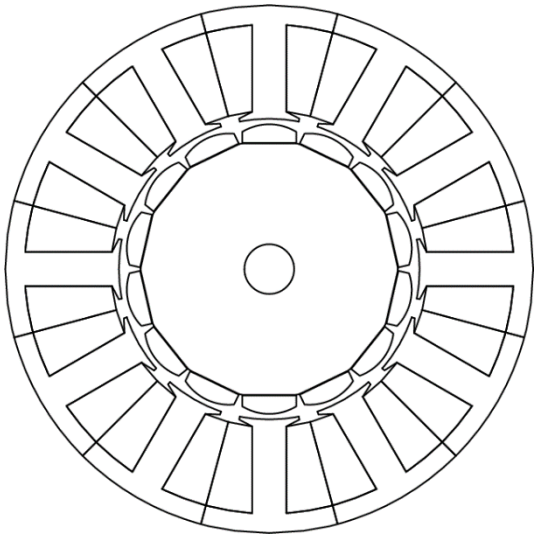
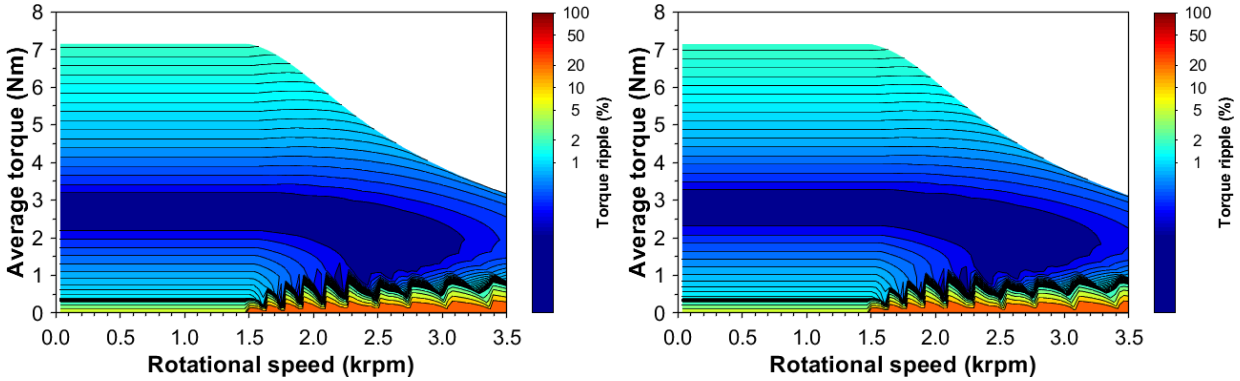


Fig. 2.59. Cross-section of optimised 12-slot/14-pole SPM motor.

The torque-speed characteristics of the motor with optimised and fixed slot opening width are shown in Fig. 2.34. The change in the torque-speed characteristic and torque ripple map due to the change in slot opening is very low. The torque ripple map of the motor is very low throughout the entire torque-speed region. The lowest torque ripple is found in the operating region between 2 and 3 Nm and extends throughout a significant range of operating speeds.




(a) Optimised slot opening width (b) Fixed slot opening width

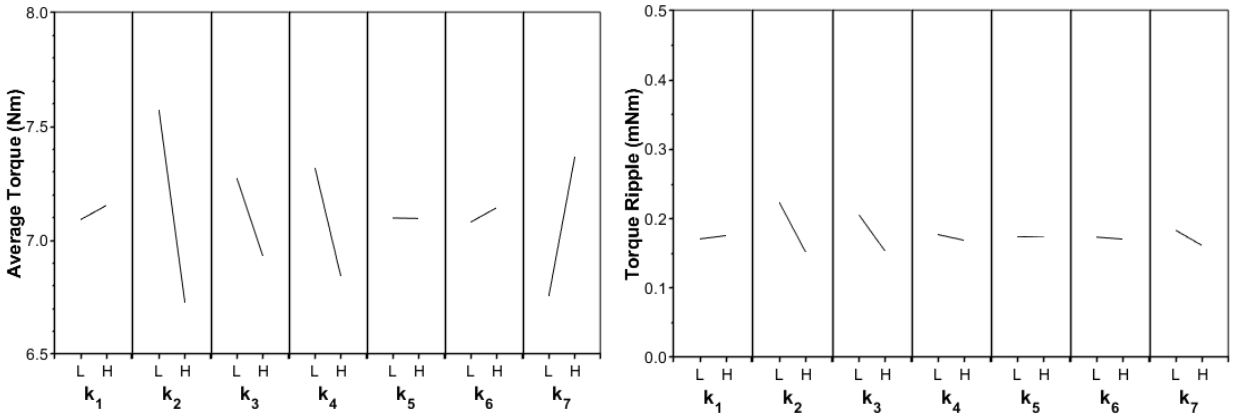
Fig. 2.60. Torque-speed characteristic and torque ripple of optimised 12-slot/14-pole SPM motor.

The main effect plots of the average torque and the torque ripple, based on a 2-level experimental design, are shown in Fig. 2.35. The two levels of each variables are set to be above and below the nominal value by the amounts listed in Table 2.21.

Table 2.21. Change in design parameters of SPM motor used in main effects analysis

| | **Design parameter** | **Units** | **Change in parameter** |
|---|---|---|---|
| $k_1$ | Pole-arc to pole-pitch ratio | N/A | ±0.025 |
| $k_2$ | Pole-shoe height | mm | ±0.5 mm |
| $k_3$ | Tooth width | mm | ±0.5 mm |
| $k_4$ | Back-iron width | mm | ±0.5 mm |
| $k_5$ | Split ratio | N/A | ±2% |
| $k_6$ | Slot opening width | mm | ±0.5 mm |
| $k_7$ | PM height | mm | ±0.5 mm |

The torque ripple of the optimised 12-slot/14-pole SPM motors is sensitive to changes in the PM pole-shoe height, PM height, and tooth width. The PM pole-shoe height and PM height also have a significant influence on the average torque. The influence of changes in the tooth width and back-iron on the average torque is lower than that of changes in PM dimensions.




(a) Average torque (b) Torque ripple

Fig. 2.61. Influence of change in design parameters on torque of optimised 12-slot/14-pole SPM motor.

## 4.3 Multi-objective Optimisation of SPM Motors

### 4.3.1 Optimisation of 12-slot/8-pole SPM Motor

The average torque and torque ripple of the solution space of the optimisation is shown in Fig. 2.36. The colour of the marker indicates the PM volume of each motor design. The PM volume of designs along the Pareto-front increases with increasing average torque. The Pareto-front extends from solutions with torque ripple below 0.5% to solutions with torque ripple of up to 7%. Three motor designs along the Pareto-front are selected to investigate the influence of design parameters on the average torque and torque ripple of the 12-slot/8-pole SPM motor.

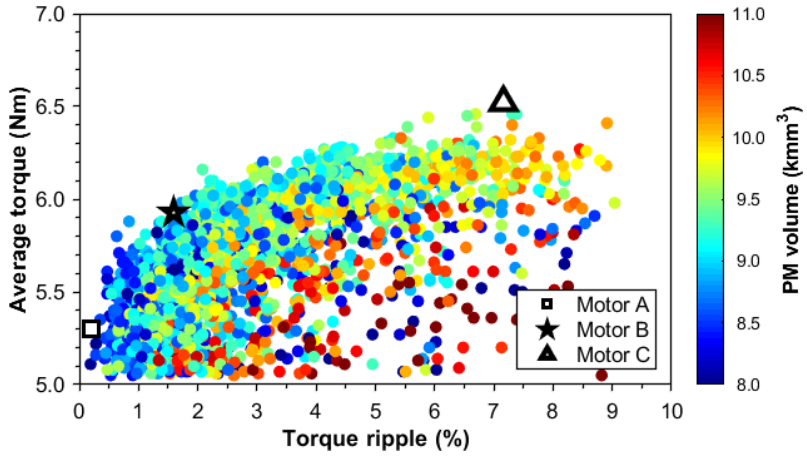


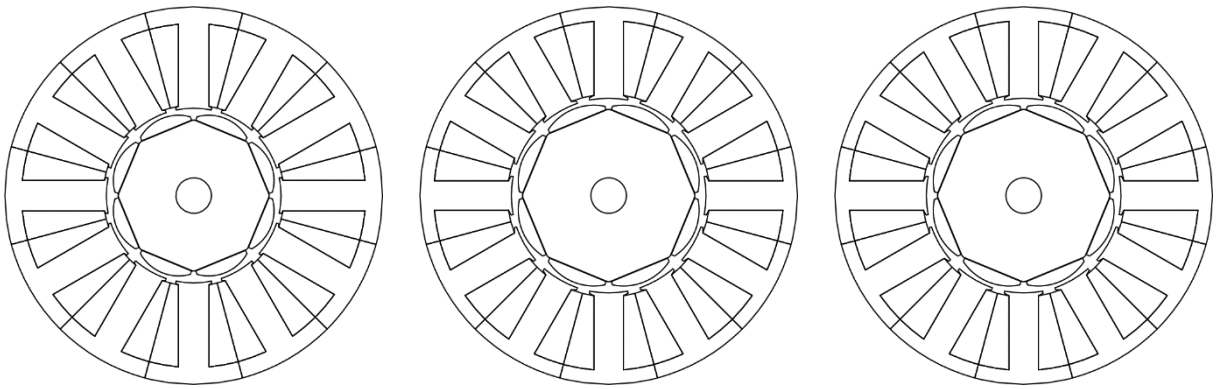

Fig. 2.62. Solution space of multi-objective optimisation of 12-slot/8-pole SPM motor.

The design parameters of the selected motor designs are listed in Table 2.9 and the motor cross-sections are illustrated in Fig. 2.37. The split ratio and PM volume of the motor designs increase with increasing average torque. The stator back-iron width and tooth width decrease with increasing average torque and torque ripple. The average torque of the motor designs varies by up to 22.6% and the torque ripple of the

motor designs varies from 0.2% to 7%. This is expected since increased pole area, increased PM volume and decreased width of the stator teeth and back-iron iron result in a significant increase of saturation of the stator iron. The stator slot opening width increases with increasing average torque and torque ripple. The PM pole-arc to pole-pitch ratio does not vary significantly between the three motor designs. However, the PM pole-shoe height of Motor A is higher than those of Motors B and C.

Table 2.22. Design parameters of optimised 12-slot/8-pole SPM motors

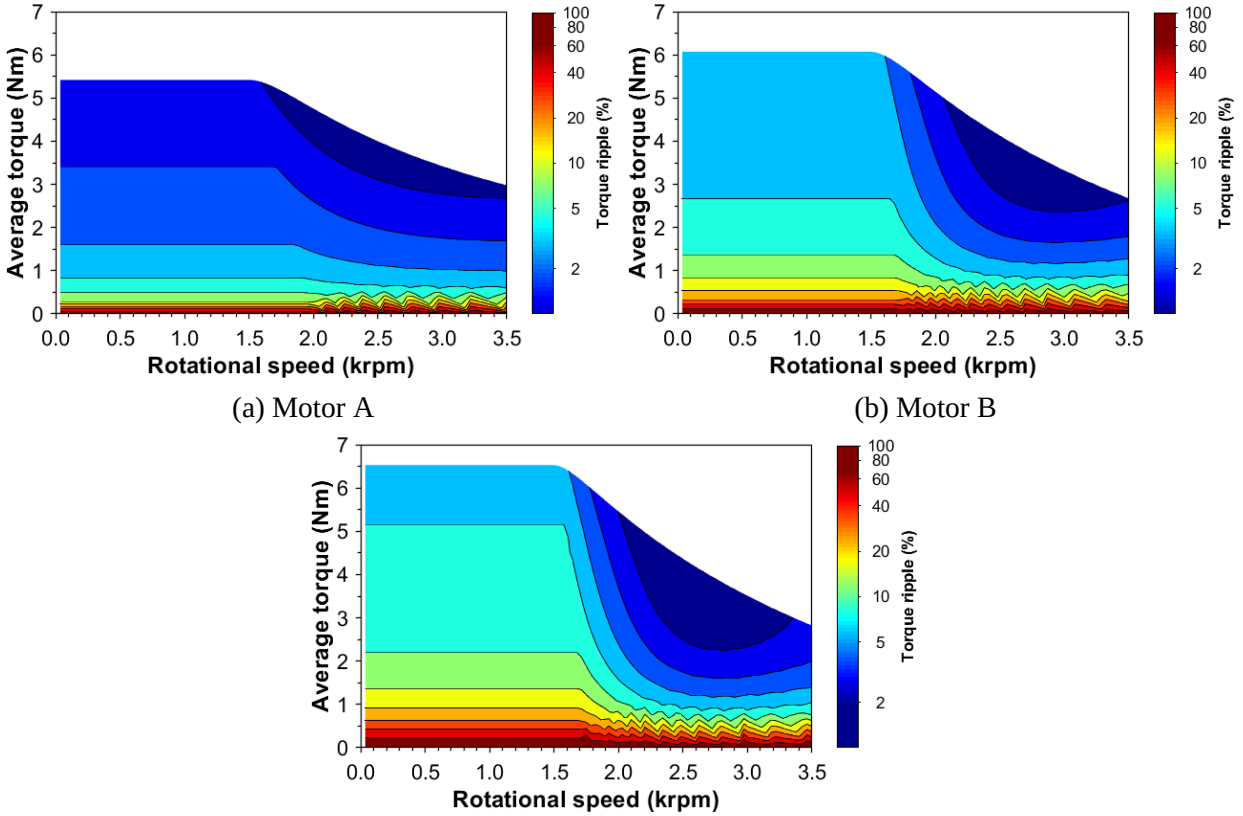
| **Parameter** | **Units** | **Values** | | |
|---|---|---|---|---|
| | | **Motor A** | **Motor B** | **Motor C** |
| Average torque | Nm | 5.3 | 5.9 | 6.5 |
| Torque ripple | % | 0.2 | 1.6 | 7.2 |
| Current advance angle | ° | 14.2 | 17.4 | 8.8 |
| Pole-arc to pole-pitch ratio | N/A | 0.889 | 0.888 | 0.907 |
| Pole-shoe height | mm | 1.01 | 0.88 | 0.88 |
| Tooth width | mm | 6.88 | 6.63 | 5.40 |
| Back-iron width | mm | 3.79 | 3.13 | 3.12 |
| Split ratio | N/A | 0.452 | 0.505 | 0.514 |
| Slot opening width | mm | 2.32 | 2.88 | 2.93 |
| PM height | mm | 2.89 | 2.90 | 2.91 |
| PM volume | $cm^3$ | 8.14 | 9.21 | 9.51 |
| Torque per Volume | Nm/L | 24.91 | 27.73 | 30.55 |
| Torque per PM Volume | $Nm/cm^3$ | 0.651 | 0.641 | 0.684 |



(a) Motor A (b) Motor B (c) Motor C

Fig. 2.63. Cross-sections of 12-slot/8-pole SPM motors selected from multi-objective optimisation solution space.

The torque-speed characteristics and the torque ripple across the operating range of the three motors are shown in Fig. 2.38. The torque ripples of the three motors increase with decreasing current magnitude since the change in absolute torque ripple due to current magnitude is lower than that of the average torque. This effect is more pronounced in the torque ripple maps of Motors B and C. Operating points in the flux-weakening region and maximum electrical load result in the lowest torque ripple.




(a) Motor A

(b) Motor B

(c) Motor C

Fig. 2.64. Torque-speed characteristics and torque ripple maps of optimised 12-slot/8-pole SPM motors.

### 4.3.2 Optimisation of 12-slot/10-pole SPM motor

The solution space of the multi-objective optimisation of the 12-slot/10-pole SPM motor is shown in Fig. 2.39. The PM volume of the solutions along the Pareto-front increases with increasing average torque and torque ripple. The design parameters and performance of three motors along the Pareto-front of the solution space are analysed.

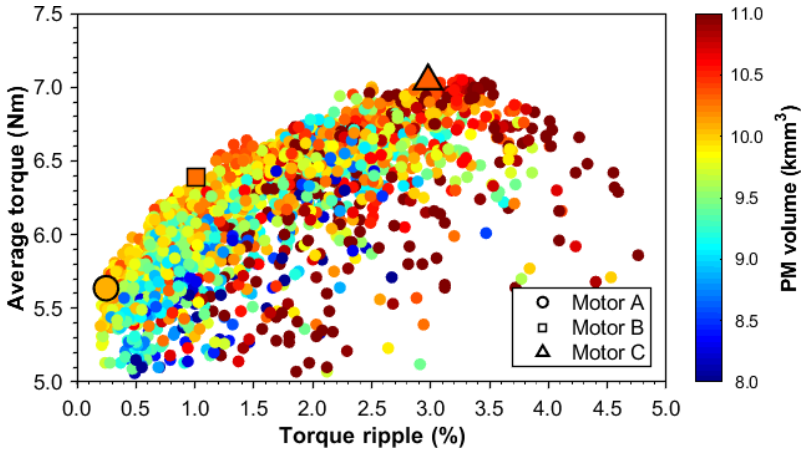



Fig. 2.65. The solution space of multi-objective optimisation of 12-slot/10-pole SPM motor.

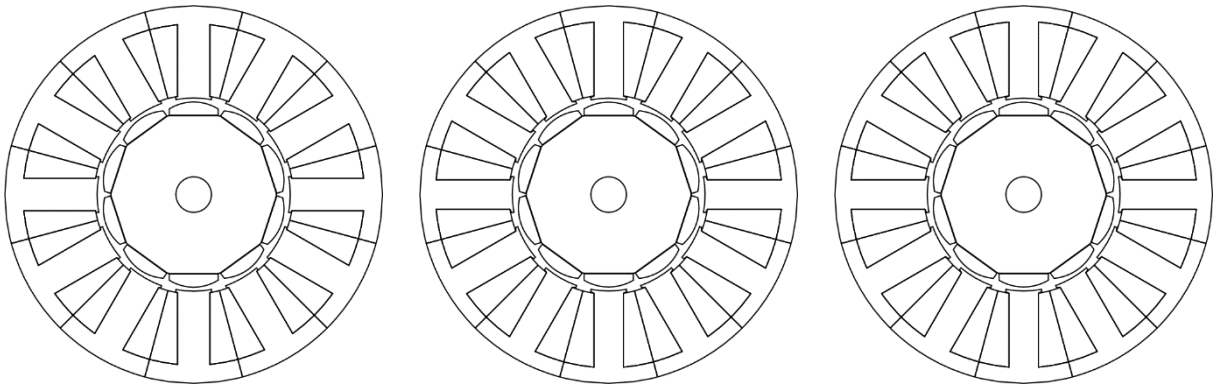
The compromise between the average torque and torque ripple, and the impact on the motor design parameters, are investigated by selecting three solutions along the Pareto-front of the solution space, as

indicated in Fig. 2.39. The cross-sections of the motors are shown in Fig. 2.40 and the design parameters are listed in Table 2.10.

The average torque of the three motors varies by up to 25% and the torque ripple varies from 0.2% to 3%. The split ratio of Motors A and B is almost identical, however, the split ratio of Motor C is 5.6% higher than that of Motor B. The PM volume and the torque per PM volume of the motors increase with increasing average torque and torque ripple. The PM volume of Motor C is 22.8% higher than that of Motor A. The stator tooth width and back-iron width decrease with increasing average torque and torque ripple. The stator slot opening width of Motors A and B is identical and the slot opening width of Motor C is narrower, 0.24 mm. The PM pole-arc to pole-pitch ratio increases with increasing average torque and torque ripple. Conversely, the PM pole-shoe height decreases, thus resulting in higher PM volume.

Table 2.23. Design parameters of optimised 12-slot/10-pole SPM motor

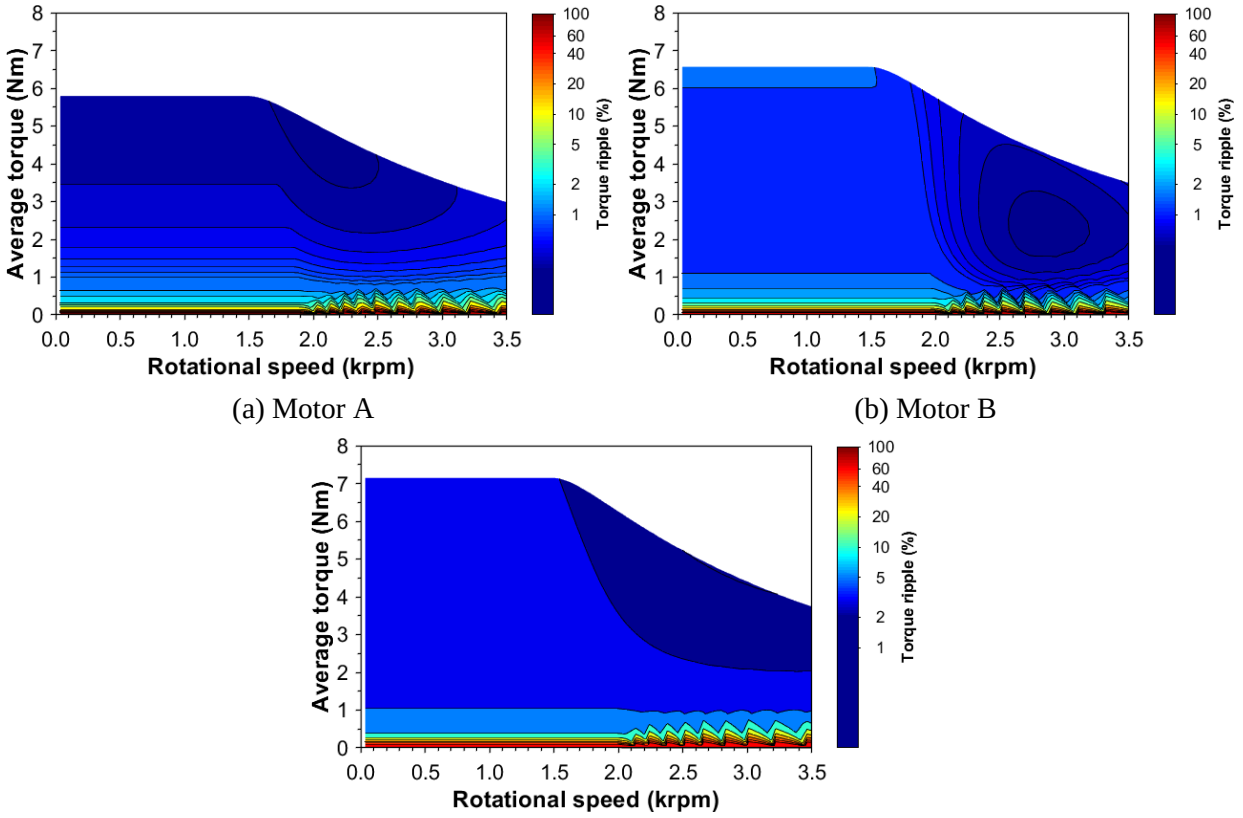
| **Parameter** | **Units** | **Values** | | |
|---|---|---|---|---|
| | | **Motor A** | **Motor B** | **Motor C** |
| Average torque | Nm | 5.6 | 6.4 | 7.0 |
| Torque ripple | % | 0.2 | 1.0 | 3.0 |
| Current advance angle | ° | 12.8 | 13.2 | 10.9 |
| Pole-arc to pole-pitch ratio | N/A | 0.889 | 0.891 | 0.898 |
| Pole-shoe height | mm | 0.81 | 0.73 | 0.74 |
| Tooth width | mm | 7.30 | 6.65 | 5.30 |
| Back-iron width | mm | 4.21 | 3.51 | 3.33 |
| Split ratio | N/A | 0.501 | 0.500 | 0.528 |
| Slot opening width | mm | 3.37 | 3.37 | 3.13 |
| PM height | mm | 2.94 | 2.96 | 2.83 |
| PM volume | $cm^3$ | 10.07 | 10.27 | 10.30 |
| Torque per Volume | Nm/L | 26.32 | 30.08 | 32.90 |
| Torque per PM Volume | $Nm/cm^3$ | 0.556 | 0.623 | 0.679 |



(a) Motor A (b) Motor B (c) Motor C

Fig. 2.66. Cross-sections of 12-slot/10-pole SPM motors selected from multi-objective optimisation solution space.

The torque-speed characteristics and the torque ripples across the operating range of the three motors are shown in Fig. 2.41. The torque ripple of the motors is lowest in the flux-weakening region. The torque ripple in the flux-weakening region of Motor A increases with in increasing rotational speed and decreasing electrical load. Motor B has low torque ripple in the constant-torque region, however, the torque ripple is higher at high and very low electrical loads. The torque ripple in the flux-weakening region is very low at a particular operating point and increases with increasing change in the electrical load and rotational speed. The torque ripple of Motor C does not vary significantly in the constant-torque region and increases at low electrical loads. Similarly, the torque ripple in the flux-weakening region is very low at high electrical loads and increases gradually with decreasing electrical load.




(a) Motor A

(b) Motor B

(c) Motor C

Fig. 2.67. Torque-speed characteristics and torque ripple maps of optimised 12-slot/10-pole SPM motors.

### 4.3.3 Optimisation of 12-slot/14-pole SPM motor

The solution space of the multi-objective optimisation of the 12-slot/14-pole SPM motor is shown in Fig. 2.42. The Pareto-front forms a quasi-linear linear line and the knee of the Pareto-front is located at a very low torque ripple. The torque ripple of 12-slot/14-pole motors is inherently low and therefore it is expected that very low torque ripples can be achieved using this topology. The PM volume of the motors along the Pareto-front is very low and increases with increasing average torque and torque ripple.

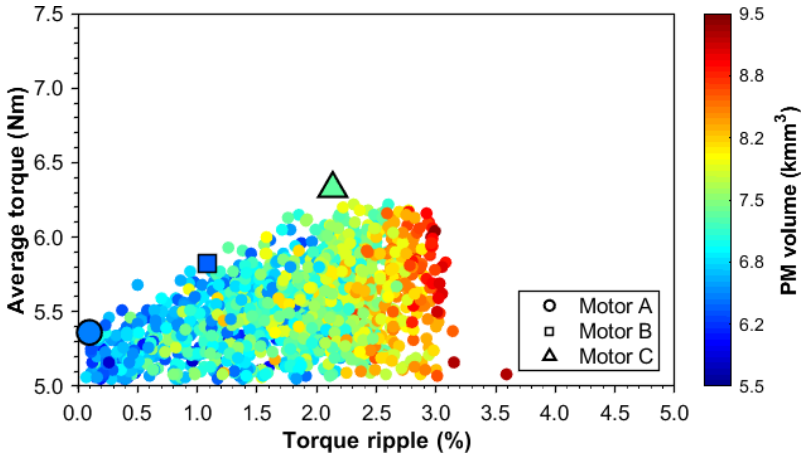
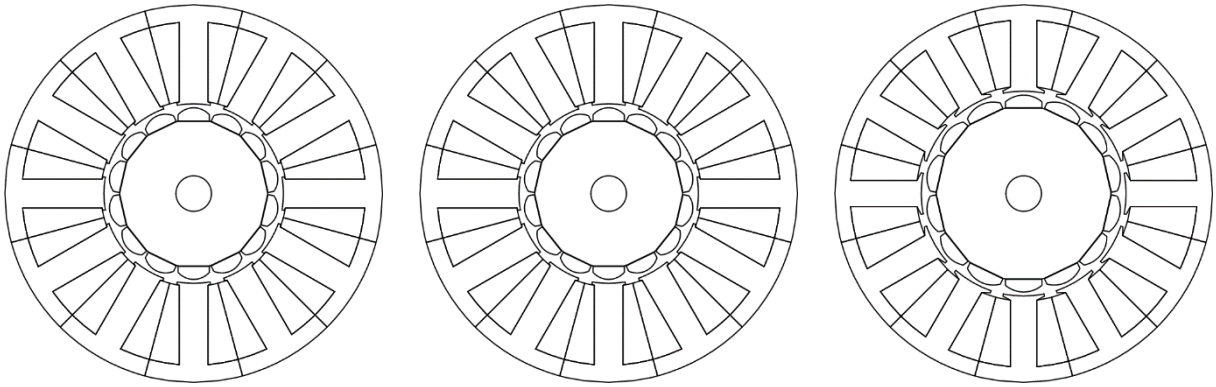



Fig. 2.68. Solution space of multi-objective optimisation of 12-slot/14-pole SPM motor.

The average torque, torque ripple, and design parameters of Motors A, B, and C indicated in Fig. 2.42 are analysed. The design parameters are listed in Table 2.11 and the cross-sections of the motors are shown in Fig. 2.43. The average torque of the three motors varies by up to 16.7% and the torque ripple varies between 0.1% and 2.1%. The PM volume of the motors increases with increasing average torque and varies by up to 13.3%. The split ratio of the motors increases with increasing average torque and torque ripple. Conversely, the stator tooth width, back-iron width, and slot opening width decrease with increasing average torque and torque ripple. The PM pole-arc to pole-pitch ratios of Motors A and C are almost identical. However, the PM pole-shoe height and PM height decrease with increasing average torque and torque ripple.

Table 2.24. Average torque and design parameters of optimised 12-slot/14-pole SPM motor

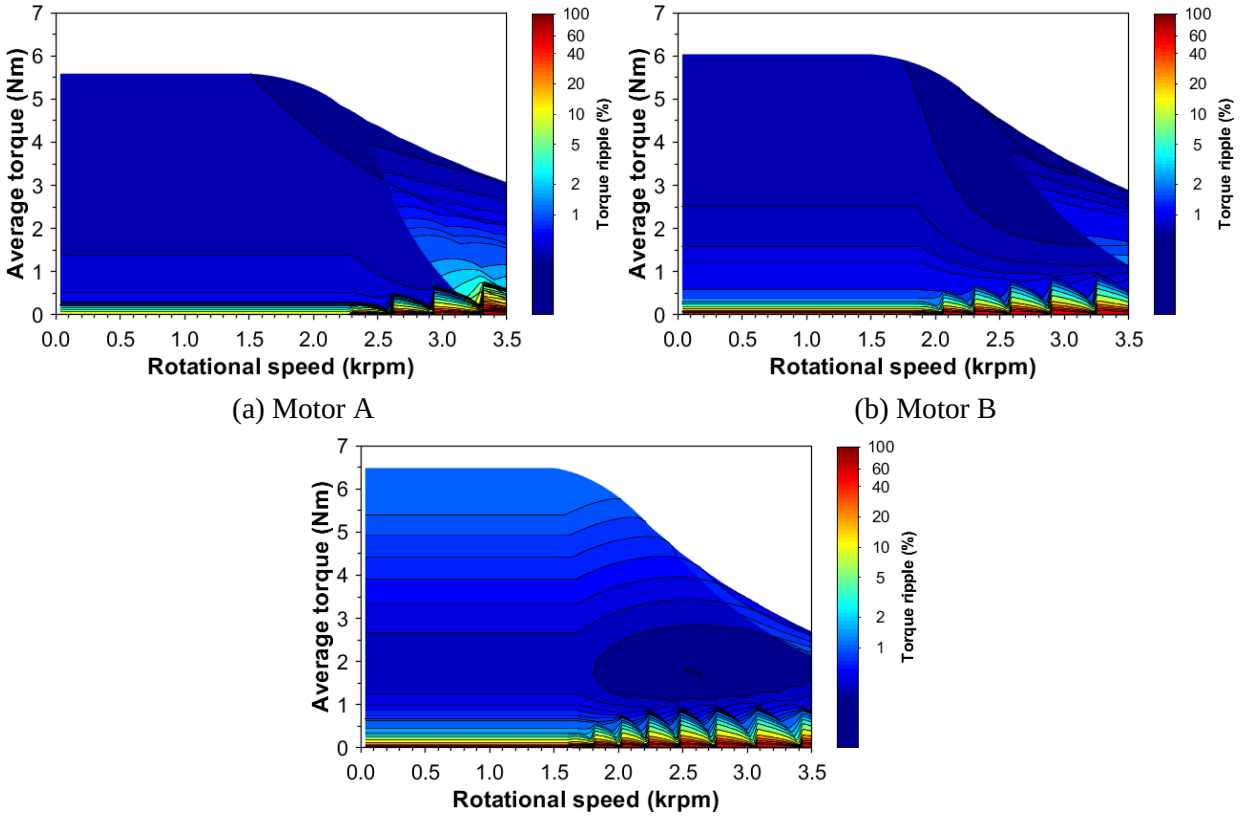
| **Parameter** | **Units** | **Values** | | |
|---|---|---|---|---|
| | | **Motor A** | **Motor B** | **Motor C** |
| Average torque | Nm | 5.4 | 5.8 | 6.3 |
| Torque ripple | % | 0.1 | 1.1 | 2.1 |
| Current advance angle | ° | 15.2 | 10.9 | 8.5 |
| Pole-arc to pole-pitch ratio | N/A | 0.873 | 0.776 | 0.876 |
| Pole-shoe height | mm | 1.24 | 0.91 | 1.10 |
| Tooth width | mm | 6.49 | 6.51 | 5.94 |
| Back-iron width | mm | 3.86 | 3.23 | 3.44 |
| Split ratio | N/A | 0.465 | 0.509 | 0.532 |
| Slot opening width | mm | 3.17 | 3.14 | 2.85 |
| PM height | mm | 2.94 | 2.89 | 2.85 |
| PM volume | $cm^3$ | 6.48 | 6.34 | 7.34 |
| Torque per Volume | Nm/L | 25.38 | 27.26 | 29.61 |
| Torque per PM Volume | $Nm/cm^3$ | 0.834 | 0.815 | 0.856 |



(a) Motor A (b) Motor B (c) Motor C

Fig. 2.69. Cross-sections of optimised 12-slot/14-pole SPM motors.

The torque-speed characteristics and the torque ripple across the operating range of the three motors are shown in Fig. 2.44. The torque ripple of the three motors is very low and there is numerical noise in the contour plots of the flux-weakening region. The torque ripple of the motors in the constant-torque region is lower than that in the flux-weakening region. The torque ripple in the flux-weakening region of Motor A and Motor B increases with decreasing electrical load and varies with rotational speed. The torque ripple of Motor C in the constant-torque region increases with increasing electrical load. The torque ripple of the Motor C at a particular operating region in the flux-weakening region is very low and increases with change in the electrical load.




(a) Motor A (b) Motor B

(c) Motor C

Fig. 2.70. Torque-speed characteristics and torque ripple maps of optimised 12-slot/14-pole SPM motors.

## 4.4 Comparison of Single-Objective and Multi-Objective Optimisation of SPM Motors

The solution spaces of the multi-objective optimisation of 12-slot/8-pole, 12-slot/10-pole, 12-slot/14-pole SPM motors, together with the motors optimised using the single-objective optimisation are shown in Fig. 2.45.

Some observations can be found further from Fig. 2.45 as follows:

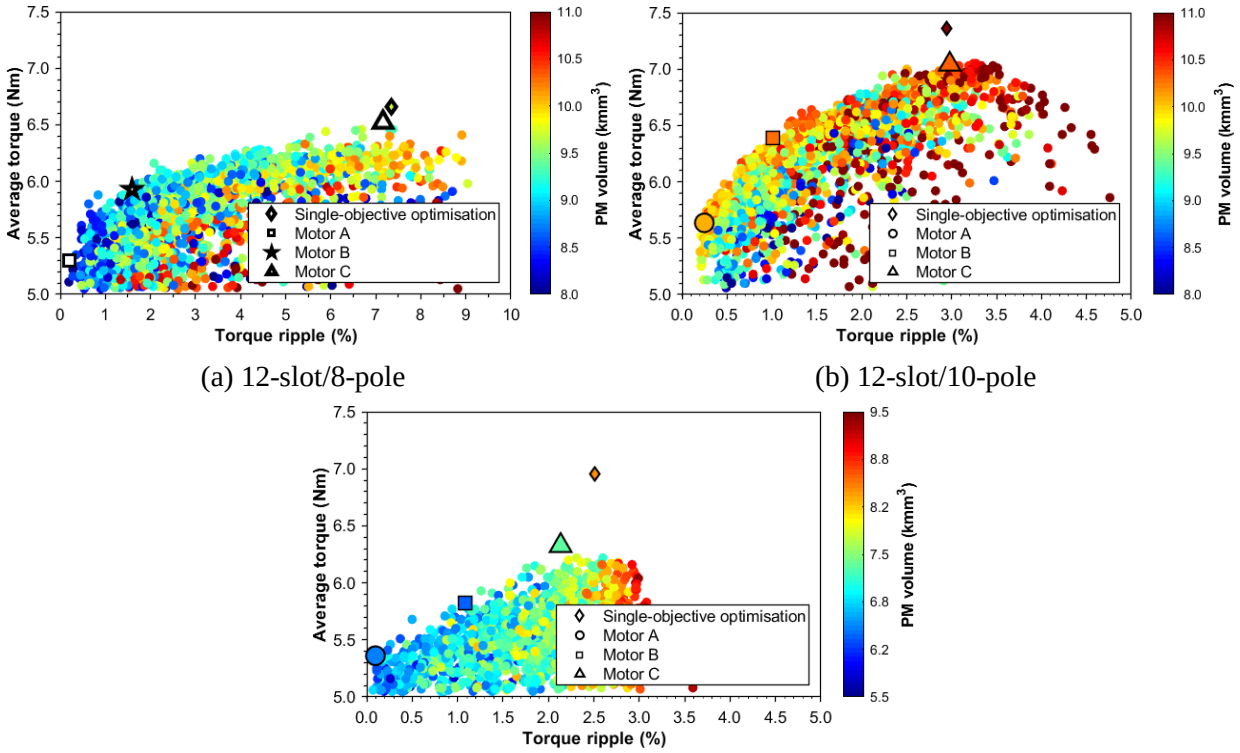
- Multi-objective optimised motors usually have lower torque ripples;
- Single-objective optimised motors for maximum average torque result in higher average torque than the multi-objective optimised motors due to the compromise amongst different objectives.

The 12-slot/8-pole SPM motor optimised for the single-objective optimisation, i.e. average torque only, lies on the upper portion of the Pareto-front, thereby indicating that the Pareto-front is a good estimation of the average torque and torque ripple limits of the motor. On the other hand, the 12-slot/10-pole and 12-slot/14-pole SPM motors optimised for the single-objective optimisation, i.e. average torque only, are well beyond the Pareto-front of the solution space of the multi-objective optimisation.

The Pareto-front of the multi-objective optimisations of the SPM motors follows a knee curve characteristic. The Pareto-front of the 12-slot/14-pole SPM motor beyond the knee of the curve follows a quasi-linear line. Thus, a lower torque ripple leads to a significantly lower average torque with respect to the other two topologies.

The solution space of the multi-objective optimisation shows that the 12-slot/10-pole SPM provides the best compromise between average torque and torque ripple at the cost of higher PM volume than those of 12-slot/8-pole and 12-slot/14-pole motors.

The design parameters of the SPM motors optimised for maximum average torque are listed in Table 2.25 and the cross-sections are shown in Fig. 2.46. The 12-slot/10-pole motor results in the highest average torque and the increase in average torque with respect to the optimised 12-slot/8-pole and 12-slot/14-pole motors is 10.5% and 5.7%, respectively. The average torque per PM volume of the 12-slot/14-pole is the 20.9% and 27.0% higher than that of the 12-slot/8-pole and 12-slot/10-pole motors, respectively. The torque ripple of the optimised motors decreases with increasing rotor pole number. The current advance angle of the optimised motors ranges decreases significantly with increasing rotor pole number. The split ratio of the motors increases with increasing rotor pole number. The dimensions of the stator back-iron and tooth widths are relatively similar. The pole-shoe height increases with increasing rotor pole number. Conversely, the pole-arc to pole-pitch ratio decreases with increasing rotor pole number.




(a) 12-slot/8-pole

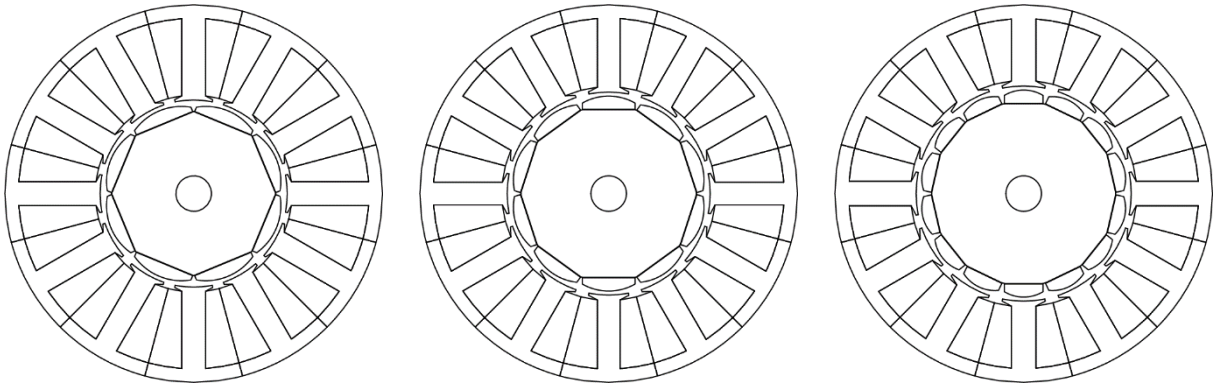
(b) 12-slot/10-pole

(c) 12-slot/14-pole

Fig. 2.71. Solution space of multi-objective optimisation and solution of single-objective optimisation of SPM motors.

Table 2.25. Design parameters of SPM motors optimised for average torque only

| **Parameter** | **Units** | **Values** | | |
|---|---|---|---|---|
| | | **12-slot/8-pole** | **12-slot/10-pole** | **12-slot/14-pole** |
| Average torque | Nm | 6.7 | 7.4 | 7.0 |
| Torque ripple | % | 6.6 | 3.1 | 1.9 |
| Current advance angle | ° | 6.8 | 0.8 | 0.3 |
| Split ratio | N/A | 0.485 | 0.527 | 0.559 |
| Back-iron width | mm | 3.05 | 3.02 | 3.12 |
| Tooth width | mm | 5.35 | 5.14 | 5.52 |
| Slot opening width | mm | 3.0 | 3.0 | 3.0 |
| PM pole-shoe height | mm | 0.71 | 0.73 | 0.79 |
| PM pole-arc to pole-pitch ratio | mm | 0.919 | 0.902 | 0.866 |
| PM height | mm | 3.00 | 2.99 | 2.97 |
| PM volume | $cm^3$ | 9.73 | 11.31 | 11.81 |
| Torque per Volume | Nm/L | 29.14 | 34.78 | 25.85 |
| Torque per PM Volume | $Nm/cm^3$ | 0.688 | 0.655 | 0.592 |

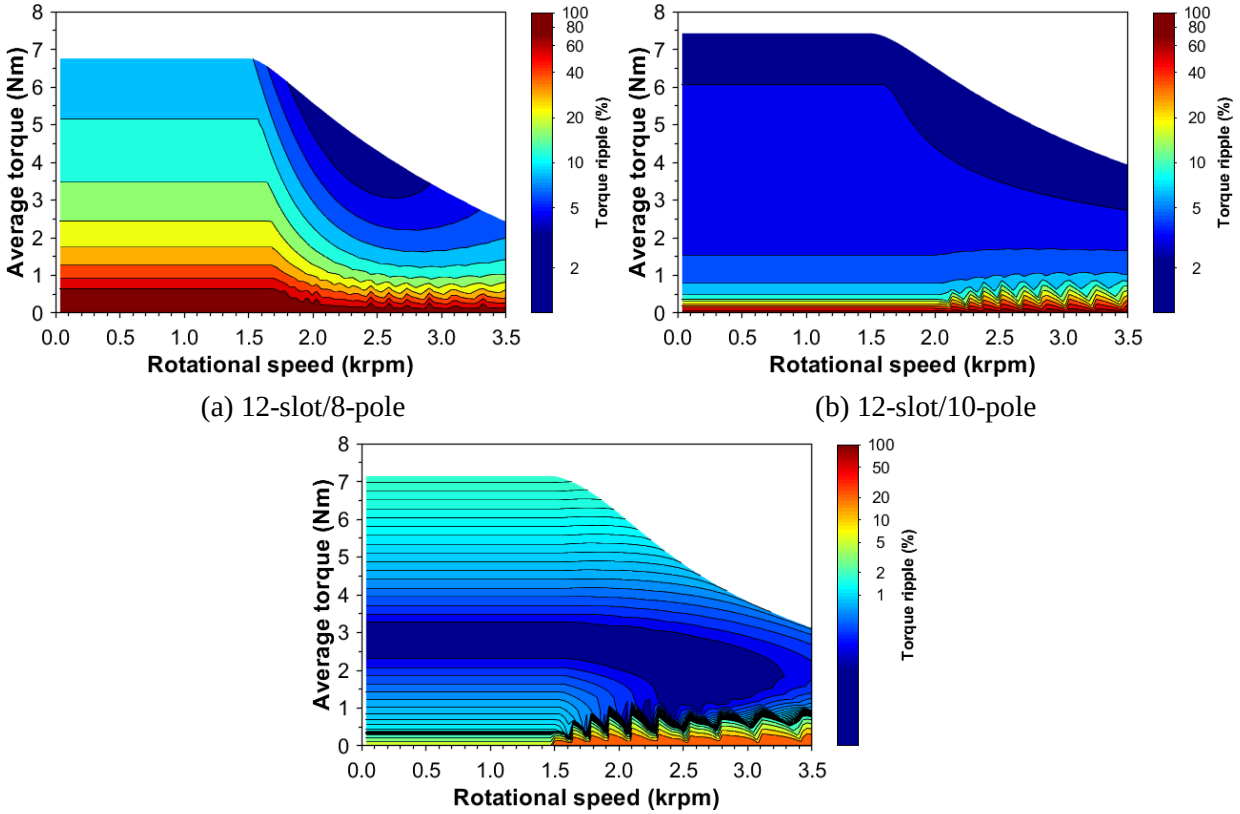


(a) 12-slot/8-pole (b) 12-slot/10-pole (c) 12-slot/14-pole

Fig. 2.72. Cross-sections of SPM motors optimised for maximum average torque only.

The torque-speed characteristics and torque ripple maps of the single-objective optimised motors are shown in Fig. 2.73. The torque ripple maps of the 12-slot/8-pole and 12-slot/10-pole motors have similar characteristics. The torque ripple in the constant torque region increases significantly with decreasing electrical load. The torque ripple in the flux-weakening region is very low at maximum electrical load and varies with rotational speed. The increase in torque ripple in the flux-weakening region with decreasing electrical load is higher in the 12-slot/8-pole motor than in the 12-slot/10-pole motor. The torque ripple of the 12-slot /14-pole motor is very low across the entire torque-speed range. The lowest torque ripple is found in the operating region between 2 and 3 Nm and extends throughout a significant range of operating speeds.

The design parameters of the multi-objective optimised 12-slot/8-pole, 12-slot/10-pole, and 12-slot/14-pole SPM motors are listed in Table 2.27 and the corresponding units are listed in Table 2.26. In general, the PM volume of the motors increases with increasing average torque and torque ripple. However, the PM volume of 12-slot/14–pole Motor B is 2.1% lower than that of Motor A. Similarly, the split ratio of the motors increases with increasing average torque and torque ripple. Conversely, the stator back-iron and tooth width decrease with increasing average torque and torque ripple. Thinner back-iron and teeth paired with higher split ratio and PM volume result in higher stator saturation and higher torque ripple. The pole-arc to pole pitch ratio of the motor of a particular topology does not vary significantly. The pole-shoe height of Motors B and C of the 12-slot/8-pole motor is identical. Similarly, the pole-shoe heights of the Motor B and Motor C of the 12-slot/10-pole motor are almost identical. However, the pole-shoe height of Motor C of the 12-slot/14-pole motor is higher than those of Motor A and Motor B of the same topology.




(a) 12-slot/8-pole

(b) 12-slot/10-pole




(c) 12-slot/14-pole

Fig. 2.73. Torque-speed characteristics and torque ripple maps of single-objective optimised SPM motors.

Table 2.26. Design parameters of SPM motors under analysis

| | **Design parameter** | **Units** |
|---|---|---|
| $k_1$ | Pole-arc to pole-pitch ratio | N/A |
| $k_2$ | Pole-shoe height | mm |
| $k_3$ | Tooth width | mm |
| $k_4$ | Back-iron width | mm |
| $k_5$ | Split ratio | N/A |
| $k_6$ | Slot opening width | mm |
| $k_7$ | PM height | mm |
| $k_8$ | PM volume | $cm^3$ |

Table 2.27. Design parameters of multi-objective optimised SPM motors

| | **Motor A** | **Motor B** | **Motor C** | **Motor A** | **Motor B** | **Motor C** | **Motor A** | **Motor B** | **Motor C** |
|---|---|---|---|---|---|---|---|---|---|
| Average Torque (Nm) | 5.3 | 5.9 | 6.5 | 5.6 | 6.4 | 7.0 | 5.4 | 5.8 | 6.3 |
| Torque ripple (%) | 0.2 | 1.6 | 7.2 | 0.2 | 1.0 | 3.0 | 0.1 | 1.1 | 2.1 |
| $k_1$ | 0.889 | 0.888 | 0.907 | 0.889 | 0.891 | 0.898 | 0.873 | 0.776 | 0.876 |
| $k_2$ | 1.01 | 0.88 | 0.88 | 0.81 | 0.73 | 0.74 | 1.24 | 0.91 | 1.10 |
| $k_3$ | 6.88 | 6.63 | 5.40 | 7.30 | 6.65 | 5.30 | 6.49 | 6.51 | 5.94 |
| $k_4$ | 3.79 | 3.13 | 3.12 | 4.21 | 3.51 | 3.33 | 3.86 | 3.23 | 3.44 |
| $k_5$ | 0.452 | 0.505 | 0.514 | 0.501 | 0.500 | 0.528 | 0.465 | 0.509 | 0.532 |
| $k_6$ | 2.32 | 2.88 | 2.93 | 3.37 | 3.37 | 3.13 | 3.17 | 3.14 | 2.85 |
| $k_7$ | 2.89 | 2.90 | 2.91 | 2.94 | 2.96 | 2.83 | 2.94 | 2.89 | 2.85 |
| $k_8$ | 8.14 | 9.21 | 9.51 | 10.07 | 10.27 | 10.30 | 6.48 | 6.34 | 7.34 |

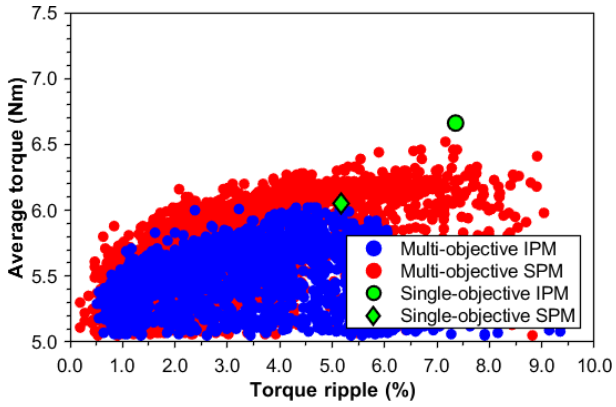
## 4.5 Comparison of Single-Objective and Multi-Objective Optimisation of IPM and SPM Motors

The solution space of the multi-objective optimisation of IPM and SPM motors as well as the average torque and torque ripple of the single-objective optimised motors are shown in Fig. 2.74.

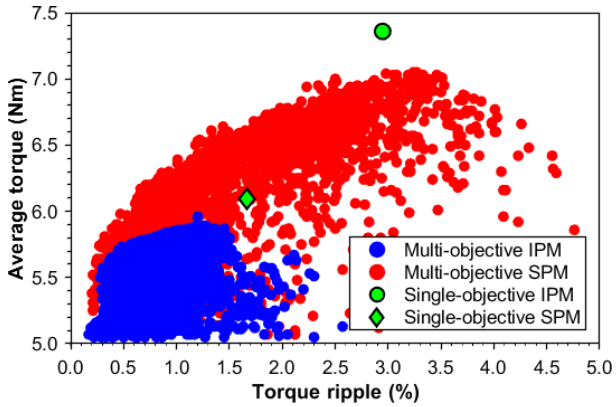
The average torque of the single-objective optimised SPM motors is significantly higher than that of the IPM motors despite the increase in effective air-gap due to the rotor sleeve. The corresponding torque ripples of the single-objective optimised 12-slot/8-pole and 12-slot/10-pole IPM motors are significantly lower than that of the SPM motors with the same slot/pole number combination. However, the torque ripple of the single-objective optimised 12-slot/14-pole IPM motor is higher than that of the 12-slot/14-pole SPM motor.

The Pareto-front of the multi-objective optimisation of the IPM and SPM motors under investigation shows that the SPM motors allow for a better compromise between the average torque and torque ripple at the optimised operating point. Thus, SPM motors can provide lower torque ripple and higher average torque than IPM motors with the same slot/pole-number combination.

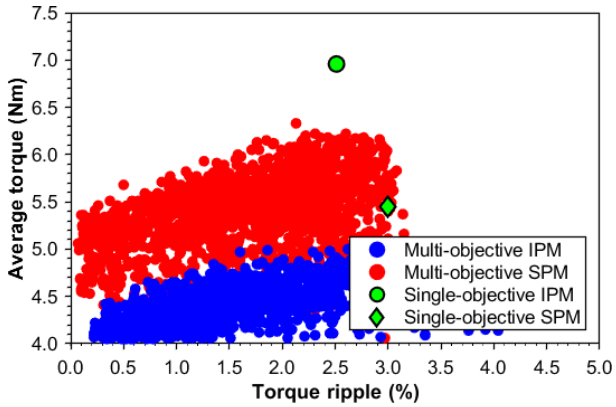
The discrepancy between the Pareto-fronts of the IPM and SPM motors increases with increasing rotor pole number. This can be attributed to the fact that the number of flux leakage paths through the rotor iron ribs of IPM motors increases with increasing rotor pole number, thus resulting in lower average torque.




(a) 12-slot/8-pole




(b) 12-slot/10-pole




(c) 12-slot/14-pole

Fig. 2.74. Solution spaces of the multi-objective optimisation and single-objective optimisation solutions of IPM and SPM motors.

The design parameters of the IPM and SPM motors optimised for maximum average torque, with unified stator slot opening width, are listed in Table 2.28. The average torque, torque ripple, and current angle at the corner point of the torque-speed characteristic are listed for comparison.

The difference in average torque between IPM and SPM motors of a given slot/pole number combination increases with increasing rotor pole number. Conversely, the difference in torque ripple decreases with increasing rotor pole number. The current angle of the motors decreases with increasing rotor pole number since the reluctance torque decreases significantly. Furthermore, the current angle of IPM motors is

significantly higher than that of SPM motors.

The average torque per PM volume of IPM motors increases with increasing rotor pole number. The 12-slot/14-pole SPM motor has the highest torque per PM volume, which is 21.1% and 24.1% higher than that of the 12-slot/8-pole SPM motor and 12-slot/10-pole SPM motors, respectively. The 12-slot/10-pole SPM motor has the highest torque density of 34.78 mNm/m$^3$, which is 37% higher than that of the 12-slot/14-pole IPM motor.

The split ratio of the IPM motors is higher than that of the SPM motors and the difference in split ratio between IPM and SPM motors of a particular slot/pole number combination decreases with increasing rotor pole number. The stator back-iron width and tooth width of the optimised IPM motors decreases with increasing rotor pole number. The pole-shoe height of the IPM and SPM motors of the 12-slot/8-pole and 12-slot/10-pole motors with a given rotor pole number is identical. The difference in pole-shoe height of the 12-slot/14-pole IPM and SPM motors is 0.02 mm. The pole-arc to pole-pitch ratio of the IPM motors is lower than that of the SPM motors.

Table 2.28. Design parameters of IPM and SPM motors optimised for maximum average torque

| | **Units** | **12-slot/8-pole** | | **12-slot/10-pole** | | **12-slot/14-pole** | |
|---|---|---|---|---|---|---|---|
| | | **IPM** | **SPM** | **IPM** | **SPM** | **IPM** | **SPM** |
| Average torque | Nm | 6.2 | 6.7 | 6.1 | 7.4 | 5.5 | 7.0 |
| Torque ripple | % | 3.0 | 6.6 | 1.7 | 3.1 | 3.0 | 1.9 |
| Current advance angle | ° | 18.9 | 6.8 | 16.5 | 0.8 | 9.9 | 0.3 |
| Axial length | mm | 37.5 | 37.5 | 37.5 | 37.5 | 37.5 | 37.5 |
| Air-gap length | mm | 0.6 | 0.9 | 0.6 | 0.6 | 0.6 | 0.9 |
| Pole-arc to pole-pitch ratio | N/A | 0.717 | 0.919 | 0.699 | 0.902 | 0.663 | 0.866 |
| Pole-arc height | mm | 0.71 | 0.71 | 0.73 | 0.73 | 0.81 | 0.79 |
| Rib width | mm | 1.26 | N/A | 0.87 | N/A | 0.90 | N/A |
| Tooth width | mm | 5.52 | 5.35 | 5.28 | 5.14 | 5.11 | 5.52 |
| Back-iron width | mm | 3.03 | 3.05 | 3.10 | 3.02 | 3.20 | 3.12 |
| Split ratio | N/A | 0.534 | 0.485 | 0.532 | 0.527 | 0.560 | 0.559 |
| Slot opening width | mm | 3.0 | 3.0 | 3.0 | 3.0 | 3.0 | 3.0 |
| PM height | mm | 2.98 | 3.00 | 2.99 | 2.99 | 2.88 | 2.97 |
| PM width | mm | 12.48 | N/A | 9.47 | N/A | 7.43 | N/A |
| PM volume | cm$^3$ | 11.17 | 9.73 | 10.60 | 11.04 | 11.23 | 11.81 |
| Torque per Volume | Nm/L | 29.14 | 31.49 | 28.67 | 34.78 | 25.85 | 25.85 |
| Torque per PM Volume | Nm/cm$^3$ | 0.555 | 0.688 | 0.575 | 0.671 | 0.490 | 0.598 |

## 4.6 Conclusion

The genetic algorithm with a population of 64 motors and 50 generations is used to optimise the 12-slot/8-pole, 12-slot/10-pole, and 12-slot/14-pole SPM motors. Single-objective optimisation is used to identify the maximum average torque for a given slot/pole number combination. Multi-objective optimisation is performed to identify the compromise between average torque and torque ripple of each topology at the corner point of the torque-speed characteristic. Three motor designs along the Pareto-front are analysed to identify the influence of design parameters on the average torque and torque ripple. The torque-speed characteristic of each optimised motors and the torque ripple across the entire torque-speed range is analysed.

Single-objective optimisation of SPM motors shows that the 12-slot/10-pole motor results in the highest average torque and the difference in average torque with respect to the optimised 12-slot/8-pole and 12-slot/14-pole motors is 10.5% and 5.7%, respectively. The 12-slot/14-pole SPM motor has the highest average torque per PM volume, 10.5% and 5.7% higher than that of the 12-slot/8-pole and 12-slot/10-pole motors, respectively. The current advance angle of the optimised motors ranges decreases significantly with increasing rotor pole number. This is due to the fact that reluctance torques in 12-slot/10-pole and 12-slot/14-pole motors are low. The torque ripple of the optimised motors decreases with increasing rotor pole number. This can be justified by the fact that the LCMs of the stator and rotor pole number of 12-slot/10-pole and 12-slot/14-pole motors are higher than that of the 12-slot/8-pole motor, thus resulting in lower cogging torque. The split ratio of the motors increases with increasing rotor pole number. The dimensions of the stator back-iron and tooth widths are relatively similar. The pole-shoe height increases with increasing rotor pole number. Conversely, the pole-arc to pole-pitch ratio decreases with increasing rotor pole number.

The torque ripple maps of the 12-slot/8-pole and 12-slot/10-pole motors have similar characteristics. The torque ripple in the constant torque region increases significantly with decreasing electrical load. The torque ripple in the flux-weakening region is very low at maximum electrical load and varies with rotational speed. The increase in torque ripple in the flux-weakening region with decreasing electrical load is higher in the 12-slot/8-pole motor than in the 12-slot/10-pole motor. The torque ripple of the 12-slot /14-pole motor is very low across the entire torque-speed range. The lowest torque ripple is found in the operating region between 2 and 3 Nm and extends throughout a significant range of operating speeds.

Designs along the Pareto-front of the multi-objective optimisation of the SPM motors under analysis are compared. The PM volume of the 12-slot/8-pole and 12-slot/10-pole SPM motors increases with increasing average torque and torque ripple. However, the PM volume of 12-slot/14–pole Motor B is 2.1% lower than that of Motor A. The split ratio of the motors increases with increasing average torque and torque ripple. Conversely, the stator back-iron and tooth width decrease with increasing average torque and torque ripple. The increase in average torque and toque ripple is attributed to the fact that larger pole are and higher PM

volume result in a higher air-gap magnetic flux density. Thinner stator back-iron and teeth result in higher saturation and an increase in torque ripple. The pole-arc to pole pitch ratio of the motor of a particular topology does not vary significantly. The pole-shoe heights of Motors B and C of the 12-slot/8-pole motor are identical. Similarly, the pole-shoe heights of the Motor B and Motor C of the 12-slot/10-pole motor are almost identical. However, the pole-shoe height of Motor C of the 12-slot/14-pole motor is higher than those of Motor A and Motor B of the same topology.

Design solutions determined using single-objective optimisation of IPM and SPM motors are compared. Furthermore, the solution space and Pareto-front of the multi-objective optimisation of the IPM and SPM motors are compared. Design optimisation of IPM and SPM motors was performed subject to identical design constraints except for the air-gap length of the motors. The air-gap of the IPM motors is fixed to 0.6 mm, however, the air-gap of the SPM motors is set to 0.9 mm to account for a rotor sleeve. It is assumed that the influence of the rotor sleeve on the electromagnetic performance is negligible.

The average torque of the single-objective optimised SPM motors is significantly higher than that of the IPM motors despite the increase in effective air-gap due to the rotor sleeve. The corresponding torque ripple of the single-objective optimised 12-slot/8-pole and 12-slot/10-pole IPM motors is significantly lower than that of the SPM motors with the same slot/pole number combination. However, the torque ripple of the single-objective optimised 12-slot/14-pole IPM motor is higher than that of the 12-slot/14-pole SPM motor.

The difference in average torque between IPM and SPM motors of a given slot/pole number combination increases with increasing rotor pole number. Conversely, the difference in torque ripple decreases with increasing rotor pole number. The current angle of the motors decreases with increasing rotor pole number since the reluctance torque decreases significantly. Furthermore, the current angle of IPM motors is significantly higher than that of SPM motors.

The average torque per PM volume of IPM motors increases with increasing rotor pole number. The 12-slot/14-pole SPM motor has the highest torque per PM volume, which is 21.1% and 24.1% higher than that of the 12-slot/8-pole SPM motor and 12-slot/10-pole SPM motors, respectively. The 12-slot/10-pole SPM motor has the highest torque density of 34.78 $mNm/m^3$, which is 37% higher than that of the 12-slot/14-pole IPM motor.

The split ratio of the IPM motors is higher than that of the SPM motors and the difference in split ratio between IPM and SPM motors of a particular slot/pole number combination decreases with increasing rotor pole number. The stator back-iron width and tooth width of the optimised IPM motors decreases with increasing rotor pole number. The pole-shoe height of the IPM and SPM motors of the 12-slot/8-pole and 12-slot/10-pole motors with a given rotor pole number is identical. The difference in pole-shoe heights of the 12-slot/14-pole IPM and SPM motors is 0.02 mm. The pole-arc to pole-pitch ratio of the IPM motors is lower than that of the SPM motors.

The Pareto-fronts of the multi-objective optimisation of the IPM and SPM motors under investigation show

that the SPM motors allow for a better compromise between the average torque and torque ripple at the optimised operating point. Thus, SPM motors can provide lower torque ripple and higher average torque than IPM motors with the same slot/pole-number combination.

The discrepancy between the Pareto-front of the IPM and SPM motors increases with increasing rotor pole number. This can be attributed to the fact that the number of flux leakage paths through the rotor ribs of IPM motors increases with increasing rotor pole number, thus resulting in lower average torque.

# 5 ANALYSIS OF COGGING TORQUE SENSITIVITY TO MANUFACTURING TOLERANCES IN IPM AND SPM MOTORS

## 5.1 Introduction

Manufacturing tolerances in mass-production processes lead to deviations from the nominal geometry that, in turn, affect the cogging torque of motors. Analysis of the influence of manufacturing tolerances on motor cogging torque is essential to quantify its sensitivity to tolerances.

The fundamental component of cogging torque of a motor without any deviations from the nominal design is defined by the Least Common Multiple (LCM) of the number of rotor PM poles and the number of stator slots, as defined in (1.1). The cogging torque of a motor is composed of the inherent Native Harmonic Components (NHCs) and Additional Harmonic Components (AHCs) , defined in (1.2), due to factors resulting from a deviation from the nominal geometry of the motor, such as manufacturing tolerances.

For instance, a 12-slot/8-pole motor without manufacturing tolerances would result in a cogging torque waveform composed of the $24^{th}$ order NHC and its higher-order multiples. Similarly, the fundamental cogging torque component of the 12-slot/10-pole and 12-slot/14-pole motors are the $60^{th}$ order component and $84^{th}$ order component, respectively.

Manufacturing tolerances introduce asymmetries in the motor resulting in cogging torque AHCs. The fundamental cogging torque AHC due to a manufacturing tolerance in the stator results in a fundamental AHC equal to the number of rotor poles. For instance, a manufacturing tolerance in the radial position of the tooth surface profile of a 12-slot/8-pole motor would result in a fundamental $8^{th}$ order (equal to rotor PM pole number) cogging torque AHC and its harmonic multiples. Similarly, a manufacturing tolerance in the rotor pole results in a fundamental $12^{th}$ order (equal to stator slot number) AHC and its harmonic multiples. Manufacturing tolerances may affect the air-gap flux density resulting in AHCs coinciding with the NHCs leading to a change in the magnitude of the harmonics inherent in the slot/pole number combination.

The magnitudes of the cogging torque AHCs depend on the type of manufacturing tolerance and its magnitude. The phase of the cogging torque AHCs is determined by the location of the manufacturing tolerance (i.e. stator tooth or rotor pole) with respect to a reference position and direction of rotation. The convention used in this chapter is that the rotor rotates clockwise and the reference point is the position in which tooth 1 is aligned with PM 1, as shown in Fig. 5.1. Furthermore, PM 1 is magnetised outwards and so forth.

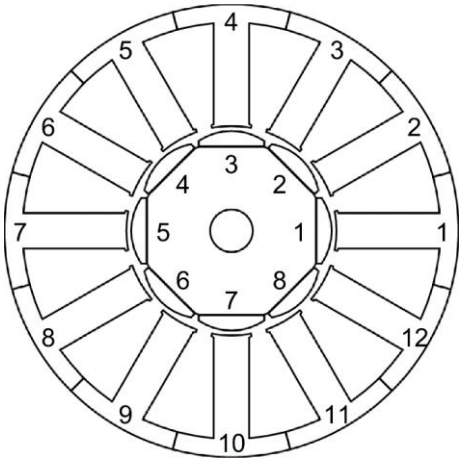



Fig. 5.1. Reference position of a 12-slot/8-pole SPM motor using the convention adopted in this study.

The phase (in degrees) of the n$^{th}$ order AHC due to a stator tolerance in the tooth N can be calculated using (5.1). Similarly, the phase of the n$^{th}$ order AHC due to a rotor tolerance in the rotor pole N can be calculated using (5.2).

$$\phi_z = N * 360° \left( \frac{\frac{360°}{N_s}}{\frac{360°}{n}} \right) \tag{5.1}$$

$$\phi_z = N * 360° \left( \frac{\frac{360°}{2p}}{\frac{360°}{n}} \right) \tag{5.2}$$

The compromise between average torque and torque ripple of IPM and SPM motors with different slot/pole number combinations is identified in Chapters 3 and 4 using multi-objective optimisation. The sensitivity of the cogging torque of a set of 12-slot/8-pole, 12-slot/10-pole, and 12-slot/14-pole IPM and SPM motors to various stator and rotor tolerances is determined in this chapter.

Prototypes of the motors under investigation could not be manufactured due to the circumstances brought by the COVID-19 pandemic at the time of writing. The prototype 12-slot/8-pole and 12-slot/10-pole IPM motors used in the study by [GE16a] were modelled using FEA to validate the efficacy of the FEA models used in this analysis.

## 5.2 Motors under Investigation

The solution space of the multi-objective optimisation of 12-slot/8-pole, 12-slot/10-pole, and 12-slot/14-pole IPM and SPM motors is shown in Fig. 5.2, Fig. 5.3, and Fig. 5.4, respectively. The solution space of IPM and SPM motors of each slot/pole number combination are superimposed to show the difference in the compromise between average torque and torque ripple.

The 12-slot/8-pole SPM motor is selected to operate around the knee point of the Pareto-front and the 12-slot/8-pole IPM motor is selected to produce a very similar average torque at a slightly different torque ripple. The same approach is applied to the 12-slot/10-pole IPM and SPM motors. The solution space of the 12-slot/14-pole IPM and SPM motors differs significantly and thus the selection of solutions on the Pareto-front with similar performance is not possible. Therefore, the motors are selected around the knee point of the Pareto-fronts of the two solution spaces. The cross-sections of the selected motors are shown in Fig. 5.5 and the design parameters are listed in Table 2.9.

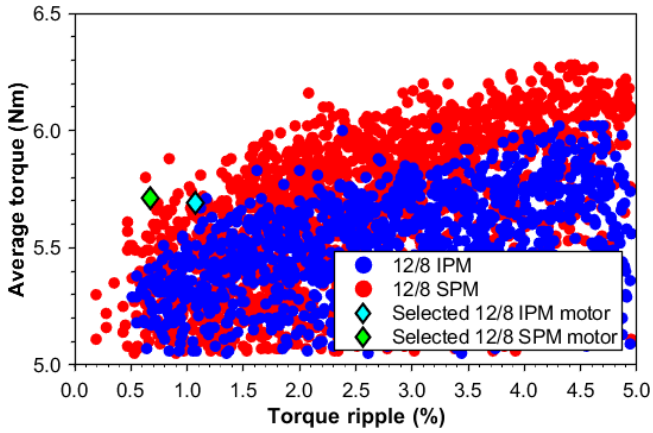



Fig. 5.2. Solution space of 12-slot/8-pole IPM and SPM motors and selected motors under investigation.

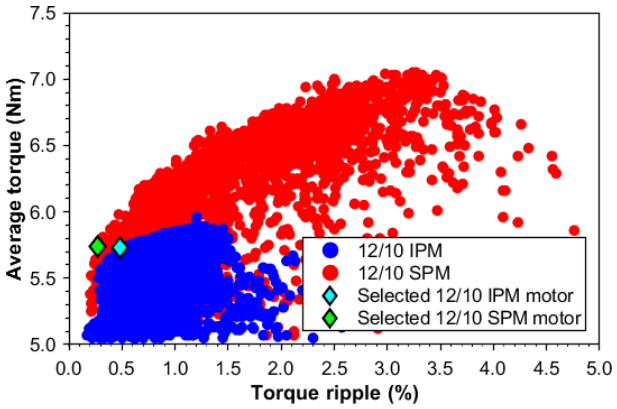



Fig. 5.3. Solution space of 12-slot/10-pole IPM and SPM motors and selected motors under investigation.

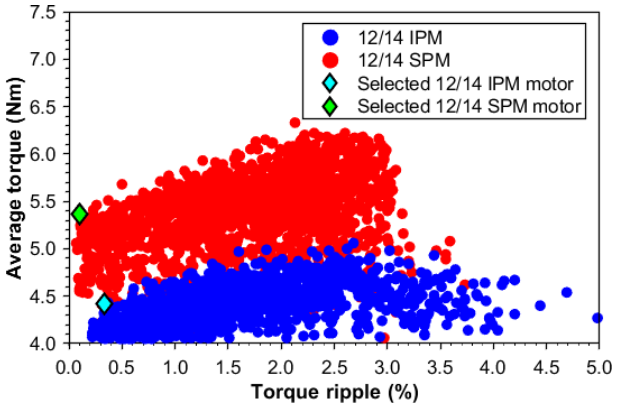
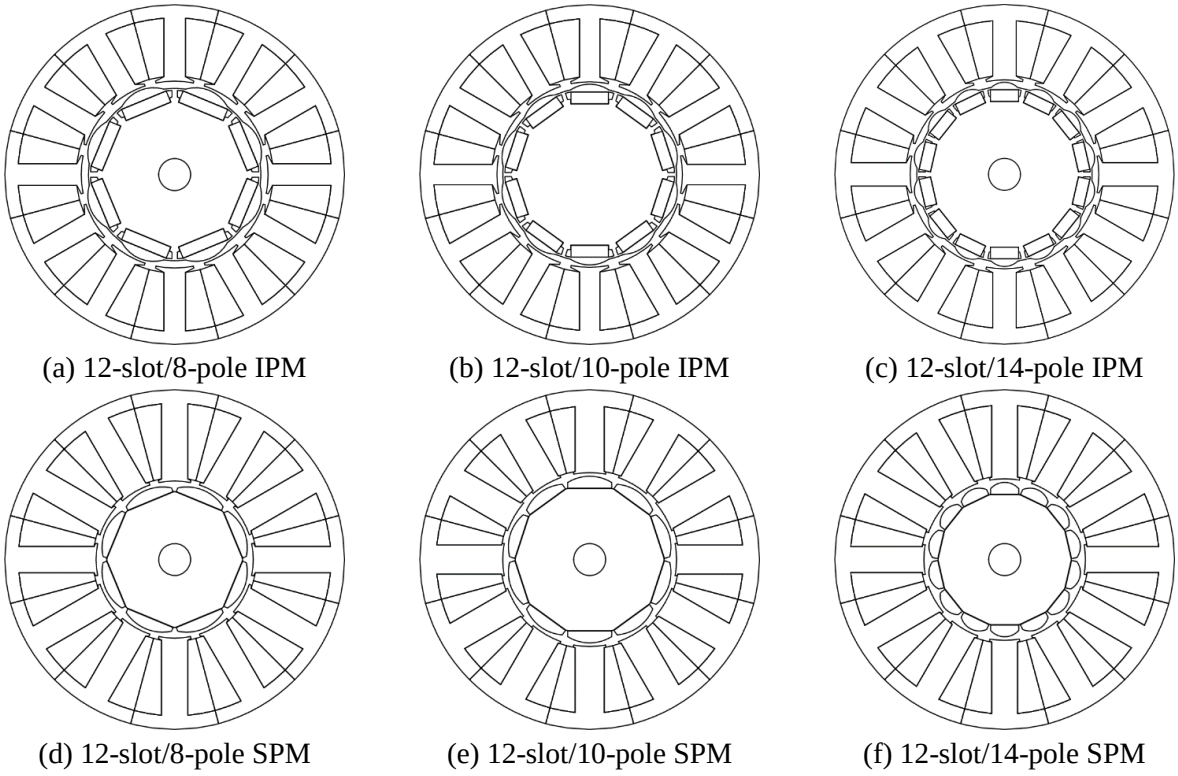



Fig. 5.4. Solution space of 12-slot/14-pole IPM and SPM motors and selected motors under investigation.



(a) 12-slot/8-pole IPM (b) 12-slot/10-pole IPM (c) 12-slot/14-pole IPM

(d) 12-slot/8-pole SPM (e) 12-slot/10-pole SPM (f) 12-slot/14-pole SPM

Fig. 5.5. Cross-sections of IPM and SPM motors under investigation.

Table 5.1. Torque and design parameters of IPM and SPM motors under investigation

| | | **12/8 IPM** | **12/8 SPM** | **12/10 IPM** | **12/10 SPM** | **12/14 IPM** | **12/14 SPM** |
|---|---|---|---|---|---|---|---|
| Average torque | Nm | 5.7 | 5.7 | 5.7 | 5.7 | 4.4 | 5.4 |
| Torque ripple | % | 1.1 | 0.7 | 0.5 | 0.3 | 0.3 | 0.1 |
| Torque per Volume | Nm/L | 26.79 | 26.79 | 26.79 | 26.79 | 20.68 | 25.38 |
| Torque per PM Volume | $Nm/cm^3$ | 0.529 | 0.678 | 0.552 | 0.565 | 0.414 | 0.596 |
| Current advance angle | ° | 16.9 | 13.9 | 13.4 | 10.8 | 17.2 | 15.2 |
| Outer diameter | mm | 85 | | | | | |
| Motor active length | mm | 37.5 | | | | | |
| Air-gap length | mm | 0.6 | 0.9 | 0.6 | 0.9 | 0.6 | 0.9 |
| Split ratio | N/A | 0.543 | 0.452 | 0.539 | 0.501 | 0.549 | 0.465 |
| Back-iron width | mm | 3.29 | 3.41 | 3.47 | 4.10 | 3.98 | 3.86 |
| Tooth width | mm | 5.39 | 6.62 | 5.12 | 7.30 | 5.85 | 6.49 |
| Slot opening width | mm | 3.0 | 3.0 | 3.0 | 3.0 | 3.0 | 3.0 |
| Pole-arc to pole-pitch ratio | N/A | 0.670 | 0.889 | 0.703 | 0.887 | 0.676 | 0.873 |
| Pole-shoe height | mm | 1.22 | 0.82 | 0.89 | 0.80 | 1.07 | 1.24 |
| Rib width | mm | 1.35 | N/A | 1.05 | N/A | 1.20 | N/A |
| PM height | mm | 2.98 | 2.89 | 2.94 | 2.95 | 2.89 | 2.94 |
| PM width | mm | 12.07 | 12.27 | 9.37 | 11.02 | 7.00 | 7.04 |
| PM remanence | T | 1.38 | | | | | |
| PM coercivity | kA/m | -1100 | | | | | |
| PM volume | $cm^3$ | 10.79 | 8.41 | 10.32 | 10.08 | 10.62 | 9.06 |

## 5.3 Manufacturing Tolerances under Investigation

The manufacturing tolerances under investigation include stator and rotor tolerances in the geometry and the PM material. It is assumed that the tolerance is uniform along the axial length of the motor and the influence of end-effects is neglected. It is generally assumed that the manufacturing tolerance on every surface in mass-production processes is ±0.05 mm [WU98].

The stator tolerances considered in this chapter, a subset of all the possible tolerances, are listed in Table 2.3. The adopted convention for tolerances in the radial position of the stator tooth profile is that a positive tolerance results in a displacement of the tooth profile that increases the air-gap (i.e. a tolerance in the outward direction) and vice-versa, as shown in Fig. 5.6. Similarly, the manufacturing tolerances in the rotors of IPM and SPM motors considered in this chapter are listed in Table 5.3 and Table 5.3, respectively.

Rotor eccentricity is a critical tolerance and has a significant effect on unbalanced magnetic forces and acoustic noise, however, the impact of eccentricity on the peak-to-peak cogging torque is low [ISL04]. Rotor eccentricity causes an asymmetric air-gap, however, the impact on the rate of change of coenergy with angular position is low [ISL11]. Therefore, rotor eccentricity is not considered in this study.

Table 5.2. Manufacturing tolerances in the stator of IPM and SPM motors considered in this analysis

| **Tolerance** | **Units** | **Values** |
|---|---|---|
| Back-iron width | mm | ±0.10 |
| Tooth width | mm | ±0.10 |
| Tooth-tip height | mm | ±0.05 |
| Tooth tip width | mm | ±0.10 |
| Tooth surface profile radial position | mm | ±0.05 |

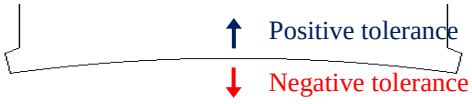



Fig. 5.6. Manufacturing tolerances in the radial position of a stator tooth.

Table 5.3. Manufacturing tolerances in the rotor of IPM motors

| **Tolerance** | **Units** | **Values** |
|---|---|---|
| Pole-shoe height | mm | ±0.05 |
| Pole-shoe width | mm | ±0.10 |
| Rib width | mm | ±0.10 |
| PM height | mm | ±0.10 |
| PM width | mm | ±0.10 |
| PM remanence | % | ±2 |

Table 5.4. Manufacturing tolerances in the rotor of SPM motors

| Tolerance | Units | Values |
|---|---|---|
| Pole-shoe height | mm | ±0.05 |
| PM height | mm | ±0.10 |
| PM width | mm | ±0.10 |
| PM remanence | % | ±2 |
| Rotor iron profile | mm | ±0.05 |

Fig. 5.7 illustrates a simplified example of the rotor geometry of a rotor pole of an IPM motor and the some of the rotor tolerances are indicated through the dashed lines and arrows. For simplicity, it is assumed that the tolerances in the cavity dimensions affect the entire cavity surface profile rather than the individual sides (i.e. the top, bottom, left, and right sides). The manufacturing tolerances affecting the rotor geometry of IPM motors considered in this chapter include:

- Variation of the rotor pole-arc height and pole-arc width
- Radial variation of the rotor iron profile
- Variation in the cavity profile
- Variation in the rotor rib width
- Variation in the PM height and width
- Radial and lateral displacement of the PM from the nominal position, as illustrated in Fig.1.2
- Variation in the remanence of the PM

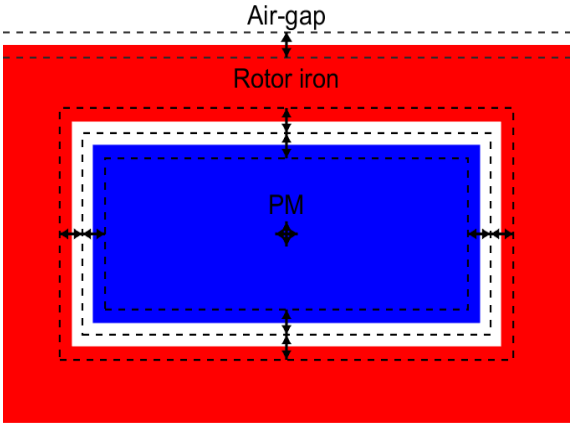



Fig. 5.7. Illustration of tolerances in a simplified rotor pole of a simplified IPM motor.

The tolerance of the rotor iron profile and the cavity profiles is ±0.05 mm and is assumed uniform for all the poles. Furthermore, any variation in the concentricity of these elements, i.e. eccentricity, is neglected. The tolerance in PM dimensions of mass-produced PMs is assumed equal to ±0.10 mm. The minimum and maximum limits of these four tolerances are summarised as follows:

- $|\delta_{sleeve}| \leq +0.05$ mm
- $|\delta_{iron}| \leq +0.05$ mm
- $|\delta_{PM\ height}| \leq +0.10$ mm
- $|\delta_{radial\ position}| \leq +0.10\ \text{mm} + \frac{1}{2}\delta_{iron\ cavity} - \frac{1}{2}\delta_{PM\ height}$

Fig. 5.8 shows a simplified rotor geometry of a rotor pole of an SPM motor and indicates some of the possible variations due to rotor manufacturing tolerances, including:

- Radial variation of the rotor sleeve profile
- Radial variation of the rotor iron profile
- Variations in the PM height and PM width
- Variation in the PM pole-arc height and pole-arc width
- Radial and lateral displacements of the PM from the nominal position
- Variation in the remanence of the PM

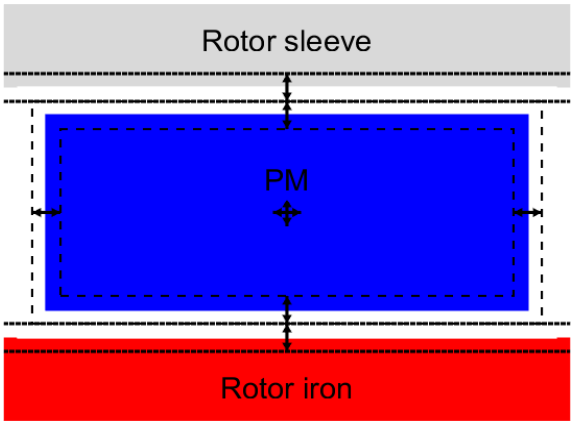



Fig. 5.8. Illustration of tolerances in a rotor pole of as simplified SPM motor.

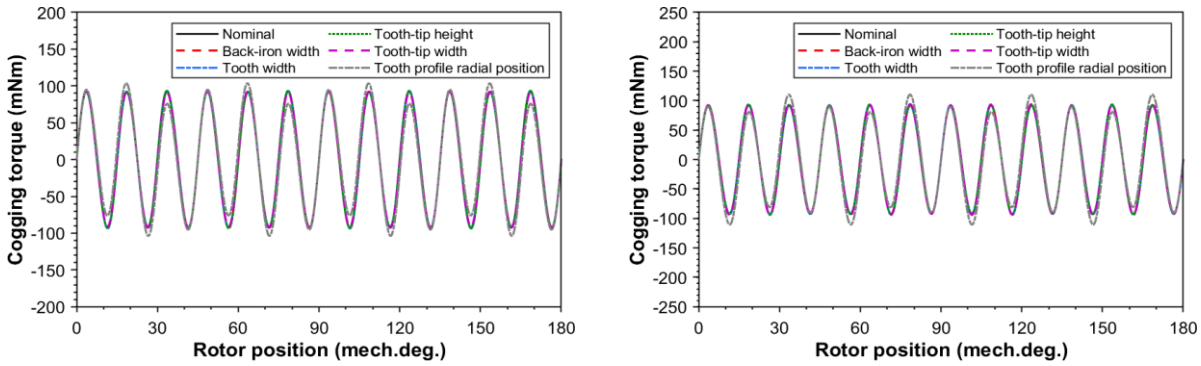
It should be noted that the adopted definition for radial variations is that a positive variation indicates a shift towards the air-gap and vice versa.It is assumed that the tolerances of the rotor sleeve and rotor iron profile are ±0.05 mm and are uniform for all the poles. Furthermore, any variations in the concentricity of these elements, i.e. eccentricity, is neglected. The tolerance in PM height of mass-produced PMs is assumed to be equal to ±0.10 mm. The radial length of the cavity between the rotor iron and the rotor sleeve is determined by the manufacturing variations in the PM height, the rotor sleeve profile, and the rotor iron profile. Therefore, the maximum possible radial displacement of the PM, with respect to the nominal PM position, is determined by the aforementioned variations. The minimum and maximum limits of these four variations are summarised as follows:

- -0.05 mm ≤ $\delta_{sleeve}$ ≤ +0.05 mm
- -0.05 mm ≤ $\delta_{iron}$ ≤ +0.05 mm
- -0.10 mm ≤ $\delta_{PM\ height}$ ≤ +0.10 mm
- -0.10 mm + $\delta_{iron} + \frac{1}{2}\delta_{PM\ height} \leq \delta_{radial\ position} \leq$ +0.10 mm +$\delta_{sleeve} - \frac{1}{2}\delta_{PM\ height}$

## 5.4 Analysis of Cogging Torque Sensitivity to Stator Tolerances in IPM Motors

### 5.4.1 Analysis of Cogging Torque Sensitivity of 12-slot/8-pole IPM motor

The cogging torque waveforms and harmonics due to positive and negative manufacturing tolerances in a single tooth of the stator of the 12-slot/8-pole motor under investigation are shown in Fig. 5.9 and Fig. 5.10, respectively. The waveforms and harmonics of the cogging torque AHCs, shown in Fig. 5.11 and Fig. 5.12, are obtained by exploiting the fact that the cogging torque is equal to the sum of the cogging torque NHCs and AHCs.




(a) Positive tolerance (b) Negative tolerance

Fig. 5.9. Influence of tolerances on cogging torque waveforms of 12-slot/8-pole IPM motor.

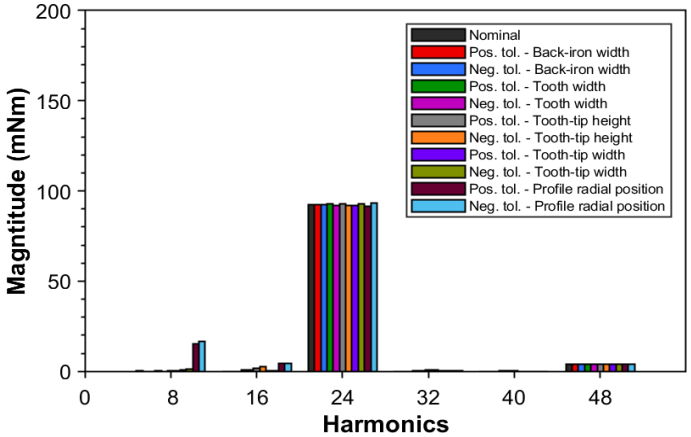


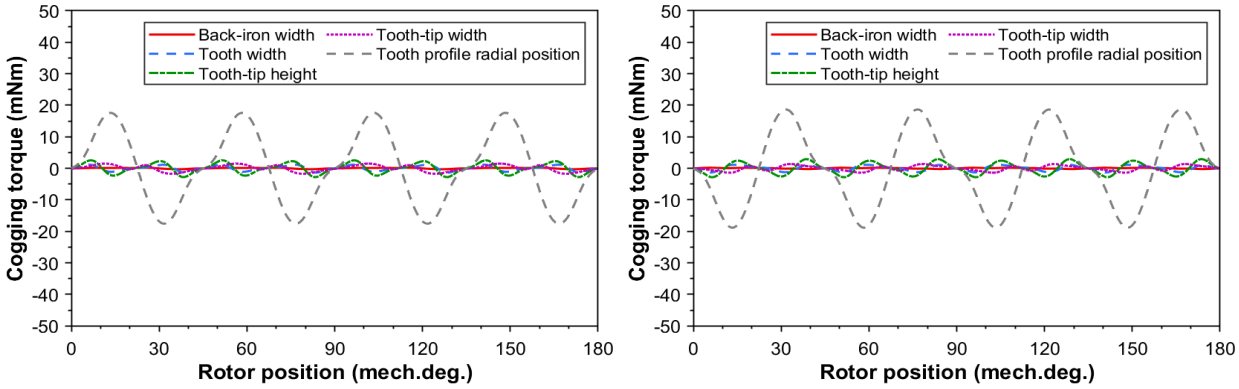

Fig. 5.10. Influence of tolerances on cogging torque harmonics of 12-slot/8-pole IPM motor.

The nominal cogging torque is primarily composed of the fundamental 24$^{th}$ order component and its harmonic multiples. The cogging torque AHCs are composed of the fundamental 8$^{th}$ order component and its harmonic multiples, as well as AHCs coinciding with the NHCs.

Manufacturing tolerances in the stator back-iron width and tooth width of a single tooth result in a very small motor asymmetry and the influence of the tolerances on the saturation under no-load condition is negligible. Therefore, the influence of tolerances in the stator back-iron width and tooth width on the cogging torque is negligible.

The influence of the tolerances in the tooth-tip height and width of a single stator tooth on the cogging torque is very small. Tolerances in the tooth-tip height result in a higher magnitude of the 16$^{th}$ order harmonic than that of 8$^{th}$ order harmonic.

Manufacturing tolerances in the radial position of the stator tooth profile have the highest influence on the cogging torque. The magnitudes of the 8$^{th}$ order torque harmonic due to positive and negative tolerances are equal to 15.6 mNm and 16.4 mNm, respectively. The magnitude of the 8$^{th}$ order harmonic due to a positive tolerance is lower than that due to a negative tolerance due to the change in air-gap length associated with the tolerance.




(a) Positive tolerance (b) Negative tolerance

Fig. 5.11. Waveforms of cogging torque AHCs due to manufacturing tolerances in 12-slot/8-pole IPM motor.

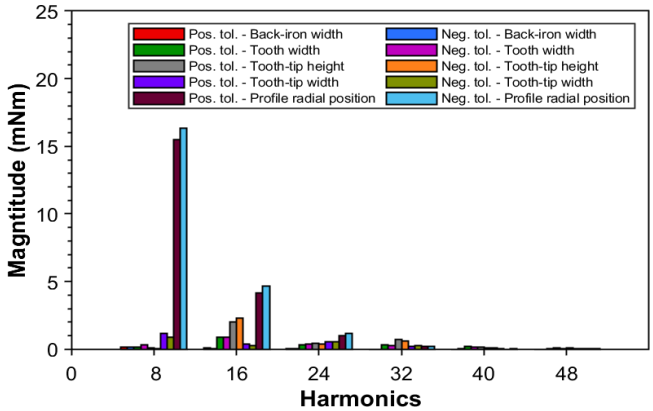
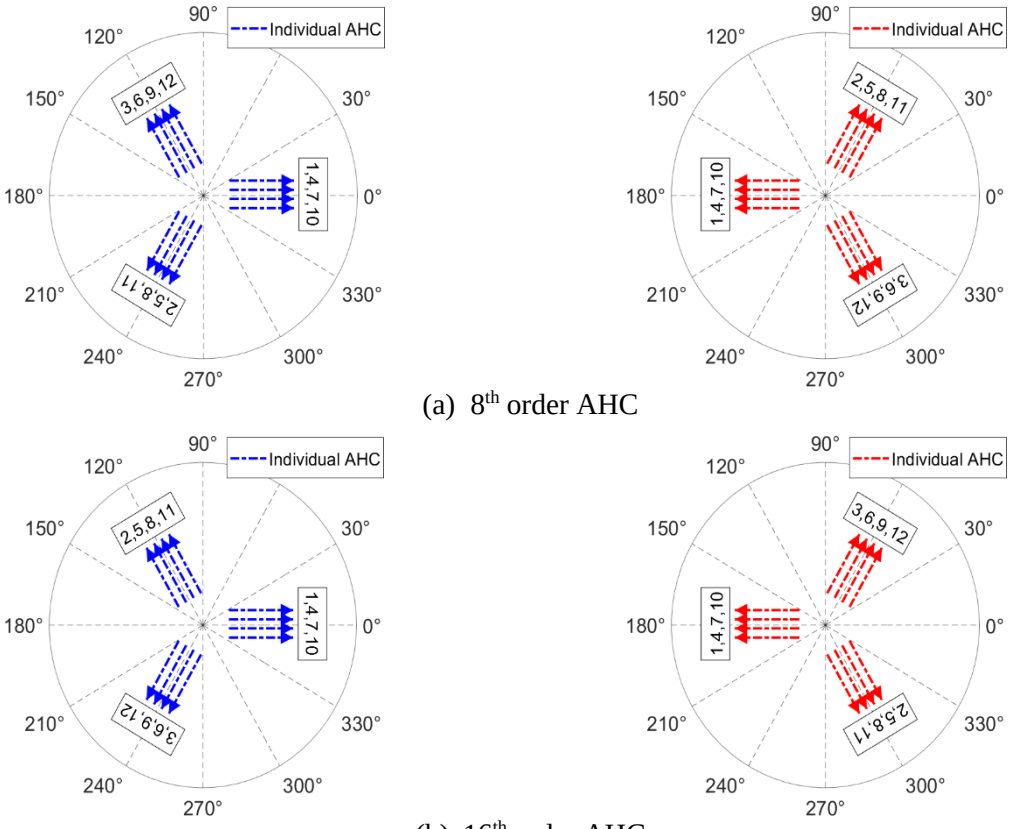



Fig. 5.12. Harmonics of AHCs due to manufacturing tolerances in 12-slot/8-pole IPM motor.

The phase of the AHCs is dependent on the direction of the variation and the location of the tooth subjected to a manufacturing tolerance. For instance, a manufacturing tolerance in the stator tooth profile radial position of tooth 1 results in a 8$^{th}$ order AHC with a phase of 0°, and a tolerance in the opposite direction results in a phase shift of 180°, as shown in Fig. 5.13.

The phase of AHCs is determined analytically using (5.1) and corroborated using FFT of the cogging torque obtained using FEA. The phases of the 8$^{th}$ and 16$^{th}$ order AHCs due to individual positive and negative tolerances of an arbitrary magnitude in the stator tooth profile radial position are shown in Fig. 5.13. The 12-slot/8-pole IPM motor has a cyclic symmetry of four, and consequently, the phases of the AHCs due to tolerances in teeth separated by a multiple of 3 slot pitches, i.e. teeth separated by an angle of 90°, are identical. The resultant AHCs due to multiple tolerances are produced by the phasor addition of the individual AHCs to individual tolerances.




(a) 8$^{th}$ order AHC

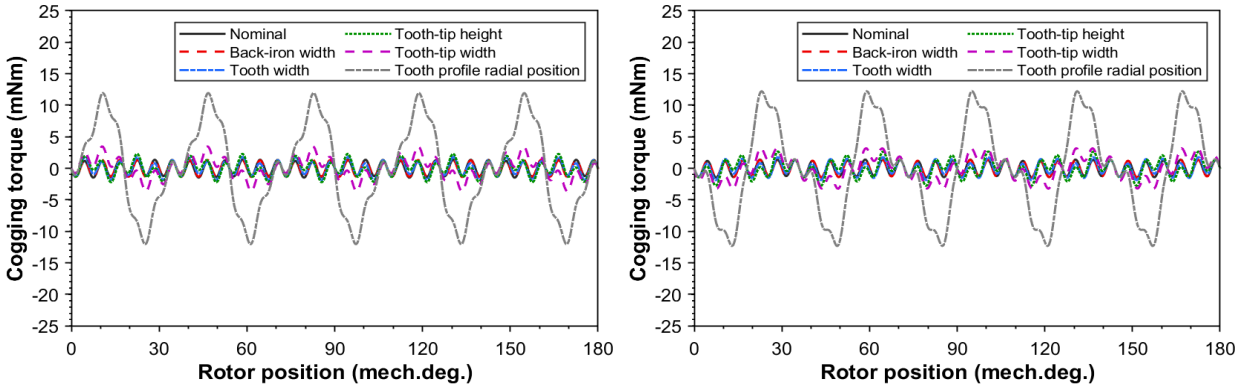
(b) 16$^{th}$ order AHC

(I) Positive tolerance (II) Negative tolerance

Fig. 5.13. Phasors of 8$^{th}$ and 16$^{th}$ order AHCs due a tolerance in tooth surface profile radial position of an individual tooth.

## 5.4.2 Analysis of Cogging Torque Sensitivity of 12-slot/10-pole IPM motor

The cogging torque waveforms and harmonics due to positive and negative manufacturing tolerances in a single tooth of the stator of the 12-slot/10-pole motor under investigation are shown in Fig. 5.14 and Fig. 5.15, respectively. The waveforms and harmonics of the cogging torque AHCs are shown in Fig. 5.16 and Fig. 5.17, respectively. The nominal cogging torque is primarily composed of the fundamental 60$^{th}$ order component. The cogging torque AHCs are composed of the fundamental 10$^{th}$ order component and its harmonic multiples, as well as the 60$^{th}$ order component. The 12-slot/10-pole IPM motor has an inherently low cogging torque and the peak-to-peak cogging torque due to tolerances in the radiation position of the stator tooth profile is up to 8.2 times that of the nominal cogging torque.




(a) Positive tolerance (b) Negative tolerance

Fig. 5.14. Influence of tolerances on cogging torque waveforms of 12-slot/10-pole IPM motor.

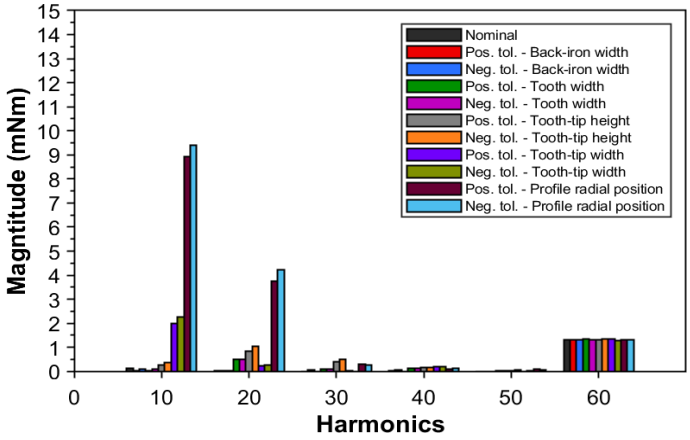
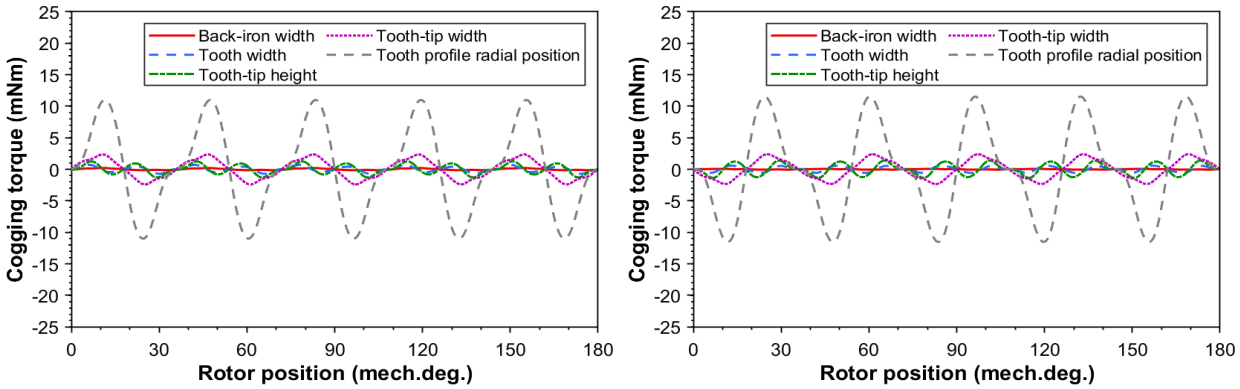



Fig. 5.15. Influence of tolerances on cogging torque harmonics of 12-slot/10-pole IPM motor.

Manufacturing tolerances in the stator back-iron width has a negligible influence on the cogging torque. Tolerances in the tooth width and tooth-tip height lead to a negligible magnitude of the fundamental 10$^{th}$ order AHC and low magnitude of the harmonic multiples, and negligible influence on the fundamental native 60$^{th}$ order component. Manufacturing tolerances in the tooth-tip width result in a low magnitude of the 10$^{th}$ order harmonic.

The highest magnitude of the 10th order harmonic and its harmonic multiples are produced by tolerances in the radial position of the stator tooth profile. The fundamental 60th order NHC is not influenced by the tolerances under investigation other than tolerances in the stator tooth profile radial position.




(a) Positive tolerance (b) Negative tolerance

Fig. 5.16. Waveforms of cogging torque AHCs due to tolerances in 12-slot/10-pole IPM motor.

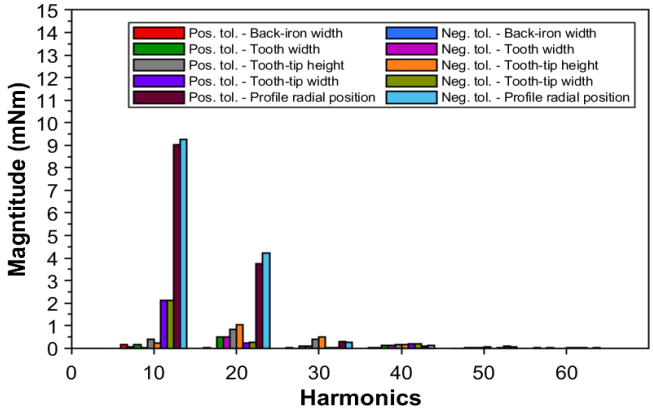
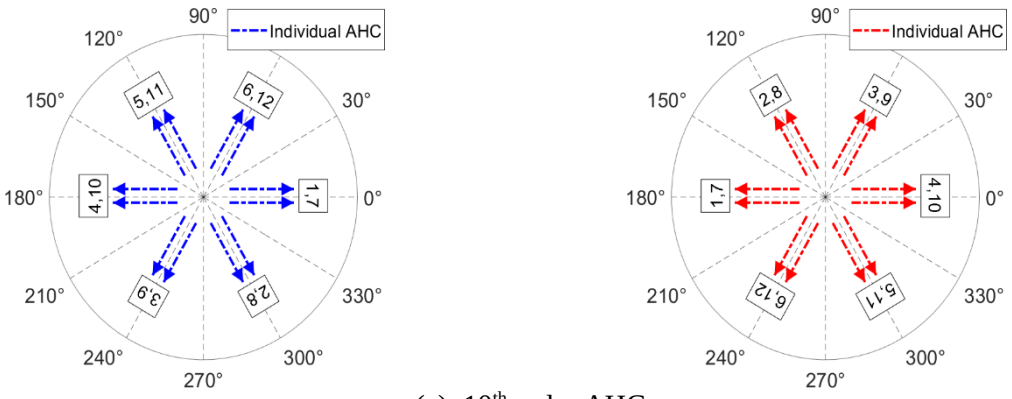
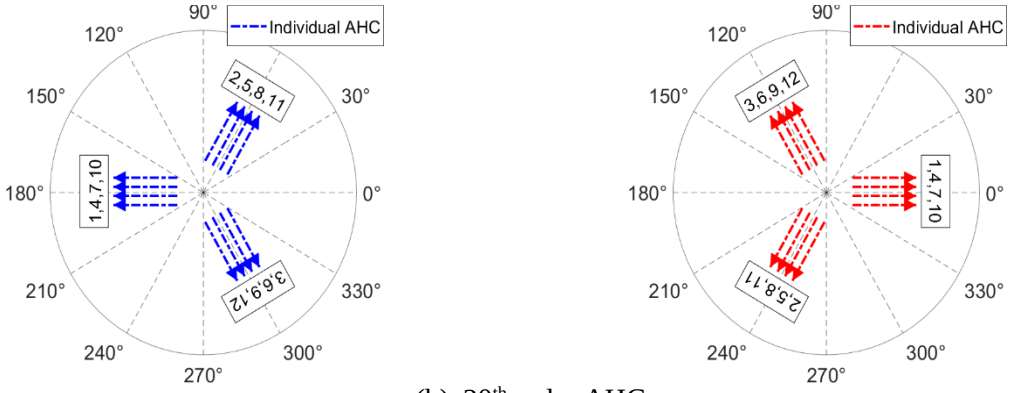



Fig. 5.17. Harmonics of AHCs due to manufacturing tolerances in 12-slot/10-pole IPM motor.

The 12-slot/10-pole IPM motor has a cyclic symmetry of two, and consequently, the phases of the AHCs due to tolerances in the same direction in teeth separated by a multiple of 180° are identical, resulting in an additive effect. Furthermore, the 12-slot/10 pole motor exhibits an anti-symmetry every 3 slot pitches. Consequently, tolerances in the same direction in teeth separated by an angle of 90° result in AHCs with opposite phases resulting in a cancelling effect. The phases of the 10th and 20th order AHCs due to individual positive and negative tolerances of an arbitrary magnitude in the stator tooth profile radial position are shown in Fig. 5.18.




(a) 10th order AHC



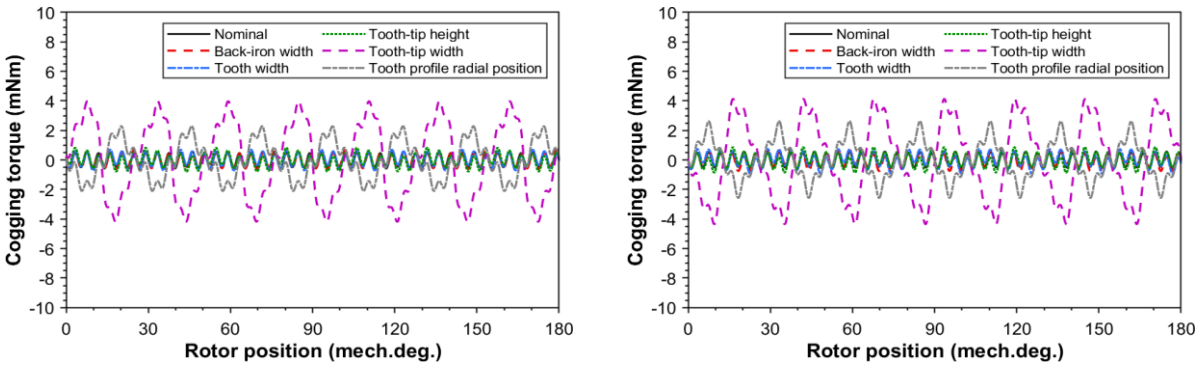

(b) 20th order AHC

(I) Positive tolerance (II) Negative tolerance

Fig. 5.18. Phasors of 10th and 20th order AHCs due a tolerance in tooth surface profile radial position of an individual tooth.

### 5.4.3 Analysis of Cogging Torque Sensitivity of 12-slot/14-pole IPM motor

The cogging torque waveforms and harmonics due to positive and negative manufacturing tolerances in a single tooth of the stator of the 12-slot/14-pole motor under investigation are shown in Fig. 5.19 and Fig. 5.20, respectively. The waveforms and harmonics of the cogging torque AHCs are shown in Fig. 5.21 and Fig. 5.22, respectively. The nominal cogging torque is primarily composed of the fundamental 84th order component. Manufacturing tolerances in the stator result in the fundamental 14th order harmonic and its harmonic multiples, as well as the 84th order component. Tolerances in the tooth-tip width and tooth profile radial position have a significant influence on the cogging torque. The influence of the other tolerances under investigation on the cogging torque is very low. The cogging torque of the 12-slot/14-pole IPM motor under investigation is more sensitive to tolerances in the tooth-tip width than the tooth profile radial position.




(a) Positive tolerance (b) Negative tolerance

Fig. 5.19. Influence of tolerances on cogging torque waveforms of 12-slot/14-pole IPM motor.

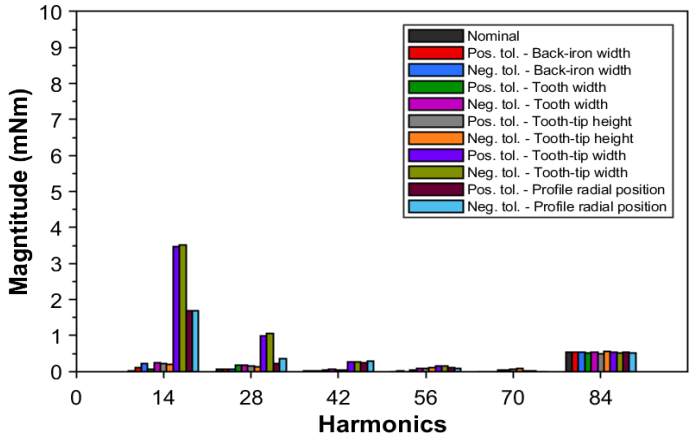
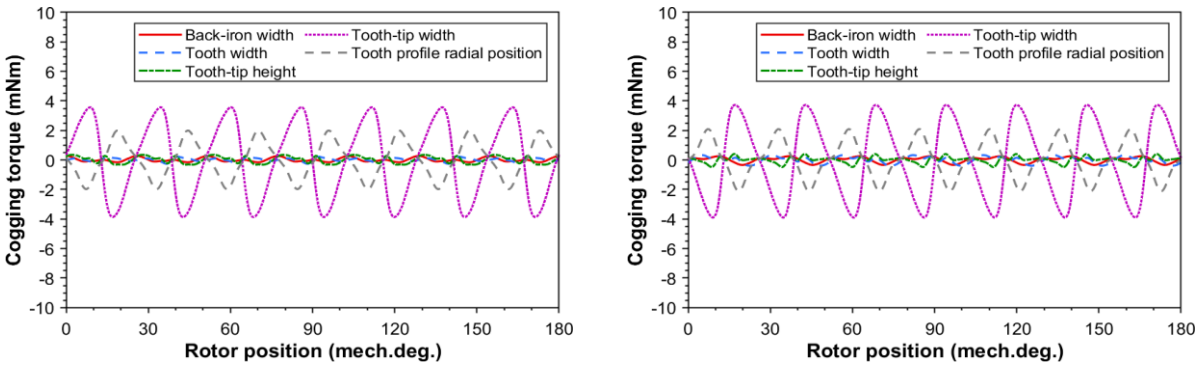



Fig. 5.20. Influence of tolerances on cogging torque harmonics of 12-slot/14-pole IPM motor.

The magnitude of the 14$^{th}$ order harmonic due to tolerances in the tooth-tip width is up to 76.6% higher than that due to tolerances in the tooth profile radial position. The magnitude of the 14$^{th}$ order harmonic due to a positive tolerance in the tooth-tip width is higher than that due to a negative tolerance since the flux linkage is increased. The influence of direction of the tolerance in the tooth profile radial position on the magnitude of the 14$^{th}$ order harmonic is negligible. The cogging torque AHC waveforms show that the 14$^{th}$ order harmonic produced by tolerances in the tooth-tip width and tooth profile radial position have opposite phases.

The phases of the AHCs are dependent on the direction of the variation and the location of the tooth subjected to a manufacturing tolerance. The 12-slot/14-pole IPM motor has a cyclic symmetry of two, and consequently, the phases of AHCs due to tolerances in teeth separated by a multiple of 180° are identical, leading to an additive effect. Furthermore, the 12-slot/10 pole motor exhibits a cyclic anti-symmetry of four. Consequently, tolerances in teeth separated by an angle of 90° result in AHCs with opposite phases, resulting in a cancelling effect. The phases of the 14$^{th}$ and 28$^{th}$ order AHCs due to individual positive and negative tolerances of an arbitrary magnitude in the stator tooth profile radial position are shown in Fig. 5.23.




(a) Positive tolerance (b) Negative tolerance

Fig. 5.21. Waveforms of cogging torque AHCs due to tolerances in 12-slot/14-pole IPM motor.

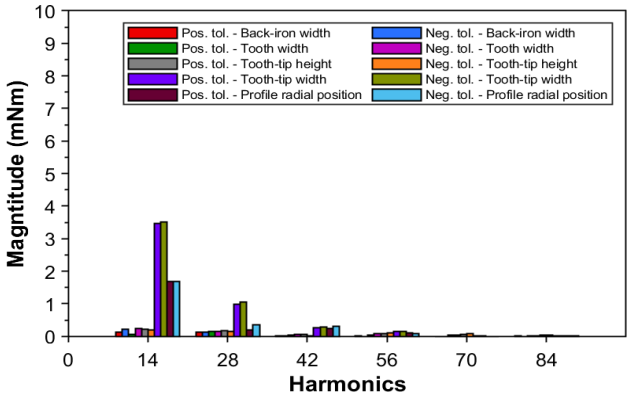
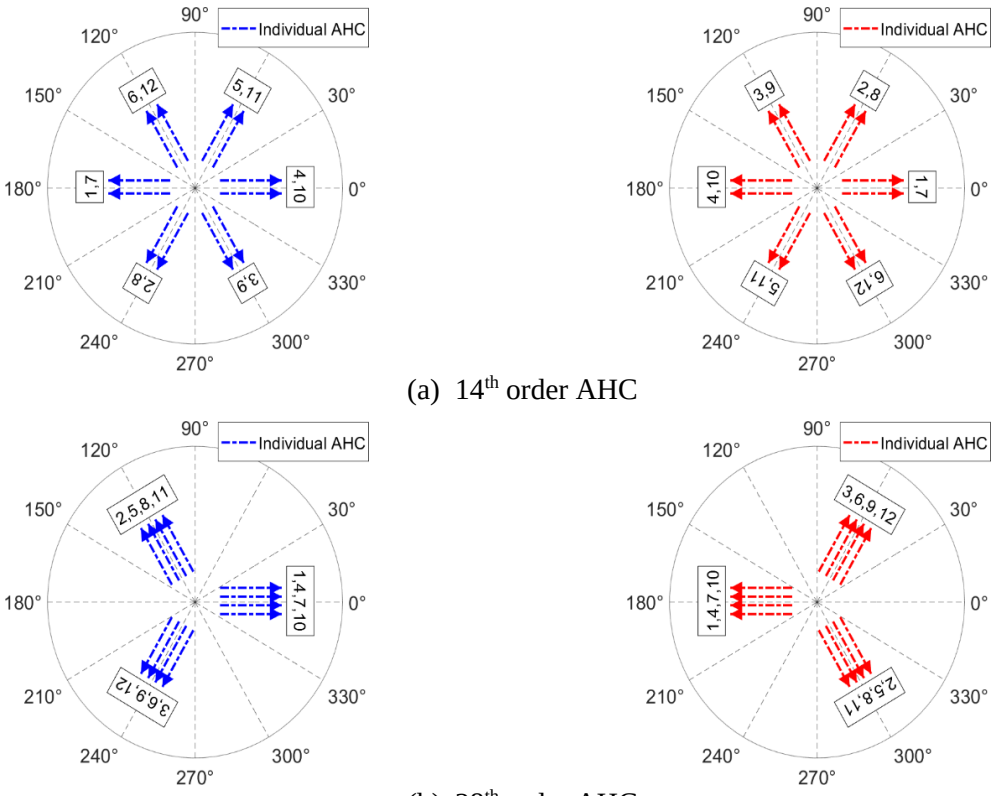



Fig. 5.22. Harmonics of AHCs due tolerances in 12-slot/14-pole IPM motor.




(a) 14th order AHC

(b) 28th order AHC

(I) Positive tolerance (II) Negative tolerance

Fig. 5.23. Phasors of 14th and 28th order AHCs due to tolerance in tooth surface profile radial position.

### 5.4.4 Comparison of Cogging Torque Sensitivity of IPM Motors

The nominal peak-to-peak cogging torque of the IPM motors under investigation decreases with increasing rotor pole number, i.e. the least common multiple, since the stator slot number is the same for three motors. The nominal peak-to-peak cogging torques of the 12-slot/8-pole, 12-slot/10-pole, and 12-slot/14-pole IPM motors are 185.7 mNm, 2.9 mNm and 1.2 mNm, respectively.

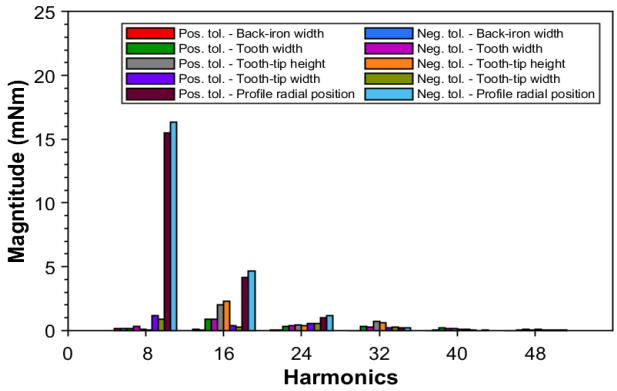
The instantaneous cogging torque is composed of NHCs and AHCs. The resultant AHCs due to multiple tolerances are determined by the phasor addition of the individual AHCs due to individual tolerances. Thus, the magnitude and phase of individual AHCs may lead to an additive or cancelling effect, as detailed in this section and supported by the phasor diagrams in Fig. 5.13, Fig. 5.18, and Fig. 5.23.

The magnitudes of the cogging torque AHCs due to manufacturing tolerances in the stator of 12-slot/8-pole, 12-slot/10-pole, and 12-slot/14-pole IPM motors are shown in Fig. 5.24. Tolerances in the stator result in AHCs with a fundamental order equal to the rotor pole number.

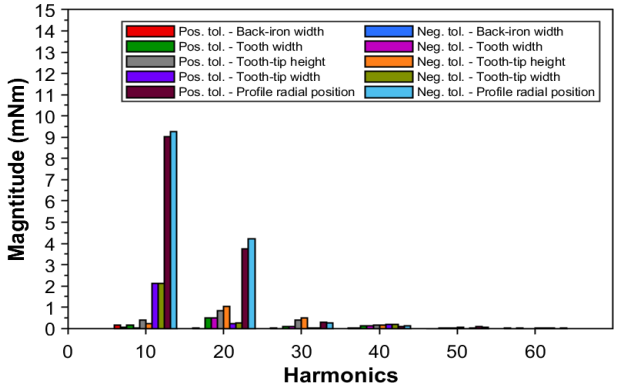
Stator tolerances in the 12-slot/8-pole motor result in AHCs coinciding with the fundamental $24^{th}$ order NHC of the motor. Tolerances in stator tooth profile radial position of the 12-slot/10-pole motor lead to AHCs coinciding with the fundamental $60^{th}$ order NHC. The magnitude of the $60^{th}$ order AHCs due to the remaining tolerances under investigation is negligible. The influence of stator tolerances on the $84^{th}$ order AHC of the 12-slot/14-pole IPM motor is negligible.

The influence of tolerances in the back-iron width and tooth width on cogging torque of the three motors is very low. Tolerances in the tooth-tip height result in a higher magnitude of the $16^{th}$ order harmonic than the $8^{th}$ order harmonic in the 12-slot/8-pole motor. Similarly, the magnitude of the $20^{th}$ order harmonic of the 12-slot/10-pole IPM motor due to tolerances in the tooth-tip height is higher than that of the $10^{th}$ order harmonic.

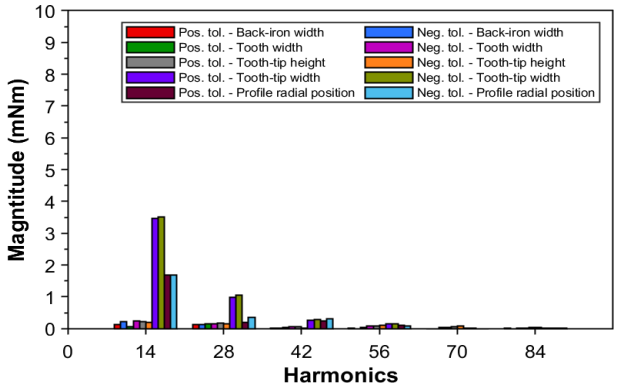
The magnitude of the fundamental AHC due to tolerances in the tooth-tip width increases with increasing rotor pole number. Conversely, the magnitude of the fundamental AHC due to tolerances in the tooth profile radial position decreases with increasing rotor pole number. The magnitude of the AHCs due to tolerances in tooth profile radial position is significantly higher than that due to the tolerances in tooth-tip width in 12-slot/8-pole and 12-slot/10-pole motors. The opposite effect is observed in the 12-slot/14-pole motor.




(a) 12-slot/8-pole IPM motor




(b) 12-slot/10-pole IPM motor




(c) 12-slot/14-pole IPM motor

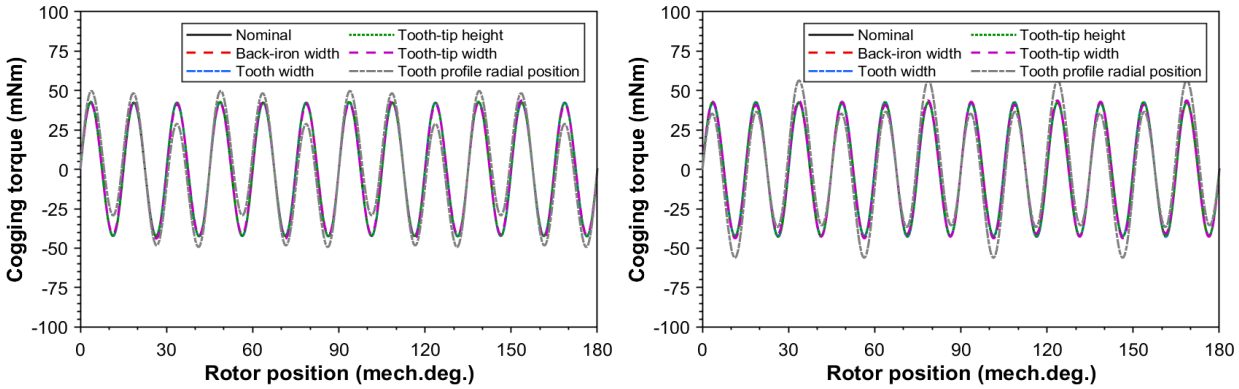
Fig. 5.24. Cogging torque AHCs due to stator manufacturing tolerances in 12-slot/8-pole, 12-slot/10-pole, and 12-slot/14-pole IPM motors

## 5.5 Analysis of Cogging Torque Sensitivity to Stator Tolerances in SPM Motors

### 5.5.1 Analysis of Cogging Torque Sensitivity of 12-slot/8-pole SPM motor

The cogging torque waveforms and harmonics due to positive and negative manufacturing tolerances in a single tooth of the stator of the 12-slot/8-pole motor under investigation are shown in Fig. 5.25 and Fig. 5.26, respectively. The waveforms and harmonics of the cogging torque AHCs, shown in Fig. 5.27 and Fig. 5.28, are obtained by exploiting the fact that the cogging torque is equal to the sum of the cogging torque NHCs and AHCs.

The nominal cogging torque is primarily composed of the fundamental 24th order component and its harmonic multiples. The cogging torque AHCs are composed of the fundamental $8^{th}$ order harmonic and its harmonic multiples, as well as AHCs coinciding with the NHCs.




(a) Positive tolerance (b) Negative tolerance

Fig. 5.25. Influence of tolerances on cogging torque waveforms of 12-slot/8-pole SPM motor.

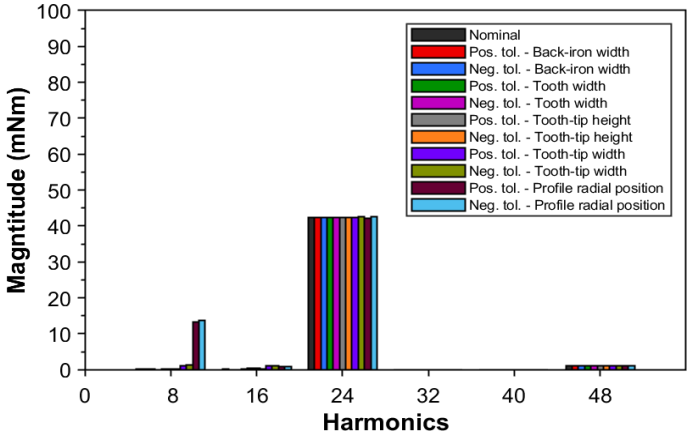
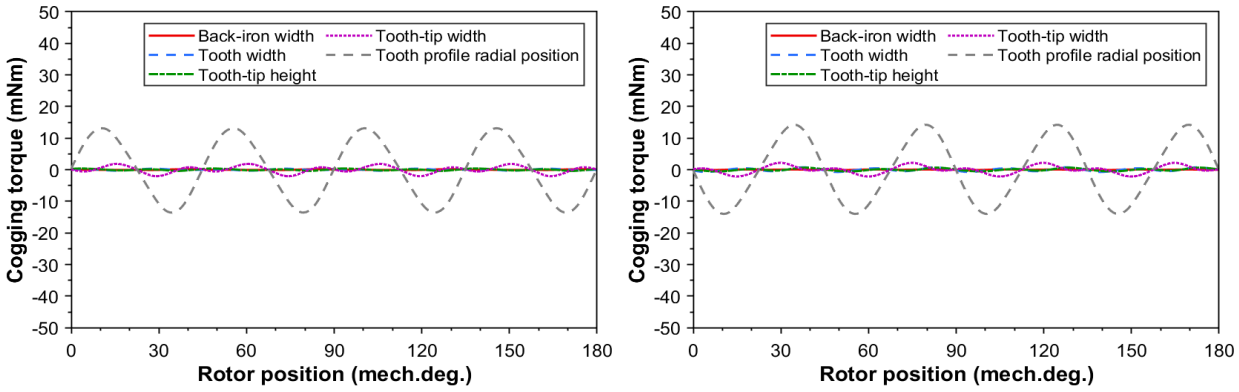



Fig. 5.26. Influence of tolerances on cogging torque harmonics of 12-slot/8-pole SPM motor.

Manufacturing tolerances in the stator back-iron width and tooth width of a single tooth result in a very small motor asymmetry and the influence of the tolerances on the saturation under no-load condition is negligible. Therefore, the influence of tolerances in the stator back-iron width and tooth width on the cogging torque is negligible.

The influence of the tolerances in the tooth-tip height and width of a single stator tooth on the cogging torque is very small. Manufacturing tolerances in the radial position of the stator tooth profile have the highest influence on the cogging torque. The magnitudes of the 8$^{th}$ order torque harmonic due to positive and negative tolerances are equal to 15.6 mNm and 16.4 mNm, respectively. The magnitude of the 8$^{th}$ order harmonic due to a positive tolerance is lower than that due to a negative tolerance due to the change in air-gap length associated with the tolerance.




(a) Positive tolerance (b) Negative tolerance

Fig. 5.27. Waveforms of cogging torque AHCs due to manufacturing tolerances in the 12-slot/8-pole SPM motor.

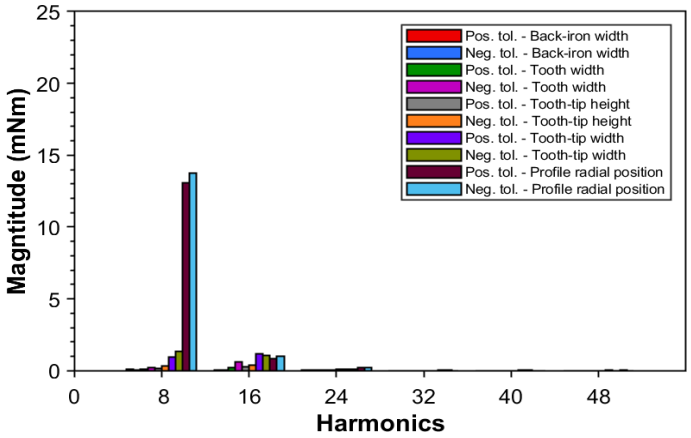
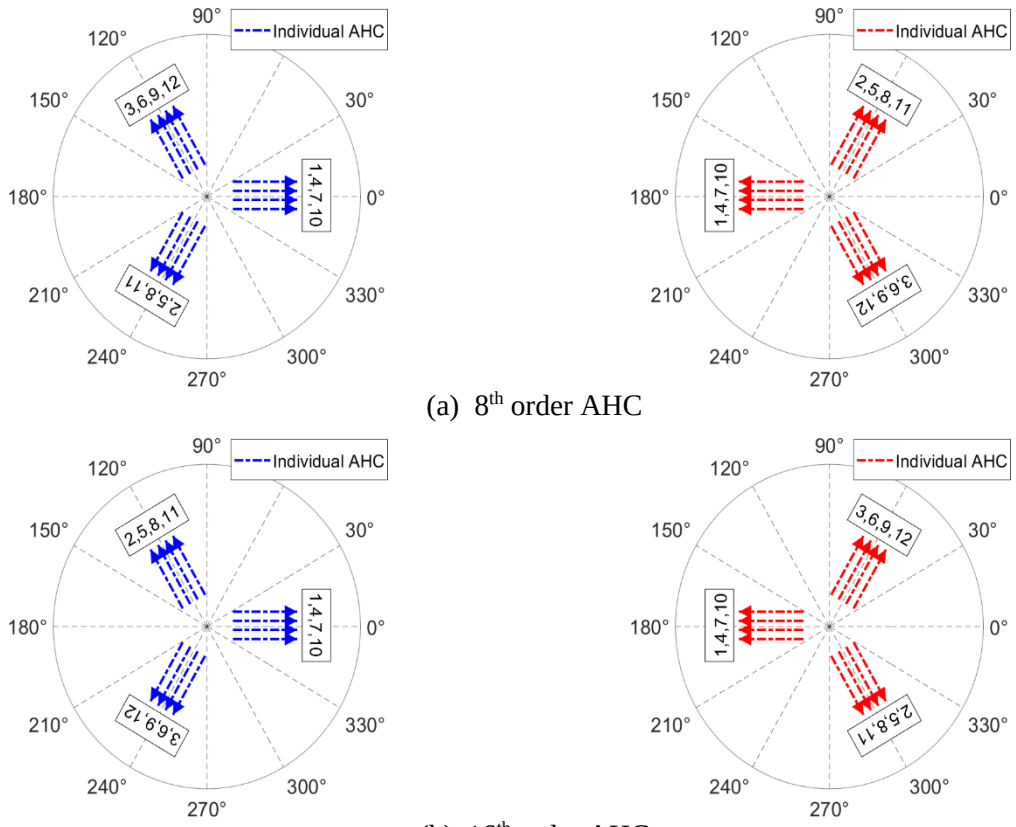



Fig. 5.28. Harmonics of AHCs due to manufacturing tolerances in the 12-slot/8-pole SPM motor.

The 12-slot/8-pole motor has a cyclic symmetry of four, and consequently, the phases of the AHCs due to tolerances in teeth separated by a multiple of 3 slot pitches are identical. The phases of the 8th and 16th order AHCs due to individual positive and negative tolerances of an arbitrary magnitude in the stator tooth profile radial position are shown in Fig. 5.29. The resultant AHCs due to multiple tolerances are produced by the phasor addition of the individual AHCs to individual tolerances.




(a) 8th order AHC

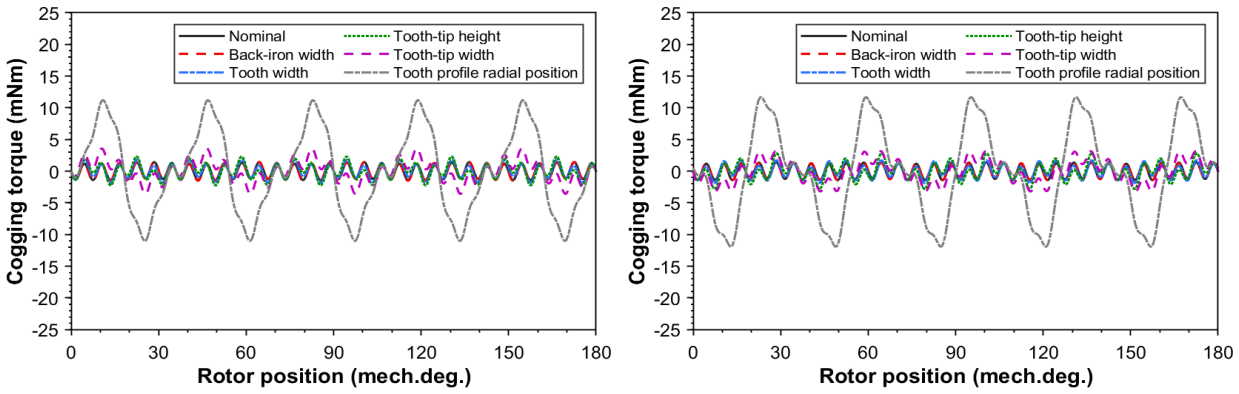
(b) 16th order AHC

(I) Positive tolerance (II) Negative tolerance

Fig. 5.29. Phasors of 8th and 16th order AHCs due a tolerance in tooth surface profile radial position of an individual tooth.

## 5.5.2 Analysis of Cogging Torque Sensitivity of 12-slot/10-pole SPM motor

The cogging torque waveforms and harmonics due to positive and negative manufacturing tolerances in a single tooth of the stator of the 12-slot/10-pole motor under investigation are shown in Fig. 5.30 and Fig. 5.31, respectively. The waveforms and harmonics of the cogging torque AHCs are shown in Fig. 5.32 and Fig. 5.33, respectively. The nominal cogging torque is primarily composed of the fundamental 60th order component. The cogging torque AHCs are composed of the fundamental 10th order harmonic and its harmonic multiples, as well as the 60th order component. The 12-slot/10-pole SPM motor has an inherently low cogging torque and the peak-to-peak cogging torque due to tolerances in the radial position of the stator tooth profile is up to 8.2 times that of the nominal cogging torque.




(a) Positive tolerance (b) Negative tolerance

Fig. 5.30. Influence of tolerances on cogging torque waveforms of 12-slot/10-pole SPM motor.

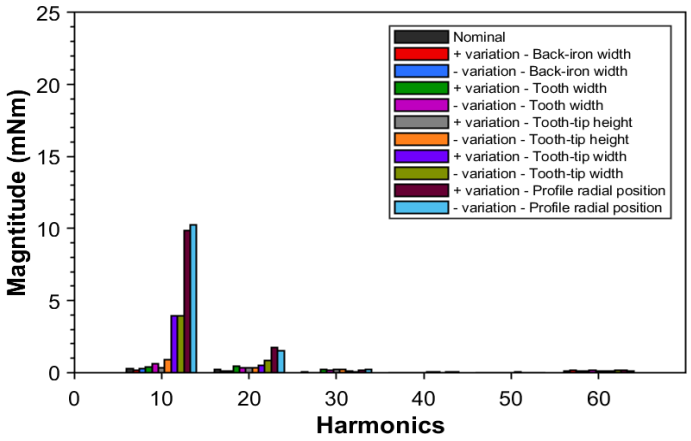
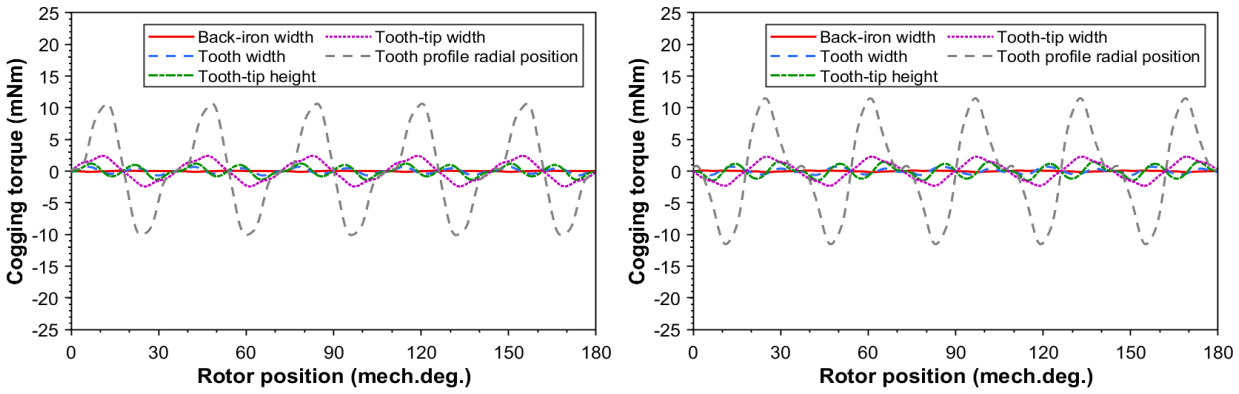



Fig. 5.31. Influence of tolerances on cogging torque harmonics of 12-slot/10-pole SPM motor.

Manufacturing tolerances in the stator back-iron width have a negligible influence on the cogging torque. Tolerances in the tooth width and tooth-tip height lead to a negligible magnitude of the fundamental $10^{th}$ order AHC and low magnitudes of the harmonic multiples, and negligible influence on the fundamental native $60^{th}$ order component. Manufacturing tolerances in the tooth-tip width result in a low magnitude of the $10^{th}$ order harmonic.

The highest magnitude of the $10^{th}$ order harmonic and its harmonic multiples are produced by tolerances in the radial position of the stator tooth profile. The fundamental $60^{th}$ order NHC is not influenced by the tolerances under investigation other than tolerances in the stator tooth profile radial position.




(a) Positive tolerance (b) Negative tolerance

Fig. 5.32. Waveforms of cogging torque AHCs due to tolerances in 12-slot/10-pole SPM motor.

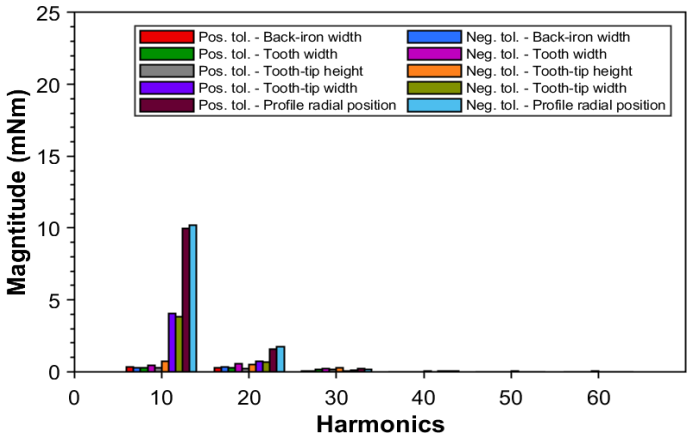
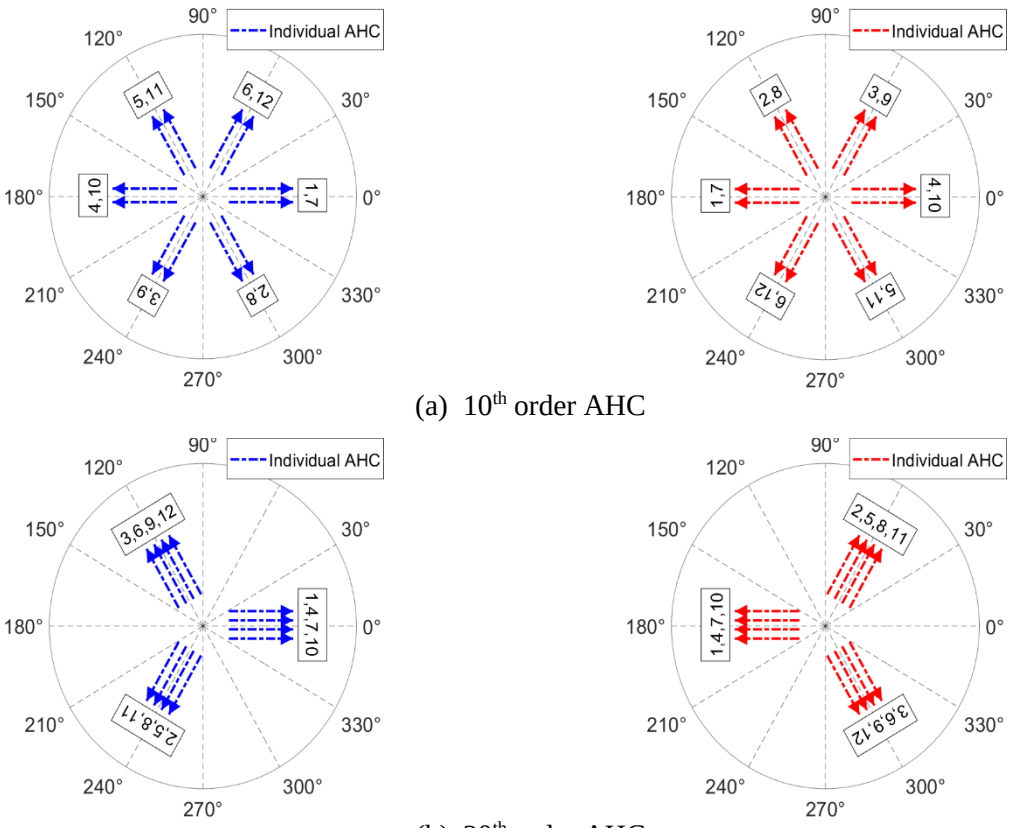



Fig. 5.33. Harmonics of AHCs due to manufacturing tolerances in 12-slot/10-pole SPM motor.

The phase of the AHCs is dependent on the direction of the variation and the location of the tooth subjected to a manufacturing tolerance. For instance, a manufacturing tolerance in the stator tooth profile radial position of tooth 1 results in a $10^{th}$ order AHC with a phase of 0°, and a tolerance in the opposite direction results in a phase shift of 180°, as shown in Fig. 5.34.

The 12-slot/10-pole SPM motor has a cyclic symmetry of two, and consequently, the phases of the AHCs due to tolerances in teeth separated by a multiple of 180° are identical, leading to an additive effect. Furthermore, the 12-slot/10 pole motor exhibits an anti-symmetry every 3 slot pitches. Consequently, tolerances in teeth separated by an angle of 90° result in AHCs with opposite phases, resulting in a cancelling effect. The phases of the $10^{th}$ and $20^{th}$ order AHCs due to individual positive and negative tolerances of an arbitrary magnitude in the stator tooth profile radial position are shown in Fig. 5.35.




(a) 10th order AHC

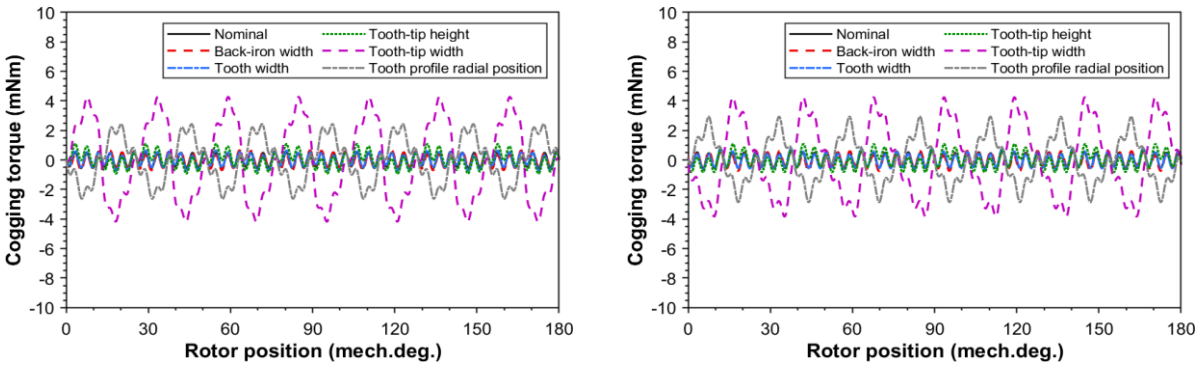
(b) 20th order AHC

(I) Positive tolerance (II) Negative tolerance

Fig. 5.34. Phasors of 10th and 20th order AHCs due a tolerance in tooth surface profile radial position of an individual tooth.

## 5.5.3 Analysis of Cogging Torque Sensitivity of 12-slot/14-pole SPM motor

The cogging torque waveforms and harmonics due to positive and negative manufacturing tolerances in a single tooth of the stator of the 12-slot/14-pole motor under investigation are shown in Fig. 5.35 and Fig. 5.36, respectively. The waveforms and harmonics of the cogging torque AHCs are shown in Fig. 5.37 and Fig. 5.38, respectively. The nominal cogging torque is primarily composed of the fundamental 84th order component. Manufacturing tolerances in the stator result in fundamental 14th order harmonic and its harmonic multiples, as well as the 84th order component. Tolerances in the tooth-tip width and tooth profile radial position have a significant influence on the cogging torque. The influence of the other tolerances under investigation on the cogging torque is very low. The cogging torque of the 12-slot/14-pole SPM motor under investigation is more sensitive to tolerances in the tooth-tip width than the tooth profile radial position. However, it is worth noting that both tooth-tip width and tooth profile radial position tolerances have larger influence on cogging torque than other parameters.




(a) Positive tolerance (b) Negative tolerance

Fig. 5.35. Influence of tolerances on cogging torque waveforms of 12-slot/14-pole SPM motor.

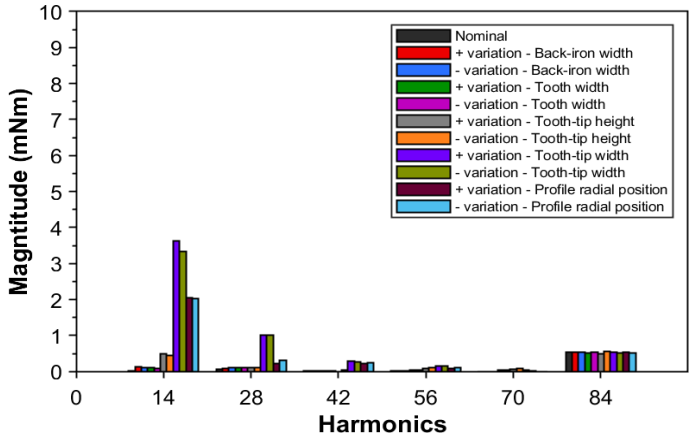
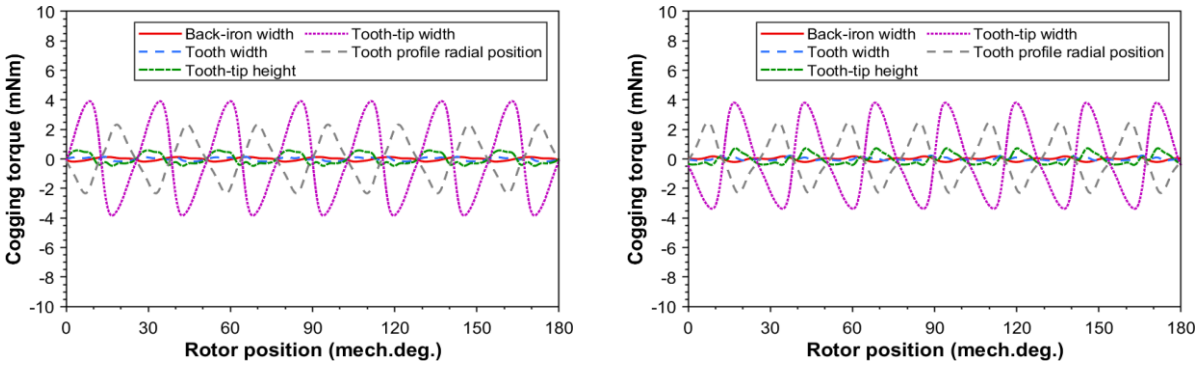



Fig. 5.36. Influence of tolerances on cogging torque harmonics of the 12-slot/14-pole SPM motor.

The magnitude of the 14$^{th}$ order harmonic due to tolerances in the tooth-tip width is up to 76.6% higher than that due to tolerances in the tooth profile radial position. The magnitude of the 14$^{th}$ order harmonic due to a positive tolerance in the tooth-tip width is higher than that due to a negative tolerance since the flux linkage is increased. The influence of direction of the tolerance in the tooth profile radial position on the magnitude of the 14$^{th}$ order harmonic is negligible. The cogging torque AHC waveforms show that the 14$^{th}$ order harmonics produced by tolerances in the tooth-tip width and tooth profile radial position have opposite phases.




(a) Positive tolerance (b) Negative tolerance

Fig. 5.37. Waveforms of cogging torque AHCs due to tolerances in 12-slot/14-pole SPM motor.

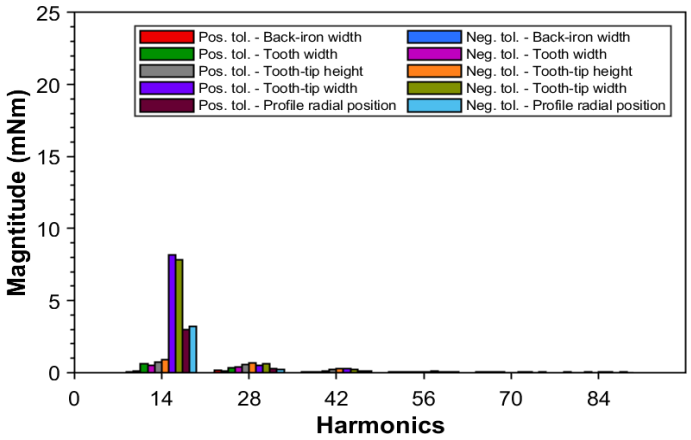
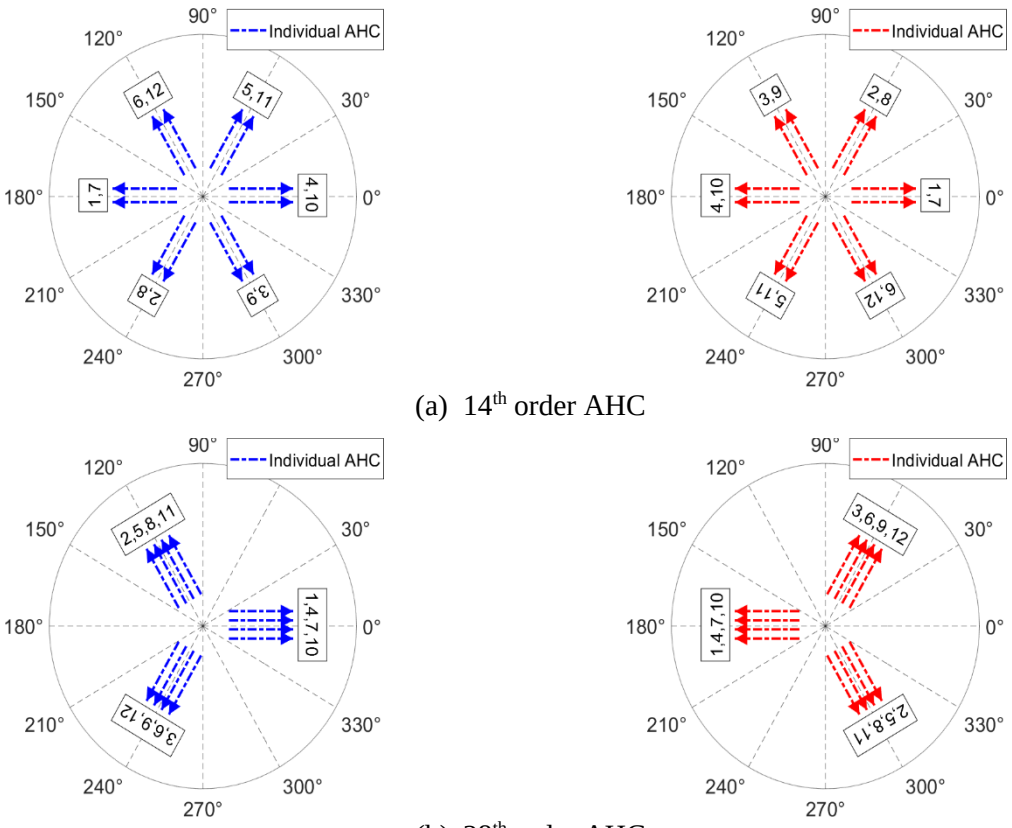



Fig. 5.38. Harmonics of AHCs due to manufacturing tolerances in 12-slot/14-pole SPM motor.

The phases of the AHCs are dependent on the direction of the variation and the location of the tooth subjected to a manufacturing tolerance. Manufacturing tolerances in the tooth-tip width of tooth 1 results in a 14$^{th}$ order AHC with a phase of 0°, and a tolerance in the opposite direction results in a phase shift of 180°, as shown in Fig. 5.39.

The 12-slot/14-pole SPM motor has a cyclic symmetry of two, and consequently, the phases of the AHCs due to tolerances in teeth separated by a multiple of 180° are identical, leading to an additive effect. Furthermore, the 12-slot/10 pole motor exhibits an anti-symmetry every 3 slot pitches. Consequently, tolerances in teeth separated by an angle of 90° result in AHCs with opposite phases resulting in a cancelling effect. The phases of the 14$^{th}$ and 28$^{th}$ order AHCs due to individual positive and negative tolerances of an arbitrary magnitude in the stator tooth profile radial position are shown in Fig. 5.39.




(a) 14th order AHC

(b) 28th order AHC

(I) Positive tolerance (II) Negative tolerance

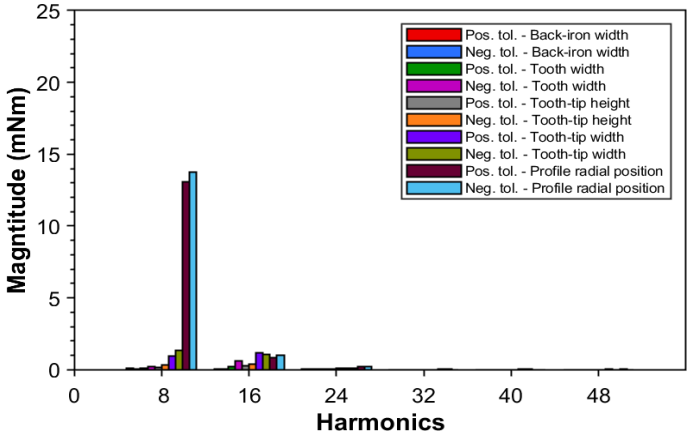
Fig. 5.39. Phasors of 14th and 28th order AHCs due to tolerance in tooth surface profile radial position of an individual tooth.

## 5.5.4 Comparison of Cogging Torque Sensitivity of SPM Motors

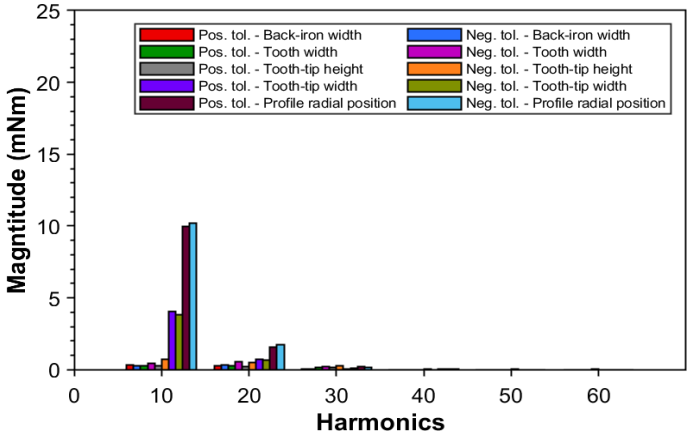
The nominal peak-to-peak cogging torque of the SPM motors under investigation decreases with increasing rotor pole number since the peak-to-peak cogging torque decreases with increasing LCM of the stator slot and rotor pole number.

Stator tolerances in the 12-slot/8-pole motor result in AHCs coinciding with the fundamental 24th order NHC of the motor. Tolerances in stator tooth profile radial position of the 12-slot/10-pole motor lead to AHCs coinciding with the fundamental 60th order NHC. The magnitudes of the 60th order AHCs due to the remaining tolerances under investigation are negligible. The influence of stator tolerances on the 84th order AHC of the 12-slot/14-pole SPM motor is negligible.

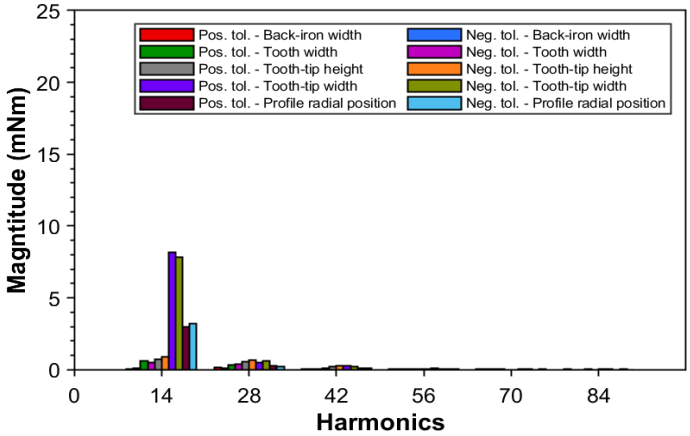
The cogging torque AHCs of the SPM motors due to stator tolerances are shown in Fig. 5.40. The influence of tolerances in the stator back-iron width, tooth width, and tooth-tip height on cogging torque is very low in all motors under analysis. The magnitude of the fundamental AHC due to tolerances in the tooth profile radial position decrease significantly with increasing rotor pole number. Conversely, the magnitude of the fundamental AHC due to tolerances in the tooth-tip width increases with increasing rotor pole number.




(a) 12-slot/8-pole SPM motor

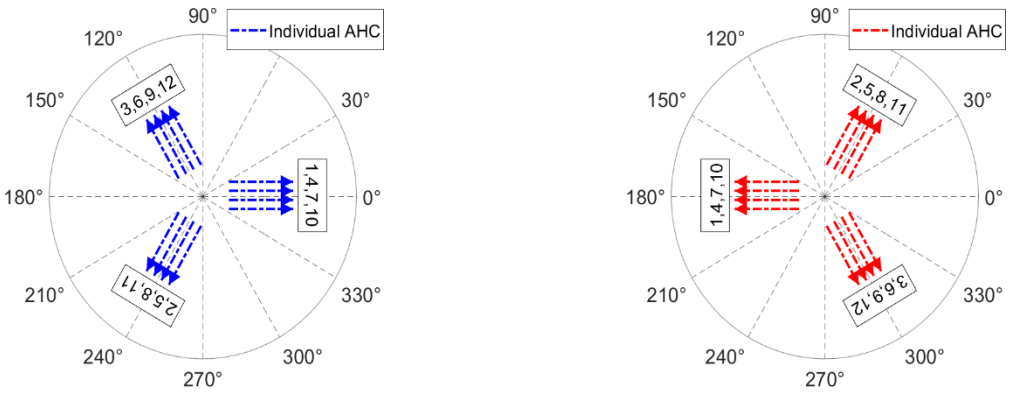



(b) 12-slot/10-pole SPM motor

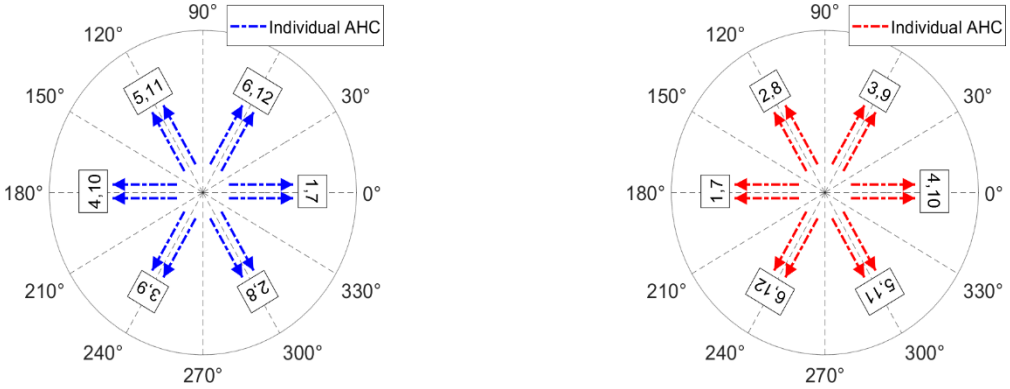



(c) 12-slot/14-pole SPM motor

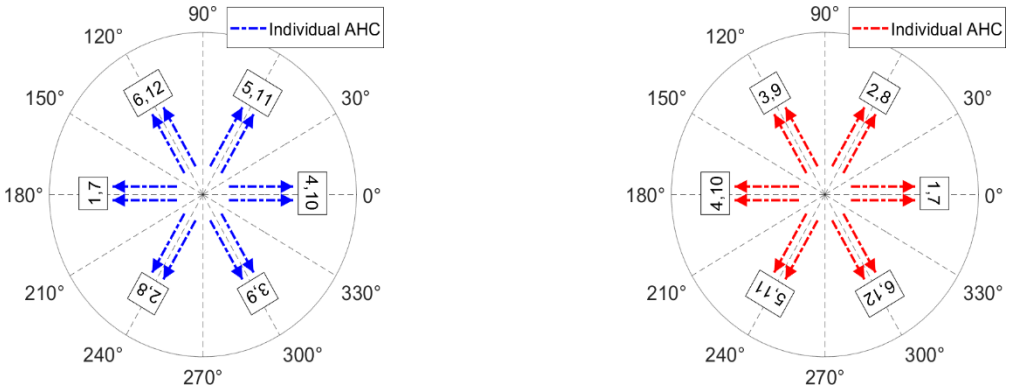
Fig. 5.40. Cogging torque AHCs due to stator manufacturing tolerances in 12-slot/8-pole, 12-slot/10-pole, and 12-slot/14-pole SPM motors




(a) 8th order AHC of the 12-slot/8-pole SPM motor




(b) 10th order AHC of the 12-slot/10-pole SPM motor




(c) 14th order AHC of the 12-slot/14-pole SPM motor

(I) Positive tolerance (II) Negative tolerance

Fig. 5.41. Phasors of fundamental AHC due to stator tolerances in tooth profile radial position of SPM motors under analysis.

## 5.6 Analysis of Cogging Torque Sensitivity to Rotor Tolerances in IPM Motors

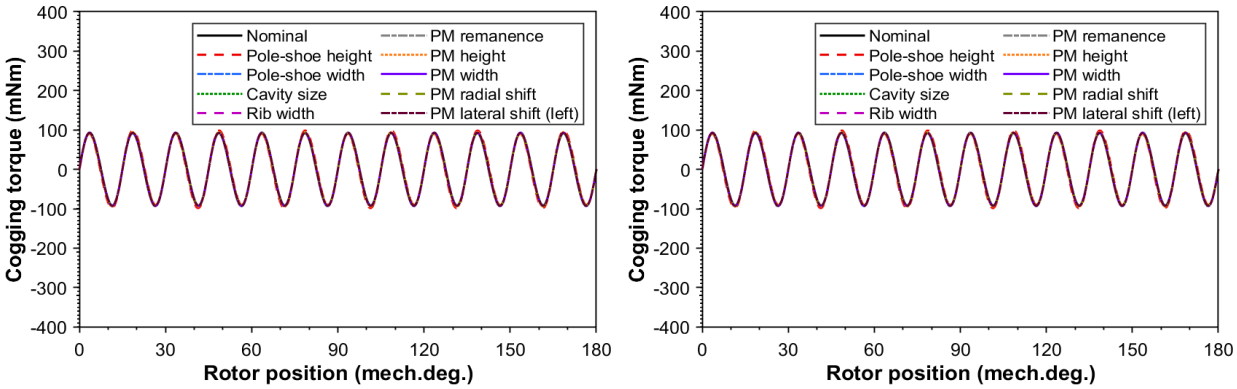
The cogging torque waveforms and harmonics due to positive and negative rotor manufacturing tolerances in the IPM motors are shown in Fig. 5.42 and Fig. 5.43, respectively. The waveforms and harmonics of the cogging torque AHCs are shown in Fig. 5.44 and Fig. 5.45, respectively.

The cogging torque of the 12-slot/8-pole motor is significantly higher than those of the 12-slot/10-pole and 12-slot/14-pole motors. Therefore, the influence of tolerances on cogging torque has a more dominant effect in 12-slot/10-pole and 12-slot/14-pole motors. The influence of rotor tolerances on the resultant native $24^{th}$ and $48^{th}$ order harmonics of the 12-slot/8-pole motor is non-negligible. The 12-slot/10-pole and 12-slot 14-pole motors have fundamental native cogging torque components of a low magnitude and the influence of rotor tolerances on the resultant native components is negligible.

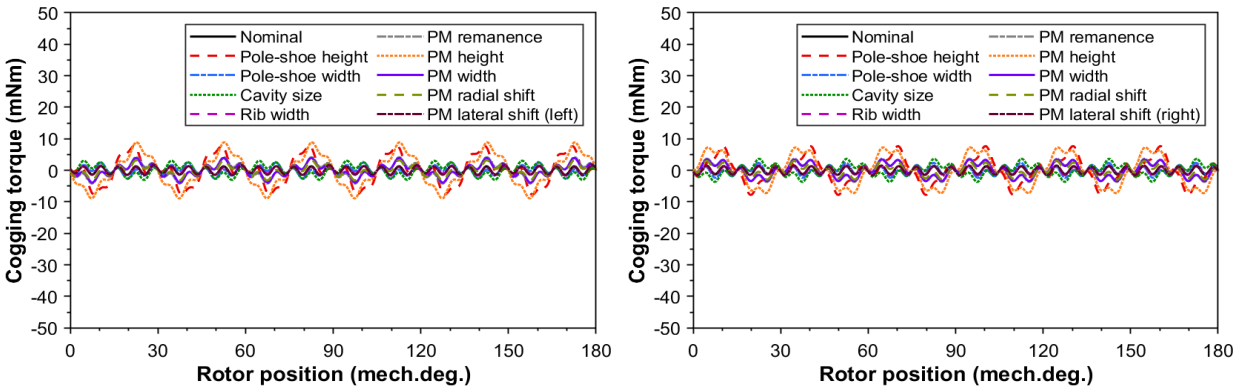
The air-gap flux density is highly influenced by the air-gap length and the PM height. Thus, the influences of tolerances in the pole-shoe height and PM height on cogging torque are significant. The magnitudes of the AHCs due to tolerances in the pole-shoe height decreases with increasing rotor pole number and this effect is attributed to the decrease in flux per pole with increasing rotor pole number.

The influence of tolerances in the lateral position of the PM in all motors is negligible. The influence of tolerances in PM width on magnitude of the AHCs of the 12-slot/8-pole motor is very low. The influence tolerances in rotor rib width is very low in 12-slot/8-pole and 12-slot/10-pole motors, but non-negligible in the 12-slot/14-pole motor. This may be attributed to the fact that the influence of flux leakage through the rotor ribs increases significantly with increasing rotor pole number.

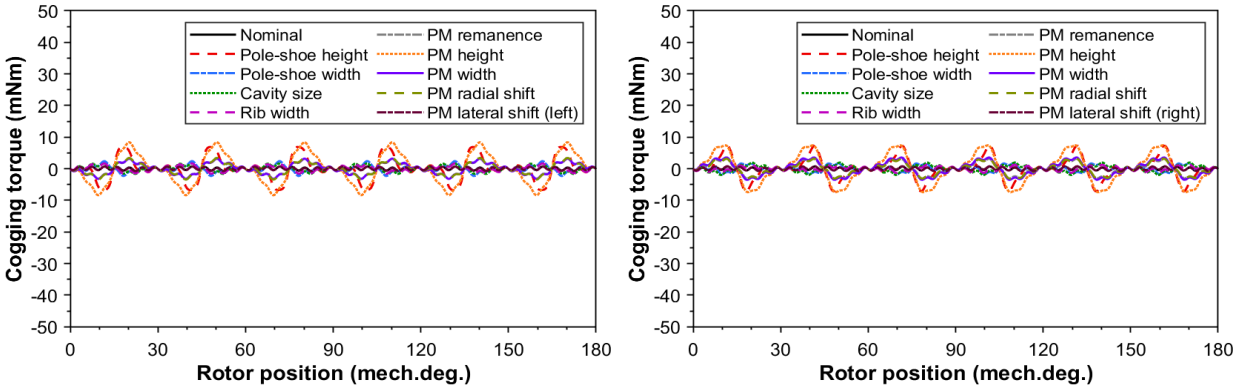
The 12-slot/8-pole motor is less sensitive to tolerances in the rotor PM than the 12-slot/10-pole and 12-slot/14-pole motors. The influence of tolerances in the rotor PM of 12-slot/10-pole and 12-slot/14-pole motors on the magnitude of the $12^{th}$ order AHC is very similar. However, the magnitude of the $24^{th}$ order AHCs of the 12-slot/14-pole motor is significantly higher than that of the 12-slot/10-pole motor.




(a) 12-slot/8-pole



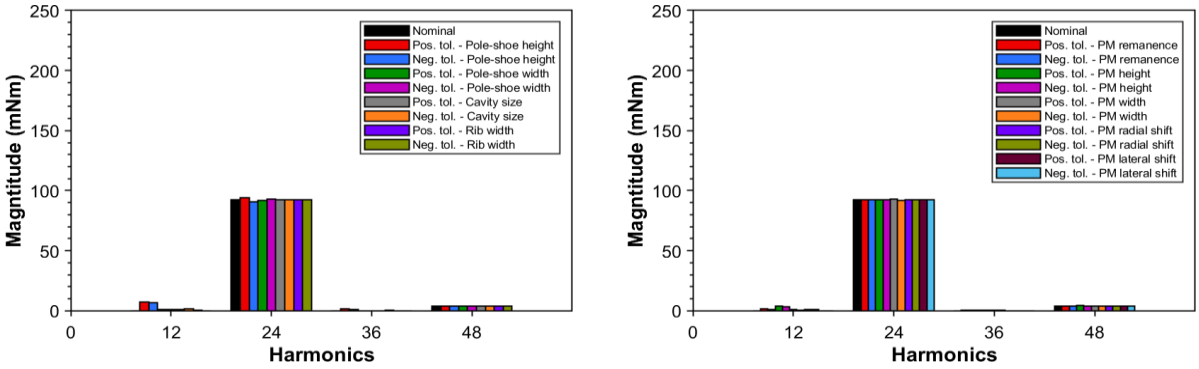

(b) 12-slot/10-pole



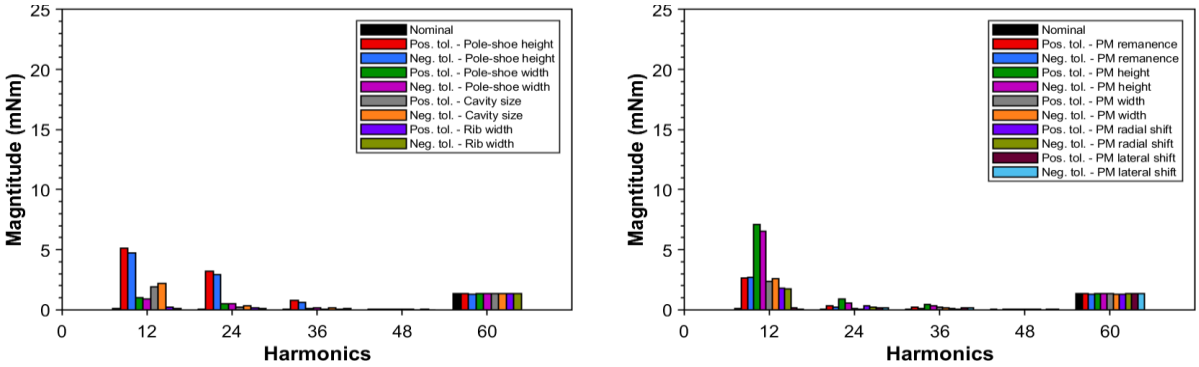

(c) 12-slot/14-pole

(I) Positive tolerance (II) Negative tolerance

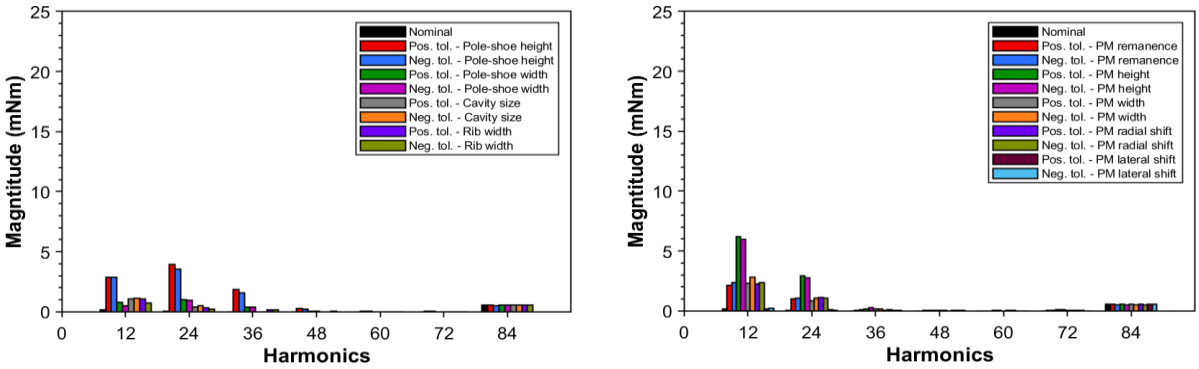
Fig. 5.42. Cogging torque waveforms of the IPM motors due to rotor tolerances.




(a) 12-slot/8-pole



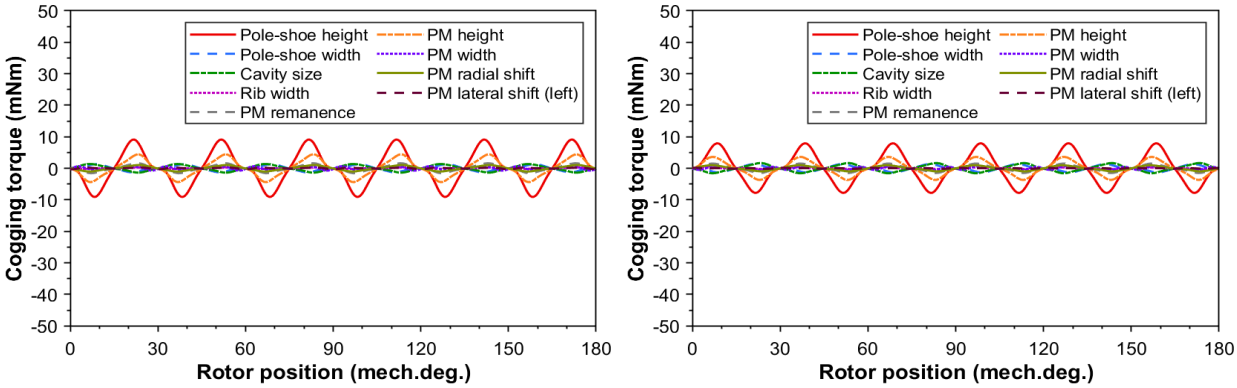

(b) 12-slot/10-pole



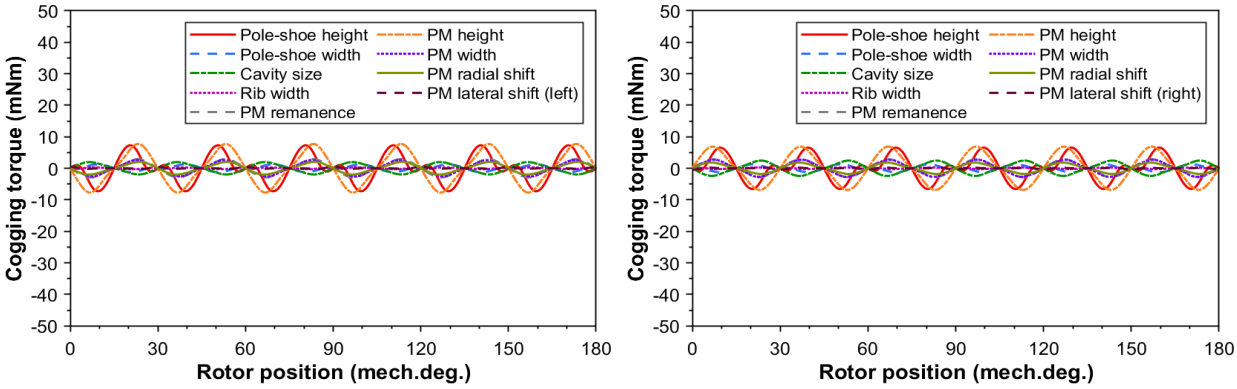

(c) 12-slot/14-pole

(I) Rotor iron tolerance (II) PM tolerance

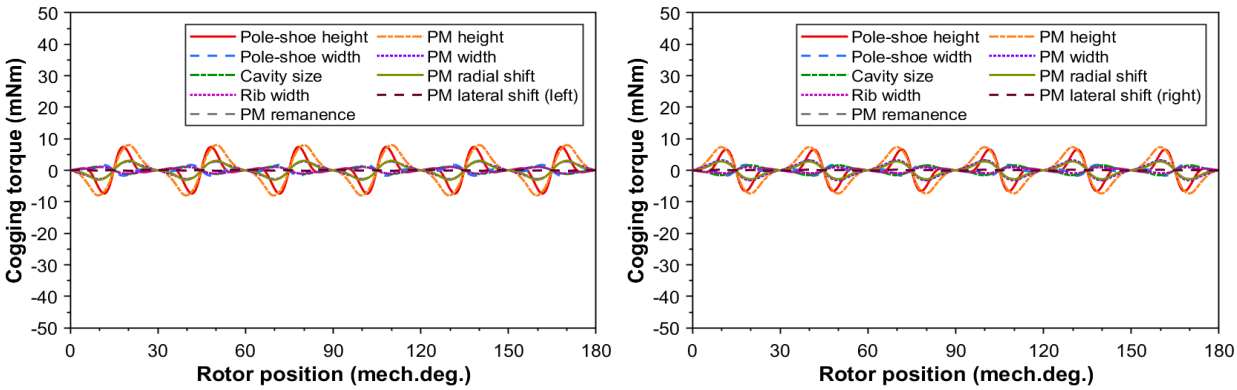
Fig. 5.43. Harmonics of cogging torque of IPM motors due to rotor tolerances.




(a) 12-slot/8-pole



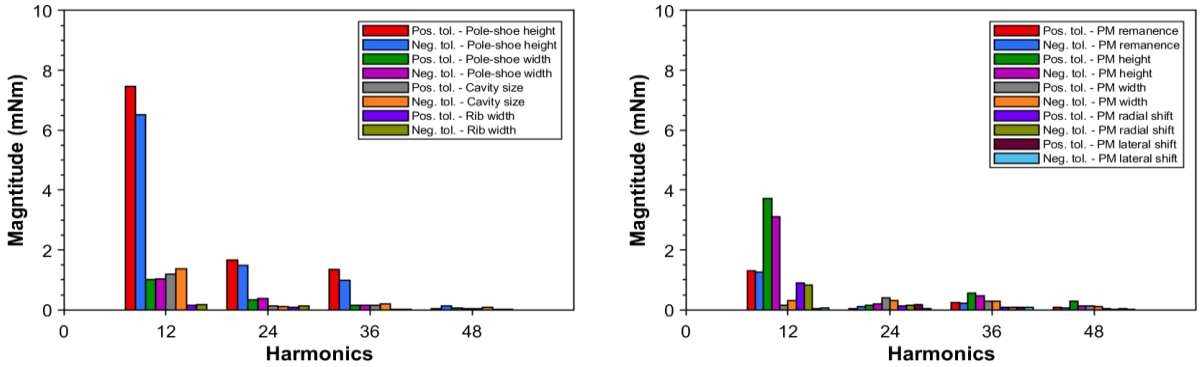

(b) 12-slot/10-pole



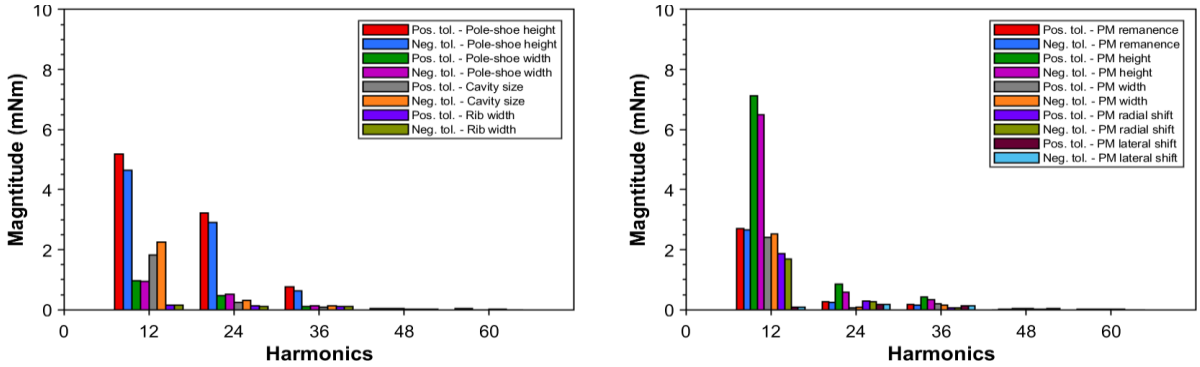

(c) 12-slot/14-pole

(I) Positive tolerance (II) Negative tolerance

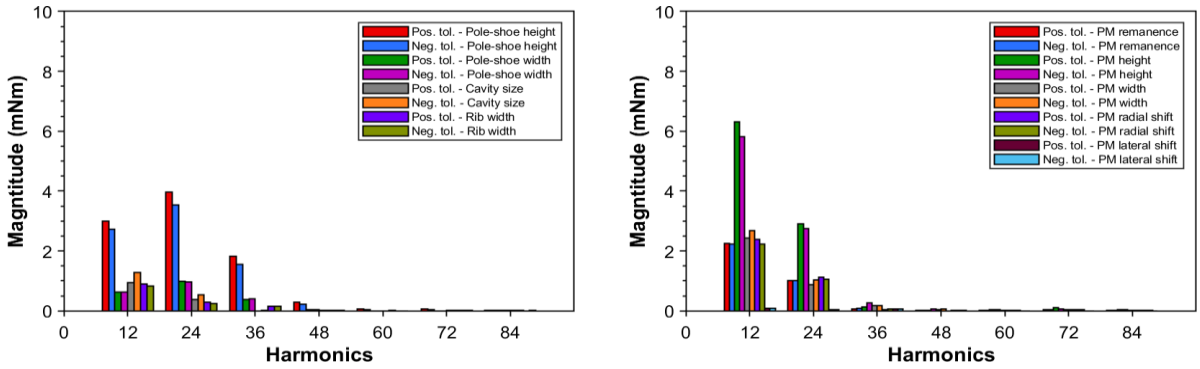
Fig. 5.44. Waveforms of cogging torque AHCs of IPM motor due to rotor tolerances.




(a) 12-slot/8-pole




(b) 12-slot/10-pole




(c) 12-slot/14-pole

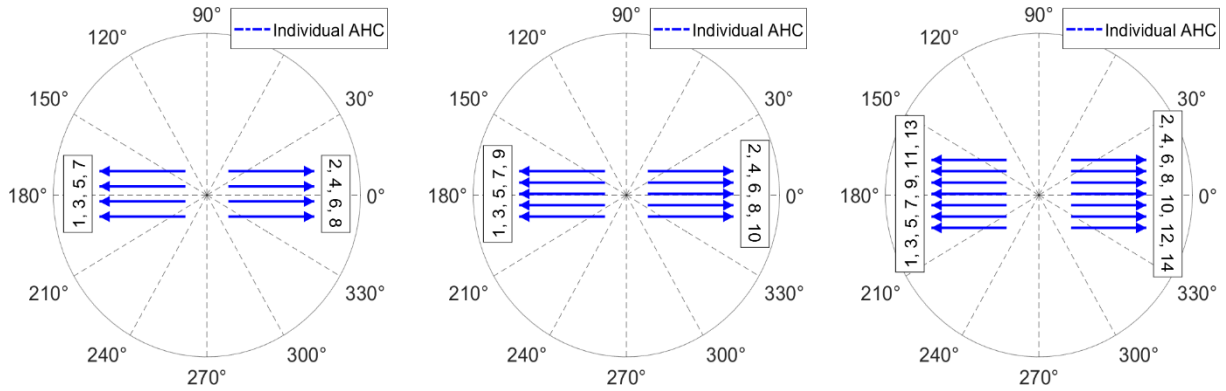
(I) Rotor iron tolerance (II) PM tolerance

Fig. 5.45. Harmonics of cogging torque AHCs of the IPM motors due to rotor tolerances.

The phase of the 12th AHCs due to a single rotor tolerance is determined by the direction of the tolerances and the affected rotor pole. The 12th order AHCs due to a negative tolerance are 180° out-of-phase with the AHCs due to positive tolerances, as shown in Fig. 5.44. Tolerances in rotor poles with the same magnetic direction and the same tolerance direction (i.e. N or S) result in AHCs with the same phase. Conversely, tolerances in opposite magnetic poles and the same tolerance direction result in AHCs 180° out-of-phase.

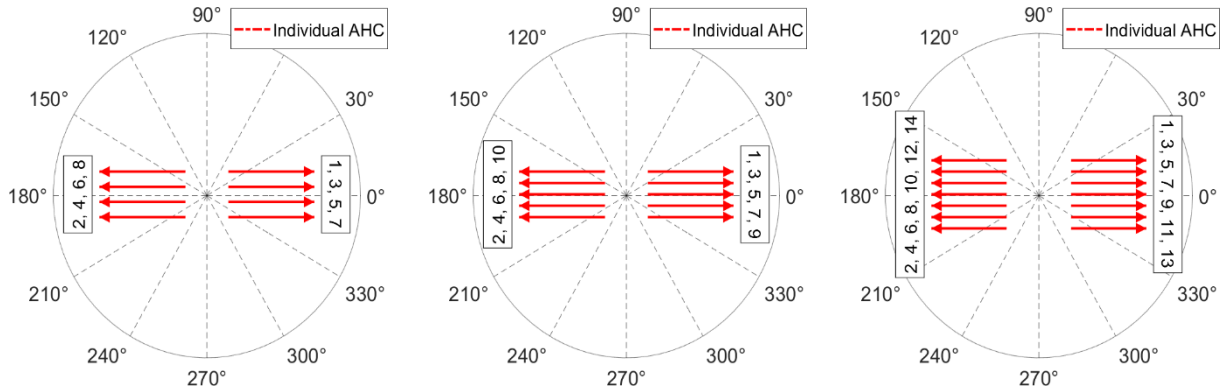
Tolerances resulting in an increase in air-gap flux density lead to fundamental AHCs with a phase of 180°, and vice-versa. For instance, positive tolerances in the pole-shoe width, cavity size, and rib width of pole 1 result in a slight reduction of air-gap flux density. Consequently, the phase difference of the fundamental AHC is 180° out-of-phase with the remaining positive tolerances under investigation.

The phasors of the individual 12th order AHCs due to a single manufacturing tolerance in a rotor pole resulting in an increase or decrease in air-gap flux density are shown in Fig. 5.46 and Fig. 5.47, respectively.




(a) 12-slot/8-pole motor (b) 12-slot/10-pole motor (c) 12-slot/14-pole motor

Fig. 5.46. Phasors of 12th order AHC due to a single tolerance in a single rotor pole resulting in an increase in air-gap flux density.




(a) 12-slot/8-pole motor (b) 12-slot/10-pole motor (c) 12-slot/14-pole motor

Fig. 5.47. Phasors of 12th order AHC due to a single tolerance in a single rotor pole resulting in a decrease in air-gap flux density.

## 5.7 Analysis of Cogging Torque Sensitivity to Rotor Manufacturing Tolerances in SPM Motors

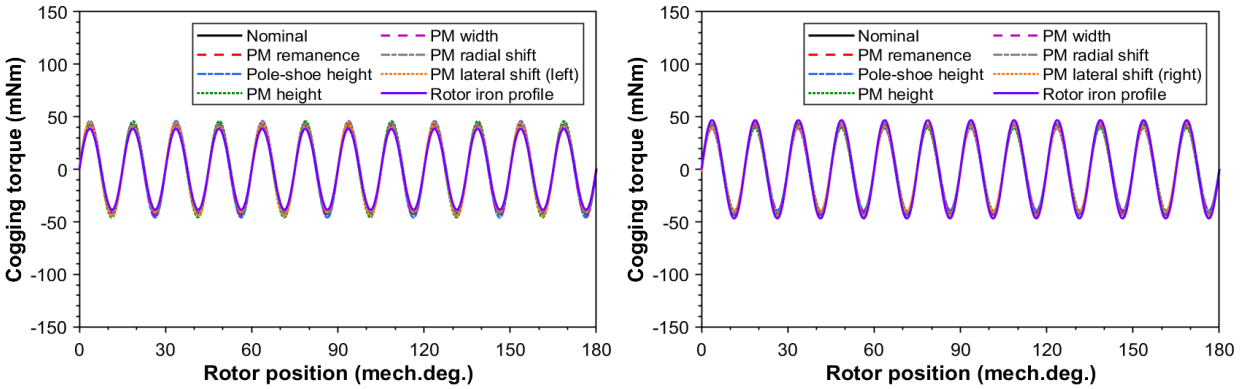
The cogging torque waveforms and harmonics due to positive and negative rotor manufacturing tolerances in the SPM motors are shown in Fig. 5.48 and Fig. 5.49, respectively. The waveforms and harmonics of the cogging torque AHCs are shown in Fig. 5.50 and Fig. 5.51, respectively.

Rotor tolerances in 12-slot motors result in a fundamental $12^{th}$ order AHC and its higher order multiples as well as AHCs coinciding with the NHCs of the motor. The cogging torque of the 12-slot/8-pole motor is significantly higher than those of the 12-slot/10-pole and 12-slot/14-pole motors. Therefore, the influence of tolerances on cogging torque has a more dominant effect in 12-slot/10-pole and 12-slot/14-pole motors.

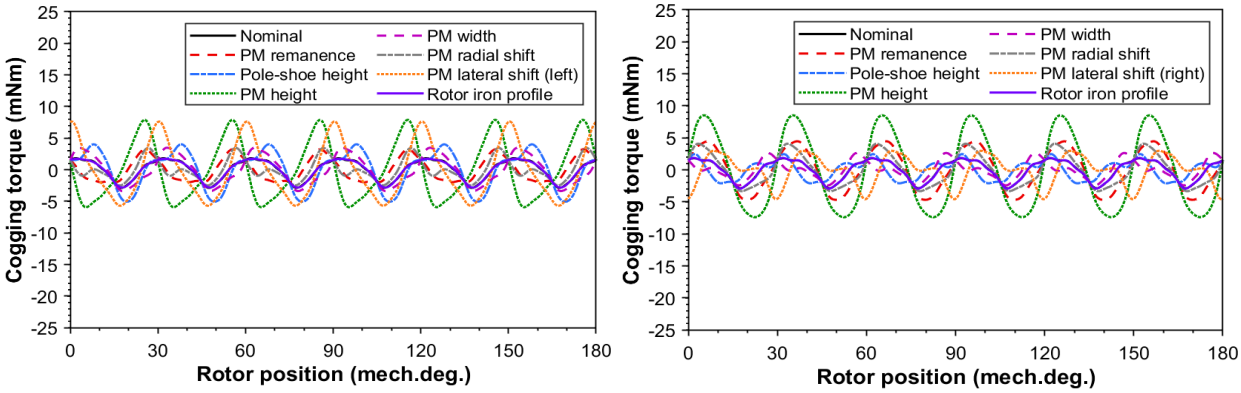
The $12^{th}$ order harmonic of the 12-slot/10-pole motor is composed of the $12^{th}$ order NHC, i.e. subharmonic of the fundamental $60^{th}$ order component, and the $12^{th}$ order fundamental AHCs due to rotor tolerances. The influence of rotor tolerances on the fundamental 84th order component and $14^{th}$ order subharmonic inherent in the 12-slot/14-pole motor under analysis is very low.

Tolerances in the rotor iron profile of SPM motors do not introduce any asymmetry in the motor geometry. The gap between the PMs and the rotor iron profile is directly affected by tolerances in the rotor iron profile, thereby affecting the air-gap flux density. Consequently, the magnitude of harmonics coinciding with the NHCs is affected. The influence of tolerances in the PM height on cogging torque increases significantly with increasing rotor pole number. Conversely, the influence of tolerances in the pole-shoe height and PM width on cogging torque decreases with increasing pole-number.

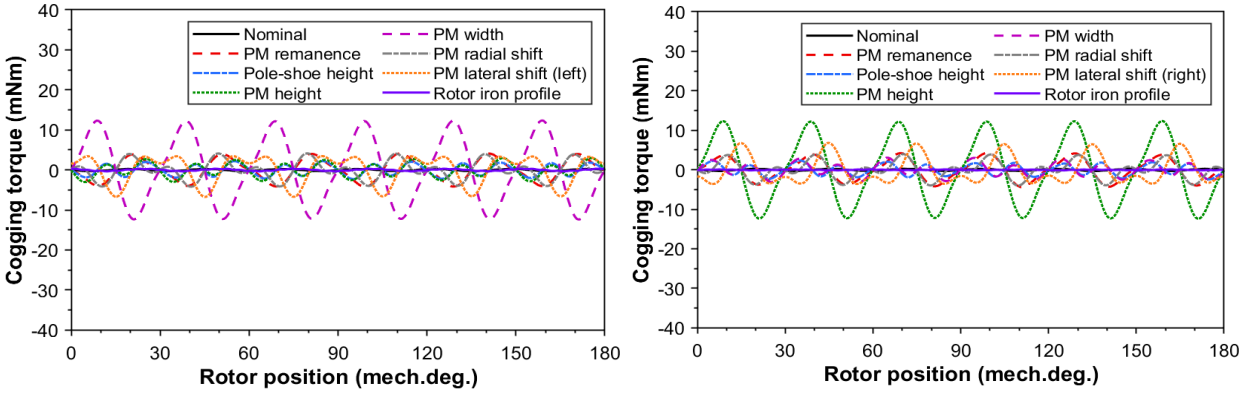
The 24th order component of the 12-slot/8-pole SPM motor is very sensitive to tolerances in the rotor iron profile. The analysed PM tolerances result in similar magnitudes of the $12^{th}$ order AHC of the 12-slot/8-pole motor. Tolerances in the PM remanence, PM radial position, and PM lateral position of the 12-slot/8-pole motor result in negligible magnitudes of the $24^{th}$ order AHC.




(a) 12-slot/8-pole



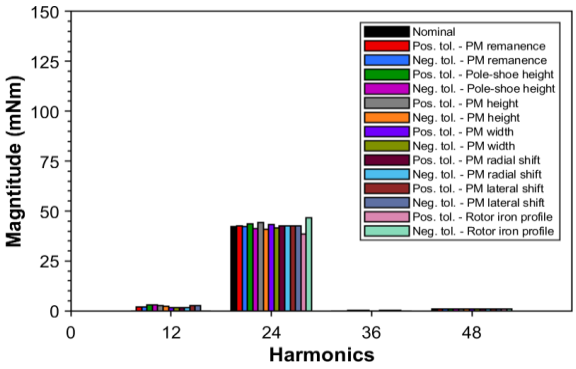

(b) 12-slot/10-pole



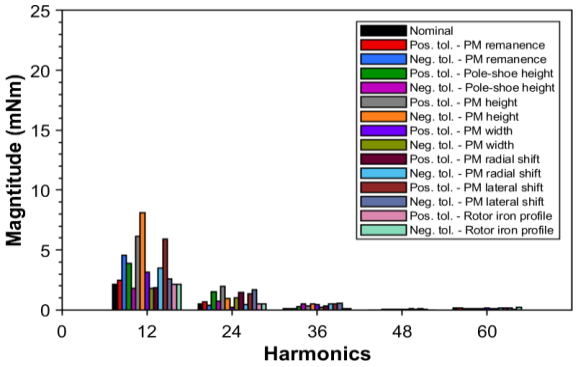

(c) 12-slot/14-pole

(I) Positive tolerance (II) Negative tolerance

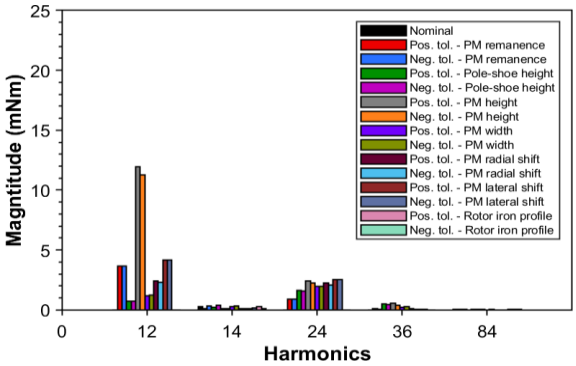
Fig. 5.48. Cogging torque waveforms of SPM motor due to rotor tolerances.




(a) 12-slot/8-pole

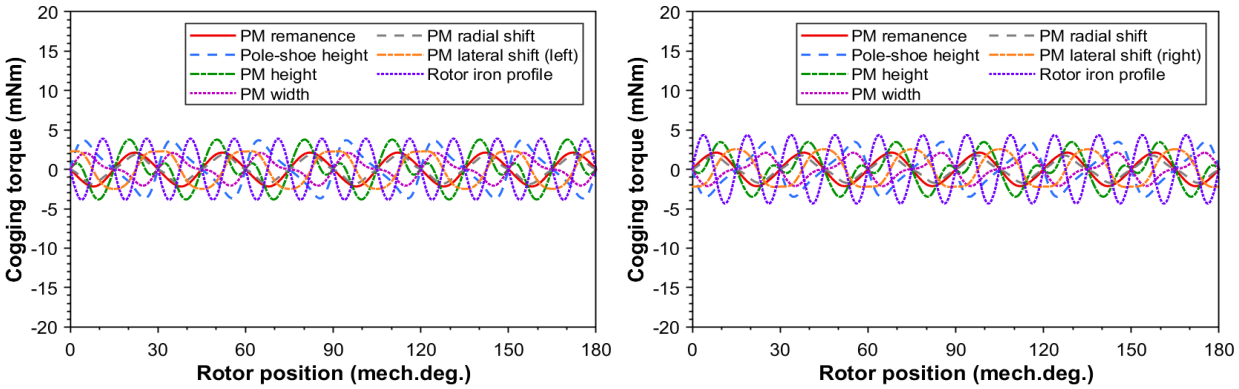



(b) 12-slot/10-pole

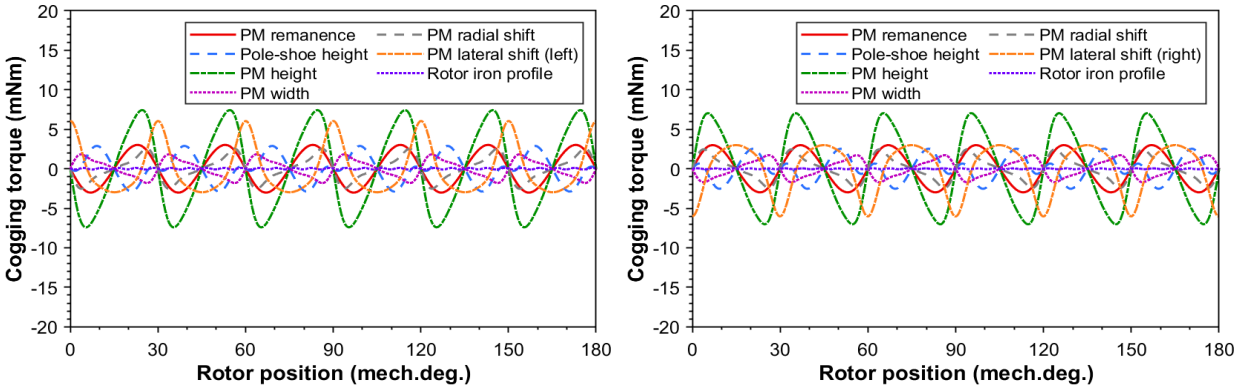



(c) 12-slot/14-pole

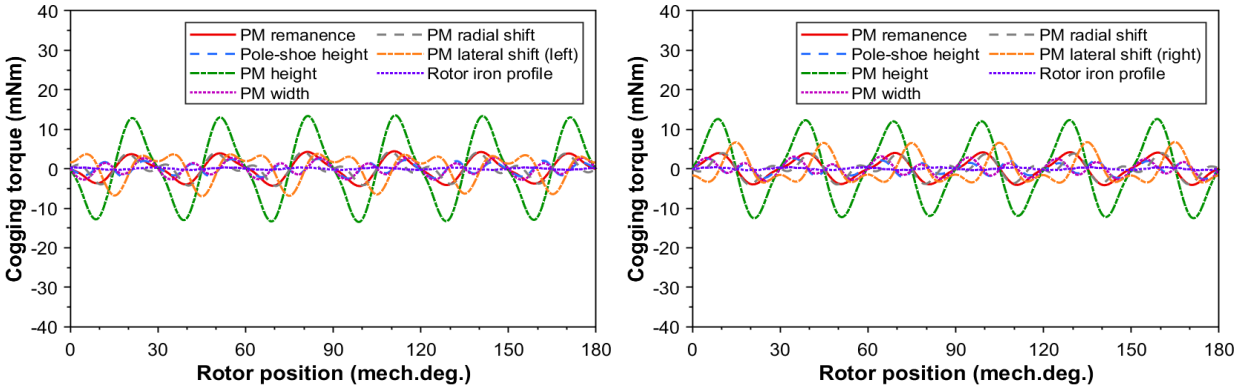
Fig. 5.49. Harmonics of cogging torque of SPM motors due to rotor tolerances.




(a) 12-slot/8-pole



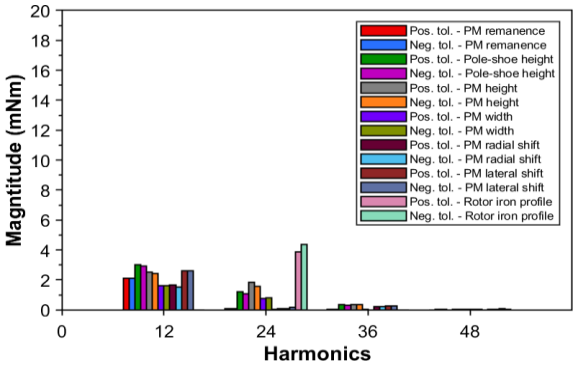

(b) 12-slot/10-pole



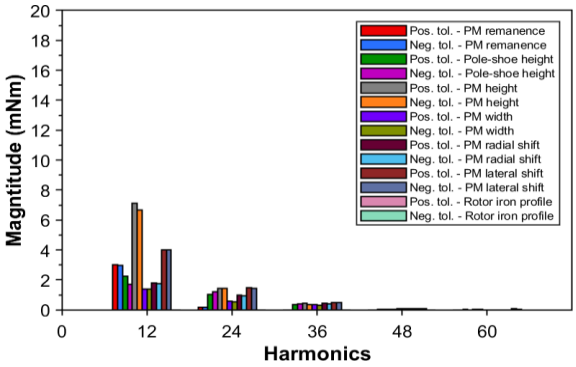

(c) 12-slot/14-pole

(I) Positive tolerance (II) Negative tolerance

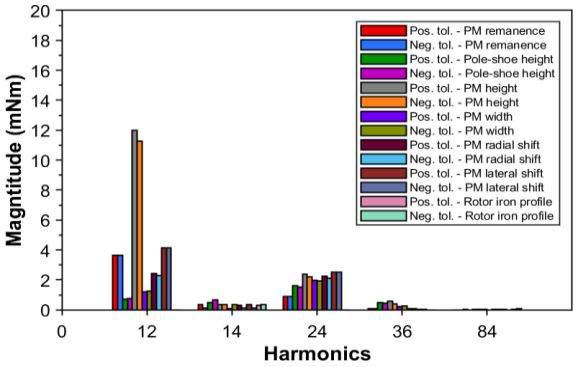
Fig. 5.50. Waveforms of cogging torque AHCs of the SPM motor due to rotor tolerances.




(a) 12-slot/8-pole




(b) 12-slot/10-pole




(c) 12-slot/14-pole

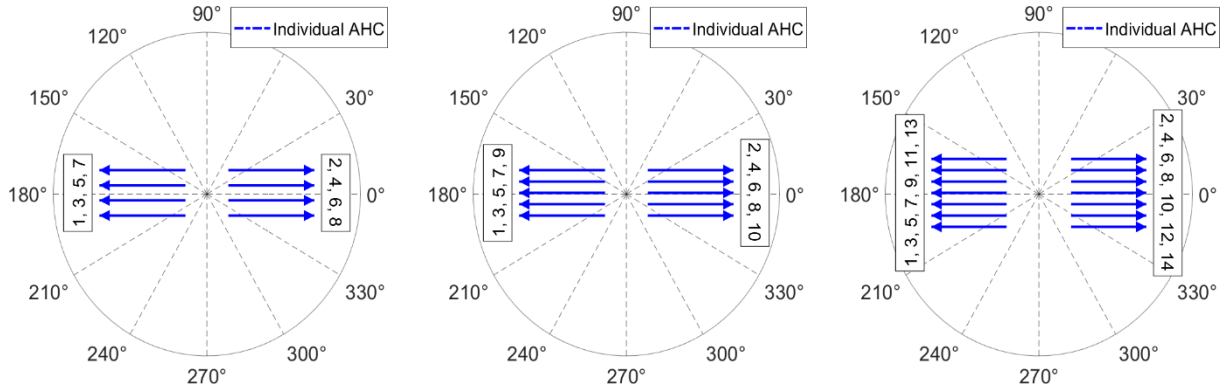
Fig. 5.51. Harmonics of cogging torque AHCs SPM motors due to rotor tolerances.

The phases of the 12$^{th}$ order AHCs due to a single rotor tolerance are determined by the direction of the tolerances and the affected rotor pole. The 12$^{th}$ order AHCs due to a negative tolerance are 180° out-of-phase with the AHCs due to positive tolerances. Tolerances in rotor poles with the same magnetic direction and the same tolerance direction (i.e. N or S) result in AHCs with the same phase. Conversely, tolerances in opposite magnetic poles and the same tolerance direction result in AHCs 180° out-of-phase.

Tolerances resulting in an increase in air-gap flux density lead to fundamental AHCs with a phase of 180°, and vice-versa. For instance, positive tolerances in the pole-shoe width, cavity size, and rib width of pole 1 result in a slight reduction of air-gap flux density. Consequently, the phase difference of the fundamental AHC is 180° out-of-phase with the remaining positive tolerances under investigation.

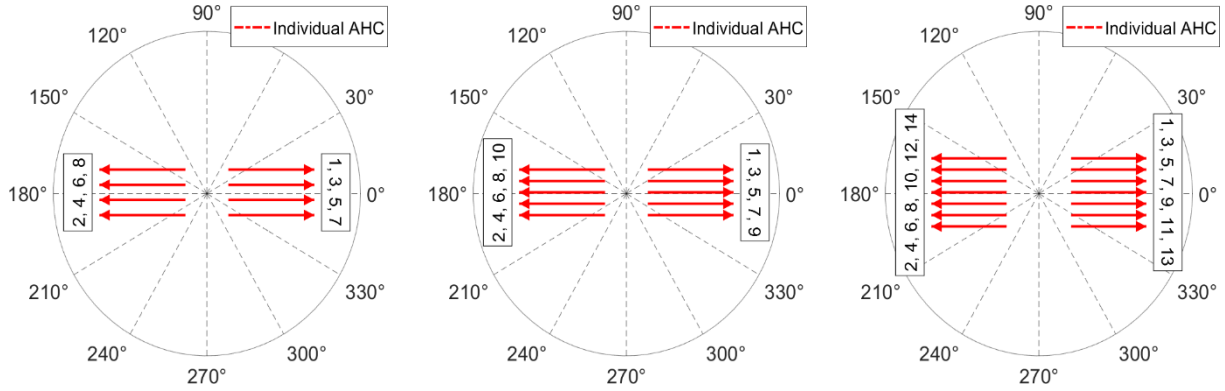
The phasors of the individual 12th order AHCs due to a single manufacturing tolerance in a rotor pole resulting in an increase or decrease in air-gap flux density are shown in Fig. 5.52 and Fig. 5.53, respectively.

Radial rotor tolerances and tolerances in the PM width of an SPM motor result in an increase or decrease in the air-gap flux density. Tolerances in the lateral position of the PM results in a drastic change in the rotor pole and, consequently, on the air-gap flux density. Therefore, the phase of AHCs due to tolerances in the lateral PM position may vary from the phases illustrated in Fig. 5.52 and Fig. 5.53.




(a) 12-slot/8-pole motor (b) 12-slot/10-pole motor (c) 12-slot/14-pole motor

Fig. 5.52. Phasors of 12th order AHC due to a single tolerance in a single rotor pole resulting in an increase in air-gap flux density.

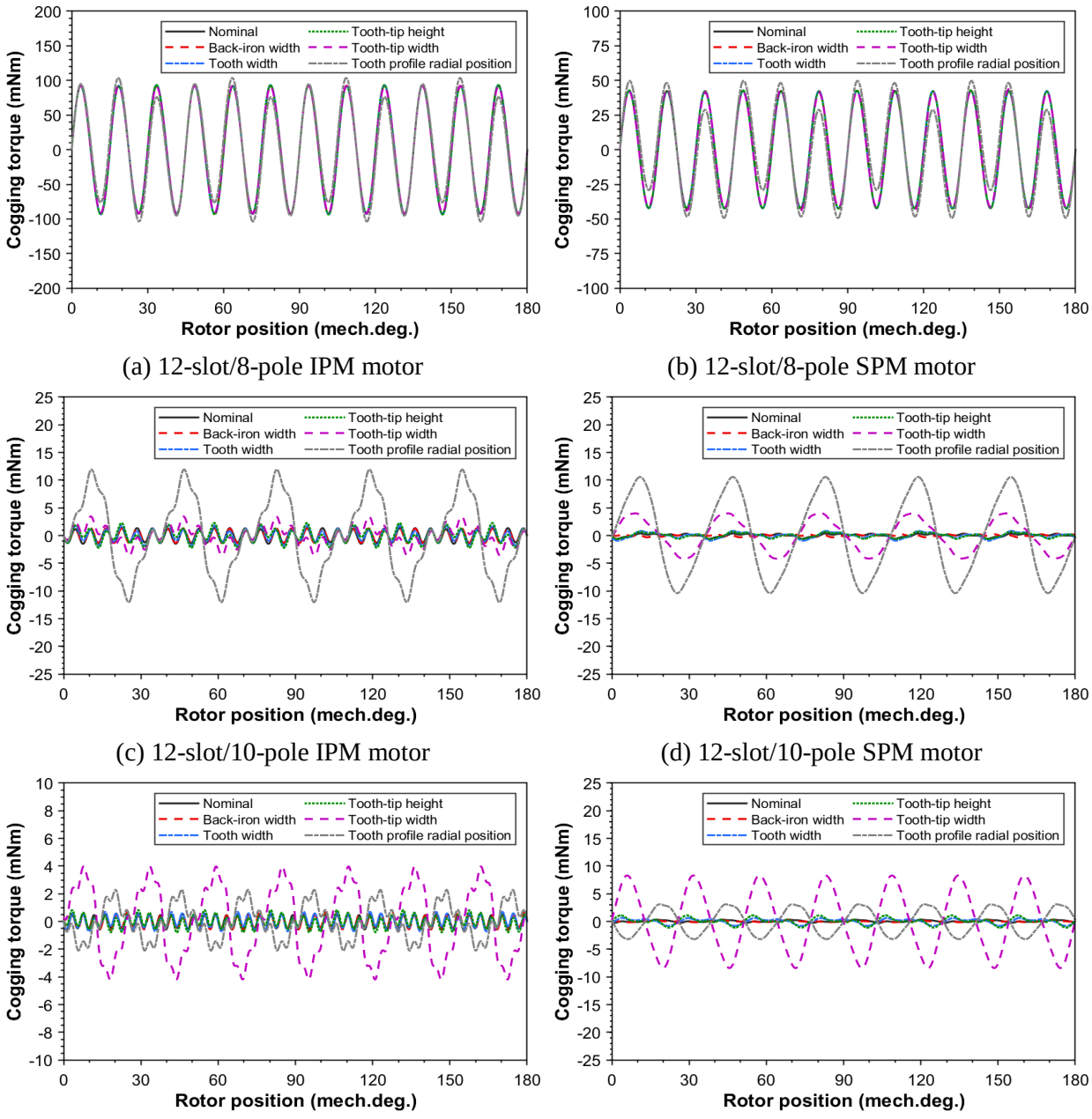



(a) 12-slot/8-pole motor (b) 12-slot/10-pole motor (c) 12-slot/14-pole motor

Fig. 5.53. Phasors of 12th order AHC due to a single tolerance in a single rotor pole resulting in a decrease in air-gap flux density.

## 5.8 Comparison of Cogging Torque Sensitivity of IPM and SPM Motors to Stator Tolerances

Cogging torques of the IPM and SPM motors given a positive stator tolerance in tooth 1 are shown in Fig. 5.54, the resulting cogging torque AHCs are shown in Fig. 5.54, the cogging torque AHC harmonics are shown in Fig. 5.55, and the cogging torque AHC phases are shown in Fig. 5.576.




(a) 12-slot/8-pole IPM motor

(b) 12-slot/8-pole SPM motor

(c) 12-slot/10-pole IPM motor

(d) 12-slot/10-pole SPM motor

(e) 12-slot/14-pole IPM motor

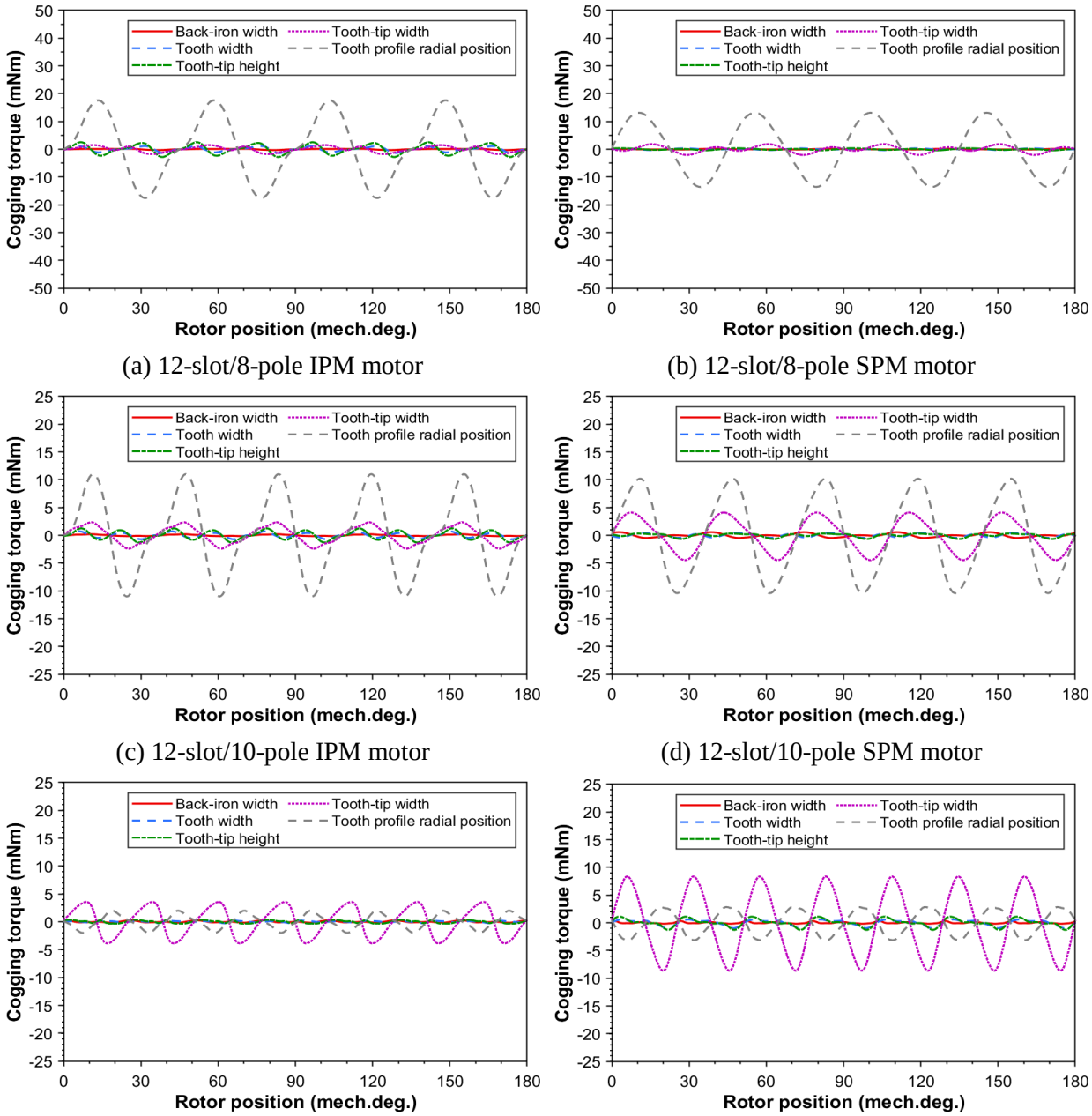
(f) 12-slot/14-pole SPM motor

Fig. 5.54. Cogging torque waveforms due to positive stator manufacturing tolerances in 12-slot/8-pole, 12-slot/10-pole, and 12-slot/14-pole motors.

The peak-to-peak cogging torque decreases significantly with increasing rotor pole number since the LCM of the stator slot and rotor pole number increases significantly. The peak-to-peak cogging torque of the

IPM motors is at the least twice as high as the SPM motors of the respective slot/pole number combination.

The 12-slot-8-pole IPM motor is most sensitive to stator tolerances and the 12-slot/14-pole IPM motor is least sensitive to stator tolerances. Sensitivity of cogging torque to tolerances in the tooth profile radial position decreases with increasing rotor pole number. Conversely, sensitivity of cogging torque to tolerances in tooth-tip width increase significantly with increasing rotor pole number. The phasors of the fundamental AHC due to tolerances in the stator tooth surface profile radial position in an individual tooth are shown in Fig. 5.57.




(a) 12-slot/8-pole IPM motor

(b) 12-slot/8-pole SPM motor

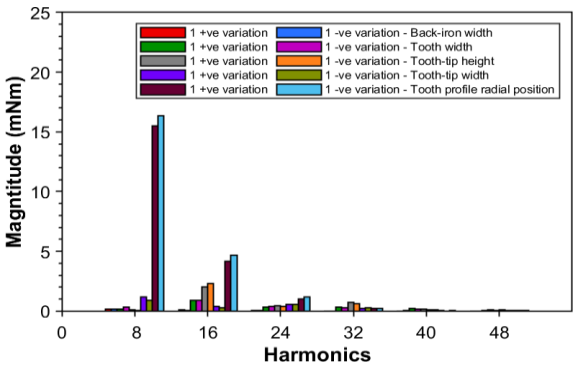
(c) 12-slot/10-pole IPM motor

(d) 12-slot/10-pole SPM motor

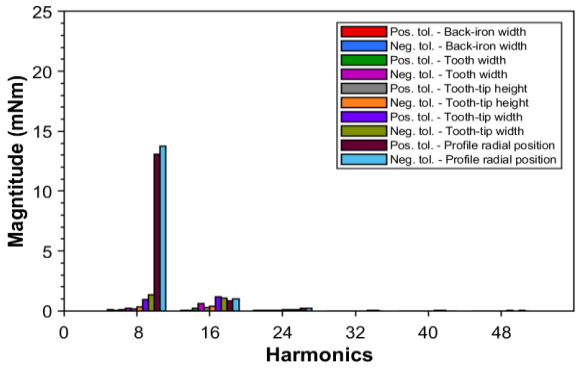
(e) 12-slot/14-pole IPM motor

(f) 12-slot/14-pole SPM motor

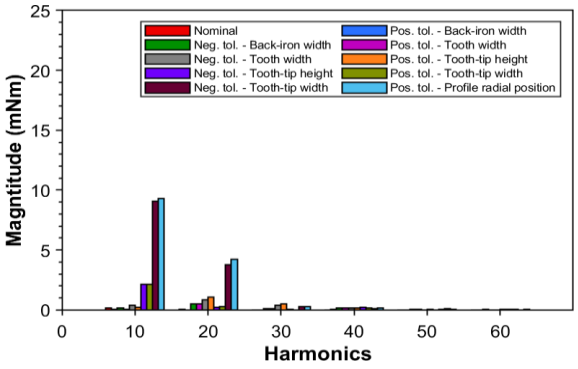
Fig. 5.55. Waveforms of cogging torque AHCs due to positive stator manufacturing tolerances in 12-slot/8-pole, 12-slot/10-pole, and 12-slot/14-pole motors.



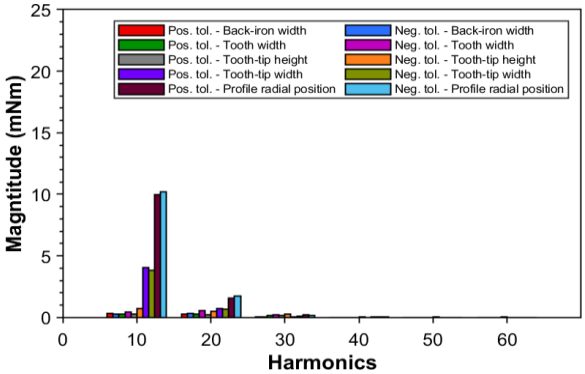

(a) 12-slot/8-pole IPM motor



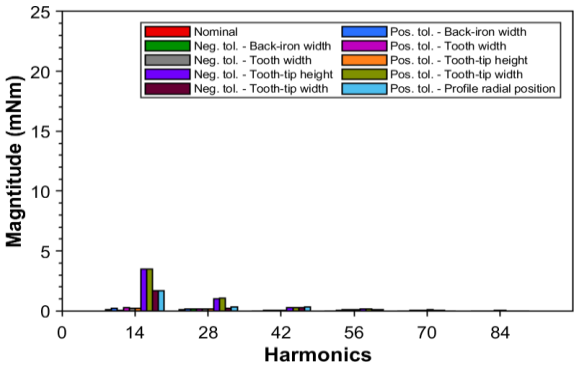

(b) 12-slot/8-pole SPM motor



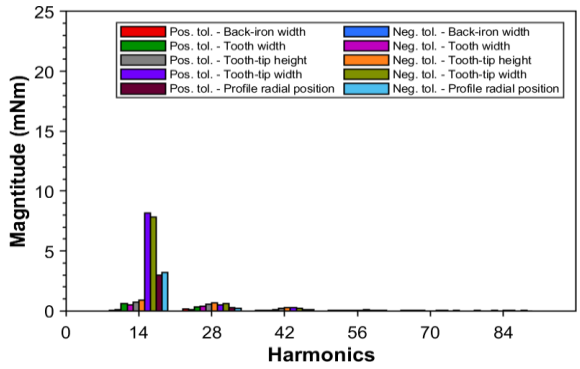

(c) 12-slot/10-pole IPM motor




(d) 12-slot/10-pole SPM motor

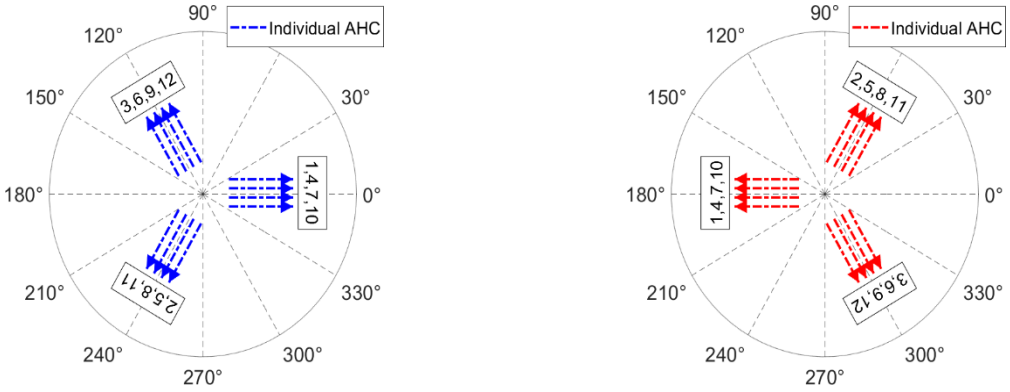



(e) 12-slot/14-pole IPM motor

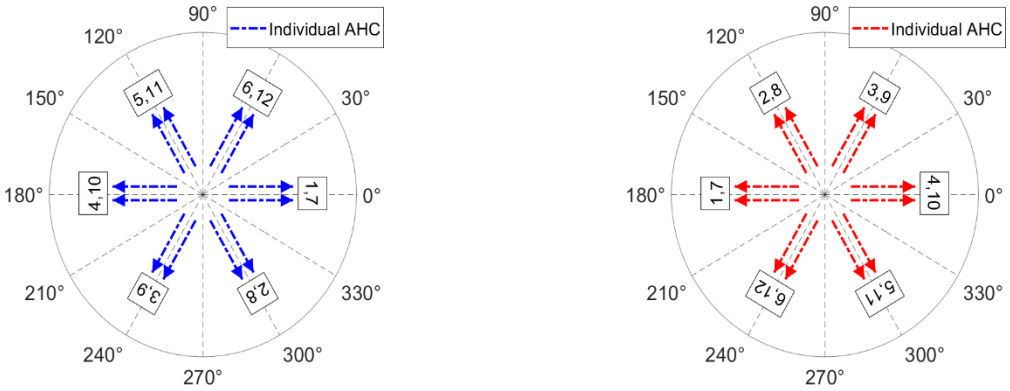



(f) 12-slot/14-pole SPM motor

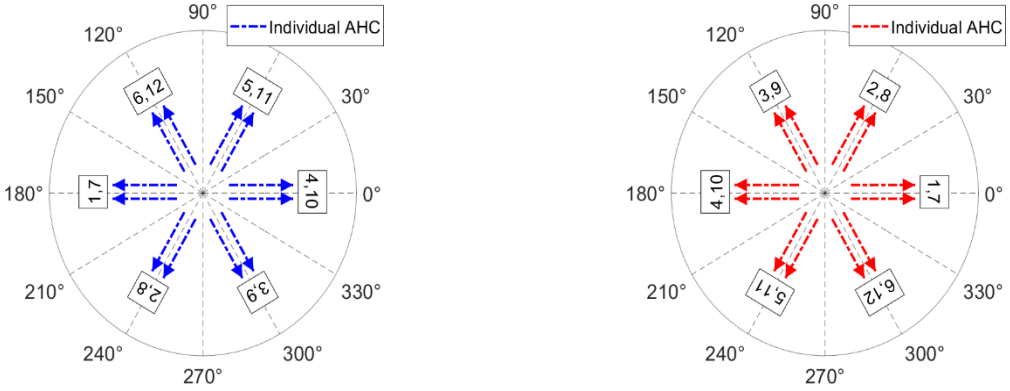
Fig. 5.56. Cogging torque AHC harmonics due to stator manufacturing tolerances in 12-slot/8-pole, 12-slot/10-pole, and 12-slot/14-pole motors.




(a) 8th order AHC of the 12-slot/8-pole motors




(b) 10th order AHC of the 12-slot/10-pole motors




(c) 14th order AHC of the 12-slot/14-pole motors

(I) Positive tolerance (II) Negative tolerance

Fig. 5.57. Phasors of fundamental AHC due to stator tolerances in tooth profile radial position of IPM and SPM motors under analysis.

## 5.9 Comparison of Cogging Torque Sensitivity of IPM and SPM Motors to Rotor Tolerances

Cogging torques of the IPM and SPM motors given a positive rotor tolerance in pole 1 are shown in Fig. 5.58, the resulting cogging torque AHCs are shown in Fig. 5.59, the cogging torque AHC harmonics are shown in Fig. 5.60.

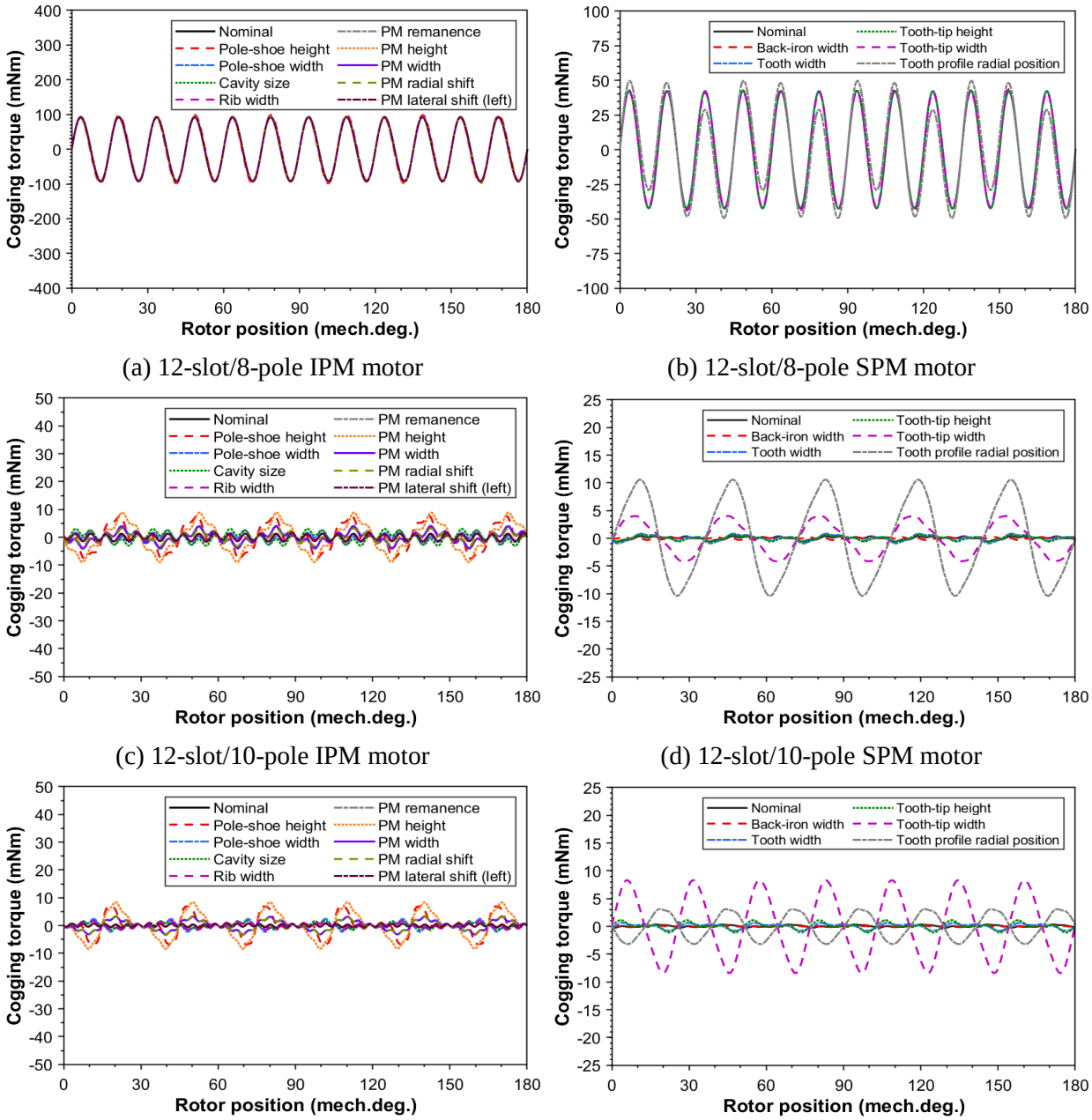
The peak-to-peak cogging torque decreases significantly with increasing rotor pole number since the LCM of the stator slot and rotor pole number increases significantly. The nominal peak-to-peak cogging torque of the IPM motors is at the least twice as high as the SPM motors of the respective slot/pole number combination.

The 12-slot-8-pole IPM motor is most sensitive to stator tolerances and the 12-slot/14-pole IPM motor is least sensitive to stator tolerances. Sensitivity of cogging torque to tolerances in the tooth profile radial position decreases with increasing rotor pole number. Conversely, sensitivity of cogging torque to tolerances in tooth-tip width increase significantly with increasing rotor pole number.

The phase of the $12^{th}$ AHCs due to a single rotor tolerance is determined by the direction of the tolerances and the affected rotor pole. The $12^{th}$ order AHCs due to a negative tolerance are 180° out-of-phase with the AHCs due to positive tolerances, as shown in Fig. 5.61 and Fig. 5.62. Tolerances in rotor poles with the same magnetic direction and the same tolerance direction (i.e. N or S) result in AHCs with the same phase. Conversely, tolerances in opposite magnetic poles and the same tolerance direction result in AHCs 180° out-of-phase.

Tolerances resulting in an increase in air-gap flux density lead to fundamental AHCs with a phase of 180°, and vice-versa. For instance, positive tolerances in the pole-shoe width, cavity size, and rib width of pole 1 result in a slight reduction of air-gap flux density. Consequently, the phase difference of the fundamental AHC is 180° out-of-phase with the remaining positive tolerances under investigation.

The phasors of the individual $12^{th}$ order AHCs due to a single manufacturing tolerance in a rotor pole resulting in an increase or decrease in air-gap flux density are shown in Fig. 5.61 and Fig. 5.62, respectively.




(a) 12-slot/8-pole IPM motor

(b) 12-slot/8-pole SPM motor

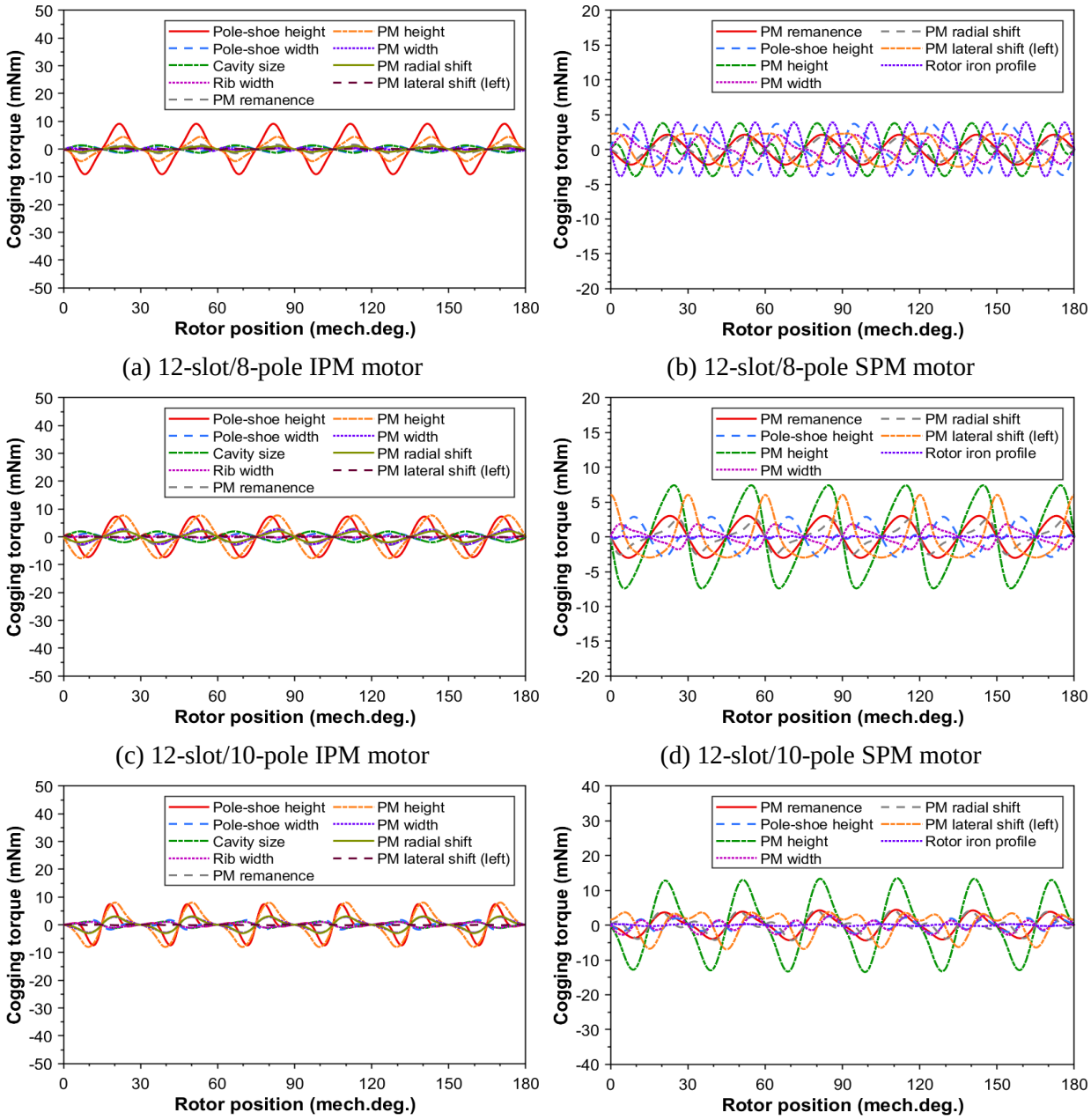
(c) 12-slot/10-pole IPM motor

(d) 12-slot/10-pole SPM motor

(e) 12-slot/14-pole IPM motor

(f) 12-slot/14-pole SPM motor

Fig. 5.58. Cogging torque waveforms due to positive rotor manufacturing tolerances in 12-slot/8-pole, 12-slot/10-pole, and 12-slot/14-pole motors.




(a) 12-slot/8-pole IPM motor

(b) 12-slot/8-pole SPM motor

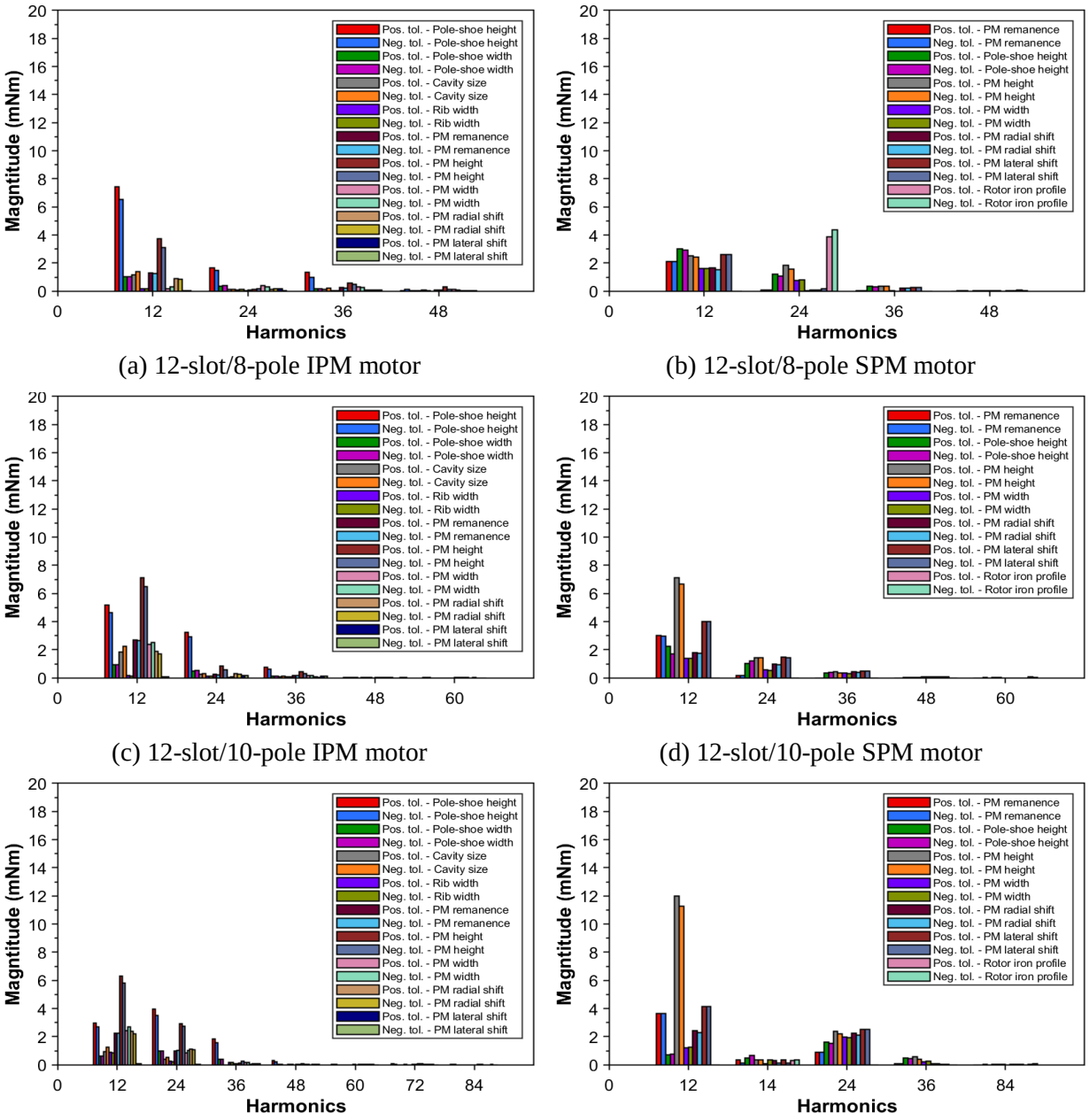
(c) 12-slot/10-pole IPM motor

(d) 12-slot/10-pole SPM motor

(e) 12-slot/14-pole IPM motor

(f) 12-slot/14-pole SPM motor

Fig. 5.59. Waveforms of cogging torque AHCs due to positive rotor manufacturing tolerances in 12-slot/8-pole, 12-slot/10-pole, and 12-slot/14-pole motors.




(a) 12-slot/8-pole IPM motor

(b) 12-slot/8-pole SPM motor

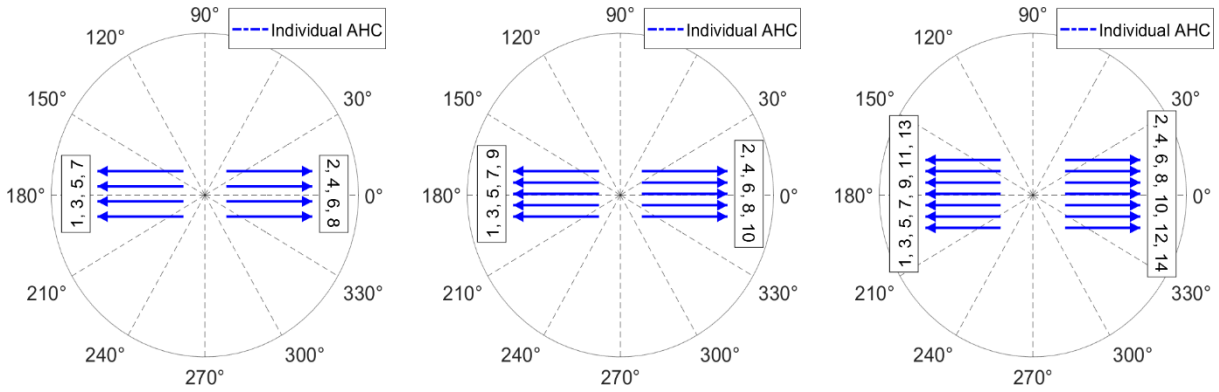
(c) 12-slot/10-pole IPM motor

(d) 12-slot/10-pole SPM motor

(e) 12-slot/14-pole IPM motor

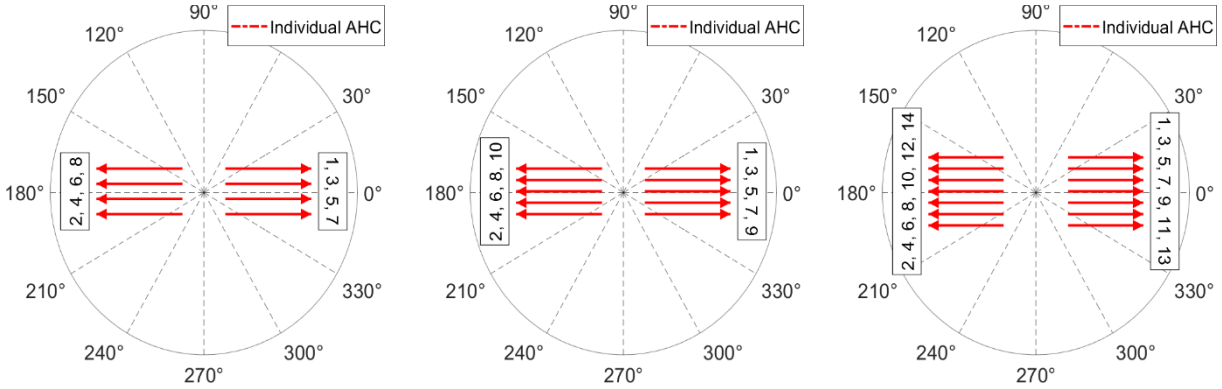
(f) 12-slot/14-pole SPM motor

Fig. 5.60. Cogging torque AHC harmonics due to rotor manufacturing tolerances in 12-slot/8-pole, 12-slot/10-pole, and 12-slot/14-pole motors.




(a) 12-slot/8-pole motor (b) 12-slot/10-pole motor (c) 12-slot/14-pole motor

Fig. 5.61. Phasors of 12th order AHC due to a single tolerance in a single rotor pole resulting in an increase in air-gap flux density.




(a) 12-slot/8-pole motor (b) 12-slot/10-pole motor (c) 12-slot/14-pole motor

Fig. 5.62. Phasors of 12th order AHC due to a single tolerance in a single rotor pole resulting in a decrease in air-gap flux density.

## 5.10 Comparison with Experimental Results

Experimental validation using the prototypes of the motors under investigation was not possible due to circumstances brought by the global COVID19 pandemic at the time of writing. A previous study by [GE16a] performed tests of the baseline 12-slot/8-pole IPM motor and a 12-slot/10-pole IPM motor. Design parameters of the two motors are listed in Table 5.5. Both motors share the same stator design and have a non-skewed rotor.

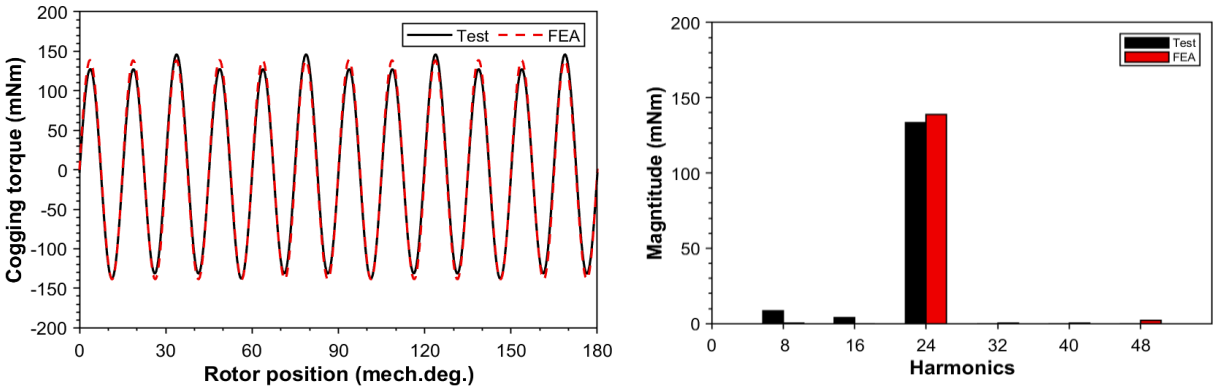
The 12-slot/8-pole and 12-slot/10-pole motors were manufactured with the nominal designs and with a deliberate manufacturing error of -0.2 mm in the tooth profile radial position of a single tooth. FEA models of the prototype motors are constructed to obtain the cogging torque of the nominal designs and the designs comprising a manufacturing error. The cogging torques obtained using FEA are compared with the experimental results obtained in [GE14] to validate the analysis method in this chapter.

Table 5.5. Design parameters of 12-slot/8-pole and 12-slot/10-pole IPM motors

| **Design parameter** | **Units** | **12-slot/8-pole IPM** | **12-slot/10-pole IPM** |
|---|---|---|---|
| Outer diameter | mm | 85 | |
| Active length | mm | 37.5 | |
| Air-gap length | mm | 0.6 | |
| Split ratio | N/A | 0.539 | |
| Back-iron width | mm | 4.0 | |
| Tooth width | mm | 7.0 | |
| Slot opening width | mm | 3.0 | |
| Pole-arc to pole-pitch ratio | N/A | 0.620 | 0.883 |
| Pole-shoe height | mm | 1.05 | |
| Rib width | mm | 1.5 | |
| PM height | mm | 2.61 | |
| PM width | mm | 12.10 | 9.68 |
| PM remanence | T | 1.32 | |
| PM coercivity | kA/m | -972.6 | |

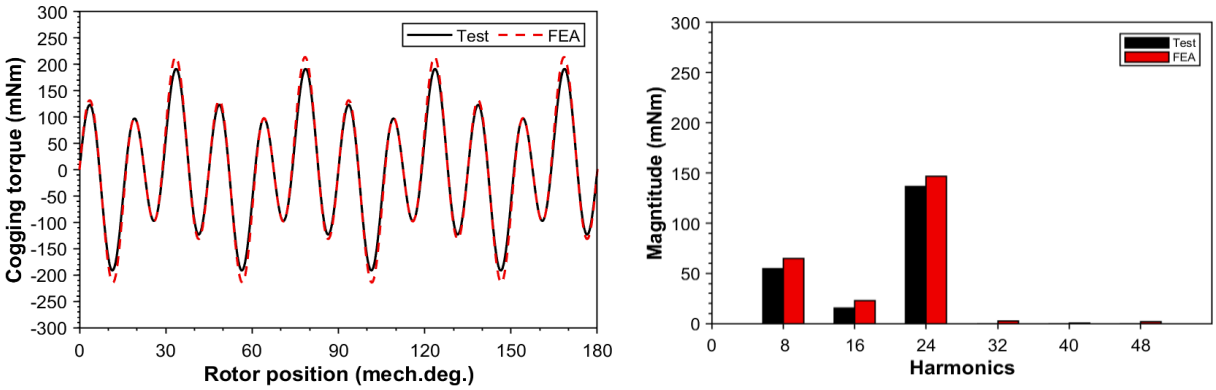
Cogging torque of the nominal 12-slot/8-pole motor design is shown in Fig. 5.63. The fundamental 24$^{th}$ order cogging torque obtained using FEA is 3.8% higher than that of the test motor. This can be attributed to slight changes in the properties of the materials and end-effects. The cogging torque of the test motor comprises the 8$^{th}$ and 16$^{th}$ order components indicating that the test motor has deviations from the nominal stator design.

Fig. 5.64 shows the cogging torque waveforms and harmonics of the 12-slot/8-pole motor with a manufacturing error of -0.2 mm in the radial position of a stator tooth profile. The cogging torque harmonics obtained using FEA are higher than those obtained experimentally. Cogging torque obtained using FEA is slightly higher than that obtained using FEA. The difference in magnitude of cogging torque harmonics can also be attributed to meshing. The magnitude of the manufacturing error under analysis is 33.3% of the minimum air-gap length. Such a significant manufacturing error in the air-gap results in an asymmetric mesh which, in turn, may affect cogging torque calculation.




(a) Waveforms (b) Harmonics

Fig. 5.63. Comparison of FE predicted and measured cogging torques of the nominal 12-slot/8-pole IPM motor.

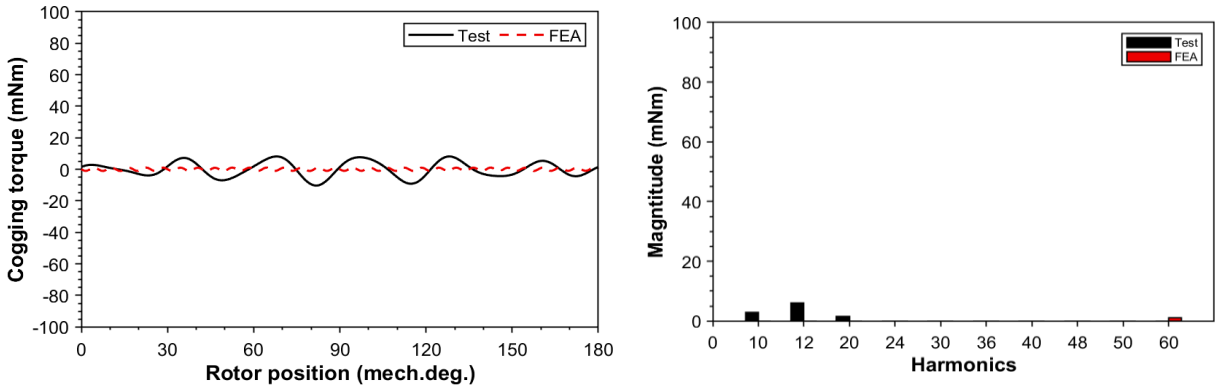



(a) Waveforms (b) Harmonics

Fig. 5.64. Comparison of FE predicted and measured cogging torques of the12-slot/8-pole IPM motor with a manufacturing error in the tooth profile radial position of -0.2 mm in a single tooth.

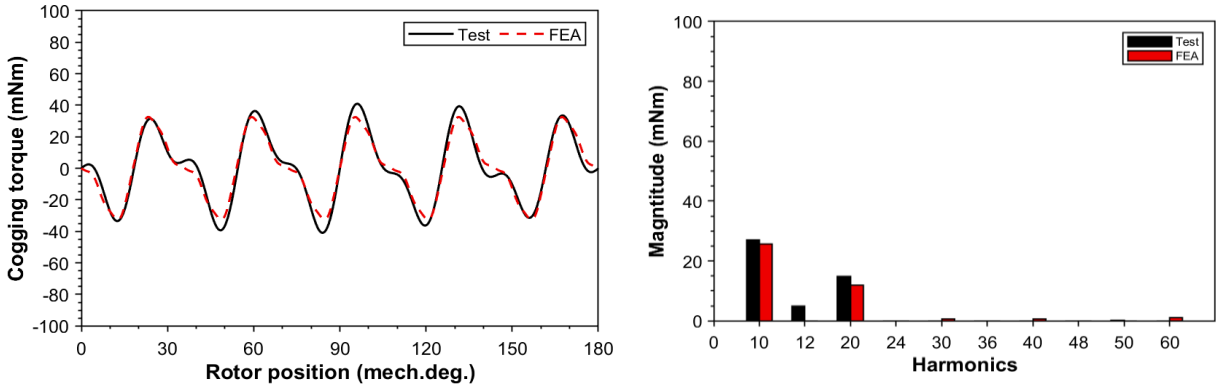
The cogging torque of the nominal 12-slot/10-pole IPM motor is shown in Fig. 5.65. The 12-slot/10-pole IPM motor has an inherently low cogging torque with a fundamental order of 60, as obtained using FEA. The test motor comprises variations from the nominal stator design resulting in the $10^{th}$ and $20^{th}$ order cogging torque components as well as variations from the nominal rotor design resulting in the $12^{th}$ order cogging torque component. The cogging torque of the test motor does not include the $60^{th}$ order component inherent in the 12-slot/10-pole motor. This can be attributed to the fact that the influence of tolerances on cogging torque of the test motor is dominant and the accuracy of test setup was not sufficient to measure the very small magnitude of the $60^{th}$ order cogging torque component.

The cogging torque of the motor with a manufacturing error of -0.2 mm in the tooth profile radial position of a single tooth is shown in Fig. 5.66. The $10^{th}$ and $20^{th}$ cogging torque components due to the manufacturing error obtained experimentally are higher than those obtained using FEA. Furthermore, the cogging torque obtained using FEA comprises a $12^{th}$ order harmonic attributed to variations from the nominal rotor design that is not present in the cogging torque obtained using FEA,




(a) Waveforms (b) Harmonics

Fig. 5.65. Comparison of FE predicted and measured cogging torques of the nominal 12-slot/10-pole IPM motor.




(a) Waveforms (b) Harmonics

Fig. 5.66. Comparison of FE predicted and measured cogging torques of the 12-slot/10-pole IPM motor with a manufacturing error in the tooth profile radial position of -0.2 mm in a single tooth.

## 5.11 Conclusion

Mass-production processes introduce deviations from the nominal motor design attributed to manufacturing tolerances which, in turn, affect cogging torque. Thus, the cogging torque of a motor is composed of the NHCs inherent in the motor topology and AHCs attributed to the asymmetries introduced by manufacturing tolerances. Analysis of the influence of manufacturing tolerances on cogging torque is essential to quantify the sensitivity to manufacturing tolerances.

Multi-objective optimisation of 12-slot/8-pole. 12-slot/10-pole, and 12-slot/14 pole IPM and SPM motors is performed to determine the compromise between the average torque and the torque ripple at base speed, as discussed in Chapters 3 and 4. Motors close to the knee point of the Pareto-front of the multi-objective optimisation are selected to obtain IPM motors with similar average torque and a reasonably low torque ripple. The solution spaces of the 12-slot/14-pole IPM and SPM motors differ significantly since the considerable flux leakage of the IPM motor results in a significant difference in average torque. Thus, the 12-slot/14-pole IPM and SPM motors at the knee point of the Pareto-front do not produce the same average

torque but operate at a similar torque ripple.

The sensitivities of the six motors selected from the solution spaces of the multi-objective optimisation to manufacturing tolerances in the stator and the rotor are investigated.

The stator tolerances under analysis are tolerances in the back-iron width, tooth width, tooth-tip height and width, and tooth surface profile radial position. Manufacturing tolerances in the stator result in AHC with a fundamental component equal to the number of rotor poles. The asymmetry introduced by stator tolerances affects the air-gap flux density resulting in AHCs coinciding with the NHCs. The magnitudes of the AHCs depend on the magnitude and direction of the tolerance. The phases of the AHCs due to a particular tolerance depend on the location of the affected tooth and the direction of the tolerance. The resultant AHCs due to multiple tolerances are equal to the phasor addition of the individual AHC due to the individual tolerances.

The magnitudes of the AHCs coinciding with the NHCs are very low in 12-slot/10-pole and 12-slot/14-pole motors. The influence of tolerances in the back-iron width and tooth width on cogging torque of the motors is very low. The magnitude of the fundamental AHC due to tolerances in the tooth-tip width increases with increasing rotor pole number. Conversely, the magnitude of the fundamental AHC due to tolerances in the tooth profile radial position decreases with increasing rotor pole number. The magnitudes of the AHCs due to tolerances in tooth profile radial position are significantly higher than those due to the tolerances in tooth-tip width in 12-slot/8-pole and 12-slot/10-pole motors. The opposite effect is observed in the 12-slot/14-pole motor.

The IPM rotor tolerances under analysis are tolerances in the pole-shoe height, pole-shoe width, cavity size, rib width, PM remanence, PM height, PM width, and PM radial and lateral displacement. The SPM rotor tolerances under analysis are tolerances in the rotor iron profile, PM remanence, PM height, PM width, and PM radial and lateral displacement.

The air-gap flux density is highly influenced by the air-gap length and the PM height. Thus, the influences of tolerances in the pole-shoe height and PM height on cogging torque are significant. The magnitudes of the AHCs due to tolerances in the pole-shoe height decrease with increasing rotor pole number and this effect is attributed to the decrease in flux per pole with increasing rotor pole number.

The influence of tolerances in the lateral position of the PM in all IPM motors is negligible. The influence of tolerances in PM width on magnitudes of the AHCs of the 12-slot/8-pole motor is very low. The influence of tolerances in rotor rib width is very low in 12-slot/8-pole and 12-slot/10-pole IPM motors, but non-negligible in the 12-slot/14-pole IPM motor. This may be attributed to the fact that the influence of flux leakage through the rotor ribs increases significantly with increasing rotor pole number.

The 12-slot/8-pole IPM motor is less sensitive to tolerances in the rotor PM than the 12-slot/10-pole and 12-slot/14-pole motors. The influences of tolerances in the rotor PM of 12-slot/10-pole and 12-slot/14-pole

IPM motors on the magnitudes of the 12$^{th}$ order AHC are very similar. However, the magnitude of the 24$^{th}$ order AHC of the 12-slot/14-pole IPM motor is significantly higher than that of the 12-slot/10-pole IPM motor.

Tolerances in the rotor iron profile of SPM motors do not introduce any asymmetry in the motor geometry. The gap between the PMs and the rotor iron profile is directly affected by tolerances in the rotor iron profile, thereby affecting the air-gap flux density. Consequently, the magnitude of harmonics coinciding with the NHCs is affected. Rotor tolerances affecting the rotor symmetry result in a fundamental 12$^{th}$ order AHC and its harmonic multiples. The influence of tolerances in the PM height on cogging torque increases significantly with increasing rotor pole number. Conversely, the influence of tolerances in the pole-shoe height and PM width on cogging torque decreases with increasing pole-number.

The 24$^{th}$ order component of the 12-slot/8-pole SPM motor is very sensitive to tolerances in the rotor iron profile. The analysed PM tolerances result in similar magnitudes of the 12$^{th}$ order AHC of the 12-slot/8-pole motor. Tolerances in the PM remanence, PM radial position, and PM lateral position of the 12-slot/8-pole motor result in negligible magnitudes of the 24$^{th}$ order AHC.

The phase of the 12th AHCs due to a single rotor tolerance is determined by the direction of the tolerances and the affected rotor pole. The 12th order AHCs due to a negative tolerance are 180° out-of-phase with the AHCs due to positive tolerances. Tolerances in rotor poles with the same magnetic direction and the same tolerance direction (i.e. N or S) result in AHCs with the same phase. Conversely, tolerances in opposite magnetic poles and the same tolerance direction result in AHCs 180° out-of-phase.

Tolerances resulting in an increase in air-gap flux density lead to fundamental AHCs with a phase of 180°, and vice-versa. For instance, positive tolerances in the pole-shoe width, cavity size, and rib width of pole 1 result in a slight reduction of air-gap flux density. Consequently, the phase difference of the fundamental AHC is 180° out-of-phase with the remaining positive tolerances under investigation.

Radial rotor tolerances and tolerances in the PM width of an SPM motor result in an increase or decrease in the air-gap flux density. Tolerances in the lateral position of the PM results in a drastic change in the rotor pole and, consequently, on the air-gap flux density. Therefore, the phase of AHCs due to tolerances in the lateral PM position may vary from the phases of AHCs illustrated in this chapter.

# 6 INVESTIGATION OF WORST SCENARIOS OF COGGING TORQUE IN IPM AND SPM MOTORS DUE TO MANUFACTURING TOLERANCES

## 6.1 Introduction

Cogging torque sensitivity of the 12-slot/8-pole, 12-slot/10-pole, and 12-slot/14-pole IPM and SPM motors to individual stator and rotor tolerance is determined in chapters 4 and 5. Mass-production processes introduce multiple tolerances in various areas of the motor design. The worst-case scenario of the cogging torque due to a tolerance in a specific motor part is attributed to particular arrangements of multiple tolerances in specific directions.

The first part of this chapter outlines the method for determination of worst-case scenarios of the cogging torque due to tolerances in radial position of the stator tooth profile of the IPM and SPM motors under investigation. The aforementioned method has been used to determine the worst-case scenarios of a 12-slot/10-pole SPM motor in [BUH20]. The worst-case scenarios of the cogging torque due to a particular type of manufacturing tolerance are determined in a systematic manner by exploiting motor symmetry and considering the possible combinations of the location and direction of the considered type of manufacturing tolerance.

The complexity of determination of the worst-case scenarios of manufacturing tolerances increases significantly with the number of considered manufacturing tolerances. Consequently, determination of the worst-case scenarios due to multiple manufacturing tolerances in a systematic manner is not feasible.

The worst-case scenarios of the cogging torque can be determined using a global search algorithm combined with a FEA model of the motor under investigation. While this method produces accurate peak-to-peak cogging torque, the computational time may be prohibitive due to the very fine mesh attributed to the low magnitude of the manufacturing tolerances and the number of iterations of the search algorithm attributed to the number of considered rotor variations.

In this chapter, a global search algorithm is combined with a simplified model based on a series of FEA simulations to obtain the worst-case scenarios with considerably lower computational effort. A sensitivity analysis of the cogging torque of the motor under investigation is performed using a FEA model for the upper and lower bounds for each of the considered manufacturing tolerances. The AHCs due to manufacturing variations are obtained by subtracting the nominal cogging torque from the cogging torque waveform due to the manufacturing variations. Therefore, the cogging torque due to a set of manufacturing variations can be obtained by summing the nominal cogging torque and the AHCs due to each manufacturing variation. The simplified cogging torque model does not account for the cross interaction

between the manufacturing variations, although the effect of the cross interaction of the variations on the cogging torque is small.

This chapter identifies the worst-case scenarios of the cogging torque of the IPM and SPM motors under investigation due to stator tolerances, rotor tolerances, and a combination of the stator and rotor tolerances considered in chapters 4 and 5.

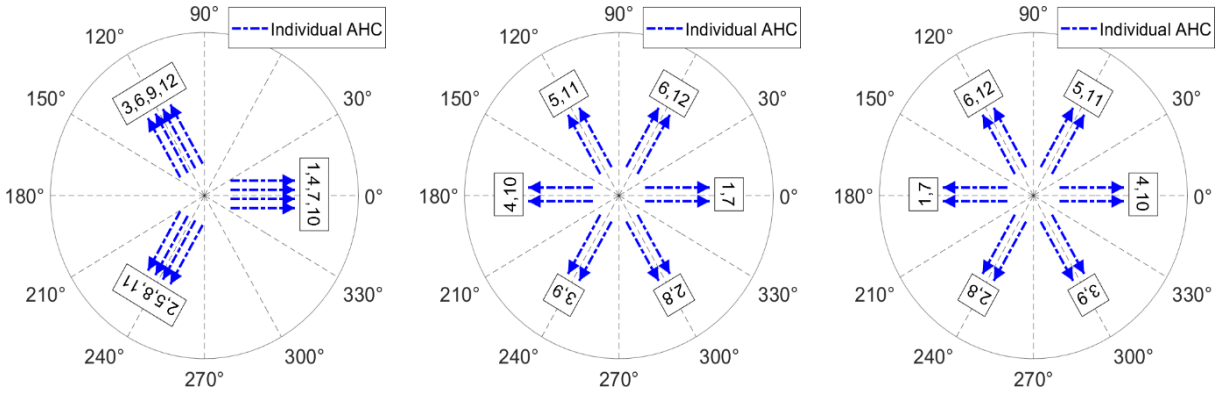
## 6.2 Determination of Worst-Case Scenarios of the Cogging Torque Due to Tolerances in the Radial Position of the Stator Teeth Profile of IPM and SPM motors

Sensitivity analysis of the cogging torque to tolerances in radial position of the stator teeth profile shows that the magnitude of the individual AHCs due to a specific tolerance is dependent on the direction of the tolerance. Furthermore, the phases of the individual AHCs due to a specific tolerance are dependent on the direction and location of the tolerance. The phases of the individual AHCs of 12-slot/8-pole, 12-slot/10-pole, and 12-slot/14-pole IPM motors are shown in Fig. 6.1 and Fig. 6.2.

The 12-slot/8-pole motor has a symmetry of four and consequently the phasors of the individual AHCs due to tolerances in teeth separated by an angle of 90°, 180°, and 270° are aligned, given that the tolerances are in the same direction. For instance, the phasors due to individual AHCs due to individual tolerances in teeth 1, 4, 7, and 10 are identical, as shown Fig. 6.1 and Fig. 6.2.

The 12-slot/10-pole and 12-slot/14-pole motors have a symmetry of two. Therefore, the phasors due to tolerances in teeth separated by an angle of 180° are aligned given that the directions of the tolerances are identical. For instance, the phasors of the individual AHCs due to individual tolerances in teeth 1 and 7, in a particular direction, are identical as shown in Fig. 6.1 and Fig. 6.2. Conversely, 12-slot/10-pole and 12-slot/14-pole motors have an anti-symmetry and consequently individual tolerance in teeth separated by an angle of 90° and 270° results in phasors of individual AHCs with opposite phases. For example, the phasor of the individual AHCs due to tolerances in tooth 1 is 180° out-of-phase with the phasor of the individual AHCs due to tolerances in teeth 4 and 10 as shown in Fig. 6.1 and Fig. 6.2.

The symmetry and anti-symmetry of the two motors are exploited to identify the worst-case scenarios of the cogging torque due to tolerances in the radial position of the stator teeth profile of 12-slot/8-pole, 12-slot/10-pole, and 12-slot/14-pole IPM and SPM motors.

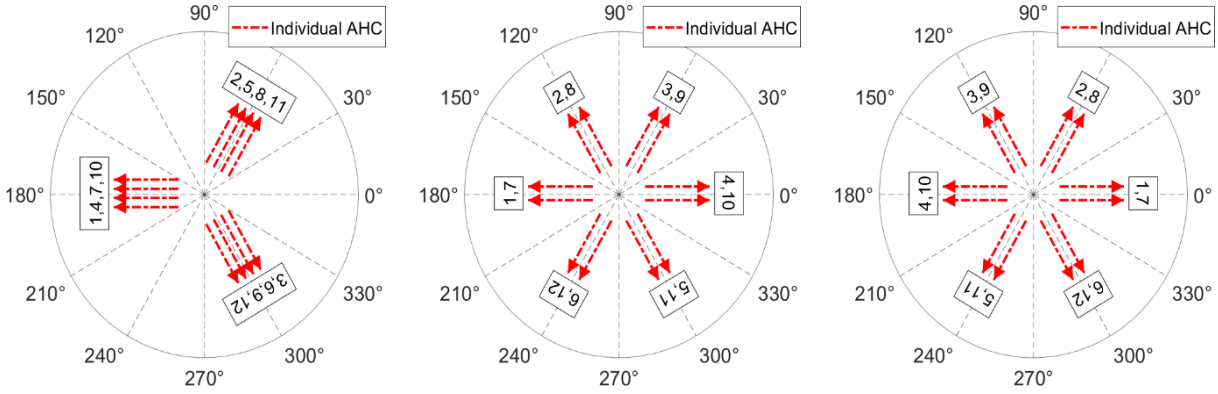



(a) 8th order AHC of 12-slot/8-pole IPM motor

(b) 10th order AHC of 12-slot/10-pole IPM motor

(c) 14th order AHC of 12-slot/14-pole IPM motor

Fig. 6.1. Phasors of the individual AHCs due to positive tolerances in IPM motors.




(a) 8th order AHC of 12-slot/8-pole IPM motor

(b) 10th order AHC of 12-slot/10-pole IPM motor

(c) 14th order AHC of 12-slot/14-pole IPM motor

Fig. 6.2. Phasors of the individual AHCs due to negative tolerances in IPM motors.

The worst-case scenarios of the cogging torque occur when the phasors of the individual AHCs due to individual tolerances are aligned resulting in the maximum magnitude of the resultant AHCs. Furthermore, the magnitudes of the individual AHCs are attributed to the magnitudes of the tolerances. It is assumed that the maximum displacement of the radial position of the stator tooth profile is ±0.05 mm.

The worst-case scenarios of the cogging torque can be determined in a systematic manner by segmenting the problem into three parts:

- Worst-case scenarios of tolerances in the inward direction only,
- Worst-case scenarios of tolerances in the outward direction only
- Worst-case scenarios of tolerances in both directions

### 6.2.1 Worst-Case Scenarios of Cogging Torque of 12-slot/8-pole IPM Motor

A. Worst-case scenarios of tolerances in the inward direction

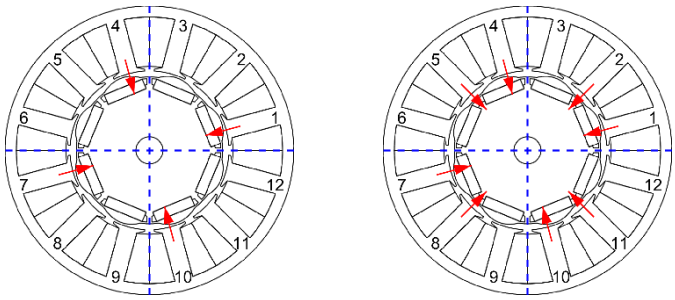
The worst-case scenarios of the cogging torque due to tolerances in the inward direction are determined by exploiting the periodic symmetry of the 12-slot/8-pole motor, indicated by blue dotted lines in Fig. 6.3. Thus, the two possible cases of tolerances in the inward direction are:

- Case 1: one tolerance per quadrant
- Case 2: two adjacent tolerances per quadrant

The case of two non-adjacent tolerances per quadrant is identical to Case 2 and is therefore not listed. Furthermore, the case of three adjacent tolerances per quadrant would be an overall decrease in the air-gap and no motor asymmetry exists, and therefore this is not the worst-case scenario of the cogging torque.

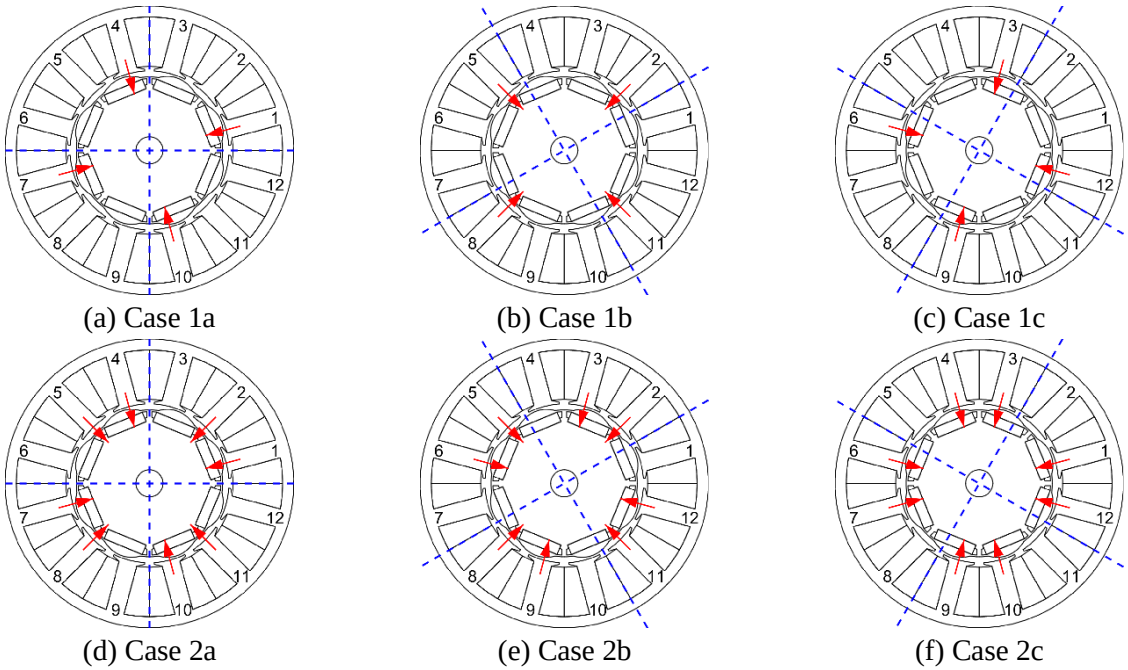
Each case is subdivided into 3 further cases (a to c) in which the tolerances are shifted by 0 to 2 slot pitches, respectively, as shown in Fig. 6.4. The two cases are indicated on the respective cross-sections in Fig. 6.3, and the resulting cogging torque waveforms and harmonics are shown in Fig. 6.5.

The magnitudes of the 24$^{th}$ and 48$^{th}$ order cogging torque harmonic components increase with increasing number of tolerances in the inward direction due to slight decrease in air-gap length. The resultant magnitudes of the 8$^{th}$ order AHC of Cases 1 and 2 are identical since the phase difference of the individual AHCs due to two adjacent tolerances is 120°. The phases of the resultant 8$^{th}$ order AHC of the two Cases are differed by 60°, and the resulting peak-to-peak cogging torque due to Case1 is higher than that due to Case 2. Thus, the worst-case scenario of cogging torque due to tolerances in the inward directions is Case 1(a to c) and the peak-to-peak cogging torque is 325.5 mNm.




(a) Case 1 (b) Case 2

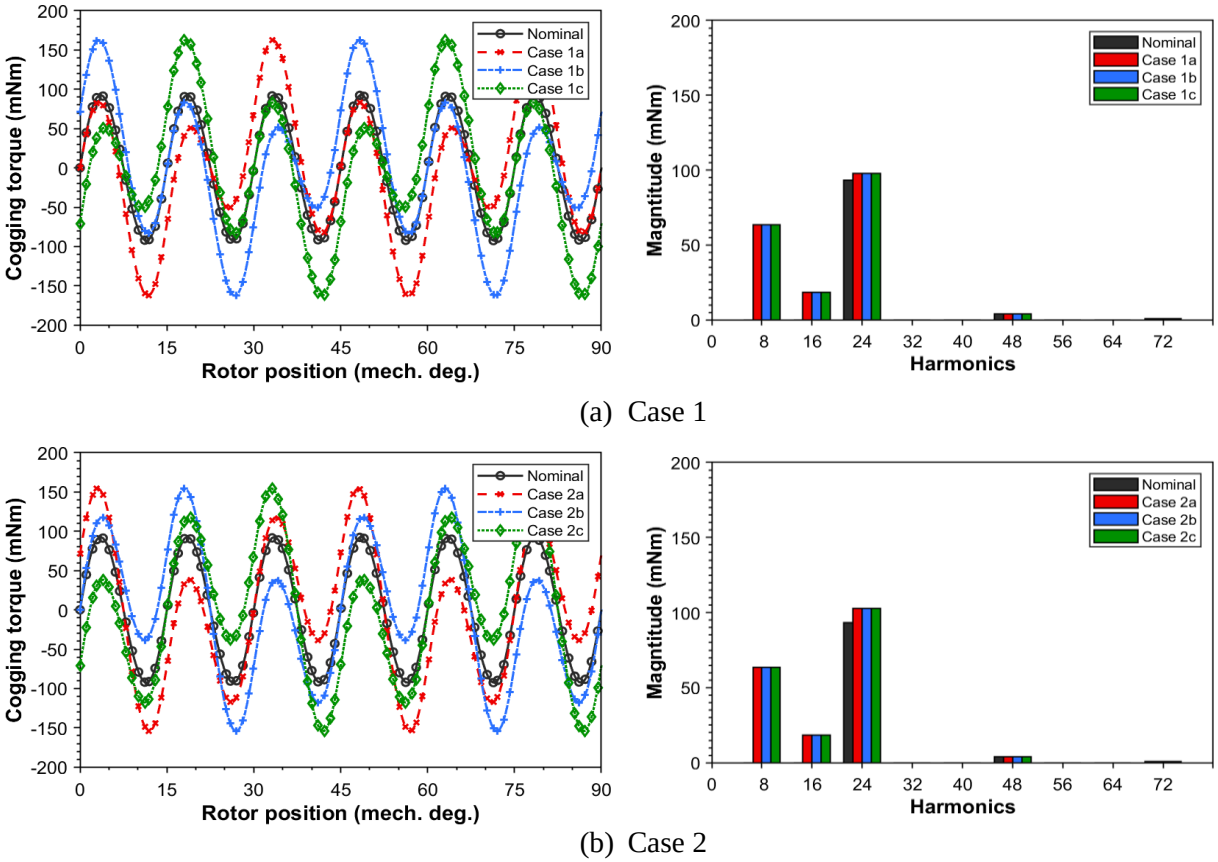
Fig. 6.3. The possible cases of tolerances in the inward direction in the 12-slot/8-pole IPM motor.



(a) Case 1a (b) Case 1b (c) Case 1c

(d) Case 2a (e) Case 2b (f) Case 2c

Fig. 6.4. Sub-cases of Case 1 and Case 2 of tolerances in the inward direction in the 12-slot/8-pole IPM motor.




(a) Case 1

(b) Case 2

(I) Waveforms (II) Harmonics

Fig. 6.5. Waveforms and harmonics of cogging torque due to the cases of tolerances in the inward direction in the 12-slot/8-pole IPM motor under investigation.

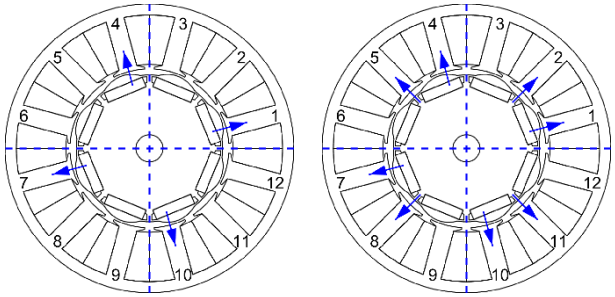
B. Worst-case scenarios of tolerances in the outward direction

The cases of tolerances identified in the previous subsection are analysed for tolerances in the outward direction, as shown in Fig. 6.6. The resulting cogging torque waveforms and harmonics are shown in

(I) Waveforms (II) Harmonics

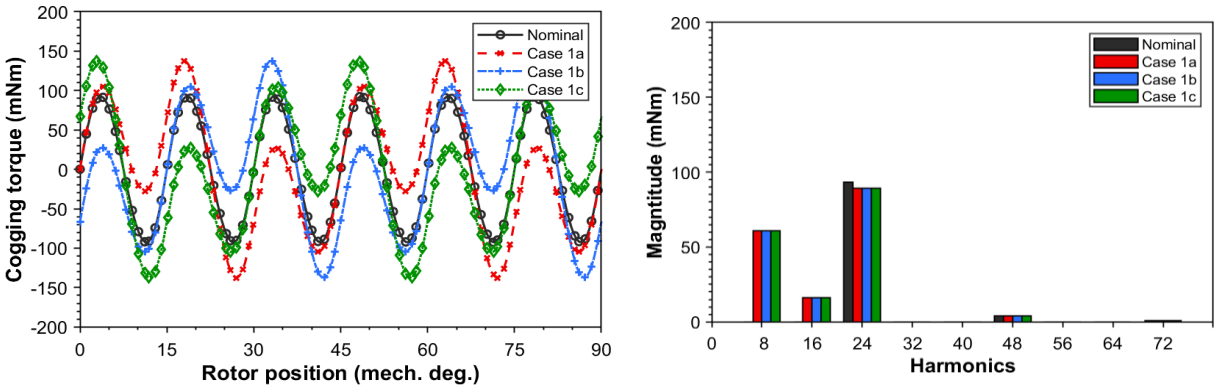
Fig. 6.7. The worst-case scenario is Case 2(a to c) and the peak-to-peak cogging torque is 294.2 mNm.

The worst-case scenario of tolerances in the outward direction results in a lower peak-to-peak cogging torque than that due to tolerances in the inward direction. This is attributed to the fact that tolerances in the outward direction result in a slight increase in air-gap length at the location of the tolerance.

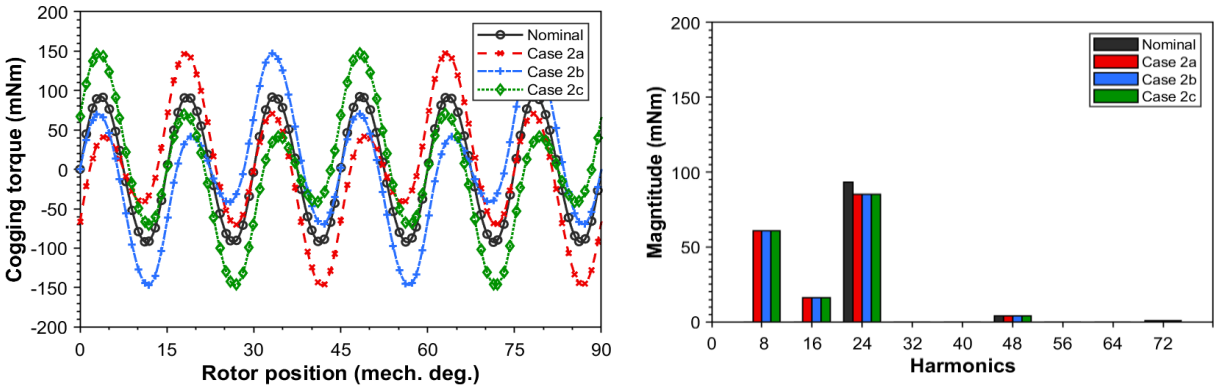



(a) Case 1 (b) Case 2

Fig. 6.6. The possible cases of tolerances in the outward direction in the 12-slot/8-pole IPM motor.



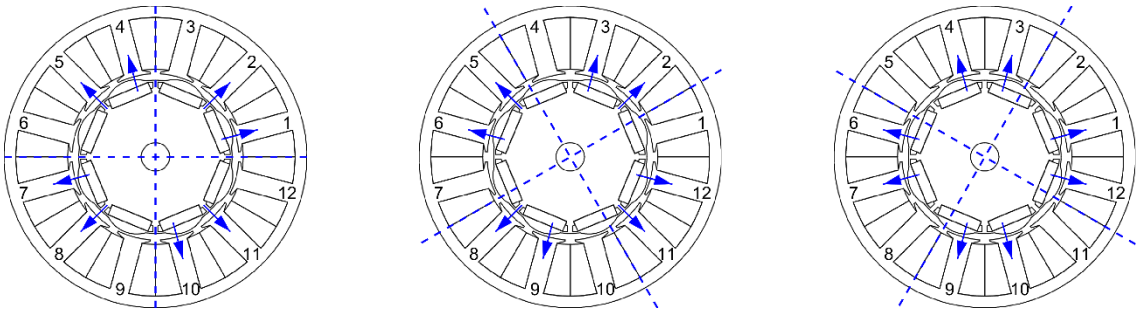

(a) Case 1




(b) Case 2

(III) Waveforms (IV) Harmonics

Fig. 6.7. Waveforms and harmonics of cogging torque due to the cases of tolerances in the outward direction in the 12-slot/8-pole IPM motor under investigation.




(a) Case 2a (b) Case 2b (c) Case 2c

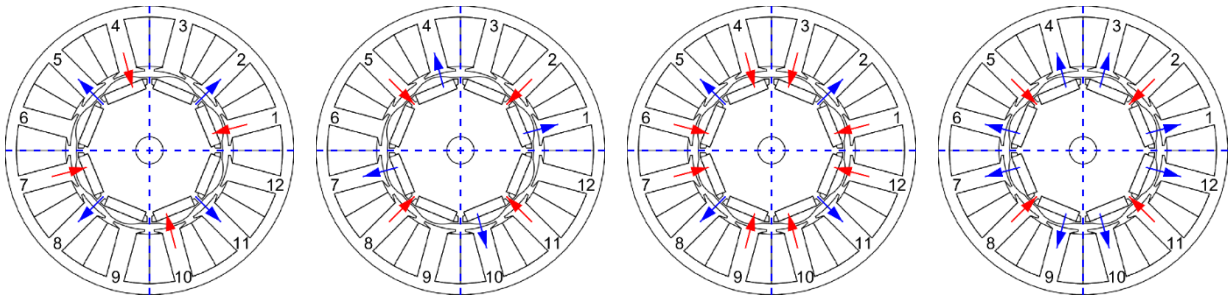
Fig. 6.8. Worst-case scenarios of tolerances in the outward direction in the 12-slot/8-pole IPM motor under investigation.

## C. Worst-case scenarios of bidirectional tolerances

The worst-case scenarios of bidirectional tolerances comprise at least two tolerances in each symmetrical quadrant. Thus, the four possible cases of bidirectional tolerances in a symmetric quadrant are:

- Case 1: two adjacent tolerances in opposite directions (i.e. one inward and one outward variation)
- Case 2: Case 1 with inverted tolerance direction
- Case 3 two non-adjacent tolerances in the same direction separated by tolerance in the opposite direction
- Case 4: Case 3 with inverted tolerance direction

The four cases, shown in Fig. 6.9, are subdivided into 3 further cases (a to c) in which the tolerances are shifted by 0 to 2 slot pitches, respectively. The cogging torque waveforms and harmonics due to the four cases are shown in Fig. 6.10.

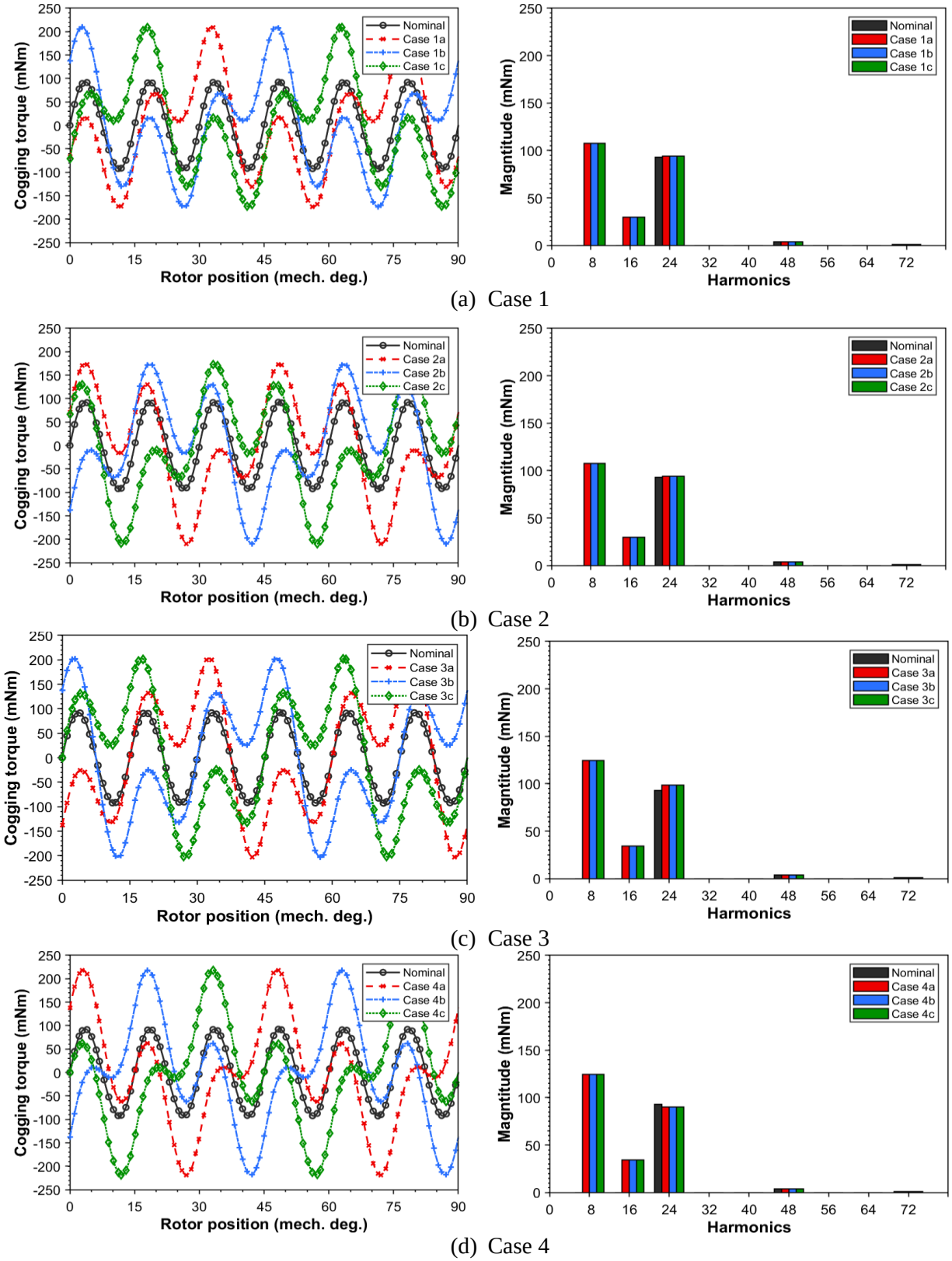



(a) Case 1 (b) Case 2 (c) Case 3 (d) Case 4

Fig. 6.9. Cases of bidirectional tolerances in the stator teeth profile radial position in the 12-slot/8-pole IPM motor.

The worst-case scenario of bidirectional variation is Case 4(a to c) and the peak-to-peak cogging torque is 436.5 mNm. Case 4 is the superposition of the worst-case scenario of tolerances in the inward direction and the worst-case scenario of tolerances in the outward direction. The magnitudes of the $8^{th}$ and $16^{th}$ order harmonic components of the cogging torque of Case 3 and Case 4 are identical. However, the phases of the resultant $8^{th}$ and $16^{th}$ order harmonic components of Case 4 result in a higher peak-to-peak cogging torque.

The tolerances of the worst-case scenarios Case 4a to Case 4c are shown in Fig. 6.11.




(a) Case 1

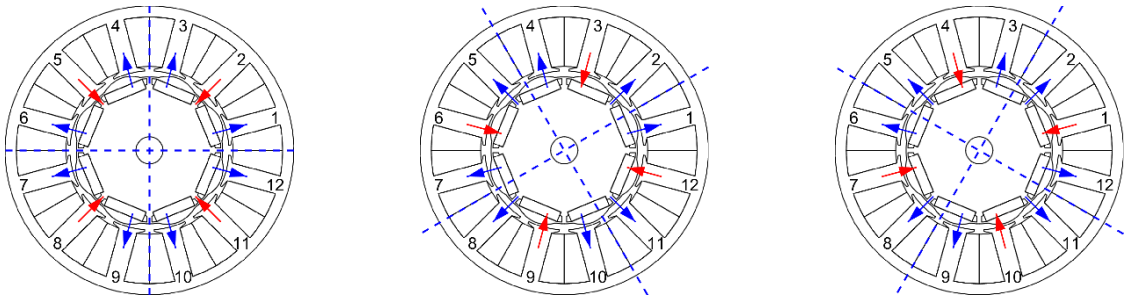
(b) Case 2

(c) Case 3

(d) Case 4

(I) Waveforms (II) Harmonics

Fig. 6.10. Waveforms and harmonics of cogging torque due to the cases of tolerances in both directions in the 12-slot/8-pole IPM motor under investigation.




(a) Case 4a (b) Case 4b (c) Case 4c

Fig. 6.11. Worst-case scenarios of bidirectional tolerances in the 12-slot/8-pole IPM motor under investigation.

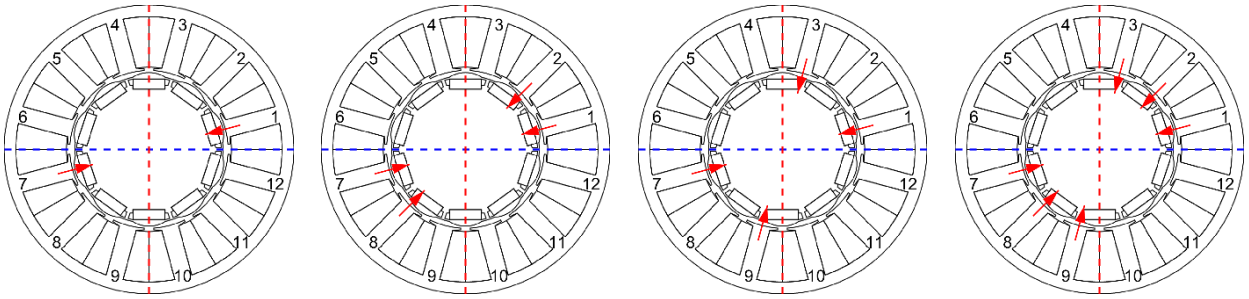
### 6.2.2 Worst-Case Scenarios of Cogging Torque of 12-slot/10-pole IPM Motor

A. Worst-case scenarios of tolerances in the inward direction

The symmetry and anti-symmetry of the 12-slot/10-pole motor are indicated by the blue and red dotted lines in Fig. 6.12, respectively. The worst-case scenarios for tolerances in a particular direction are obtained by exploiting the additive and cancelling effects on the resultant AHCs due to the inherent symmetry and anti-symmetry of the motor. Therefore, the four possible cases of tolerances in the inward direction are:

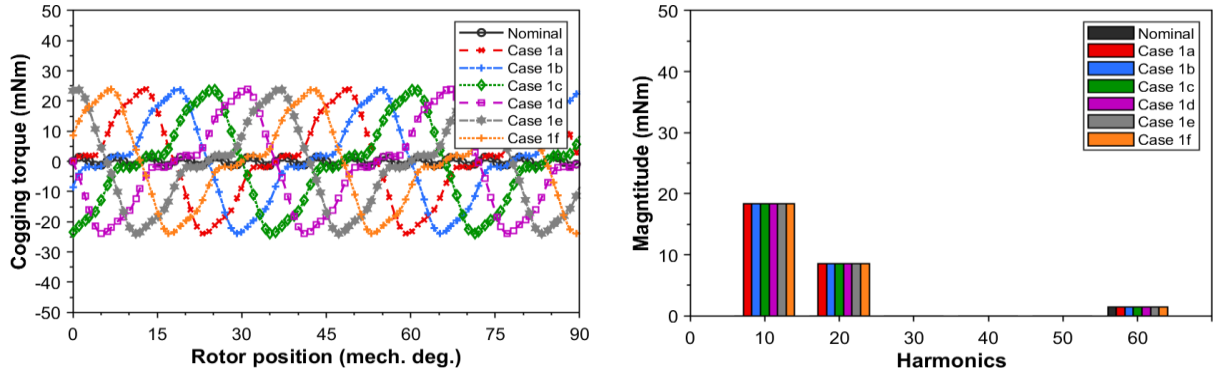
- Case 1: one tolerance
- Case 2: two adjacent tolerances
- Case 3: two tolerances separated by a slot pitch
- Case 4: three adjacent tolerances

The four cases, shown in Fig. 6.12, are subdivided into 6 further cases (a to f) in which the tolerances are shifted by 0 to 5 slot pitches, respectively. The cogging torque waveforms and harmonics of the worst-case scenarios in the inward direction are shown in Fig. 6.18. The worst-case scenario of the cogging torque due to tolerances in the inward directions is Case 4(a to f) and the peak-to-peak cogging torque is 75.1 mNm.

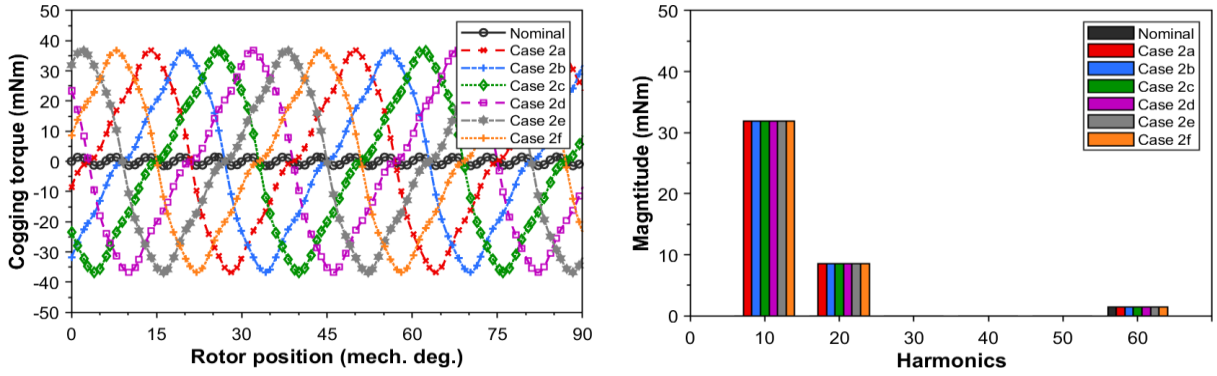



(a) Case 1 (b) Case 2 (c) Case 3 (d) Case 4

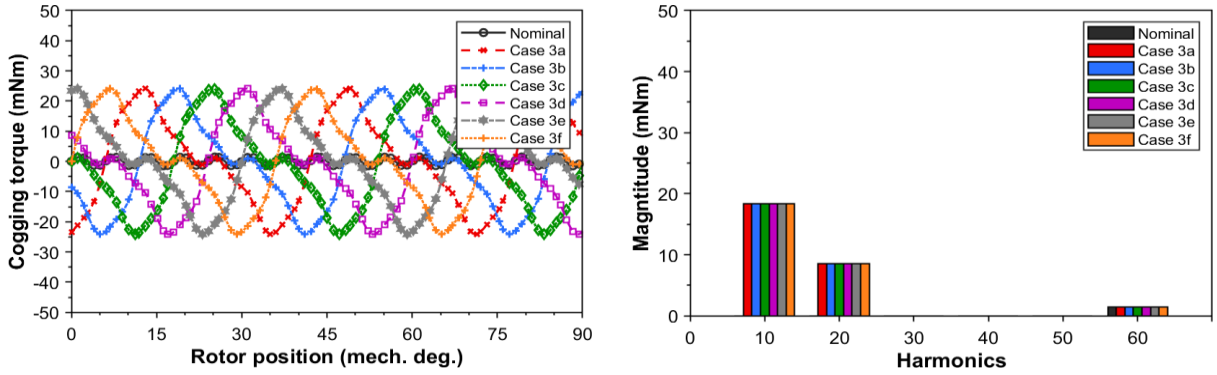
Fig. 6.12. The possible cases of tolerances in the inward direction in the 12-slot/10-pole IPM motor.



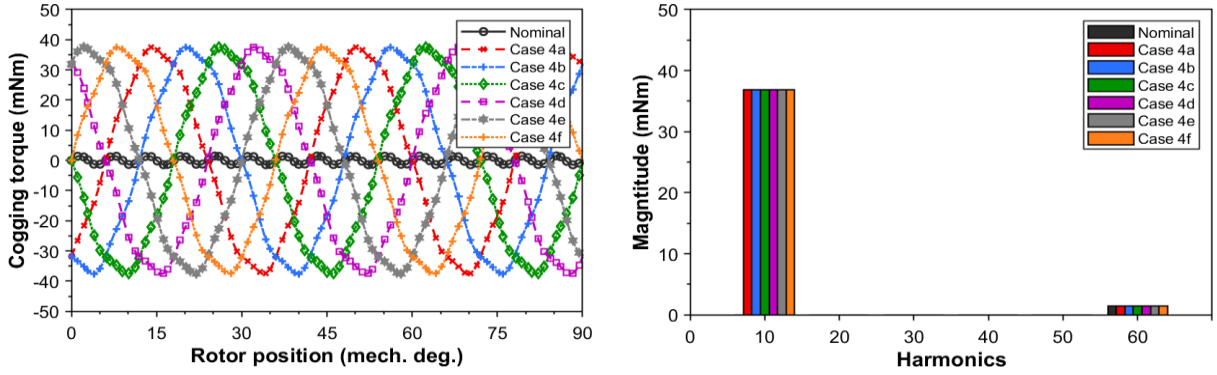

(a) Case 1




(b) Case 2




(c) Case 3




(d) Case 4

(I) Waveforms (II) Harmonics

Fig. 6.13. Waveforms and harmonics of cogging torque waveforms due to the possible cases of tolerances in the inward direction in the 12-slot/10-pole IPM motor.

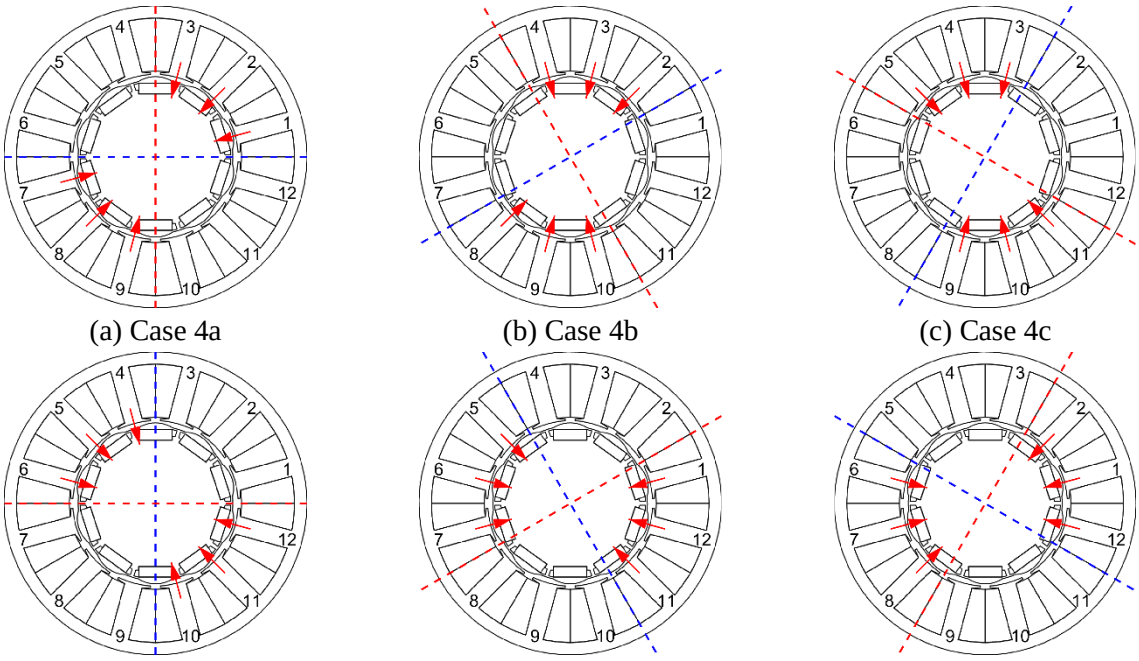



Fig. 6.14. Sub-cases of the worst-case scenario of tolerances in the inward direction in the 12-slot/10-pole IPM motor.

## B. Worst-case scenarios of tolerances in the outward direction

The directions of the tolerances in the identified possible cases of tolerances in the inward direction are reversed, as shown in Fig. 6.15. The cogging torque waveforms and harmonics of each case, including sub-cases in which the tolerances are shifted by 0 to 5 slot pitches, are shown in Fig. 6.16.

The worst-case scenario is Case 4(a to f) and the peak-to-peak cogging torque is 71.5 mNm. The worst-case scenario of tolerances in the outward direction results in a lower peak-to-peak cogging torque than that of tolerances in the inward directions due to the change in air-gap length caused by manufacturing tolerances.

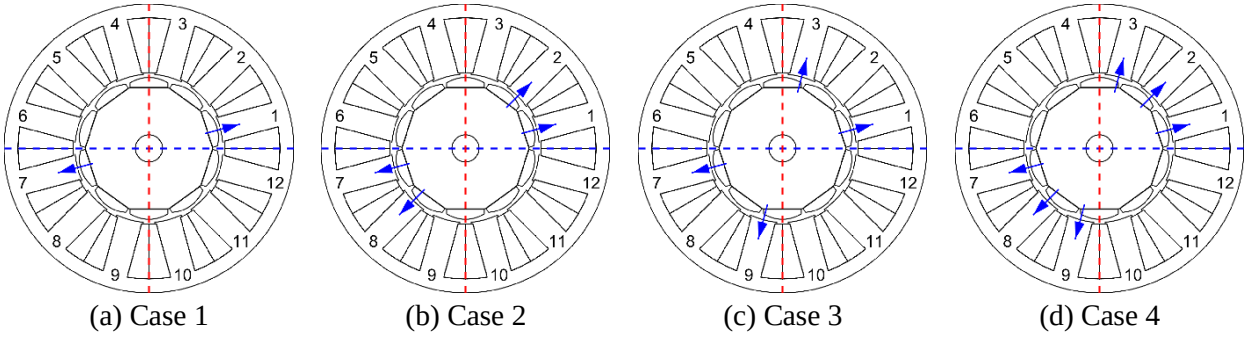
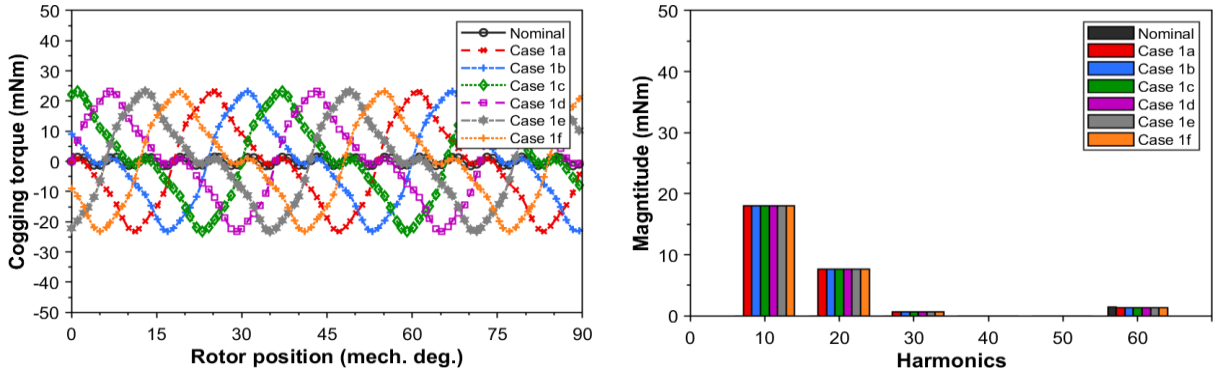
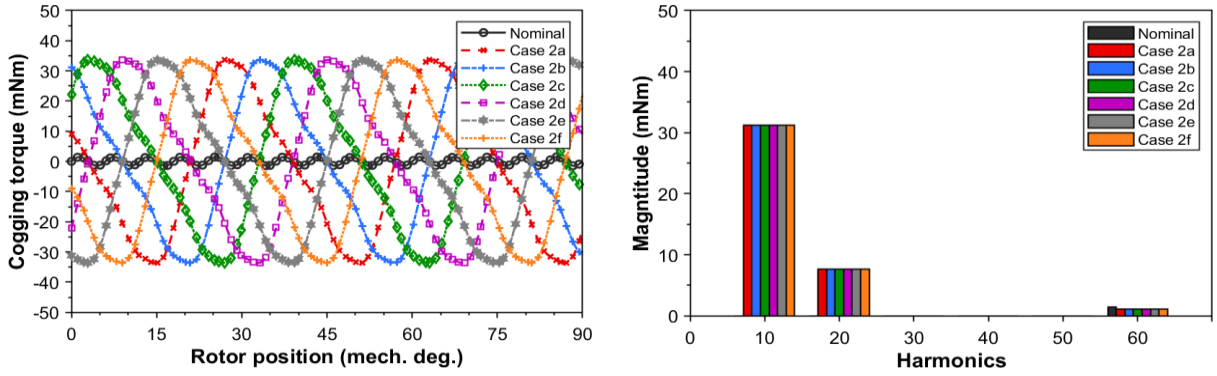


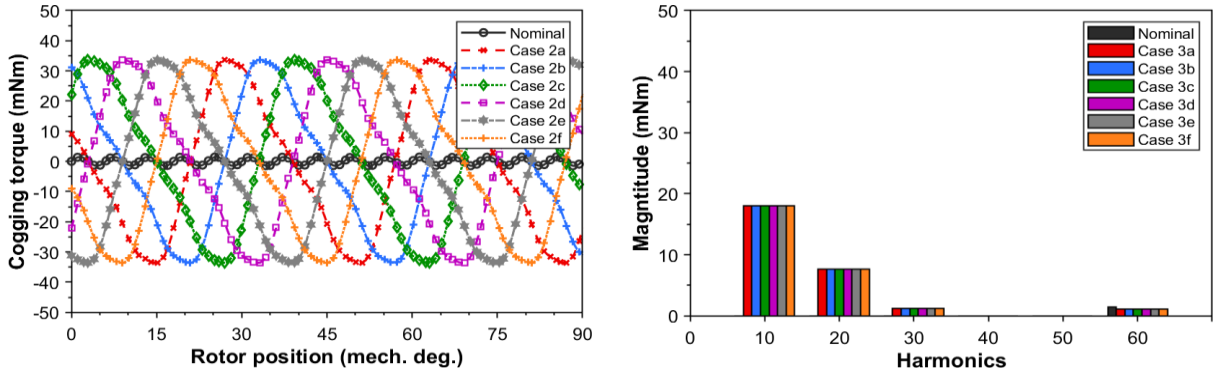

Fig. 6.15. The possible cases of tolerances in the outward direction.



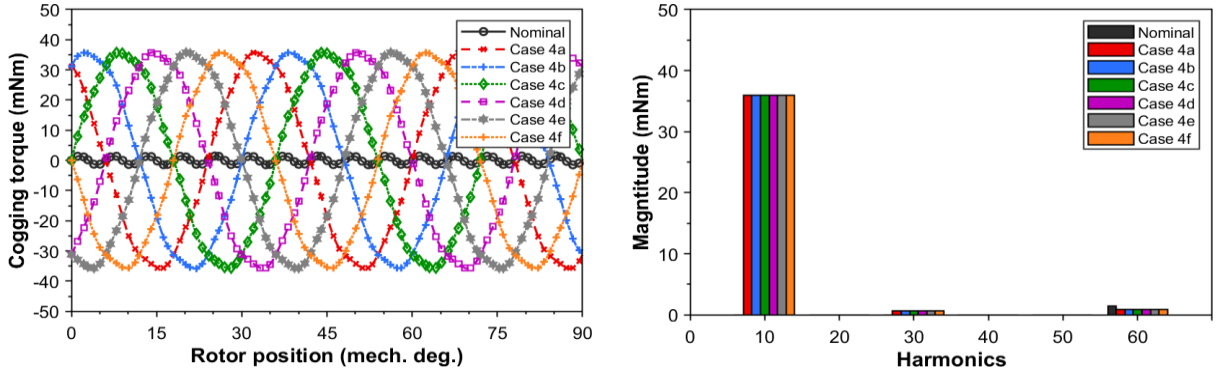

(a) Case 1




(b) Case 2



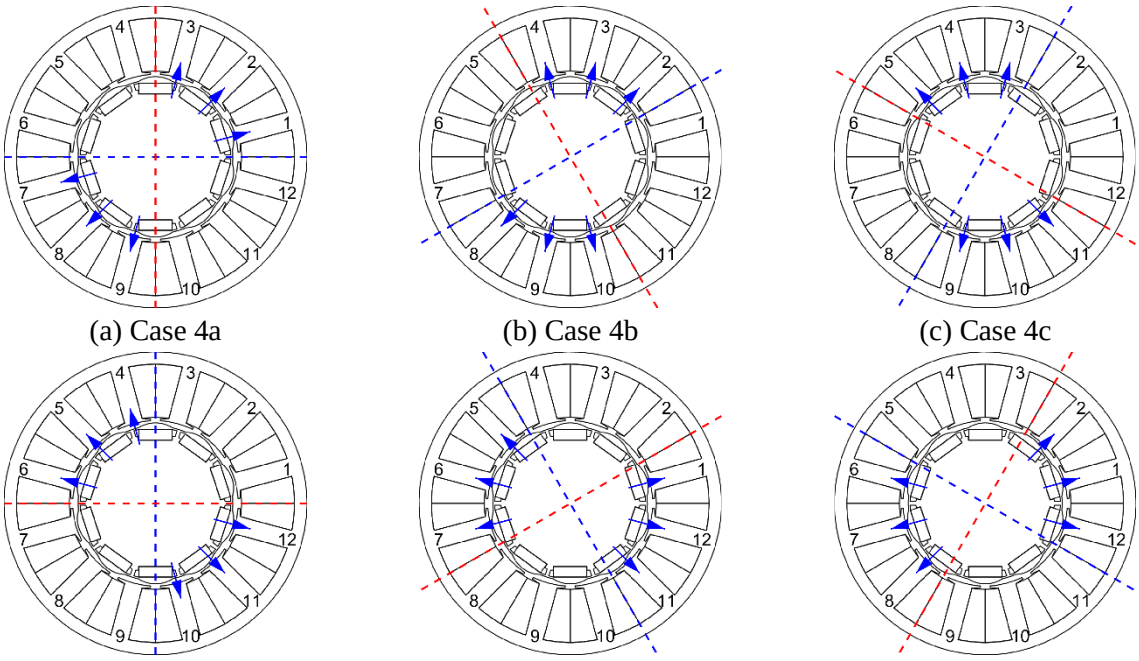

(c) Case 3




(d) Case 4

(I) Waveforms (II) Harmonics

Fig. 6.16. Waveforms and harmonics of cogging torque waveforms due to the possible cases of tolerances in the outward direction in the 12-slot/10-pole IPM motor.




(a) Case 4a (b) Case 4b (c) Case 4c

(d) Case 4d (e) Case 4e (f) Case 4f

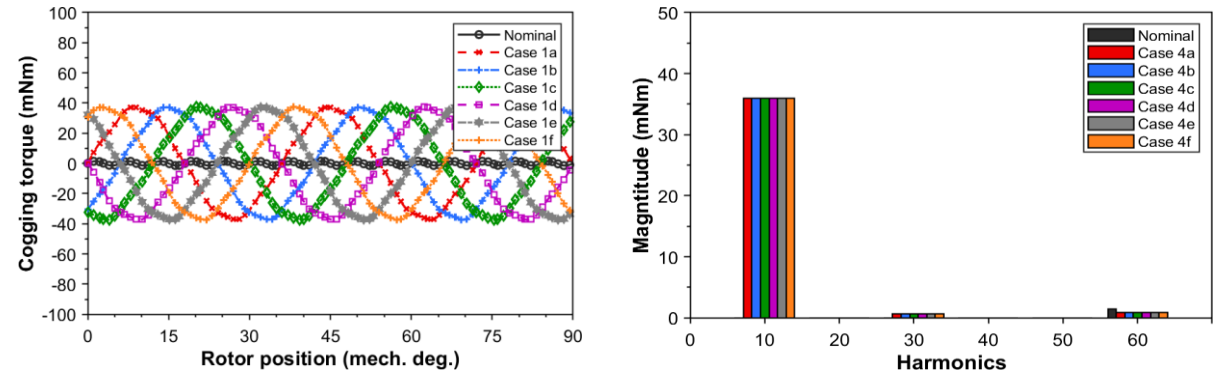
Fig. 6.17. Sub-cases of the worst-case scenario of tolerances in the outward direction in the 12-slot/10-pole IPM motor.

## C. Worst-case scenarios of bidirectional tolerances

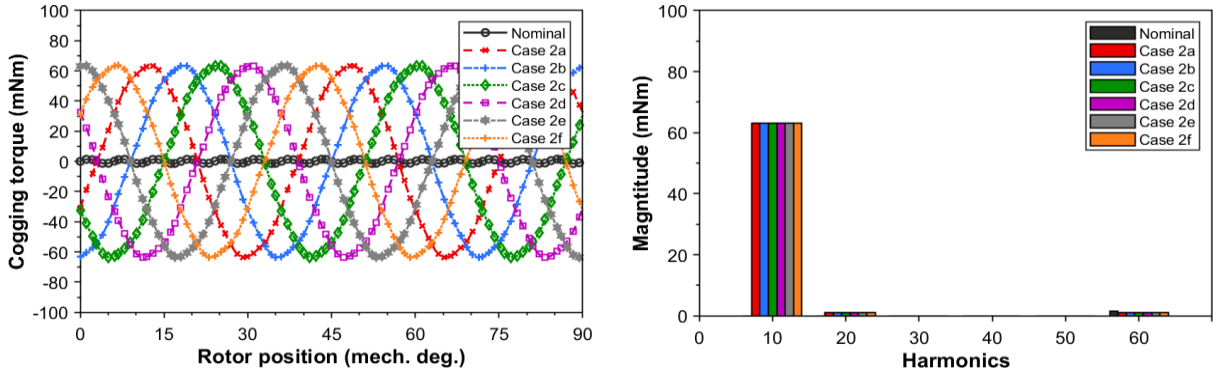
The possible cases of bidirectional tolerances are determined by exploiting the symmetry and anti-symmetry of the 12-slot/10-pole motor. Therefore, the tolerances in each quadrant for the respective cases are as follows:

- Case 1: one tolerance
- Case 2: two adjacent tolerances in the same direction
- Case 3: two tolerances in the same direction separated by a slot pitch
- Case 4: two non-adjacent tolerances in the same directions separated a tolerance in the opposite direction
- Case 5: three adjacent tolerances in same direction.

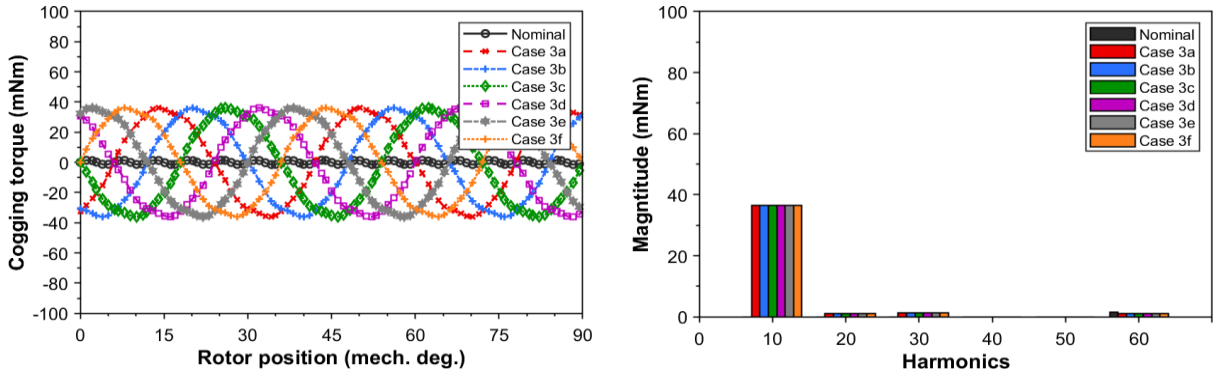
The five cases, shown in Fig. 6.20, are further subdivided into 6 further cases (a to f) in which the tolerances are shifted by 0 to 5 slot pitches, respectively. The waveforms and harmonics of cogging torque due to the possible cases are shown in Fig. 6.18 and Fig. 6.19. The worst-case scenario is Case 5(a to f) and the peak-to-peak cogging torque is 144.8 mNm. The tolerances of Cases 5a to 5f are shown in Fig. 6.21.



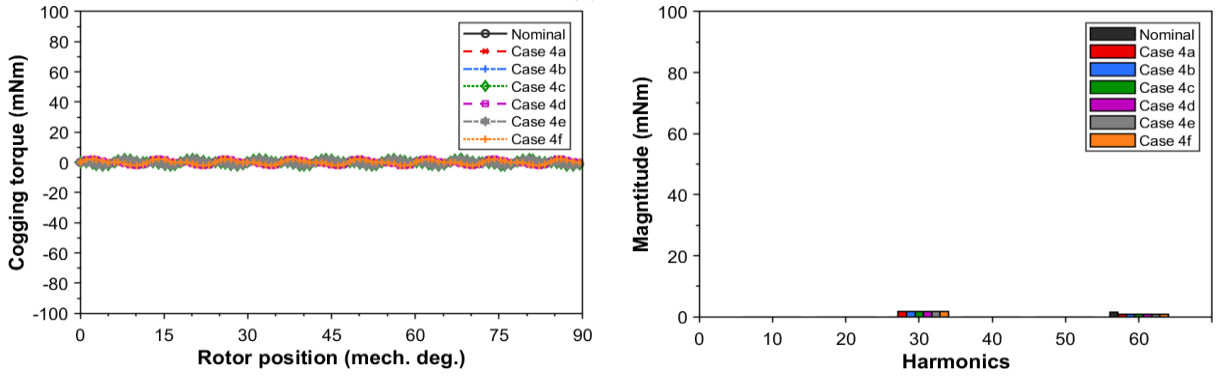

(a) Case 1




(b) Case 2



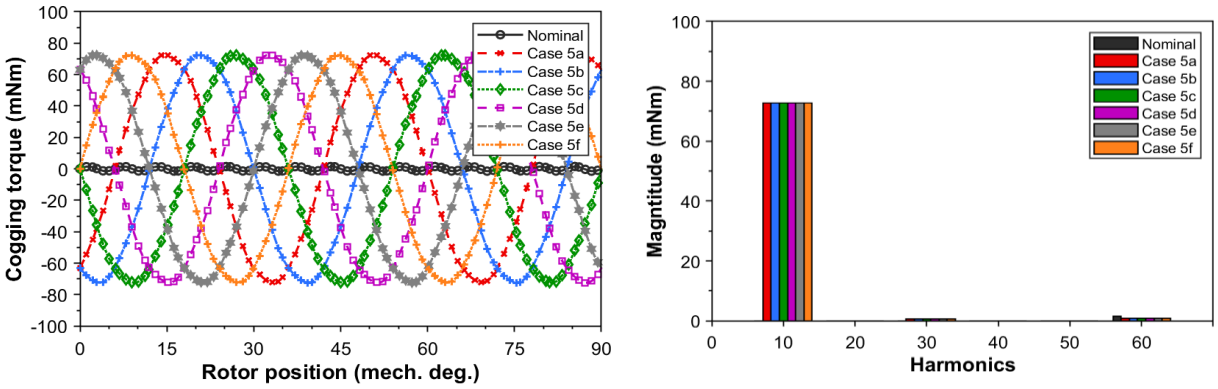

(c) Case 3




(d) Case 4

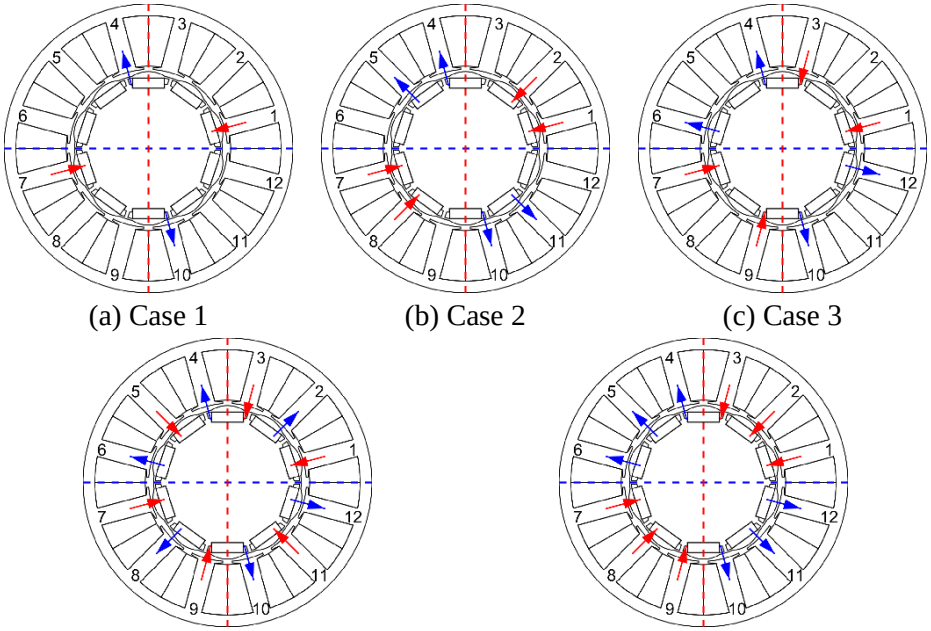
(I) Waveforms (II) Harmonics

Fig. 6.18. Waveforms and harmonics of cogging torque due to cases 1 to 4 of bidirectional tolerances in the 12-slot/10-pole IPM motor.




(a) Waveforms (b) Harmonics

Fig. 6.19. Waveforms and harmonics of cogging torque due to the worst-case scenario Case 5 of bidirectional tolerances in the 12-slot/10-pole IPM motor.



(a) Case 1 (b) Case 2 (c) Case 3

(d) Case 4 (e) Case 5

Fig. 6.20. The possible cases of bidirectional tolerances in the 12-slot/10-pole IPM motor.

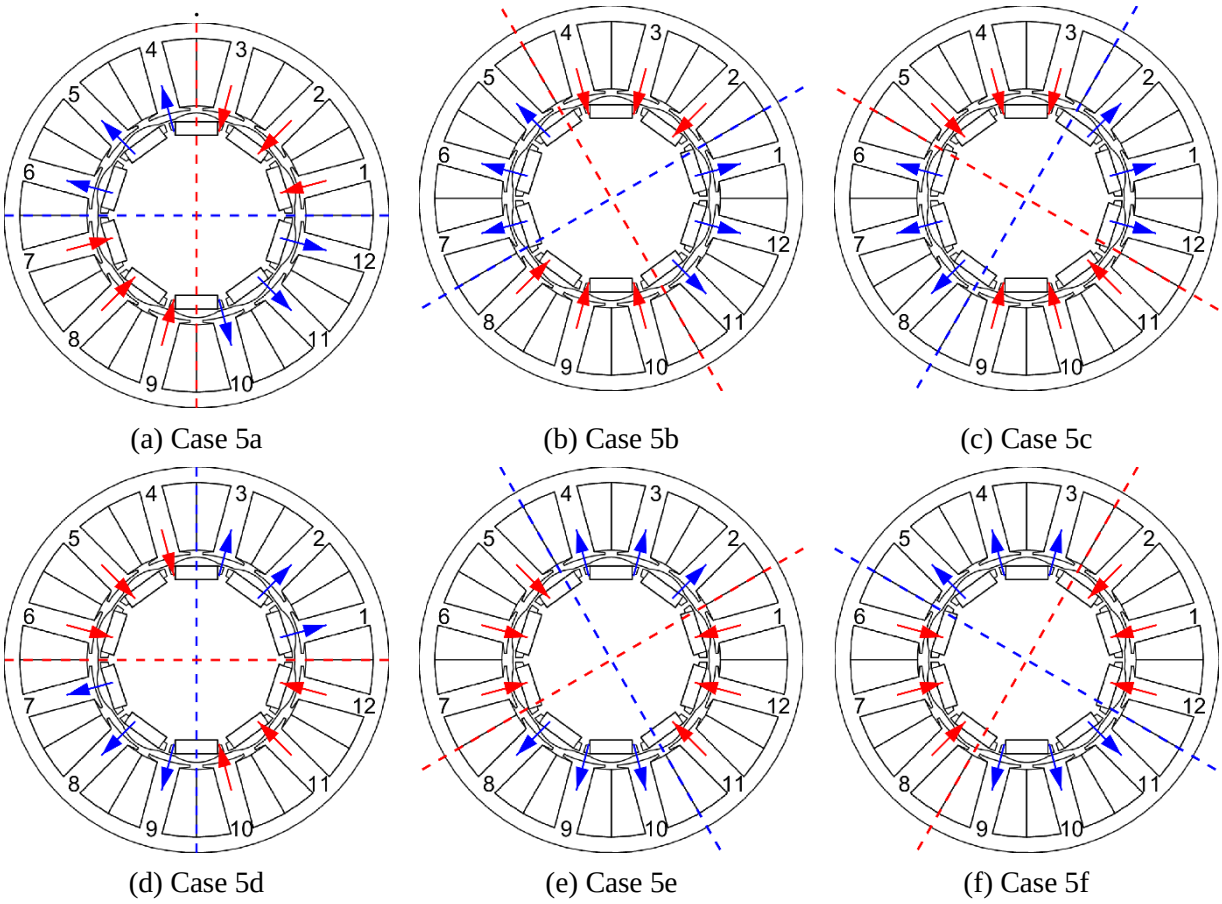



Fig. 6.21. Worst-case scenarios of bidirectional tolerances in the 12-slot/10-pole IPM motor.

.

### 6.2.3 Worst-Case Scenarios of Cogging Torque of 12-slot/14-pole IPM Motor

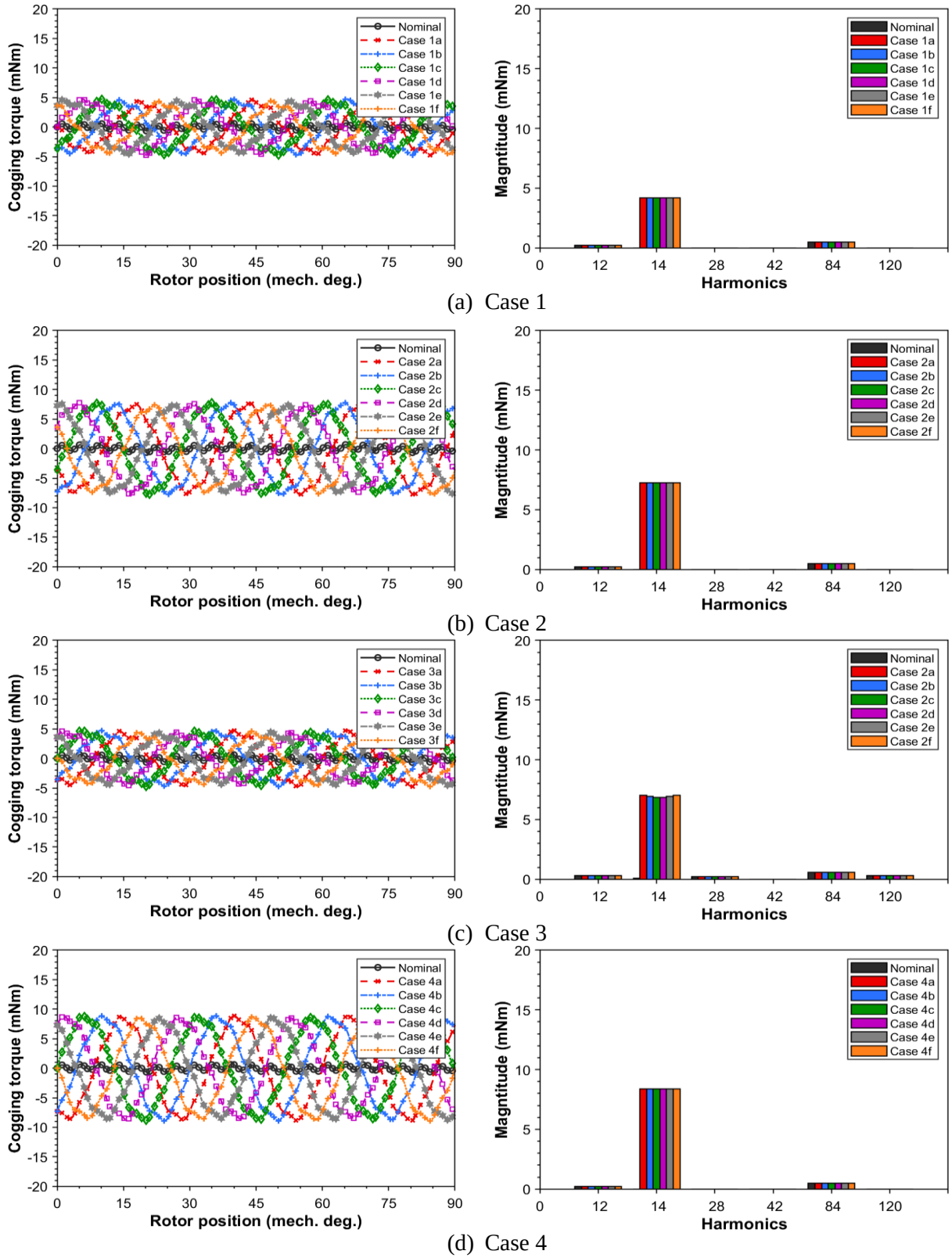
A. Worst-case scenarios of tolerances in the inward direction

The symmetry and anti-symmetry of the 12-slot/14-pole motor are indicated by the blue and red dotted lines in Fig. 6.23, respectively. The worst-case scenarios for tolerances in a particular direction are obtained by exploiting the additive and cancelling effects on the resultant AHCs due to the inherent symmetry and anti-symmetry of the motor. Therefore, the four possible cases of tolerances in the inward direction in the first and third quadrants are:

- Case 1: one tolerance
- Case 2: two adjacent tolerances
- Case 3: two tolerances separated by a slot pitch
- Case 4: three adjacent tolerances

The four cases, shown in Fig. 6.23, are subdivided into 6 further cases (a to f) in which the layouts in are shifted by 0 to 5 slot pitches, respectively. The cogging torque waveforms and harmonics of the worst-case

scenarios in the inward direction are shown in Fig. 6.22. The worst-case scenario of the cogging torque due to tolerances in the inward directions is Case 4(a to f) and the peak-to-peak cogging torque is 19.2 mNm.




(a) Case 1

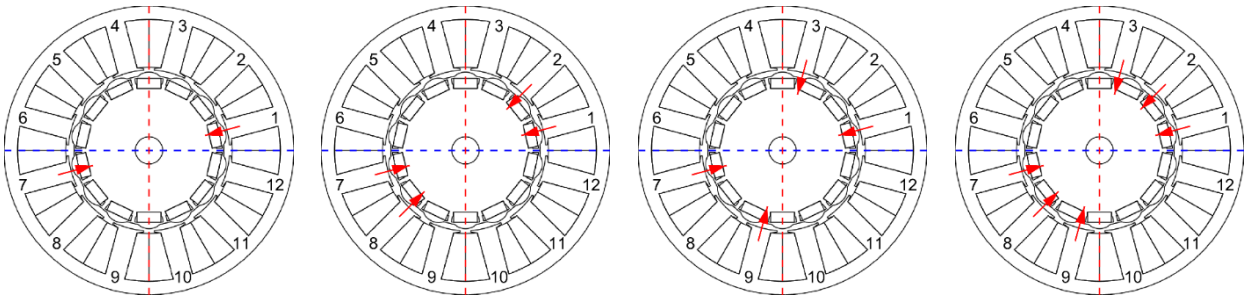
(b) Case 2

(c) Case 3

(d) Case 4

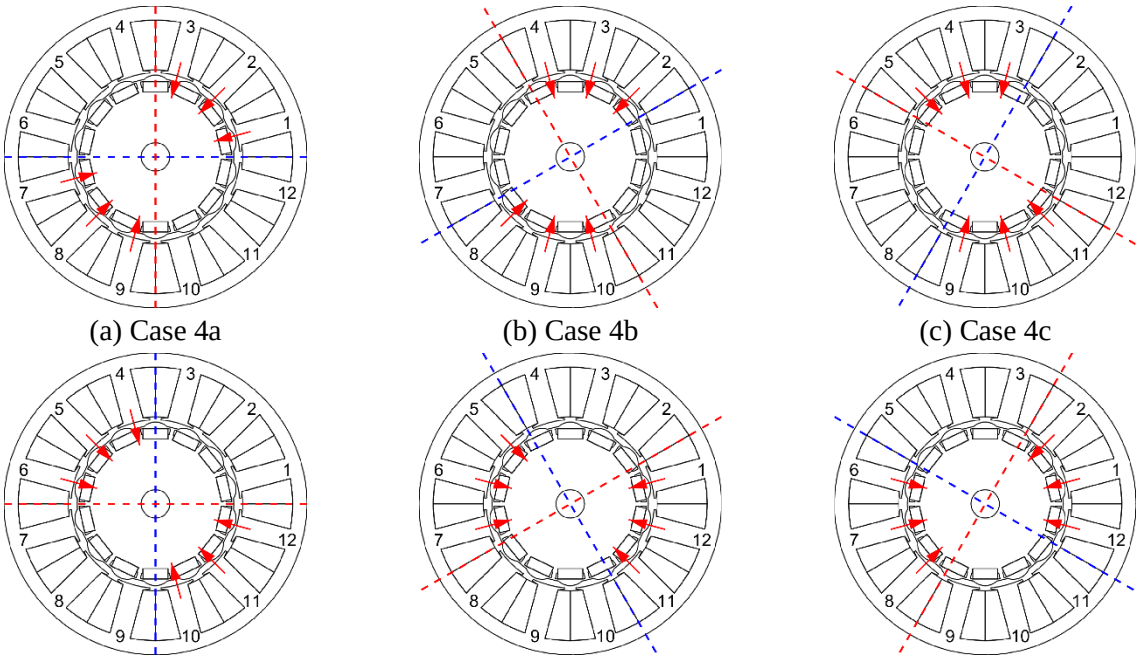
(I) Waveforms (II) Harmonics

Fig. 6.22. Waveforms and harmonics of cogging torque due to the possible cases of tolerances in the inward direction in the 12-slot/14-pole IPM motor.



(a) Case 1 (b) Case 2 (c) Case 3 (d) Case 4

Fig. 6.23. The possible cases of tolerances in the inward direction in the 12-slot/14-pole IPM motor.



(a) Case 4a (b) Case 4b (c) Case 4c

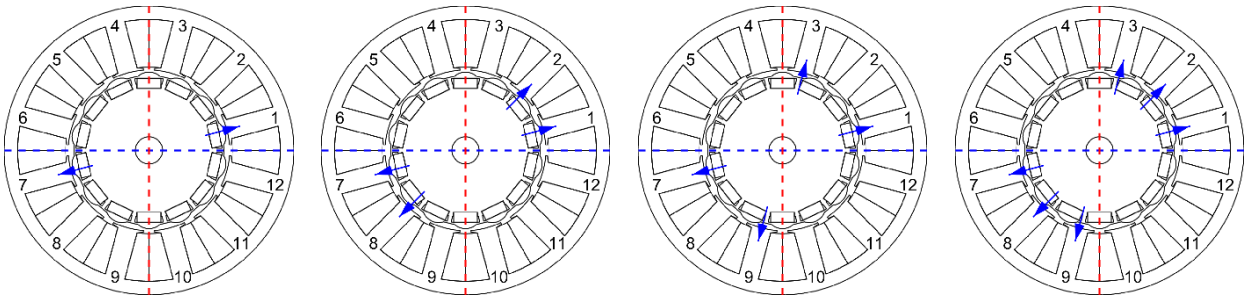
(d) Case 4d (e) Case 4e (f) Case 4f

Fig. 6.24. Sub-cases of the worst-case scenario of tolerances in the inward direction in the 12-slot/14-pole IPM motor.

## B. Worst-case scenarios of tolerances in the outward direction

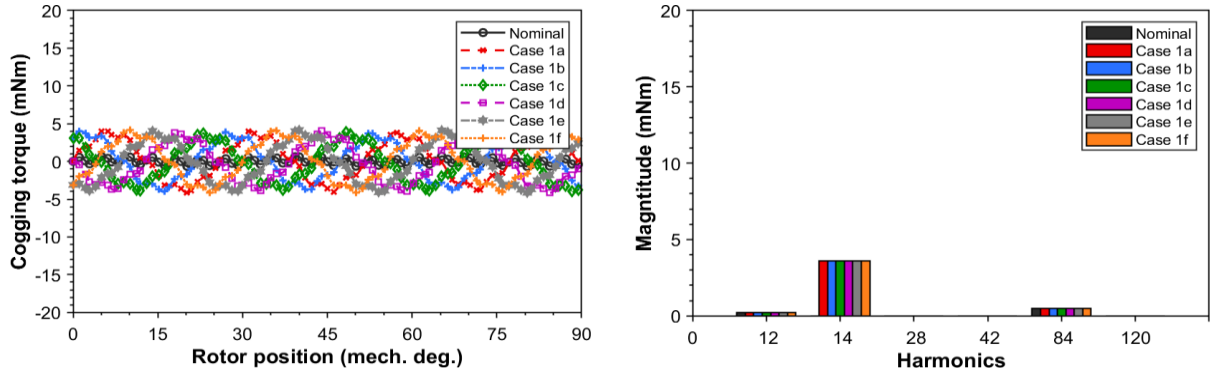
The directions of the tolerances in the identified possible cases of tolerances in the inward direction are reversed, as shown in Fig. 6.25. The cogging torque waveforms and harmonics of each case, including sub-cases in which the tolerances are shifted by 0 to 5 slot pitches, are shown in Fig. 6.27.

The worst-case scenario is Case 4(a to f) and the peak-to-peak cogging torque is 17.8 mNm. The worst-case scenario of tolerances in the outward direction results in a lower peak-to-peak cogging torque than that of tolerances in the inward directions due to the change in air-gap length caused by manufacturing tolerances.

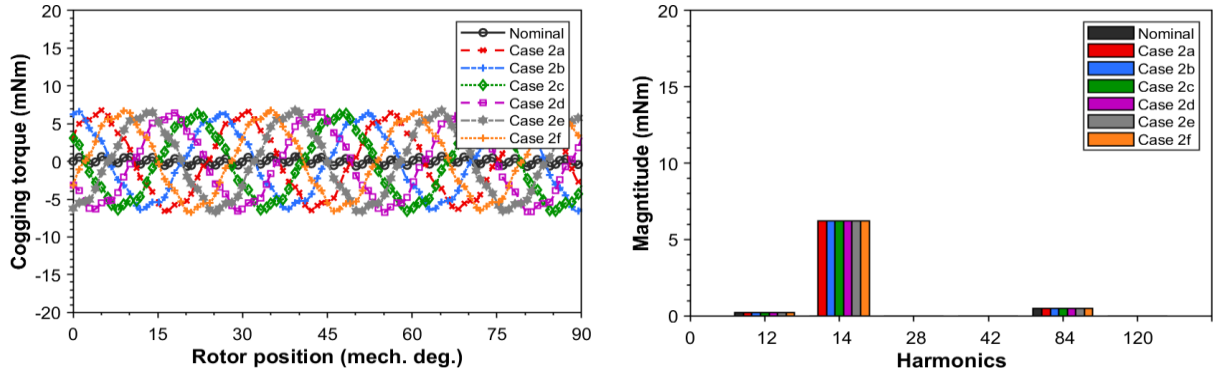


(a) Case 1 (b) Case 2 (c) Case 3 (d) Case 4

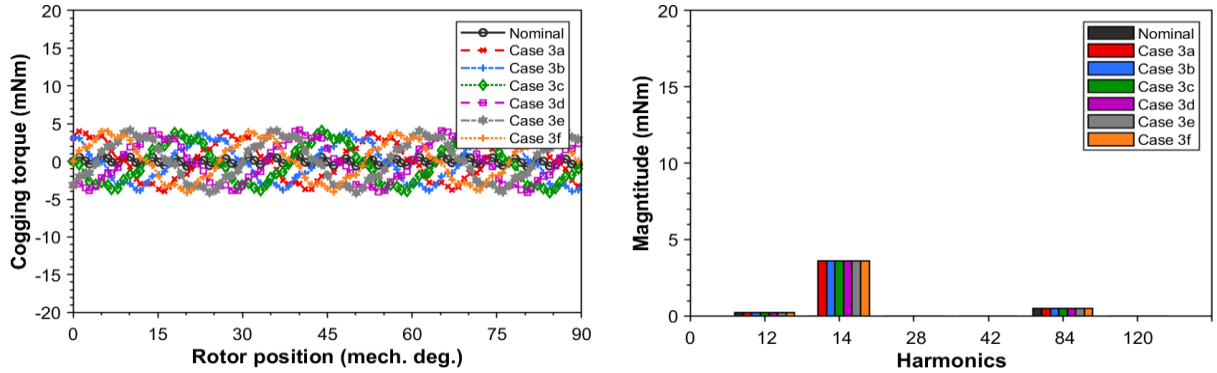
Fig. 6.25. The possible cases of tolerances in the outward direction in the 12-slot/14-pole IPM motor.



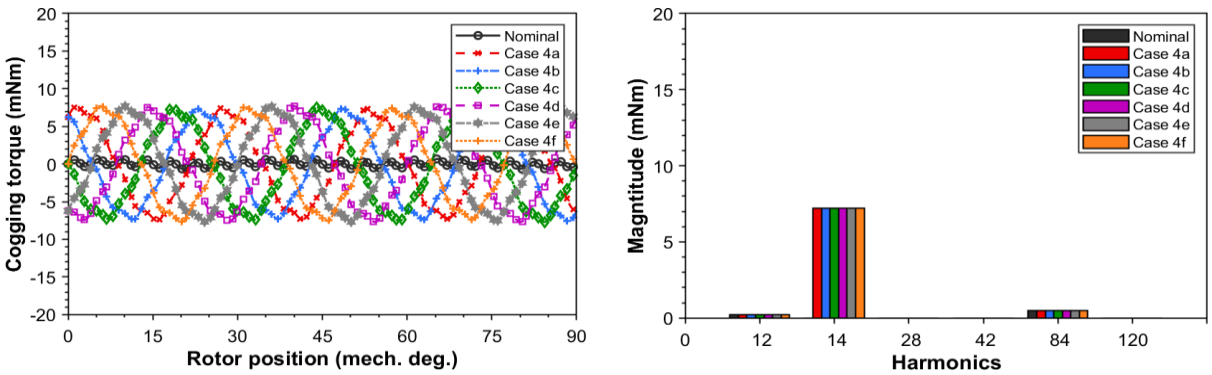

(a) Case 1




(b) Case 2



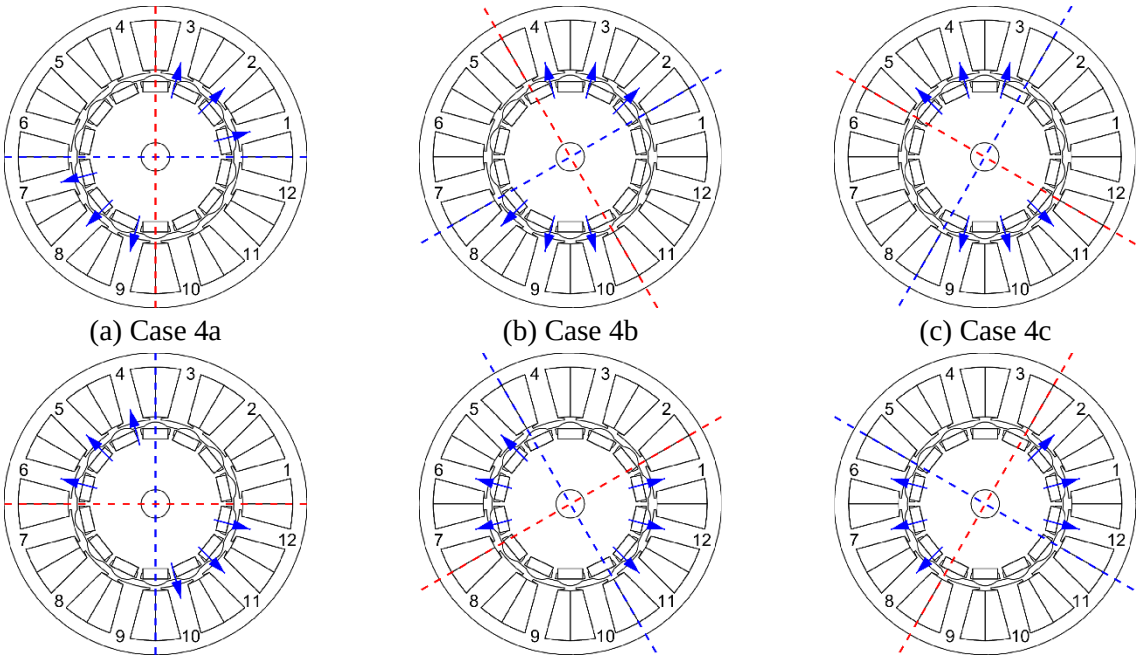

(c) Case 3




(d) Case 4

(I) Waveforms (II) Harmonics

Fig. 6.26. Waveforms and harmonics of cogging torque due to the possible cases of tolerances in the outward direction in the 12-slot/14-pole IPM motor.



(a) Case 4a (b) Case 4b (c) Case 4c

(d) Case 4d (e) Case 4e (f) Case 4f

Fig. 6.27. Sub-cases of the worst-case scenario of tolerances in the outward direction in the 12-slot/14-pole IPM motor.

## C. Worst-case scenarios of bidirectional tolerances

The inherent symmetry and anti-symmetry of the motor is again exploited to determine the worst-case scenarios of bidirectional tolerances. Therefore, the tolerances in each quadrant for the respective cases are as follows:

- Case 1: one tolerance
- Case 2: two adjacent tolerances in the same direction
- Case 3: two tolerances in the same direction separated by a slot pitch
- Case 4: two non-adjacent tolerances in the same directions separated a tolerance in the opposite direction
- Case 5: three adjacent tolerances in same direction.

The five cases, shown in Fig. 6.28, are further subdivided into 6 further cases (a to f) in which the tolerances are shifted by 0 to 5 slot pitches, respectively. The cogging torque waveforms of the possible cases are shown in Fig. 6.29 and Fig. 6.30. The worst-case scenario is Case 5(a to f) and the peak-to-peak cogging torque is 32.0 mNm. The tolerances of Cases 5a to 5f are shown in Fig. 6.31.

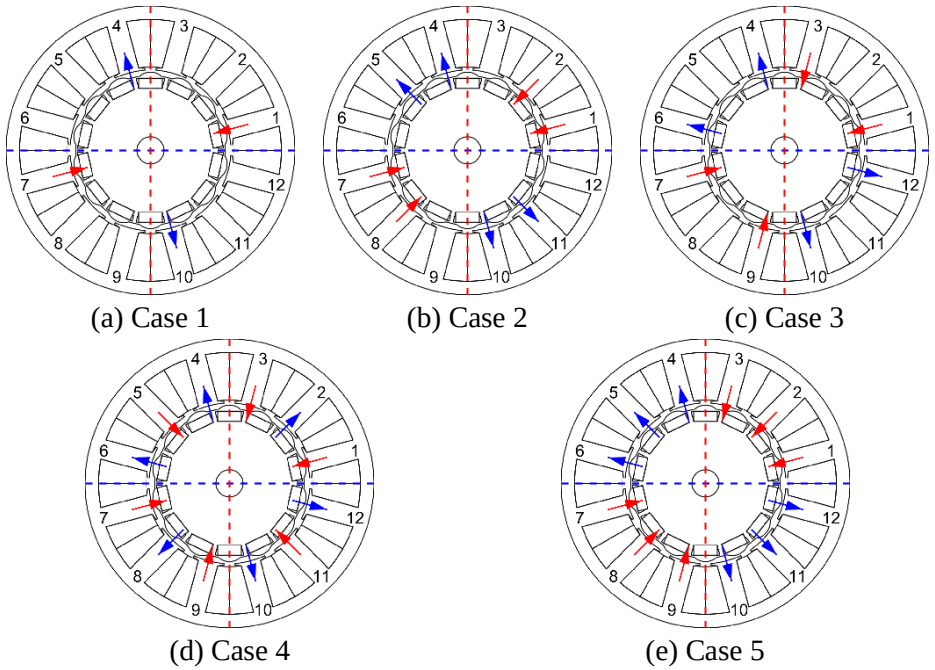
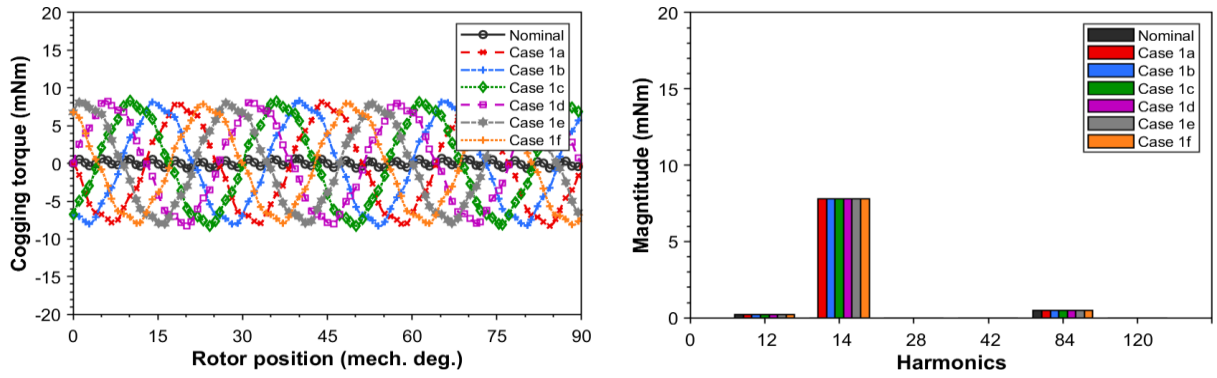
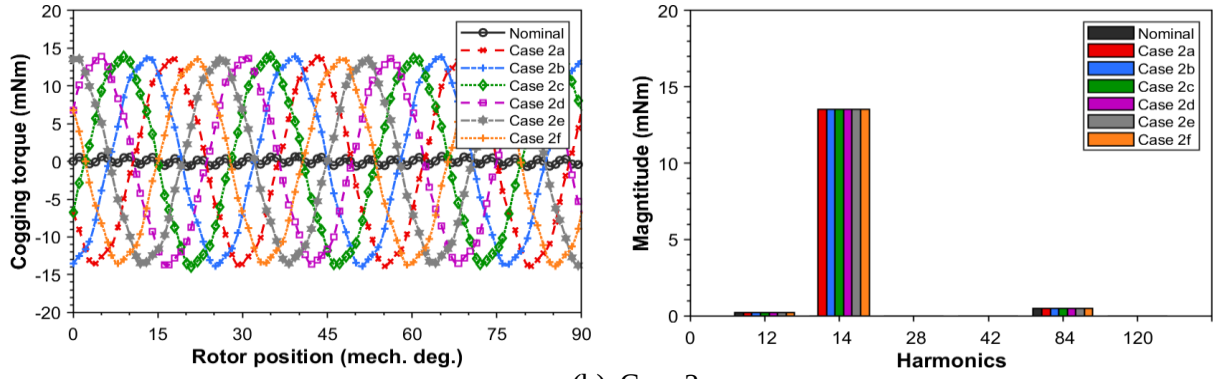


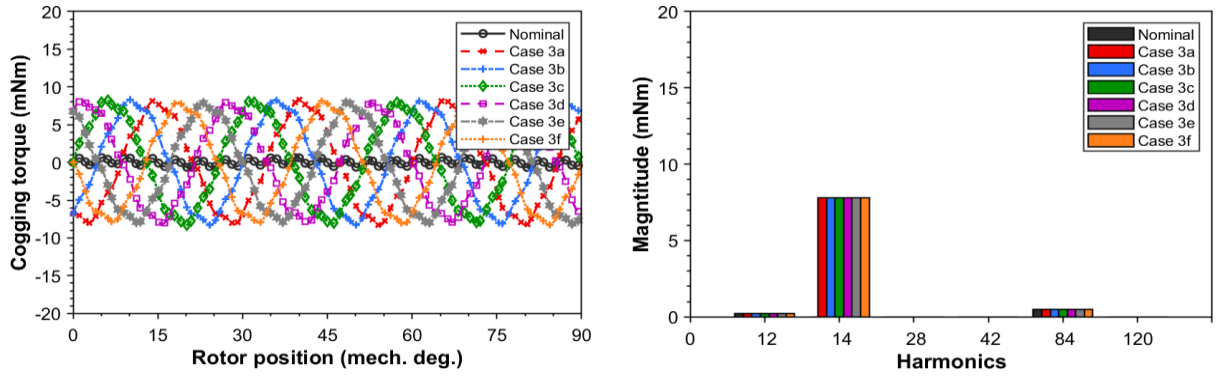

Fig. 6.28. The possible cases of bidirectional tolerances in the 12-slot/14-pole IPM motor.



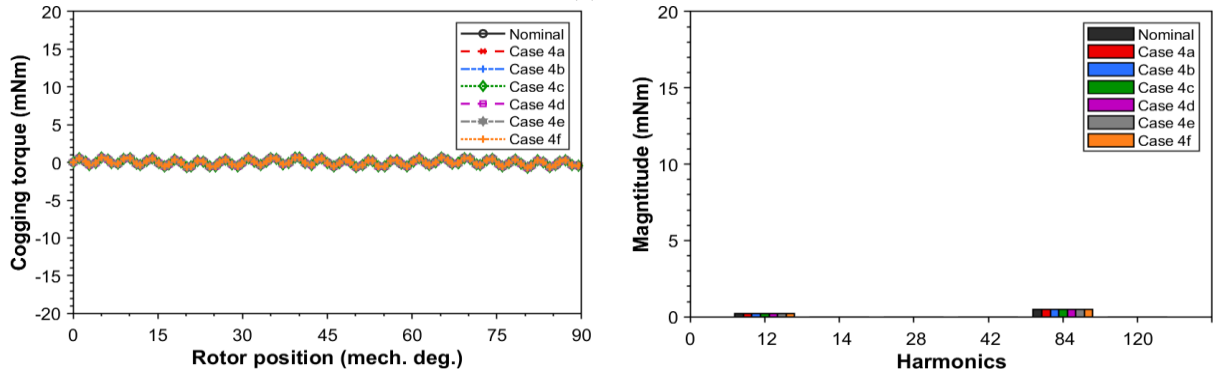

(a) Case 1




(b) Case 2



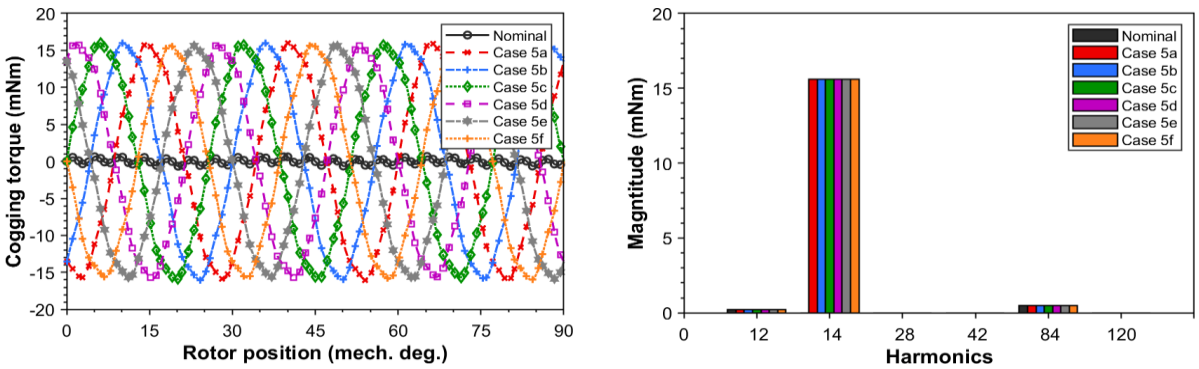

(c) Case 3




(d) Case 4

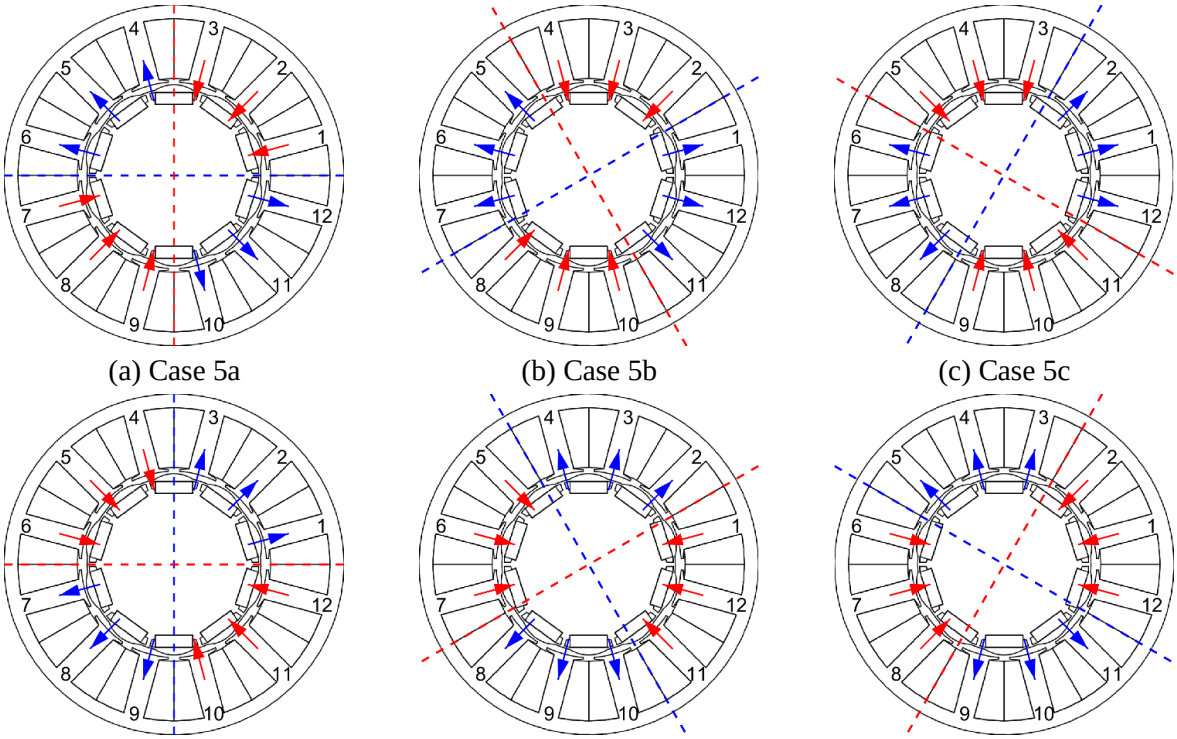
(I) Waveforms (II) Harmonics

Fig. 6.29. Waveforms and harmonics of cogging torque due to the possible cases 1 to 4 of bidirectional tolerances in the 12-slot/14-pole IPM motor.




(a) Waveforms (b) Harmonics

Fig. 6.30. Waveforms and harmonics of cogging torque due to Case 5 of bidirectional tolerances in the 12-slot/14-pole IPM motor.



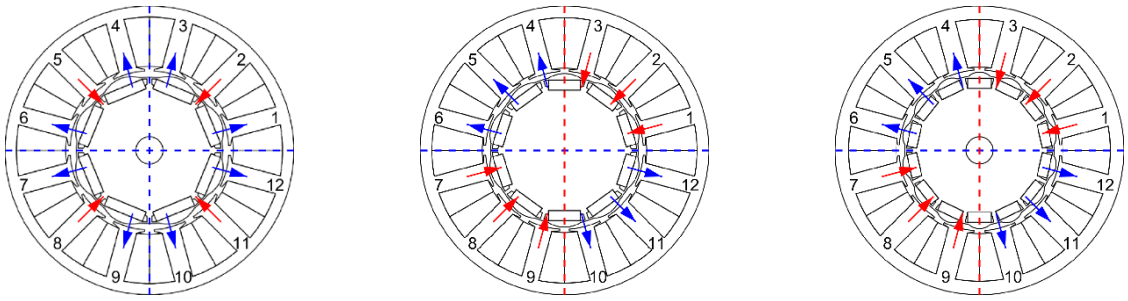
(a) Case 5a (b) Case 5b (c) Case 5c

(d) Case 5d (e) Case 5e (f) Case 5f

Fig. 6.31. The worst-case scenarios of bidirectional tolerances in the 12-slot/14-pole IPM motor.

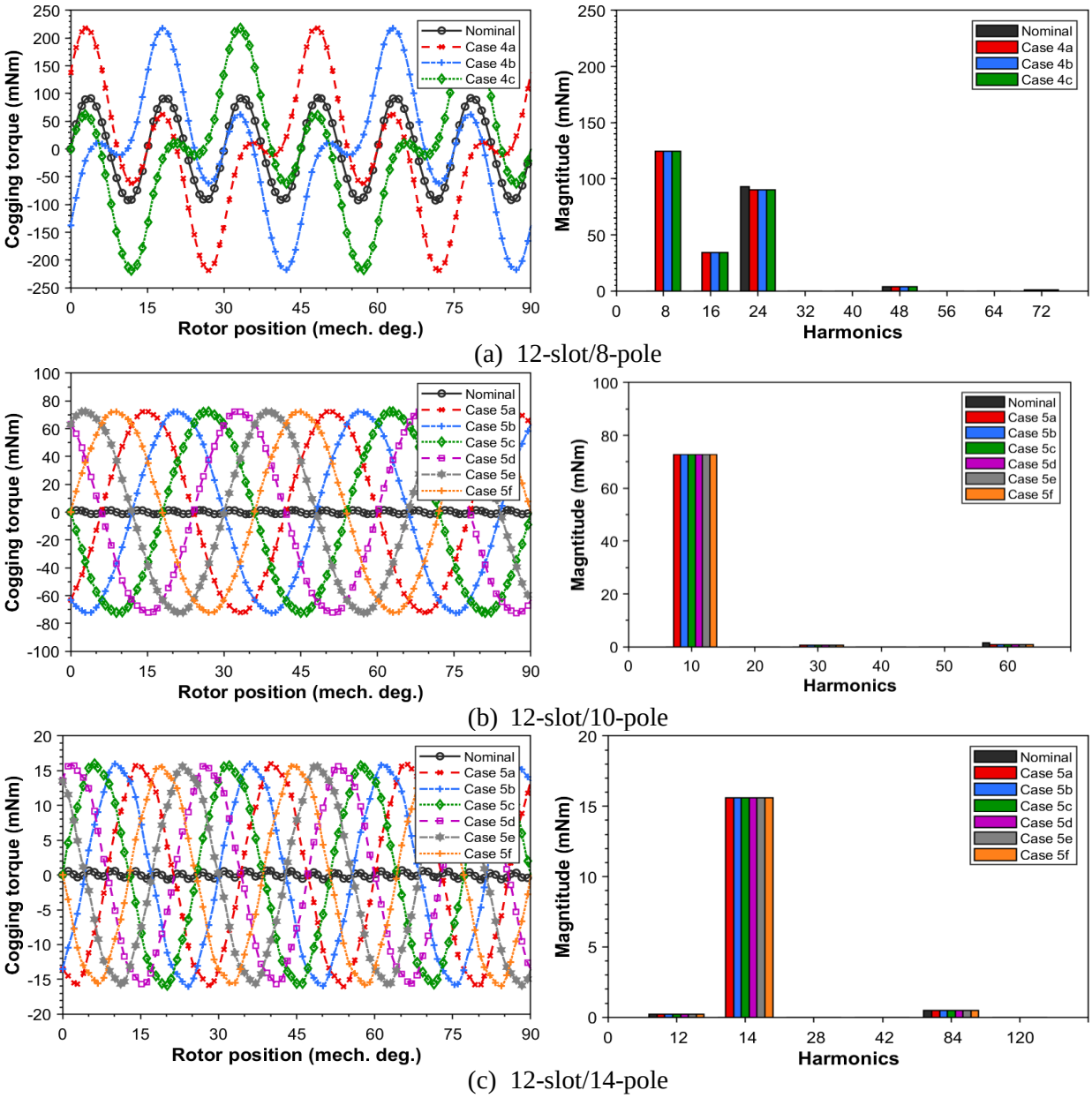
### 6.2.4 Comparison of Worst-Case Scenarios of Cogging Torque of IPM Motors with Different Slot/Pole Number Combinations

Worst-case scenarios of tolerances in the radial position of the stator teeth profile of the IPM motors under investigation are shown in Fig. 6.32. Blue and red dotted lines indicate the inherent symmetry and anti-symmetry of the motors, respectively. Waveforms and harmonics of the cogging torque of the worst-case scenarios are shown in Fig. 6.33. The cogging torque of the sub-cases, in which the tolerances are shifted by a number of slot pitches, are also shown in Fig. 6.33. The directions of the tolerances reflect the periodicity of the motor, equal to the GCD of the stator slot and rotor pole numbers. The cogging torque attributed to the worst-case scenarios decreases significantly with increasing rotor pole number.



(a) 12-slot/8-pole (b) 12-slot/10-pole (c) 12-slot/14-pole

Fig. 6.32. Worst-case scenarios of bidirectional tolerances in IPM motors




(a) 12-slot/8-pole

(b) 12-slot/10-pole

(c) 12-slot/14-pole

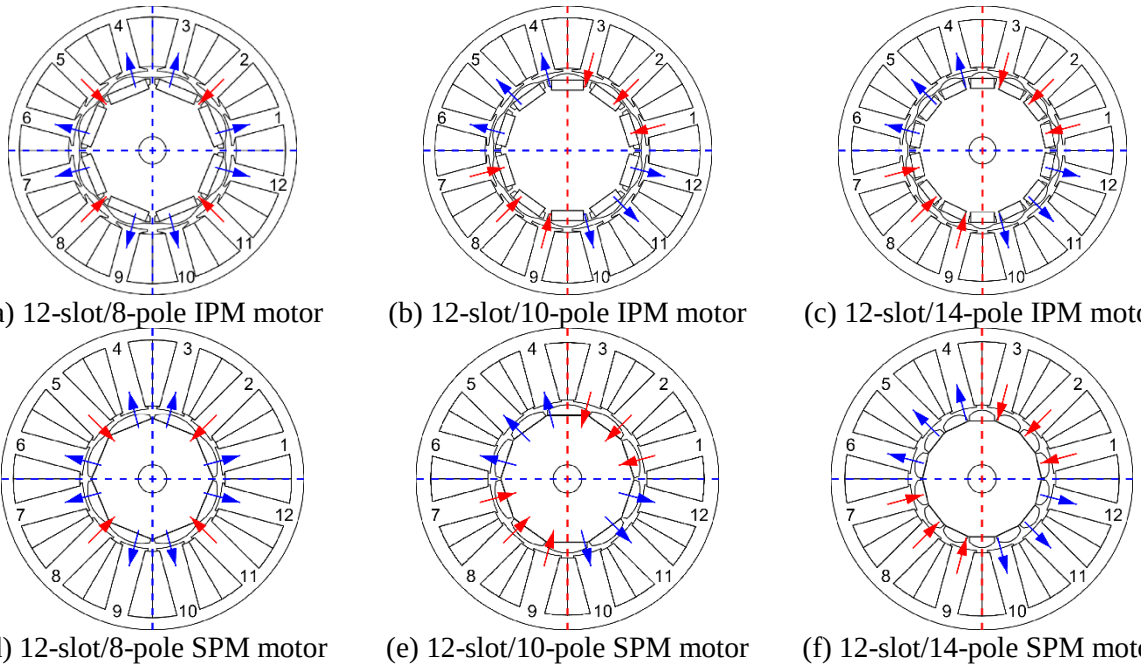
(I) Waveforms (II) Harmonics

Fig. 6.33. Waveforms and harmonics of cogging torque due to the worst-case scenarios of bidirectional tolerances in IPM motors.

### 6.2.5 Comparison of Worst-Case Scenarios of Cogging Torque of IPM and SPM Motors

Worst-case scenarios of tolerances in the radial position of the stator teeth profile of the SPM motors are determined using the same methodology applied for tolerances in IPM motors. Motor cross-sections, waveforms, and harmonics of the cases of tolerances in the inward direction, outward direction, and both directions are shown in Appendix B. The identified worst-case scenarios for tolerances in the inward direction, outward direction and bidirectional tolerances are identical to those of IPM motors, as shown in Fig. 6.34. Waveforms and harmonics of the cogging torque of the worst-case scenarios and the corresponding sub-cases are shown in Fig. 6.35 and Fig. 6.36, respectively.

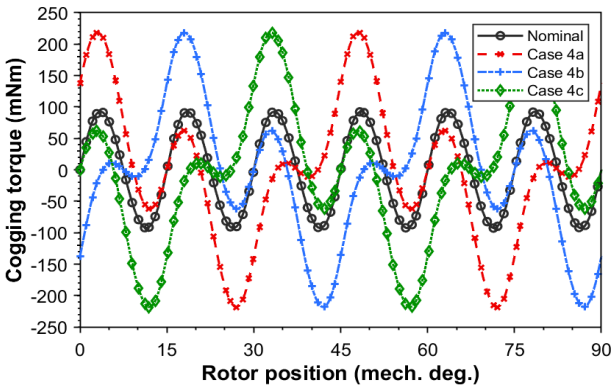
The periodicity of the motor, equal to the GCD of the stator slot and rotor pole numbers, is reflected in the direction of the tolerances. For instance, the 12-slot/8-pole motor has a periodicity of four and consequently the worst-case scenario is composed of four orthogonal tolerances in the inward direction and four orthogonal sets of two adjacent tolerances in the opposite direction. Similarly, the worst-case of the 12-slot/10-pole and 12-slot/14-pole motors, both having a periodicity of two, is composed of two diametrically opposite quadrants with tolerances in the same direction and tolerances in the opposing direction in the remaining quadrants. The peak-to-peak cogging torque attributed to the worst-case scenarios decreases significantly with increasing rotor pole number. The peak-to-peak cogging torque attributed to the worst-case scenarios of the 12-slot/8-pole IPM motor is 45.8% higher than that of the 12-slot/8-pole SPM motor. Similarly, the worst-case peak-to-peak cogging torque of the 12-slot/14-pole IPM motor is 74.8% higher than that of the 12-slot/14-pole SPM motor. The 12-slot/10-pole SPM has a 10.9% higher worst-case peak-to-peak cogging torque than the 12-slot/10-pole IPM motor.



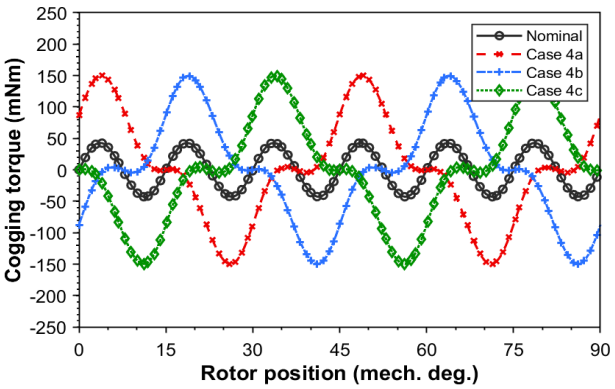
(a) 12-slot/8-pole IPM motor (b) 12-slot/10-pole IPM motor (c) 12-slot/14-pole IPM motor

(d) 12-slot/8-pole SPM motor (e) 12-slot/10-pole SPM motor (f) 12-slot/14-pole SPM motor

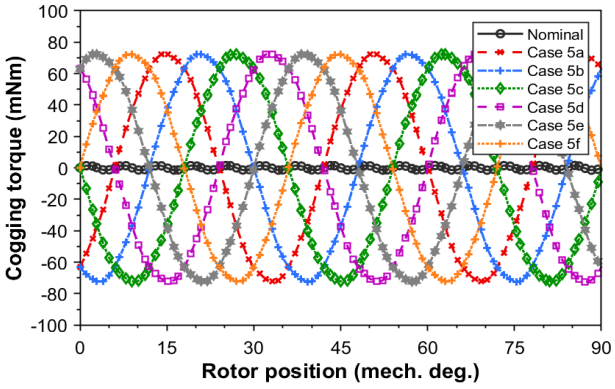
Fig. 6.34. Worst-case scenarios of tolerances in IPM and SPM motors



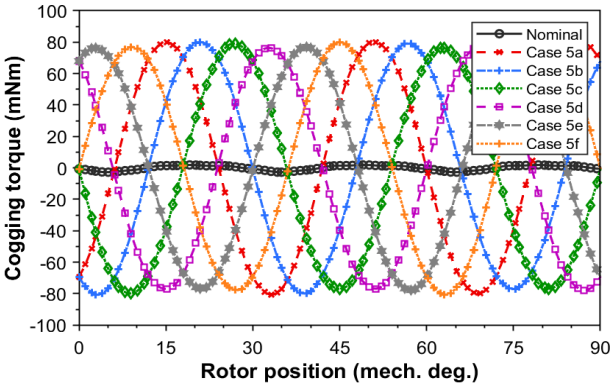

(a) 12-slot/8-pole IPM



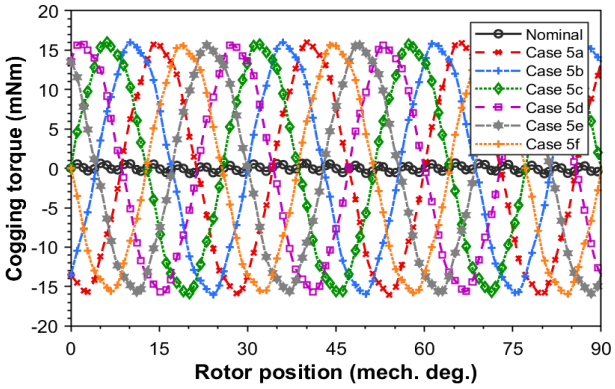

(b) 12-slot/8-pole SPM



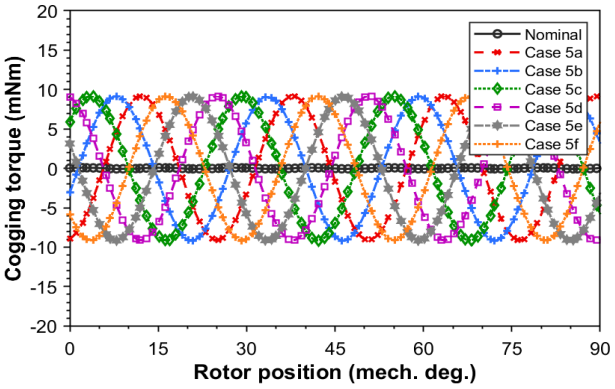

(c) 12-slot/10-pole IPM




(d) 12-slot/10-pole SPM

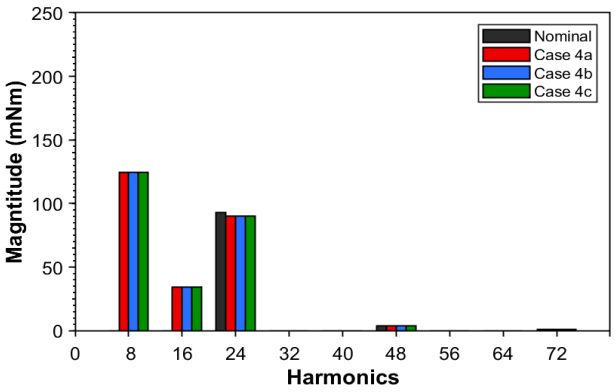



(e) 12-slot/14-pole IPM

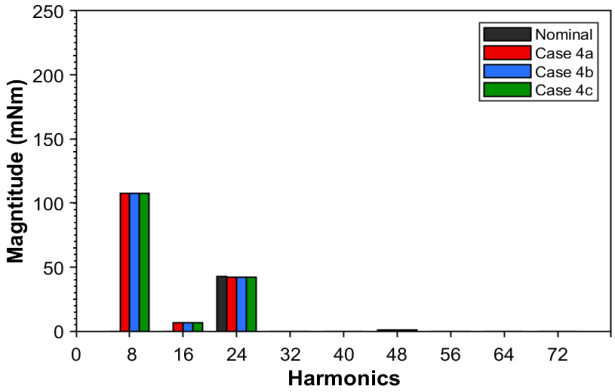



(f) 12-slot/14-pole SPM

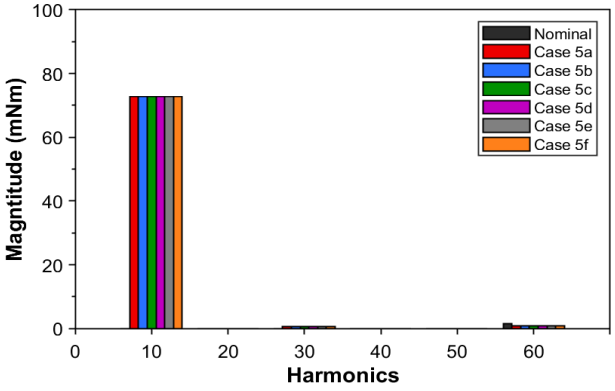
Fig. 6.35. Cogging torque due to the worst-case scenarios of bidirectional tolerances in IPM and SPM motors.



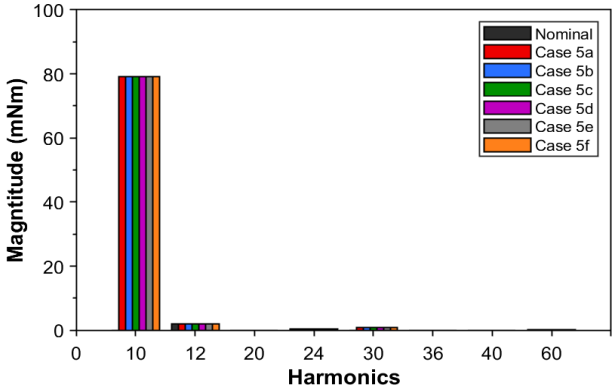

(a) 12-slot/8-pole IPM motor



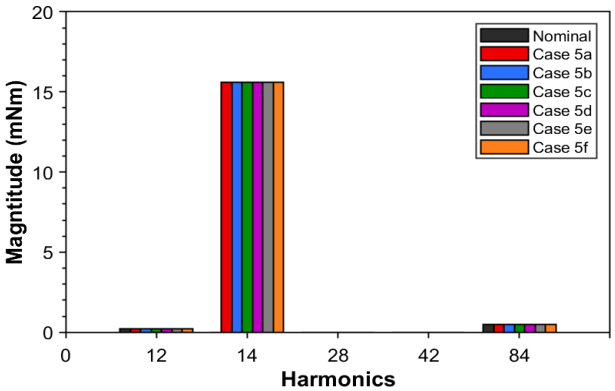

(b) 12-slot/8-pole SPM motor



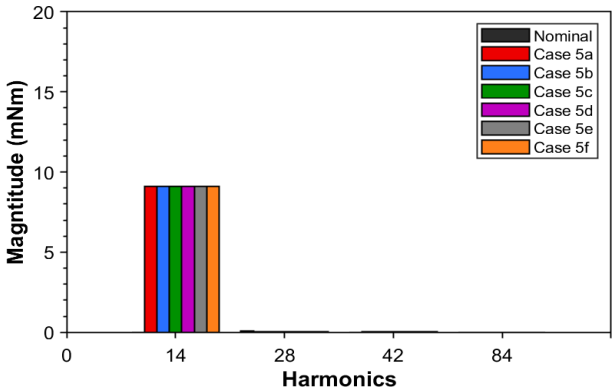

(c) 12-slot/10-pole IPM motor




(d) 12-slot/10-pole SPM motor




(e) 12-slot/14-pole IPM motor




(f) 12-slot/14-pole SPM motor

Fig. 6.36. Cogging torque harmonics due to the worst-case scenarios of bidirectional tolerances in IPM and SPM motors.

## 6.3 Investigation of Worst-Case Scenarios Due to Stator Tolerances in IPM motors

The worst-case scenarios of cogging torque due to stator tolerances in 12-slot/8-pole, 12-slot/10-pole, and 12-slot/14-pole IPM motors under investigation are identified using the global search algorithm combined with a simplified analytical model based on a series of FEA simulations. The directions of tolerances in stator teeth 1 to 6 are indicated in Table 6.1, Table 6.2, Table 6.3, respectively. The directions of tolerances in teeth 7 to 12 are identical to those of tolerances in teeth 1 to 6, respectively, due to the geometrical symmetry of the motors under investigation. The tolerances of the worst-case scenarios are illustrated in a simplified stator geometry in Fig. 6.37. The worst-case scenarios are composed of 6 sub-cases in which the direction of the tolerances are shifted by 0 to 5 slot pitches, respectively.

The 12-slot/8-pole IPM motor has a geometrical symmetry of four, and thus tolerances separated by an angle of 90° result in an additive effect. The worst-case scenario of the cogging torque is composed of tolerances in teeth 1 to 3 identical to the tolerances in teeth 4 to 6, respectively. The directions of tolerances in the tooth-tip with and tooth profile radial position are identical. Furthermore, the directions of tolerances in the tooth-tip height are opposite those of tolerances in the tooth-tip width and tooth profile radial position.

The 12-slot/10-pole and 12-slot/14-pole motors exhibit rotational symmetry every 180° and anti-symmetry every 90°. Thus, tolerances in the same direction separated by an angle of 180° result in an additive effect. Similarly, tolerances in the same direction separated by an angle of 90° result in a cancelling effect. Consequently, the worst-case scenario is composed of tolerances in teeth 1 to 3 and teeth 4 to 6, respectively, in opposite directions.

The worst-case scenario of the 12-slot/10-pole motor is composed of tolerances in the tooth-tip width and tooth profile radial position in the same direction. The worst-case scenario tolerances in tooth-tip height of the 12-slot/10-pole motor in adjacent teeth are in alternate directions. Tolerances in the tooth-tip height and tooth-tip width of the worst-case scenario of the 12-slot/14-pole IPM motor are in the same direction and opposite to those of the tolerances in the tooth profile radial position.

Table 6.1. Directions of tolerances in worst-case scenario of cogging torque due to stator tolerances in 12-slot/8-pole IPM motor

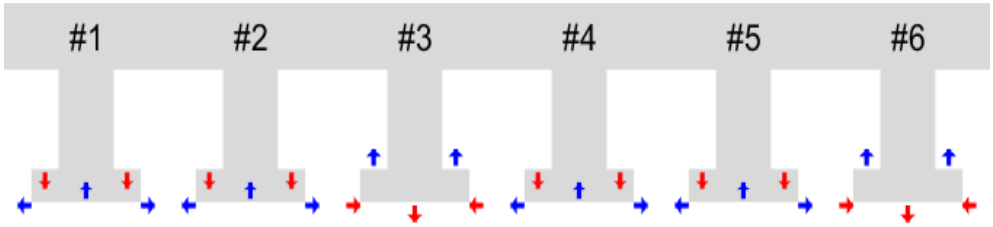
| **Tolerances** | **Tooth 1** | **Tooth 2** | **Tooth 3** | **Tooth 4** | **Tooth 5** | **Tooth 6** |
|---|---|---|---|---|---|---|
| Tooth-tip height | ▼ | ▼ | ▲ | ▼ | ▼ | ▲ |
| Tooth-tip width | ▲ | ▲ | ▼ | ▲ | ▲ | ▼ |
| Tooth profile radial position | ▲ | ▲ | ▼ | ▲ | ▲ | ▼ |

Table 6.2. Directions of tolerances in worst-case scenario of cogging torque due to stator tolerances in 12-slot/10-pole IPM motor

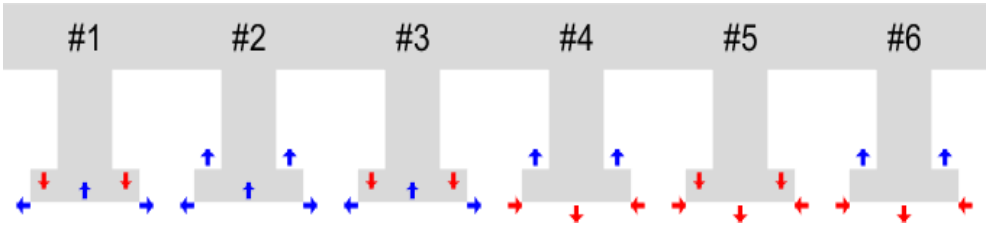
| **Tolerances** | **Tooth 1** | **Tooth 2** | **Tooth 3** | **Tooth 4** | **Tooth 5** | **Tooth 6** |
|---|---|---|---|---|---|---|
| Tooth-tip height | ▼ | ▲ | ▼ | ▲ | ▼ | ▲ |
| Tooth-tip width | ▲ | ▲ | ▲ | ▼ | ▼ | ▼ |
| Tooth profile radial position | ▲ | ▲ | ▲ | ▼ | ▼ | ▼ |

Table 6.3. Directions of tolerances in worst-case scenario of cogging torque due to stator tolerances in 12-slot/14-pole IPM motor

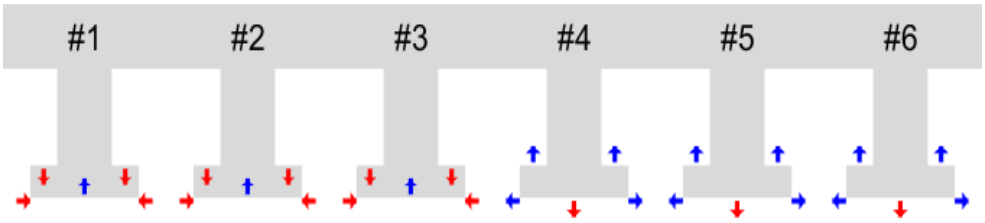
| **Tolerances** | **Tooth 1** | **Tooth 2** | **Tooth 3** | **Tooth 4** | **Tooth 5** | **Tooth 6** |
|---|---|---|---|---|---|---|
| Tooth-tip height | ▼ | ▼ | ▼ | ▲ | ▲ | ▲ |
| Tooth-tip width | ▼ | ▼ | ▼ | ▲ | ▲ | ▲ |
| Tooth profile radial position | ▲ | ▲ | ▲ | ▼ | ▼ | ▼ |




(a) 12-slot/8-pole



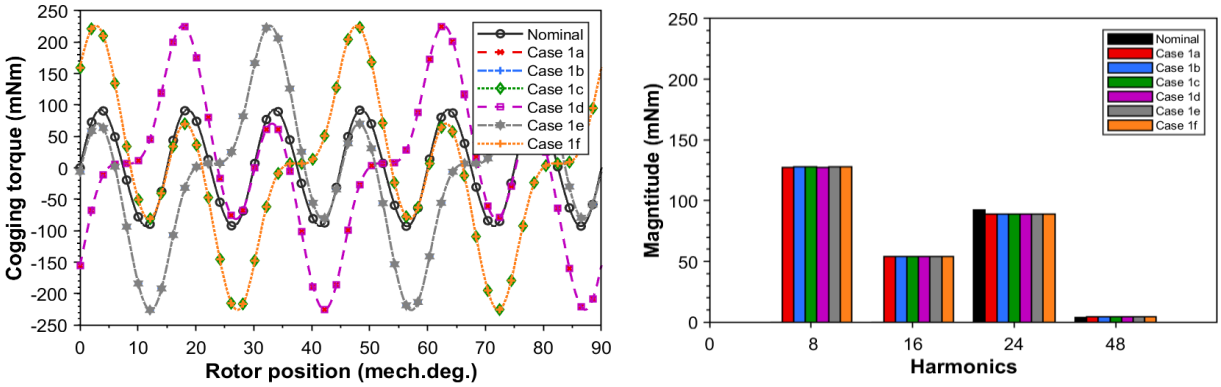

(b) 12-slot/10-pole



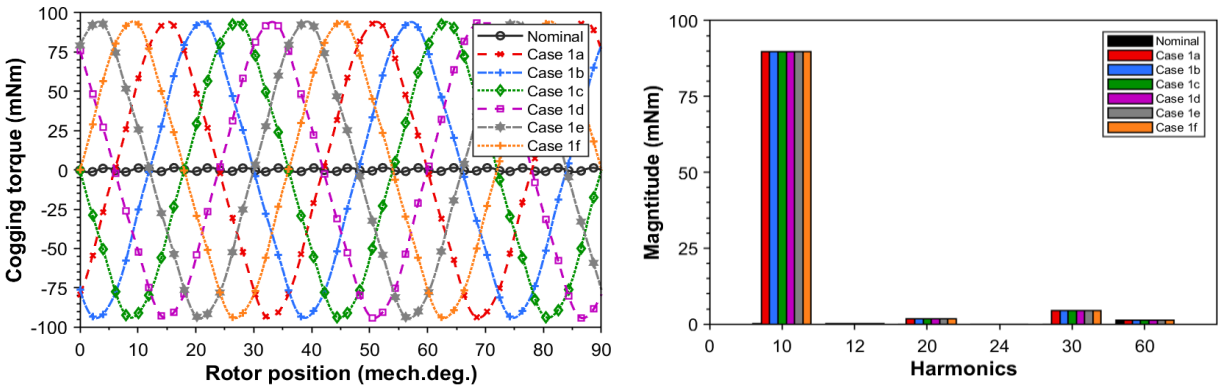

(c) 12-slot/14-pole

Fig. 6.37. Simplified IPM stator geometry including worst-case scenario tolerances in a 180° segment.

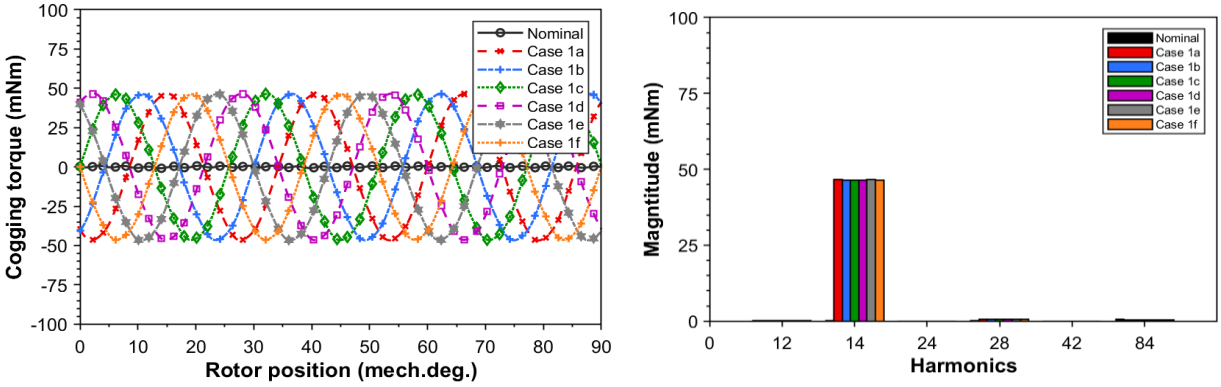
The cogging torque waveforms and harmonics of the worst-case scenarios of the IPM motors under investigation are shown in Fig. 6.38. The maximum peak-to-peak cogging torques of the 12-slot/8-pole, 12-slot/10-pole, and 12-slot/14-pole motors are 452.3 mNm, 188.8mNm, and 93.7mNm, respectively. The peak-to-peak cogging torque of the worst-case scenario sub-cases varies by up to 0.9 mNm. The cogging torque of the worst-case scenarios is the resultant of the superposition of the nominal cogging torque and the cogging torque AHCs due to tolerances. Therefore, the peak-to-peak cogging torque is dependent on the phase of individual cogging torque harmonics. Furthermore, numerical noise may contribute to the slight difference in peak-to-peak cogging torque of the sub-cases of the worst-case scenario.




(a) 12-slot/8-pole




(b) 12-slot/10-pole




(c) 12-slot/14-pole

(I) Waveforms (II) Harmonics

Fig. 6.38. Waveforms and harmonics of cogging torque due to the possible cases of tolerances in the inward direction in the 12-slot/14-pole IPM motor.

## 6.4 Investigation of Worst-Case Scenarios Due to Stator Tolerances in SPM motors

The worst-case scenarios of cogging torque due to stator tolerances in 12-slot/8-pole, 12-slot/10-pole, and 12-slot/14-pole IPM motors under investigation are identified using the global search algorithm. The directions of tolerances in stator teeth 1 to 6 are indicated in Table 6.4, Table 6.5, and Table 6.6, respectively. The directions of tolerances in teeth 7 to 12 are identical to those of tolerances in teeth 1 to 6, respectively, due to the geometrical symmetry of the motors under investigation. The worst-case scenarios are composed of 6 sub-cases in which the directions of the tolerances are shifted by 0 to 5 slot pitches, respectively.

The worst-case scenario tolerances in teeth 1 to 3 of the 12-slot/8-pole IPM motor are identical to tolerances in teeth 4 to 6, respectively, due to the geometrical symmetry of the motor. The directions of the analysed tolerances in a particular tooth are identical.

The 12-slot/10-pole and 12-slot/14-pole motors comprise rotational symmetry every 180° and anti-symmetry every 90°. Thus, tolerances in the same direction separated by an angle of 180° result in an additive effect. Similarly, tolerances in the same direction separated by an angle of 90° result in a cancelling effect. Consequently, the worst-case scenario is composed of tolerances in teeth 1 to 3 and teeth 4 to 6, respectively, in opposite directions.

The directions of tolerances in the tooth profile radial position of the 12-slot/14-pole motor are opposite to those of the tolerances in the tooth-tip height and width.

Table 6.4. Directions of tolerances in worst-case scenario of cogging torque due to stator tolerances in 12-slot/8-pole SPM motor

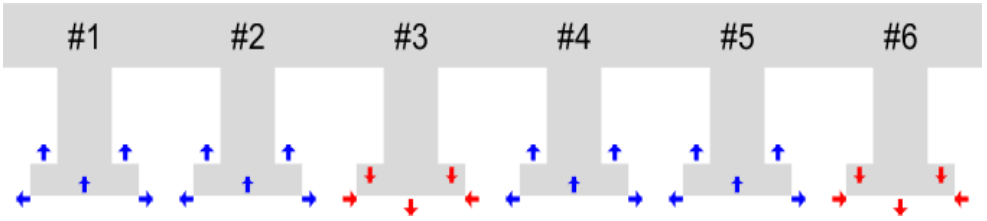
| **Tolerances** | **Tooth 1** | **Tooth 2** | **Tooth 3** | **Tooth 4** | **Tooth 5** | **Tooth 6** |
|---|---|---|---|---|---|---|
| Tooth-tip height | ▲ | ▲ | ▼ | ▲ | ▲ | ▼ |
| Tooth-tip width | ▲ | ▲ | ▼ | ▲ | ▲ | ▼ |
| Tooth profile radial position | ▲ | ▲ | ▼ | ▲ | ▲ | ▼ |

Table 6.5. Directions of tolerances in worst-case scenario of cogging torque due to stator tolerances in 12-slot/10-pole SPM motor

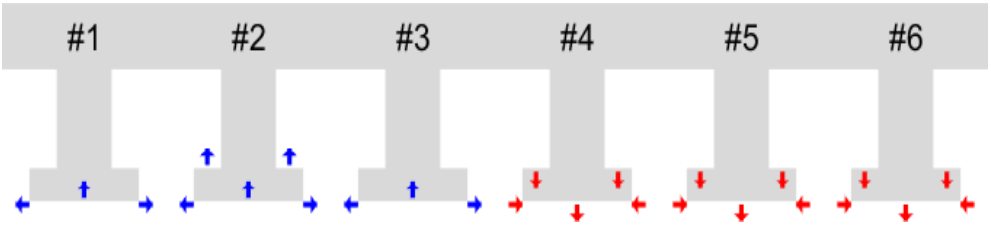
| **Tolerances** | **Tooth 1** | **Tooth 2** | **Tooth 3** | **Tooth 4** | **Tooth 5** | **Tooth 6** |
|---|---|---|---|---|---|---|
| Tooth-tip height | N/A | ▲ | N/A | ▼ | ▼ | ▼ |
| Tooth-tip width | ▲ | ▲ | ▲ | ▼ | ▼ | ▼ |
| Tooth profile radial position | ▲ | ▲ | ▲ | ▼ | ▼ | ▼ |

Table 6.6. Directions of tolerances in worst-case scenario of cogging torque due to stator tolerances in 12-slot/14-pole SPM motor

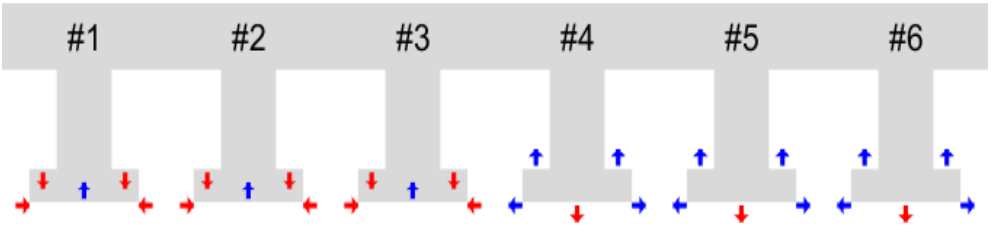
| **Tolerances** | **Tooth 1** | **Tooth 2** | **Tooth 3** | **Tooth 4** | **Tooth 5** | **Tooth 6** |
|---|---|---|---|---|---|---|
| Tooth-tip height | ▼ | ▼ | ▼ | ▲ | ▲ | ▲ |
| Tooth-tip width | ▼ | ▼ | ▼ | ▲ | ▲ | ▲ |
| Tooth profile radial position | ▲ | ▲ | ▲ | ▼ | ▼ | ▼ |




(a) 12-slot/8-pole



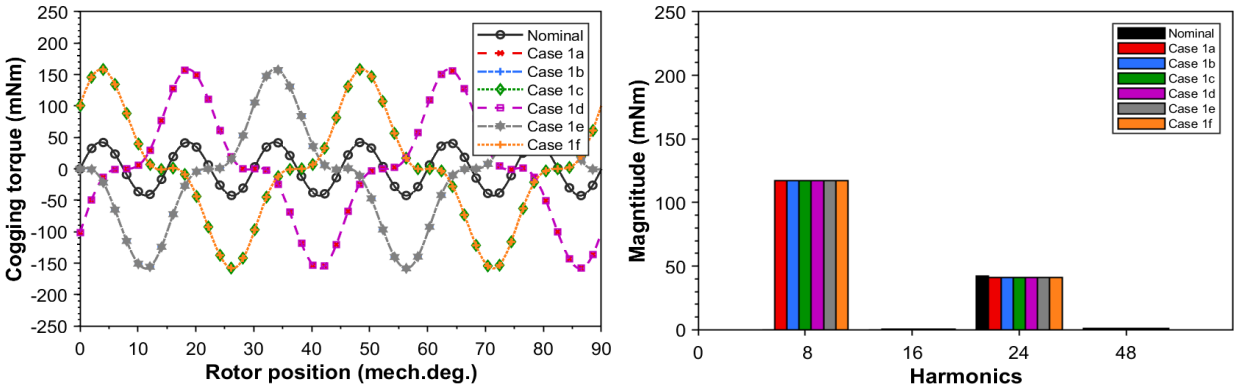

(a) 12-slot/10-pole



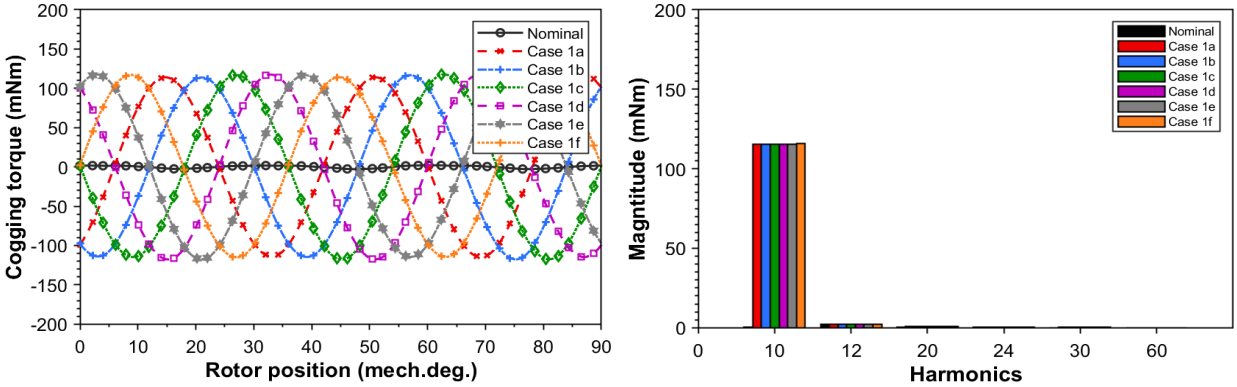

(c) 12-slot/14-pole

Fig. 6.39. Simplified SPM stator geometry including worst-case scenario tolerances in a 180° segment.

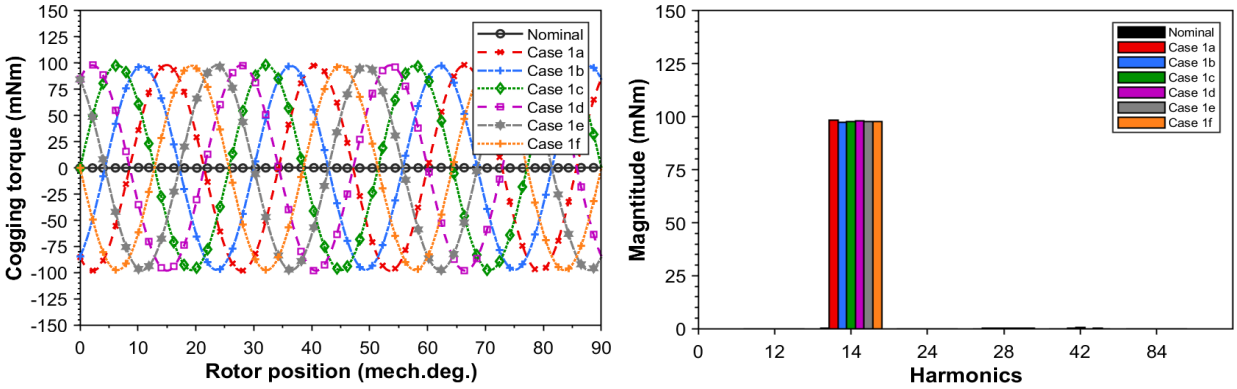
The cogging torque waveforms and harmonics of the worst-case scenarios of the SPM motors under investigation are shown in Fig. 6.40. The maximum peak-to-peak cogging torques of the 12-slot/8-pole, 12-slot/10-pole, and 12-slot/14-pole SPM motors are 316.6 mNm, 236.0 mNm, and 196.4 mNm, respectively. The peak-to-peak cogging torques of the 12-slot/10-pole and 12-slot/14-pole vary by up to 1 mNm and 2.1 mNm, respectively. The variation in peak-to-peak cogging torque in sub-cases Case1a to e is attributed to superposition of the nominal cogging torque and cogging torque AHCs as well as numerical noise.




(a) 12-slot/8-pole




(b) 12-slot/10-pole



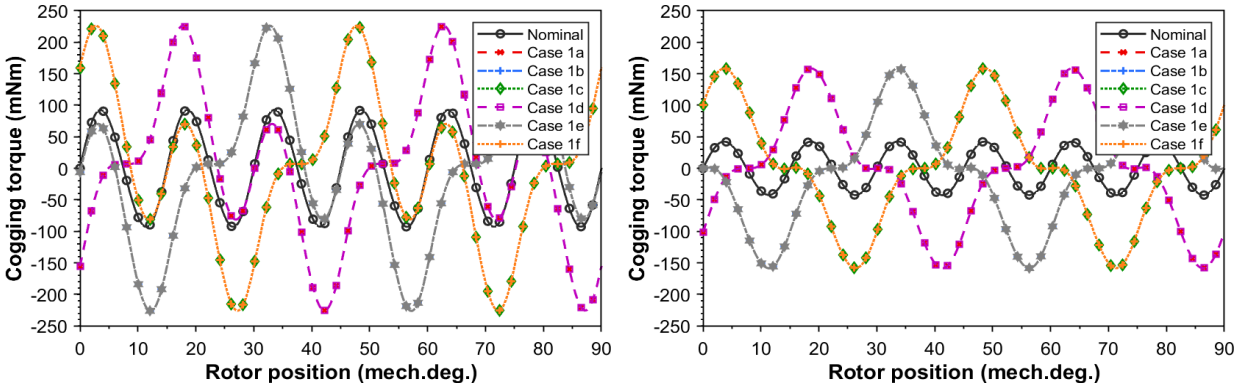

(c) 12-slot/14-pole

(I) Waveforms (II) Harmonics

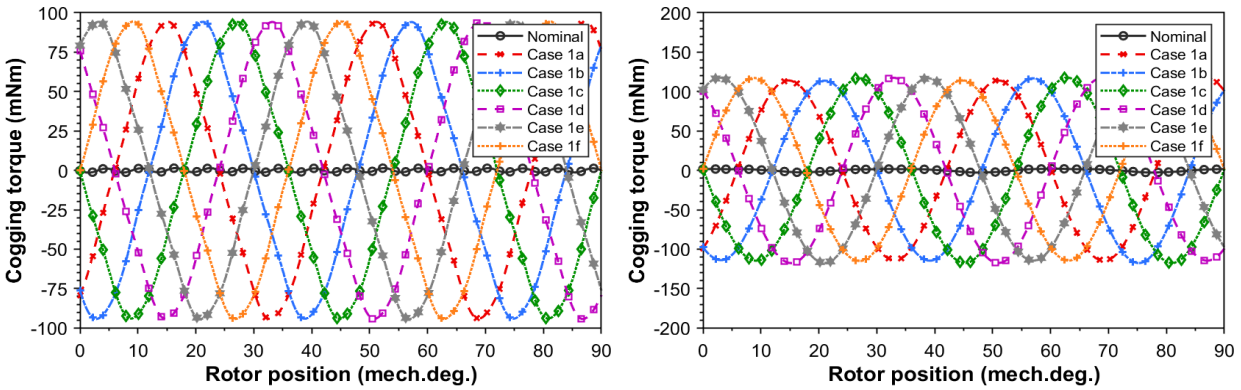
Fig. 6.40. Waveforms and harmonics of cogging torque due to worst-case scenarios of stator tolerances in SPM motors.

## 6.5 Comparison of Cogging Torque Worst-Case Scenarios Due to Stator Tolerances only in IPM and SPM motors

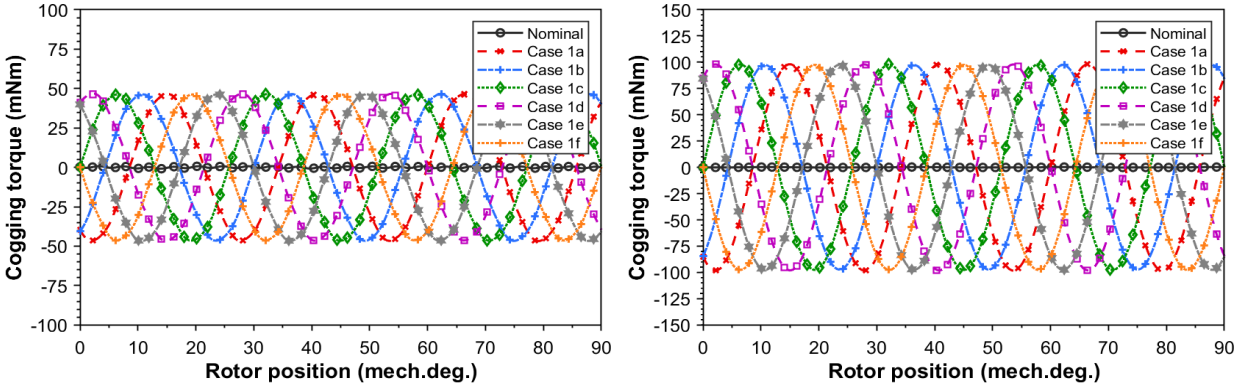
Cogging torque waveforms and harmonics due to the worst-cases of rotor tolerances in the analysed IPM and SPM motors are shown in Fig. 6.41 and Fig. 6.42, respectively.




(a) 12-slot/8-pole




(b) 12-slot/10-pole

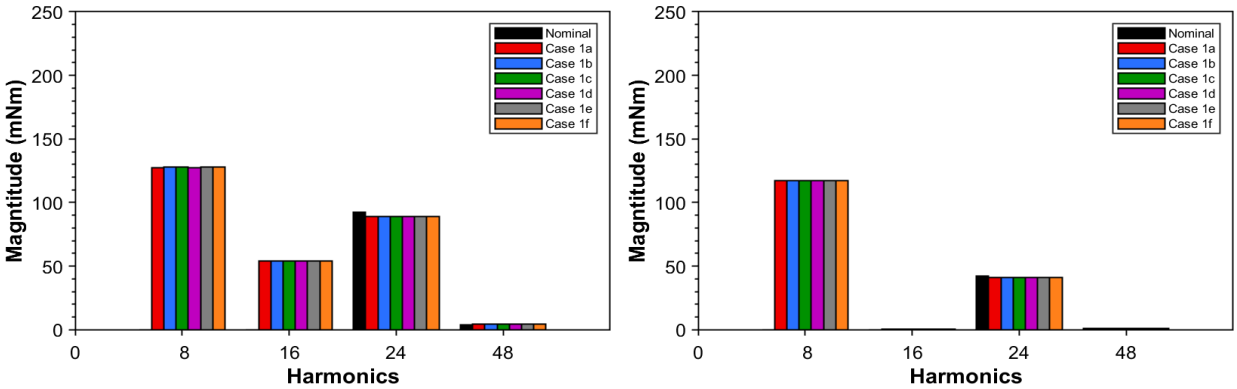



(c) 12-slot/14-pole

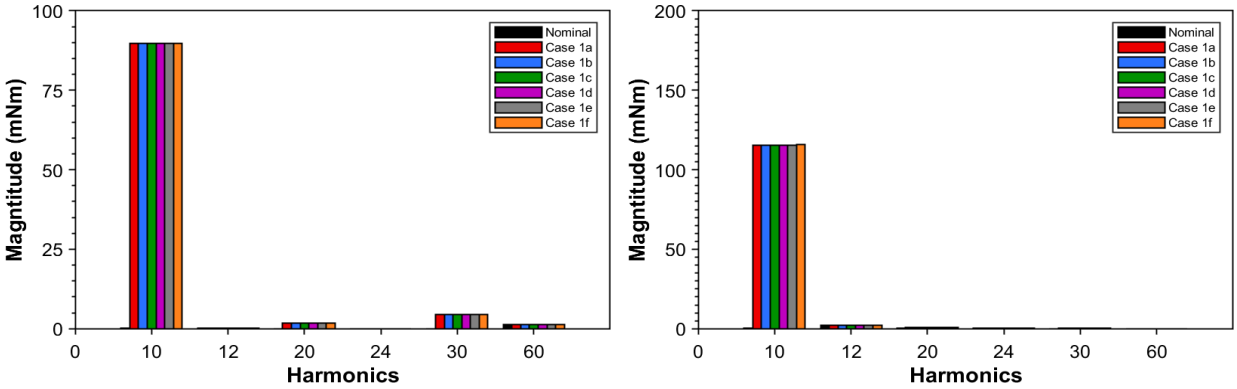
(I) IPM (II) SPM

Fig. 6.41. Cogging torque waveforms due to worst-case scenarios of stator tolerances in IPM and SPM motors.

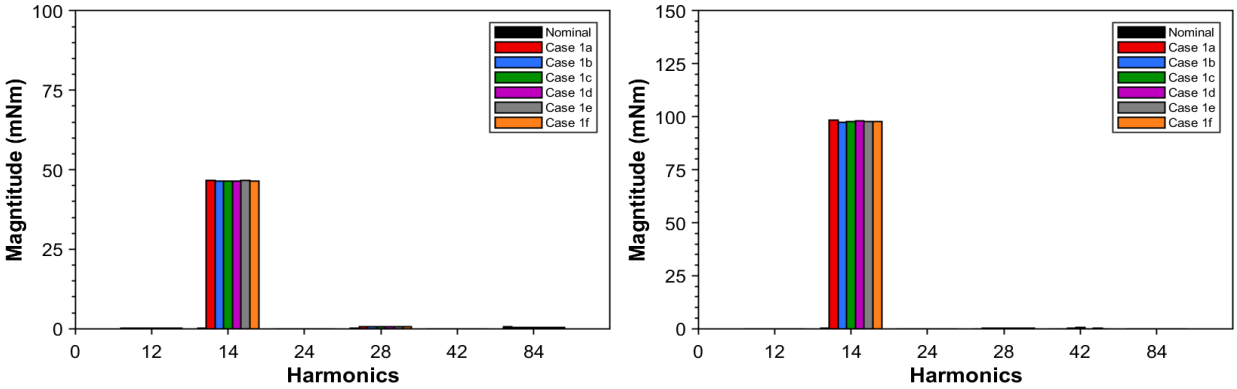
The peak-to-peak cogging torque of the IPM motors due to worst-case scenarios of stator tolerances decreases significantly with increasing rotor pole number. The peak to peak cogging torque of the 12-slot/8-pole SPM motor is higher than those of the 12-slot/10-pole and 12-slot 14-pole SPM motors. The peak-to-peak cogging torques of the 12-slot/10-pole and 12-slot 14-pole SPM motors are comparable. The cogging torque of the 12-slot/8-pole IPM motor is higher than that of the 12-slot/8-pole SPM motor. The cogging torque of the 12-slot/10-pole SPM motor is higher than that of the 12-slot/10-pole IPM motor. The cogging torque of the 12-slot/14-pole SPM motor is significantly higher than that of the 12-slot/14-pole IPM motor.




(a) 12-slot/8-pole




(b) 12-slot/10-pole




(c) 12-slot/14-pole

(I) IPM (II) SPM

Fig. 6.42. Cogging torque harmonics due to worst-case scenarios of stator tolerances in IPM and SPM motors.

## 6.6 Investigation of Worst-Case Scenario of Cogging Torque Due to Rotor Tolerances in IPM motors

### 6.6.1 Worst-Case Scenarios of Cogging Torque of 12-slot/8-pole IPM Motor

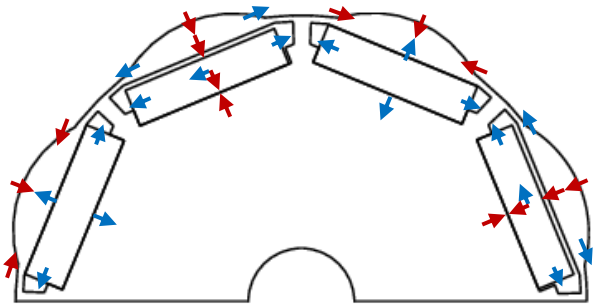
The worst-case scenarios of cogging torque due to rotor tolerances are Case 1 and Case 2. The worst-case scenarios are composed of two sub-cases, e.g. Case 1a and Case 1b, in which the tolerances are shifted by 0 to 1 pole pitch, respectively. The direction of the tolerances in poles 1 and 2 resulting in worst-case scenarios Cases 1 and 2 are indicated in Table 6.7. The 12-slot/8-pole motor has a geometrical symmetry of four therefore the AHCs due to tolerances in a particular direction separated by an angle of 90° are identical. The arrows indicate an increase, decrease, or shift of each of the considered tolerances. Furthermore, blue and red arrows indicate positive and negative tolerances, respectively, for easier interpretation.

Case 1 and Case 2 are identical except for the direction of the tolerance in the PM lateral position. The magnitude of the cogging torque AHCs due to tolerances in the PM lateral position is dependent on the magnitude and direction of the tolerance, however, the influence of the tolerance direction is low.

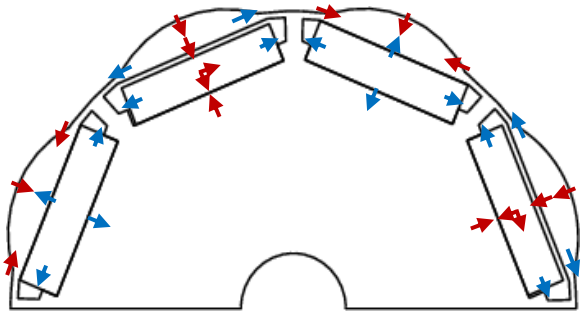
Table 6.7. Directions of tolerances in worst-case scenarios of cogging torque due to rotor tolerances in 12-slot/8-pole IPM motor

| | **Case 1a** | | **Case 1b** | | **Case 2a** | | **Case 2b** | |
|---|---|---|---|---|---|---|---|---|
| **Tolerances** | **Pole 1** | **Pole 2** | **Pole 1** | **Pole 2** | **Pole 1** | **Pole 2** | **Pole 1** | **Pole 2** |
| Pole-shoe height | ▼ | ▲ | ▲ | ▼ | ▼ | ▲ | ▲ | ▼ |
| Pole-shoe width | ▲ | ▼ | ▼ | ▲ | ▲ | ▼ | ▼ | ▲ |
| Cavity size | ▲ | ▼ | ▼ | ▲ | ▲ | ▼ | ▼ | ▲ |
| PM remanence | ▼ | ▲ | ▲ | ▼ | ▼ | ▲ | ▲ | ▼ |
| PM height | ▼ | ▲ | ▲ | ▼ | ▼ | ▲ | ▲ | ▼ |
| PM width | ▲ | ▲ | ▲ | ▲ | ▲ | ▲ | ▲ | ▲ |
| PM radial shift | ▼ | N/A | N/A | ▼ | ▼ | N/A | N/A | ▼ |
| PM lateral shift | ◄ | N/A | N/A | ◄ | ► | N/A | N/A | ► |
| Rib width | ▼ | ▲ | ▲ | ▼ | ▼ | ▲ | ▲ | ▼ |

The sensitivity analysis of the rotor tolerances shows that tolerances in adjacent poles in the same direction result in out-of-phase AHCs. Conversely, tolerances in adjacent poles in opposite directions result in AHCs with the same phase resulting in an additive effect. Thus, the worst-case scenarios are composed of tolerances in adjacent poles in opposing directions. A negative tolerance in the cavity size and positive tolerance in the PM height and width results in no room for PM radial or lateral displacement.



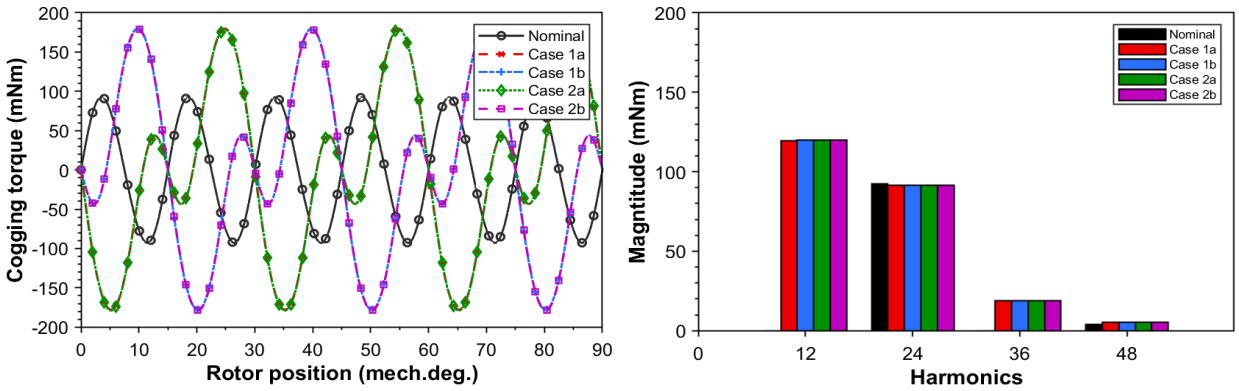
(a) 12-slot/8-pole Case 1a



(b) 12-slot/8-pole Case 2a

Fig. 6.43. Worst-case scenario tolerances in a 180° segment of 12-slot/8-pole IPM motor.

The cogging torque waveforms and harmonics of the four worst-case scenarios of the 12-slot/8-pole IPM motor are shown in Fig. 6.44. The peak-to-peak cogging torques of the four worst-case scenarios are all 357.6 mNm.




(a) Waveforms (b) Harmonics

Fig. 6.44. Waveforms and harmonics of cogging torque of 12-slot/8-pole IPM motor due to worst-case scenarios of rotor tolerances.

### 6.6.2 Worst-Case Scenarios of Cogging Torque of 12-slot/10-pole IPM Motor

The directions of the tolerances in poles 1 to 5 attributed to the worst-case scenario (Case 1) are indicated in Table 6.8. The 12-slot/10-pole motor has a symmetry of two and therefore the effect of tolerances separated by an angle of 180° is identical. Thus, tolerances in poles 6 to 10 are identical to tolerances in poles 1 to 5, respectively. Tolerances due to the worst-case scenario are indicated in a simplified IPM rotor geometry in Fig. 6.45. Tolerances due to the worst-case scenario are symmetrical about pole 3 resulting in identical tolerances in poles 1 and 5 and in poles 2 and 4.

Table 6.8. Directions of tolerances in worst-case scenario (Case 1) of cogging torque due to rotor tolerances in 12-slot/10-pole IPM motor

| **Tolerances** | **Pole 1** | **Pole 2** | **Pole 3** | **Pole 4** | **Pole 5** |
|---|---|---|---|---|---|
| Pole-shoe height | ▼ | ▲ | ▲ | ▲ | ▼ |
| Pole-shoe width | ▲ | ▼ | ▼ | ▼ | ▲ |
| Cavity size | ▼ | ▲ | ▼ | ▲ | ▼ |
| PM remanence | ▼ | ▲ | ▲ | ▲ | ▼ |
| PM height | ▼ | ▲ | ▲ | ▲ | ▼ |
| PM width | ▼ | ▲ | ▲ | ▲ | ▼ |
| PM radial shift | ▼ | ▲ | N/A | ▲ | ▼ |
| PM lateral shift | ► | ◄ | N/A | ► | ◄ |
| Rib width | ▲ | ▲ | ▼ | ▲ | ▲ |

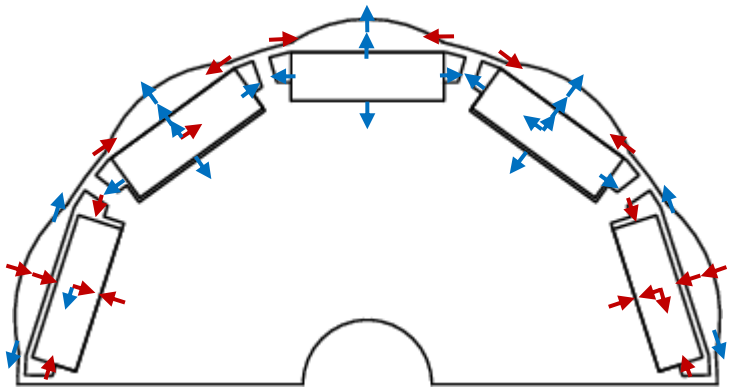
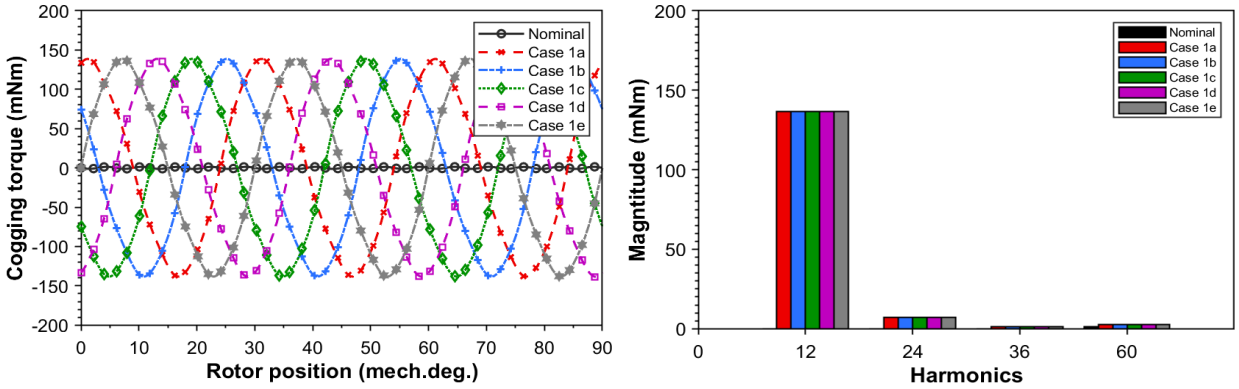


Fig. 6.45. Worst-case scenario of tolerances in 12-slot/10-pole IPM motor.

The 12-slot/10-pole motor has a symmetry of two and therefore the five sub-cases of the identified worst-case scenario are analysed for completeness. The cogging torque waveforms and harmonics of the sub-cases in which the tolerances are shifted by 0 to 4 pole pitches, respectively, are shown in Fig. 6.46.

The maximum peak-to-peak cogging torque of the worst-case scenarios is 277.2 mNm and the maximum cogging torque variation between sub-cases is 0.3 mNm. The cogging torque of the worst-case scenarios is the resultant of the superposition of the nominal cogging torque and the cogging torque AHCs due to tolerances. Therefore, the peak-to-peak cogging torque is dependent on the phase of individual cogging torque harmonics. Furthermore, numerical noise may contribute to the slight difference in peak-to-peak cogging toque of the sub-cases of the worst-case scenario.




(a) Waveforms (b) Harmonics

Fig. 6.46. Waveforms and harmonics of the cogging torque of the 12-slot/10-pole IPM motor due to sub-cases of worst-case scenario.

## 6.6.3 Worst-Case Scenarios of Cogging Torque of 12-slot/14-pole IPM Motor

The directions of the tolerances in poles 1 to 7 attributed to the worst-case scenario (Case 1) are indicated in Table 6.9. The 12-slot/14-pole motor has a symmetry of two and therefore the effect of tolerances separated by an angle of 180° is identical. Thus, tolerances in pole 8 to 14 are identical to tolerances in pole 1 to 7, respectively. Tolerances due to the worst-case scenario are indicated in a simplified IPM rotor geometry in Fig. 6.47. All tolerances in poles 1 to 3, other than tolerances in cavity size and PM lateral position, are in the opposite direction of the respective tolerances in poles 4 to 7.

The cogging torque waveforms and harmonics of the worst-case scenarios are shown in Fig. 6.48. The maximum peak-to-peak cogging torque of the worst-case scenarios is 382.5 mNm and the maximum variation of the peak-to-peak cogging torque between sub-cases is 0.6 mNm.

Table 6.9. Directions of tolerances in worst-case scenario (Case 1) of cogging torque due to rotor tolerances in 12-slot/14-pole IPM motor

| Tolerances | Pole 1 | Pole 2 | Pole 3 | Pole 4 | Pole 5 | Pole 6 | Pole 7 |
|---|---|---|---|---|---|---|---|
| Pole-shoe height | ▼ | ▼ | ▼ | ▲ | ▲ | ▲ | ▲ |
| Pole-shoe width | ▲ | ▲ | ▲ | ▼ | ▼ | ▼ | ▼ |
| Cavity size | ▲ | ▲ | ▲ | ▲ | ▲ | ▲ | ▲ |
| PM remanence | ▼ | ▼ | ▼ | ▲ | ▲ | ▲ | ▲ |
| PM height | ▼ | ▼ | ▼ | ▲ | ▲ | ▲ | ▲ |
| PM width | ▼ | ▼ | ▼ | ▲ | ▲ | ▲ | ▲ |
| PM radial shift | ▼ | ▼ | ▼ | ▲ | ▲ | ▲ | ▲ |
| PM lateral shift | ◀ | ▶ | ◀ | ▶ | ▶ | ◀ | ◀ |
| Rib width | ▲ | ▲ | ▲ | ▼ | ▼ | ▼ | ▼ |

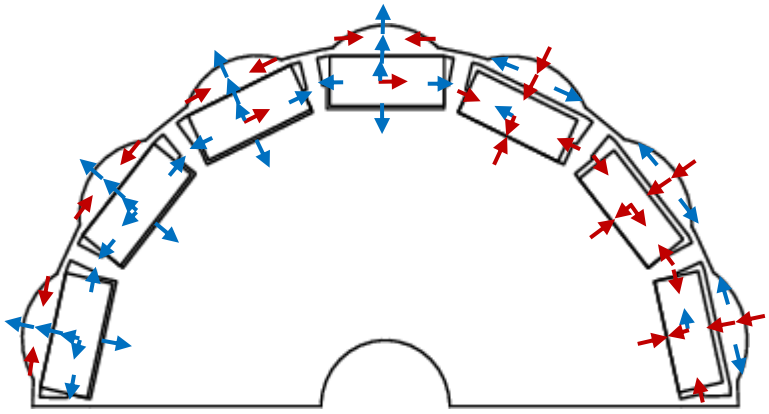
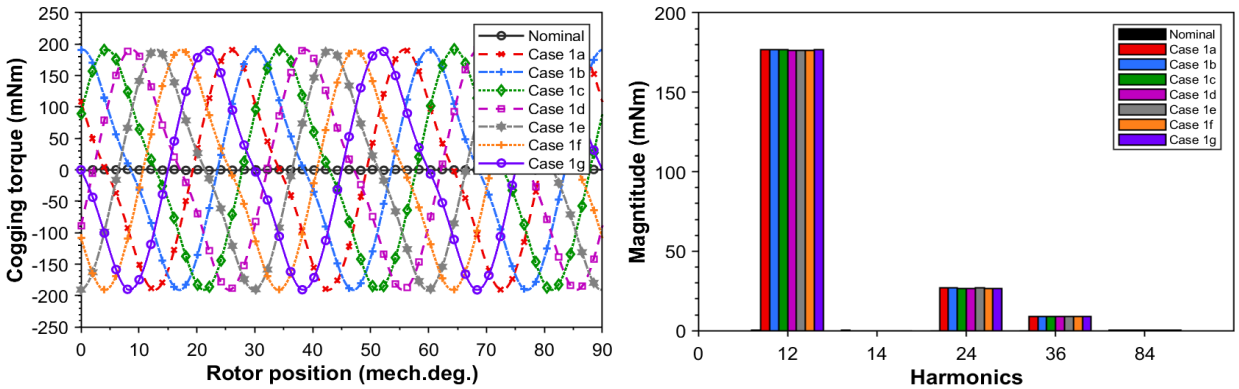


Fig. 6.47. Worst-case scenario of tolerances in 12-slot/14-pole IPM motor.




(a) Waveforms (b) Harmonics

Fig. 6.48. Waveforms and harmonics of the cogging torque of the 12-slot/14-pole IPM motor due to sub-cases of worst-case scenario.

## 6.7 Investigation of Worst-Case Scenario of Cogging Torque Due to Rotor Tolerances in SPM motors

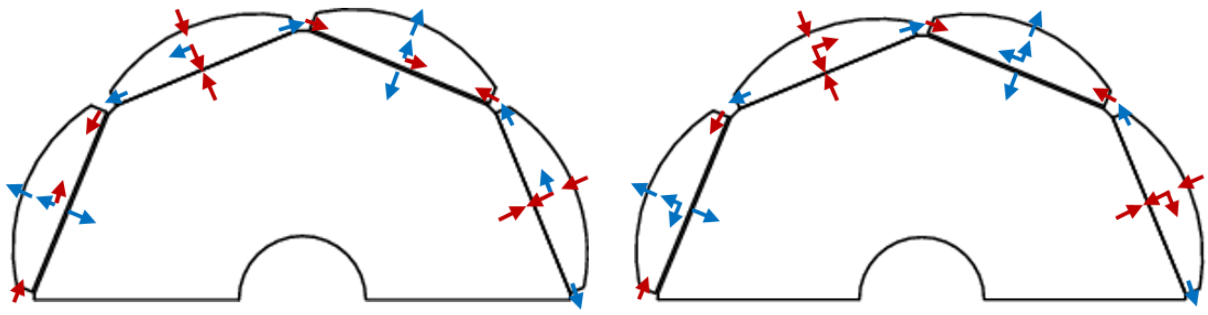
### 6.7.1 Worst-Case Scenarios of Cogging Torque of 12-slot/8-pole SPM Motor

The global search algorithm converges to two worst-case scenarios, Cases 1 and 2, in which the directions of all the considered tolerances are identical, however, the direction of the tolerance in the lateral displacement of the PMs is reversed. Influence of PM polarity and the considered tolerances of the worst-cases on the magnitude of the AHCs due to the worst-case tolerances in lateral PM displacement is very low.

The worst-case scenarios are composed of two sub-cases, e.g. Case 1a and Case 1b, in which the tolerances are shifted by 0 to 1 pole pitch, respectively. The 12-slot/8-pole motor has a geometrical symmetry of four and therefore the AHCs due to tolerances in a particular direction separated by an angle of 90° are identical. The directions of the tolerances in poles 1 and 2 resulting in worst-case scenarios Cases 1 and 2 are indicated in Table 6.10. The arrows indicate an increase, decrease, or shift of each of the considered tolerances. Furthermore, blue and red arrows indicate positive and negative tolerances, respectively, for easier interpretation.

The worst-case scenarios comprise a positive tolerance in the rotor sleeve profile. This tolerance does not result in any asymmetry or cogging torque AHCs but allows for a higher possible displacement of the PMs from the nominal position.

The tolerances resulting in the worst-case scenarios Cases 1 and 2, and the corresponding sub-cases are indicated in a simplified SPM rotor geometry in Fig. 6.49 shows a 180° segment of the rotor geometry, for simplicity. Tolerances in the opposite 180° segment are identical due to rotational symmetry.



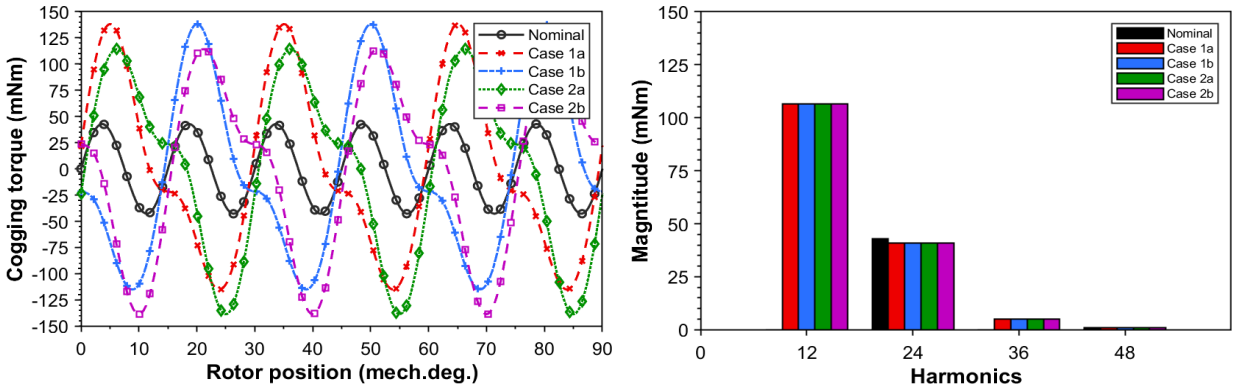
(a) 12-slot/8-pole Case 1a (b) 12-slot/8-pole Case 2a

Fig. 6.49. Worst-case scenario tolerances in a 180° segment of 12-slot/8-pole SPM motor.

Table 6.10. Directions of tolerances in worst-case scenarios of cogging torque due to rotor tolerances in 12-slot/8-pole SPM motor

| Tolerances | Case 1a | | Case 1b | | Case 2a | | Case 2b | |
|---|---|---|---|---|---|---|---|---|
| | Pole 1 | Pole 2 | Pole 1 | Pole 2 | Pole 1 | Pole 2 | Pole 1 | Pole 2 |
| PM remanence | ▼ | ▲ | ▲ | ▼ | ▼ | ▲ | ▲ | ▼ |
| PM height | ▼ | ▲ | ▲ | ▼ | ▼ | ▲ | ▲ | ▼ |
| PM width | ▲ | ▼ | ▼ | ▲ | ▲ | ▼ | ▼ | ▲ |
| PM pole-shoe height | ▲ | ▼ | ▼ | ▲ | ▲ | ▼ | ▼ | ▲ |
| PM radial shift | ▼ | ▲ | ▲ | ▼ | ▼ | ▲ | ▲ | ▼ |
| PM lateral shift | ◀ | ▶ | ▶ | ◀ | ▶ | ◀ | ◀ | ▶ |
| Rotor iron profile | N/A | N/A | N/A | N/A | N/A | N/A | N/A | N/A |
| Rotor sleeve profile | ▲ | ▲ | ▲ | ▲ | ▲ | ▲ | ▲ | ▲ |

The cogging torque waveforms and harmonics of the four worst-case scenarios of the 12-slot/8-pole SPM motor are shown in Fig. 6.50. The difference in magnitudes of the cogging torque harmonics of the four cases is negligible. The magnitude of the 24$^{th}$ order harmonic of the worst-case scenarios is slightly lower that the nominal magnitude and this is attributed to the difference in PM volume, remanence, and position due to rotor tolerances.




(a) Waveforms (b) Harmonics

Fig. 6.50. Waveforms and harmonics of cogging torque of 12-slot/8-pole SPM motor due to worst-case scenarios of rotor tolerances.

## 6.7.2 Worst-Case Scenarios of Cogging Torque of 12-slot/10-pole SPM Motor

The direction of the tolerances in poles 1 to 5 attributed to the worst-case scenario (Case 1) is indicated in Table 6.11. The 12-slot/10-pole motor has a symmetry of two and therefore the effect of tolerances separated by an angle of 180° is identical. Thus, tolerances in pole 6 to 10 are identical to tolerances in poles 1 to 5, respectively. Tolerances due to the worst-case scenario are indicated in a simplified SPM rotor geometry in Fig. 6.51. Tolerances due to the worst-case scenario are symmetric about pole 3 resulting in identical tolerances in poles 1 and 5 and in poles 2 and 4.

Table 6.11. Directions of tolerances in worst-case scenario (Case 1) of cogging torque due to rotor tolerances in 12-slot/10-pole SPM motor

| **Tolerances** | **Pole 1** | **Pole 2** | **Pole 3** | **Pole 4** | **Pole 5** |
|---|---|---|---|---|---|
| PM remanence | ▼ | ▲ | ▲ | ▲ | ▼ |
| PM height | ▼ | ▲ | ▲ | ▲ | ▼ |
| PM width | ▲ | ▼ | ▼ | ▼ | ▲ |
| PM pole-shoe height | ▲ | ▼ | ▼ | ▼ | ▲ |
| PM radial shift | ▼ | ▲ | ▲ | ▲ | ▼ |
| PM lateral shift | ◄ | ◄ | N/A | ► | ► |
| Rotor iron profile | ▼ | ▼ | ▼ | ▼ | ▼ |
| Rotor sleeve profile | ▲ | ▲ | ▲ | ▲ | ▲ |

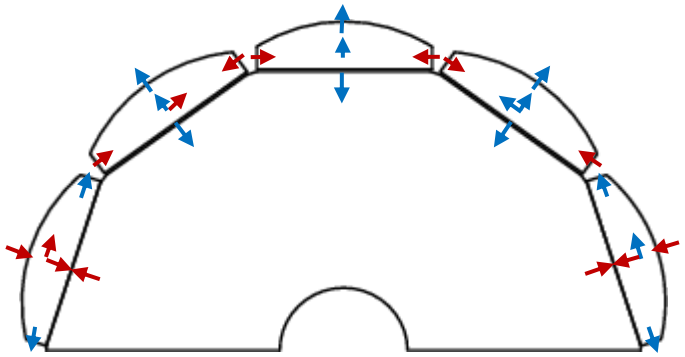
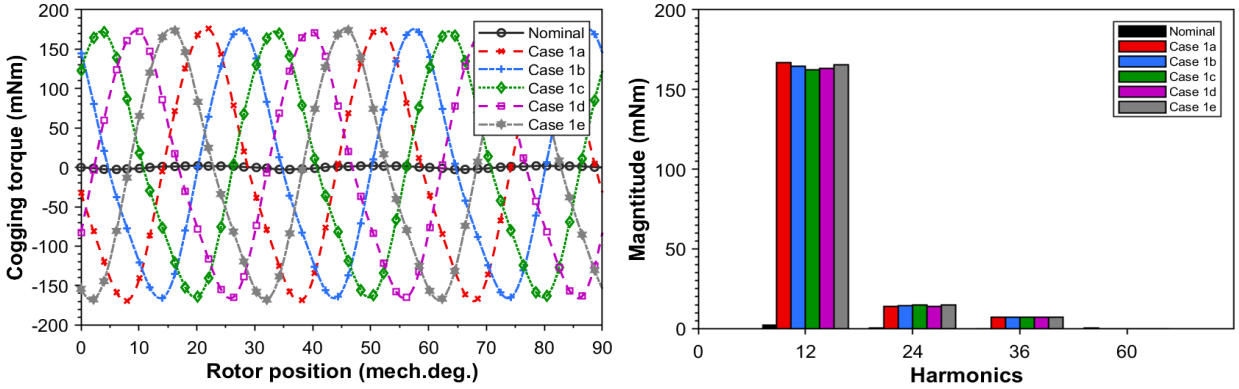


Fig. 6.51. Worst-case scenario tolerances in a 180° segment of a 12-slot/10-pole SPM motor.

The 12-slot/10-pole motor has a symmetry of two and therefore the five sub-cases of the identified worst-case scenario are analysed for completeness. The cogging torque waveforms and harmonics of the sub-cases in which the tolerances are shifted by 0 to 4 pole pitches, respectively, are shown in Fig. 6.52.

The peak-to-peak cogging of the worst-case scenario is 346.7 mNm. The magnitudes of the resultant AHCs

vary with each sub-case since the phases of the individual AHCs depend on the location of the poles affected by a specific tolerance. Consequently, the peak-to-peak cogging torque of the sub-cases varies by up to 9.3 mNm. Case 1a results in the highest peak-to-peak cogging torque and is the worst-case scenario of rotor tolerances in the 12-slot/10-pole SPM motor under investigation.




(a) Waveforms (b) Harmonics

Fig. 6.52. Waveforms and harmonics of the cogging torque of the 12-slot/10-pole SPM motor due to sub-cases of worst-case scenario.

## 6.7.3 Worst-Case Scenarios of Cogging Torque of 12-slot/14-pole SPM Motor

The directions of the tolerances in poles 1 to 5 attributed to the worst-case scenario (Case 1) are indicated in Table 6.11. The 12-slot/14-pole motor has a symmetry of two and therefore the effect of tolerances separated by an angle of 180° is identical. Thus, tolerances in pole 6 to 10 are identical to tolerances in pole 1 to 5, respectively. Tolerances due to the worst-case scenario are indicated in a simplified SPM rotor geometry in Fig. 6.53. Tolerances in PM remanence, PM height, PM width and PM radial shift are in the same direction in every pole. Tolerance in the rotor iron profile is at the nominal value and the tolerance in rotor sleeve profile is positive, thus allowing a higher PM radial displacement. Tolerances in the PM lateral position in pole 1 and pole 3 have opposite directions. Similarly, tolerances in the PM lateral position in poles 4 and 5 are opposite the respective tolerances in poles 6 and 7. Tolerances in the PM pole-shoe height in poles 1 to 3 are identical to tolerances in poles 5 and 6 and opposite tolerances in poles 4 and 7.

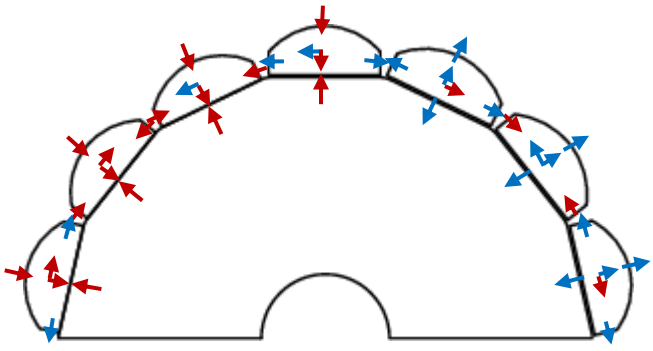
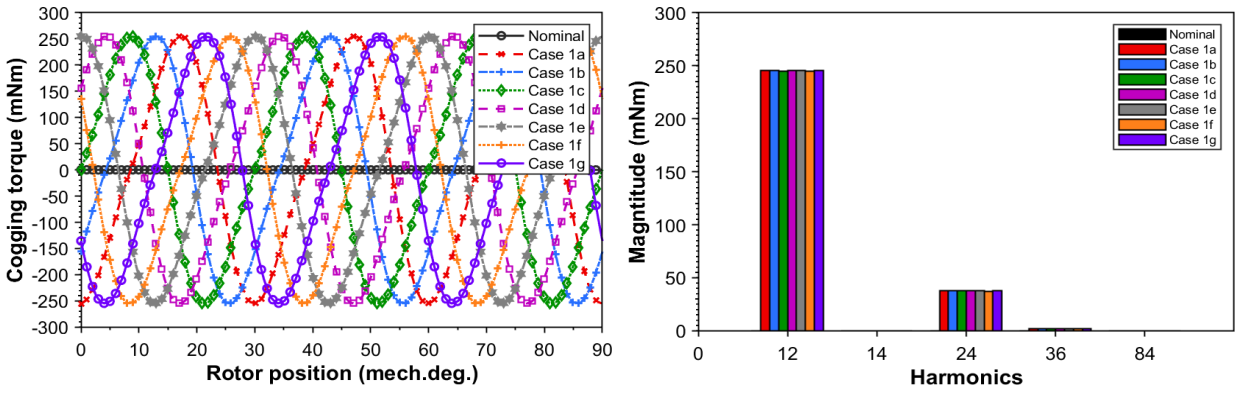


Fig. 6.53. Worst-case scenario tolerances in a 180° segment of a 12-slot/14-pole SPM motor.

Table 6.12. Directions of tolerances in worst-case scenario (Case 1) of cogging torque due to rotor tolerances in 12-slot/14-pole SPM motor

| Tolerances | Pole 1 | Pole 2 | Pole 3 | Pole 4 | Pole 5 | Pole 6 | Pole 7 |
|---|---|---|---|---|---|---|---|
| PM remanence | ▲ | ▲ | ▲ | ▼ | ▼ | ▼ | ▼ |
| PM height | ▲ | ▲ | ▲ | ▼ | ▼ | ▼ | ▼ |
| PM width | ▲ | ▼ | ▲ | ▲ | ▼ | ▼ | ▲ |
| PM pole-shoe height | ▲ | ▼ | ▲ | ▲ | ▼ | ▼ | ▲ |
| PM radial shift | ▲ | ▲ | ▲ | ▼ | ▼ | ▼ | ▼ |
| PM lateral shift | ▶ | ◀ | ◀ | ◀ | ◀ | ▶ | ▶ |
| Rotor iron profile | ▼ | ▼ | ▼ | ▼ | ▼ | ▼ | ▼ |
| Rotor sleeve profile | ▲ | ▲ | ▲ | ▲ | ▲ | ▲ | ▲ |

The 12-slot/14-pole motor has a symmetry of two and therefore the seven sub-cases of the identified worst-case scenario are analysed for completeness. The cogging torque waveforms and harmonics of the sub-cases in which the tolerances are shifted by 0 to 6 pole pitches, respectively, are shown in Fig. 6.54. The maximum peak-to-peak cogging torque is 513.6 mNm. The peak-to-peak cogging torque of the 7 sub-cases varies by up to 0.1 mNm, which can be attributed to numerical noise. Thus, Cases 1a to 1g are the worst-case scenarios of the cogging torque of the 12-slot/14-pole SPM motor under investigation.

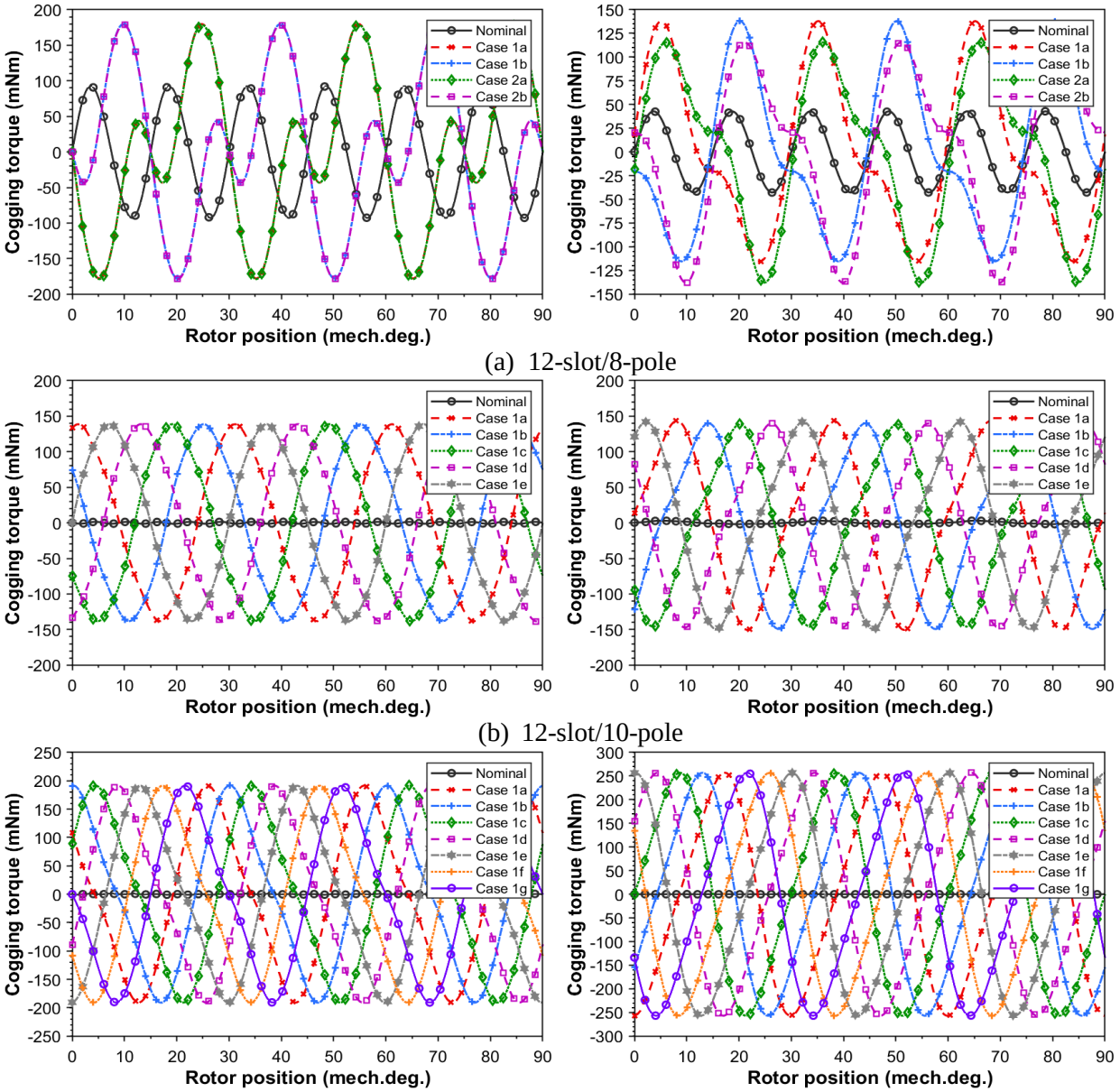



(a) Waveforms (b) Harmonics

Fig. 6.54. Waveforms and harmonics of the cogging torque of the 12-slot/14-pole SPM motor due to sub-cases of worst-case scenario.

## 6.8 Comparison of Cogging Torque Worst-Case Scenarios Due to Rotor Tolerances only in IPM and SPM motors

Cogging torque waveforms and harmonics due to the worst-cases of rotor tolerances in the analysed IPM and SPM motors are shown in Fig. 6.55 and Fig. 6.56, respectively.



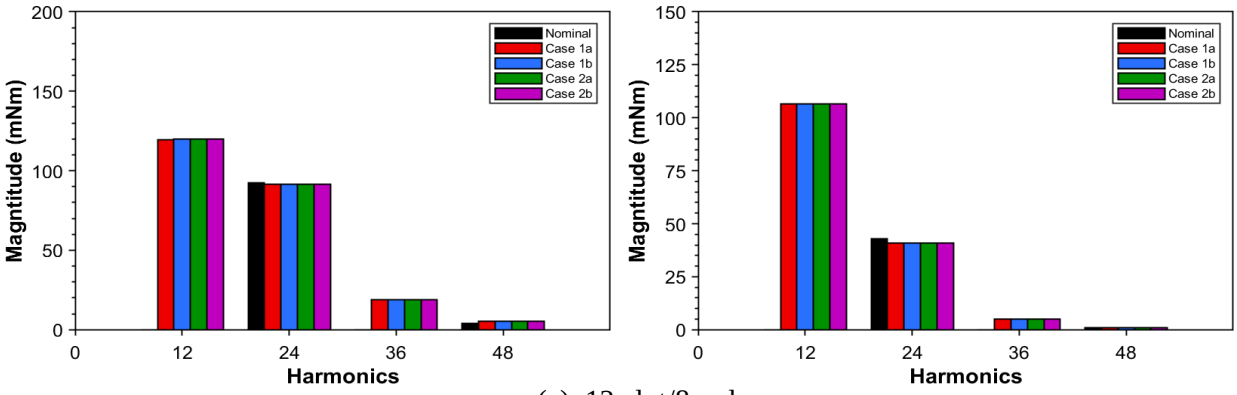

(a) 12-slot/8-pole

(b) 12-slot/10-pole

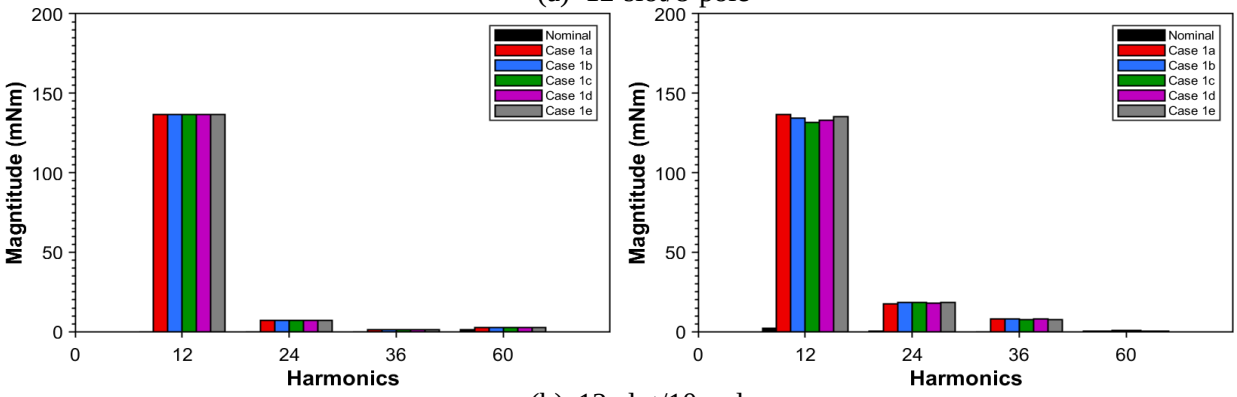
(c) 12-slot/14-pole

(I) IPM (II) SPM

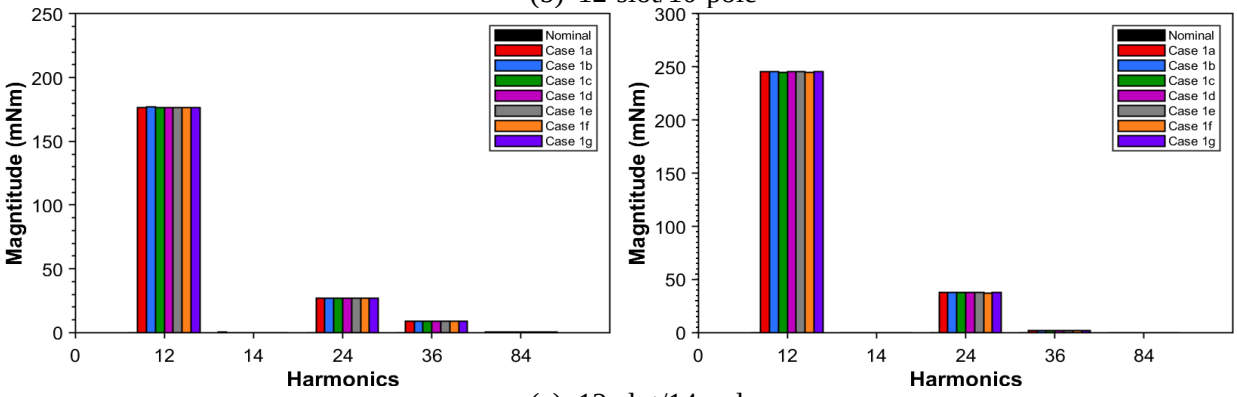
Fig. 6.55. Cogging torque waveforms due to worst-case scenarios of rotor tolerances in PM motors.




(a) 12-slot/8-pole




(b) 12-slot/10-pole




(c) 12-slot/14-pole

(I) IPM (II) SPM

Fig. 6.56. Cogging torque harmonics due to worst-case scenarios of rotor tolerances in PM motors.

The magnitude of the 12$^{th}$ order cogging torque component increases with increasing rotor pole number. This is expected since a higher rotor pole number results in an increased number of possible rotor tolerances, which in turn leads to cogging torque AHCs.

The peak-to-peak cogging torque of the 12-slot/8-pole IPM motor is higher than that of the 12-slot/8-pole SPM motor despite the lower magnitude of the 12$^{th}$ order cogging torque component. This is due to the fact that the nominal cogging torque of the IPM motor is higher than that of the SPM motor under investigation. The 12-slot/10-pole motors have similar magnitude of the 12$^{th}$ order cogging torque component and very low nominal cogging torque, thus resulting in similar peak-to-peak cogging torque.

The 24th and 36th order cogging torque components of the 12-slot/10-pole SPM motor are higher than those of the 12-slot/10-pole IPM motor. The 12th order cogging torque component of the 12-slot/14-pole SPM motor is higher than that of the 12-slot/14-pole IPM motor. Consequently, the peak-to-peak cogging torque of the 12-slot/14-pole SPM motor is higher than that of the 12-slot/14-pole IPM motor.

## 6.9 Investigation of Worst-Case Scenario of Cogging Torque Due to Combined Stator and Rotor Tolerances in IPM motors

### 6.9.1 Worst-Case Scenarios of Cogging Torque of 12-slot/8-pole IPM Motor

The worst-case scenario of cogging torque of the 12-slot/ 8-pole IPM motor due to combined stator and rotor tolerances under investigation is identified using the global search algorithm. The cross-section of the motor including the worst-case scenario tolerances is shown in Fig. 6.57.

The directions of the tolerances in the stator and rotor are listed in Table 6.13 and Table 6.14, respectively. The arrows indicate an increase, or a decrease, or a shift of each of the considered tolerances. Furthermore, blue and red arrows indicate positive and negative tolerances, respectively. The directions of the stator and rotor tolerances are indicated graphically in Fig. 6.58 and Fig. 6.59, respectively. The phases of cogging torque AHCs due to tolerances in a motor dimension separated by an angle of 90° are identical in a 12-slot/8-pole motor. For instance, the directions of tolerances in teeth 1, 4, 7, and 10 resulting in the worst-case scenario are identical. Similarly, the directions of tolerances in poles 1, 3, 5, and 7 resulting in the worst-case scenario are identical

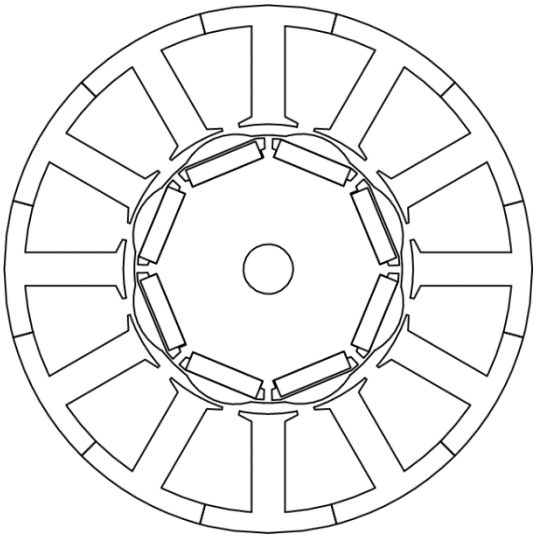


Fig. 6.57. Worst-case scenario tolerances in a 180° segment of 12-slot/8-pole IPM motor.

The directions of the stator tolerances in the tooth-tip height, tooth-tip width, and tooth profile radial position of the worst-case scenario of any given tooth are identical. The worst-case scenario results in four orthogonal tolerances towards the air-gap and four orthogonal sets of two adjacent tolerances towards the stator back iron.

Tolerances in the PM height, PM remanence, PM radial shift, pole-shoe height and rib-width of a particular rotor pole are in the same direction. Similarly, tolerances in the cavity size and pole-shoe width of a particular rotor pole are in the same direction and opposite to that of the aforementioned tolerances. Tolerances in the PM width of all rotor poles are positive, thus resulting in an increase in PM width. The tolerances in the radial and lateral shifts of the PM of pole 2 are zero since the reduced cavity size and the increased PM dimensions result in no further space in the cavity.

Table 6.13. Directions of stator tolerances in worst-case scenario of cogging torque due to stator and rotor tolerances in 12-slot/8-pole IPM motor

| **Tolerances** | **Tooth 1** | **Tooth 2** | **Tooth 3** | **Tooth 4** | **Tooth 5** | **Tooth 6** |
|---|---|---|---|---|---|---|
| Tooth-tip height | ▼ | ▲ | ▲ | ▼ | ▲ | ▲ |
| Tooth-tip width | ▼ | ▲ | ▲ | ▼ | ▲ | ▲ |
| Tooth profile radial position | ▼ | ▲ | ▲ | ▼ | ▲ | ▲ |

Table 6.14. Directions of rotor tolerances in worst-case scenario of cogging torque due to stator and rotor tolerances in 12-slot/8-pole IPM motor

| **Tolerances** | **Pole 1** | **Pole 2** | **Pole 3** | **Pole 4** |
|---|---|---|---|---|
| Pole-shoe height | ▼ | ▲ | ▼ | ▲ |
| Pole-shoe width | ▲ | ▼ | ▲ | ▼ |
| Cavity size | ▲ | ▼ | ▲ | ▼ |
| PM remanence | ▼ | ▲ | ▼ | ▲ |
| PM height | ▼ | ▲ | ▼ | ▲ |
| PM width | ▲ | ▲ | ▲ | ▲ |
| PM radial shift | ▼ | N/A | ▼ | N/A |
| PM lateral shift | ◀ | N/A | ◀ | N/A |
| Rib width | ▼ | ▲ | ▼ | ▲ |

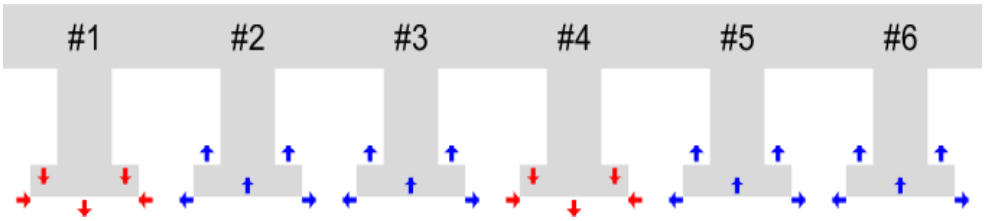



Fig. 6.58. Simplified IPM stator geometry including worst-case scenario tolerances in a 180° segment.

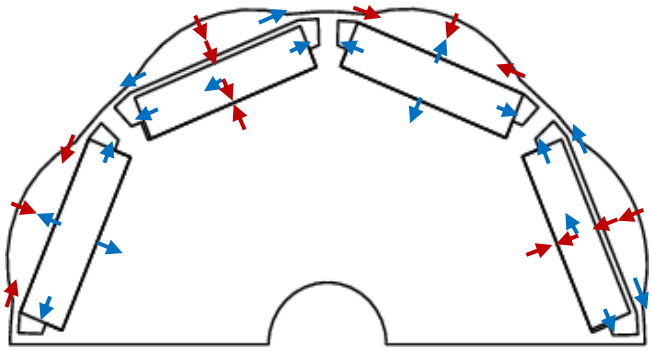
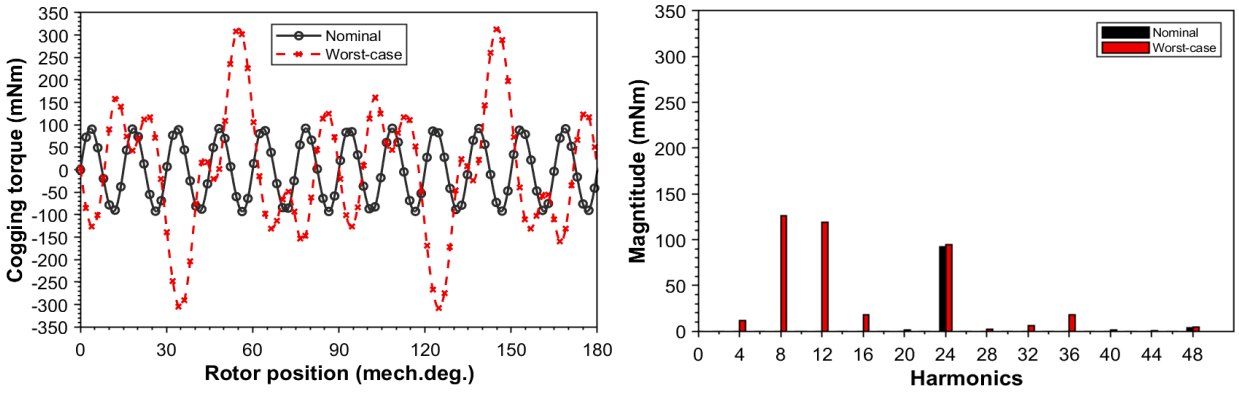


Fig. 6.59. Worst-case scenario tolerances in a 180° segment of 12-slot/8-pole IPM motor.

The cogging torque waveforms and harmonics of the worst-case scenario of the cogging torque of the 12-slot/8-pole IPM motor are shown in Fig. 6.60. The peak-to-peak cogging torque of the worst-case scenario is 622.4 mNm, 335.3% higher than the nominal peak-to-peak cogging torque.

The magnitude of the native 24$^{th}$ and 48$^{th}$ order cogging torque components of the worst-case scenario is 2.2% and 22% higher than the nominal, respectively. Stator tolerances result in the 8$^{th}$ order cogging torque component and its harmonics and rotor tolerances result in the 12$^{th}$ order cogging torque component and its harmonics. The magnitude of the 8$^{th}$ order harmonic component is 5.7% higher than that of the 12$^{th}$ order harmonic component. The interaction of the cogging toque AHCs due to stator and rotor tolerances result in a small magnitude of the 4$^{th}$ order harmonic component due to modulation.




(a) Waveforms (b) Harmonics

Fig. 6.60. Waveforms and harmonics of cogging torque of 12-slot/8-pole IPM motor due to worst-case scenario of stator and rotor tolerances.

### 6.9.2 Worst-Case Scenarios of Cogging Torque of 12-slot/10-pole IPM Motor

The worst-case scenario of cogging torque of the 12-slot/ 10-pole IPM motor due to combined stator and rotor tolerances under investigation is identified and the cross-section of the motor including the worst-case scenario tolerances is shown in Fig. 6.61. The directions of the tolerances in the stator and rotor are listed in Table 6.15 and Table 6.16, respectively. The directions of the stator and rotor tolerances are indicated graphically in Fig. 6.62 and Fig. 6.63, respectively.

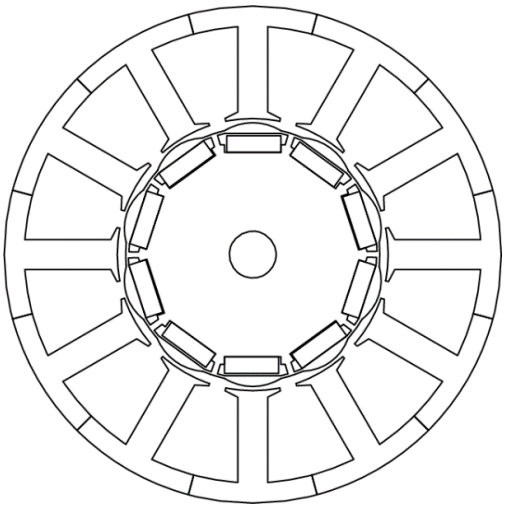


Fig. 6.61. Worst-case scenario tolerances in a 180° segment of 12-slot/10-pole IPM motor.

The directions of worst-case scenario tolerances in the tooth profile radial position and tooth-tip width of a particular tooth are identical. The directions of the aforementioned tolerances in teeth 3, 4 and 5 are identical and opposing the direction of the same tolerances in teeth 6, 7 and 8. Thus, the tolerances form adjacent sets of three teeth and the direction of the tolerances differs between adjacent sets. Tolerances in the tooth-tip height in adjacent teeth are in opposing directions.

Worst-case scenario tolerances in the PM height, PM width, PM radial shift, and pole-shoe height of a given rotor pole are in the same direction. The PM radial and lateral shift of poles 5 and 10 is zero since the decrease in cavity size paired with the increase in PM dimensions results in no room for PM displacement. Tolerances in the pole-shoe width and rib width of any particular rotor pole are in the same direction.

Table 6.15. Directions of stator tolerances in worst-case scenario of cogging torque due to tolerances in 12-slot/10-pole IPM motor

| **Tolerances** | **Tooth 1** | **Tooth 2** | **Tooth 3** | **Tooth 4** | **Tooth 5** | **Tooth 6** |
|---|---|---|---|---|---|---|
| Tooth-tip height | ▼ | ▲ | ▼ | ▲ | ▼ | ▲ |
| Tooth-tip width | ▼ | ▼ | ▲ | ▲ | ▲ | ▼ |
| Tooth profile radial position | ▼ | ▼ | ▲ | ▲ | ▲ | ▼ |

Table 6.16. Directions of rotor tolerances in worst-case scenario of cogging torque due to tolerances in 12-slot/10-pole IPM motor

| Tolerances | Pole 1 | Pole 2 | Pole 3 | Pole 4 | Pole 5 |
|---|---|---|---|---|---|
| Pole-shoe height | ▲ | ▼ | ▼ | ▲ | ▲ |
| Pole-shoe width | ▼ | ▲ | ▲ | ▼ | ▼ |
| Cavity size | ▲ | ▲ | ▲ | ▲ | ▼ |
| PM remanence | ▲ | ▼ | ▼ | ▲ | ▲ |
| PM height | ▲ | ▼ | ▼ | ▲ | ▲ |
| PM width | ▲ | ▼ | ▼ | ▲ | ▲ |
| PM radial shift | ▲ | ▼ | ▼ | ▲ | N/A |
| PM lateral shift | ► | ◄ | ► | ◄ | N/A |
| Rib width | ▲ | ▲ | ▲ | ▲ | ▼ |

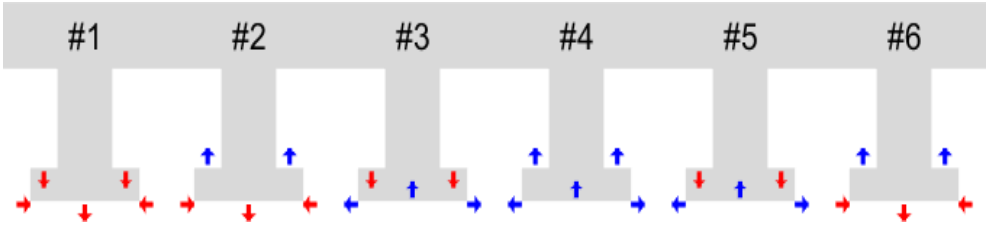



Fig. 6.62. Simplified IPM stator geometry including worst-case scenario tolerances in a 180° segment.

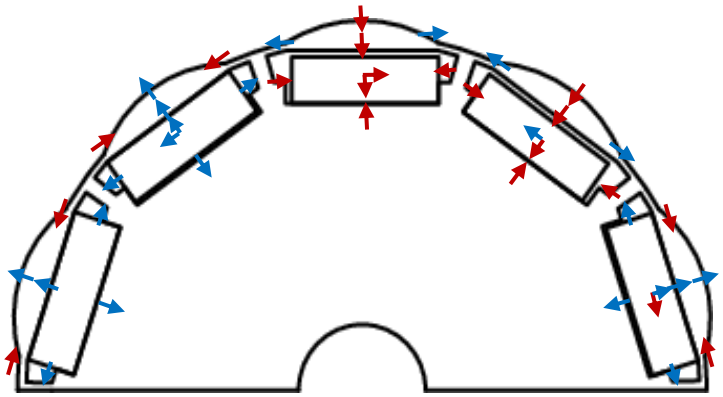
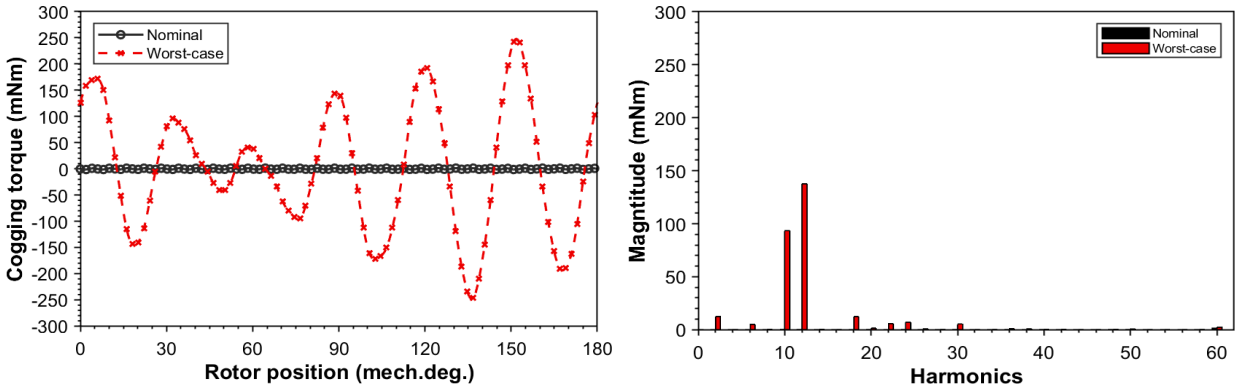


Fig. 6.63. Worst-case scenario tolerances in a 180° segment of 12-slot/10-pole IPM motor.

The cogging torque waveforms and harmonics of the worst-case scenario of the cogging torque of the 12-slot/10-pole IPM motor are shown in Fig. 6.64. The peak-to-peak cogging torque of the worst-case scenario is 496.8 mNm. The magnitude of the $10^{th}$ and $12^{th}$ order cogging torque components is 93.4mNm and

137.6 mNm, respectively.




(a) Waveforms (b) Harmonics

Fig. 6.64. Waveforms and harmonics of cogging torque of 12-slot/10-pole IPM motor due to worst-case scenario of stator and rotor tolerances.

### 6.9.3 Worst-Case Scenarios of Cogging Torque of 12-slot/14-pole IPM Motor

The worst-case scenario of cogging torque of the 12-slot/ 14-pole IPM motor due to combined stator and rotor tolerances under investigation is identified and the cross-section of the motor including the worst-case scenario tolerances is shown in Fig. 6.68. The directions of the tolerances in the stator and rotor are listed in Table 6.17 and Table 6.18, respectively. The directions of the stator and rotor tolerances are indicated graphically in Fig. 6.66 and Fig. 6.67, respectively.

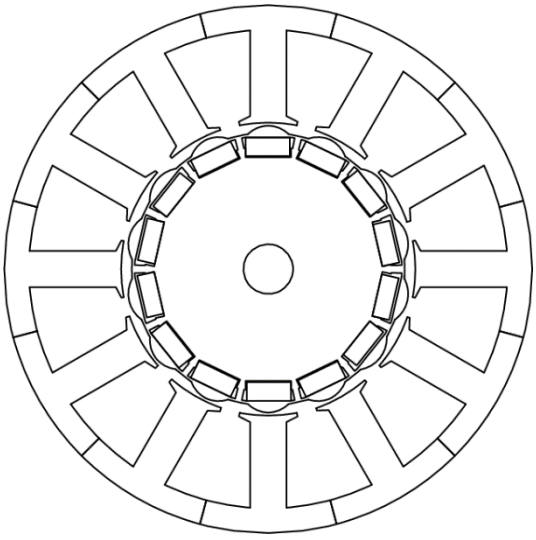


Fig. 6.65. Worst-case scenario tolerances in a 180° segment of 12-slot/14-pole IPM motor.

The directions of tolerances in the tooth-tip height and width of any given tooth is identical and opposes the direction of tolerances in the tooth profile radial position of the same tooth. Tolerances in teeth 2, 3, and 4 are identical, and in the opposite direction of tolerances in teeth 5, 6, and 7, and so forth,

The directions of tolerances in the pole-shoe height, PM height, width, remanence and radial shift of any given pole are identical. Similarly, the directions of tolerances in the pole-shoe height and rib width of any

given pole are identical and in the opposite direction of the aforementioned tolerances.

Tolerances in the PM lateral shift of poles 6 and 1 are in opposing directions. Similarly, tolerances in the PM lateral shift of poles 2 and 3 and 4 are in opposite directions of tolerances in poles 4 and 5. The influence of the direction of the tolerances in the PM lateral displacement of pole 7 on the cogging torque is very low.

Table 6.17. Directions of tolerances in worst-case scenario of cogging torque due to stator tolerances in 12-slot/14-pole IPM motor

| **Tolerances** | **Tooth 1** | **Tooth 2** | **Tooth 3** | **Tooth 4** | **Tooth 5** | **Tooth 6** |
|---|---|---|---|---|---|---|
| Tooth-tip height | ▲ | ▼ | ▼ | ▼ | ▲ | ▲ |
| Tooth-tip width | ▲ | ▼ | ▼ | ▼ | ▲ | ▲ |
| Tooth profile radial position | ▼ | ▲ | ▲ | ▲ | ▼ | ▼ |

Table 6.18. Directions of rotor tolerances in worst-case scenario of cogging torque due to in 12-slot/14-pole IPM motor

| **Tolerances** | **Pole 1** | **Pole 2** | **Pole 3** | **Pole 4** | **Pole 5** | **Pole 6** | **Pole 7** |
|---|---|---|---|---|---|---|---|
| Pole-shoe height | ▼ | ▲ | ▲ | ▲ | ▲ | ▼ | ▼ |
| Pole-shoe width | ▲ | ▼ | ▼ | ▼ | ▼ | ▲ | ▲ |
| Cavity size | ▲ | ▲ | ▲ | ▲ | ▲ | ▲ | ▲ |
| PM remanence | ▼ | ▲ | ▲ | ▲ | ▲ | ▼ | ▼ |
| PM height | ▼ | ▲ | ▲ | ▲ | ▲ | ▼ | ▼ |
| PM width | ▼ | ▲ | ▲ | ▲ | ▲ | ▼ | ▼ |
| PM radial shift | ▼ | ▲ | ▲ | ▲ | ▲ | ▼ | ▼ |
| PM lateral shift | ► | ► | ► | ◄ | ◄ | ◄ | ► |
| Rib width | ▲ | ▼ | ▼ | ▼ | ▼ | ▲ | ▲ |

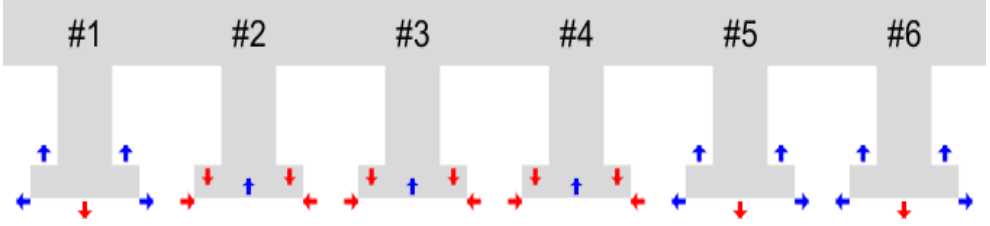



Fig. 6.66. Simplified IPM stator geometry including worst-case scenario tolerances in a 180° segment.

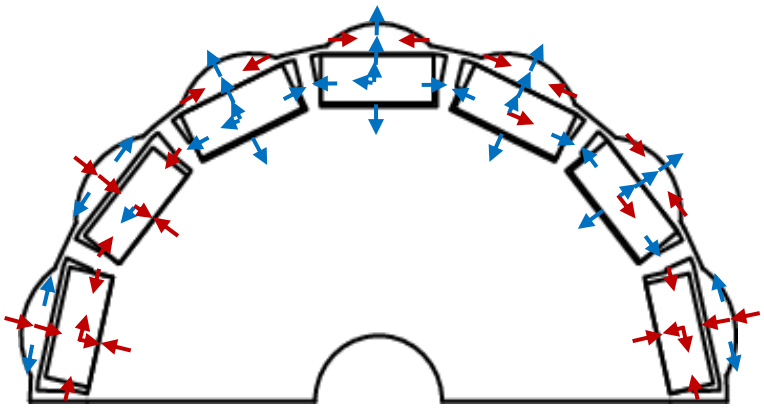
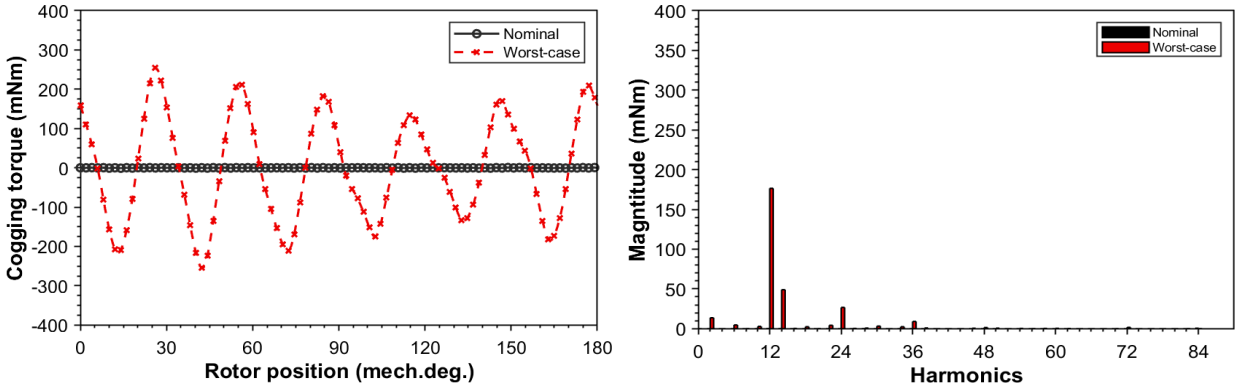


Fig. 6.67. Worst-case scenario tolerances in a 180° segment of 12-slot/14-pole IPM motor.

The cogging torque waveforms and harmonics of the worst-case scenario of the cogging torque of the 12-slot/14-pole IPM motor are shown in Fig. 6.68. The peak-to-peak cogging torque of the worst-case scenario is 510.3 mNm. The magnitude of the $12^{th}$ and $14^{th}$ order cogging torque components are 176.7 mNm and 49.1 mNm, respectively.




(a) Waveforms (b) Harmonics

Fig. 6.68. Waveforms and harmonics of cogging torque of 12-slot/14-pole IPM motor due to worst-case scenario of stator and rotor tolerances.

## 6.10 Investigation of Worst-Case Scenario of Cogging Torque Due to Combined Stator and Rotor Tolerances in SPM motors

### 6.10.1 Worst-Case Scenarios of Cogging Torque of 12-slot/8-pole SPM Motor

The worst-case scenario of cogging torque of the 12-slot/8-pole SPM motor due to combined stator and rotor tolerances under investigation is identified using the global search algorithm. The cross-section of the motor including the worst-case scenario tolerances is shown in Fig. 6.69.

The directions of the worst-case tolerances in the stator and rotor are listed in Table 6.19 and Table 6.20,

respectively. The arrows indicate an increase, a decrease, or a shift of each of the considered tolerances. Furthermore, blue and red arrows indicate positive and negative tolerances, respectively. The worst-case stator and rotor tolerances are shown graphically in Fig. 6.70 and Fig. 6.71, respectively.

The phases of individual cogging torque AHCs due to tolerances in a motor dimension separated by an angle of 90° are identical in a 12-slot/8-pole motor. For instance, the directions of tolerances in teeth 1, 4, 7, and 10 resulting in the worst-case scenario are identical. Similarly, the directions of tolerances in poles 1, 3, 5, and 7 resulting in the worst-case scenario are identical. Thus, for simplicity, only tolerances in a 180° are shown in the figures and tables.

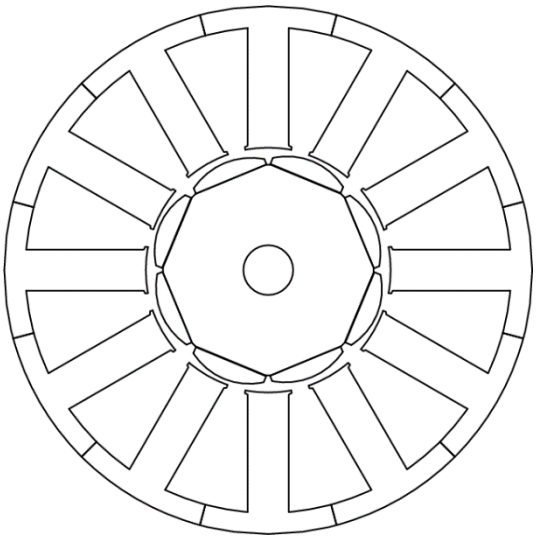


Fig. 6.69. Worst-case scenario tolerances in a 180° segment of 12-slot/8-pole SPM motor.

The directions of the stator tolerances in the tooth-tip height and tooth profile radial position of the worst-case scenario are identical. The worst-case scenario results in four orthogonal tolerances towards the air-gap and four orthogonal sets of two adjacent tolerances towards the stator back iron. The worst-case scenario tolerances in the tooth-tip height of teeth 1, 2, 4 and 5 are zero.

The directions of the worst-case scenario tolerances in the PM width and the PM height are identical. Similarly, the directions of tolerances in the PM height, PM remanence, and PM radial displacement are identical. Tolerances in the rotor sleeve profile and rotor iron profile are in opposite directions, thus allowing for the maximum possible radial displacement of the PMs. Tolerances in the lateral displacement of the PM of adjacent teeth are in opposing directions.

Table 6.19. Directions of stator tolerances in worst-case scenario of cogging torque due to stator and rotor tolerances in 12-slot/8-pole SPM motor

| **Tolerances** | **Tooth 1** | **Tooth 2** | **Tooth 3** | **Tooth 4** | **Tooth 5** | **Tooth 6** |
|---|---|---|---|---|---|---|
| Tooth-tip height | N/A | N/A | ▼ | N/A | N/A | ▼ |
| Tooth-tip width | ▲ | ▲ | ▼ | ▲ | ▲ | ▼ |
| Tooth profile radial position | ▲ | ▲ | ▼ | ▲ | ▲ | ▼ |

Table 6.20. Directions of rotor tolerances in worst-case scenario of cogging torque due to stator and rotor tolerances in 12-slot/8-pole SPM motor

| **Tolerances** | **Pole 1** | **Pole 2** | **Pole 3** | **Pole 4** |
|---|---|---|---|---|
| Rotor sleeve profile | ▲ | ▲ | ▲ | ▲ |
| PM pole-shoe height | ▲ | ▼ | ▲ | ▼ |
| PM width | ▲ | ▼ | ▲ | ▼ |
| PM height | ▼ | ▲ | ▼ | ▲ |
| PM remanence | ▼ | ▲ | ▼ | ▲ |
| PM radial shift | ▼ | ▲ | ▼ | ▲ |
| PM lateral shift | ► | ◄ | ► | ◄ |
| Rotor iron profile | ▼ | ▼ | ▼ | ▼ |

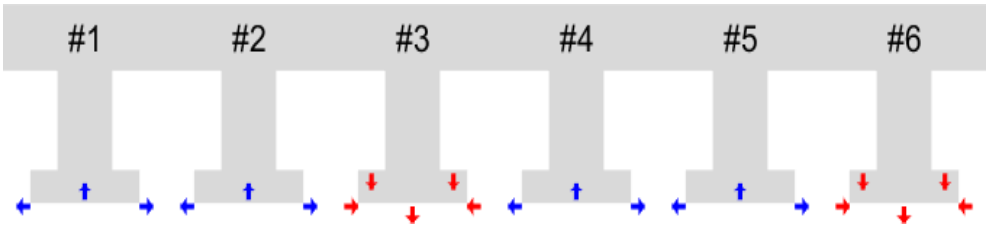



Fig. 6.70. Simplified SPM stator geometry including worst-case scenario tolerances in a 180° segment.

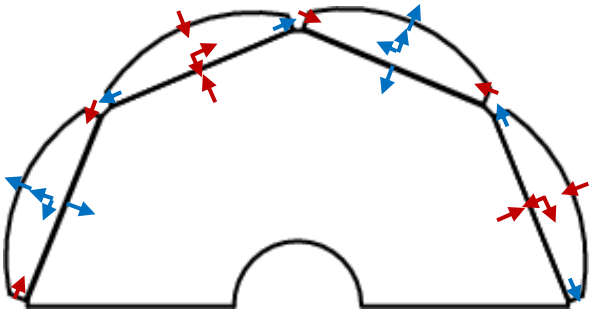
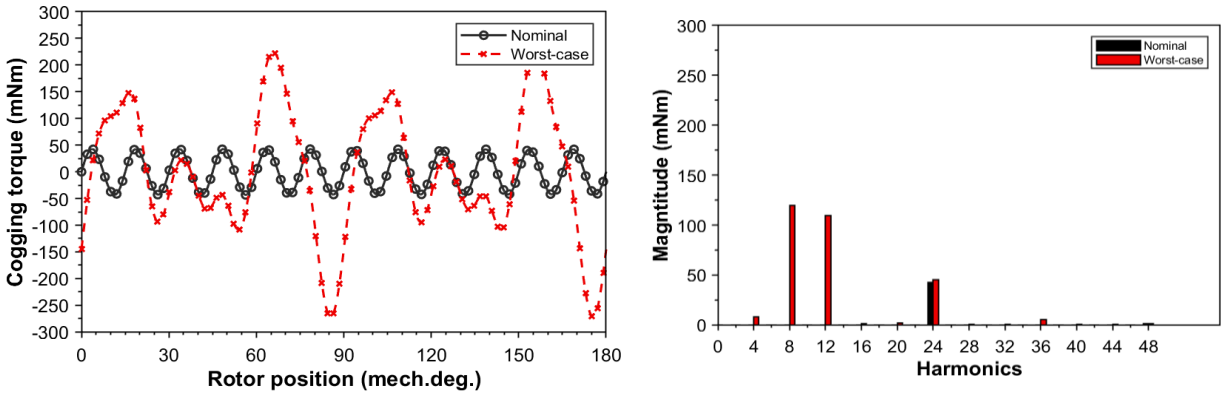


Fig. 6.71. Worst-case scenario tolerances in a 180° segment of 12-slot/8-pole SPM motor.

The cogging torque waveforms and harmonics of the worst-case scenario of the cogging torque of the 12-slot/8-pole SPM motor are shown in Fig. 6.72. The peak-to-peak cogging torque of the worst-case scenario is 498.9 mNm, 583% higher than the nominal peak-to-peak cogging torque. The magnitude of the 24$^{th}$ order cogging torque component of the worst-case scenario is 5.4% higher than the nominal value.

Stator tolerances result in a fundamental 8$^{th}$ order cogging torque AHC of 119.4 mNm and rotor tolerances result in a fundamental 12$^{th}$ order cogging torque AHC of 109.2 mNm. Thus, stator tolerances have a higher influence on the cogging torque of the worst-case scenario. The cogging torque of the worst-case scenario comprises a small magnitude of the 4$^{th}$ order cogging torque component due to modulation of the 8$^{th}$ and 12$^{th}$ order cogging torque components.




(a) Waveforms (b) Harmonics

Fig. 6.72. Waveforms and harmonics of cogging torque of 12-slot/8-pole SPM motor due to worst-case scenario of stator and rotor tolerances.

## 6.10.2 Worst-Case Scenarios of Cogging Torque of 12-slot/10-pole SPM Motor

The worst-case scenario of cogging torque of the 12-slot/ 10-pole SPM motor due to combined stator and rotor tolerances under investigation is identified and the cross-section of the motor including the worst-case scenario tolerances is shown in Fig. 6.73. The directions of the tolerances in the stator and rotor are listed in Table 6.21 and

Table 6.22, respectively. The directions of the stator and rotor tolerances are indicated graphically in Fig. 6.74 and Fig. 6.75, respectively.

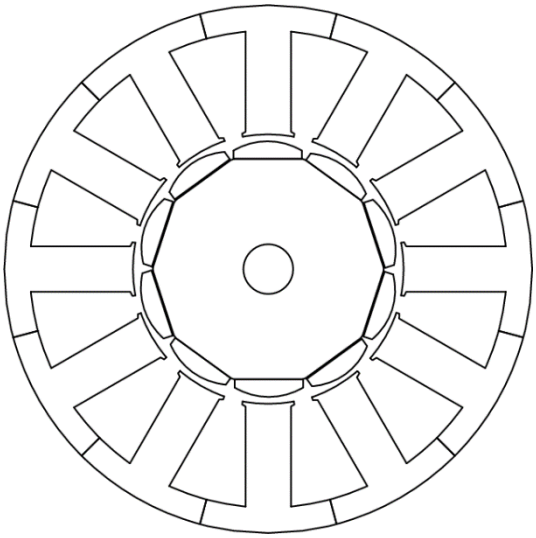


Fig. 6.73. Worst-case scenario tolerances in a 180° segment of 12-slot/10-pole SPM motor.

The directions of tolerances in the tooth-tip height, tooth-tip width, and tooth profile radial position of a given tooth are identical. The directions of the tolerances form adjacent sets of three teeth in a particular direction with different directions in adjacent sets. For instance, the directions of tolerances in teeth 2, 3 and 4 are positive, the directions of tolerances in teeth 5, 6, and 7 are negative, and so forth,

The directions of tolerance in the rotor pole-shoe-height and PM width of a particular rotor pole are identical. The directions of tolerances in the PM height, remanence and radial position of any given rotor pole are identical and opposite the direction of tolerances in the PM width and pole-shoe height. The direction of tolerances in the rotor sleeve and rotor iron profile are opposite, thus allowing for maximum radial PM displacement. The directions of tolerances in the PM pole-shoe height, width, height, remanence, and radial position of poles 1, 4, and 5 are identical and opposite those of poles 2 and 5. Tolerances in the PM lateral position of pole 2 and 3 are in opposite directions. Similarly, tolerances in the PM lateral position poles 1 and 4 are in opposite directions.

Table 6.21. Directions of stator tolerances in worst-case scenario of cogging torque due to tolerances in 12-slot/10-pole SPM motor

| **Tolerances** | **Tooth 1** | **Tooth 2** | **Tooth 3** | **Tooth 4** | **Tooth 5** | **Tooth 6** |
|---|---|---|---|---|---|---|
| Tooth-tip height | ▼ | ▲ | ▲ | ▲ | ▼ | ▼ |
| Tooth-tip width | ▼ | ▲ | ▲ | ▲ | ▼ | ▼ |
| Tooth profile radial position | ▼ | ▲ | ▲ | ▲ | ▼ | ▼ |

Table 6.22. Directions of tolerances in worst-case scenario of cogging torque due to tolerances in 12-slot/10-pole SPM motor

| **Tolerances** | **Pole 1** | **Pole 2** | **Pole 3** | **Pole 4** | **Pole 5** |
|---|---|---|---|---|---|
| Rotor sleeve profile | ▲ | ▲ | ▲ | ▲ | ▲ |
| PM pole-shoe height | ▼ | ▲ | ▲ | ▼ | ▼ |
| PM width | ▼ | ▲ | ▲ | ▼ | ▼ |
| PM height | ▲ | ▼ | ▼ | ▲ | ▲ |
| PM remanence | ▲ | ▼ | ▼ | ▲ | ▲ |
| PM radial shift | ▲ | ▼ | ▼ | ▲ | ▲ |
| PM lateral shift | ▶ | ▶ | ◀ | ◀ | ▶ |
| Rotor iron profile | ▼ | ▼ | ▼ | ▼ | ▼ |

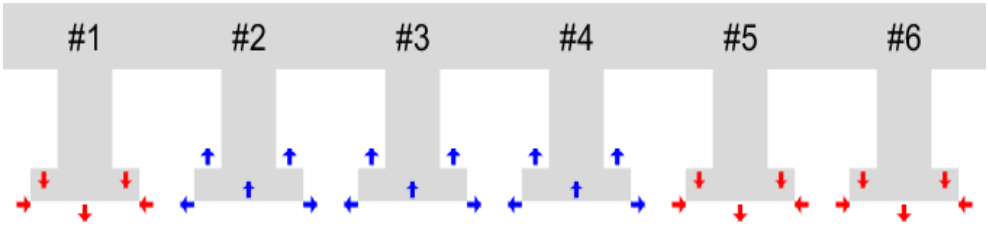



Fig. 6.74. Simplified SPM stator geometry including worst-case scenario tolerances in a 180° segment.

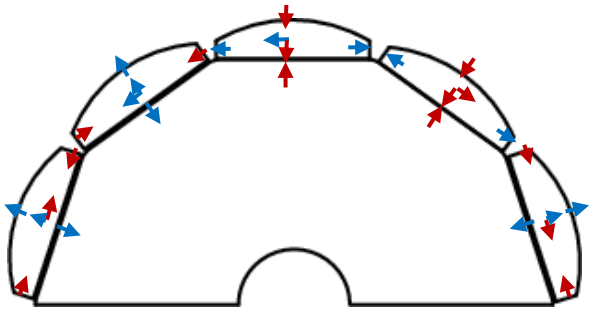
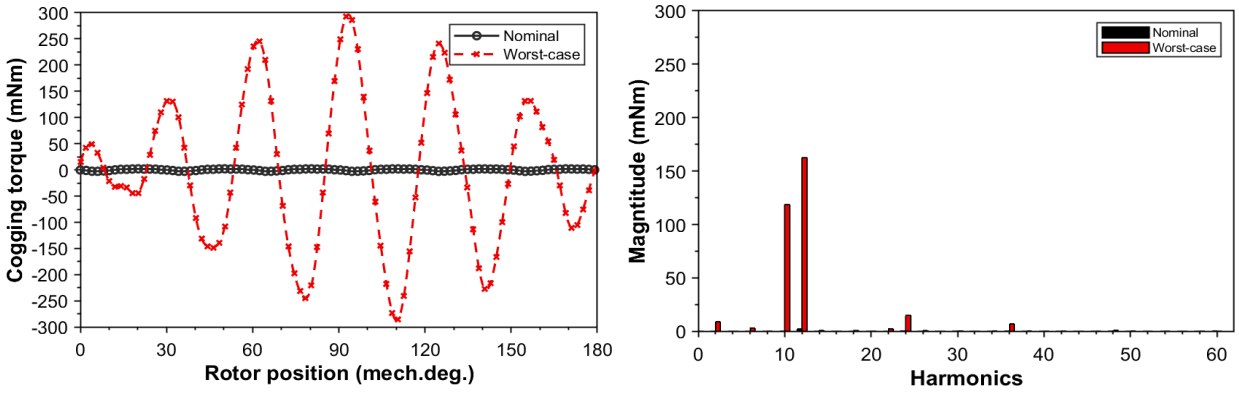


Fig. 6.75. Worst-case scenario tolerances in a 180° segment of 12-slot/10-pole SPM motor.

The cogging torque waveforms and harmonics of the worst-case scenario of the cogging torque of the 12-slot/10-pole SPM motor are shown in Fig. 6.76. The nominal peak-to-peak cogging torque and the peak-to-peak cogging torque of the worst-case scenario are 5.0 mNm and 581.3 mNm, respectively.

Stator tolerances result in $10^{th}$ order cogging torque component of 118.6 mNm and rotor tolerances result

in a 12th order cogging torque component of 162.5 mNm. Thus, rotor tolerances have a higher influence on the cogging torque of the worst-case scenario due to combined stator and rotor tolerances.




(a) Waveforms (b) Harmonics

Fig. 6.76. Waveforms and harmonics of cogging torque of 12-slot/10-pole SPM motor due to worst-case scenario of stator and rotor tolerances.

## 6.10.3Worst-Case Scenarios of Cogging Torque of 12-slot/14-pole SPM Motor

The worst-case scenario of cogging torque of the 12-slot/ 14-pole SPM motor due to combined stator and rotor tolerances under investigation is identified and the cross-section of the motor including the worst-case scenario tolerances is shown in Fig. 6.77. The directions of the tolerances in the stator and rotor are listed in Table 6.23 and Table 6.24, respectively. The directions of the stator and rotor tolerances are indicated graphically in Fig. 6.78 and Fig. 6.79, respectively.

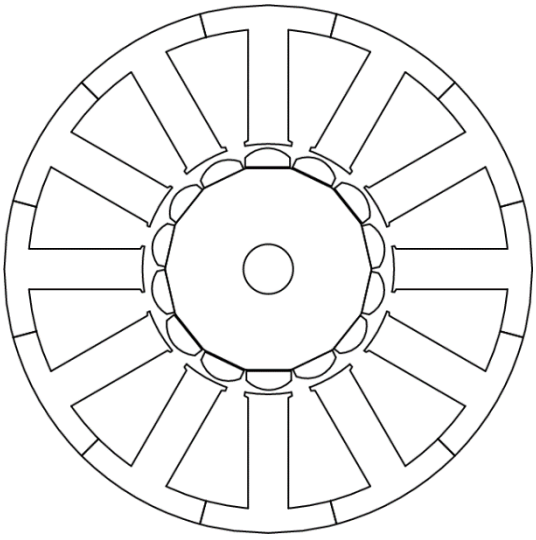


Fig. 6.77. Worst-case scenario tolerances in a 180° segment of 12-slot/14-pole SPM motor.

The directions of tolerances in the tooth-tip height and tooth-tip width of a particular tooth are identical and opposing the direction of tolerances in the radial position of the tooth profile. The directions of tolerances in teeth 3, 4 and 5 are identical and opposite the direction of tolerances in teeth 6, 7, and 8. Thus,

the worst-case scenario is composed of adjacent sets of three teeth in a given direction. Adjacent sets are composed of tolerances in opposite directions.

The directions of tolerances in the rotor sleeve and rotor iron profile are in opposing direction permitting a higher maximum radial displacement of the PMs. The direction of tolerances in the PM pole-shoe height and PM width are identical. Similarly, the direction of tolerances in the PM height, remanence, and radial shift are identical.

The directions of tolerances in the PM width and pole-shoe height of pole 3 opposes the direction of the same tolerances in poles 2 and 4. Similarly, the directions of the aforementioned tolerances in poles 6 and 7 oppose the directions of the same tolerances in poles 5 and 8. Tolerances in the PM lateral displacement of poles 2 and 4 are in opposing directions. Similarly, the directions of tolerances in poles 5 and 6 oppose the direction of the same tolerances in poles 7 and 8.

Table 6.23. Directions of stator tolerances in worst-case scenario of cogging torque due to tolerances in 12-slot/14-pole SPM motor

| **Tolerances** | **Tooth 1** | **Tooth 2** | **Tooth 3** | **Tooth 4** | **Tooth 5** | **Tooth 6** |
|---|---|---|---|---|---|---|
| Tooth-tip height | ▲ | ▲ | ▼ | ▼ | ▼ | ▲ |
| Tooth-tip width | ▲ | ▲ | ▼ | ▼ | ▼ | ▲ |
| Tooth profile radial position | ▼ | ▼ | ▲ | ▲ | ▲ | ▼ |

Table 6.24. Directions of tolerances in worst-case scenario of cogging torque due to tolerances in 12-slot/14-pole SPM motor

| **Tolerances** | **Pole 1** | **Pole 2** | **Pole 3** | **Pole 4** | **Pole 5** | **Pole 6** | **Pole 7** |
|---|---|---|---|---|---|---|---|
| Rotor sleeve profile | ▲ | ▲ | ▲ | ▲ | ▲ | ▲ | ▲ |
| PM pole-shoe height | ▲ | ▲ | ▼ | ▲ | ▲ | ▼ | ▼ |
| PM width | ▲ | ▲ | ▼ | ▲ | ▲ | ▼ | ▼ |
| PM height | ▼ | ▲ | ▲ | ▲ | ▼ | ▼ | ▼ |
| PM remanence | ▼ | ▲ | ▲ | ▲ | ▼ | ▼ | ▼ |
| PM radial shift | ▼ | ▲ | ▲ | ▲ | ▼ | ▼ | ▼ |
| PM lateral shift | ► | ► | ◄ | ◄ | ◄ | ◄ | ► |
| Rotor iron profile | ▼ | ▼ | ▼ | ▼ | ▼ | ▼ | ▼ |

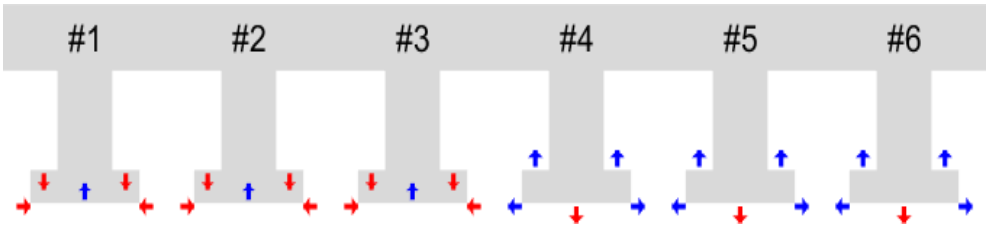



Fig. 6.78. Simplified SPM stator geometry including worst-case scenario tolerances in a 180° segment.

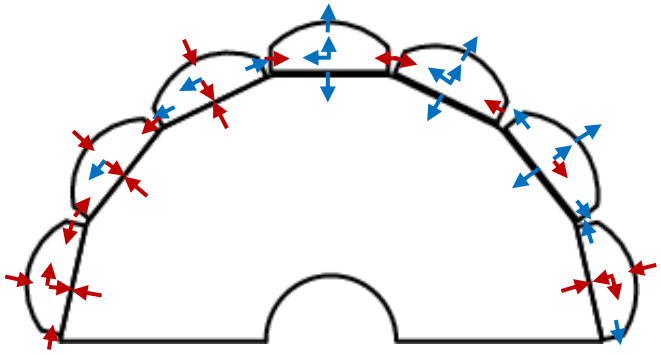
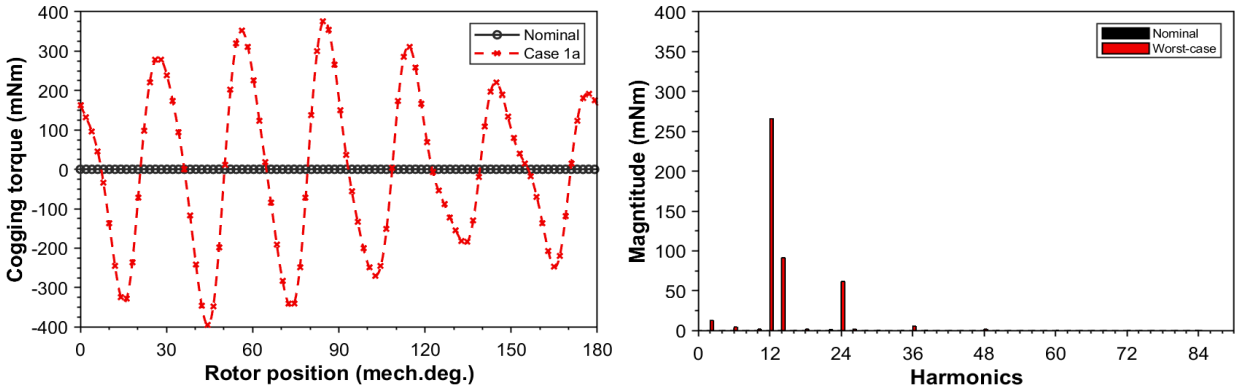


Fig. 6.79. Worst-case scenario tolerances in a 180° segment of 12-slot/14-pole SPM motor.

The cogging torque waveforms and harmonics of the worst-case scenario of the cogging torque of the 12-slot/14-pole SPM motor are shown in Fig. 6.80. The peak-to-peak cogging torque of the nominal and worst-case scenario are 0.3 mNm and 773.4 mNm respectively.

The fundamental cogging torque AHCs due to stator and rotor tolerances are the $14^{th}$ and $12^{th}$ cogging torque components, respectively. The magnitude of the $14^{th}$ and $12^{th}$ order cogging torque components is 91.3 mNm and 266.0 mNm, respectively. Thus, rotor tolerances have a significantly higher influence on the cogging torque of the worst-case scenario.

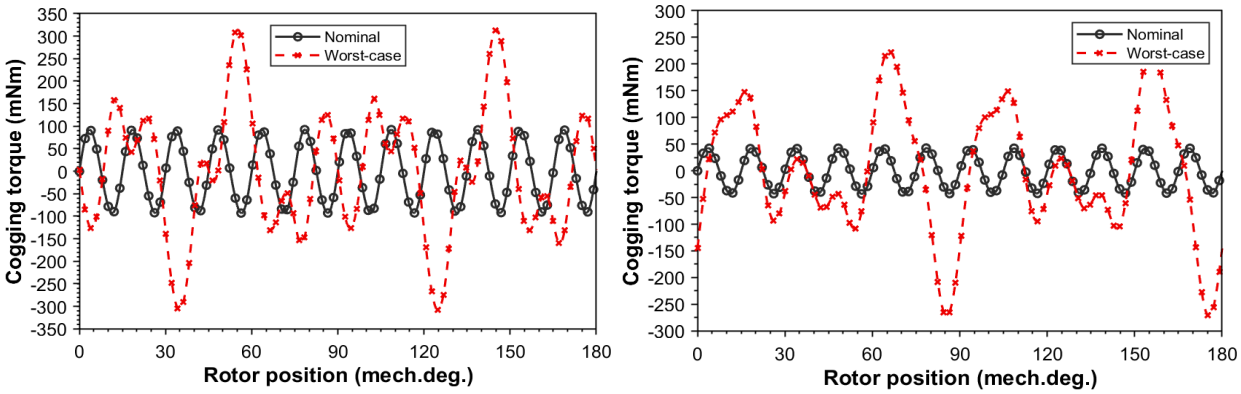



(a) Waveforms (b) Harmonics

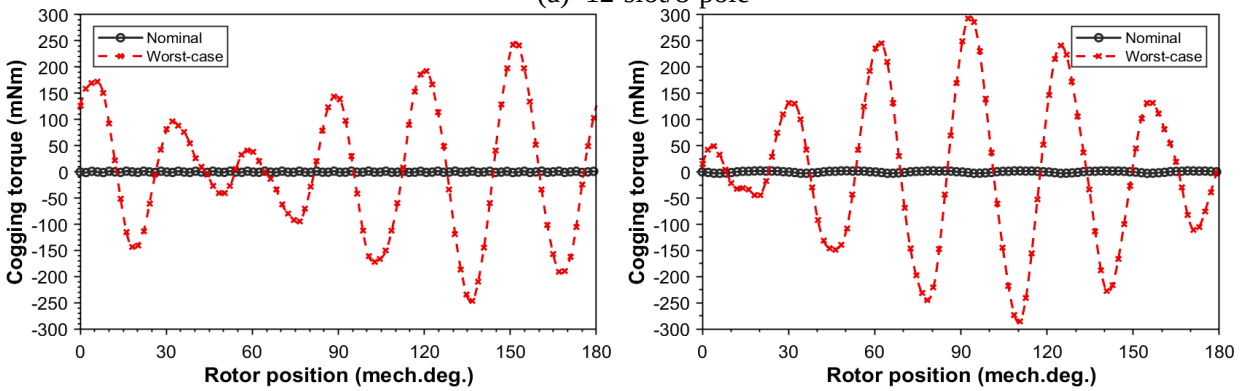
Fig. 6.80. Waveforms and harmonics of cogging torque of 12-slot/14-pole SPM motor due to worst-case scenario of stator and rotor tolerances.

## 6.11 Comparison of Cogging Torque Worst-Case Scenarios Due to Combined Stator and Rotor Tolerances in IPM and SPM motors

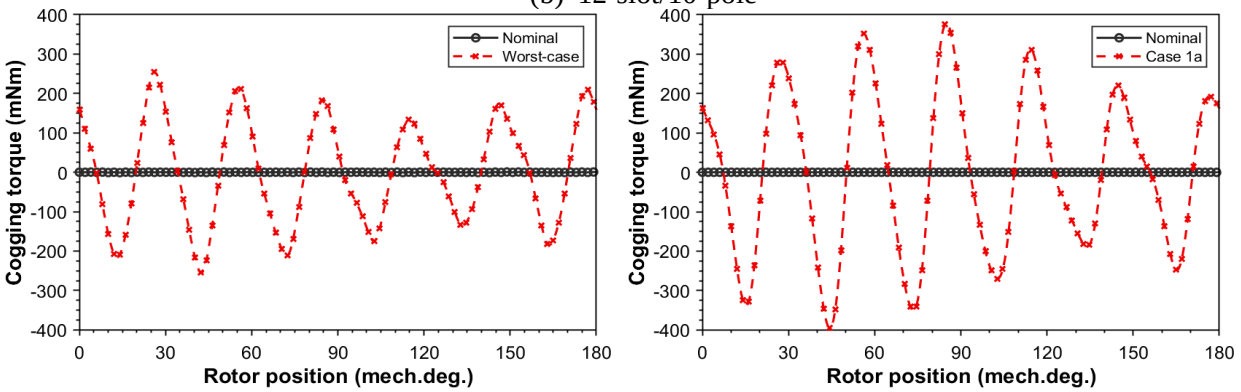
Cogging torque waveforms and harmonics due to the worst-cases of rotor tolerances in the analysed IPM and SPM motors are shown in Fig. 6.81 and Fig. 6.82, respectively. The 12-slot/14-pole SPM motor has the highest peak-to-peak cogging torque followed by the 12-slot/8-pole IPM motor. The peak-to-peak cogging torque of IPM motors decreases with increasing pole number. Conversely, the peak-to-peak cogging torque of SPM motors increases with increasing pole number.




(a) 12-slot/8-pole



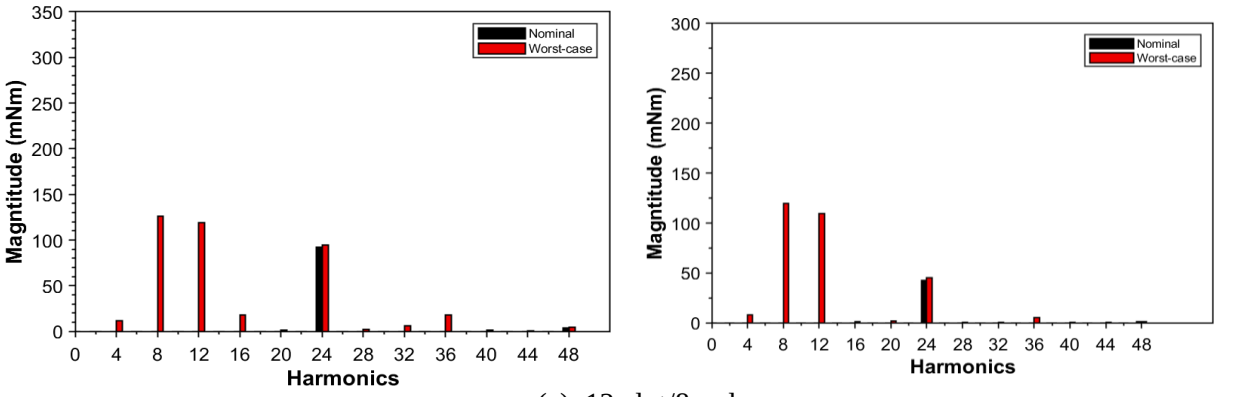

(b) 12-slot/10-pole



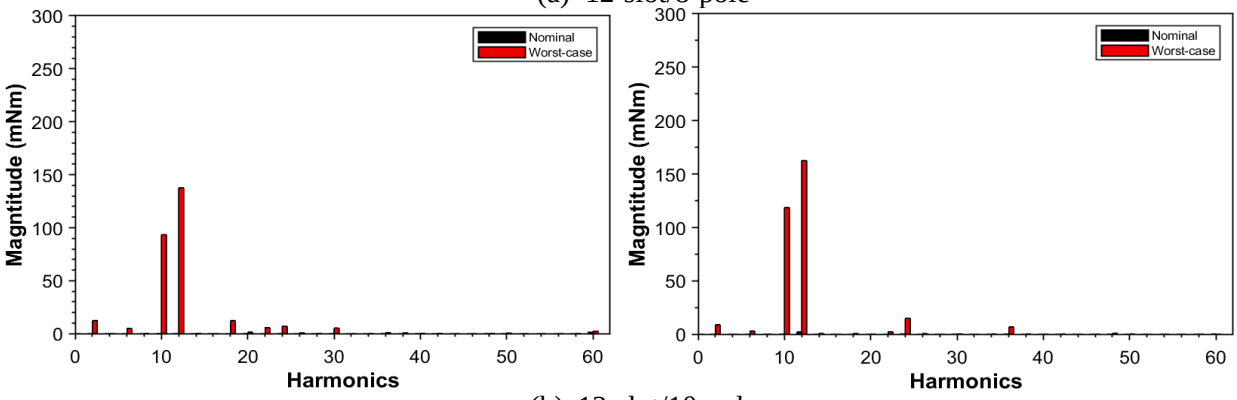

(c) 12-slot/14-pole

(I) IPM (II) SPM

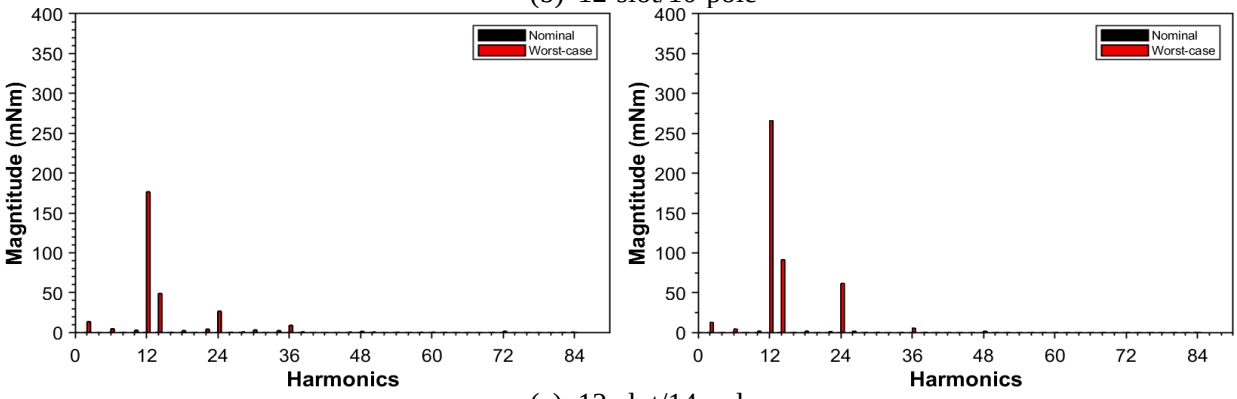
Fig. 6.81. Cogging torque waveforms due to worst-case scenarios of combined stator and rotor tolerances in IPM and SM motors.




(a) 12-slot/8-pole




(b) 12-slot/10-pole




(c) 12-slot/14-pole

(I) IPM (II) SPM

Fig. 6.82. Cogging torque harmonics due to worst-case scenarios of combined stator and rotor tolerances in IPM and SM motors.

## 6.12 Conclusion

The sensitivity analyses of the optimised 12-slot/8-pole, 12-slot/10-pole, and 12-slot/14-pole IPM and SPM motor designs show that manufacturing tolerances result in individual cogging torque AHCs of a given magnitude and phase. The worst-case scenario of the cogging torque is produced by a particular arrangement of manufacturing tolerances.

The worst-case scenarios due to manufacturing tolerances due to tolerances in radial position of the stator tooth profile of the IPM and SPM motors under investigation are determined using the method outlined in

in [BUH20]. Manufacturing tolerances in the inward direction, outward directions and both directions are considered to identify the worst-case scenarios.

Determination of the worst-case scenarios of tolerances in multiple stator and rotor dimensions using a systematic manner is very complex. The worst-case scenarios can also be determined using a global search algorithm combined with a FEA model of the motor under investigation. This method required a very high computational effort due to the fine mesh of the FEA model attributed to the low magnitude of the manufacturing tolerances.

A global search algorithm is combined with a simplified model based on a series of FEA simulations to obtain the worst-case scenarios with low computational effort. The simplified model is constructed using a sensitivity analysis of the cogging torque due to the upper and lower bounds for each of the considered manufacturing tolerances. The AHCs due to manufacturing variations are obtained by subtracting the nominal cogging torque from the cogging torque waveform due to the manufacturing variations. Therefore, the cogging torque due to a set of manufacturing variations can be obtained by summing the nominal cogging torque and the AHCs due to each manufacturing variation. It is assumed that the cross-interaction between manufacturing tolerances is negligible. Furthermore, it is assumed that the magnitude of the cogging torque AHCs varies linearly with the magnitude of the corresponding manufacturing tolerances. This is justified by the fact that the magnitudes of the manufacturing tolerances are very low.

The worst-case scenarios of the cogging torque due to stator tolerances, rotor tolerances, and combined stator and rotor tolerances of the motors under investigation are identified. The cogging torque of the worst-case scenario due to stator tolerances only, rotor tolerances only, and combined stator and rotor tolerances is listed in Table 6.25. Thus, the peak-to-peak cogging torque due to the worst-case scenario decreases with increasing rotor pole number in IPM motors. Conversely, the worst-case cogging torque increases with increasing rotor pole number in SPM motors.

Table 6.25. Worst-case cogging torque due to stator tolerances only, rotor tolerances only, and combined stator and rotor tolerances

| **Units: (mNm)** | **Stator tolerances** | | **Rotor tolerances** | | **Stator and rotor tolerances** | |
|---|---|---|---|---|---|---|
| | **IPM** | **SPM** | **IPM** | **SPM** | **IPM** | **SPM** |
| 12-slot/8-pole | 452.3 | 316.6 | 357.6 | 235.5 | 622.4 | 489.9 |
| 12-slot/10-pole | 188.8 | 236.0 | 277.2 | 346.7 | 496.8 | 581.3 |
| 12-slot/14-pole | 93.7 | 196.4 | 382.5 | 513.6 | 510.3 | 773.4 |

# 7 UNCERTAINTY ANALYSIS OF COGGING TORQUE IN IPM AND SPM MOTORS DUE TO MANUFACTURING TOLERANCES

## 7.1 Introduction

Manufacturing tolerances in the stator and rotor of PM motors lead to cogging torque AHCs that in turn affect the peak-to-peak cogging torque. The sensitivity analysis of the cogging torque due to manufacturing tolerances carried out in Chapter 5 identifies the magnitude and phase of the cogging torque AHCs in the 12-slot/8-pole, 12-slot/10-pole, and 12-slot/14-pole IPM and SPM motors under investigation.

Particular arrangements of manufacturing tolerances of the maximum possible magnitude in given directions result in the worst-case scenarios of the peak-to-peak cogging torque due to manufacturing tolerances. The worst-case scenarios provide a good indication of the expected influence of manufacturing tolerances in a given set of motors with different topologies. The likelihood of occurrence of the worst-case scenarios of the cogging torque of different motors may be low and not necessarily indicative of the uncertainty of the cogging torque due to manufacturing tolerances.

The uncertainty of the peak-to-peak cogging torque of the 12-slot/8-pole, 12-slot/10-pole, and 12-slot/14-pole IPM and SPM motors under investigation is quantified using Monte Carlo simulations accounting for the stochastic nature manufacturing processes.

The uncertainty of the cogging torque due to manufacturing tolerances can be quantified through a statistical analysis of the cogging torque of a set of motors. This can be performed experimentally using a set of manufactured motors, or numerically using an analytical or finite-element model of a motor with variations defined by a statistical distribution that accounts for the stochastic nature of manufacturing tolerances.

Pina Ortega et al. [ORT16] proposes an analytical model of a 12-slot/8-pole SPM motor, including the effects of manufacturing tolerances and concluded that there is a good agreement between the measured cogging torque and the cogging torque obtained numerically using the proposed analytical model and a finite-element model of the manufactured motors. Manufacturing tolerances have been considered in the motor design process in [OMB07b, HEI11, KIM18]. However, the influence of manufacturing tolerances on the cogging torque components produced by the manufacturing tolerances has not been fully explored.

Generally, it is assumed that the manufacturing tolerance in mass-production processes is ±0.05 mm [WU98] and that the probability density of manufacturing tolerances follows the normal (or Gaussian) distribution with a mean of 0 mm and a standard deviation of 0.05/3 mm, as shown in Fig. 7.1.

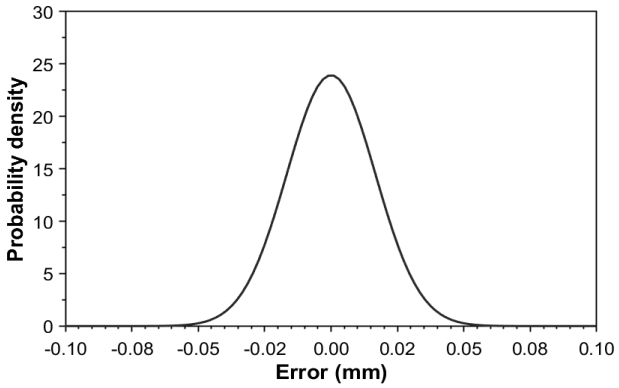



Fig. 7.1. Probability density function of the manufacturing variations.

The Monte Carlo method is used to generate 100 motor designs with manufacturing tolerances having the probability density in Fig. 7.1, which are then modelled using the finite-element method. The distributions of number of occurrences of the cogging torque of the sample motors are analysed to identify the uncertainty due to manufacturing tolerances. The influence of sample size on the uncertainty of the peak-to-peak cogging torque is investigated in Appendix C. It is determined that the influence of sample size on the uncertainty of the peak-to-peak cogging torque is low and hence a sample of 100 motors is sufficient for the foregoing investigation.

The variation of the peak-to-peak cogging torque and cogging torque components due to manufacturing tolerances is illustrated using histograms. The exact distribution of a the peak-to-peak cogging torque and its harmonics is not known and therefore well-known mathematical distributions, such as the normal distribution, are fitted to the data to provide an indication of the change in the mean of the given quantity from the nominal value.

The uncertainty of the peak-to-peak cogging torque is a product of the accumulation of cogging torque AHCs of random magnitude and phase due to the randomness of several manufacturing tolerances. Thus, it is expected that the statistical distributions of the cogging torque and its harmonics exhibit a degree of positive skewness. Skewness refers to the fact that the distribution is not symmetric about the mean of the distribution. The standard normal distribution does not account for skewness and thus another statistical distribution is also used to better represent the statistical distribution of the data. Various statistical distributions that account for skewness, with the most widely used being the lognormal and log-logistic distributions [DEY10]. Both normal and log-logistic distributions are fitted to each of the analysed quantities to quantify the deviation from a standard normal distribution and the degree of skewness. The statistical dispersion of a normal distribution can be quantified using traditional measures such as standard deviation and range, or more robust measures such as the interquartile range and the median absolute range. The interquartile range is a more effective and robust measure to quantify the spread of distributions with a certain degree of skewness. The interquartile range is equal to the difference between the third quartile and first quartile, i.e. the range of the middle 50% of a probability density function.

The uncertainty of the cogging torque is analysed for the stator and rotor tolerances investigated in the

previous chapter. The uncertainties due to stator tolerances only, rotor tolerances only, and combined stator and rotor tolerances are analysed to determine the influence of the various tolerances on the uncertainty of the cogging torque.

The manufacturing tolerances of PM motors considered in this analysis are:

Stator of IPM and SPM motors:

- Tooth-tip height
- Tooth-tip width
- Tooth profile radial positon

Rotors of IPM motors:

- Pole-shoe height
- Pole-shoe width
- Cavity size
- PM height
- PM width
- PM remanence
- PM radial displacement
- PM lateral displacement
- Rib width

Rotors of SPM motors:

- Rotor sleeve profile (which affects the tolerances in the PM radial displacement)
- PM pole-shoe height
- PM height
- PM width
- PM remanence
- PM radial displacement
- PM lateral displacement
- Rotor iron profile

## 7.2 Uncertainty Analysis of Cogging Torque in IPM and SPM Motors due to Stator Tolerances

The distributions of the number of occurrences of the peak-to-peak cogging torque and the fitted distributions of the IPM and SPM motors under investigation due to stator tolerances only are shown in Fig. 7.2.

The differences between the modes of the fitted log-logistic distribution and the nominal peak-to-peak cogging torque of the 12-slot/8-pole, 12-slot/10-pole, and 12-slot/14-pole IPM motors (Fig. 7.2 I) are 23.3 mNm, 18.3 mNm, and 7.9 mNm, respectively. Similarly, the differences between the modes of the fitted log-logistic distribution and the nominal peak-to-peak cogging torque of the 12-slot/8-pole, 12-slot/10-pole, and 12-slot/14-pole SPM (Fig. 7.2 II) motors are 20.2 mNm, 14.9 mNm, and 10.7 mNm, respectively. Thus, the variation of the mode of the fitted log-logistic distribution from the nominal peak-to-peak cogging torque of IPM and SPM motors decreases with increasing rotor pole number. The difference between the modes of the fitted log-logistic distribution and the nominal peak-to-peak cogging torque of the 12-slot/8-pole and 12-slot/10-pole IPM motors (Fig. 7.2 Ia, Fig. 7.2 Ib). is higher than that of the corresponding SPM motors (Fig. 7.2 IIa, Fig. 7.2 IIb). Conversely, the difference between the modes of the fitted log-logistic distribution and the nominal peak-to-peak cogging torque of the 12-slot/14-pole IPM motor (Fig. 7.2 Ic) is lower than that of the corresponding SPM motor (Fig. 7.2 IIc).

The interquartile ranges of the fitted log-logistic distributions of the 12-slot/8-pole, 12-slot/10-pole, and 12-slot/14-pole IPM motors are 18.3 mNm, 7.5 mNm, and 5.2 mNm, respectively. Thus, the spread of the distribution of the peak-to-peak cogging torque of IPM motor decreases significantly with increasing rotor pole number. The interquartile ranges of the fitted log-logistic distributions of the 12-slot/8-pole, 12-slot/10-pole, and 12-slot/14-pole SPM motors are 16.2 mNm, 17.3 mNm, and 13.3 mNm, respectively. Thus, the spread of the distributions of the IPM motors decreases with increasing rotor pole number. The distribution of the 12-slot/10-pole SPM motor has a higher spread than that of the 12-slot/8-pole and 12-slot/14-pole SPM motors. Conversely, the spreads of the distributions of the 12-slot/10-pole and 12-slot/14-pole IPM motors are lower than those of the corresponding SPM motors.

The skewness of the distributions of the peak-to-peak cogging torque of the 12-slot/8-pole and 12-slot/14-pole IPM motors are comparable. The skewness of the distribution of the 12-slot/10-pole IPM motor is significantly higher than those of the 12-slot/8-pole and 12-slot/14-pole IPM motors. The skewness of the distribution of the 12-slot/8-pole SPM motor is very low. Furthermore, the skewness of the 12-slot/10-pole SPM motor is higher than that of the 12-slot/14-pole SPM motor. Thus, the skewness of the distributions of the 12-slot/8-pole motors is very low. Furthermore, the skewness of the distributions of the 12-slot/10-pole motors is the highest among the investigated topologies.

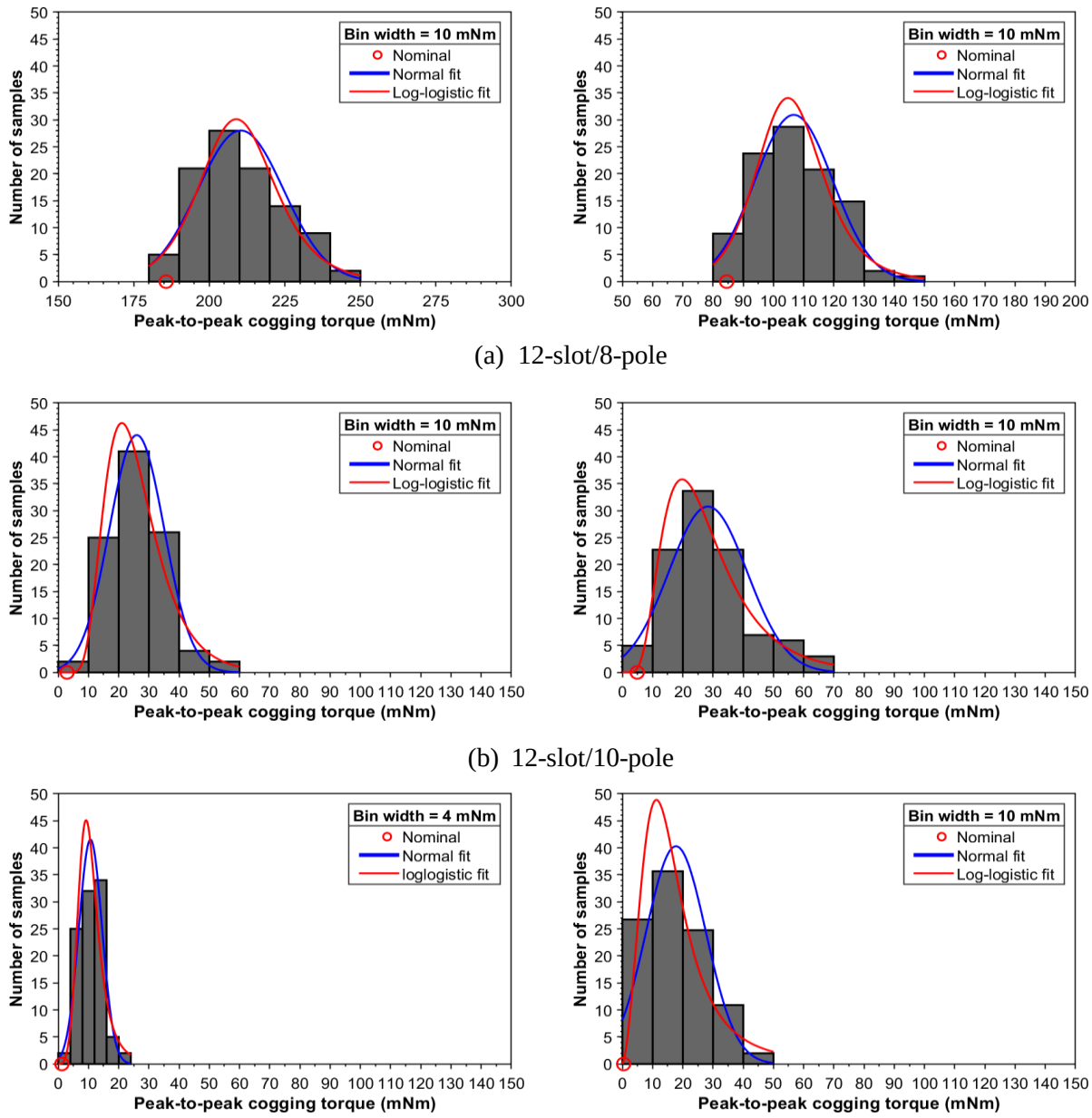
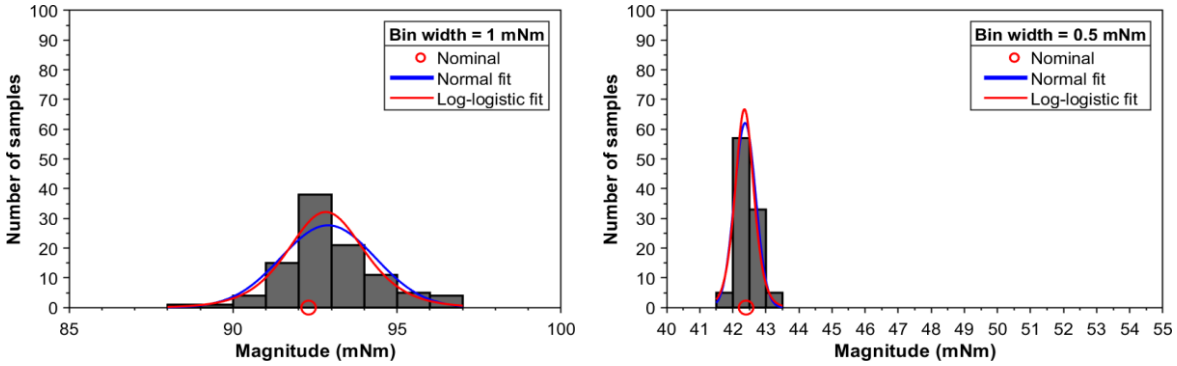



Fig. 7.2. Distribution of number of occurrences of peak-to-peak cogging torque of IPM and SPM motors due to stator tolerances only.

The distributions of number of occurrences of the native 24$^{th}$ order cogging torque components of the 12-slot/8-pole IPM and SPM motors are shown in Fig. 7.3. The skewness of the fitted log-logistic distributions of the 12-slot/8-pole IPM and SPM motors are very low. The difference between the modes of the fitted log-logistic distribution and the nominal magnitude of the 24$^{th}$ order cogging torque harmonic of the 12-slot/8-pole IPM and SPM motors are 0.5 mNm and 0.1 mNm, respectively. The interquartile ranges of the fitted log-logistic distributions of the IPM and SPM motors are 1.7 mNm and 0.4 mNm, respectively. Thus, the dispersion of the fitted log-logistic distribution is approximately 4 times higher than that of the SPM motor.

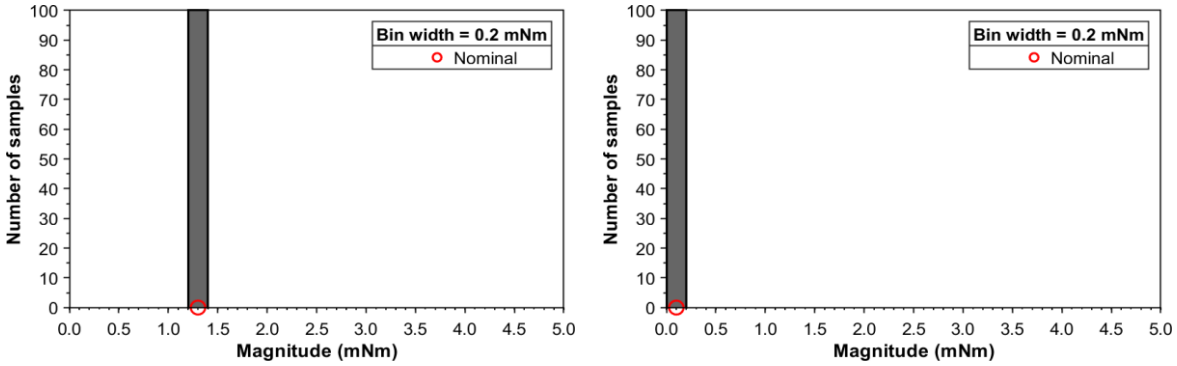
The distributions of number of occurrences of the native 60$^{th}$ order cogging torque components of the 12-slot/10-pole IPM and SPM motors are shown in Fig. 7.4. The magnitudes of the 60$^{th}$ order cogging torque component of the IPM and SPM motors fall within the bin of 0.2 mNm. Thus, the magnitude of the 60$^{th}$ order cogging torque component is not influenced by stator manufacturing tolerances.

The distributions of number of occurrences of the native 84$^{th}$ order cogging torque components of the 12-slot/14-pole IPM and SPM motors are shown in Fig. 7.5. The nominal magnitude of the 84$^{th}$ order cogging torque harmonic of both motors is very low. Thus, the influence of numerical noise on the fitted distributions may be non-negligible. The skewness of the fitted log-logistic distribution of the 12–slot/14-pole SPM motor is higher than that of the IPM motor. The interquartile range of the fitted log-logistic distributions of the IPM and SPM motors is 0.05 mNm and 0.04 mNm, respectively. Thus, the distribution of the 84$^{th}$ order cogging torque component of the IPM motor has a slightly higher dispersion than that of the SPM motor.



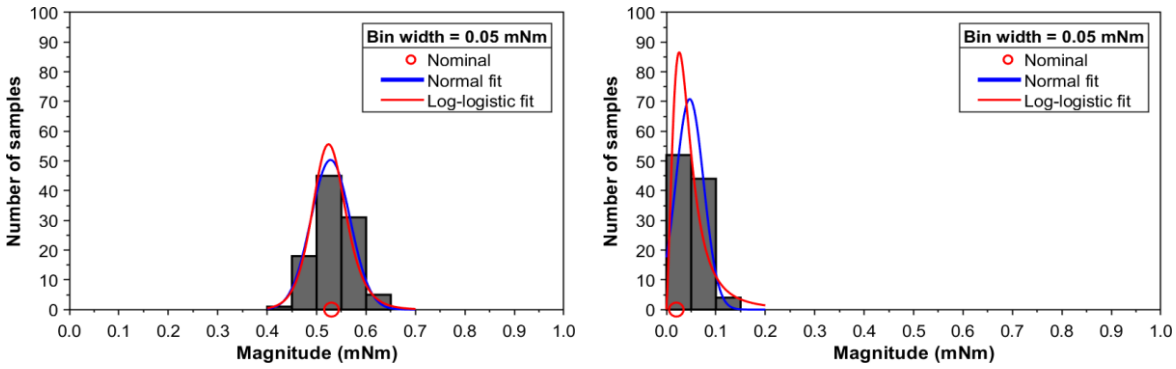

(a) IPM (b) SPM

Fig. 7.3. Distribution of number of occurrences of 24$^{th}$ order cogging torque components of 12-slot/8-pole IPM and SPM motors due to stator tolerances only.




(a) IPM (b) SPM

Fig. 7.4. Distribution of number of occurrences of 60$^{th}$ order cogging torque components of 12-slot/10-pole IPM and SPM motors due to stator tolerances only.




(a) IPM (b) SPM

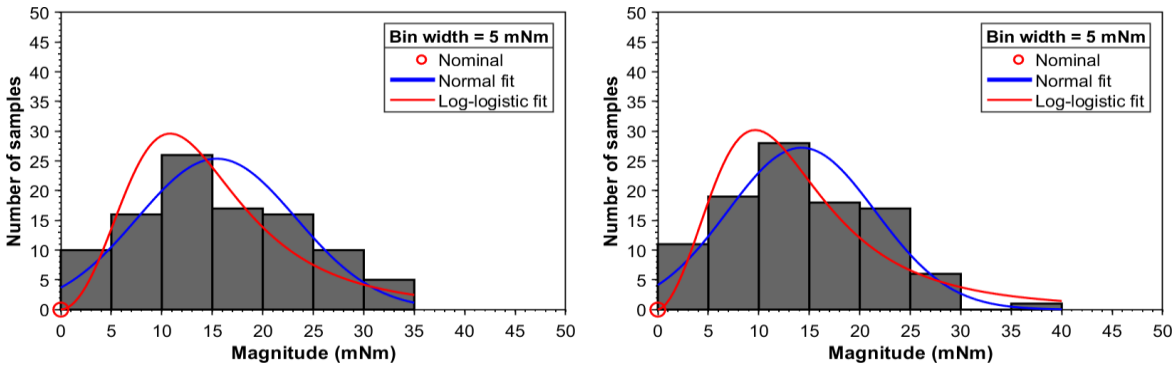
Fig. 7.5. Distribution of number of occurrences of 84th order cogging torque components of 12-slot/14-pole IPM and SPM motors due to stator tolerances only.

The distributions of number of occurrences of the 8th order cogging torque AHC of the 12-slot/8-pole IPM and SPM motors are shown in Fig. 7.6. The difference between the modes of the fitted log-logistic distribution and the mean of the fitted normal distribution of both IPM and SPM motors is 4.5 mNm, Thus, the skewness of the fitted log-logistic distributions of both motors are almost identical. The interquartile ranges of the fitted log-logistic distributions of the IPM and SPM motors are 10.7 mNm and 10.8 mNm, respectively. Thus, the dispersions of the fitted log-logistic distributions of both motors are high and almost identical.

The distributions of number of occurrences of the 10th order cogging torque AHC of the 12-slot/10-pole IPM and SPM motors are shown in Fig. 7.7. The differences between the modes of the fitted log-logistic distribution and the mean of the fitted normal distribution of the IPM and SPM motors are 3.2 mNm and 4.0 mNm, respectively. The interquartile ranges of the fitted log-logistic distributions of the IPM and SPM motors are 7.5 mNm and 8.8 mNm, respectively. Thus, the skewness and dispersion of the fitted log-logistic distribution of the SPM motor are higher than those of the IPM motor.

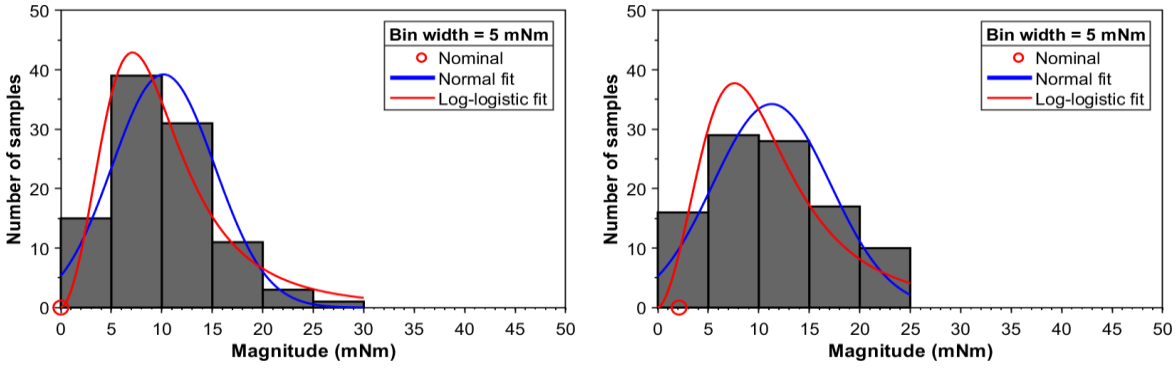
The distributions of number of occurrences of the 14th order cogging torque AHC of the 12-slot/14-pole IPM and SPM motors are shown in Fig. 7.8. The differences between the modes of the fitted log-logistic distribution and the mean of the fitted normal distribution of both IPM and SPM motors are 1.2 mNm and 3.4 mNm, respectively. Thus, the skewness of the fitted log-logistic distribution of the SPM motor is significantly higher than that of the IPM motor. The interquartile ranges of the fitted log-logistic distributions of the IPM and SPM motors are 3.0 mNm and 6.8 mNm, respectively. Thus, the dispersion of the fitted log-logistic distribution of the SPM motor is significantly higher than that of the IPM motor.

The skewness and dispersion of the fitted log-logistic distributions of the cogging torque AHCs of the SPM motors are higher than those of the IPM motors. Furthermore, the skewness and dispersion decrease with increasing rotor pole number and the rate of decrease is higher in IPM motors.



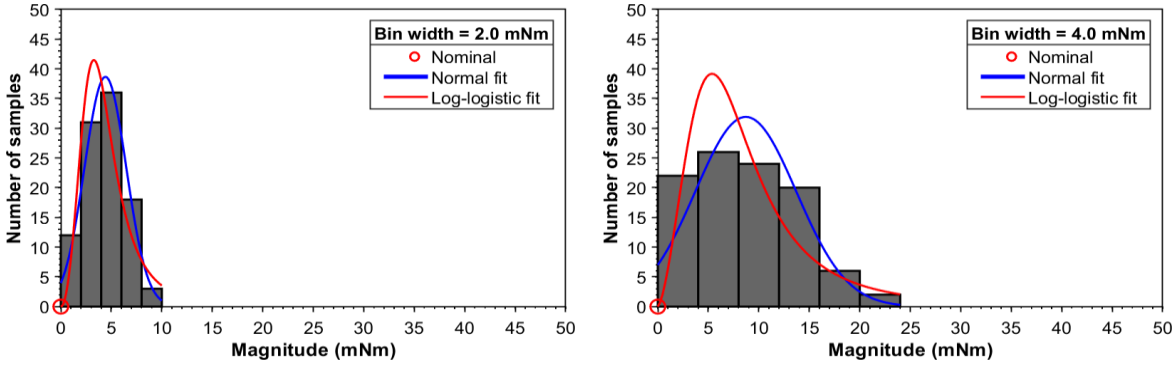

(a) IPM (b) SPM

Fig. 7.6. Distribution of number of occurrences of 8th order cogging torque components of 12-slot/8-pole IPM and SPM motors due to stator tolerances only.




(a) IPM (b) SPM

Fig. 7.7. Distribution of number of occurrences of 10th order cogging torque components of 12-slot/10-pole IPM and SPM motors due to stator tolerances only.




(a) IPM (b) SPM

Fig. 7.8. Distribution of number of occurrences of 14th order cogging torque components of 12-slot/14-pole IPM and SPM motors due to stator tolerances only.

## 7.3 Uncertainty Analysis of Cogging Torque of IPM and SPM Motors due to Rotor Tolerances

The distributions of the number of occurrences of the peak-to-peak cogging torque and the fitted distributions of the IPM and SPM motors under investigation due to rotor tolerances only are shown in Fig. 7.9.

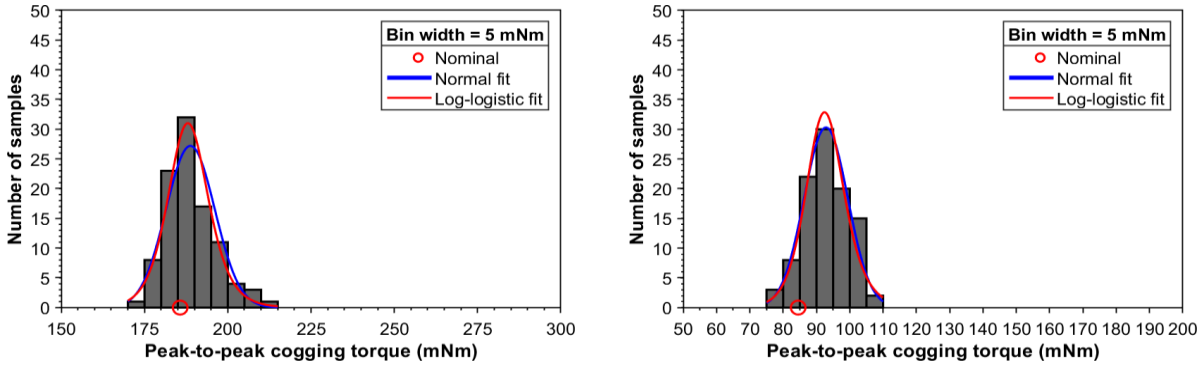
The differences between the modes of the fitted log-logistic distribution and the nominal peak-to-peak cogging torque of the 12-slot/8-pole, 12-slot/10-pole, and 12-slot/14-pole IPM motors (Fig. 7.9.I) are 2.5 mNm, 18.2 mNm, and 28.2 mNm, respectively. The differences between the modes of the fitted log-logistic distribution and the nominal peak-to-peak cogging torque of the 12-slot/8-pole, 12-slot/10-pole, and 12-slot/14-pole SPM motors (Fig. 7.9.II) are 7.8 mNm, 15.8 mNm, and 36.9 mNm, respectively. The difference of the modes of the fitted distribution from the nominal cogging torque is expected to increase with increasing rotor pole number since the number of manufacturing tolerances increases linearly with increasing rotor pole number. The lowest difference in nominal cogging torque due to rotor tolerances is attributed to the 12-slot/8-pole IPM motor and the highest difference is attributed to the 12-slot/14-pole SPM motor.

The interquartile ranges of the fitted log-logistic distributions of the 12-slot/8-pole, 12-slot/10-pole, and 12-slot/14-pole IPM motors (Fig. 7.9.I) are 8.6 mNm, 13.3 mNm, and 12.2 mNm, respectively. The interquartile ranges of the fitted log-logistic distributions of the 12-slot/8-pole, 12-slot/10-pole, and 12-slot/14-pole SPM motors (Fig. 7.9.II) are 8.4 mNm, 12.3 mNm, and 22.1 mNm, respectively. This indicates that the spread of the fitted distribution of the SPM motors increases significantly with increasing rotor pole number. This results in an increased likelihood of the cogging torque falling within a wider range with respect to the nominal cogging torque. The dispersions of the fitted distributions of the cogging torque of the 12-slot/8-pole and 12-slot/10-pole IPM motors are comparable to those of the corresponding SPM motors. However, the dispersion of the fitted distribution of the 12-slot/14-pole SPM motor is almost twice that of the 12-slot/14-pole IPM motor. The skewness of the fitted log-logistic distribution follows closely the characteristic of the dispersion of the fitted distributions. The skewness of the fitted log-logistic distributions of the 12-slot/8-pole IPM and SPM motors is the lowest among the fitted distributions of the motors under investigation.

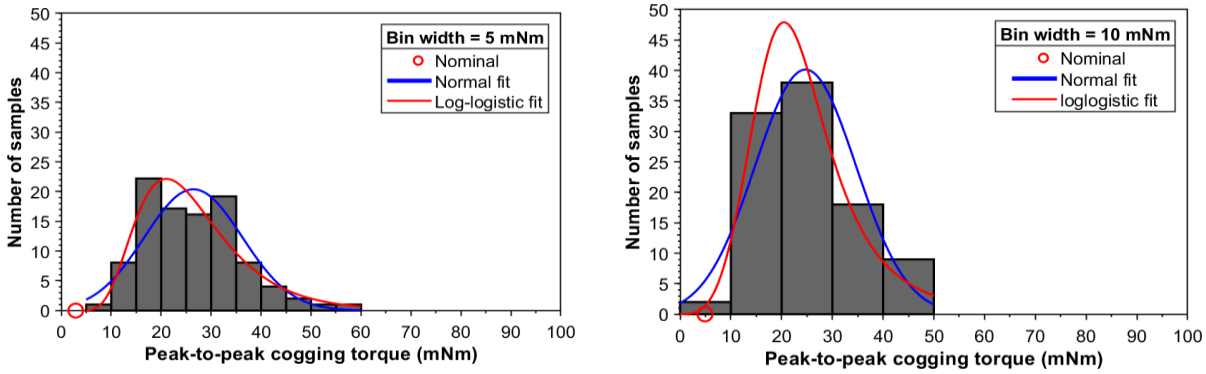
The distributions of the number of occurrences of the peak-to-peak cogging torque and the fitted distributions of the IPM and SPM motors under investigation due to rotor tolerances only are shown in Fig. 7.9.

The differences between the modes of the fitted log-logistic distribution and the nominal peak-to-peak cogging torque of the 12-slot/8-pole, 12-slot/10-pole, and 12-slot/14-pole IPM motors (Fig. 7.9.I) are 2.5 mNm, 18.2 mNm, and 28.2 mNm, respectively. The differences between the modes of the fitted log-

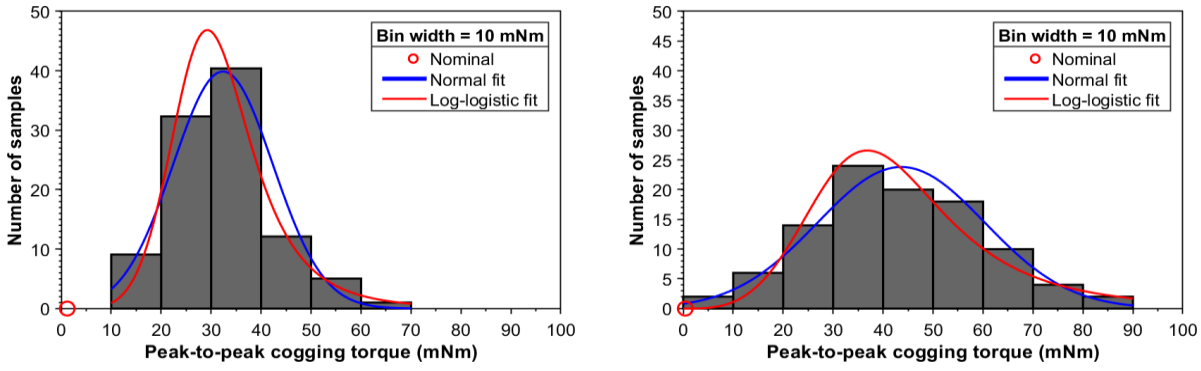
logistic distribution and the nominal peak-to-peak cogging torque of the 12-slot/8-pole, 12-slot/10-pole, and 12-slot/14-pole SPM motors (Fig. 7.9.II) are 7.8 mNm, 15.8 mNm, and 36.9 mNm, respectively. The difference of the modes of the fitted distribution from the nominal cogging torque is expected to increase with increasing rotor pole number since the number of manufacturing tolerances increases linearly with increasing rotor pole number. The lowest difference in nominal cogging torque due to rotor tolerances is attributed to the 12-slot/8-pole IPM motor and the highest difference is attributed to the 12-slot/14-pole SPM motor.




(a) 12-slot/8-pole




(b) 12-slot/10-pole




(c) 12-slot/14-pole

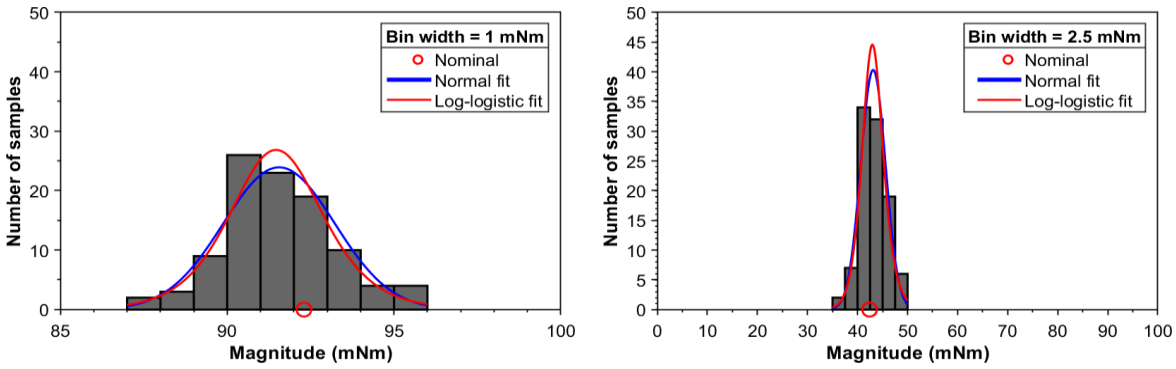
(I) IPM (II) SPM

Fig. 7.9. Distributions of number of occurrences of peak-to-peak cogging torque of IPM and SPM motors due to rotor tolerances only.

The distributions of number of occurrences of the native 24th order cogging torque components of the 12-slot/8-pole IPM and SPM motors are shown in Fig. 7.10. The differences between the modes of the fitted log-logistic distribution and the nominal magnitude of the 24th order cogging torque harmonic of the 12-slot/8-pole IPM and SPM motors are 0.8 mNm and 0.6 mNm, respectively. The interquartile ranges of the fitted log-logistic distributions of the IPM and SPM motors are 2.0 mNm and 3.1 mNm, respectively. Thus, the skewness of the fitted log-logistic distributions of the 12-slot/8-pole IPM and SPM motors is very low. The dispersion of the fitted log-logistic distribution of the 12-slot/8-pole SPM motor is higher than that of the 12-slot/8-pole IPM motor.

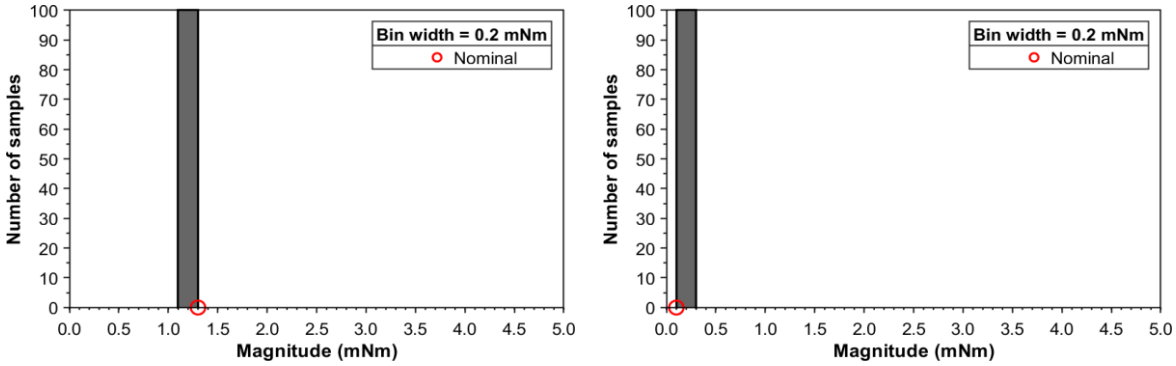
The bin widths of the native 60th order cogging torque component of the 12-slot/10-pole IPM and SPM (Fig. 7.11.) motors are very low, indicating that the magnitude of the native harmonic is insensitive to rotor tolerances. Similarly, the magnitude of the 84th order cogging torque component of the 12-slot/14-pole SPM motor, shown in Fig. 7.12, is not sensitive to rotor tolerances. The magnitude of the 84th order component is higher than the nominal value and this may be attributed to numerical noise.

The distribution of the fitted log-logistic distribution of the 12-slot/14-pole IPM motor, shown in Fig. 7.12, has very low skewness. The interquartile range of the fitted log-logistic distribution is 0.1 Nm. Thus, the dispersion of the distribution of the native 84th order component of the 12-slot/14-pole IPM motor is significantly lower than the dispersion of the distribution of the 24th order component of the 12-slot/8-pole motors (Fig. 7.10).



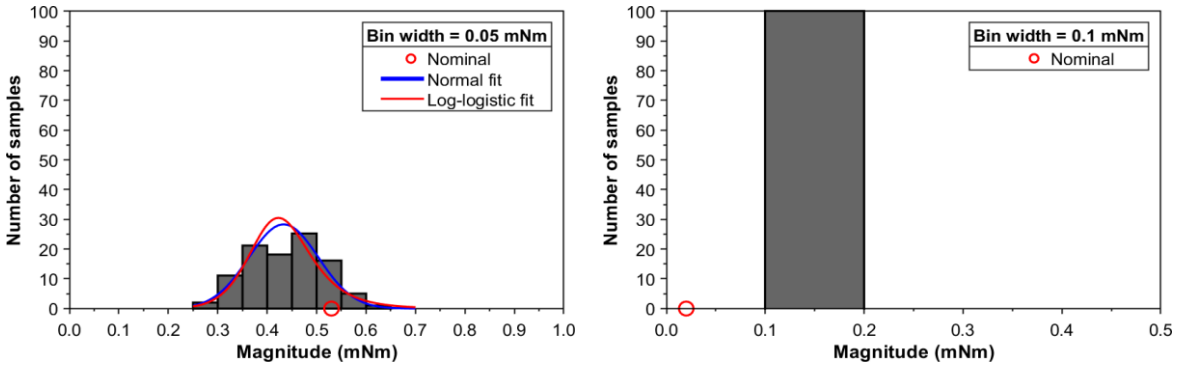

(a) IPM (b) SPM

Fig. 7.10. Distributions of number of occurrences of 24th order cogging torque components of 12-slot/8-pole IPM and SPM motors due to rotor tolerances only.



(a) IPM (b) SPM

Fig. 7.11. Distributions of number of occurrences of 60th order cogging torque components of 12-slot/10-pole IPM and SPM motors due to rotor tolerances only.




(a) IPM (b) SPM

Fig. 7.12. Distributions of number of occurrences of 84th order cogging torque components of 12-slot/14-pole IPM and SPM motors due to rotor tolerances only.

The distributions of the number of occurrences of the 12th order cogging torque AHC and the fitted distributions of the IPM and SPM motors under investigation due to rotor tolerances only are shown in Fig. 7.13.

The modes of the fitted log-logistic distribution of the 12th order cogging torque component of the 12-slot/8-pole, 12-slot/10-pole, and 12-slot/14-pole IPM motors (Fig. 7.13.I) are 2.3 mNm, 6.7 mNm, and 8.7 mNm, respectively. The modes of the fitted log-logistic distribution of the 12-slot/8-pole, 12-slot/10-pole, and 12-slot/14-pole SPM motors ((Fig. 7.13.II) are 3.9 mNm, 6.3 mNm, and 11.3 mNm, respectively.

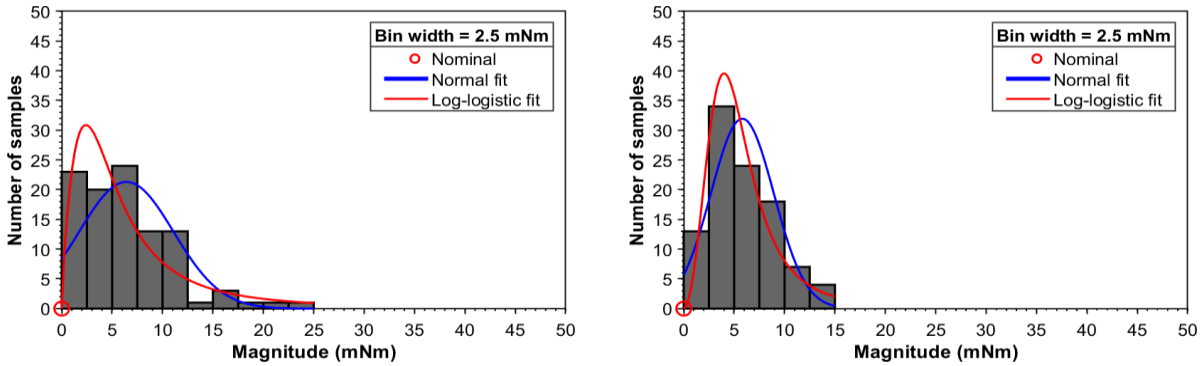
The modes of the fitted log-logistic distribution of the 12th order cogging torque component increases with increasing rotor pole number. The modes of the distributions of the 12-slot/8-pole and 12-slot/14-pole SPM motors are higher than the modes of the corresponding IPM motors. The 12-slot/10-pole IPM and SPM motor have similar modes of the fitted distribution of the 12th order cogging torque component.

The skewness of the fitted distributions of the 12th order cogging torque component of the 12-slot/8-pole and 12-slot/10-pole IPM motors is almost identical and comparable to that of the 12-slot/14-pole SPM motor. The distribution of the 12-slot/8-pole SPM motor (Fig. 7.13.Ia) exhibits the lowest skewness among the analysed motors.

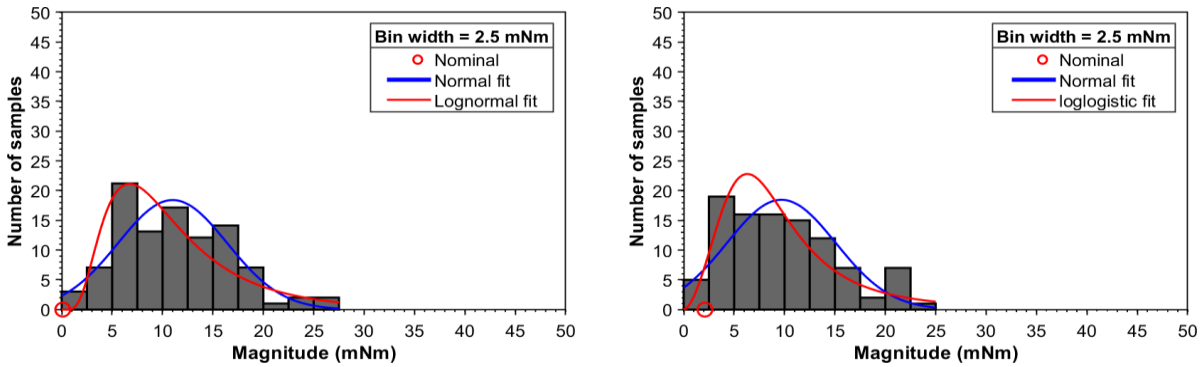
The interquartile ranges of the fitted log-logistic distribution of the 12th order cogging torque component of the 12-slot/8-pole, 12-slot/10-pole, and 12-slot/14-pole IPM motors (Fig. 7.13.I) are 6.7 mNm, 7.8 mNm, and 6.5 mNm, respectively. The interquartile ranges of the fitted log-logistic distribution of the 12th order cogging torque component of the 12-slot/8-pole, 12-slot/10-pole, and 12-slot/14-pole SPM motors ((Fig. 7.13.II) are 4.0 mNm, 7.1 mNm, and 10.9 mNm, respectively.

The dispersions of the distributions of the SPM motors increase with increasing rotor pole number. The

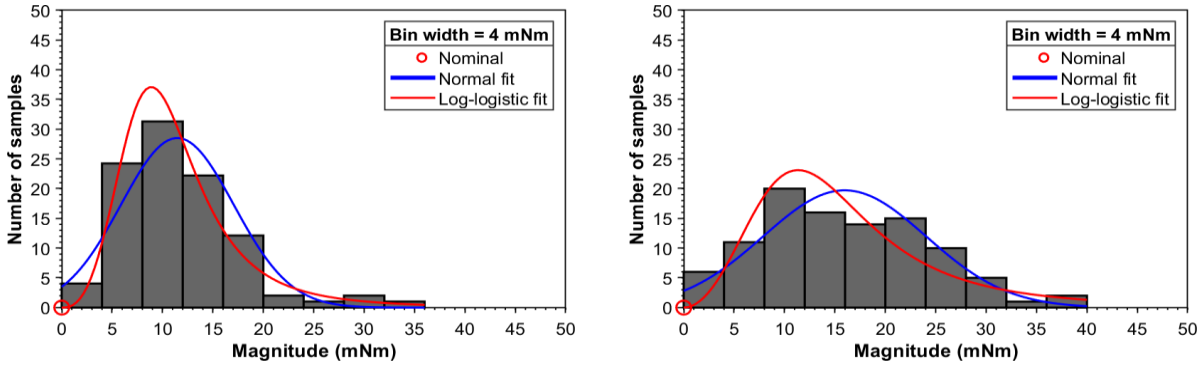
dispersions of the distributions of the 12-slot/8-pole IPM and 12-slot/14-pole IPM motors are comparable and lower than that of the 12-slot/10-pole IPM motor.




(a) 12-slot/8-pole




(b) 12-slot/10-pole




(c) 12-slot/14-pole

(I) IPM (II) SPM

Fig. 7.13. Distributions of number of occurrences of 12$^{th}$ order cogging torque components of IPM and SPM motors due to stator tolerances only.

## 7.4 Uncertainty Analysis of Cogging Torque of IPM and SPM Motors due to Stator and Rotor Tolerances

The distributions of the number of occurrences of the peak-to-peak cogging torque and the fitted distributions of the IPM and SPM motors under investigation due to combined stator and rotor tolerances are shown in Fig. 6.40.

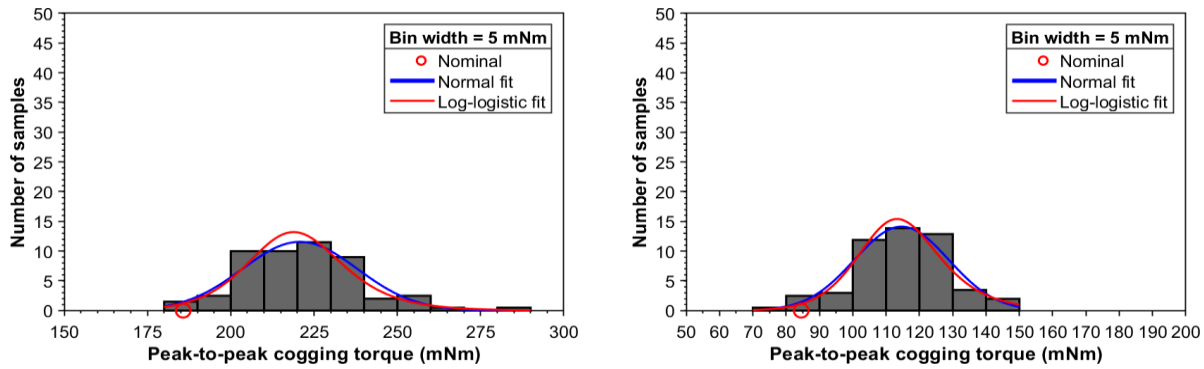
The differences between the modes of the fitted log-logistic distribution and the nominal peak-to-peak cogging torque of the 12-slot/8-pole, 12-slot/10-pole, and 12-slot/14-pole IPM motors (Fig. 6.40.I) are 33.2 mNm, 38.9 mNm, and 37.7 mNm, respectively. The differences between the modes of the fitted log-logistic distribution and the nominal peak-to-peak cogging torque of the 12-slot/8-pole, 12-slot/10-pole, and 12-slot/14-pole SPM motors (Fig. 6.40.II) are 29.1 mNm, 36.0 mNm, and 53.0 mNm, respectively. Thus, the discrepancy increases with increasing rotor pole number.

The differences between the modes of the fitted log-logistic distribution and the nominal peak-to-peak cogging torque of the 12-slot/8-pole, 12-slot/10-pole IPM motors are slightly higher than the corresponding SPM motors. Conversely, the difference between the modes of the fitted log-logistic distribution and the nominal peak-to-peak cogging torque of the 12-slot/14-pole SPM motor is higher than that of the 12-slot/14-pole IPM motor.

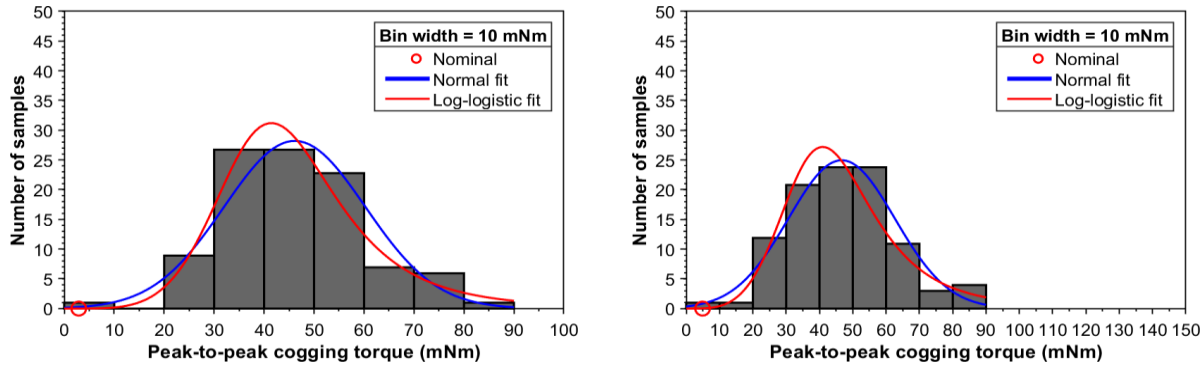
The skewness of the distributions of the 12-slot/8-pole motors is very low. The skewness of the distributions of the 12-slot/10-pole is of similar magnitude. However, the skewness of the distribution of the 12-slot/14-pole SPM motor is about twice that of the 12-slot/14-pole IPM motor.

The interquartile ranges of the fitted log-logistic distributions of the 12-slot/8-pole, 12-slot/10-pole, and 12-slot/14-pole IPM motors are 20.8 mNm, 18.4 mNm, and 15.9 mNm, respectively. The interquartile ranges of the fitted log-logistic distributions of the 12-slot/8-pole, 12-slot/10-pole, and 12-slot/14-pole SPM motors are 17.9 mNm, 21.4 mNm, and 27.7 mNm, respectively. This indicates that the spread of the fitted distribution of the SPM motors increases significantly with increasing rotor pole number. This results in an increased likelihood of the cogging torque falling within a wider range with respect to the nominal cogging torque.

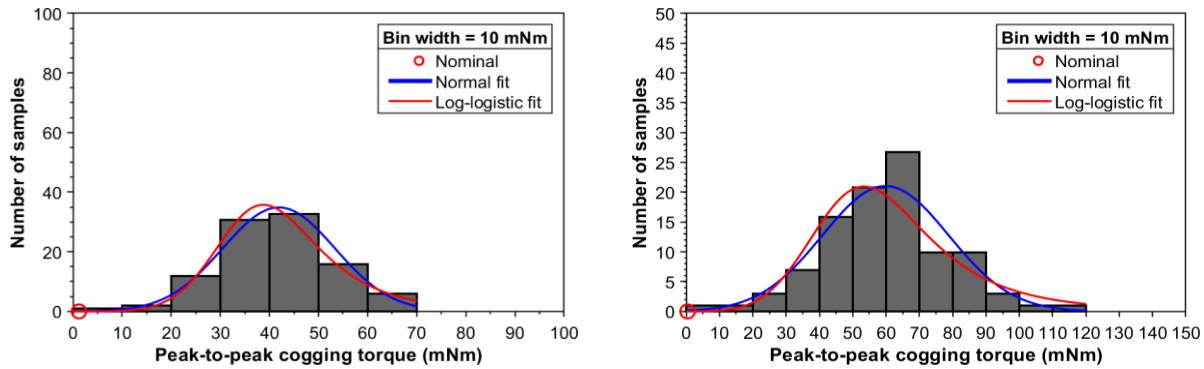
The dispersion of the distributions of the IPM motors decreases with increasing rotor pole number. On the other hand, the dispersion of the distributions of the SPM motors increases with increasing rotor pole number.




(a) 12-slot/8-pole




(b) 12-slot/10-pole

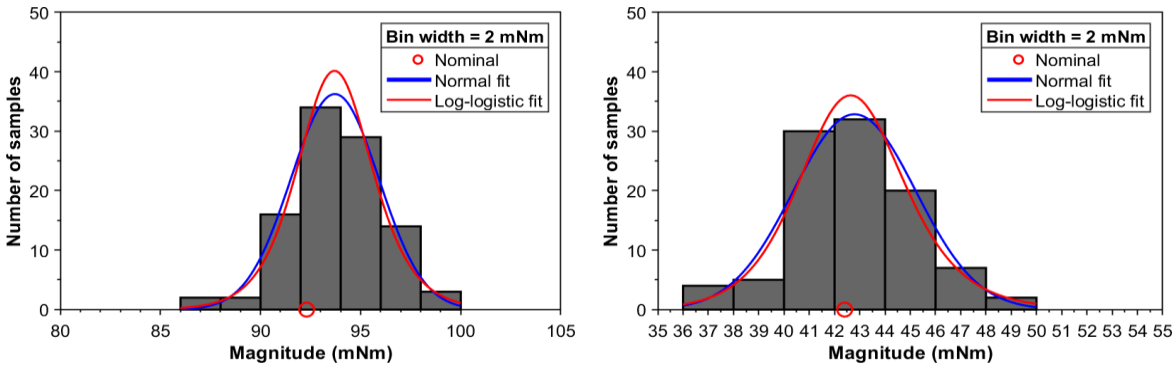



(c) 12-slot/14-pole

(I) IPM (II) SPM

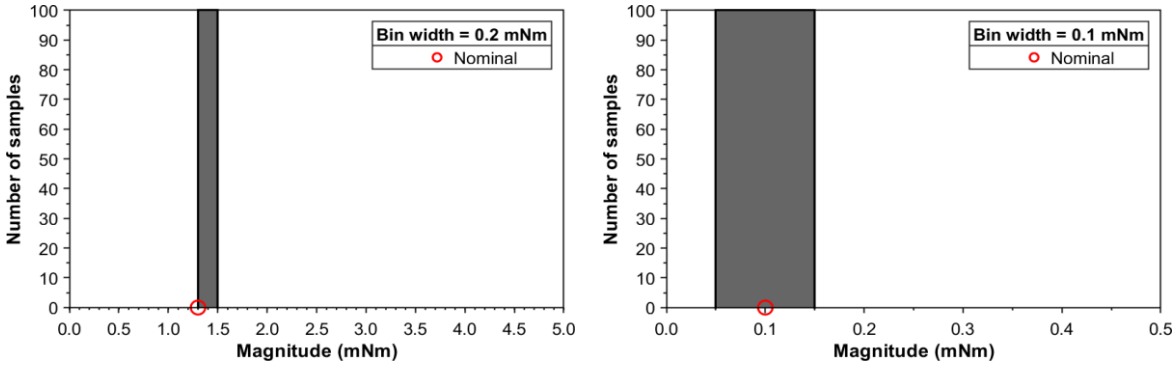
Fig. 7.14. Distributions of number of occurrences of peak-to-peak cogging torque of IPM and SPM motors due to combined stator and rotor tolerances.

The distributions of number of occurrences of the native 24$^{th}$ order cogging torque components of the 12-slot/8-pole IPM and SPM motors are shown in Fig. 7.15. The differences between the modes of the fitted log-logistic distribution and the nominal magnitude of the 24$^{th}$ order cogging torque harmonic of the 12-slot/8-pole IPM and SPM motors are 1.3 mNm and 0.2 mNm, respectively. The interquartile ranges of the fitted log-logistic distributions of the IPM and SPM motors are 2.7 mNm and 3.1 mNm, respectively. Thus, the skewness of the fitted log-logistic distributions of the 12-slot/8-pole IPM and SPM motors is very low. The dispersion of the fitted log-logistic distribution of the 12-slot/8-pole SPM motor is higher than that of the 12-slot/8-pole IPM motor.



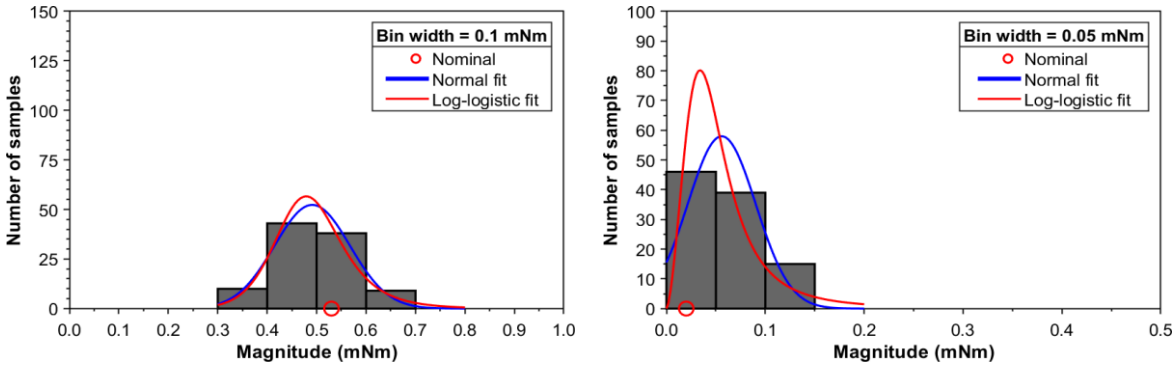

(a) IPM (b) SPM

Fig. 7.15. Distributions of number of occurrences of 24th order cogging torque components of 12-slot/8-pole IPM and SPM motors due to combined stator and rotor tolerances.




(a) IPM (b) SPM

Fig. 7.16. Distributions of number of occurrences of 60th order cogging torque components of 12-slot/10-pole IPM and SPM motors due to combined stator and rotor tolerances.




(a) IPM (b) SPM

Fig. 7.17. Distributions of number of occurrences of 84th order cogging torque components of 12-slot/14-pole IPM and SPM motors due to combined stator and rotor tolerances.

The bin width of the native 60th order cogging torque component of the 12-slot/10-pole IPM and SPM Fig. 7.16.) motors is very low, indicating that the magnitude of the native harmonic is insensitive to stator and rotor tolerances. Similarly, the uncertainty of the magnitude of the 84th order cogging torque component of the 12-slot/14-pole SPM motor, shown in Fig. 7.17, is low. The magnitude of the 84th order component is higher than the nominal value and this may be attributed to numerical noise.

The difference between the modes of the fitted log-logistic distribution and the nominal magnitude of the 84$^{th}$ order cogging torque harmonic of the 12-slot/14-pole IPM motor, shown in Fig. 7.17, is less than 0.1 mNm. The interquartile range of the fitted log-logistic distribution is 0.1 mNm.

The fitted log-logistic distribution of the native cogging torque components is low. The dispersion of the native 24$^{th}$ order component of the 12-slot/8-pole SPM motor is high, indicating a significant probability that the magnitude of the native 24$^{th}$ order component is different from the nominal value.

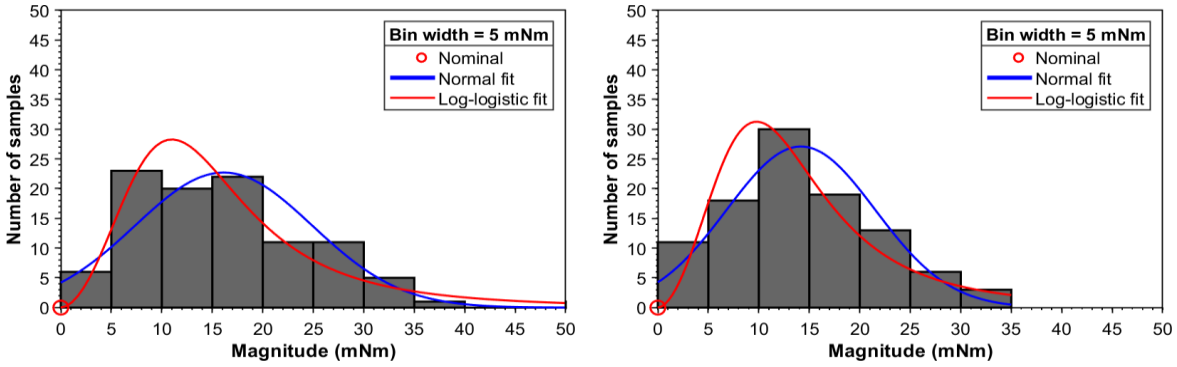
The distributions of number of occurrences of the 8$^{th}$ order cogging torque AHC of the 12-slot/8-pole IPM and SPM motors are shown in Fig. 7.18. The modes of the fitted log-logistic distributions of the 12-slot/8-pole IPM and SPM motors are 11.1 mNm and 9.9 mNm, respectively. The differences between the modes of the fitted log-logistic distribution and the mean of the fitted normal distribution of the IPM and SPM motors are 5.0 mNm and 4.3 mNm, respectively. The interquartile ranges of the fitted log-logistic distributions of the IPM and SPM motors are 11.3 mNm and 10.3 mNm, respectively. Therefore, the distributions of the 8$^{th}$ order cogging torque components of 12-slot/8-pole IPM and SPM motor have similar characteristics. The mode, skewness and dispersion of the fitted log-logistic distribution of the SPM motor are slightly lower than those of the IPM motor.

The distributions of number of occurrences of the 10$^{th}$ order cogging torque AHC of the 12-slot/10-pole IPM and SPM motors are shown in Fig. 7.19. The modes of the fitted log-logistic distributions of the 12-slot/10-pole IPM and SPM motors are 7.5 mNm and 7.6 mNm, respectively. The differences between the modes of the fitted log-logistic distribution and the mean of the fitted normal distribution of the IPM and SPM motors are 2.0 mNm and 3.7 mNm, respectively. The interquartile ranges of the fitted log-logistic distributions of the IPM and SPM motors are 5.7 mNm and 8.6 mNm, respectively. Therefore, the skewness and dispersion of the fitted log-logistic distribution of the 12-slot/10-pole SPM motor are significantly higher than those of the corresponding IPM motor.

The distributions of number of occurrences of the 14$^{th}$ order cogging torque AHC of the 12-slot/14-pole IPM and SPM motors are shown in Fig. 7.20. The modes of the fitted log-logistic distributions of the 12-slot/14-pole IPM and SPM motors are 2.5 mNm and 6.5 mNm, respectively. The differences between the modes of the fitted log-logistic distribution and the mean of the fitted normal distribution of the IPM and SPM motors are 1.5 mNm and 2.6 mNm, respectively. The interquartile ranges of the fitted log-logistic distributions of the IPM and SPM motors are 3.0 mNm and 6.2 mNm, respectively. The mode, skewness and dispersion of the fitted log-logistic distribution of the 12-slot/14-pole SPM motor are about twice those of the corresponding IPM motor.

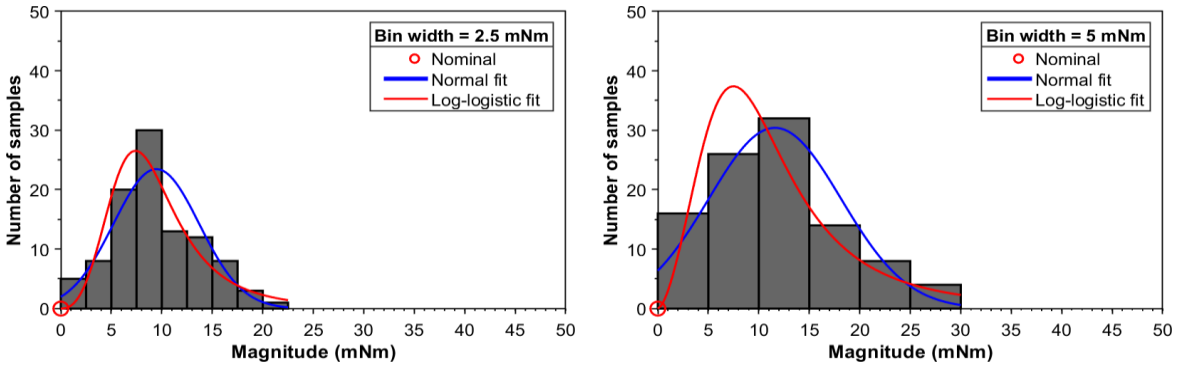
Tolerances in the stator geometry result in the 8$^{th}$ order, 10$^{th}$ order, and 14$^{th}$ order cogging torque AHCs in 12-slot/8-pole, 12-slot/10-pole, and 12-slot/14-pole motors, respectively. The modes and degrees of skewness and dispersions of the fitted distributions of the cogging torque AHCs under investigation are attributed to stator tolerances, and decrease with increasing rotor pole number. The difference between the

dispersions of the distribution of the IPM and SPM motors of the same rotor pole number increases with increasing rotor pole number.



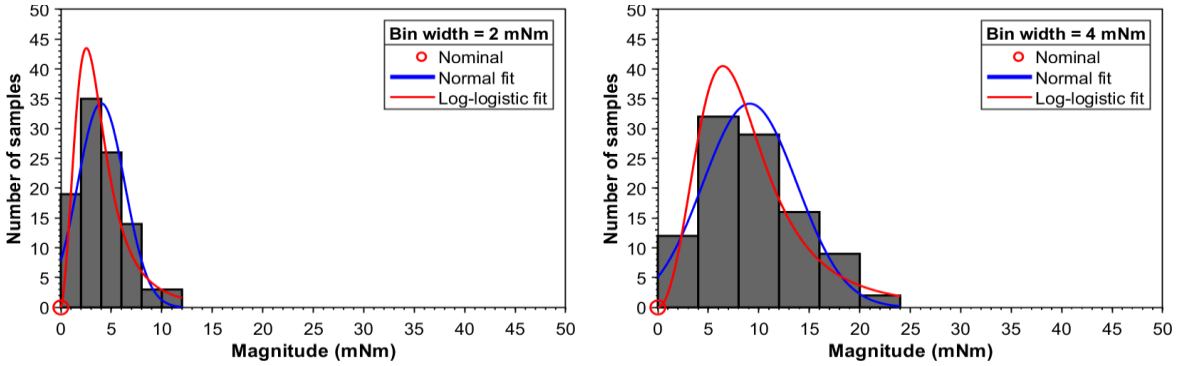

(a) IPM (b) SPM

Fig. 7.18. Distributions of number of occurrences of 8$^{th}$ order cogging torque components of 12-slot/8-pole IPM and SPM motors due to combined stator and rotor tolerances.




(a) IPM (b) SPM

Fig. 7.19. Distributions of number of occurrences of 10$^{th}$ order cogging torque components of 12-slot/10-pole IPM and SPM motors due to combined stator and rotor tolerances.




(a) IPM (b) SPM

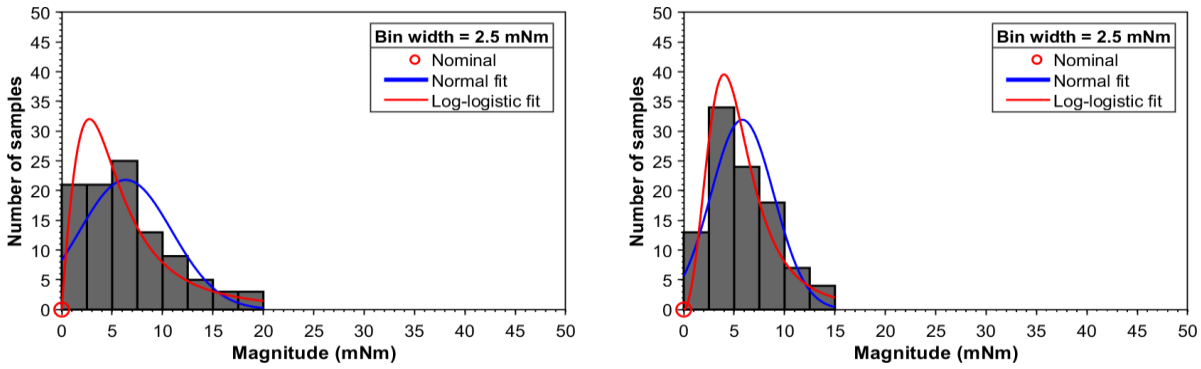
Fig. 7.20. Distributions of number of occurrences of 14$^{th}$ order cogging torque components of 12-slot/14-pole IPM and SPM motors due to combined stator and rotor tolerances.

The distributions of the number of occurrences of the 12th order cogging torque AHC and the fitted distributions of the IPM and SPM motors under investigation due to combined stator and rotor tolerances are shown in Fig. 7.21.

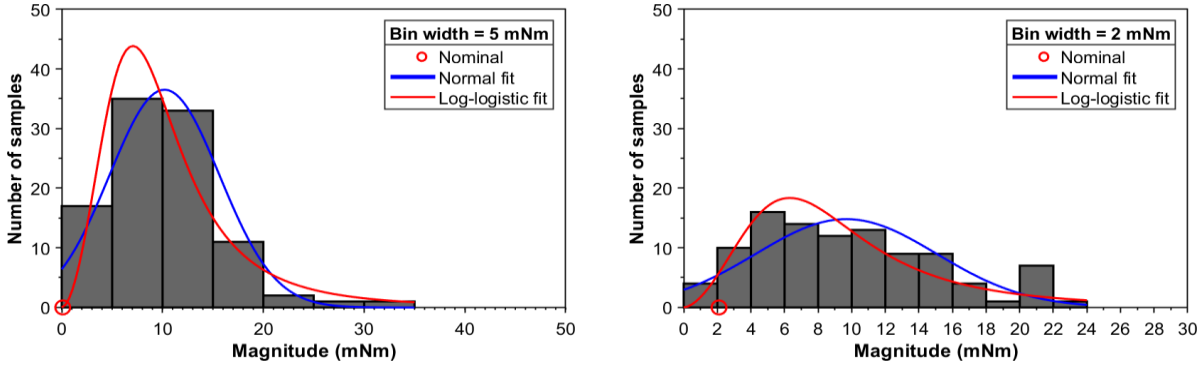
The modes of the fitted log-logistic distribution of the 12-slot/8-pole, 12-slot/10-pole, and 12-slot/14-pole IPM motors (Fig. 7.21.I) are 2.8 mNm, 7.0 mNm, and 8.5 mNm, respectively. The modes of the fitted log-logistic distribution of the 12-slot/8-pole, 12-slot/10-pole, and 12-slot/14-pole SPM motors (Fig. 7.21.II) are 3.9 mNm, 6.3 mNm, and 11.3 mNm, respectively.

The interquartile ranges of the fitted log-logistic distributions of the 12-slot/8-pole, 12-slot/10-pole, and 12-slot/14-pole IPM motors are 6.0 mNm, 7.3 mNm, and 8.3 mNm, respectively. The interquartile ranges of the fitted log-logistic distributions of the 12-slot/8-pole, 12-slot/10-pole, and 12-slot/14-pole SPM motors are 4.0 mNm, 7.1 mNm, and 10.8 mNm, respectively.

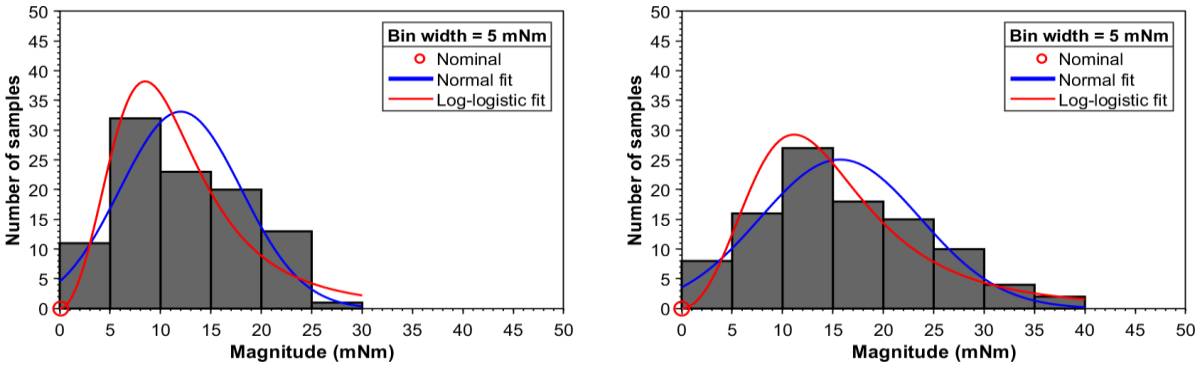
The modes of the fitted distribution of the 12th order components of the IPM and SPM motors increase with increasing pole number. This is expected since the number of rotor tolerances increases with increasing rotor pole number. The skewness of the fitted distribution of the 12th order component of the IPM motors does not vary significantly with rotor pole number. On the other hand, the skewness of the distributions of the SPM motors increases with increasing rotor pole number. The dispersions of the fitted distribution of the IPM and SPM motors increase with increasing rotor pole number.




(a) 12-slot/8-pole




(b) 12-slot/10-pole




(c) 12-slot/14-pole

(I) IPM (II) SPM

Fig. 7.21. Distributions of number of occurrences of 12th order cogging torque AHC of IPM and SPM motors due to combined stator and rotor tolerances.

## 7.5 Conclusion

This chapter has investigated the uncertainty of the peak-to-peak cogging torque, cogging torque NHCs and cogging torque AHCs due to stator tolerances, rotor tolerances, and combined stator and rotor tolerances. Uncertainty of various parameters is quantified using Monte-Carlo simulations with a sample size of 100 motors. It is assumed that the probability density of manufacturing tolerances follows the normal distribution as shown in Fig. 7.1. Normal and log-logistic distributions are fitted to the distributions of number of occurrences of the analysed parameters to more accurately identify the skewness and dispersion of the distributions. The differences between modes of the fitted log-logistic distribution and nominal peak-to-peak cogging torque due to stator tolerances, rotor tolerances, and combined stator and rotor tolerances are listed in Table 6.25. The interquartile ranges of the fitted log-logistic distributions of the peak-to-peak cogging torque due to stator tolerances, rotor tolerances, and combined stator and rotor tolerances are listed in Table 7.2.

Table 7.1. Difference between modes of the fitted log-logistic distribution and nominal peak-to-peak cogging torque due to tolerances

| **Units: (mNm)** | **Stator tolerances** | | **Rotor tolerances** | | **Stator and rotor tolerances** | |
|---|---|---|---|---|---|---|
| | **IPM** | **SPM** | **IPM** | **SPM** | **IPM** | **SPM** |
| 12-slot/8-pole | 23.3 | 20.2 | 2.5 | 7.8 | 33.2 | 29.1 |
| 12-slot/10-pole | 18.3 | 14.9 | 18.2 | 15.8 | 38.9 | 36.0 |
| 12-slot/14-pole | 7.9 | 10.7 | 28.2 | 36.9 | 37.7 | 53.0 |

Table 7.2. Interquartile ranges of the fitted log-logistic distributions of the peak-to-peak cogging torque due to tolerances

| Units: (mNm) | Stator tolerances | | Rotor tolerances | | Stator and rotor tolerances | |
|---|---|---|---|---|---|---|
| | IPM | SPM | IPM | SPM | IPM | SPM |
| 12-slot/8-pole | 18.3 | 16.2 | 8.6 | 8.4 | 20.8 | 17.9 |
| 12-slot/10-pole | 7.5 | 17.3 | 13.3 | 12.3 | 18.4 | 21.4 |
| 12-slot/14-pole | 5.2 | 13.3 | 12.2 | 22.1 | 15.9 | 27.7 |

Stator tolerances result in a higher probability of deviation from the nominal peak-to-peak cogging torque in motors with lower rotor pole number. The differences between the modes of the fitted distribution and the nominal peak-to-peak cogging torque due to stator tolerances (Fig. 7.2) are higher in 12-slot/8-pole and 12-slot/10-pole IPM motors than that of the corresponding SPM motors. The dispersion of the distributions of IPM motors decreases significantly with increasing rotor pole number, resulting in a lower range of possible peak-to-peak cogging torque. Thus, the peak-to-peak cogging torques of the 12-slot/14-pole and 12-slot/8-pole IPM motors exhibit the lowest and highest uncertainty due to stator tolerances.

The uncertainties of the native $24^{th}$ order cogging torque component of the 12-slot/8-pole IPM and SPM motors (Fig. 7.3) due to stator tolerances are significantly higher than the uncertainties of the native cogging torque components of the 12-slot/10-pole and 12-slot/14-pole motors. The dispersion of the native $24^{th}$ order component of the IPM motor is about four times higher than that of the SPM motor.

The skewness and dispersion of the fitted log-logistic distributions of the cogging torque AHCs of SPM motors due to stator tolerances are higher than the skewness and dispersion of IPM motors (Fig. 7.6-Fig. 7.8). Furthermore, the skewness and dispersion decrease with increasing rotor pole number and the rate of decrease is higher in IPM motors. Therefore, the peak to-peak cogging torques of IPM motors with higher rotor pole number are less susceptible to uncertainty due to stator tolerances.

The number of rotor tolerances increases with increasing rotor pole number. Therefore, the dispersion of the fitted log-logistic distribution and the difference of the modes of the fitted distribution from the nominal cogging torque increase with increasing rotor pole number (Fig. 7.9). The lowest difference in nominal cogging torque due to rotor tolerances is attributed to the 12-slot/8-pole IPM motor and the highest difference is attributed to the 12-slot/14-pole SPM motor.

The skewness and dispersion of the fitted log-logistic distribution of the native $24^{th}$ order cogging torque components of the 12-slot/8-pole IPM and SPM motor due to stator tolerances (Fig. 7.3) and rotor tolerances (Fig. 7.10) do not vary significantly. The mode of the fitted log-logistic distribution of the $24^{th}$ order component due to stator tolerances in the 12-slot/8-pole IPM motor is slightly higher than the nominal

value. Conversely, the mode of the fitted log-logistic distribution of the 24$^{th}$ order component of the 12-slot/8-pole SPM motor due to stator tolerances is slightly lower than the nominal value.

The distributions of the number of occurrences of the peak-to-peak cogging torque of IPM and SPM motors subjected to combined stator and rotor tolerances are shown in Fig. 6.40. The properties of the fitted log-logistic distributions of the 12-slot/10-pole IPM and SPM motors are similar. The difference between the modes of the fitted log-logistic distribution and the nominal peak-to-peak cogging torque increases with increasing rotor pole number. Furthermore, the skewness of the fitted log-logistic distributions increases with increasing rotor pole number. The dispersion of the distributions of the IPM motors decreases with increasing rotor pole number. On the other hand, the dispersion of the distributions of the SPM motors increases with increasing rotor pole number.

The distributions of number of occurrences of the native 24$^{th}$ order cogging torque components of the 12-slot/8-pole IPM and SPM motors subjected to stator and rotor tolerances are shown in Fig. 7.15. The differences between the modes of the fitted log-logistic distribution and the nominal magnitude of the 24$^{th}$ order cogging torque harmonic of the 12-slot/8-pole IPM and SPM motors are 1.3 mNm and 0.2 mNm, respectively. The skewness and dispersion of the fitted log-logistic distributions of the 12-slot/8-pole IPM and SPM motor are almost identical. The uncertainties of the native cogging torque components of the 12-slot/10-pole and 12-slot/14-pole motors are very low.

Tolerances in the stator geometry result in cogging torque AHCs with an order equal to the rotor pole number. The modes, degrees of skewness, and dispersions of the fitted distributions of the cogging torque AHCs attributed to stator tolerances decrease with increasing rotor pole number. The difference between the dispersion of the distribution of the IPM and SPM motors of the same rotor pole number increases with increasing rotor pole number.

Tolerances in the rotor geometry result in the 12$^{th}$ order cogging torque AHCs .The dispersion and modes of the fitted distribution of the 12$^{th}$ order components of the IPM and SPM motors increase with increasing pole number. The skewness of the fitted distribution of the 12$^{th}$ order component of the IPM motors does not vary significantly with rotor pole number. On the other hand, the skewness of the distributions of the SPM motors increases with increasing rotor pole number.

The difference of the modes of the fitted distributions of the native 24$^{th}$ order cogging torque component of the 12-slot/8-pole IPM motor from the nominal value due to stator and rotor tolerances is equivalent to the sum of the difference due to stator tolerances only and rotor tolerances only. This indicates that the influence of stator and rotor tolerances on the native 24$^{th}$ order component is additive and that rotor tolerances contribute to up to 61.5% of the difference of the mode of the distribution from the nominal value. The difference of the modes of the fitted distributions of the native 24$^{th}$ order cogging torque component of the 12-slot/8-pole SPM motor is very low.

The dispersion of the fitted distribution of the 24$^{th}$ order component of the 12-slot/8-pole SPM motor due

to stator tolerances is very low. The dispersion due to stator and rotor tolerances is very similar to that of the distribution due to rotor tolerances only. Therefore, the dispersion of the fitted distribution is mostly attributed to rotor tolerances.

The characteristics of the fitted distributions of the cogging torque AHCs equal to the rotor pole number of motors subjected to rotor tolerances only and combined stator and rotor tolerances are very similar. The properties of the fitted distributions of the $12^{th}$ order AHC due to stator tolerances only and combined stator and rotor tolerances are also similar.

# 8 CONCLUSIONS AND DISCUSSION

## 8.1 Motivation and Methodology

PMSMs are extensively used in a wide variety of applications, including automotive industry, due to their advantages in terms of power density, efficiency, and reliability [ZHU14]. Power steering systems reduce the torque that the driver has to apply, filter interference from the road surface, and provide useful feedback [HAR17]. EPS systems present significant improvements in functionality, weight, volume, and efficiency of the power steering system, leading to better mileage and lower emissions [BUR03, GAE17].

There are various PMSM topologies with varying slot, winding, and rotor configurations as outlined in Chapter 1. The two most commonly used PM motor topologies are SPM motors and IPM motors. The interaction of the stator teeth and the rotor PM field results in no-load torque pulsation, commonly referred to as cogging torque.

Global optimisation is used extensively to identify one or more solutions from a solution space that satisfy one or more objective functions subject to a number of constraints on the design variables [MAR04]. The main difference between single-objective and multi-objective problems is that the outcome of a multi-objective optimisation problem is a set of solutions with varying degrees of each objectives rather than one solution. Multi-objective optimisation of conflicting objectives can be used to identify a set of Pareto-optimal solutions forming a Pareto-front. The preferred solution can then be determined a posteriori.

Mass production processes inevitably lead to manufacturing tolerances resulting in deviations from the nominal motor geometry. Consequently, manufacturing tolerances lead to a variation in the expected performance of a motor. Manufacturing tolerances may affect the assembly of stator and rotor laminations, magnet dimensions and placement, and stator and rotor concentricity among other factors [ISL04].

EPS systems have stringent requirements on motor volume and torque ripple among other factors. Various motor topologies have been optimised for EPS applications including SPM motors [DUA09, DUA13, LIP15], IPM motors [BIA02, PEL10, ALO11].

The main objectives of the thesis are as follows:

- Analysis of the performances of a baseline 12-slot/8-pole IPM motor
- Single-objective optimisation of IPM and SPM motors of different slot/pole number combinations for maximum average torque
- Multi-objective optimisation of IPM and SPM motors of different slot/pole number combinations for maximum average torque and minimum torque ripple
- Identification of a set of multi-objective optimised IPM and SPM motors of different slot/pole number combinations with the same volume and similar torque performance
- Analysis of cogging torque sensitivity of multi-objective optimised motors to manufacturing tolerances
- Identification of worst-case scenarios of cogging torque due to manufacturing tolerances
- Analysis of cogging torque uncertainty due to manufacturing tolerances

## 8.2 Electromagnetic Performance of Baseline IPM Motor

The electromagnetic performance of the baseline 12-slot/8-pole IPM motor, shown in Fig. 2.1, is analysed using 2D FEA. The motor torque is analysed under no-load and on-load condition given zero d-axis current. The peak-to-peak cogging torque is 19.4 mNm, the on-load average torque is 4.6 Nm, and the torque ripple is 34.6 mNm.

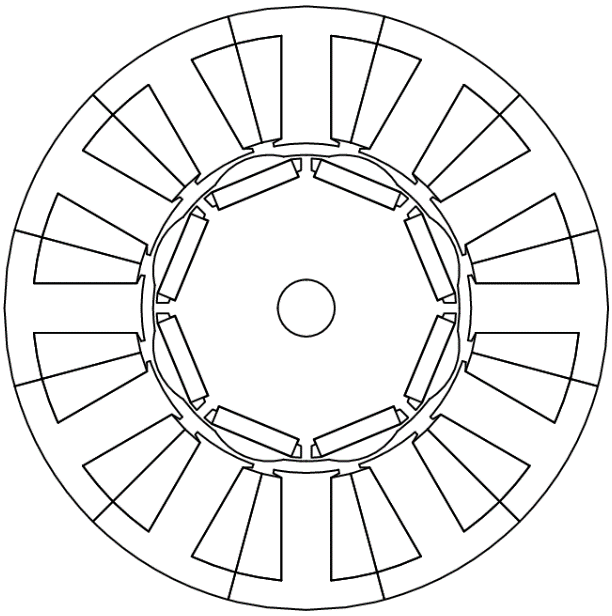


Fig. 8.1. Cross-section of baseline 12-slot/8-pole IPM motor.

The influence of design parameters on the no-load and on-load torque of the motor given zero d-axis current is investigated. The influence of changes in the split ratio, stator back-iron width, and rib width on the cogging torque is not significant. The cogging toque increases with increasing slot opening width. The influence of the pole-shoe height on the cogging torque decreases with increasing pole-arc to pole-pitch ratio.

The average torque is sensitive to changes in the split ratio, stator back-iron width, stator tooth width, and pole-shoe dimensions due to the significant impact on the air-gap magnetic flux density and the operating point of the stator material. Similarly, the torque ripple is very sensitive to changes in the stator back-iron width, stator tooth width, and pole-shoe dimensions.

The influences of electric load and current angle on the motor inductances and torque characteristics are investigated. The d-axis inductance is lower than the q-axis inductance resulting in reluctance torque. The influence of the q-axis current on the d-axis inductance is fairly low. Conversely, the influence of negative d-axis current on the q-axis inductance is significant due to the inherent flux weakening effect attributed to negative d-axis currents. The average torque increases linearly with load and the relative torque ripple decreases with increasing load.

Analysis of the influence of the current angle on the average torque shows that the maximum average torque occurs at a current angle of 8.3° and that the magnitude of the reluctance torque decreases with decreasing load level. The sensitivity of the absolute torque ripple to current angle increases significantly with increasing load. Maps of the torque ripple and current angle across the entire torque-speed operating range of the motor were calculated. The torque ripple does not vary significantly in the constant torque region and increases significantly with increasing rotational speed due to the increase in current angle.

A prototype of the baseline motor with some minor modifications to the PM material and the rotor step-skewing angles has been tested in a previous study [GE16]. The 2D FEA model used in this analysis was adapted to the prototype and the cogging torque of the motor with and without rotor step-skew was analysed. The difference peak-to-peak cogging torque of the motor without rotor step-skew obtained experimentally and using 2D FEA is 5%. The cogging torque of the motor with rotor step-skew obtained using 2D FEA is negligible compared that obtained experimentally. This discrepancy is due to the fact that axial effects such as end-effects and interaction between rotor steps are not accounted for in 2D FEA. It is shown that the measured peak cogging torque and harmonics are significantly higher than those obtained using 2D FEA, attributed to imperfections in the stator and the rotor, which clearly demand an in-depth investigation on the influence of manufacturing tolerance and imperfections, as discussed in subsequent chapters.

## 8.3 Single-Objective and Multi-Objective Optimisation of IPM and SPM Motors

The solution space of the multi-objective optimisation of IPM and SPM motors as well as the average torque and torque ripple of the single-objective optimised motors are shown in Fig 4.22.

The average torque of the single-objective optimised SPM motors is significantly higher than that of the IPM motors despite the increase in effective air-gap due to the rotor sleeve. The corresponding torque ripples of the single-objective optimised 12-slot/8-pole and 12-slot/10-pole IPM motors are significantly lower than that of the SPM motors with the same slot/pole number combination. However, the torque ripple of the single-objective optimised 12-slot/14-pole IPM motor is higher than that of the 12-slot/14-pole SPM motor.

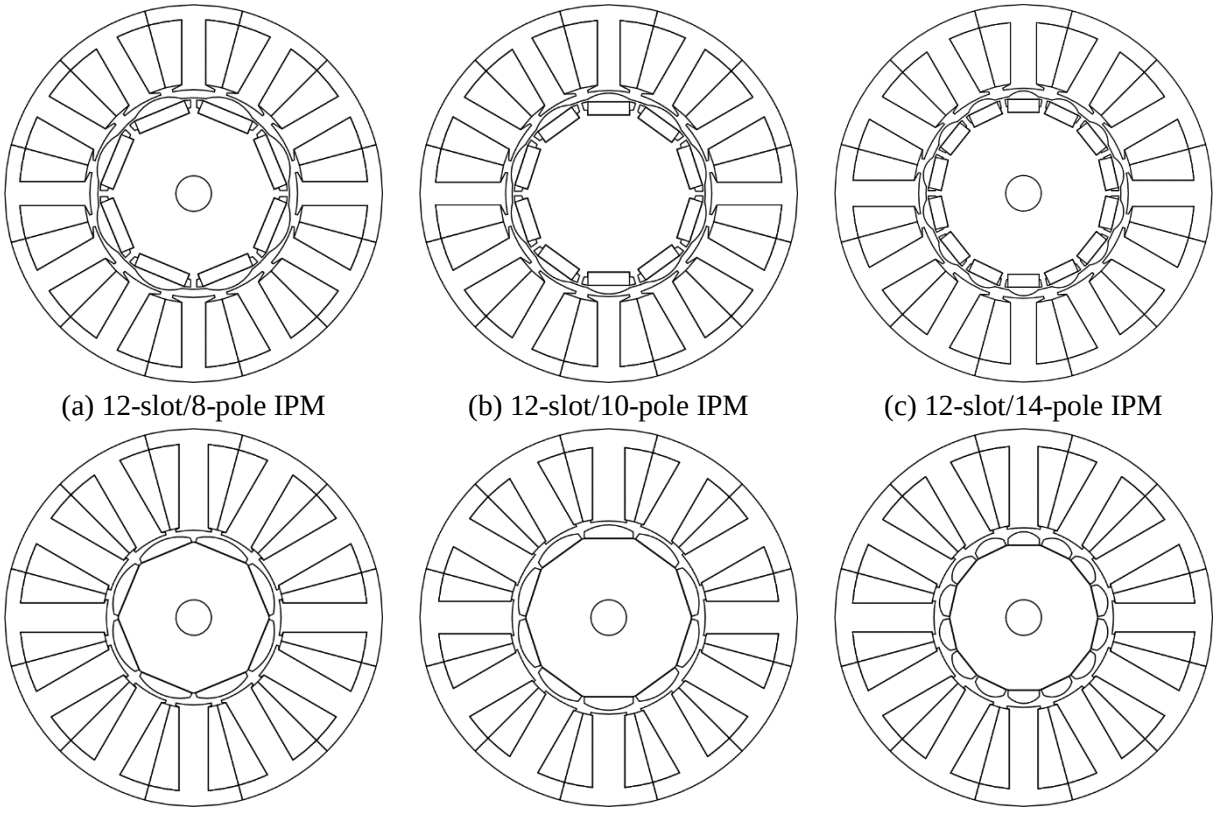
The Pareto-front of the multi-objective optimisation of the IPM and SPM motors under investigation shows that the SPM motors allow for a better compromise between the average torque and torque ripple at the optimised operating point. Thus, SPM motors can provide lower torque ripple and higher average torque than IPM motors with the same slot/pole-number combination. The discrepancy between the Pareto-fronts of the IPM and SPM motors increases with increasing rotor pole number. This can be attributed to the fact that the number of flux leakage paths through the rotor iron ribs of IPM motors increases with increasing rotor pole number, thus resulting in lower average torque.

The design of the IPM and SPM motors optimised for maximum average torque, with unified stator slot opening width, is analysed. The difference in average torque between IPM and SPM motors of a given slot/pole number combination increases with increasing rotor pole number. Conversely, the difference in torque ripple decreases with increasing rotor pole number. The current angle of the motors decreases with increasing rotor pole number since the reluctance torque decreases significantly. Furthermore, the current angle of IPM motors is significantly higher than that of SPM motors.

The average torque per PM volume of IPM motors increases with increasing rotor pole number. The 12-slot/14-pole SPM motor has the highest torque per PM volume, which is 21.1% and 24.1% higher than those of the 12-slot/8-pole SPM motor and 12-slot/10-pole SPM motors, respectively. The 12-slot/10-pole SPM motor has the highest torque density of 34.78 $mNm/m^3$, which is 37% higher than that of the 12-slot/14-pole IPM motor.

The split ratio of the IPM motors is higher than that of the SPM motors and the difference in split ratios between IPM and SPM motors of a particular slot/pole number combination decreases with increasing rotor pole number. The stator back-iron width and tooth width of the optimised IPM motors decreases with increasing rotor pole number. The pole-shoe heights of the IPM and SPM motors of the 12-slot/8-pole and 12-slot/10-pole motors with a given rotor pole number are identical. The pole-arc to pole-pitch ratios of the IPM motors are lower than those of the SPM motors.

The solution spaces of the multi-objective optimisation of 12-slot/8-pole, 12-slot/10-pole and 12-slot/14-pole IPM motors and the corresponding SPM motors with the same slot/pole number combination were superimposed. Motors around the knee of the Pareto-front with similar average torque and torque ripple at the optimised operating point are selected to enable a fair comparison. The discrepancy between the Pareto-front of the 12-slot/14-pole IPM and SPM motors is significant resulting in a discrepancy in average torque of the selected motors. The cross-sections of the selected motor are re-iterated in Fig. 8.3.



(a) 12-slot/8-pole IPM (b) 12-slot/10-pole IPM (c) 12-slot/14-pole IPM

(d) 12-slot/8-pole SPM (e) 12-slot/10-pole SPM (f) 12-slot/14-pole SPM

Fig. 8.2. Cross-sections of IPM and SPM motors under investigation.

## 8.4 Cogging Torque Sensitivity to Manufacturing Tolerances in IPM and SPM Motors

Manufacturing tolerances in mass-production processes lead to deviations from the nominal geometry that, in turn, affect the cogging torque of motors. Thus, quantification of sensitivity of the cogging torque due to manufacturing tolerances in the IPM and SPM motors under investigation is essential.

The cogging torque of a motor is composed of the inherent Native Harmonic Components (NHCs) and Additional Harmonic Components (AHCs), defined in Section 5.1, due manufacturing tolerances. The fundamental component of cogging torque of a motor without any deviations from the nominal design is defined by the Least Common Multiple (LCM) of the number of rotor PM poles ($2p$) and the number of

stator slots ($N_s$), as defined in Section 5.1,

Therefore, a 12-slot/8-pole motor without manufacturing tolerances would result in a cogging torque waveform composed of the 24$^{th}$ order NHC and its higher-order multiples. Similarly, the fundamental cogging torque component of the 12-slot/10-pole and 12-slot/14-pole motors are the 60th order component and 84th order component, respectively.

The fundamental cogging torque AHC due to a manufacturing tolerance in the stator results in a fundamental AHC equal to the number of rotor poles. Manufacturing tolerances in the rotor poles result in a fundamental AHC equal to stator slot number AHC and its harmonic multiples. Manufacturing tolerances may affect the air-gap flux density resulting in AHCs coinciding with the NHCs leading to a change in the magnitude of the native cogging torque components. The magnitudes of the AHCs coinciding with the NHCs are very low in 12-slot/10-pole and 12-slot/14-pole motors. The magnitude and phase of individual cogging torque AHCs due to a particular tolerance depend on the magnitude, direction, and location of the tolerance. The resultant AHCs due to multiple tolerances are equal to the phasor addition of the individual AHC due to the individual tolerances.

The stator tolerances under analysis are tolerances in the back-iron width, tooth width, tooth-tip height and width, and tooth surface profile radial position. The influence of tolerances in the back-iron width and tooth width on cogging torque of the motors is very low. The magnitude of the fundamental AHC due to tolerances in the tooth-tip width increases with increasing rotor pole number. Conversely, the magnitude of the fundamental AHC due to tolerances in the tooth profile radial position decreases with increasing rotor pole number. The magnitudes of the AHCs due to tolerances in tooth profile radial position are significantly higher than those due to the tolerances in tooth-tip width in 12-slot/8-pole and 12-slot/10-pole motors. The opposite effect is observed in the 12-slot/14-pole motor.

The IPM rotor tolerances under analysis are tolerances in the pole-shoe height, pole-shoe width, cavity size, rib width, PM remanence, PM height, PM width, and PM radial and lateral displacement. The SPM rotor tolerances under analysis are tolerances in the rotor iron profile, PM remanence, PM height, PM width, and PM radial and lateral displacement.

The air-gap flux density is highly influenced by the air-gap length and the PM height. Thus, the influences of tolerances in the pole-shoe height and PM height on cogging torque are significant. The magnitudes of the AHCs due to tolerances in the pole-shoe height decrease with increasing rotor pole number and this effect is attributed to the decrease in flux per pole with increasing rotor pole number.

The influence of tolerances in the lateral position of the PM in all IPM motors is negligible. The influence of tolerances in PM width on magnitudes of the AHCs of the 12-slot/8-pole motor is very low. The influence of tolerances in rotor rib width is very low in 12-slot/8-pole and 12-slot/10-pole IPM motors, but non-negligible in the 12-slot/14-pole IPM motor.

The 12-slot/8-pole IPM motor is less sensitive to tolerances in the rotor PM than the 12-slot/10-pole and 12-slot/14-pole motors. The influences of tolerances in the rotor PM of 12-slot/10-pole and 12-slot/14-pole IPM motors on the magnitudes of the 12$^{th}$ order AHC are very similar.

Tolerances in the rotor iron profile of SPM motors do not introduce any asymmetry in the motor geometry. The gap between the PMs and the rotor iron profile is directly affected by tolerances in the rotor iron profile, thereby affecting the air-gap flux density. Consequently, the magnitude of harmonics coinciding with the NHCs is affected. The influence of tolerances in the PM height on cogging torque increases significantly with increasing rotor pole number. Conversely, the influence of tolerances in the pole-shoe height and PM width on cogging torque decreases with increasing pole-number.

The native 24$^{th}$ order cogging torque component of the 12-slot/8-pole SPM motor is very sensitive to tolerances in the rotor iron profile. The analysed PM tolerances result in similar magnitudes of the 12$^{th}$ order AHC of the 12-slot/8-pole motor. Tolerances in the PM remanence, PM radial position, and PM lateral position of the 12-slot/8-pole motor result in negligible magnitudes of the 24$^{th}$ order AHC.

The phase of the 12th AHCs due to a single rotor tolerance is determined by the direction of the tolerances and the affected rotor pole. The 12$^{th}$ order AHCs due to a negative tolerance are 180° out-of-phase with the AHCs due to positive tolerances. Tolerances in rotor poles with the same magnetic direction and the same tolerance direction (i.e. N or S) result in AHCs with the same phase. Conversely, tolerances in opposite magnetic poles and the same tolerance direction result in AHCs 180° out-of-phase.

Tolerances resulting in an increase in air-gap flux density lead to fundamental AHCs with a phase of 180°, and vice-versa. For instance, positive tolerances in the pole-shoe width, cavity size, and rib width of pole 1 result in a slight reduction of air-gap flux density. Consequently, the phase difference of the fundamental AHC is 180° out-of-phase with the remaining positive tolerances under investigation.

The phases of AHCs due to tolerances in the lateral PM position result in irregular phases since the asymmetry introduced by the tolerance results in a complete change of the rotor pole rather than a slight change in the magnitude of the air-gap flux density at the affected pole.

## 8.5 Worst Scenarios of Cogging Torque in IPM and SPM Motors

The worst-case scenarios due to manufacturing tolerances due to tolerances in radial position of the stator tooth profile of the IPM and SPM motors under investigation were determined using the method outlined in in [BUH20]. Determination of the worst-case scenarios of tolerances in multiple stator and rotor dimensions using the method in [BUH20] is very complex.

The worst case scenarios are determined using a global search algorithm combined with a simplified model based on a series of FEA simulations. This method achieves a very high decrease in computational effort with respect to the global search algorithm combined with a FEA model. It is assumed that the cross-

interaction between manufacturing tolerances is negligible and that the magnitude of the cogging torque AHCs varies linearly with the magnitude of the corresponding manufacturing tolerances. This is justified by the fact that the magnitudes of the manufacturing tolerances are very low.

The simplified model is constructed using a sensitivity analysis of the cogging torque due to the upper and lower bounds for each of the considered manufacturing tolerances. The AHCs due to manufacturing variations are obtained by subtracting the nominal cogging torque from the cogging torque waveform due to the manufacturing variations. The cogging torque due to a set of manufacturing variations of a particular magnitude and direction is obtained by summing the nominal cogging torque and the AHCs due to each manufacturing variation.

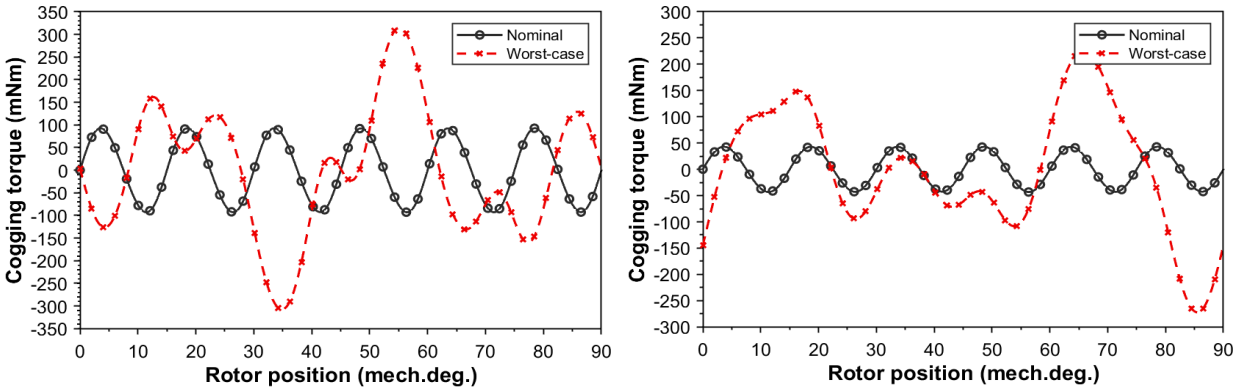
The worst-case scenarios of the cogging torque due to stator tolerances only, rotor tolerances only, and combined stator and rotor tolerances of the motors under investigation are identified. The peak-to-peak cogging torque of the worst-case scenarios is listed in Table 8.2.

Table 8.1. Worst-case cogging torque due to stator tolerances only, rotor tolerances only, and combined stator and rotor tolerances

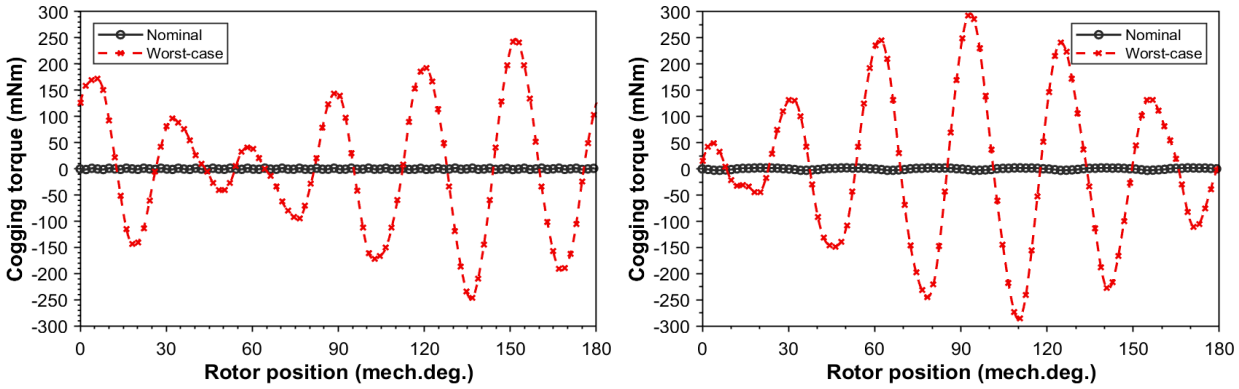
| **Units: (mNm)** | **Stator tolerances** | | **Rotor tolerances** | | **Stator and rotor tolerances** | |
|---|---|---|---|---|---|---|
| | **IPM** | **SPM** | **IPM** | **SPM** | **IPM** | **SPM** |
| 12-slot/8-pole | 452.3 | 316.6 | 357.6 | 235.5 | 622.4 | 489.9 |
| 12-slot/10-pole | 188.8 | 236.0 | 277.2 | 346.7 | 496.8 | 581.3 |
| 12-slot/14-pole | 93.7 | 196.4 | 382.5 | 513.6 | 510.3 | 773.4 |

The worst-case cogging torque of the SPM motors due to rotor tolerances increases with increasing rotor pole number. The worst-case cogging torque of the 12-slot/10-pole IPM is lower the worst-case cogging torques of 12-slot/8-pole and 12-slot/14-pole IPM motors. This is attributed to the fact that the nominal cogging torque of the 12-slot/8-pole IPM motor is significantly higher than the cogging torques of the 12-slot/10-pole and 12-slot/14-pole IPM motors.

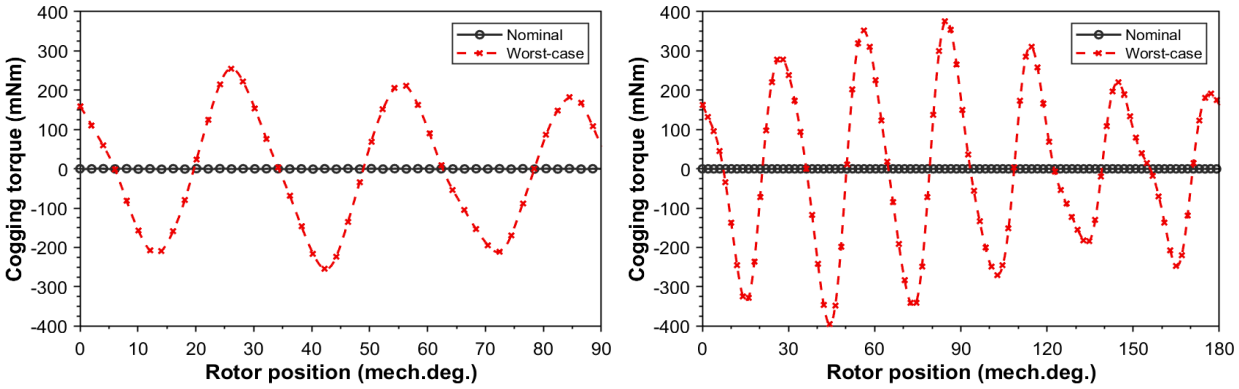
Therefore, the worst-case cogging torque AHCs due to stator tolerances decrease with increasing rotor pole number. Conversely, the worst-case cogging torque AHCs due to rotor tolerances increase with increasing rotor pole number. The peak-to-peak cogging torque due to the worst-case scenario decreases with increasing rotor pole number in IPM motors. Conversely, the worst-case cogging torque increases with increasing rotor pole number in SPM motors. The worst-case scenario cogging torque and harmonics are shown in Fig. 6.38 and Fig. 8.4, respectively.




(a) 12-slot/8-pole



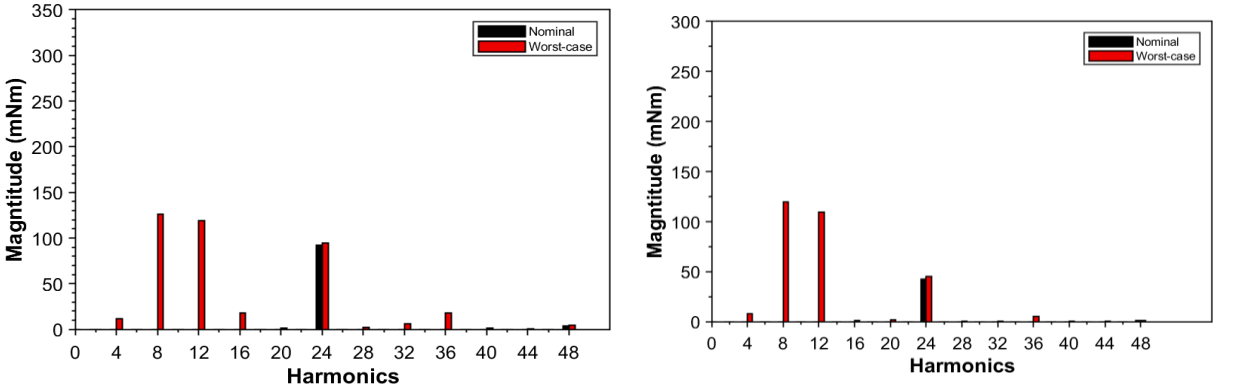

(b) 12-slot/10-pole



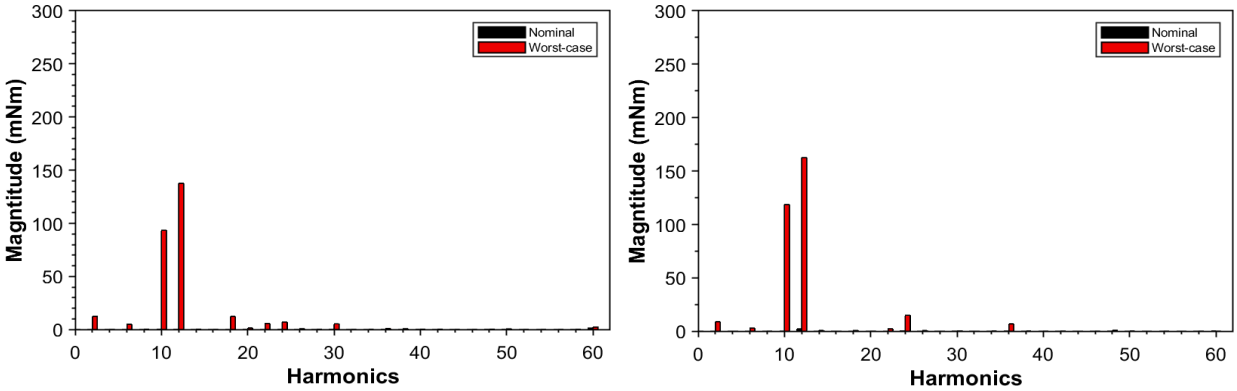

(c) 12-slot/14-pole

(I) IPM (II) SPM

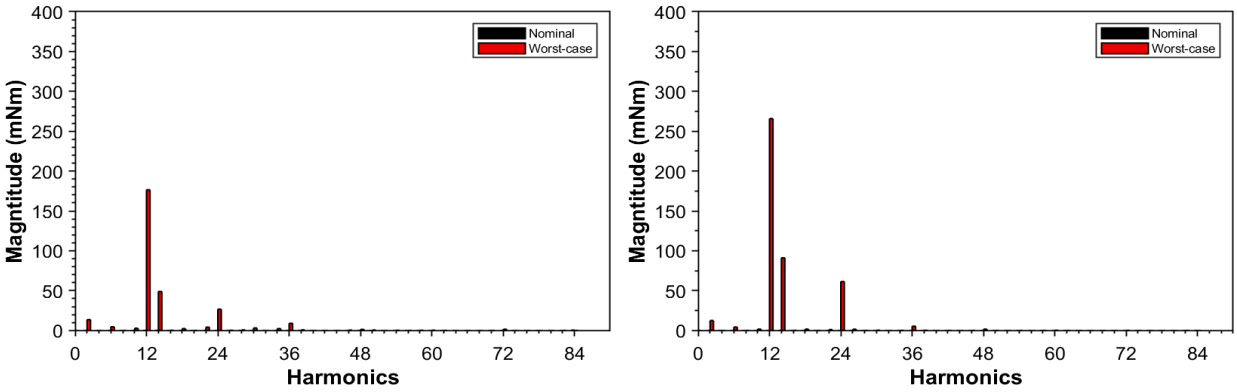
Fig. 8.3. Waveforms and harmonics of the cogging torque due to the possible cases of tolerances in the inward direction in the 12-slot/14-pole IPM motor.




(a) 12-slot/8-pole




(b) 12-slot/10-pole




(c) 12-slot/14-pole

(I) IPM (II) SPM

Fig. 8.4. Waveforms and harmonics of the cogging torque due to the possible cases of tolerances in the inward direction in the 12-slot/14-pole IPM motor.

## 8.6 Uncertainty of Cogging Torque Due to Manufacturing Tolerances in IPM and SPM motors

The uncertainties of the peak-to-peak cogging torque, cogging torque NHCs and cogging torque AHCs due to stator tolerances, rotor tolerances, and both stator and rotor tolerances are quantified using Monte-Carlo simulations with a sample size of 100 motors. It is assumed that the probability density of manufacturing tolerances follows the normal distribution as shown in Fig. 7.1. Normal and log-logistic distributions are fitted to the distributions of number of occurrences of the analysed parameters to identify the skewness and dispersion of the distributions.

The distributions of the number of occurrences of the peak-to-peak cogging torque of IPM and SPM motors subjected to both stator and rotor tolerances are shown in Fig. 7.14. The properties of the fitted log-logistic distributions of the 12-slot/10-pole IPM and SPM motors are similar. The difference between the modes of the fitted log-logistic distribution and the nominal peak-to-peak cogging torque increases with increasing rotor pole number. Furthermore, the skewness of the fitted log-logistic distributions increases with increasing rotor pole number. The dispersion of the distributions of the IPM motors decreases with increasing rotor pole number. On the other hand, the dispersion of the distributions of the SPM motors increases with increasing rotor pole number.

Therefore, the 12-slot/14-pole SPM motor results in the highest distribution dispersion and highest difference between the modes of the fitted distribution and the nominal peak-to-peak cogging torque. The 12-slot/8-pole IPM motor results in the lowest difference between the modes of the fitted distribution and the nominal peak-to-peak cogging torque. The 12-slot14-pole IPM motor has the lowest distribution dispersion.

The uncertainty of the peak-to-peak cogging torque due to stator tolerances decreases with increasing rotor pole number. Conversely, the uncertainty of the peak-to-peak cogging torque due to rotor tolerances increases significantly with increasing rotor pole number.

The uncertainties of the cogging torque NHCs of 12-slot/10-pole and 12-slot/14-pole motors due to tolerances are very low.

The difference of the modes of the fitted distributions of the native $24^{th}$ order cogging torque NHC of the 12-slot/8-pole IPM motor from the nominal value due to stator and rotor tolerances is equivalent to the sum of the difference due to stator tolerances only and rotor tolerances only. This indicates that the influence of stator and rotor tolerances on the native $24^{th}$ order component is additive and that rotor tolerances contribute to up to 61.5% of the difference of the mode of the distribution from the nominal value. The difference of the modes of the fitted distributions of the native 24th order cogging torque component of the 12-slot/8-pole SPM motor is very low.

The dispersion of the fitted distribution of the 24$^{th}$ order component of the 12-slot/8-pole SPM motor due to stator tolerances is very low. The dispersion due to stator and rotor tolerances is very similar to that of the distribution due to rotor tolerances only. Therefore, the dispersion of the fitted distribution is mostly attributed to rotor tolerances.

Table 8.2. Difference between modes of the fitted log-logistic distribution and nominal peak-to-peak cogging torque due to tolerances

| **Units: (mNm)** | **Stator tolerances** | | **Rotor tolerances** | | **Stator and rotor tolerances** | |
|---|---|---|---|---|---|---|
| | **IPM** | **SPM** | **IPM** | **SPM** | **IPM** | **SPM** |
| 12-slot/8-pole | 23.3 | 20.2 | 2.5 | 7.8 | 33.2 | 29.1 |
| 12-slot/10-pole | 18.3 | 14.9 | 18.2 | 15.8 | 38.9 | 36.0 |
| 12-slot/14-pole | 7.9 | 10.7 | 28.2 | 36.9 | 37.7 | 53.0 |

Table 8.3. Interquartile ranges of the fitted log-logistic distributions of the peak-to-peak cogging torque due to tolerances

| **Units: (mNm)** | **Stator tolerances** | | **Rotor tolerances** | | **Stator and rotor tolerances** | |
|---|---|---|---|---|---|---|
| | **IPM** | **SPM** | **IPM** | **SPM** | **IPM** | **SPM** |
| 12-slot/8-pole | 18.3 | 16.2 | 8.6 | 8.4 | 20.8 | 17.9 |
| 12-slot/10-pole | 7.5 | 17.3 | 13.3 | 12.3 | 18.4 | 21.4 |
| 12-slot/14-pole | 5.2 | 13.3 | 12.2 | 22.1 | 15.9 | 27.7 |

## 8.7 Future Work

The work carried out in this thesis has been based on analyses using 2D FEA models. The influence of manufacturing tolerances on 3D effects of the motor could be investigated using 3D FEA models. Furthermore, tolerances in the stator and rotor that vary along the axial length of the motor could be investigated. Examples of such tolerances include bends in stator teeth modules due to the winding process and tolerances in rotor step skew angles.

The foregoing investigation has been focused on the influence of manufacturing tolerances on the cogging torque. The analyses could be applied to motors at a particular operating point to determine the influence of manufacturing tolerances on the on-load average torque and torque ripple. This is particularly relevant for the 12-slot/8-pole motors since this research has concluded that the uncertainty of the native cogging torque components due to manufacturing tolerances is non-negligible.

The methodology adopted in this thesis could be applied to determine the sensitivity, worst-cases, and uncertainty of unbalanced magnetic forces in IPM and SPM motors. Furthermore, the analyses of unbalanced magnetic forces could be extended to quantification of the uncertainty of the noise and vibration performance of IPM and SPM motors for EPS applications.

# REFERENCES


[ALO11] P. Alotto, M. Barcaro, N. Bianchi, and M. Guarnieri, “Optimization of interior PM motors with Machaon rotor flux barriers,” in IEEE Transactions on Magnetics, vol. 47, no. 5, pp. 958–961, 2011.

[BEN05] A. Benedetti, N. Bianchi, S. Bolognani, M. Dai Pre, P. Molari, P.Morelli, M. Tomasini, L. Tubiana, and M. Zigliotto, “PM motor drives for steer-by-wire applications,” in Fourtieth IAS Annual Meeting. Conference Record of the 2005 Industry Applications Conference, 2005, vol. 4, pp. 2857–2864.

[BIA00] N. Bianchi and S. Bolognani, “Reducing torque ripple in PM synchronous motors by pole-shifting,” in International Conference on Electrical Machines, 2000, pp. 1222–1226.

[BIA02] N. Bianchi and A. Canova, “FEM analysis and optimisation design of an IPM synchronous motor,” in IEE Conference Publication, 2002, no. 487, pp. 49–54.

[BIA02a] N. Bianchi and S. Bolognani, “Design techniques for reducing the cogging torque in surface-mounted PM motors,” IEEE Transactions on Industry Applications, vol. 38, no. 5, pp. 1259–1265, 2002.

[BIA06] N. Bianchi, M. D. Pre, and S. Bolognani, “Design of a fault-tolerant IPM motor for electric power steering,” IEEE Trans. Veh. Technol., vol. 55, no. 4, pp. 1102–1111, 2006.

[BIA06a] N. Bianchi, S. Bolognani, and M. Dai Pré, “Magnetic loading of fractional-slot three phase PM motors with non-overlapped coils,” in Industry Applications Conference, 2006. 41st IAS Annual Meeting. Conference Record of the 2006 IEEE, 2006, vol. 1, pp. 35–43.

[BRA20] G. Bramerdorfer, “A general investigation of the sensitiveness of brushless permanent magnet synchronous machines considering magnet tolerances,” IEEE Trans. Magn., 2020.

[BRE00] C. Breton, J. Bartolomé, J. A. Benito, G. Tassinario, I. Flotats, C. W. Lu, and B. J. Chalmers, “Influence of machine symmetry on reduction of cogging torque in permanent-magnet brushless motors,” IEEE Transactions on Magnetics, vol. 36, no. 5, pp. 3819–3823, 2000.

[BUH20] K. Buhagiar, Z. Q. Zhu, and D. Moule, “Investigation of worst-case scenarios of cogging torque due to manufacturing tolerances in stator teeth profile of 12-slot/10-pole surface permanent magnet motors,” IET International Conference on Power Electronics, Machines and Drives, (PEMD), 2020.

[BUR03] A. W. Burton, “Innovation drivers for electric power-assisted steering,” *IEEE Control Syst.*, vol. 23, no. 6, pp. 30–39, Dec. 2003.

[CAR14] E. Carraro, N. Bianchi, S. Zhang, and M. Koch, “Permanent magnet volume minimization of spoke type fractional slot synchronous motors,” in 2014 IEEE Energy Conversion Congress and Exposition (ECCE), 2014, pp. 4180–4187.

[CAR18] E. Carraro, N. Bianchi, S. Zhang, and M. Koch, “Design and performance comparison of fractional slot concentrated winding spoke type synchronous motors with different slot-pole combinations,” in IEEE Transactions on Industry Applications, vol. 54, no. 3, pp. 2276–2284, 2018.

[CHE12] L. Chen, J. Wang, P. Lombard, P. Lazari, and V. Leconte, “Design optimisation of permanent magnet assisted synchronous reluctance machines for electric vehicle applications,” in Proceedings - 2012 20th International Conference on Electrical Machines, ICEM 2012, 2012, pp. 2647–2653.

[CHE14] X. Chen, J. Wang, V. I. Patel, P. Lazari, L. Chen, and P. Lombard, “Reluctance torque evaluation for interior permanent magnet machines using frozen permeability,” 2014.

[CHU13] W. Q. Chu and Z. Q. Zhu, “Investigation of torque ripples in permanent magnet synchronous machines with skewing,” IEEE Transactions on Magnetics, vol. 49, no. 3, pp. 1211–1220, 2013.

[COE11] I. Coenen, M. Herranz Gracia, and K. Hameyer, “Influence and evaluation of non-ideal manufacturing process on the cogging torque of a permanent magnet excited synchronous machine,” COMPEL-The international journal for computation and mathematics in electrical and electronic engineering, vol. 30, no. 3, pp. 876–884, 2011.

[COE12] I. Coenen, M. van der Giet, and K. Hameyer, “Manufacturing tolerances: Estimation and prediction of cogging torque influenced by magnetization faults,” IEEE Transactions on Magnetics, vol. 48, no. 5, pp. 1932–1936, 2012.

[DEB01] K. Deb, “Multi-objective optimization using evolutionary algorithms: an introduction multi-objective optimization using evolutionary algorithms: an introduction,” Wiley-Interscience Ser. Syst. Optim., no. June, pp. 1–24, 2001.

[DEY10] A. K. Dey and D. Kundu, “Discriminating between the log-normal and log-logistic distributions,” Commun. Stat. - Theory Methods, vol. 39, no. 2, pp. 280–292, 2010.

[DUA09] Y. Duan, R. G. Harley, and T. G. Habetler, “A useful multi-objective optimization design method for PM motors considering nonlinear material properties,” in 2009 IEEE Energy Conversion Congress and Exposition, ECCE 2009, 2009, pp. 187–193.

[DUA13] Y. Duan and D. M. Ionel, “A review of recent developments in electrical machine design optimization methods with a permanent-magnet synchronous motor benchmark study,” IEEE Transactions on Industry Applications, vol. 49, no. 3. pp. 1268–1275, 2013.

[ELR05] A. M. El-Refaie amd T. M. Jahns, “Optimal flux weakening in surface PM machines using fractional-slot concentrated windings,” IEEE Trans. Ind. Appl., vol. 41, no. 3, pp. 790–800, 2005.

[EVA10] S. A. Evans, “Salient pole shoe shapes of interior permanent magnet synchronous machines,” in 2010 XIX International Conference on Electrical Machines (ICEM), 2010, pp. 1–6.

[FEI10] W. Fei and P. C.-K. Luk, “A new technique of cogging torque suppression in direct-drive permanent-magnet brushless machines,” IEEE Transactions on Industry Applications, vol. 46, no. 4, pp. 1332–1340, 2010.

[GAE17] A. Gaedke, M. Heger, M. Sprinzl, S. Grüner, and A. Vähning, “Electric power steering systems,” in *Steering Handbook*, M. Harrer and P. Pfeffer, Eds. Springer International Publishing, 2017, pp. 403–467.

[GAS08] L. Gašparin, A. Černigoj, S. Markič, and R. Fišer, “Prediction of cogging torque level in PM motors due to assembly tolerances in mass-production,” COMPEL-The international journal for computation and mathematics in electrical and electronic engineering, vol. 27, no. 4, pp. 911–918, 2008.

[GAS09] L. Gasparin, A. Cernigoj, S. Markic, and R. Fiser, “Additional cogging torque components in permanent-magnet motors due to manufacturing imperfections,” IEEE Transactions on Magnetics, vol. 45, no. 3, pp. 1210–1213, 2009.

[GE14] X. Ge, Y. Zhou, and Z. Q. Zhu, “TRW EPS Motor Project Report,” 2014.

[GE16] X. Ge, Z. Q. Zhu, G. Kemp, D. Moule, and C. Williams, “Optimal step-skew methods for cogging torque reduction accounting for 3-dimensional effect of interior permanent magnet machines,” IEEE Trans. Energy Convers., 2016.

[GE16a] X. Ge, “Investigation of Interior Permanent Magnet Machines and Variable Reluctance Resolvers Accounting for Manufacturing Issues.” PhD thesis, University of Sheffield, 2016.

[GE17] X. Ge and Z. Q. Zhu, “Sensitivity of manufacturing tolerances on cogging torque in interior permanent magnet machines with different slot/pole number combinations,” IEEE Trans. Ind. Appl., vol. 53, no. 4, pp. 3557–3567, 2017.

[GIE02] J. F. Gieras, Permanent Magnet Motor Technology Design and Applications. CRC Press, 2002.

[GOP21] D. Gope and S. K. Goel, “Design optimization of permanent magnet synchronous motor using Taguchi method and experimental validation,” Int. J. Emerg. Electr. Power Syst., 2021.

[GOS13] J. Goss, R. Wrobel, P. Mellor, and D. Staton, “The design of AC permanent magnet motors for electric vehicles: A design methodology,” in Proceedings of the 2013 IEEE International Electric Machines and Drives Conference, IEMDC 2013, 2013, pp. 871–878.

[HAN10] S.-H. Han, T. M. Jahns, W. L. Soong, M. K. Güven, and M. S. Illindala, “Torque ripple reduction in interior permanent magnet synchronous machines using stators with odd number of slots per pole pair,” IEEE Transactions on Energy Conversion, vol. 25, no. 1, pp. 118–127, 2010.

[HAR17] M. Harrer and P. Pfeffer, “Steering Handbook,” 2017.

[HEI11] Heins, G., Brown, T., Thiele, M.:“Statistical analysis of the effect of magnet placement on cogging torque in fractional pitch permanent magnet motors,” IEEE Trans. Magn., vol. 47, no. 8, pp. 2142–2148, 2011.

[HOL02] D. J. Holt, Electric steering: a revolution in steering technology. Warrendale, Pa. (400 Commonwealth Dr., Wallendale PA USA): Society of Automotive Engineers, 2002.

[HOM14] T. Homem-de-Mello and G. Bayraksan, “Monte Carlo sampling-based methods for stochastic optimization,” Surveys in Operations Research and Management Science, vol. 19, no. 1. pp. 56–85, 2014.

[HUA01] S. Huang, M. Aydin, and T. A. Lipo, “Torque quality assessment and sizing optimization for surface mounted permanent magnet machines,” in Industry Applications Conference, 2001. Thirty-Sixth IAS Annual Meeting. Conference Record of the 2001 IEEE, 2001, vol. 3, pp. 1603–1610.

[HUA20] W. Huang, J. Wang, J. Zhao, L. Zhou, and Z. Zhang, “Demagnetization analysis and magnet design of permanent magnet synchronous motor for electric power steering applications,” in 2020 IEEE 1st China International Youth Conference on Electrical Engineering, CIYCEE 2020, 2020, pp. 1–6.

[HWA00] S.-M. Hwang, J.-B. Eom, G.-B. Hwang, W.-B. Jeong, and Y.-H. Jung, “Cogging torque and acoustic noise reduction in permanent magnet motors by teeth pairing,” IEEE Transactions on Magnetics, vol. 36, no. 5, pp. 3144–3146, 2000.

[HWA07] K. Y. Hwang, S. B. Rhee, J. S. Lee, and B. Il Kwon, “Shape optimization of rotor pole in spoke type permanent magnet motor for reducing partial demagnetization effect and cogging torque,” in Proceeding of International Conference on Electrical Machines and Systems, ICEMS 2007, 2007, pp. 955–960.

[ISL04] M. S. Islam, S. Mir, and T. Sebastian, “Issues in reducing the cogging torque of mass-produced permanent-magnet brushless DC motor,” IEEE Transactions on Industry Applications, vol. 40, no. 3, pp. 813–820, 2004.

[ISL09] R. Islam, I. Husain, A. Fardoun, and K. McLaughlin, “Permanent-magnet synchronous motor magnet designs with skewing for torque ripple and cogging torque reduction,” IEEE Transactions on Industry Applications, vol. 45, no. 1, pp. 152–160, 2009.

[ISL11] M. S. Islam, R. Islam, T. Sebastian, A. Chandy, and S. A. Ozsoylu, “Cogging torque minimization in PM motors using robust design approach,” IEEE Transactions on Industry Applications, vol. 47, no. 4, pp. 1661–1669, 2011.

[JAH96] T. M. Jahns and W. L. Soong, “Pulsating torque minimization techniques for permanent magnet AC motor drives-a review,” IEEE Transactions on Industrial Electronics, vol. 43, no. 2, pp. 321–330,1996.

[JUN17] C. S. Jun and B. Il Kwon, “Process capability control procedure for electrical machines by using a six-sigma process for achieving six-sigma quality level,” IET Electr. Power Appl., 2017.

[KHA14] M. A. Khan, I. Husain, M. R. Islam, and J. T. Klass, “Design of experiments to address manufacturing tolerances and process variations influencing cogging torque and back EMF in the mass production of the permanent-magnet synchronous motors,” IEEE Transactions on Industry Applications, vol. 50, no. 1, pp. 346–355, 2014.

[KIM05] S.-I. Kim, J.-Y. Lee, Y.-K. Kim, J.-P. Hong, Y. Hur, and Y.-H. Jung, “Optimization for reduction of torque ripple in interior permanent magnet motor by using the Taguchi method,” IEEE Transactions on Magnetics, vol. 41, no. 5, pp. 1796–1799, 2005.

[KIM14] Y.-B. Kim, H.-J. Kim, K.-T. Jung, and J.-P. Hong, “Influence of manufacturing tolerances on cogging torque of IPMSM for EPS application,” in 2014 17th International Conference on Electrical Machines and Systems (ICEMS), 2014, pp. 382–386.

[KIM16] K. S. Kim, K. T. Jung, J. M. Kim, J. P. Hong, and S. Il Kim, “Taguchi robust optimum design for reducing the cogging torque of EPS motors considering magnetic unbalance caused by manufacturing tolerances of PM,” IET Electr. Power Appl., vol. 10, no. 9, pp. 909–915, Nov. 2016.

[KIM16a] J.-M. Kim, M.-H. Yoon, J.-P. Hong, and S.-I. Kim, “Analysis of cogging torque caused by manufacturing tolerances of surface-mounted permanent magnet synchronous motor for electric power steering,” *IET Electr. Power Appl.*, vol. 10, no. 8, pp. 691–696, 2016.

[KIM18] Kim, T., Chowdhury, M., Islam, M., Gebregergis, A., et al.: “Tolerance study to forecast performances of permanent magnet synchronous machines using segmented stator for mass production,” IEEE Trans. Ind. Appl., vol. 54, no. 5, pp. 4333–4342, Sep. 2018.

[KIM20] K. S. Kim and B. H. Lee, “Taguchi robust design for the multi-response considering the manufacturing tolerance used in high-speed air blower motor,” IET Electr. Power Appl., vol. 14, no. 7, pp. 1141–1147, Jul. 2020.

[KIO06] A. Kioumarsi, M. Moallem, and B. Fahimi, “Mitigation of torque ripple in interior permanent magnet motors by optimal shape design,” IEEE Transactions on Magnetics, vol. 42, no. 11, pp. 3706–3711, 2006.

[KOH03] C. S. Koh and J.-S. Seol, “New cogging-torque reduction method for brushless permanent-magnet motors,” IEEE Transactions on Magnetics, vol. 39, no. 6, pp. 3503–3506, 2003.

[KOL20] J. Kolb and K. Hameyer, “Sensitivity analysis of manufacturing tolerances in permanent magnet synchronous machines with stator segmentation,” IEEE Trans. Energy Convers., vol. 35, no. 4, pp. 2210–2221, 2020.

[KRA13] P. Krause, O. Wasynczuk, S. D. Sudhoff, and S. Pekarek, Analysis of electric machinery and drive systems, vol. 75. John Wiley & Sons, 2013.

[LAT06] R. Lateb, N. Takorabet, and F. Meibody-Tabar, “Effect of magnet segmentation on the cogging torque in surface-mounted permanent-magnet motors,” IEEE Transactions on Magnetics, vol. 42, no. 3, pp. 442–445, 2006.

[LEE14] S. J. Lee, S. I. Kim, and J. P. Hong, “Characteristics of PM synchronous motors according to pole-slot combinations for EPS applications,” *Int. J. Automot. Technol.*, vol. 15, no. 7, pp. 1183–1187, 2014.

[LEE14a] S. Lee, K. Kim, S. Cho, J. Jang, T. Lee, and J. Hong, “Optimal design of interior permanent magnet synchronous motor considering the manufacturing tolerances using Taguchi robust design,” IET Electric Power Applications, vol. 8, no. 1, pp. 23–28, 2014.

[LEE20] B. H. Lee and J. W. Jung, “Robust design for reducing cogging torque in surface-mounted permanent magnet synchronous motor considering tolerances of sub-components,” IET Electr. Power Appl., vol. 14, no. 3, pp. 448–456, 2020.

[LEI19] G. Lei, C. Liu, Y. Li, D. Chen, Y. Guo, and J. Zhu, “Robust design optimization of a high-temperature superconducting linear synchronous motor based on Taguchi method,” IEEE Trans. Appl. Supercond., vol. 29, no. 2, 2019.

[LI88] T. Li and G. Slemon, “Reduction of cogging torque in permanent magnet motors,” IEEE Transactions on magnetics, vol. 24, no. 6, pp. 2901–2903, 1988.

[LIM15] S. Lim, S. Min, and J.-P. Hong, “Optimal rotor design of IPM motor for improving torque performance considering thermal demagnetization of magnet,” IEEE Trans. Magn., vol. 51, no. 3, pp. 1–5, 2015.

[LIP15] W. Zhao, T. A. Lipo, and B. Il Kwon, “Optimal design of a novel asymmetrical rotor structure to obtain torque and efficiency improvement in surface inset PM motors,” IEEE Trans. Magn., vol. 51, no. 3, 2015.

[MA16] J. Ma, and Z. Q. Zhu, “TRW EPS Motor Project Report.” 2016.

[MAR88] M. Marinescu and N. Marinescu, “Numerical computation of torques in permanent magnet motors by Maxwell stresses and energy method,” IEEE Transactions on Magnetics, vol. 24, no. 1, pp. 463–466, Jan. 1988.

[MUE19] C. Mülder, M. Franck, M. Schroder, M. Balluff, A. Wanke, and K. Hameyer, “Impact study of isolated and correlated manufacturing tolerances of a permanent magnet synchronous machine for traction drives,” in 2019 IEEE International Electric Machines and Drives Conference, IEMDC 2019, 2019.

[NIS21] “Electro-Hydraulic power steering system | NISSAN | TECHNOLOGICAL DEVELOPMENT ACTIVITIES.” [Online]. Available: https://www.nissan-global.com/EN/TECHNOLOGY/OVERVIEW/ehpss.html. [Accessed: 20-Feb-2021].

[OMB07] G. Ombach and J. Junak, “Two rotors designs’ comparison of permanent magnet brushless synchronous motor for an electric power steering application,” in *Power Electronics and Applications, 2007 European Conference on*, 2007, pp. 1–9.

[OMB07a] G. Ombach and J. Junak, “Design of PM brushless motor taking into account tolerances of mass production-six sigma design method,” in Industry Applications Conference, 2007. 42nd IAS Annual Meeting. Conference Record of the 2007 IEEE, 2007, pp. 2139–2146.

[OMB07b] Ombach, G. „Junak, J.: “Design of PM brushless motor taking into account tolerances of mass production - Six sigma design method,” Conf. Rec. - IAS Annu. Meet. (IEEE Ind. Appl. Soc.), pp. 2139–2146, 2007.

[OMB11] G. Ombach and J. Junak, “Torque ripple optimization of skewed IPM motor for field weakening operation,” in 2011 International Conference on Electrical Machines and Systems (ICEMS), 2011, pp. 1–7.

[ORT16] Pina Ortega, A. J., Paul, Islam, A., et al.: “Analytical Model for Predicting Effects of Manufacturing Variations on Cogging Torque in Surface-Mounted Permanent Magnet Motors,” IEEE Trans. Ind. Appl., vol. 52, no. 4, pp. 3050–3061, Jul. 2016

[PAT18] M. Patel and D. A. Desai, “Critical review and analysis of measuring the success of Six Sigma implementation in manufacturing sector,” International Journal of Quality and Reliability Management. 2018.

[PAU19] S. Paul, D. Harris, Z. Wan, and J. Klass, “Robust design approach of permanent magnet synchronous motors for torque ripple minimization,” in 2019 IEEE International Electric Machines and Drives Conference, IEMDC 2019, 2019.

[PEL10] G. Pellegrino and F. Cupertino, “FEA-based multi-objective optimization of IPM motor design including rotor losses,” in 2010 IEEE Energy Conversion Congress and Exposition, ECCE 2010 - Proceedings, 2010, pp. 3659–3666.

[PUC05] J. Puchinger and G. R. Raidl, “Combining metaheuristics and exact algorithms in combinatorial optimization: A survey and classification,” in Lecture Notes in Computer Science, 2005, vol. 3562, no. PART II, pp. 41–53.

[RAF20] V. Rafiee and J. Faiz, “Uncertainty quantification of permanent magnet motor using response surface surrogate modeling,” in 2020 11th Power Electronics, Drive Systems, and Technologies Conference, PEDSTC 2020, 2020.

[RAH14] M. M. Rahman, K. T. Kim, and J. Hur, “Design and optimization of neodymium-free SPOKE-type motor with segmented wing-shaped PM,” IEEE Trans. Magn., vol. 50, no. 2, 2014.

[SAH15] S. Saha, S.-A. Kim, and Y.-H. Cho, “Optimal rotor shape design for minimizing cogging torque of spoke type BLAC motor for EPS,” in *Industrial Electronics and Applications (ICIEA), 2015 IEEE 10th Conference on*, 2015, pp. 1313–1318.

[SAL12] N. Salkind, “Main Effects,” in Encyclopedia of Research Design, SAGE Publications, Inc., 2012.

[SCH06] C. Schlensok, M. H. Gracia, and K. Hameyer, “Combined numerical and analytical method for geometry optimization of a PM motor,” *IEEE Trans. Magn. MAG*, vol. 42, no. 4, p. 1211, 2006.

[SCH90] R. F. Schiferl and T. A. Lipo, “Power capability of salient pole permanent magnet synchronous motor in variable speed drive applications,” IEEE Trans. Ind. Appl., vol. 26, no. 1, pp. 115–123, Jan./Feb. 1990.

[SHA12] S. Q. A. Shah, T. A. Lipo, and B.-I. Kwon, “Modeling of novel permanent magnet pole shape SPM motor for reducing torque pulsation,” IEEE Transactions on Magnetics, vol. 48, no. 11, pp. 4626–4629, 2012.

[SHU16] A. L. Shuraiji Al-Lami and Z. Q. Zhu, “TRW EPS Motor Project Report.” 2016.

[SI16] M. Si, X. Y. Yang, S. W. Zhao, and S. Gong, “Design and analysis of a novel spoke-type permanent magnet synchronous motor,” IET Electr. Power Appl., vol. 10, no. 6, pp. 571–580, Jul. 2016.

[SIM12] J. Sim, J. Jung, Y. Kim, B. Lee, and J. Hong, “Optimum design of SPMSM with concentrated windings and unequal tooth widths for EPS,” in *2012 IEEE Vehicle Power and Propulsion Conference*, 2012, pp. 191–195.

[SOO94] W. Soong and T. J. E. Miller, “Field weakening performance of brushless synchronous AC motor drives,” Proc. IEE—Elect. Power Appl., vol. 141, no. 6, pp. 331–340, Nov. 1994.

[STI16] S. Stipetic, D. Zarko, and M. Kovacic, “Optimised design of permanent magnet assisted synchronous reluctance motor series using combined analytical-finite element analysis based approach,” IET Electr. Power Appl., vol. 10, no. 5, pp. 330–338, May 2016.

[SUD14] S. D. Sudhoff, “Optimization-Based Design,” in Power Magnetic Devices, John Wiley & Sons, Inc., 2014, pp. 1–44.

[TAL09] E. G. Talbi, Metaheuristics: From Design to Implementation. 2009.

[TAR19] N. Taran, V. Rallabandi, D. M. Ionel, P. Zhou, M. Thiele, and G. Heins, “A systematic study on the effects of dimensional and materials tolerances on permanent magnet synchronous machines based on the IEEE Std 1812,” IEEE Trans. Ind. Appl., 2019.

[TSU92] K. L. Tsui, “An Overview of Taguchi Method and Newly Developed Statistical Methods for Robust Design,” IIE Trans. (Institute Ind. Eng., vol. 24, no. 5, pp. 44–57, 1992.

[UGR07] Z. Ugray, L. Lasdon, J. Plummer, F. Glover, J. Kelly, and R. Martí, “Scatter search and local nlp solvers: a multistart framework for global optimization,” INFORMS Journal on Computing, Vol. 19, No. 3, 2007, pp. 328–340.

[WAH13] Z. Wahid and N. Nadir, “Improvement of one factor at a time through design of experiments,” World Applied Sciences Journal, vol. 21, pp. 56–61, 2013.

[WAN11] C. F. Wang, J.-X. Shen, P. C.-K. Luk, W.-Z. Fei, and M.-J. Jin, “Design issues of an IPM motor for EPS,” COMPEL Int J Comput. Maths Electr. Electron. Eng, vol. 31, no. 1, pp. 71–87, 2011.0

[WAN11a] A. Wang, Y. Jia, and W. L. Soong, “Comparison of five topologies for an interior permanent-magnet machine for a hybrid electric vehicle,” IEEE Transactions on Magnetics, vol. 47, no. 10, pp. 3606–3609, 2011.

[WAN12] K. Wang, Z. Q. Zhu, G. Ombach, and W. Chlebosz, “Optimal rotor shape with third harmonic for maximizing torque and minimizing torque ripple in IPM motors,” in 2012 XXth International Conference on Electrical Machines (ICEM), 2012, pp. 397–403.

[WAN12] K. Wang, Z. Q. Zhu, G. Ombach, and W. Chlebosz, “Optimal rotor shape with third harmonic for maximizing torque and minimizing torque ripple in IPM motors,” in 2012 XXth International Conference on Electrical Machines (ICEM), 2012, pp. 397–403.

[WAN14] K. Wang, Z. Q. Zhu, G. Ombach, and W. Chlebosz, “Average torque improvement of interior permanent-magnet machine using third harmonic in rotor shape,” IEEE Transactions on Industrial Electronics, vol. 61, no. 9, pp. 5047–5057, 2014.

[WAN14a] K. Wang, Z. Q. Zhu, G. Ombach, and W. Chlebosz, “Torque ripple and magnetic forces on teeth in IPM machines,” COMPEL: The International Journal for Computation and Mathematics in Electrical and Electronic Engineering, vol. 33, no. 5, pp. 1487–1501, 2014.

[WON01] T. Wong, “Hydraulic power steering system design and optimization simulation,” in *SAE Technical Papers*, 2001.

[WU09] L. J. Wu, Z. Q. Zhu, J. T. Chen, Z. P. Xia, and G. W. Jewell, “Optimal split ratio in fractional-slot interior permanent magnet machines with non-overlapping windings,” in IEEE International Electric Machines and Drives Conference, 2009, pp. 1721–1728.

[WU98] Wu, C.-C., Chen, Z.,Tang, G.-R.,: “Component tolerance design for minimum quality loss and manufacturing cost,” Comput. Ind., vol. 35, no. 3, pp. 223–232, Apr. 1998

[WUE13] M. Würges, “New Electrical Power Steering Systems,” in Encyclopedia of Automotive Engineering, John Wiley & Sons, Ltd, 2013, pp. 1–17.

[YAN05] Y. Yang, X. Wang, R. Zhang, C. Zhu, and T. Ding, “Research of cogging torque reduction by different slot width pairing permanent magnet motors,” in Electrical Machines and Systems, 2005. ICEMS 2005. Proceedings of the Eighth International Conference on, 2005, vol. 1, pp. 367–370.

[YAN07] Y. Yang, X. Wang, X. Leng, D. Wang, and S. Liu, “Reducing cogging torque in surface-mounted permanent magnet motors by teeth notching,” in Industrial Electronics and Applications, 2007. ICIEA 2007. 2nd IEEE Conference on, 2007, pp. 265–268.

[YAN20] Y. Yang, N. Bianchi, G. Bramerdorfer, C. Zhang, and S. Zhang, “Methods to improve the cogging torque robustness under manufacturing tolerances for the permanent magnet synchronous machine,” IEEE Trans. Energy Convers., 2020.

[ZF21] “Electrically Powered Steering – Column Drive - ZF.” [Online]. Available: https://www.zf.com/products/en/cars/products_31872.html. [Accessed: 20-Feb-2021].

[ZHA14] P. Zhang et al., “Multi-objective tradeoffs in the design optimization of a brushless permanent-magnet machine with fractional-slot concentrated windings,” IEEE Trans. Ind. Appl., vol. 50, no. 5, pp. 3285–3294, 2014.

[ZHA14a] W. Zhao, T. A. Lipo, and B.-I. Kwon, “Material-efficient permanent-magnet shape for torque pulsation minimization in SPM motors for automotive applications,” IEEE Transactions on Industrial Electronics, vol. 61, no. 10, pp. 5779–5787, 2014.

[ZHA15] W. Zhao, T. A. Lipo, and B. Il Kwon, “Torque Pulsation Minimization in Spoke-type Interior Permanent Magnet Motors with Skewing and Sinusoidal Permanent Magnet Configurations,” IEEE Trans. Magn., vol. 51, no. 11, 2015.

[ZHU00] Z. Q. Zhu and D. Howe, “Influence of design parameters on cogging torque in permanent magnet machines,” IEEE Transactions on Energy Conversion, vol. 15, no. 4, pp. 407–412, 2000.

[ZHU03] Z. Q. Zhu, S. Ruangsinchaiwanich, N. Schofield, and D. Howe, “Reduction of cogging torque in interior-magnet brushless machines,” IEEE Transactions on Magnetics, vol. 39, no. 5, pp. 3238–3240, 2003.

[ZHU08] Z. Q. Zhu, J. T. Chen, L. J. Wu, and D. Howe, “Influence of stator asymmetry on cogging torque of permanent magnet brushless machines,” IEEE Transactions on Magnetics, vol. 44, no. 11, pp. 3851–3854, 2008.

[ZHU09] L. Zhu, S. Z. Jiang, Z. Q. Zhu, and C. C. Chan, “Analytical methods for minimizing cogging torque in permanent-magnet machines,” IEEE transactions on magnetics, vol. 45, no. 4, pp. 2023–2031, 2009.

[ZHU09a] Zhu, Z. Q., et al., “Influence of slot and pole number combination on radial force and vibration modes in fractional slot PM brushless machines having single-and double-layer windings,” IEEE Energy Conversion Congress and Exposition, 2009.

[ZHU12] Z. Q. Zhu, K. Wang, and G. Ombach, “Optimal magnet shaping with third order harmonic for maximum torque in brushless AC machines,” in 6th IET International Conference on Power Electronics, Machines and Drives (PEMD 2012), 2012, pp. 1–6.

[ZHU12a] Z. Q. Zhu, Z. Azar, and G. Ombach, “Influence of additional air gaps between stator segments on cogging torque of permanent-magnet machines having modular stators,” IEEE Transactions on Magnetics, vol. 48, no. 6, pp. 2049–2055, 2012.

[ZHU14] Z. Q. Zhu, “Permanent magnet machines for traction applications,” Encyclopaedia of Automotive Engineering, 2014.

# APPENDIX A
# CALCULATION OF THE TORQUE-SPEED CHARACTERISTICS OF PM MOTORS

## A.1 Calculation of the Torque-speed Envelope of PM Motors

The operating points of a PM motor are determined by a vector control scheme aimed at exploiting the characteristics of a motor to obtain maximum performance. This section is based on calculation of the operating points of the motor using the Maximum Torque per Ampere (MTPA) control algorithm. The MTPA control algorithm determines the minimum current magnitude and the corresponding current advance angle required at a specific operating point in the torque-speed range of the motor. The MTPA control algorithm neglects motor losses such as mechanical losses, iron losses, and copper losses.

The torque-speed envelope of the motor defines the maximum average torque of the motor that can be obtained throughout the speed range of the motor given constraints on the maximum voltage and maximum current of the motor.

The average torque of a PM motor can be approximated analytically using Equation A.1, where p is the pole-pair number, $\Psi_d$ and $\Psi_q$ are the d- and q- axes flux linkages, and $I_d$ and $I_q$ are the d- and q- axes current vectors. The constraints on the voltage and the current are determined by Equations A.2 and A.3, where $\omega_s$ is the rotational speed. The voltage limit $V_{lim}$ and the maximum current $I_{max}$ are defined by the specifications of the inverter used in the particular application.

$$T = \frac{3}{2} p(\Psi_d I_q - \Psi q I_d) \tag{A.1}$$

$$V_{lim} \geq \omega_s \sqrt{\Psi_d^2 + \Psi_q^2} \tag{A.2}$$

$$I_{max} \geq \sqrt{\mathrm{I}_d^2 + \mathrm{I}_q^2} \tag{A.3}$$

Cross-coupling of the d- and q- axes flux linkages is a result of the saturation in the magnetic material due to the d- and q- axes currents. Therefore, accurate calculation of the average torque requires the flux linkages to be expressed as a function of $I_d$ and $I_q$, as indicated in Equation A.4.

$$T = \frac{3}{2} p\big(\Psi_d(I_d, I_q) I_q - \Psi q(I_d, I_q) I_d\big) \tag{A.4}$$

Goss et al. [GOS13] obtained the d- and q- axes flux linkages over a range of $I_d$ and $I_q$ using 2D FEA. The

variation of the flux linkages with $I_d$ and $I_q$ was expressed as a second order polynomial function and the coefficients were determined using a least squares fitting of the data obtained using FEA computations. The torque-speed envelope is then obtained by calculating the maximum average torque using Equation A.1 for a given speed $\omega_s$ and maximum current $I_{max}$ over the speed range of the motor.

## A.2 Calculation of Efficiency Maps and Other Parameter Maps

Calculation of the maps of motor parameters over the entire torque-speed range of the motor is essential to determine the performance of the motor and identify phenomena that may not fit the requirements of the application.

Efficiency can be determined by calculating the copper losses, iron losses, and mechanical losses of the motor for a given input power. The efficiency map can be therefore generated by calculating the losses at a range of operating points across the torque-speed curve of the motor. The iron losses of the motor at any given current magnitude and rotational speed can be determined analytically, using FEA, or using a computationally efficient method such as that outlined in [GOS13]. The latter method uses two time-stepping FEA calculations to determine the iron losses as a function of the d-axis current, q-axis current and rotational speed.

Certain applications have torque ripple requirements that extend over the operational range of the motor. Therefore, torque ripple maps are required to understand the influence of the d- and q-axes current vectors on the torque ripple of the motor. For simplicity, it is assumed that the torque ripple is a function of the d- and q-axes current vectors and is independent of rotational speed. The torque ripple of the motor can be expressed as a polynomial function of the d- and q-axes current vectors and the coefficients can be determined using a least squares fitting of the data obtained using FEA computations. For simplicity, it is assumed that the torque ripple can be approximated by a second order polynomial function, however, it is possible that the torque ripple of a motor requires a higher-order polynomial function, and in turn, inaccuracies due to under-fitting may arise.

RSM uses a design of experiments to express the response variables as a function of a number of independent variables. The complexity of the RSM, and consequently the computational effort, increases significantly with the number of independent variables and the accuracy of the response surfaces is closely related to the chosen design of experiments.

The response variables of interest are the torque, torque ripple and the d- and q- axis flux linkages. The independent variables are the d- and q-axes currents. A three-level factorial design is used to determine the response surfaces as a function of the two independent variables and it is assumed that the response surfaces can be approximated by a pure quadratic function. Response surfaces defined by higher order functions, such as cubic functions, can be accounted for choosing a different design of experiment that allows for regression of a higher-order functions with a low error. The three-level factorial design of, $i_d$ and $i_q$ results

in 9 runs and the values for each run are listed in Table A.1.

Table A.1. The three-level factorial design for two independent variables.

| **Run** | $i_d$ **(p.u.)** | $i_q$ **(p.u.)** |
|---|---|---|
| **1** | -1 | 0 |
| **2** | -1 | 0.5 |
| **3** | -1 | 1 |
| **4** | -0.5 | 0 |
| **5** | -0.5 | 0.5 |
| **6** | -0.5 | 1 |
| **7** | 0 | 0 |
| **8** | 0 | 0.5 |
| **9** | 0 | 1 |

# APPENDIX B
# DETERMINATION OF WORST-CASE SCENARIOS OF THE COGGING TORQUE DUE TO TOLERANCES IN THE RADIAL POSITION OF THE STATOR TEETH PROFILE OF SPM MOTORS

## B.1 Worst-Case Scenarios of Cogging Torque of 12-slot/8-pole SPM Motor

A. Worst-case scenarios of tolerances in the inward direction

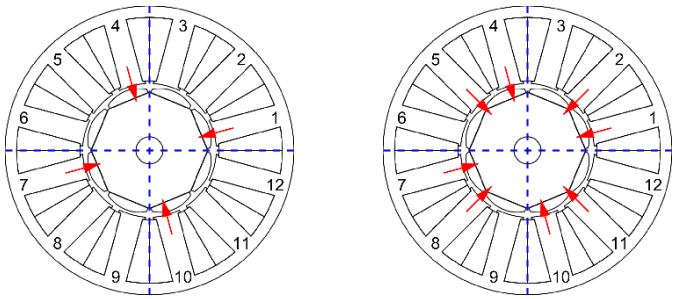
The worst-case scenarios if the cogging torque due to tolerances in the inward direction are determined by exploiting the periodic symmetry of the 12-slot/8-pole motor, indicated by blue dotted lines in Fig. B.1. Thus, the two possible cases of tolerances in the inward direction are:

- Case 1: one tolerance per quadrant
- Case 2: two adjacent tolerances per quadrant

The case of two non-adjacent tolerances per quadrant is identical to Case 2 and is therefore not listed. Furthermore, the case of three adjacent tolerances per quadrant would in an overall decrease in the air-gap and no motor asymmetry and therefore this is not the worst-case scenario of the cogging torque.

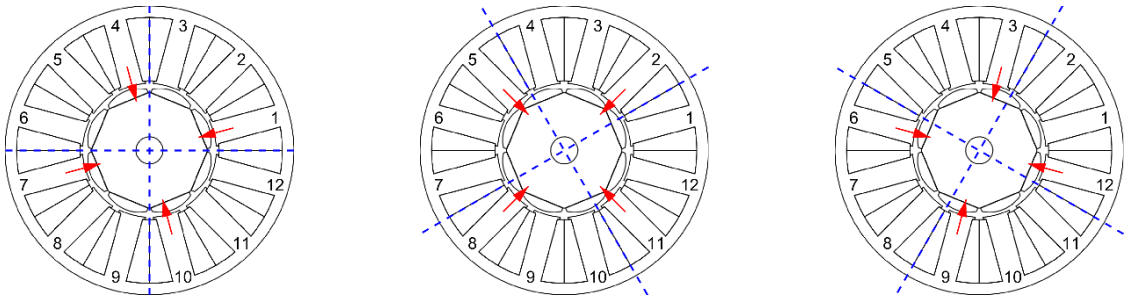
Each case is subdivided into 3 further cases (a to c) in which the tolerances are shifted by 0 to 2 slot pitches, respectively, shown in Fig. B.2. The two cases are indicated on the respective cross-sections in Fig. B.2. and the resulting cogging torque waveforms and harmonics are shown in Fig. B.3.

The magnitude of the $24^{th}$ and $48^{th}$ order cogging torque harmonic components increase with increasing number of tolerances in the inward direction due to slight decrease in air-gap length. The resultant magnitude of the $8^{th}$ order AHC of Cases 1 and 2 are identical since the phase difference of the individual AHCs due to two adjacent tolerances is 120°. The phases of the resultant $8^{th}$ order AHC of the two Cases is differ by 60°, and the resulting peak-to-peak cogging torque due to Case1 is higher than that due to Case 2. Thus, the worst-case scenario of cogging torque due to tolerances in the inward directions is Case 1(a to c) and the peak-to-peak cogging torque is 197.6 mNm.

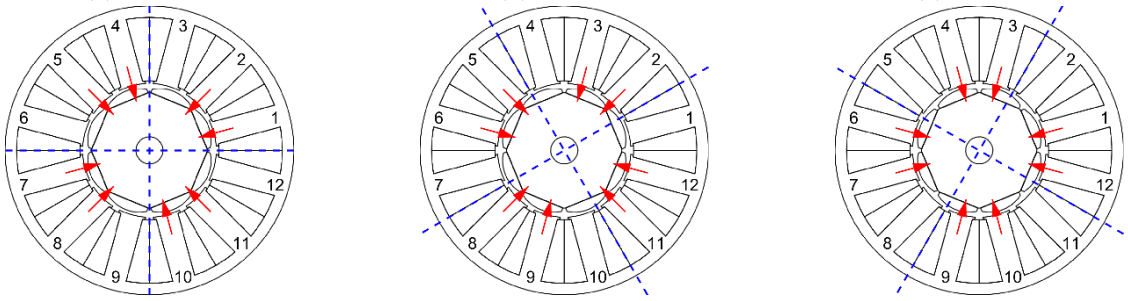



(a) Case 1 (b) Case 2

Fig. B.1. The possible cases of tolerances in the inward direction in the 12-slot/8-pole SPM motor.

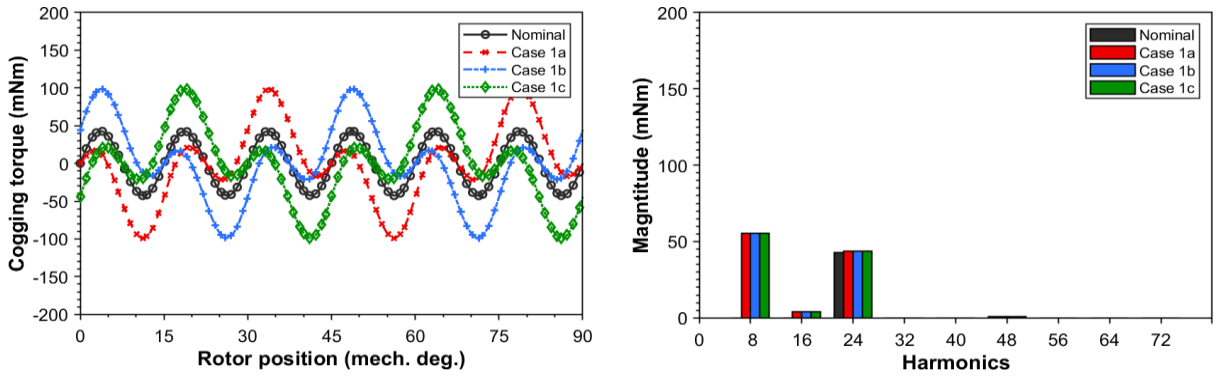



(a) Case 1a (b) Case 1b (c) Case 1c

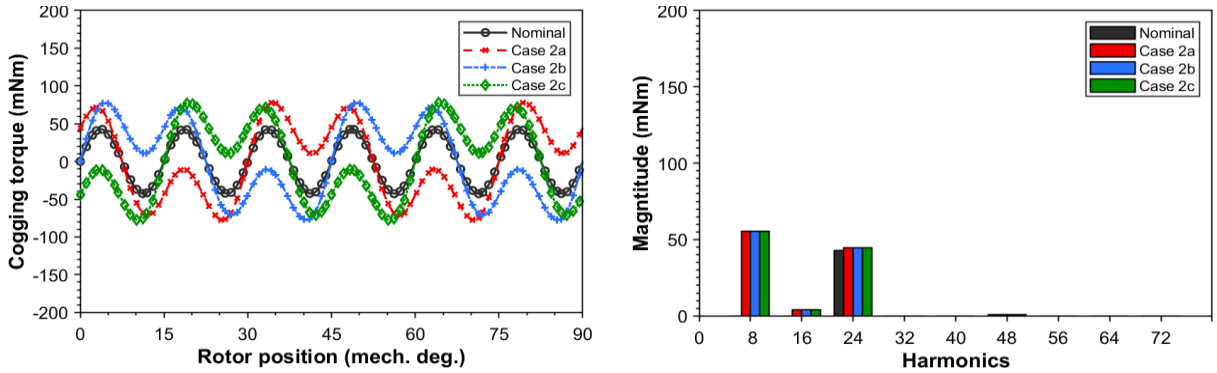



(d) Case 2a (e) Case 2b (f) Case 2c

Fig. B.2. Sub-cases of Case 1 and Case 2 of tolerances in the inward direction in the 12-slot/8-pole SPM motor.




(a) Case 1




(b) Case 2

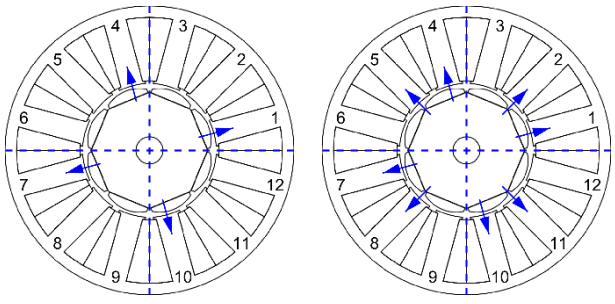
(I) Waveforms (II) Harmonics

Fig. B.3. Waveforms and harmonics of cogging torque due to the cases of tolerances in the inward direction in the 12-slot/8-pole SPM motor under investigation.

## B. Worst-case scenarios of tolerances in the outward direction

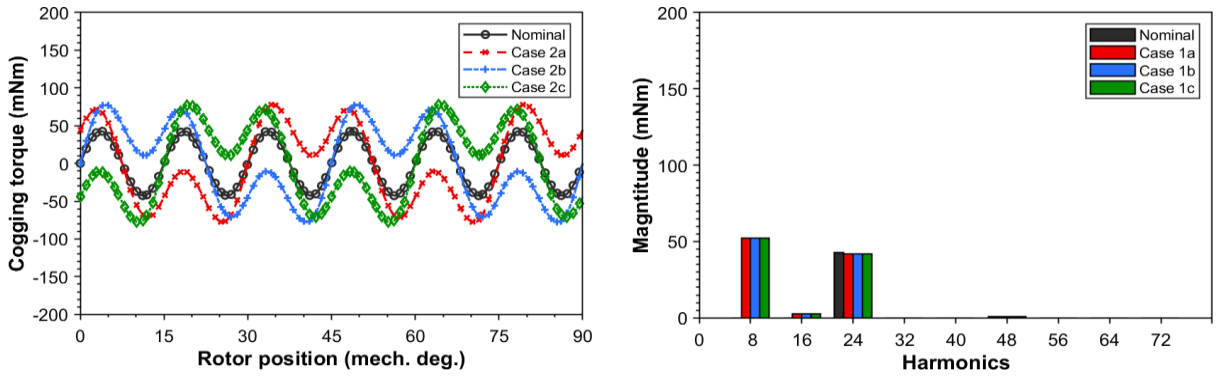
The cases of tolerances identified in the previous subsection are analysed for tolerances in the outward direction, as shown in Fig. B.4. The resulting cogging torque waveforms and harmonics are shown in Fig. B.5. The worst-case scenario is Case 2(a to c) and the peak-to-peak cogging torque is 187.2 mNm.

The worst-case scenario of tolerances in the outward direction results in a lower peak-to-peak cogging torque than that due to tolerances in the inward direction. This is attributed to the fact that tolerances in the outward direction result in a slight increase in air-gap length at the location of the tolerance.

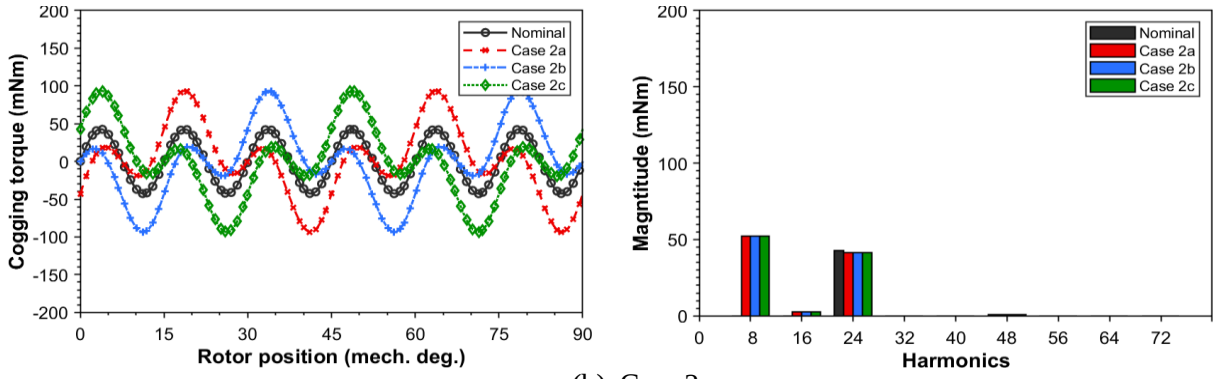


(a) Case 1 (b) Case 2

Fig. B.4. The possible cases of tolerances in the outward direction in the 12-slot/8-pole SPM motor



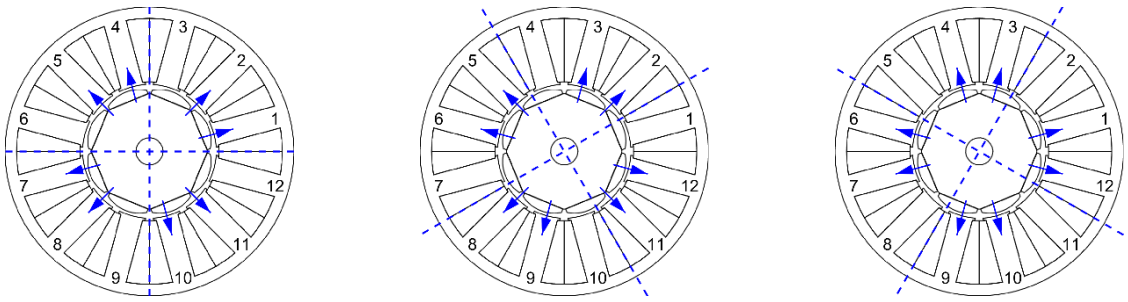

(a) Case 1




(b) Case 2

(I) Waveforms (II) Harmonics

Fig. B.5. Waveforms and harmonics of cogging torque due to the cases of tolerances in the outward direction in the 12-slot/8-pole SPM motor under investigation.



(a) Case 2a (b) Case 2b (c) Case 2c

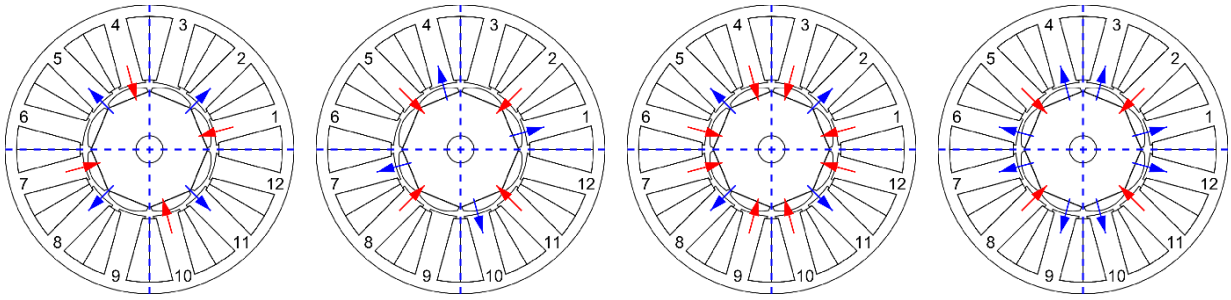
Fig. B.6. Worst-case scenarios of tolerances in the outward direction in the 12-slot/8-pole SPM motor under investigation.

## C. Worst-case scenarios of bidirectional tolerances

The worst-case scenarios of bidirectional tolerances comprise at least two tolerances in each symmetric quadrant. Thus, the four possible cases of bidirectional tolerances in a symmetric quadrant are:

- Case 1: two adjacent tolerances in opposite directions (i.e. one inward and one outward variation)
- Case 2: Case 1 with inverted tolerance direction
- Case 3 two non-adjacent tolerances in the same direction separated by tolerance in the opposite direction
- Case 4: Case 3 with inverted tolerance direction

The four cases, shown in Fig. B.7, are subdivided into 3 further cases (a to c) in which the tolerances are shifted by 0 to 2 slot pitches, respectively. The cogging torque waveforms and harmonics due to the four cases are shown in Fig. B.8.

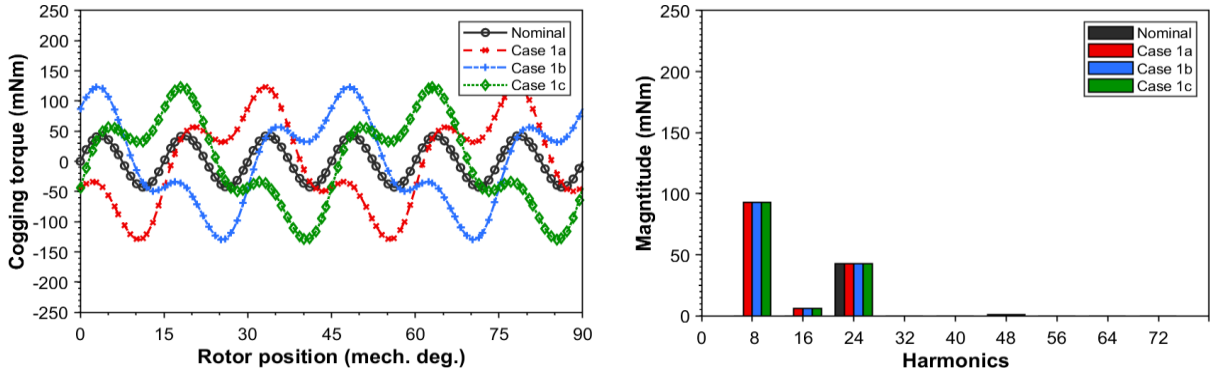



(a) Case 1 (b) Case 2 (c) Case 3 (d) Case 4

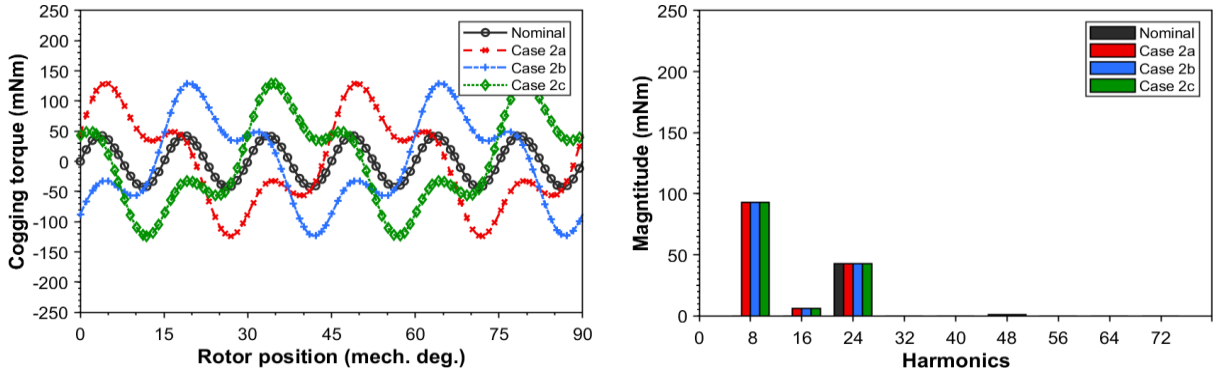
Fig. B.7. Cases of bidirectional tolerances in the stator teeth profile radial position in the 12-slot/8-pole SPM motor.

The worst-case scenario of bidirectional variation is Case 4(a to c) and the peak-to-peak cogging torque is 299.3 mNm**.** Case 4 is the superposition of the worst-case scenario of tolerances in the inward direction and the worst-case scenario of tolerances in the outward direction

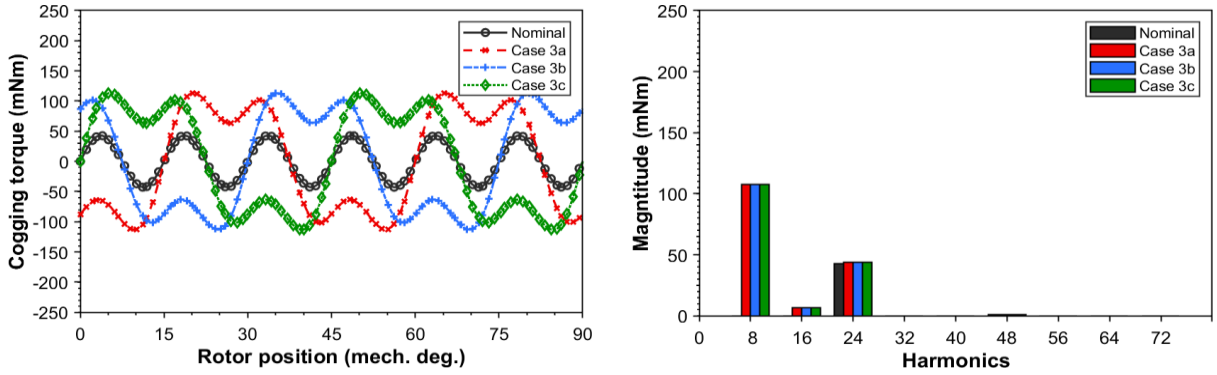
The magnitudes of the $8^{th}$ and $16^{th}$ order harmonic components of the cogging torque of Case 3 and Case 4 are identical. However, the phases of the resultant $8^{th}$ and $16^{th}$ order harmonic components of Case 4 result in a higher peak-to-peak cogging torque. The tolerances of the worst-case scenarios Case 4a to Case 4c are shown in Fig. B.9.



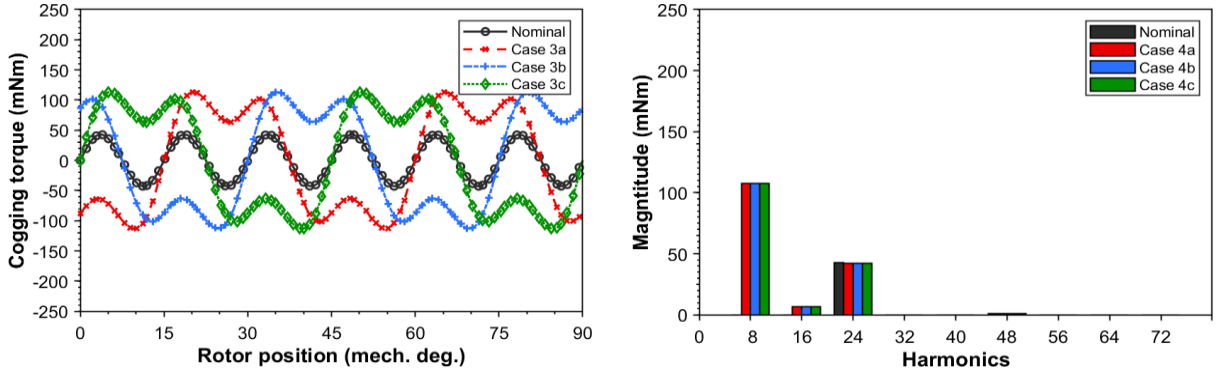

(a) Case 1




(b) Case 2



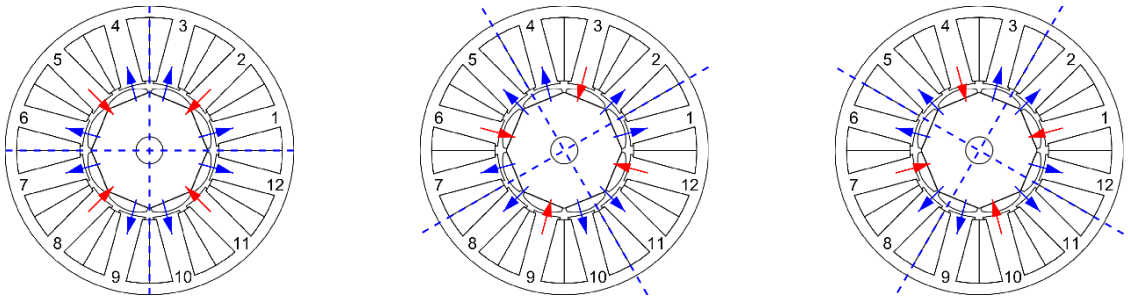

(c) Case 3




(d) Case 4

(I) Waveforms (II) Harmonics

Fig. B.8. Waveforms and harmonics of cogging torque due to the cases of tolerances in both directions in the 12-slot/8-pole SPM motor under investigation.




(a) Case 4a (b) Case 4b (c) Case 4c

Fig. B.9. Worst-case scenarios of bidirectional tolerances in the 12-slot/8-pole SPM motor under investigation.

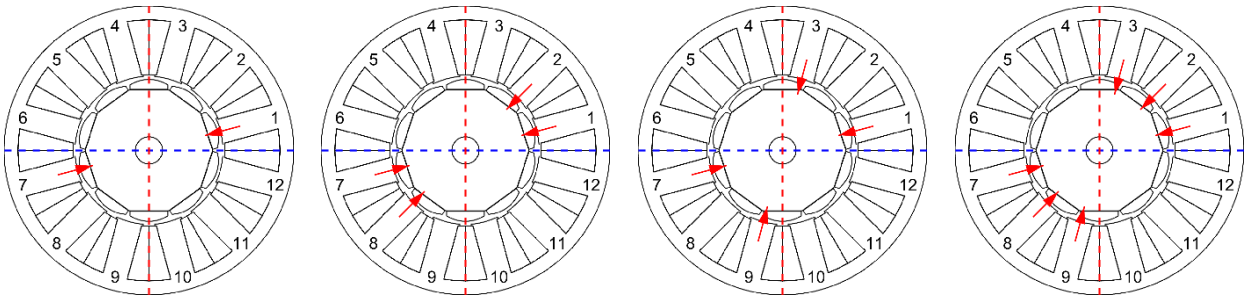
## B.2 Worst-Case Scenarios of Cogging Torque of 12-slot/10-pole SPM Motor

A. Worst-case scenarios of tolerances in the inward direction

The symmetry and anti-symmetry of the 12-slot/10-pole motor are indicated by the blue and red dotted lines in Fig. B.10, respectively. The worst-case scenarios for tolerances in a particular direction are obtained by exploiting the additive and cancelling effects on the resultant AHCs due to the inherent symmetry and anti-symmetry of the motor. Therefore, the four possible cases of tolerances in the inward direction are:

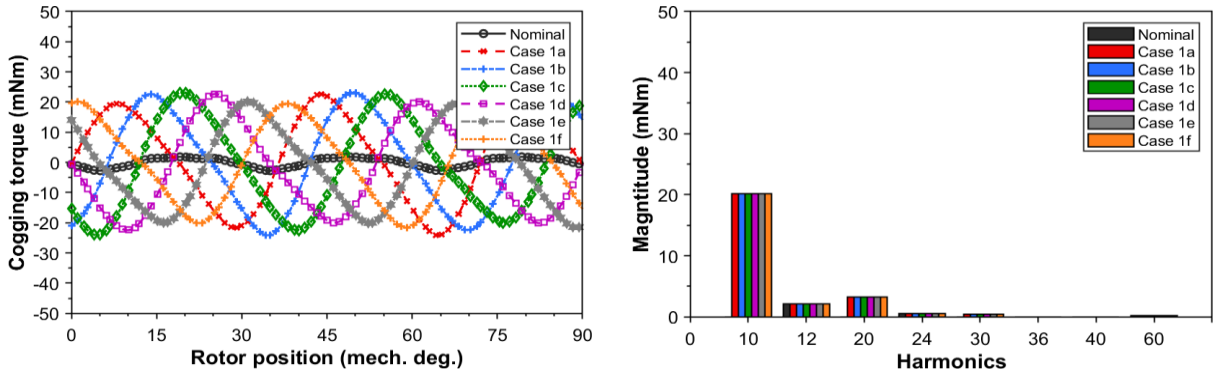
- Case 1: one tolerance
- Case 2: two adjacent tolerances
- Case 3: two tolerances separated by a slot pitch
- Case 4: three adjacent tolerances

The four cases, shown in Fig. B.10, are subdivided into 6 further cases (a to f) in which the tolerances in are shifted by 0 to 5 slot pitches, respectively. The cogging torque waveforms and harmonics of the worst-case scenarios in the inward direction are shown in Fig. B.11. The worst-case scenario of the cogging torque due to tolerances in the inward directions is Case 4(a to f) and the peak-to-peak cogging torque is 83.9 mNm.

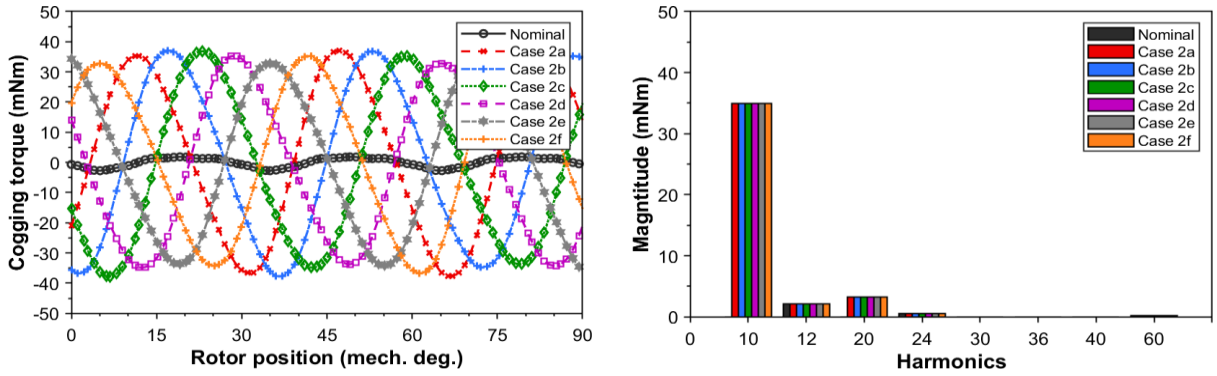



(a) Case 1 (b) Case 2 (c) Case 3 (d) Case 4

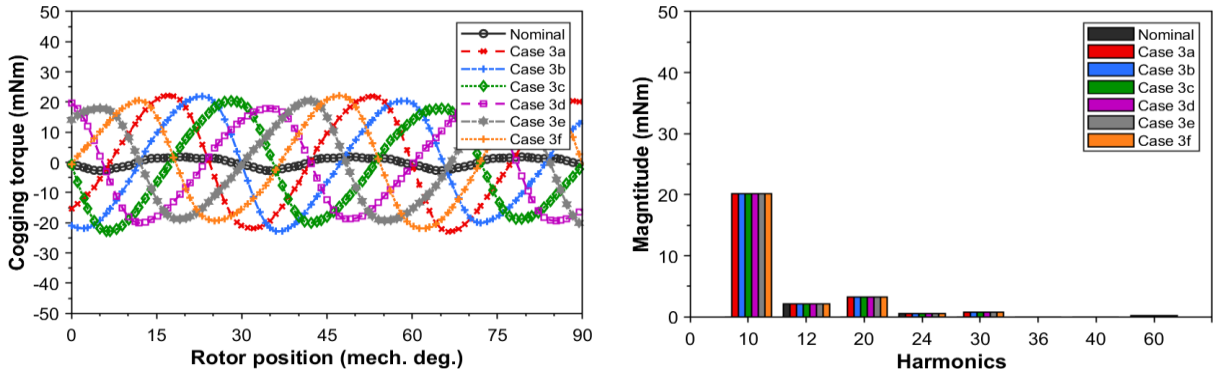
Fig. B.10. The possible cases of tolerances in the inward direction in the 12-slot/10-pole SPM motor.



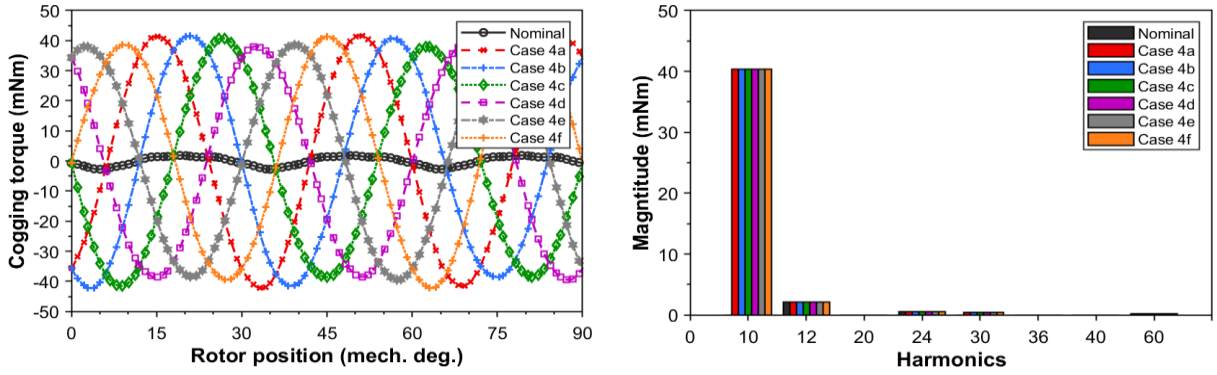

(a) Case 1




(b) Case 2



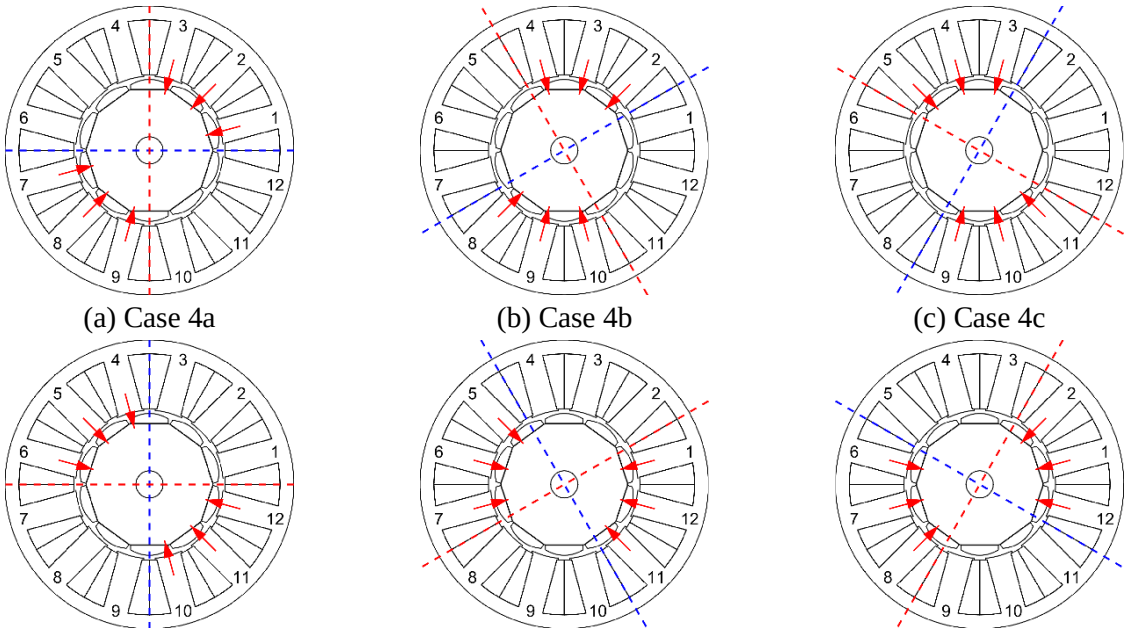

(c) Case 3




(d) Case 4

(I) Waveforms (II) Harmonics

Fig. B.11. Waveforms and harmonics of cogging torque waveforms due to the possible cases of tolerances in the inward direction in the 12-slot/10-pole SPM motor.



(a) Case 4a (b) Case 4b (c) Case 4c

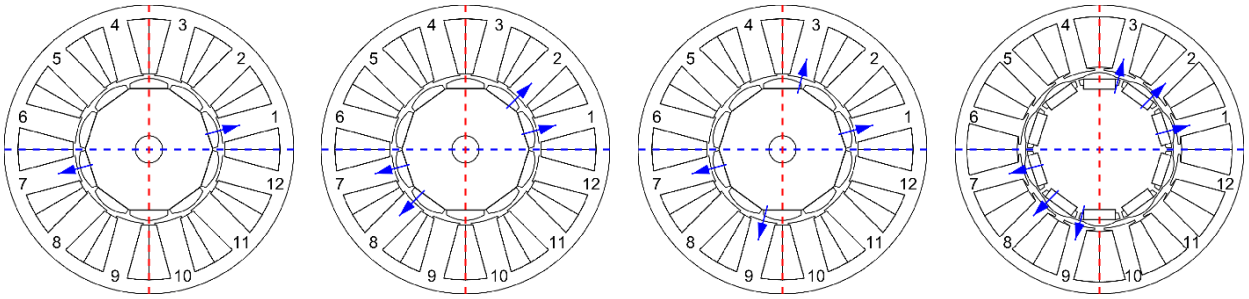
(d) Case 4d (e) Case 4e (f) Case 4f

Fig. B.12. Sub-cases of the worst-case scenario of tolerances in the inward direction in the 12-slot/10-pole SPM motor.

## B. Worst-case scenarios of tolerances in the outward direction

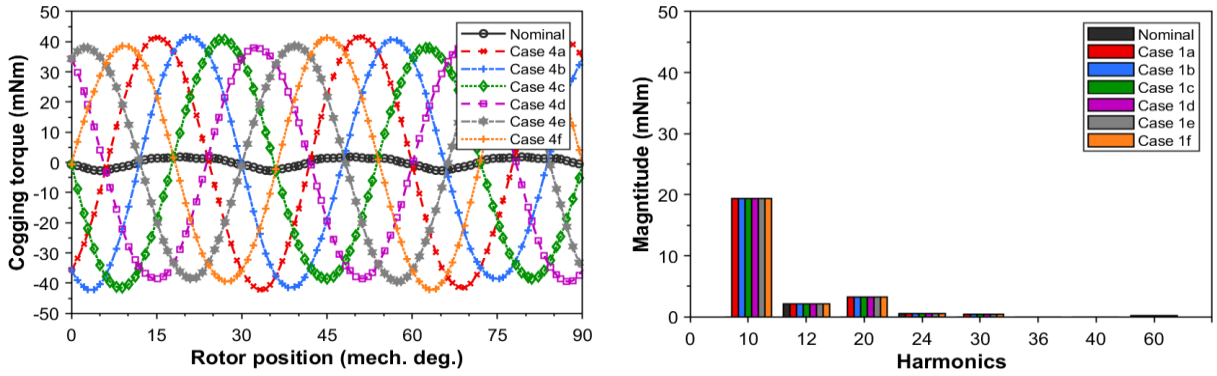
The direction of the tolerances in the identified possible cases of tolerances in the inward direction is reversed, as shown in Fig. B.13. The cogging torque waveforms and harmonics of each case, including sub-cases in which the tolerances are shifted by 0 to 5 slot pitches, are shown in Fig. B.14.

The worst-case scenario is Case 4(a to f) and the peak-to-peak cogging torque is 80.7 mNm. The worst-case scenario of tolerances in the outward direction results in a lower peak-to-peak cogging torque than that of tolerances in the inward directions due to the change in air-gap length caused by manufacturing tolerances.

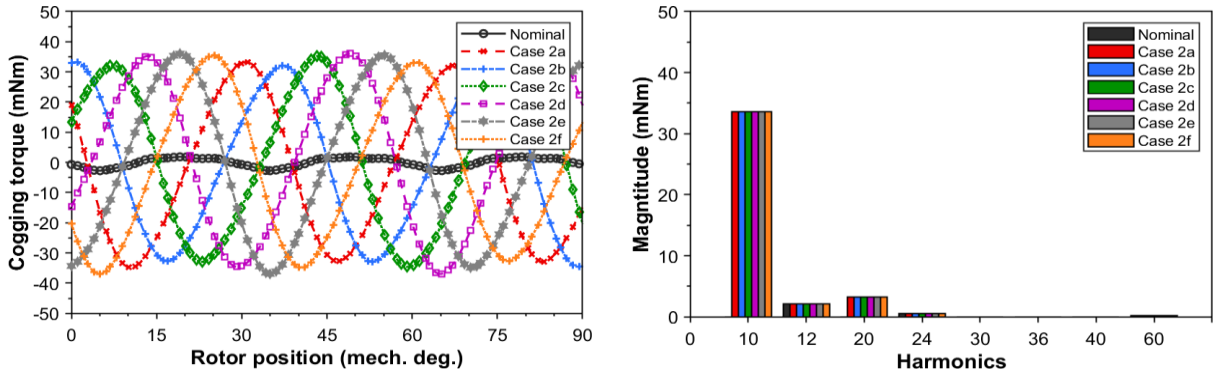


(a) Case 1 (b) Case 2 (c) Case 3 (d) Case 4

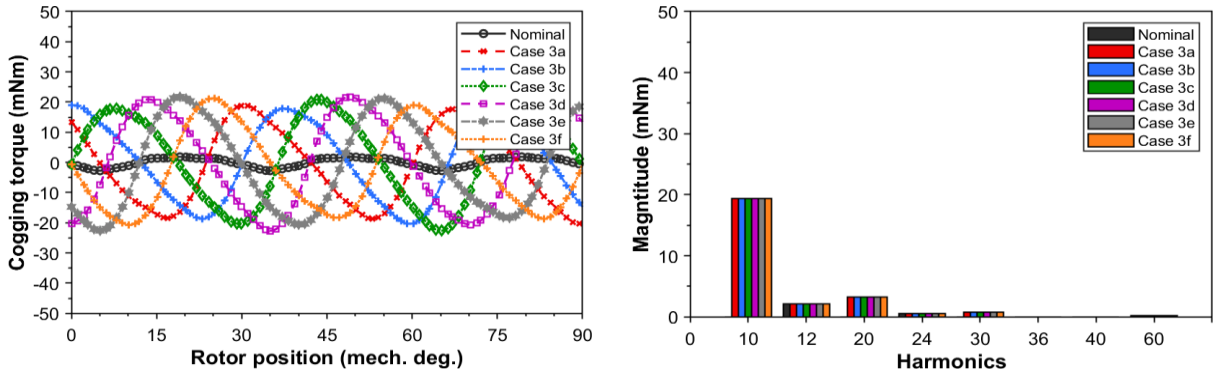
Fig. B.13. The possible cases of tolerances in the outward direction.



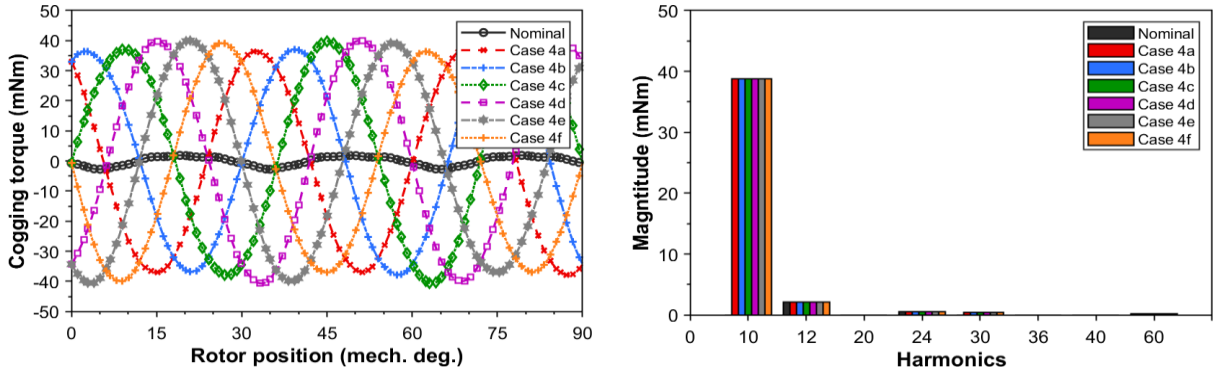

(a) Case 1




(b) Case 2



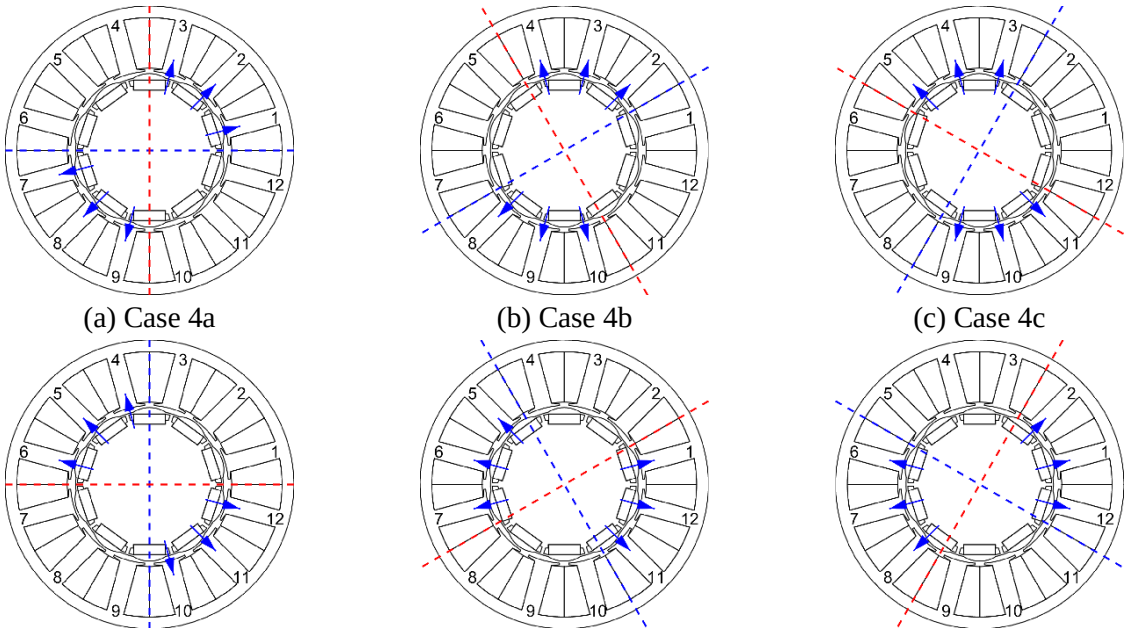

(c) Case 3




(d) Case 4

(I) Waveforms (II) Harmonics

Fig. B.14. Waveforms and harmonics of cogging torque waveforms due to the possible cases of tolerances in the outward direction in the 12-slot/10-pole SPM motor.



(a) Case 4a (b) Case 4b (c) Case 4c

(d) Case 4d (e) Case 4e (f) Case 4f

Fig. B.15. Sub-cases of the worst-case scenario of tolerances in the outward direction in the 12-slot/10-pole SPM motor.

## C. Worst-case scenarios of bidirectional tolerances

The possible cases of bidirectional tolerances are determined by exploiting the symmetry and anti-symmetry of the 12-slot/10-pole motor. Therefore, the tolerances in each quadrant for the respective cases are as follows:

- Case 1: one tolerance
- Case 2: two adjacent tolerances in the same direction
- Case 3: two tolerances in the same direction separated by a slot pitch
- Case 4: two non-adjacent tolerances in the same directions separated a tolerance in the opposite direction
- Case 5: three adjacent tolerances in same direction.

The five cases, shown in Fig. B.16, are further subdivided into 6 further cases (a to f) in which the tolerances are shifted by 0 to 5 slot pitches, respectively. The Waveforms and harmonics of cogging torque due to the possible cases are shown in Fig. B.17 and Fig. B.18. The worst-case scenario is Case 5(a to f) and the peak-to-peak cogging torque is 160.6 mNm. The tolerances of Cases 5a to 5f are shown in Fig. B.19.

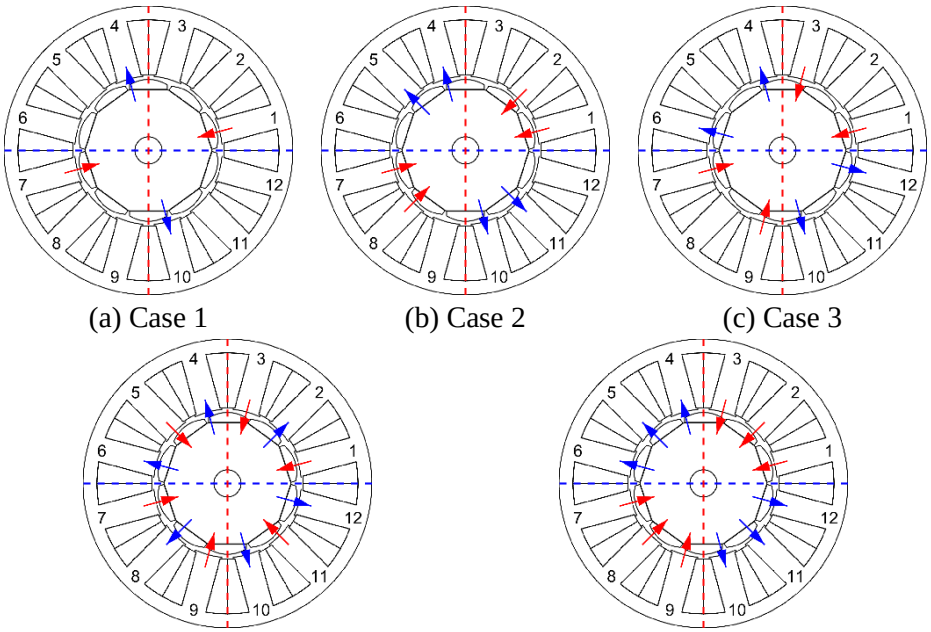
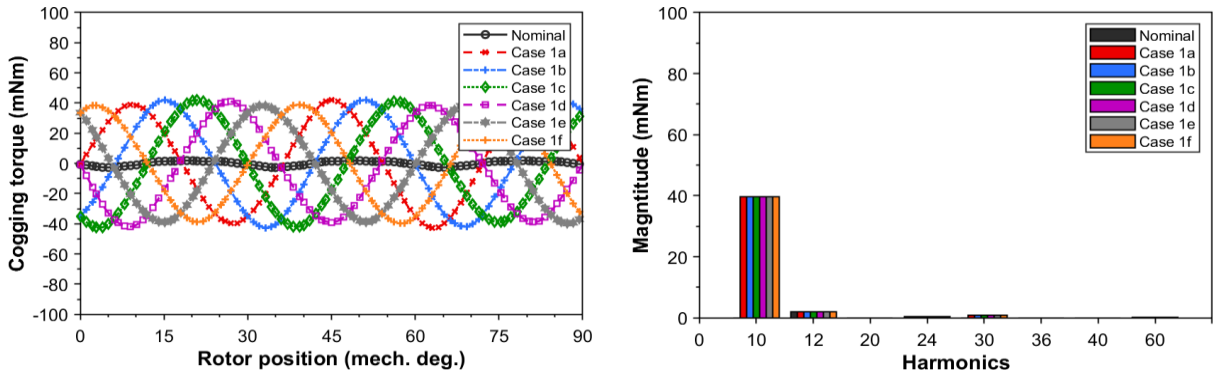
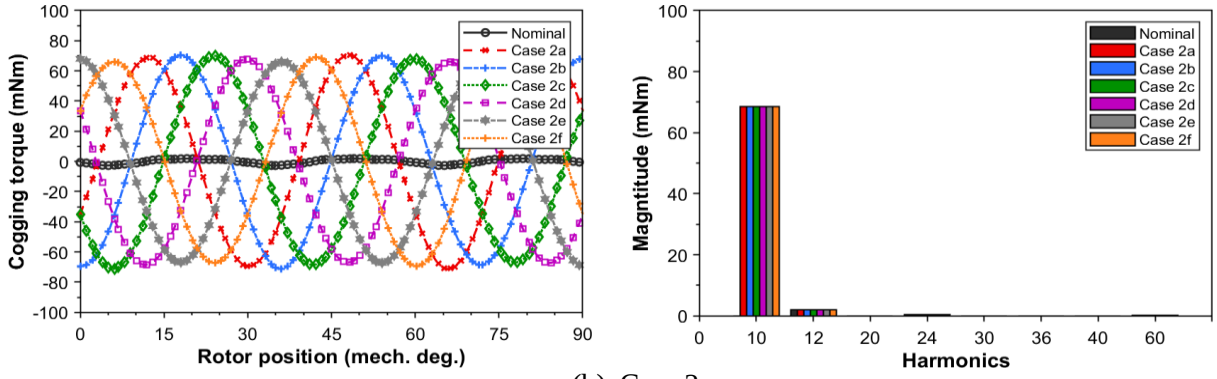


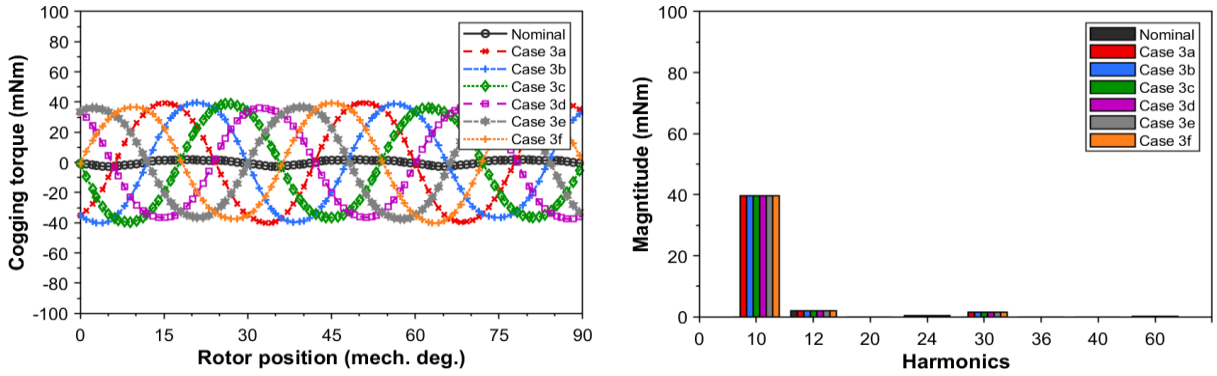

Fig. B.16. The possible cases of bidirectional tolerances in the 12-slot/10-pole SPM motor.



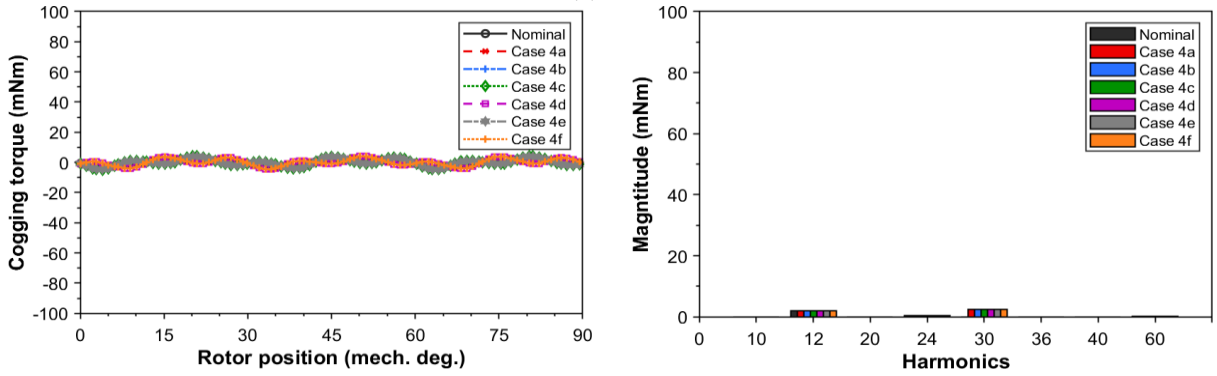

(a) Case 1




(b) Case 2



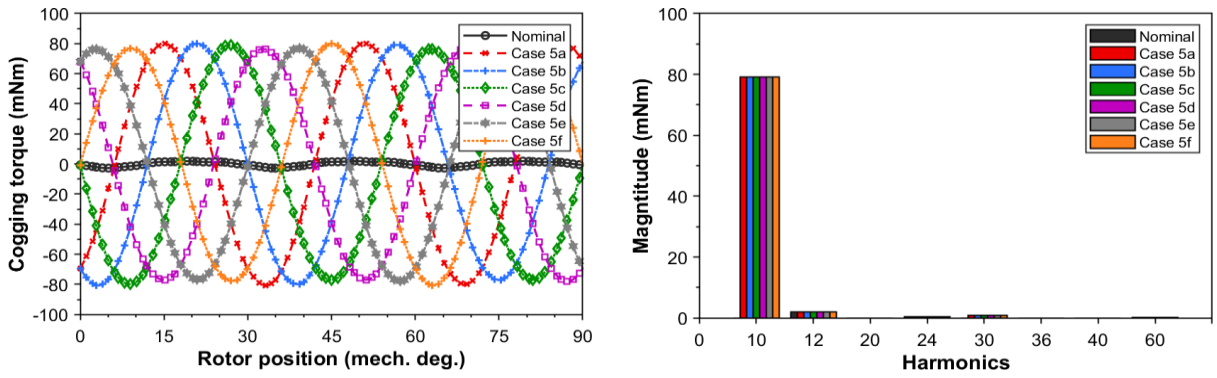

(c) Case 3




(d) Case 4

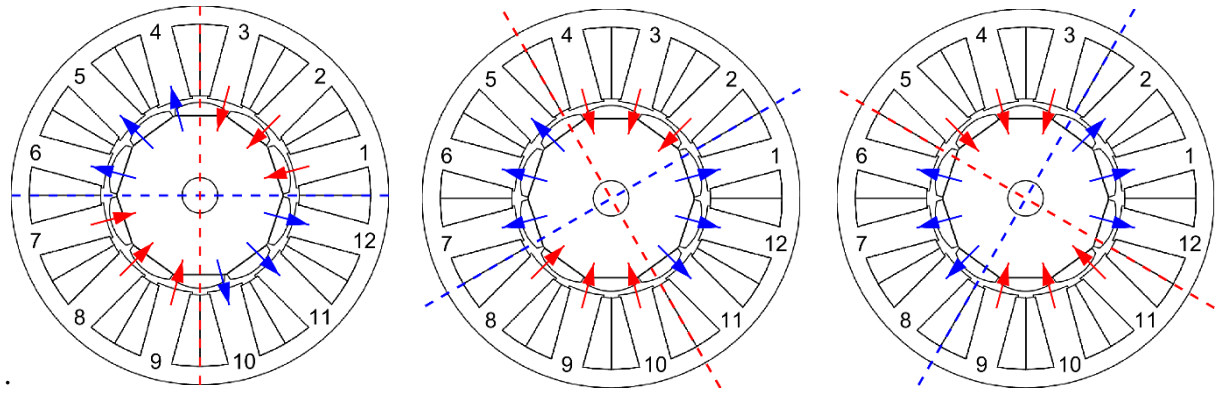
(I) Waveforms (II) Harmonics

Fig. B.17. Waveforms and harmonics of cogging torque due to cases 1 to 4 of bidirectional tolerances in the 12-slot/10-pole SPM motor.

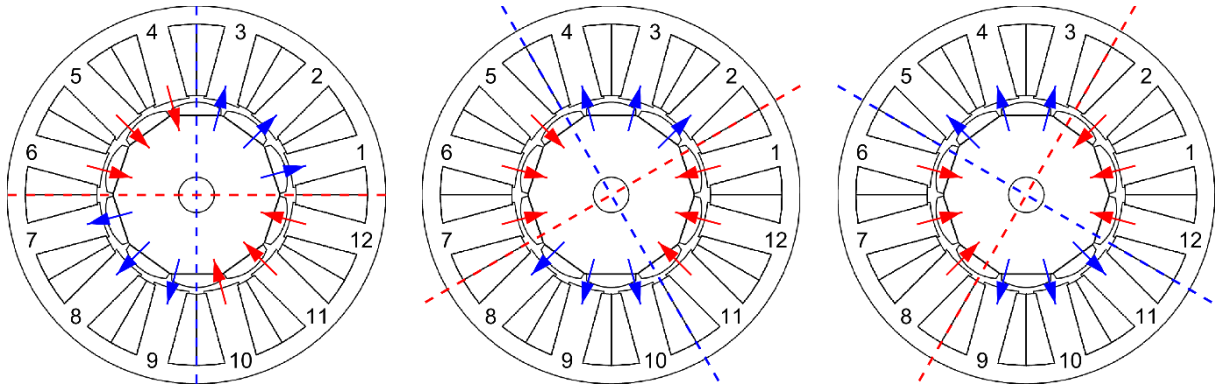



(a) Waveforms (b) Harmonics

Fig. B.18. Waveforms and harmonics of cogging torque due to the worst-case scenario Case 5 of bidirectional tolerances in the 12-slot/10-pole SPM motor.



(a) Case 5a (b) Case 5b (c) Case 5c



(d) Case 5d (e) Case 5e (f) Case 5f

Fig. B.19. Worst-case scenarios of bidirectional tolerances in the 12-slot/10-pole SPM motor.

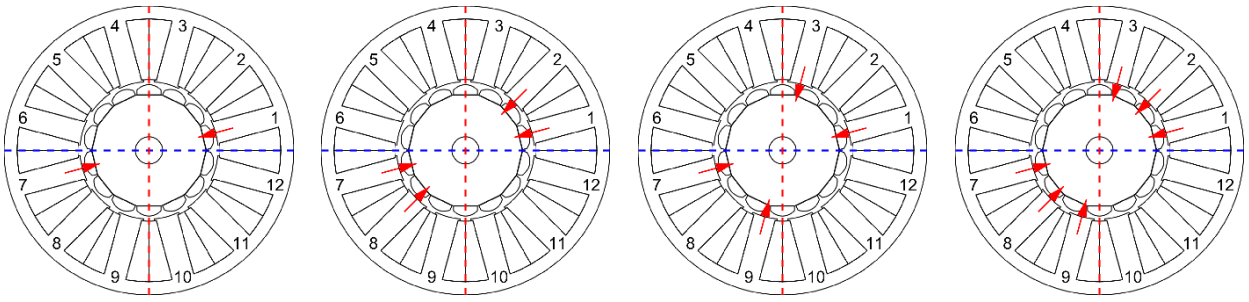
# B.3 Worst-Case Scenarios of Cogging Torque of 12-slot/14-pole SPM Motor

A. Worst-case scenarios of tolerances in the inward direction

The symmetry and anti-symmetry of the 12-slot/14-pole motor is indicated by the blue and red dotted lines in Fig. B.20, respectively. The worst-case scenarios for tolerances in a particular direction are obtained by exploiting the additive and cancelling effects on the resultant AHCs due to the inherent symmetry and anti-symmetry of the motor. Therefore, the four possible cases of tolerances in the inward direction in the first and third quadrant are:

- Case 1: one tolerance
- Case 2: two adjacent tolerances
- Case 3: two tolerances separated by a slot pitch
- Case 4: three adjacent tolerances

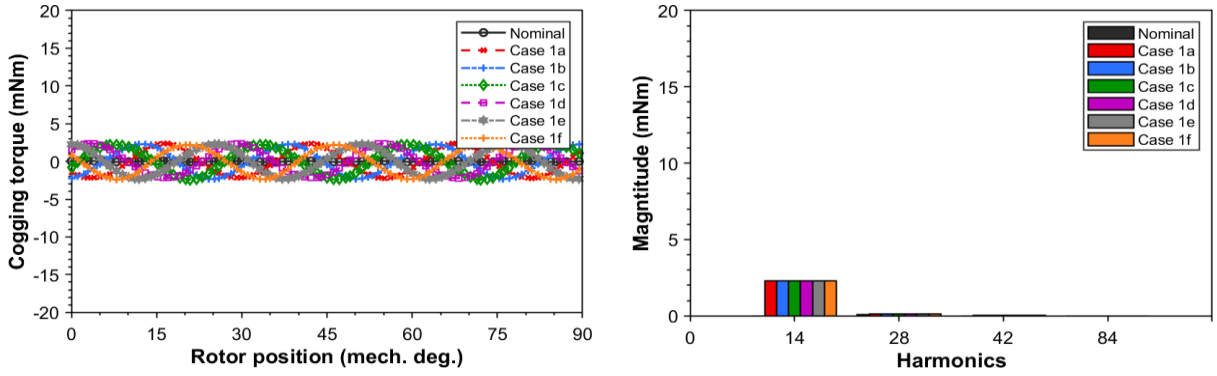
The four cases, shown in Fig. B.20, are subdivided into 6 further cases (a to f) in which the layouts in are shifted by 0 to 5 slot pitches, respectively. The cogging torque waveforms and harmonics of the worst-case scenarios in the inward direction are shown in Fig. B.21. The worst-case scenario of the cogging torque due to tolerances in the inward directions is Case 4(a to f) and the peak-to-peak cogging torque is 9.3 mNm.



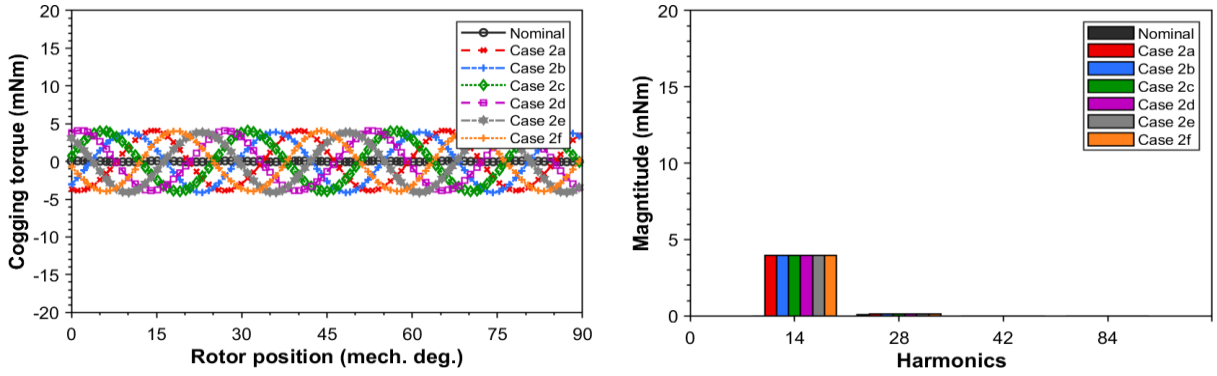

(a) Case 1 (b) Case 2 (c) Case 3 (d) Case 4

Fig. B.20. The possible cases of tolerances in the inward direction in the 12-slot/14-pole SPM motor.

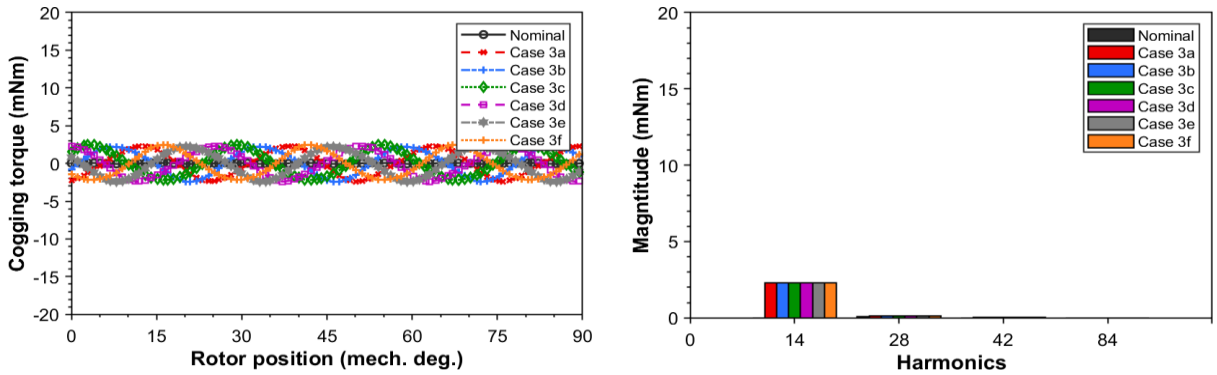
.



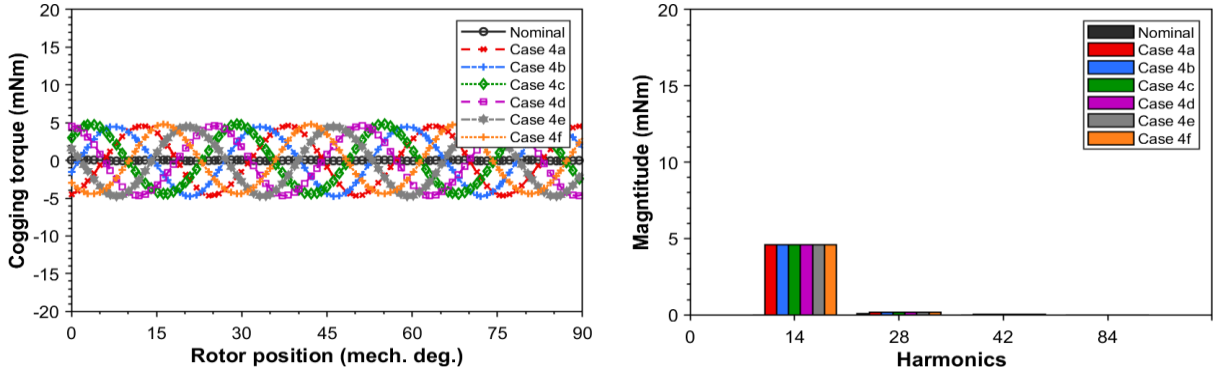

(a) Case 1




(b) Case 2




(c) Case 3




(d) Case 4

(I) Waveforms (II) Harmonics

Fig. B.21. Waveforms and harmonics of cogging torque due to the possible cases of tolerances in the inward direction in the 12-slot/14-pole SPM motor.

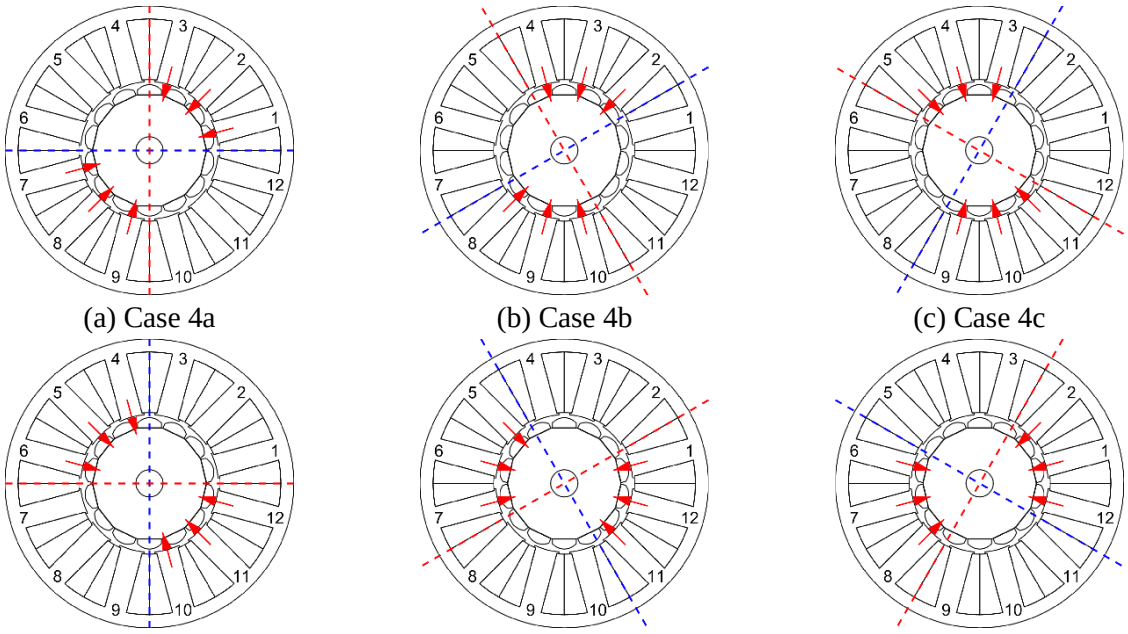



Fig. B.22. Sub-cases of the worst-case scenario of tolerances in the inward direction in the 12-slot/14-pole SPM motor.

## B. Worst-case scenarios of tolerances in the outward direction

The direction of the tolerances in the identified possible cases of tolerances in the inward direction is reversed, as shown in Fig. B.23. The cogging torque waveforms and harmonics of each case, including sub-cases in which the tolerances are shifted by 0 to 5 slot pitches, are shown in Fig. B.24.

The worst-case scenario is Case 4(a to f) and the peak-to-peak cogging torque is 9.1 mNm. The worst-case scenario of tolerances in the outward direction results in a lower peak-to-peak cogging torque than that of tolerances in the inward directions due to the change in air-gap length caused by manufacturing tolerances.

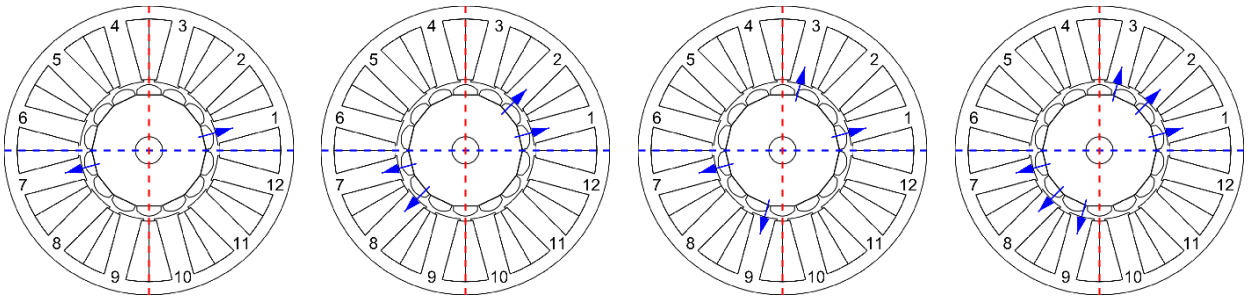
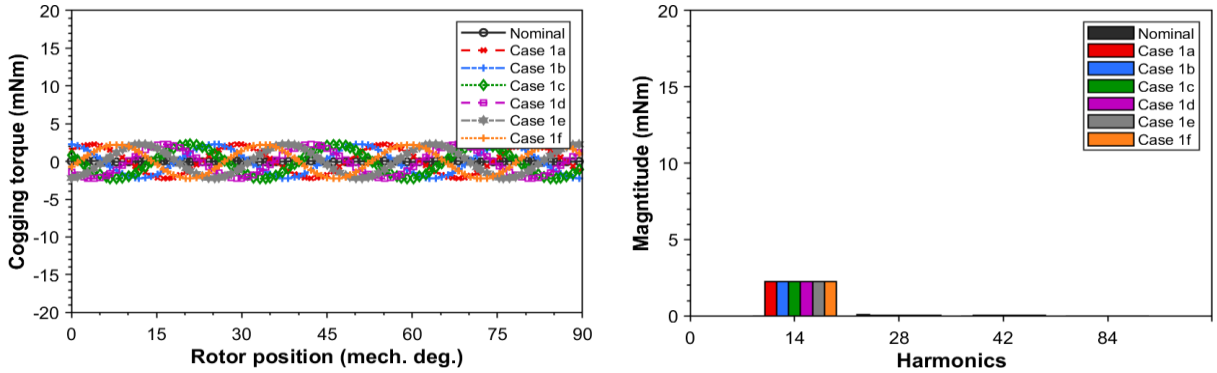
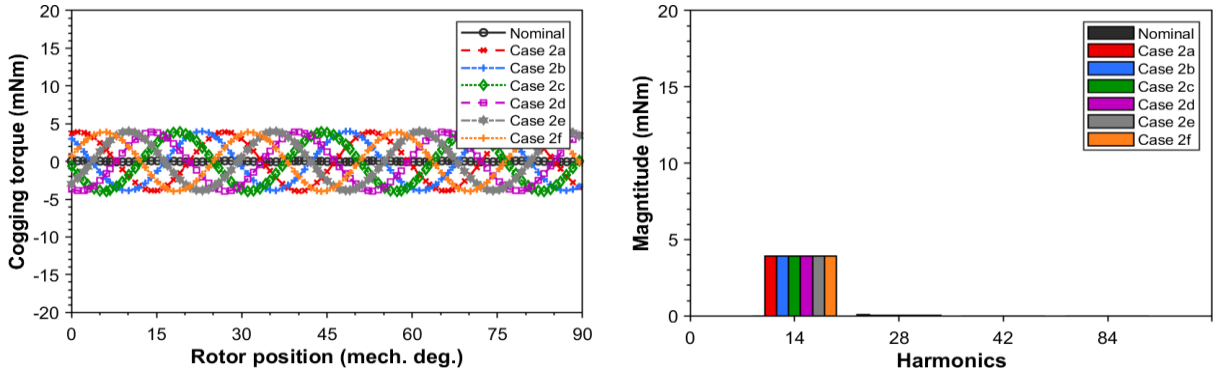


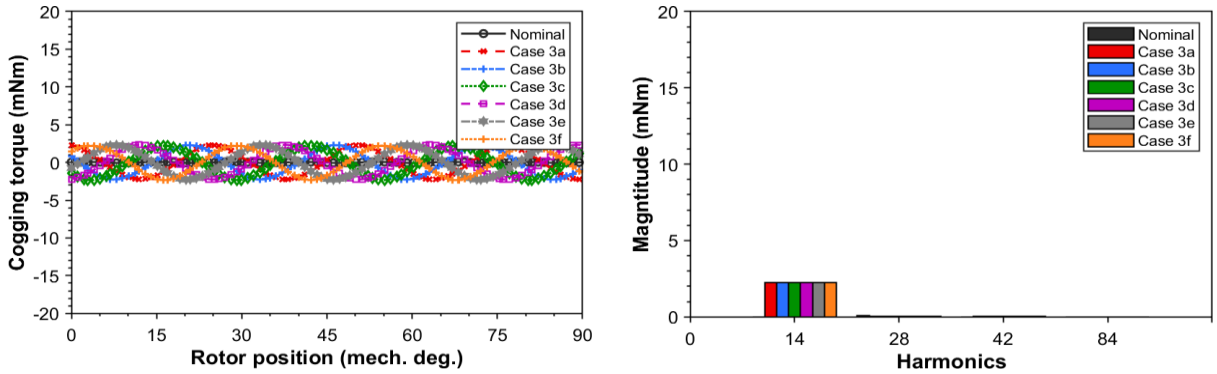

Fig. B.23. The possible cases of tolerances in the outward direction in the 12-slot/14-pole SPM motor.



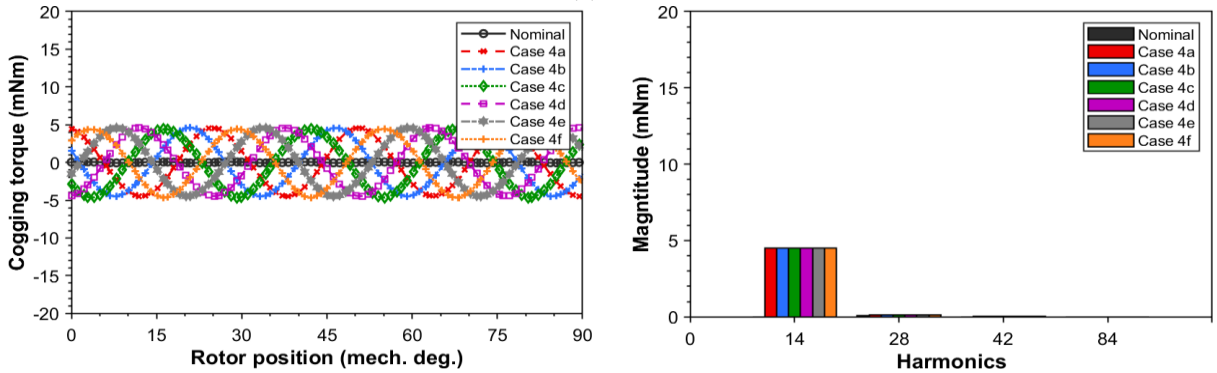

(a) Case 1




(b) Case 2



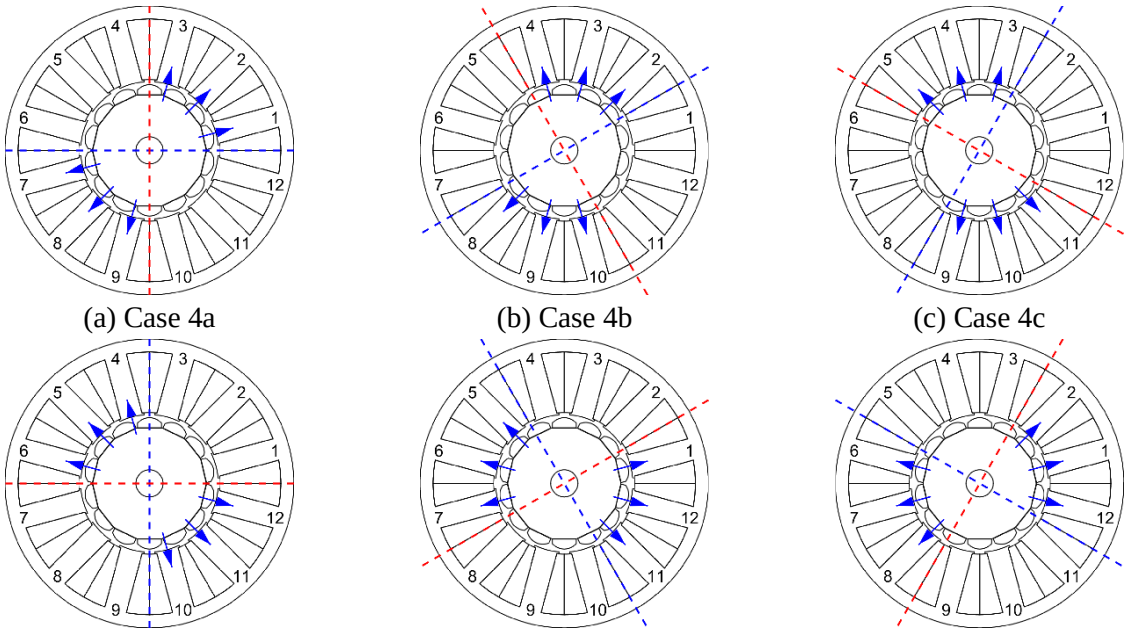

(c) Case 3




(d) Case 4

(I) Waveforms (II) Harmonics

Fig. B.24. Waveforms and harmonics of cogging torque due to the possible cases of tolerances in the outward direction in the 12-slot/14-pole SPM motor.




(a) Case 4a (b) Case 4b (c) Case 4c

(d) Case 4d (e) Case 4e (f) Case 4f

Fig. B.25. Sub-cases of the worst-case scenario of tolerances in the outward direction in the 12-slot/14-pole SPM motor.

## C. Worst-case scenarios of bidirectional tolerances

The inherent symmetry and anti-symmetry of the motor is again exploited to determine the worst-case scenarios of bidirectional tolerances. Therefore, the tolerances in each quadrant for the respective cases are as follows:

- Case 1: one tolerance
- Case 2: two adjacent tolerances in the same direction
- Case 3: two tolerances in the same direction separated by a slot pitch
- Case 4: two non-adjacent tolerances in the same directions separated a tolerance in the opposite direction
- Case 5: three adjacent tolerances in same direction.

The five cases, shown in Fig. B.26, are further subdivided into 6 further cases (a to f) in which the tolerances are shifted by 0 to 5 slot pitches, respectively. The cogging torque waveforms of the possible cases are shown in Fig. B.28 and Fig. B.29. The worst-case scenario is Case 5(a to f) and the peak-to-peak cogging torque is 18.3 mNm. The tolerances of Cases 5a to 5f are shown in Fig. B.27.

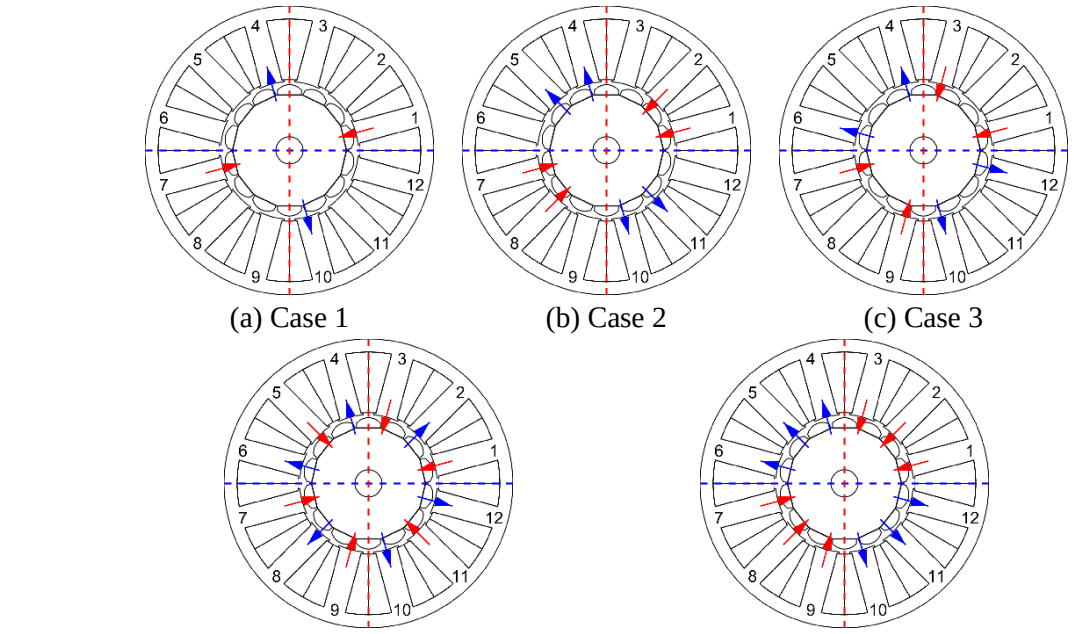



Fig. B.26. The possible cases of bidirectional tolerances in the 12-slot/14-pole SPM motor.

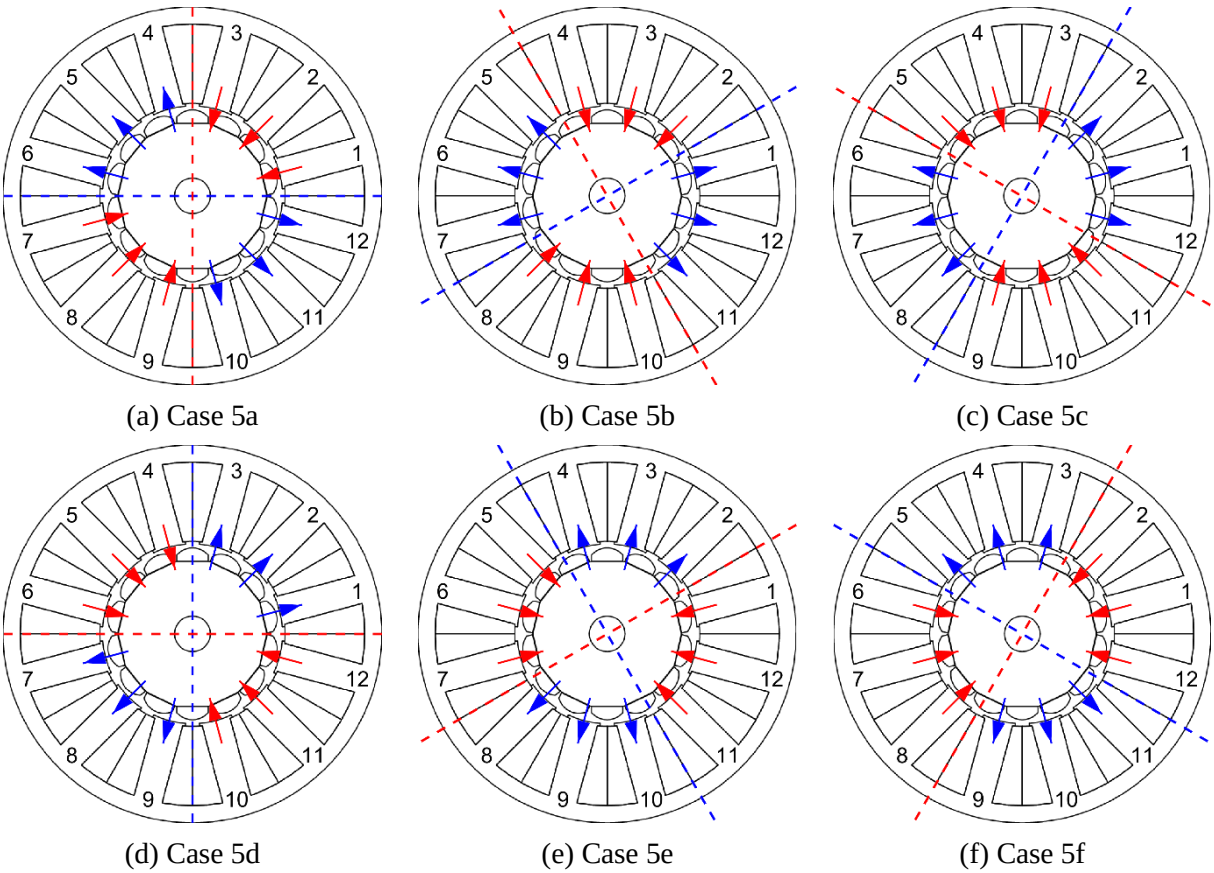
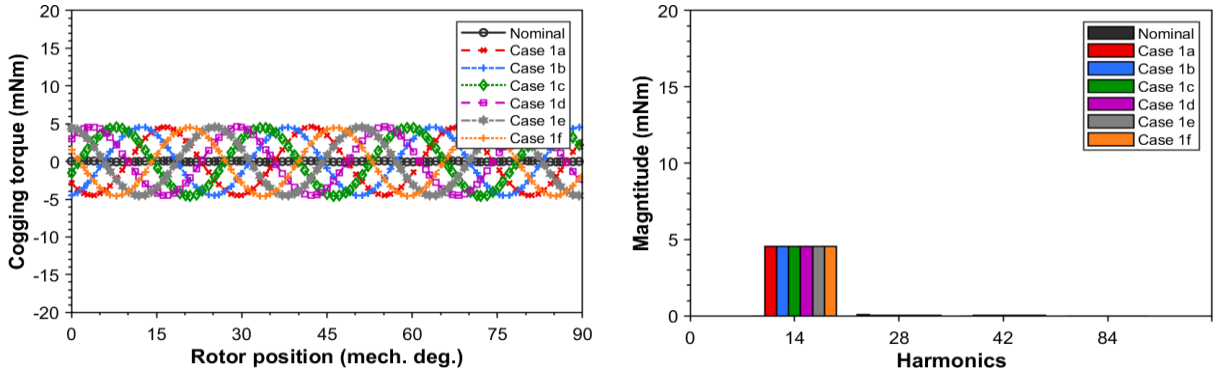
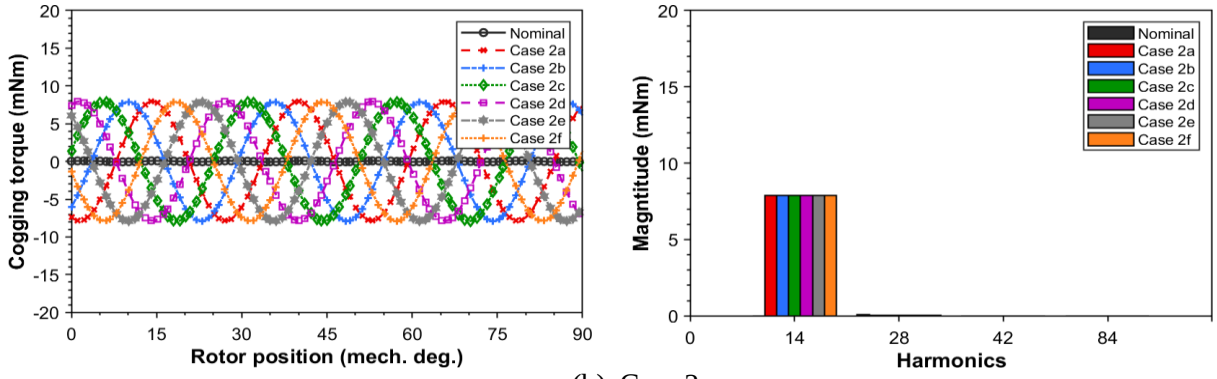


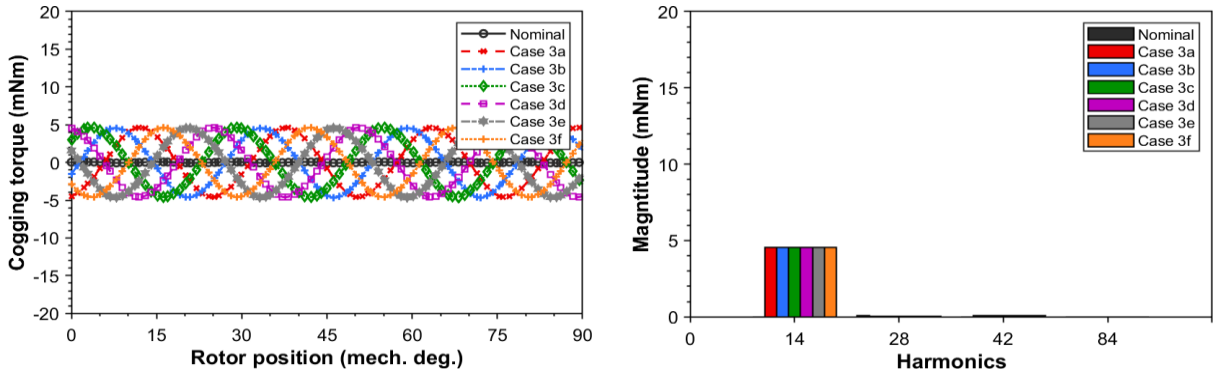

Fig. B.27. The worst-case scenarios of bidirectional tolerances in the 12-slot/14-pole SPM motor.



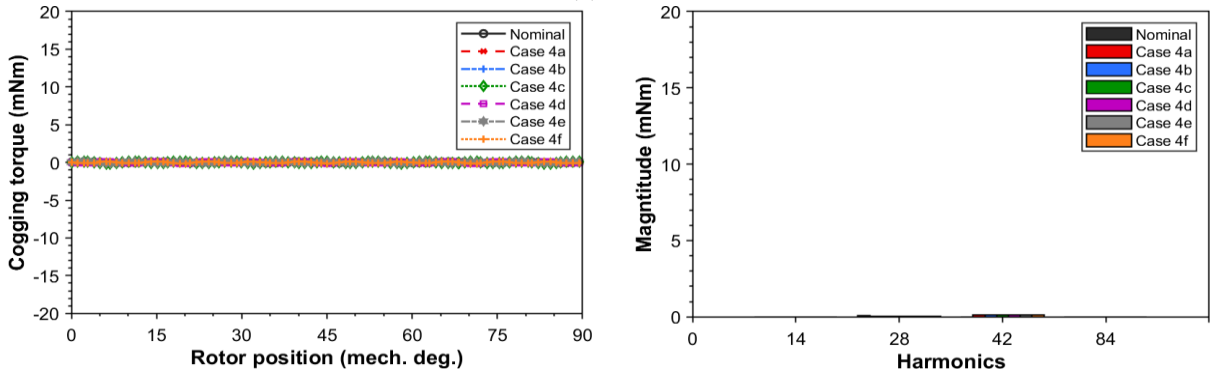

(a) Case 1




(b) Case 2



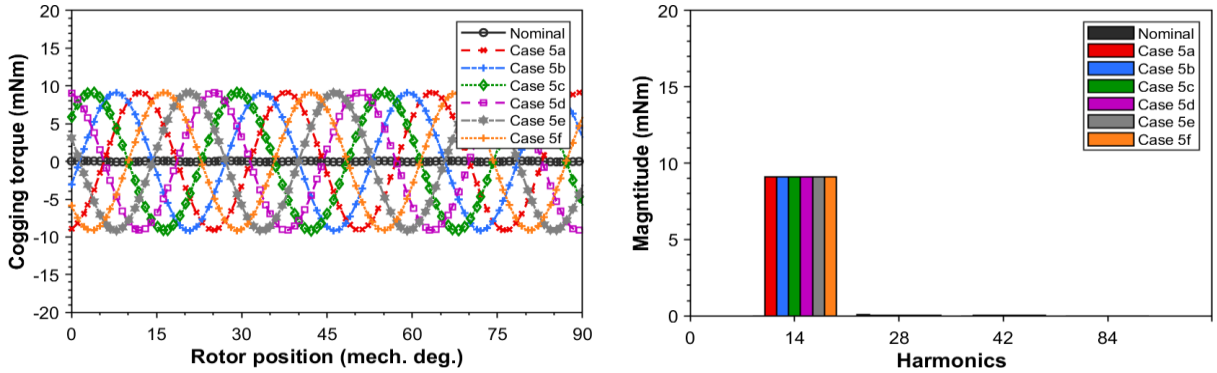

(c) Case 3




(d) Case 4

(I) Waveforms (II) Harmonics

Fig. B.28. Waveforms and harmonics of cogging torque due to the possible cases 1 to 4 of bidirectional tolerances in the 12-slot/14-pole SPM motor.



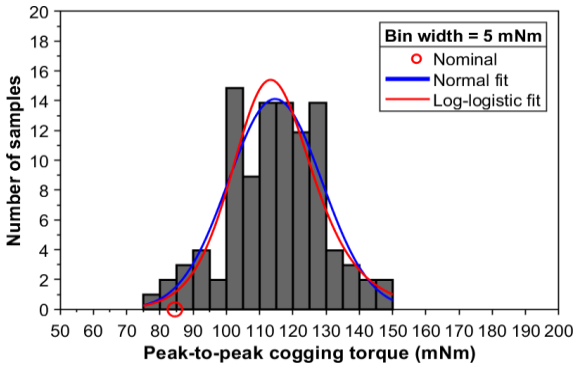

(a) Waveforms (b) Harmonics

Fig. B.29. Waveforms and harmonics of cogging torque due to Case 5 of bidirectional tolerances in the 12-slot/14-pole SPM motor.

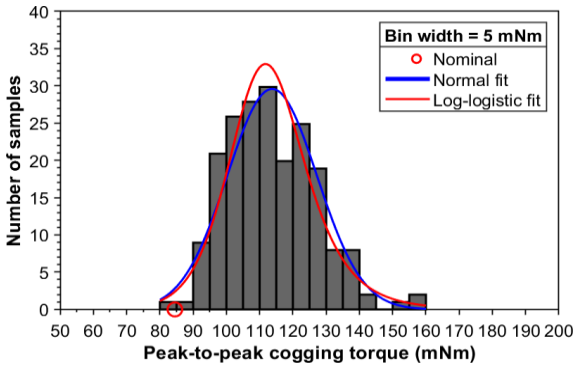
# APPENDIX C

# ANALYSIS OF INFLUENCE OF SAMPLE SIZE ON COGGING TORQUE UNCERTAINTY

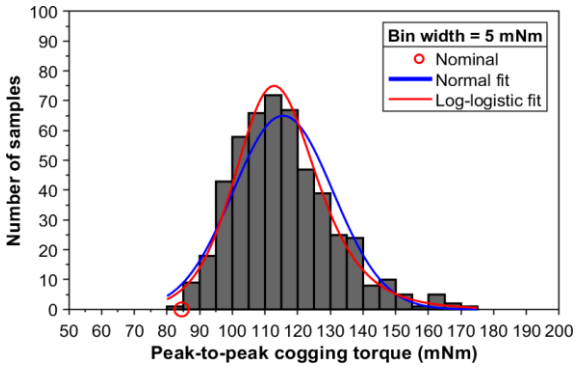
The distributions of number of occurrences of peak-to-peak cogging torque of the 12-slot/8-pole SPM motor is shown in Fig. C.1. The influence of sample size on the distribution of number of occurrences and fitted distributions is low.




(a) 100 motors




(b) 200 motors

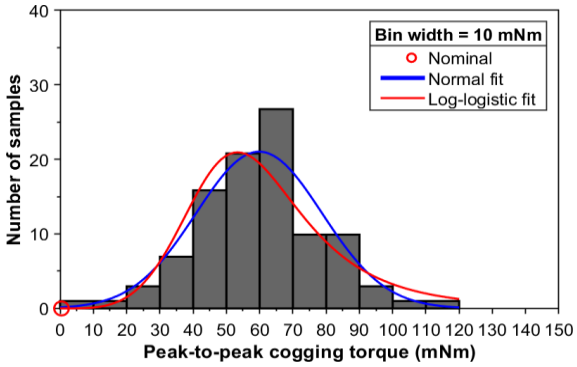



(c) 500 motors

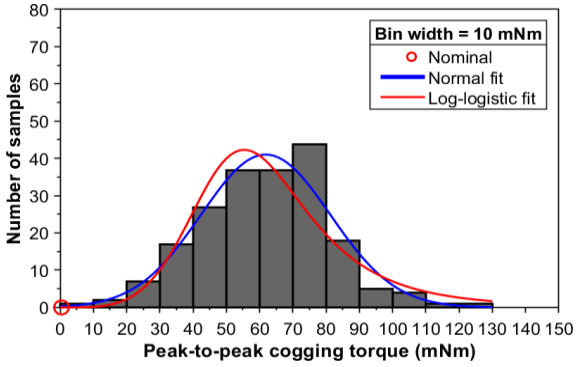
Fig. C.1. Distribution of number of occurrences of peak-to-peak cogging torque of 12-slot/8-pole SPM motor with different sample sizes.

The influence of sample size on the distributions of number of occurrences of the 12-slot/14-pole SPM motor to determine the influence of increase in tolerances attributed to higher pole numbers. Fig. C.2 shows

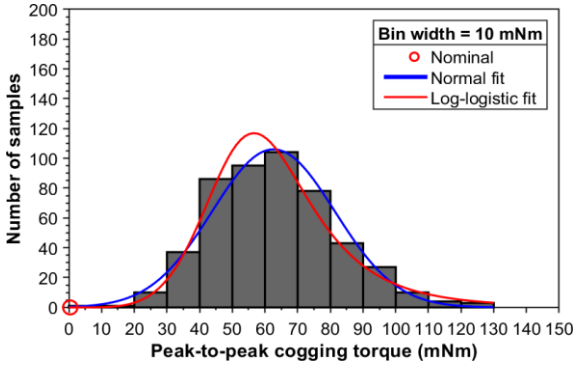
that there is good agreement between the distributions of number of occurrences with different sample sizes and that the difference in properties of the fitted distributions is low. Therefore, a sample size of 100 motors is suitable for analysis of cogging torque uncertainty.




(a) 100 motors




(b) 200 motors




(c) 500 motors

Fig. C.2. Distribution of number of occurrences of peak-to-peak cogging torque of 12-slot/14-pole SPM motor with different sample sizes.